Compression de mélanges liquides et silice par chocs générés par laser jusqu'à des conditions thermodynamiques extrêmes d'intérêt pour les modèles des intérieurs planétaires

Marco Guarguaglini

université PARIS-SACLAY

NNT : 2019SACLX075

Thèse de doctorat

Laser-driven shock compression of liquid mixtures and silica up to extreme thermodynamic conditions of interest for planetary interior models

Thèse de doctorat de l'Université Paris-Saclay
préparée à l'École Polytechnique

Ecole doctorale n°572 Ondes et Matière (EDOM)
Spécialité de doctorat : Physique

Thèse présentée et soutenue à Palaiseau, le 15 novembre 2019, par

MARCO GUARGUAGLINI

Composition du Jury :

Stefan Hüller Directeur de Recherche, École Polytechnique (CPhT)	Président
Sakura Pascarelli Scientific Director, European XFEL	Rapporteure
Thibaut de Rességuier Directeur de Recherche, ISAE-ENSMA (Institut Pprime)	Rapporteur
François Guyot Directeur de Recherche, Muséum National d'Histoire Naturelle (IMPMC)	Examinateur
Paul Loubeyre Directeur de Recherche, CEA (DAM, DIF)	Examinateur
Alessandra Benuzzi-Mounaix Directrice de Recherche, École Polytechnique (LULI)	Directrice de thèse
Alessandra Ravasio Chargée de Recherche, École Polytechnique (LULI)	Directrice de thèse

To the Rt Rev. Abbot Bernardo Gianni, O.S.B.
and all the Brothers of the abbey of
San Miniato al Monte (Florence, Italy)

Acknowledgments

I have conducted this PhD under a financement from the École Polytechnique. *I acknowledge financial support to the research presented in this Thesis from the* Agence Nationale de la Recherche *grant no. ANR-16-CE31-0008 to project POMPEI (principal investigator: Alessandra Ravasio), the* Japanese Society for the Promotion of Science *core-to-core program on International Alliance for Material Science in Extreme States with High Power Laser and XFEL, the* International Joint Research Promotion Program *at the* Osaka University*, and the* European Research Council *Advanced Grant to project "Planetary Diversity: The experimental Terapascal perspective" (principal investigator: Guillaume Fiquet). Complementary trainings necessary for the validation of this PhD have been funded by the* Université Paris–Saclay *and by the* Erasmus+ *program.*

I start the professional part of these Acknowledgments by thanking my supervisors, Alessandra Ravasio and Alessandra Benuzzi-Mounaix, for their guidance throughout this long and challenging journey. I thank Sakura Pascarelli and Thibaut de Rességuier for their useful corrections and suggestions for this Thesis and François Guyot, Stefan Hüller, and Paul Loubeyre for their interesting inputs during the discussion. A warm thank goes to Tommaso Vinci, who taught me a lot about the different aspects of this work, from the use of data analysis and simulation softwares to the preparation and conduction of the experimental campaigns. I also want to thank my teammates Riccardo Bolis and Jean-Alexis Hernandez, not only for their support but also for the many good moments we shared, and Erik Brambrink for his good advices and the always useful discussions. A very special thank to Frédéric Lefevre, for his tireless work on targets and especially for his crucial contribution to the design and testing of cryostatic cells and their filling system.
I thank the many colleagues I have had the pleasure to work with in the context of our national and international collaborations. Between them, Sandra Ninet, Frédéric Datchi, Guillaume Morard, François Guyot, and Guillaume Fiquet (Sorbonne Université, Paris, France), Adrien Denoeud (CEA, France), Raffaella Torchio (ESRF, Grenoble, France), François Soubiran (ENS Lyon, France), Ronald Redmer, Martin French, Mandy Bethkenhagen (Rostock University, Germany), Anja Schuster (HZDR, Dresden, Germany), Norimasa Ozaki, Yohei Fujimoto, Yuhei Umeda (Osaka University, Japan).
Many thanks go to the members of the LULI support teams and to the LULI2000 facil-

ity staff, whose contribution to the preparation of the experiments and to their success has been critical. I would like to thank also the staff of the other facilities I used during my work, GEKKO XII (Osaka, Japan) and SLAC-LCLS (Menlo Park, California, USA). During these three years I also worked as Teaching Assistant. I therefore want to thank my colleagues at the Department of Physics *of the* École Polytechnique*, and in particular Guilhem Gallot and Geraud Chandèze, for their invaluable support I could count on to accomplish my teaching duties.*

On a more personal note, I warmly thank my whole family, and especially my parents, for their continuous support and advice. To all my friends, currently scattered around the world (Pisa, Paris, Bordeaux, Liverpool, Boston, ...): thank you, David, Nour, Riccardo and Marta (and the young Pietro and Costanza!), Francesco, Ludovico, Alison, Stefano, Elisabetta, and all the rest of you, for your support and the great moments we shared. A warm thank to the ArteMusica *choir in Verrières-le-Buisson, who welcomed me as a tenor and with whom I shared many joyful musical moments.*

Contents

Introduction

> When he gave to the sea his decree, that the waters should not pass his commandment: when he appointed the foundations of the earth:
> Then I was by him, as one brought up with him: and I was daily his delight, rejoicing always before him.
>
> PROVERBS 8, 29–30

Wandering stars

LOOKING AT THE celestial vault at night has captivated the curiosity and provoked the reverence of mankind since the ancient times. Early Greek astronomers, after noticing the peculiar path followed by certain objects across the sky, coined the term πλανήτης ἀστέρες: wandering stars, that constitutes the etymology of the word "planet" in many modern languages. As an evidence of the special consideration reserved to planets by many human cultures, we only mention a very well known fact: in many Western languages, the planets visible to the naked eye have been named after Greek–Roman gods: Mercury, Venus, Mars, Jupiter, and Saturn. The outermost planets Uranus and Neptune, discovered in 1781 and 1846, respectively (see Table 0.1 for an essential chronology), have followed the same naming tradition.

The natural and millenary human appeal for planets has been reignited in 1992 – four and a half centuries after the appearance of the *De revolutionibus orbium coelestium* [Kopernikus (1543)] that triggered the Copernican Revolution – by the first confirmed discovery [Wolszczan (1994)] of an extrasolar planet, *i.e.* a planet orbiting around a star other than our Sun. The discovery has been made by means of the radial velocity technique, that consists in detecting small Doppler shifts in the colour signature of the host star due to the movement caused by the gravitational interaction with the planet. This method has remained the principal mean of detecting extrasolar planets (or *exoplanets*) until the launch of the *Kepler* space telescope in 2009 [kepler.nasa.gov]. *Kepler*, which has been active in the discovery of exoplanets until 2018, used a different approach, called transit method, that consists in detecting the drop in the observed brightness of the host star when the planet transits between the star and the observer.

Today, more than four thousand extrasolar planets in more than three thousand different systems have been discovered [exoplanet.eu], opening a whole new, thrilling domain in the context of planetary science. The quest for inhabitable planets is open, as eventually will be that for *inhabited* worlds, giving satisfaction to the philosophical theories of Giordano Bruno, a XVI-century Dominican friar who, in his dialogue *De l'infinito, universo e mondi* [Bruno (1584)], made the character Fracastorio say:

> ...we can think that countless stars host many other moons, many other terrestrial globes, many other worlds similar to this one.

Table 0.1 – Key events in history concerning the philosophical and scientific study of planets.

Year	Event
17$^{\text{th}}$ c. BC	The **Babylonians** observe and note the periodic motion of Venus.
7$^{\text{th}}$ c. BC	The *Venus tablet of Ammisaduqa*, containing recordings of the motion of Venus, is written in **Babylon**.
ca. 260 BC	**Aristarchus of Samos** elaborates a heliocentric theory.
ca. 150	**C. Ptolemy** writes the *Almagest*, canonising the geocentric model.
1543	**N. Copernicus** publishes *De revolutionibus orbium coelestium*, scientifically presenting the heliocentric theory.
1584	**G. Bruno** publishes the philosophical dialogue *De l'infinito, universo e mondi*, containing the theory of the existence of countless inhabited worlds.
1609–19	**J. Kepler** elaborates his three laws of planetary motion.
1632	**G. Galilei** publishes the *Dialogo sopra i due massimi sistemi del mondo*, defending the Copernican theory against the Ptolemaic system.
1687	**I. Newton** formulates the theories of the laws of motion and universal gravitation.
1781	**W. Herschel** discovers Uranus.
1796	**P.-S. de Laplace**, in his *Exposition du système du monde*, proposes the theory that the Solar System has formed from the condensation of a protosolar nebula.
1846	**U. Le Verrier** and **J. C. Adams** discover Neptune.
1961	First fly-by of Venus by the Soviet *Venera 1*.
1965	First fly-by of Mars by NASA's *Mariner 4*.
1970	The Soviet *Venera 7* is the first space probe to land on a planet and transmit data back to Earth.
1973	First fly-by of Jupiter by NASA's *Pioneer 10*.
1986	First fly-by of Uranus by NASA's *Voyager 2*.
1988	First detection of an exoplanet: Gamma Cephei Ab, confirmed in 2002.
1992	First confirmed detection of an exoplanet: PSR B1257+12 B and C.
2018	The NASA's *InSight* robotic lander lands on the surface of Mars.
2019	Today, more than 4000 exoplanets belonging to more than 3000 different systems have been discovered.

The exploration of planets

Studying these "countless worlds" requires in the first place the collection of a data set as wide and complete as possible for each planet. A fairly natural starting point is the investigation of the planet on the surface of which we live, the Earth. On the one hand, we have a direct access to its surface and atmosphere: we can study their

composition, structure, and evolution. On the other hand, a diverse set of methods has been developed to indirectly characterise the interior of our planet, which is not directly accessible. First, the precise measurement of the magnetic and gravitational fields on the surface as well as the observation of the surface and of the ocean floors can be used to infer the structure and activity of the interior; besides, we dispose of samples from the interior brought to the surface by the eruption of volcanoes. Second, the huge amount of available seismic wave data provides fundamental insights about the nature and depth of different layers of the interior [Nolet (2008)]. For instance, the fact that seismographs beyond an angular distance of around 110° from the epicenter of an earthquake do not detect S waves (which are transverse polarisation waves) has been taken as an evidence of the existence of a liquid outer core, in which the propagation of S waves is not possible [Eales (2009)].

The other planets of our Solar System are studied either through distant observation or by sending space probes, either for a flyby, that allows to take data relative to the outer atmosphere, or for landing on the surface in the case of rocky planets. We cite as examples the NASA's *Voyager 2* probe [see Figure 0.1 (left)], that visited all the four giant planets of the Solar System and has been up to now the only probe to flyby Uranus and Neptune, and the Soviet *Venera 7* that has been the first spacecraft to successfully land on the surface of another planet (Venus) and send back to the Earth data about the atmospheric composition, dominated by carbon dioxide, and surface temperature, which is about 750 K [Reeves (1994)].

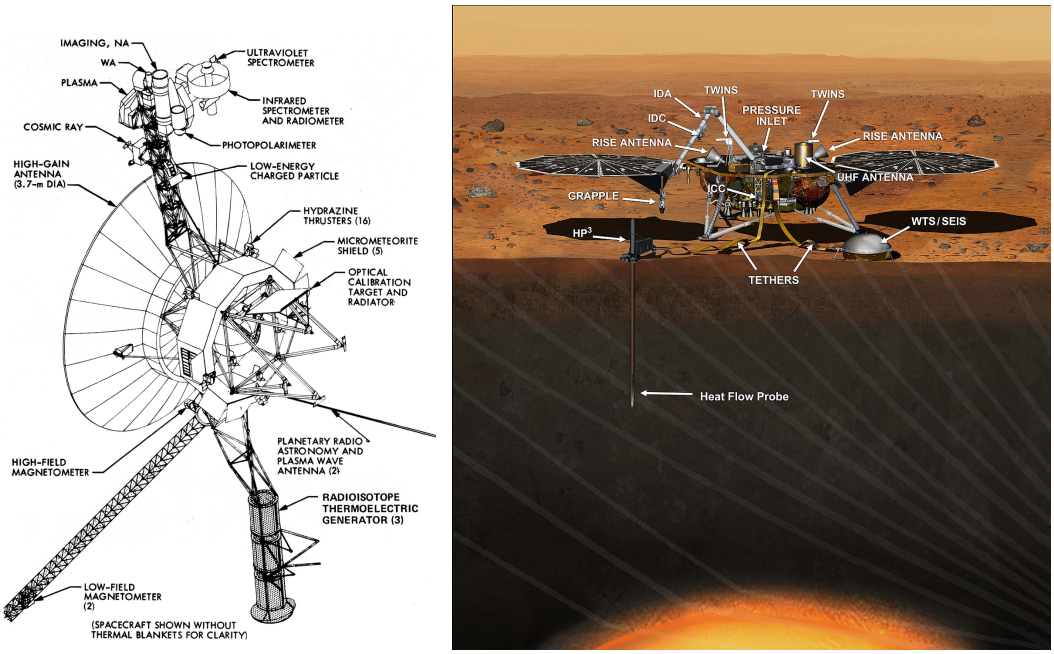

Figure 0.1 – Different generations and types of space probes in comparison. **Left.** Diagram of the *Voyager* spacecrafts highlighting instruments and systems. Of particular interest in our context are the magnetometers and the UV and IR spectrometers. Source: NASA/JPL, Voyager Bulletin, no. 13. **Right.** Artist's concept of *InSight* lander on Mars. To be noticed: the SEIS seismometer, the HP^3 self-penetrating heat flow probe, and the RISE radio antenna that provides measurements of the planetary rotation. Online: `http://photojournal.jpl.nasa.gov/catalog/PIA17358`.

Together, observation and probes allow to collect a diverse set of information about mass, radii, shape, rotational velocity, atmospheric and surface composition, luminosity, gravitational and magnetic fields. However, the interiors of Solar planets remain essentially unexplored: until today, space probes had only access to the atmosphere and surface. The mission *InSight* [mars.nasa.gov/insight], active from 2018, is the first one whose scientific goals are the measurement of the seismic activity and the internal heat flow of Mars, to elaborate models of the deep interiors and study the early geological evolution of the planet [see Figure 0.1 (right)].

Characterising exoplanets is obviously far more challenging. Distant observation allows the measurement of just a few basic data, such as mass, radius, host star type, orbital radius and period. The knowledge of two extensive properties such as mass and radius is however sufficient to estimate a first key intensive parameter: the mean density. This allows a first rough determination of the composition of the exoplanet – in particular, it permits to distinguish hydrogen- and helium-rich planets, "icy" planets mainly composed by water–methane–ammonia mixtures, and rocky planets, in increasing order of mean density. With the parameter of mean density playing a fundamental role, as it is the primary parameter used to determine the planetary composition, Solar planets are employed as paradigms for the classification of exoplanets – identified as super-Earths, mini-Neptunes, hot-Jupiters, etc. If, on the one hand, the visit of rocky Solar planets with space probes progresses uninterruptedly (in particular, visiting Uranus and Neptune is a priority for both NASA and ESA) and programs for the human exploration of Mars become a reality, on the other hand the visit of extrasolar planets by space probes will remain impossible until a very distant future because of the involved distances – the closest star hosting a discovered exoplanet, Proxima Centauri, is 4.2 light years away from the Solar System [Anglada-Escudé et al. (2016)].

Models and open questions

The data collected by distant observation and space probes serve as essential constraints for planetary models, which should describe the formation, evolution, and current structure of planets within a unified framework. Within this context, a key aspect is the modelling of planetary interiors, which is essential to provide fundamental answers about how the planets have evolved, why their surface have their current structure, how the planetary magnetic fields have been formed and are currently sustained, and more.

Notwithstanding the fact that planetary interior models can be extremely elaborated, they are all based upon a same basic set of ingredients. The first, that constitutes one of the criteria of the International Astronomical Union for determining if a celestial object can be classified as a planet [IAU (2006)], is the assumption of hydrostatic equilibrium: the gravitational force towards the center is balanced by a pressure-gradient force, so that the pressure increases when approaching the center of the planet. The second key ingredient is the *equation of state* of the components of the interior, that is, a relation between density, pressure, and temperature providing one of the state variables as a function of the other two. Finally, independent information is needed about the temperature interior profile, that requires the study of the heat flow from the internal layers towards the surface of the planet. The heat sources

can be radioactive materials or have a primordial origin, as the planet gradually cools down from its initial conditions. Heat is transported via conduction, convection, or radiation mechanisms depending on the properties of the different layers, which should be characterised. Additionally, interior models should provide an explanation of the origin and sustaining mechanism of planetary magnetic fields. According to the widely accepted dynamo theory, rotation and convection of electrically conducting materials in the interior generate a magnetic field that sustains their motion in a feedback process. A rough criterion for determining if a dynamo can be sustained inside a planet is determining if magnetic induction dominates over diffusion. This requires the precise knowledge of the electrical conductivity of the components of the dynamo-active layers at the relevant thermodynamic conditions as well as the length and velocity scales of the motion of the conductive layers.

Hereafter we summarise the currently accepted models of the planets of our Solar System and of similar exoplanets, highlighting the open questions that need to be solved.

Rocky planets

The four inner planets of our Solar System – Mercury, Venus, Earth, and Mars – are called rocky (or terrestrial) planets. They are limited in size in comparison to the four outer planets and exhibit higher densities. They possess only a few satellites and no ring systems. Rocky planets have solid surfaces, characterised by geological features such such as craters and mountains. Their mantles are primarily composed by magnesium oxide – iron oxide – silica (MgO–FeO–SiO_2) systems, while their cores are made of iron (Fe) and possibly nickel (Ni).

Throughout their history, rocky planets underwent differentiation and gravitational separation. These processes have been primarily controlled by the melting curve of their major components [Millot et al. (2015)]. Also the locations of core-mantle boundaries (CMB) are primarily determined by the melting curves [Stixrude (2014)]. Finally, melting is critical in giant impacts scenarios, since such impacts caused the formation of a magma ocean whose consequent freezing and re-solidification may have driven the planet's thermal history.

The four rocky planets exhibit diverse scenarios concerning the presence and structure of magnetic fields. Mercury's magnetic field is probably sustained by a dynamo. Venus has a very low magnetic field, without an active dynamo and without proof that a dynamo has been sustained throughout its history. Our Earth has a mostly dipolar and slightly tilted magnetic field, that represents one of the key factor that permitted the development of life on its surface, as it screened it from harmful Solar radiation. The Earth's magnetic field is currently sustained by a dynamo, active in the liquid iron-rich outer core. Finally, Mars exhibits a strong remnant field, formerly sustained by a dynamo. The understanding of the dynamo process inside rocky planets requires the thorough characterisation of the equation of state, transport properties, and electrical conductivity of warm dense iron. Additionally, studying the conductivity of silicates at conditions typical of super-Earths' interiors is crucial to understand if they are capable of sustaining a planetary dynamo inside these planets, where convecting magma oceans are expected to exist [Stanley and Glatzmaier (2010); Soubiran and Militzer (2018)].

It should be noticed that many discovered exoplanets are rocky planets. Obviously, the discovery of new exoplanets of this type is particularly exciting in the context of the quest for habitable planets.

Gas giants

The four outer Solar planets – Jupiter, Saturn, Uranus, and Neptune – are called giant planets since their size is far greater than the inner planets. In particular, Jupiter and Saturn are called gas giants as they are primarily composed by hydrogen (H) and helium (He), together with heavier elements (mainly water and ammonia in their atmospheres). The term gas giant can be misleading, as it describes the composition rather than the phase present inside those planets. Indeed, because of the high pressures and temperatures, hydrogen is supposed to be present in the molecular phase in their outer layers and in a liquid metallic phase in their deep interiors. The gas giants probably possess cores composed by molten rocks and high-pressure ices, although their masses and compositions are still debated. Proposed interior models of Jupiter and Saturn are shown in Figure 0.2.

Both Jupiter and Saturn exhibit magnetic fields generated by active dynamos. The dynamo-active region of Jupiter is extended up to outer layers, whereas in Saturn it is located in the deep interiors. Both magnetic fields are mainly dipolar, but the Jupiter's one is tilted with respect to the spin axis whereas the Saturn's one is axisymmetric.

One of the key open questions to be solved in order to drastically improve models of giant planets concerns the identification of the thermodynamic conditions at which the phase separation of helium from hydrogen takes place. Such phase separation would give birth to an inhomogeneous region in which helium droplets form and fall down to deeper planetary layers due to gravity [Guillot (2005)].

Icy giants

The two outermost planets of the Solar System, Uranus and Neptune, are called icy giant planets as they exhibit intermediate densities between terrestrial planets and gas giants. As in the case of the latter, the term ice is relative to the composition rather than a phase. According to current models, the icy giants' atmospheres are primarily composed by hydrogen and helium whereas their deep interiors are assumed to be composed by mixtures of water, methane, and ammonia (the planetary ices) at high-pressure phases. The existence and precise composition of a rocky core remain elusive since it has a small influence on the observable parameters. Tentative interior profiles of Uranus and Neptune are shown in Figure 0.2.

Despite their similar structures, Uranus and Neptune exhibit different luminosities. While the Neptune's value suggests an internal heat source, Uranus' low luminosity indicates that it is presently in thermal equilibrium with the radiation received from the Sun. The Uranus' low luminosity has questioned the validity of the general assumption that the planetary interior profiles are adiabatic. A non-adiabatic model including a thermal boundary layer (TBL) has been developed by Nettelmann et al. (2016) to fit the low luminosity value of Uranus. This model predicts temperatures 2 to 3 times warmer than adiabatic models [Redmer et al. (2011); Bethkenhagen et al. (2017)] in

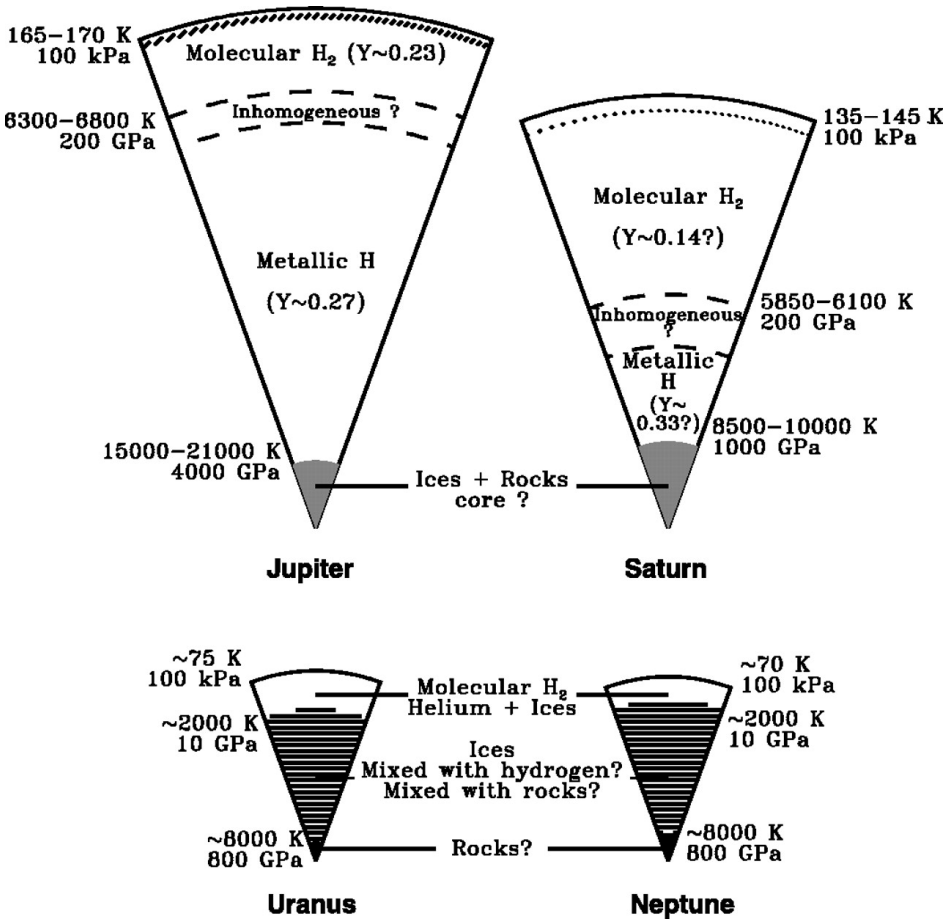

Figure 0.2 – Interior models of the four giant planets of the Solar System. The hashed region indicates a possible radiative zone (a zone in which heat is transported towards the exterior mainly via radiation). Helium mass mixing ratios (Y) are indicated. The size of the central rock and ice cores of Jupiter and Saturn is very uncertain; the actual structures of Uranus and Neptune may be significantly different from the models shown. From Guillot (1999), who adapted and updated it from Stevenson (1982).

the deep interior of the planet. As a consequence, there is a great uncertainty about the interior profile of Uranus.

The magnetic fields of the two icy giants, measured by the *Voyager 2* space probe [Ness et al. (1986); Ness et al. (1989)], are highly non-dipolar and non-axisymmetric, unlike those of the majority of planets, including the Earth. These strange features can be explained if we assume that the magnetic fields originate in a thin dynamo-active outer shell [Stanley and Bloxham (2004); Nellis (2015)].

Several discovered exoplanets have been classified as icy giants because of their similarity with Uranus and Neptune. Such exoplanets are included in the categories of mini-Neptunes (planets less massive than Neptune but with a similar, thick envelope made of H, He, and ices) and hot Neptunes (with a similar size to Neptune's, but orbiting closer to their stars).

Characterising matter at planetary interior conditions

Improving planetary models and solving the outstanding questions we have presented requires a thorough investigation of the physics of planetary interiors. In particular, we have seen that the properties of crucial importance are the equation of state, the heat transport properties, and the electrical conductivity of the components of the interiors. Those materials experience extreme thermodynamic conditions: pressures of several megabar (1 Mbar = 100 GPa) and temperatures of a few thousand Kelvin. Such conditions belong to a regime called "Warm Dense Matter" (WDM), which is at the interface between the well-established condensed matter and plasma domains (ad depicted in Figure 0.3) and particularly challenging to characterise. This constitutes an additional reason to study these states, as the frontiers of the region of the phase diagram in which the behaviour of matter is well described by theories shall be broadened.

As we have already pointed out, the interiors of planets other than the Earth are difficult, if not impossible, to access, with the partial and recent exception of Mars. Therefore, the characterisation of planetary interiors must be achieved by models using reliable inputs on the behaviour of matter at extreme conditions. Within this context, computer simulations provide a crucial contribution, as they can be used to predict the behaviour of matter at extreme conditions. However, this approach is quite challenging, due to the elusive theoretical description of the WDM regime. Indeed, WDM is partially or highly coupled (the electrical potential between charged particles is of the same magnitude or dominates over thermal energy) and partially degenerate (the quantum wavefunctions of atoms partially overlap). It also displays a complex physical-chemical behaviour as distinct states of ions, atoms, molecules, clusters, and lattices often coexist. The absence of a theory satisfactorily describing the WDM regime requires an approach based only on the first principles of quantum mechanics: *ab initio* calculations. Within this framework, a quantum treatment of electrons is done using density functional theory, while the motion of ions is simulated via classical molecular dynamics [French et al. (2012)]. However, this kind of simulations suffer from long computation times and their results need in any case an experimental validation.

The basic challenges of any experimental approach are the generation of WDM states in the laboratory and their characterisation. The extreme conditions of interest can be achieved via static and dynamic methods. Figure 0.4 shows three of such methods. Static methods, typically using Diamond Anvil Cells (DAC) allow precise measurements but are limited in pressure and temperature. Dynamic methods are based on the propagation of compression waves (which can be generated with different methods: explosion, magnetic pinch, gas-gun, high-power laser ablation) and permit to explore higher pressures and temperatures compared to static methods. Dynamic methods allow the generation of the desired states for very short times (from the microsecond to the nanosecond scale), which may complicate their characterisation and require in any case ultrafast diagnostics. In the context of dynamic methods, the simplest possible approach is single-shock compression of a material starting from ambient conditions. This method allows to explore a locus of thermodynamic states called principal Hugoniot curve [Hugoniot (1887)]. The loading of a shock wave is a highly

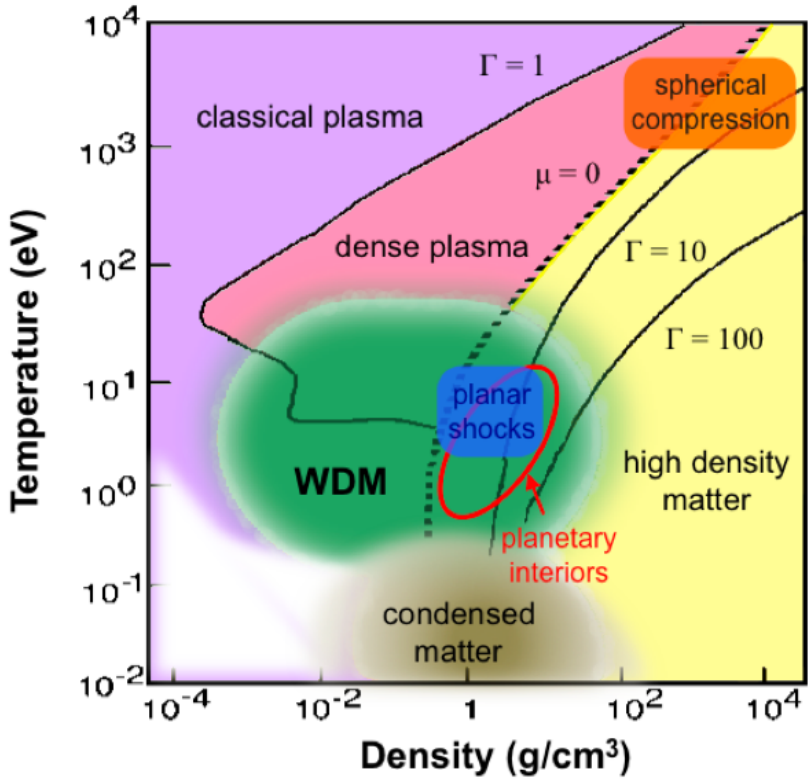

Figure 0.3 – Phase diagram of aluminum (a standard material for the study of WDM) in the temperature – density plane. Temperature is expressed in elettronvolt: 1 eV $\simeq$ 11605 K. Warm Dense Matter conditions correspond to the green area. The WDM domain is at the interface between the condensed matter (brown area on the bottom), plasma (violet area on the left top), and high density matter (yellow area on the right) domains. The black solid curves are iso-Γ curves (Γ, the plasma coupling, is the ratio between the Coulomb and thermal energy). The black dashed curve, which indicates the condition $\mu = 0$, where μ is the chemical potential (or, equivalently, $T = T_F$, where T_F is the Fermi temperature), separates quantum degenerate states (on the right) from classical states (on the left). From Lee et al. (2004).

entropic phenomenon: this means that a huge fraction of the shock wave energy is employed in heating, instead than compressing, the sample. For this reason, single-shock loading permits to study high temperature conditions. Such conditions are much higher than those generally encountered in planetary interiors, but interesting for the study of early planetary histories, the interiors giant and hot exoplanets, and planetary impacts with giant astronomical objects. Those high-pressure / high-temperature conditions are also of primary interest for the characterisation of the WDM regime and as a benchmark of *ab initio* simulations. However, the generation and characterisation of moderate-temperature states remains essential to directly probe planetary interiors' conditions and to extend the frontiers of the charted region of the phase diagram of WDM. To achieve lower temperature conditions, the main strategy consists in increasing the density of the sample prior to shock loading, in order to decrease the entropy jump associated to the propagation of the shock wave. This can be done statically (using a DAC) or dynamically (*e.g.* with the propagation a weak shock wave prior to

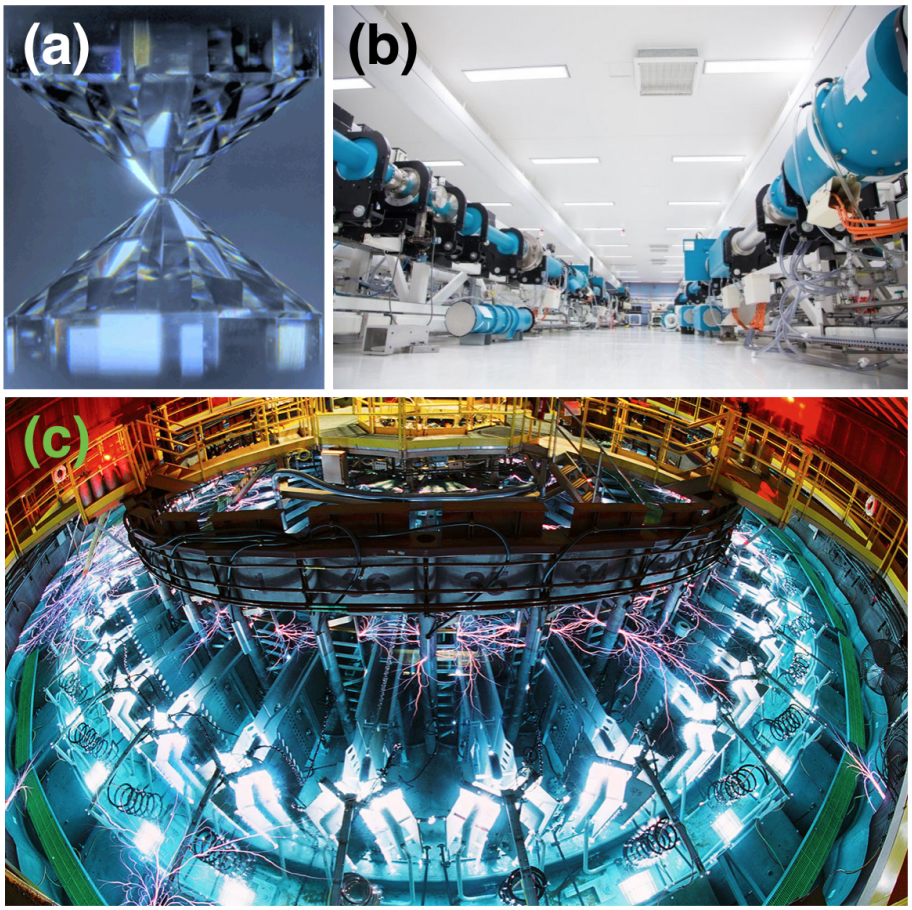

Figure 0.4 – Different compression methods to achieve Warm Dense Matter conditions. **(a).** Detail of a Diamond Anvil Cell (source: www.spring8.or.jp). **(b).** High-power laser ablation: the LULI2000 laser hall (Palaiseau, France – source: www.polytechnique.edu). **(c).** Magnetic pinch: the Sandia Z machine (Albuquerque, New Mexico, USA – source: www.sciencemag.org).

the main shock). On the one hand, coupling DAC and shock compression is challenging, mainly because of the difficult optical access to the target and of the important thickness of the anvil, which complicates the propagation of the shock wave; on the other hand, also the propagation of two shocks is challenging as it requires considerable simulation efforts to carefully shape the laser pulse profiles and a complicated analysis to determine the double-shocked state from the observables. The combination of the described static and dynamic methods, including pre-compression strategies, allows to span a wide region of the phase diagram encompassing diverse phases and conditions.

State of the art

In this Thesis, we have performed an extensive work to characterise high pressure equations of state, optical and electrical properties of materials of interest for planetary science. Here we present a general state of the art of the key interior components. The efforts in pursuing such research testify the importance of furnishing reliable inputs

on the components' properties, via simulations and experiments, in order to improve planetary models.

MgO–FeO–SiO_2 systems

Magnesium oxide – iron oxide – silica (MgO–FeO–SiO_2) systems are the major components of the mantles of rocky planets and are also probably present inside the cores of giant planets.

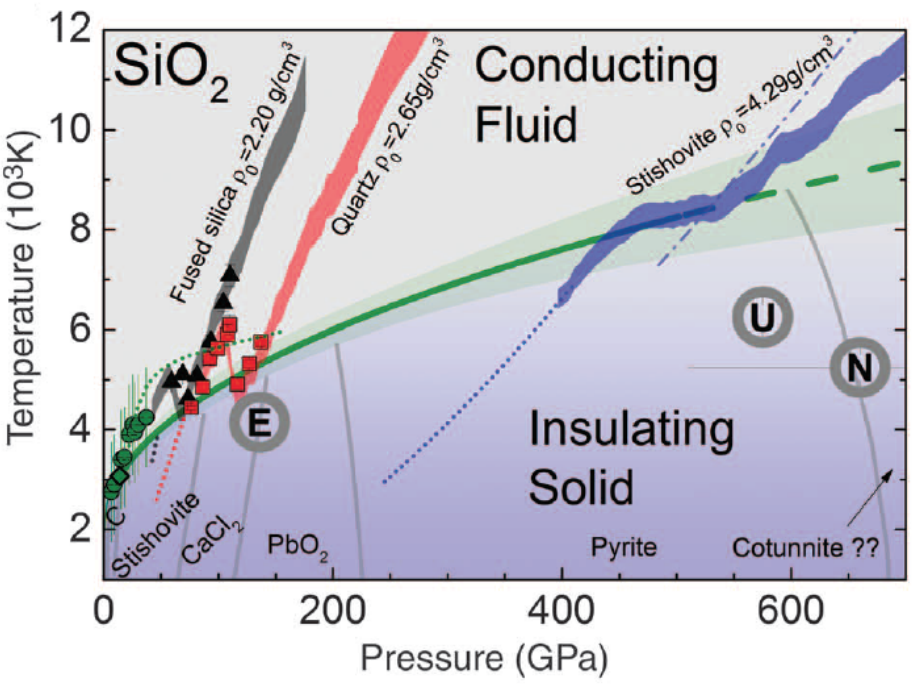

Figure 0.5 – Phase diagram of silica, displaying low-pressure phases (stishovite, $CaCl_2$, PbO_2) and the phase transition between insulating solid and conducting fluid (green curve). The principal Hugoniot curves starting from three different initial phases – fused silica (grey curve), α-quartz (red curve), and stishovite (blue curve) – are shown. Adapted from Millot et al. (2015).

Silica. The silica (SiO_2) end-member is not only interesting for planetary science but also a valid case study for the behaviour of matter at WDM conditions [Denoeud et al. (2016a)] and a standard material for shock compression, especially in the form of α-quartz [Barrios et al. (2010); Brygoo et al. (2015); Sekine et al. (2016)]. Its equation of state, phase diagram, and optical-electrical properties have been extensively characterised on a wide set of thermodynamic conditions by *ab initio* simulations [Laudernet et al. (2004); Mazevet et al. (2015); Qi et al. (2015); Denoeud et al. (2016a); Scipioni et al. (2017); Soubiran and Militzer (2018)]. Recent works by Mazevet et al. (2015) and Scipioni et al. (2017) predict a non-monotonic dependence on pressure of the conductivity of silica for temperatures below $20 \cdot 10^3$ K, as a consequence of a charge-ordering breaking mechanism. The prediction of such non-monotonic dependence, which may have an important role in the magnetic field generation in early Earth and super-Earth planets, needed an experimental validation at the beginning of this Thesis. On

the experimental point of view, the equation of state and optical properties along the principal Hugoniot associated to different initial phases (fused silica, α-quartz, and stishovite) have been extensively studied up to very high pressures (around 20 Mbar) using different compression methods such as gas-guns and high-power lasers [Lyzenga and Ahrens (1980); Lyzenga et al. (1983); Boslough (1988); Trunin (2001); Luo et al. (2004); Hicks et al. (2005); Hicks et al. (2006); Knudson and Desjarlais (2009); Millot et al. (2015)]. Figure 0.5 shows the phase diagram of silica, highlighting the Hugoniot curves starting from the different low-pressure phases. However, the experimental studies of silica are not limited to the Hugoniot curves. Indeed, the α-quartz adiabatic release [Knudson and Desjarlais (2013); Desjarlais et al. (2017)], the sound velocity of silica [McCoy et al. (2016)], and the effect of static pre-compression on α-quartz properties [Brygoo et al. (2015)] have been characterised, providing essential insights to widen our understanding of this material off the Hugoniot conditions. A XANES (X-ray Absorption Near-Edge Spectroscopy) study by Denoeud et al. (2016a) could characterise the structural properties of silica off the α-quartz Hugoniot using shock reverberation (for higher densities) and release (for lower densities).

Magnesium oxide. The equation of state and phase diagram of the magnesium oxide (MgO) end-member of the components of the mantles of rocky planets have been extensively studied by *ab initio* simulations [Cebulla and Redmer (2014); Root et al. (2015); Miyanishi et al. (2015); Soubiran and Militzer (2018); Musella et al. (2019)] and shock-compression experiments [McWilliams et al. (2012); Coppari et al. (2013); Root et al. (2015); Bolis et al. (2016)]. Whether some phase transitions, such as the solid-solid B1-B2 transition and melting, occur in a dynamic-compression context and at which conditions of pressure and temperature is still questioned.

Magnesium oxide – silica systems. MgO–SiO_2 systems, such as $MgSiO_3$ and Mg_2SiO_4, in both their glass and crystalline (enstatite, forsterite) forms, have been the object of several simulation studies [Boates and Bonev (2013); Militzer (2013); Soubiran and Militzer (2018)] but are still far from being satisfactorily characterised in the laboratory [Spaulding et al. (2012); Coppari et al. (2013); Sekine et al. (2016); Bolis et al. (2016)], especially at high pressures above 2 Mbar, and debates about the occurrence of different phase transitions along their Hugoniot curves are currently ongoing. Moreover, alloys including both Fe and Mg essentially still need to be characterised.

Iron and nickel

Iron is the main component of the core of rocky planets, where also nickel is believed to be present. Moreover, it is of crucial important for the modelling of iron planets – a proposed type of exoplanet in which the mantle is not present or is very thin compared to the iron-rich core [Seager et al. (2007)].

The equation of state and phase diagram of iron have been quite extensively characterised by *ab initio* calculations [Alfè et al. (2002); Sun et al. (2018)] and experimental studies including static compression [Williams et al. (1987); Boehler (1993); Anzellini et al. (2013); Aquilanti et al. (2015)] and shock compression methods [Brown and McQueen (1986); Yoo et al. (1993); Nguyen and Holmes (2004); Huser et al. (2005)], that

have recently included X-ray diagnostics such as absorption spectroscopy [Harmand et al. (2015)] and diffraction [Denoeud et al. (2016b)]. The precise determination of the melting curve of iron is crucial for the modelling of the core of rocky planets, which has a major impact on various processes such as the global heat flux, convection, and dynamo action. In particular, the knowledge of the iron melting curve is necessary to determine the conditions of the inner core boundary (ICB) inside the Earth and to understand in which percentage iron is present in its solid and liquid phase in super-Earths' interiors – which is essential to model their magnetic fields. The identification of the boundaries between the different solid phases (bcc at low pressures and temperatures, fcc at higher temperatures, hcp at high pressures) is also important for structural models of the cores. Transport properties and electrical conductivity in the liquid phase of iron are in their turn essential for the modelling of planetary dynamos.

As iron is present together with nickel in the cores of rocky planets, the study of pure nickel and of iron-nickel alloys is also necessary to achieve more precise and consistent models [McQueen and Marsh (1966); Jarmakani et al. (2008)].

Hydrogen and helium

Hydrogen and helium are the two most abundant elements in the Universe and the main components of the interiors of gas giants and of the atmospheres of icy giants. They are also present in the interiors of the latter together with planetary ices.

Hydrogen. Hydrogen has been studied at planetary interiors conditions via *ab initio* simulations and experiments [Nellis et al. (1999); Fortov et al. (2003); Zaghoo and Silvera (2017)], which also studied the deuterium isotope [Celliers et al. (2018)]. With the increase of pressure and temperature, hydrogen undergoes a transition from a molecular state to a fluid, metallic-like state [Zaghoo and Silvera (2017); Loubeyre et al. (2019)]. Experiments show that this transition takes place at thermodynamic conditions close to those of the envelope-mantle boundary in icy giant planets, so that conducting hydrogen may have a predominant role in the generation of magnetic fields in a thin dynamo-active layer [Nellis (2017)]. The precise determination of the conductivity dependence on pressure and temperature is also necessary to understand the boundaries of the dynamo-active region inside gas giant planets.

Helium. Helium has also been characterised by *ab initio* studies [Kietzmann et al. (2007); Soubiran et al. (2012)] and experiments [Nellis et al. (1984); Eggert et al. (2008); Celliers et al. (2010)]. The precise determination of the insulator-to-conductor transition is crucial to improve dynamo models for the gas giants. A key question concerns the phase separation of helium from hydrogen, which has a huge impact on the structural models of Jupiter and Saturn [Guillot (2005)].

Ices

Planetary ices consist in mixtures of water, methane, and ammonia. They represent the major components of the deep interiors of icy giant planets but are also present in the atmospheres of gas giants. These components have been studied in both their

pure and mixed form via calculations and experiments. However, they are the less characterised by experimental means between the key planetary components. Except for pure water, no data obtained with laser-driven shock compression are available and the reached pressures and temperatures reached are limited.

Water. The equation of state [French et al. (2009); Knudson et al. (2012); Kimura et al. (2015)] and optical-electrical properties [Celliers et al. (2004); French and Redmer (2011); Batani et al. (2015); Jakubowska et al. (2019)], including conductivity, of pure water at WDM conditions have been extensively characterised up to pressures of several megabar, both through simulations and experiments. The latter have employed different compression methods: single-shock loading starting from ambient conditions [Mitchell and Nellis (1982); Lyzenga et al. (1982); Celliers et al. (2004); Knudson et al. (2012); Henry (2003); Kimura et al. (2015)], single-shock loading from statically pre-compressed conditions [Henry (2003); Kimura et al. (2015); Millot et al. (2018) and multiple shock loading [Mitchell and Nellis (1982); Knudson et al. (2012)]. Nevertheless, the water phase diagram at the icy giants interiors conditions remains unclear, given that an exotic superionic phase – in which oxygen atoms are arranged in a lattice but protons are highly diffusive – has been identified since the pioneering work of Cavazzoni et al. (1999) but has been experimentally probed only by Millot et al. (2018, 2019).

Methane. The other fundamental components of planetary ices – methane, ammonia, and their mixtures, such as the "synthetic Uranus" prepared by Nellis et al. (1997) – have been scarcely studied, up to pressures which are too low to be of planetary interest. Hugoniot curves of statically pre-compressed liquid methane starting from different densities have been obtained via *ab initio* calculations by Sherman et al. (2012). Experimental studies are limited to low pressures [Nellis et al. (2001)], so that there is the need of high-pressure experimental data to verify the simulations.

Ammonia. Ammonia has been studied by several *ab initio* simulation works [Cavazzoni et al. (1999); Ojwang et al. (2012); Bethkenhagen et al. (2013); Li et al. (2013, 2017)]. As in water, a superionic phase has been identified, in which the nitrogen atoms are arranged in a lattice whereas protons are free to diffuse. Experimental studies involve DACs [Ninet and Datchi (2008); Li et al. (2009); Ninet et al. (2012)] and dynamic compression [Kovel (1973); Dick (1981); Mitchell and Nellis (1982); Nellis et al. (1988); Radousky et al. (1990); Nellis et al. (1997)]. The superionic phase has been observed for the first time by Ninet et al. (2012) via Raman spectroscopy and X-ray diffraction (XRD). Dynamic compression studies are limited to pressures of 0.7 Mbar (see Figure 0.6). The only available data concern the equation of state Hugoniot curve. Neither temperature – except two data points at 48 and 61 GPa from Radousky et al. (1990) – nor shock-front reflectivity data are provided. Experimental studies of ammonia are complicated by the chemical aggressiveness of ammonia, which limits the choice of materials for the target cells.

Mixtures. The few experimental studies on icy mixtures of water, alcohol, and ammonia have primarily characterised their equation of state and electrical conductivity,

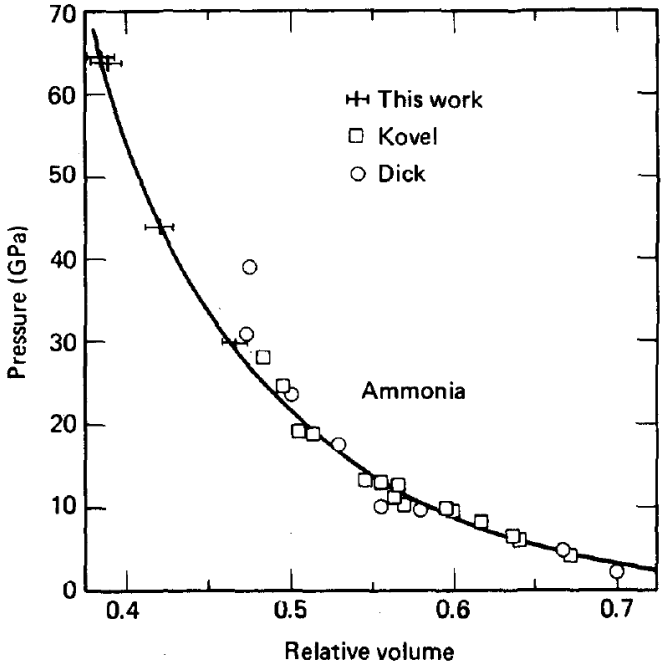

Figure 0.6 – Shock-compression studies of pure liquid ammonia in the pressure – relative volume (V/V_0) plane. Before this Thesis, the explored conditions were limited to pressures of 0.7 Mbar. From Mitchell and Nellis (1982).

using single-shock compression – thus exploring thermodynamic conditions along the principal Hugoniot curve [Radousky et al. (1990); Nellis et al. (1997); Chau et al. (2011)], or double-shock compression, which allowed to probe lower temperatures [Nellis et al. (1997); Chau et al. (2011)]. However, the existing experimental data are limited in pressure and almost completely miss reflectivity and temperature measurements. This represents a major hindrance for the understanding of the thermal history of the icy giants and of the role of icy mixtures in the generation of planetary magnetic fields. A considerable effort is thus necessary for the characterisation of these mixtures at conditions more similar to those typical of planetary interiors (high pressures, moderate temperatures) and for the measurement of temperature and reflectivity. Another critical aspect is the individuation of the boundaries of the superionic phase for such mixtures.

Objectives and challenges of this study

This research has two main scientific objectives, which we present here below.

(i) Since the icy giant planets of our Solar system – Uranus and Neptune – are still far from being described by reliable models, and given the high fraction of discovered exoplanets which exhibit mass and size similar to our icy giants [Fressin et al. (2013)], we aim at furnishing more essential data about the components of their deep interiors: water, methane, and ammonia, in both their pure and mixed form. First, we want to characterise the equation of state and optical properties of these components along their principal Hugoniot curves, as there is a lack of data even

at such conditions. Our data will be primarily interesting for benchmarking *ab initio* simulations. Moreover, we want to start characterising the icy mixtures at off-Hugoniot conditions, reaching states more similar to those expected in icy giants' interiors.

(ii) We want to extend the study of silica – a key component of the interiors of rocky planets – to thermodynamic conditions up to now unexplored. A considerable effort will be made in going beyond simplistic models to estimate the electrical conductivity of warm dense silica (which is essential to model the generation of magnetic fields via a dynamo action) from the measurements of equation of state and optical properties.

The objective (i) faces a challenge involving the conception and realisation of target cells suitable for the laser-driven shock compression of liquid samples, including highly corrosive liquid ammonia. Both objectives demand to develop and apply, in addition to the single-shock compression technique, static and dynamic pre-compression methods with the aim of exploring a range of thermodynamic conditions as wide as possible. This in necessary in order to probe the interiors of a vast and diverse collection of Solar and extrasolar planets. In particular, with this aim, we developed a method which allows to directly probe the thermodynamic state and optical properties of a double-shocked sample.

Thesis plan

This Thesis is divided into three Parts. **Part I** (including Chapters 1–3) treats the generalities of the domain of planetary science in the laboratory. **Part II** (including Chapters 4–5 and a Discussion) describes the experimental work done on several components of icy giant planets (pure water, a synthetic planetary mixture of water, ethanol, and ammonia, and pure liquid ammonia). **Part III** (including Chapter 6 and a Discussion) displays the work done to characterise relevant properties of the components of rocky planets (silica and silicate minerals).

- **Part I: Planetary science in the laboratory**
  - **Chapter 1** presents the domain of planetary science and the scientific interest of the study of planetary interiors. Our current knowledge about rocky and icy giant planets is discussed, outlining its limits and the questions that are still open.
  - **Chapter 2** is devoted to the description of the Warm Dense Matter regime and of the methods used to generate, diagnose, and simulate it. A particular attention is given to the experimental method of laser-driven shock compression.
  - **Chapter 3** treats the compression method beyond single-shock loading with the aim of probing a wider region of the phase diagram. First, it describes the coupling between Diamon Anvil Cells and shock loading to statically pre-compress samples. Then, it introduces a novel method to characterise dynamically pre-compressed materials.

- **Part II: Experimental study of components of icy giant planets**
  - **Chapter 4** presents the state of the art of the characterisation of pure water and of planetary mixtures relevant for the icy giants. It then describes the experimental study of the equation of state and optical-electrical properties of pure water and of a synthetic planetary mixture (SPM) along their principal Hugoniot curves and their statically and dynamically pre-compressed Hugoniot curves.
  - **Chapter 5** treats the experimental study of pure liquid ammonia, after describing its state of the art. It shows the conception, assembly, and filling of target cells with liquid ammonia. It then provides the equation of state and optical reflectivity results along the liquid ammonia principal Hugoniot and statically pre-compressed Hugoniot curves.
  - A **General discussion** presents the consequences for planetary science and the study of WDM of the work described in this Part.
- **Part III: Experimental study of components of rocky planets**
  - **Chapter 6** is devoted to the study of the electrical conductivity behaviour of dynamically pre-compressed warm dense silica.
  - A **General discussion** presents the consequences for planetary science and the study of WDM of the work described in this Part.

In the **Conclusions and perspectives**, we will sum up the main technical and scientific advancements of the work described in this Thesis and propose some possible axes of future work. After the complete **Bibliography**, we will list in the **Outreach** the publications and presentations concerning the scientific work described in this Thesis. Finally, a **List of acronyms** will be provided.

Part I:

Planetary science in the laboratory

> Canst thou bind the sweet influences of Pleiades,
> or loose the bands of Orion?
> Canst thou bring forth Mazzaroth in his season?
> or canst thou guide Arcturus with his sons?
> Knowest thou the ordinances of heaven?
> canst thou set the dominion thereof in the earth?
>
> Job 38, 31–33

Chapter 1

Outstanding questions in planetary science

In this Chapter we will motivate the scientific goals of the experimental work presented in this Thesis. First, we will introduce the context of planetary science. We will then present the foundations of the models describing the interior structure of planets, the generation of planetary magnetic fields, and the evolution of planets. We will highlight the necessity of characterising the behaviour of the components of their interiors at the relevant thermodynamic conditions, which is the subject of this Thesis. We will then overview the measurable planetary parameters for our Earth, the other Solar planets, and the exoplanets, explaining how they can be used to constrain planetary models. Finally, the current knowledge of terrestrial and icy giant planets (whose interior components are the object of this study) will be discussed, with particular attention to the limits and outstanding questions.

Contents

1.1 Context

Our Earth is part of a system of objects orbiting around their host star, the Sun, to which they are gravitationally bound – the *Solar System*. This System, an artistic depiction of which is shown in Figure 1.1, features a remarkably diverse set of components, from very low-mass and low-size objects such as dust clouds, comets, and asteroids (organised in belts) to the most massive objects: *planets*. Precisely encasing all the different celestial objects in proper definitions has proved to be a rather difficult task. In particular, in the last decades there has been much debate about the definition of a planet, and whether this category should include mid-sized objects located in the peripheral region of the System. With the aim of solving this dispute, the *International Astronomical Union* [IAU (2006)] has proposed this set of definitions (my emphasis):

> The IAU [...] resolves that planets and other bodies, except satellites, in our Solar System be defined into three distinct categories in the following way:
>
> 1. A planet is a celestial body that
>   (a) is in orbit around the Sun,
>   (b) has sufficient mass for its self-gravity to overcome rigid body forces so that it assumes a hydrostatic equilibrium (nearly round) shape, and
>   (c) has cleared the neighbourhood around its orbit.
> 2. A "dwarf planet" is a celestial body that
>   (a) is in orbit around the Sun,
>   (b) has sufficient mass for its self-gravity to overcome rigid body forces so that it assumes a hydrostatic equilibrium (nearly round) shape,
>   (c) has *not* cleared the neighbourhood around its orbit, and
>   (d) is not a satellite.
> 3. All other objects, except satellites, orbiting the Sun shall be referred to collectively as "Small Solar System Bodies".

The definition (1) of a planet only applies to eight celestial bodies: Mercury, Venus, the Earth, Mars, Jupiter, Saturn, Uranus, and Neptune. Five mid-sized objects (Ceres, Pluto, Eris, Makemake, and Haumea) are not included in the definition (1) but are considered *dwarf planets* according to definition (2). Definition (1) also requires that the object orbits around the Sun to be defined a planet. However, according to our current knowledge of the observable Universe, the Solar System is not an exceptional keystone in its architecture. Instead, planetary systems appear to be very common: at least one planet per host star is predicted to exist in our galaxy, the Milky Way [Cassan et al. (2012)]. These objects are called *extrasolar planets* (or *exoplanets*).

In this Chapter, when presenting Solar planetary data, we will consider the eight planets according to the definition (1) for the sake of simplicity. However, independently from the global validity of this definition, in the context of this Thesis we will refer to planets, dwarf planets, and extrasolar planets as simply planets. Indeed, the birth, evolution, and structure of these objects can be described within a unified framework by the same planetary models. All of such models are built upon some basic assumptions, such that of *hydrostatic equilibrium* in the planetary interiors, and on our

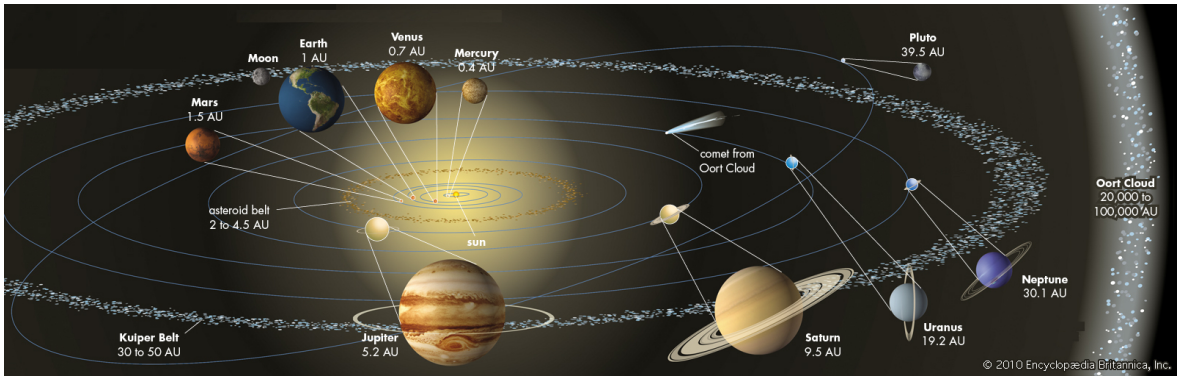

Figure 1.1 – Artistic view of the Solar System. The distance between each object and the Sun is reported in astronomical units (1 AU $\simeq 1.5 \cdot 10^8$ km). The inner planets (Mercury, Venus, Earth, and Mars) and the Moon are shown in scale to each other; so are the outer planets (Jupiter, Saturn, Uranus, and Neptune) and Pluto. Other depicted objects include the asteroid belt (formed by rocky and metallic asteroids), the Kuiper Belt (formed by icy asteroids), and the Oort Cloud (composed of icy planetesimals). From Owen (2019). Online: www.britannica.com.

knowledge of the behaviour of the components of planetary interiors and of the physical processes that take place in the interiors. Planetary interiors cannot be directly probed, and even indirect probing (such as the analysis of seismic waves) is nowadays limited to our Earth, with a few partial exceptions. The thermodynamic conditions typical of the interiors have thus to be reproduced by other means: this is the main goal of the work presented in this Thesis. The observation and measurement of some planetary properties – between them, gravitational fields, magnetic fields, luminosities – represent essential benchmarks for planetary models, which are constrained to reproduce the measured values.

1.2 Planetary models

In this Section we will present the foundations of planetary models. In particular, we will focus on the internal structure, the generation of magnetic fields via planetary dynamos, and the evolution of planets. Throughout the Section, we will highlight the importance of the knowledge of the behaviour of matter in planetary interiors.

1.2.1 Internal structure

Models structurally describing the interior profiles are all based upon the same set of basic assumptions. The governing equations of the interior structure expressing such assumptions are shown in Table 1.1 together with their physical meaning. A simplified scenario is considered in which secondary effects such as rotation are neglected and the planet is assumed to be spherically symmetric ($R_{pol} = R_{eq} = R$).

The first equation of Table 1.1 expresses the assumption of hydrostatic equilibrium, according to which the gravitational force towards the center is balanced by a pressure-

Table 1.1 – Equations describing the interior structure of an ideal non-rotating, spherically symmetric planet, expressed in their differential form. P, ρ, g, m, and T only depend on the radius r. The equation-of-state density function ρ_{EOS} depends on both pressure and temperature.

Physical meaning	**Differential form**
Hydrostatic equilibrium	$\frac{dP}{dr} = -\rho g$
Contribution to gravity (Gauss)	$\frac{dg}{dr} = \frac{G}{r^2}\left[\frac{dm}{dr} - \frac{2m}{r}\right]$
Contribution to mass	$\frac{dm}{dr} = 4\pi r^2 \rho$
Temperature profile	$\frac{dT}{dr} = \left.\frac{dT}{dr}\right\|_{\mathrm{conv}} + \left.\frac{dT}{dr}\right\|_{\mathrm{cond}}$
EOS-determined density	$\frac{d\rho}{dr} = \frac{\partial \rho_{\mathrm{EOS}}}{\partial P}\frac{dP}{dr} + \frac{\partial \rho_{\mathrm{EOS}}}{\partial T}\frac{dT}{dr}$

gradient force. In its integral form, it reads:

$$P(r) = P(0) - \int_0^r \rho(r')g(r')dr', \tag{1.1}$$

where $P(r)$ is the local pressure at a distance r from the center, $\rho(r)$ the local mass density, and $g(r)$ the local gravitational field. The latter can be easily obtained via the Gauss' theorem:

$$g(r) = \frac{Gm(r)}{r^2}, \tag{1.2}$$

where G is the universal gravitational constant and $m(r)$ is the mass of the portion of the planet from the center to the radius r:

$$m(r) = \int_0^r \rho(r')4\pi r'^2 dr'. \tag{1.3}$$

Equation 1.1 tells us that pressure increases when approaching to the center of the planet and reaches a maximum value P_{max} at the center ($P_{\mathrm{max}} = P_0$). If the very simplistic assumption that density is constant over the whole internal profile is made, the system composed by equations 1.1-1.3 can be solved without the need of any other information. This assumption is not completely unrealistic in the case of rocky planets that are not internally differentiated and are composed by materials with a very high adiabatic bulk modulus $K_S = \rho\,(\partial P/\partial \rho)_S$, since it represents the theoretical limit $K_S \to \infty$. Within this approximation, the local density everywhere corresponds to the mean density (see equation 1.17) and the pressure in the center of the planet becomes

$$P_{\mathrm{max}} = \frac{2\pi}{3} G\bar{\rho}^2 R^2. \tag{1.4}$$

For the Earth ($\bar{\rho} \simeq 5.51$ g/cm^3 and $R \simeq 6370$ km), the formula in equation 1.4 gives a maximum internal pressure of about 170 GPa, whereas accurate models [Alfè et al. (2007)] predict an inner core pressure around 360 GPa [Alfè et al. (2007)]. The simplistic uniform-density approximation is therefore able to provide the correct order of magnitude (at least for rocky planets, composed by materials with high bulk moduli) but considerably underestimates the pressure values. Indeed, the interiors of rocky planets are differentiated and the cores possess a significantly higher density than the mantles, increasing the values of $m(r)$ at low radii (see equation 1.3) and hence the value of $P_{\max}$. However, by substituting the definition of mean density in equation 1.4 and neglecting numerical factors, one can obtain a rough scaling law of the maximum internal pressure as a function of mass and radius of the planet:

$$P_{\max} \propto \frac{GM^2}{R^4}. \tag{1.5}$$

From equation 1.5 we can estimate that the interiors of the Solar and known extra-solar planets experience a vast range of pressures, reaching values around 100 Mbar. In any case, despite the usefulness of simple scaling laws such as that provided in equation 1.5 (especially for exoplanets of which we only know mass and radius), solving the system of equations 1.1-1.3 by taking into account the real response to gravitational compression of the planetary interior components rather than using simplistic approximations requires the knowledge of their *equation of state* – a relation between density, pressure, and temperature that can be described as an implicit surface in the (ρ, P, T) space:

$$f_{\mathrm{EOS}}(\rho, P, T) = 0. \tag{1.6}$$

If the equation of state is known, one of the three state variables ρ, P, and T can be expressed as a function of the other two. For instance, $\rho = \rho_{\mathrm{EOS}}(P, T)$. The density of a planetary layer can thus be determined from its pressure and temperature as

$$\rho(r) = \rho_{\mathrm{EOS}}[P(r), T(r)]. \tag{1.7}$$

Equation 1.7 highlights how a precise knowledge of the equations of state of the major planetary interior components is essential to build consistent structural models. An application of this principle is provided in Figure 1.2, that shows the mass–radius diagram for some low-mass exoplanets in comparison with the mass–radius relations predicted using the equations of state of several components (water, silicates, iron) assuming a homogeneous interior composition (solid curves) or internal differentiation (dashed curves). In the latter case, the considered structure models are water-worlds (composed by a metallic core, a rocky mantle, and an icy envelope), Earth-like planets (iron core, silicate mantle), and Mercury-type planets (huge iron core, thin silicate mantle).

However, the knowledge of the EOS of the planetary components is not sufficient to build a planetary model: additional information about the temperature profile $T(r)$ is needed to close the system of equations 1.1, 1.2, 1.3, and 1.7 (that is also provided in Table 1.1). Indeed, equation 1.7 provides a local relation between density and pressure only if $T(r)$ is known. It is therefore crucial to characterise the heat flow from the internal layers towards the surface of the planet. Heat can be produced by radioactive sources (such as ^{232}T and ^{238}U inside the Earth) or have a primordial origin, as the

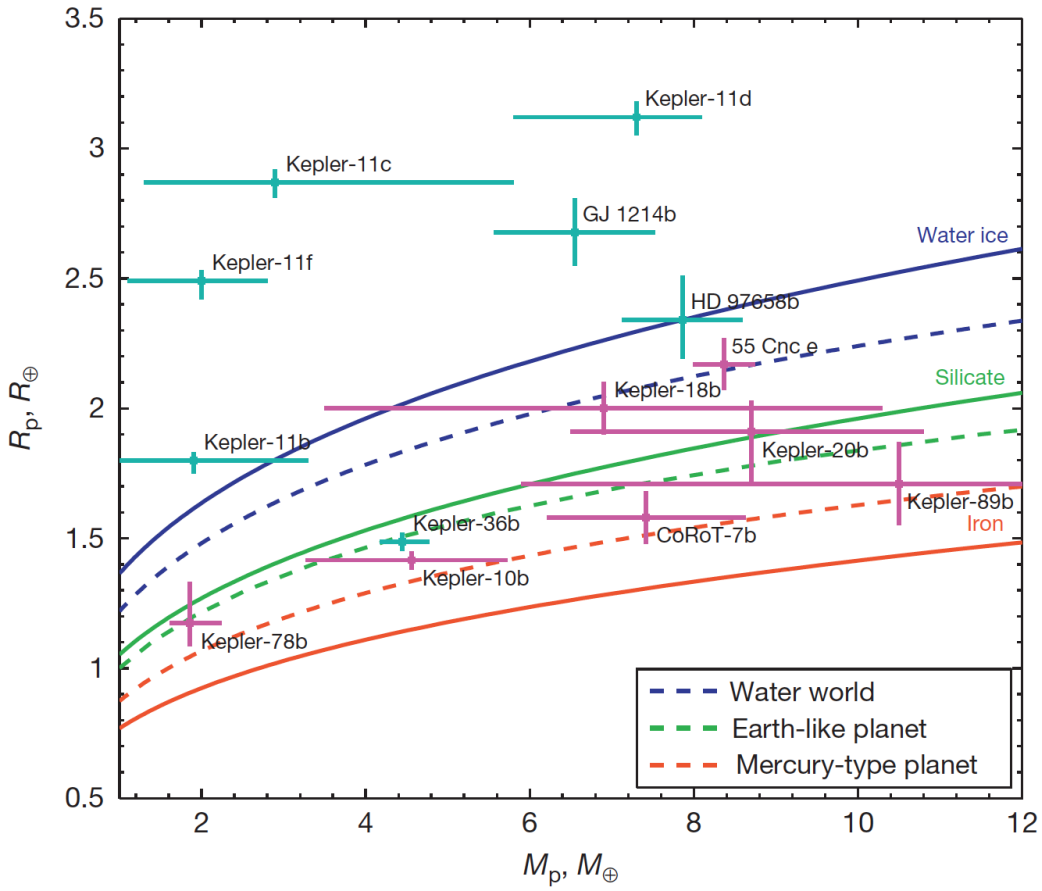

Figure 1.2 – Mass–radius planetary diagram. The points with error bars are examples of low-mass exoplanets (cyan: equilibrium temperature between $500 - 1000$ K; magenta: between $1000 - 2000$ K). The solid curves are the mass–radius relations for planets solely composed by water, silicates, and iron, based on our knowledge of the equations of state of such components. The dashed curves correspond to differentiated models: water worlds (with a metallic core, a rocky mantle and a considerable icy envelope), Earth-like planets (iron core, silicate mantle), and Mercury-type planets (with a huge iron core and a thin silicate-based mantle). Mass and radius are expressed in Earth units. From Wagner (2014).

planet gradually cools down from its initial conditions. It can be transported via conduction, convection, or radiation, depending on the properties of the considered layer. Inside convective layers of the planetary interior, the temperature gradient is essentially adiabatic:

$$\frac{dT}{dr} \simeq \left.\frac{dT}{dr}\right|_{\text{conv}} = -\left(\frac{\rho g \gamma}{K_S}\right) T, \tag{1.8}$$

where γ is the Grüneisen parameter: $\gamma = \frac{V}{C_V}\left(\frac{\partial P}{\partial T}\right)_V$. Across the boundary between distinct layers (such as the Core-Mantle Boundary inside the Earth), convection does not take place and heat transport becomes a conductive process:

$$\frac{dT}{dr} \simeq \left.\frac{dT}{dr}\right|_{\text{cond}} = -\frac{q_b}{k}, \tag{1.9}$$

where q_b is the heat flux across the boundary and k the thermal conductivity. In terrestrial planets, the same mechanism drives the temperature gradient near the surface,

such as in the lithosphere in the Earth, where convective currents do not occur. Conduction is the dominant process also in the inner core, mostly composed by solid iron that does not convect. The temperature profiles in planetary interiors strongly depend on the planet's size and type. However, temperature generally spans values up to a few 10^3 K in rocky planets and to $\sim 10^4$ K in giant planets.

Although the interior model we depicted is sufficient to bring out all the key parameters, we must highlight that equation 1.1 does not consider the effect of rotation on hydrostatic equilibrium. As we said in Section 1.3.2, rotation makes oblate, rather than spherical, the form of the planet and introduces an asymmetry in the planetary mass distribution. If rotation is taken into account, equation 1.1 becomes

$$\nabla P(r,\theta) = -\rho(r,\theta)\left[\mathbf{g}(r,\theta) + \mathbf{\Omega}(\mathbf{r},\theta) \times (\mathbf{\Omega}(\mathbf{r},\theta) \times \mathbf{r})\right], \tag{1.10}$$

where P and g are now expressed as functions of r and θ instead of the sole r, and a centrifugal term $-\mathbf{\Omega} \times (\mathbf{\Omega} \times \mathbf{r})$, depending on the angular rotation velocity $\Omega(r,\theta)$, is now present. The discrepancy between the model results using equation 1.10 and those using equation 1.1 depends on the value of the rotation parameter (defined in equation 1.19).

The density profile $\rho(r,\theta)$ given as output by an interior model must respect the constraints given by measurements: as we will see in Sections 1.3.1 and 1.3.2, the first key constraint is the mean planetary density, extracted from the observed mass and size of the planet. Additional essential constraints, which encode information about the density distribution inside the planet, are the planet's moment of inertia and the moments of its gravitational field.

1.2.2 Dynamos

According to the widely accepted dynamo theory, the rotation and convection of electrically conducting internal layers of a planet can generate and sustain a magnetic field. The theory predicts that a small seed magnetic field existing in the active region generates small currents in the rotating and convecting fluid via the Lorentz force. Those currents exercise a feedback action on the magnetic field via the Ampere's law, until a saturation regime is reached.

The first fundamental governing equation of a planetary dynamo is the magnetic induction equation describing the dynamics of the magnetic field:

$$\frac{\partial \mathbf{B}}{\partial t} = -\nabla \times \left(\frac{1}{\mu\sigma_{\mathrm{DC}}}\nabla \times \mathbf{B}\right) + \nabla \times (\mathbf{u} \times \mathbf{B}), \tag{1.11}$$

where μ is the magnetic permeability of the material, σ_{DC} its static electrical conductivity, and $\mathbf{u}$ the fluid velocity. The first term on the right side represents magnetic diffusion and the second term represents induction.

The second key equation is the momentum equation

$$\rho\frac{D\mathbf{u}}{Dt} = -\nabla P + \rho\mathbf{g} + \nabla \cdot \tau + 2\rho\,(\mathbf{\Omega} \times \mathbf{u}) + \rho\left[\mathbf{\Omega} \times (\mathbf{\Omega} \times \mathbf{r})\right] + \mathbf{J} \times \mathbf{B}, \tag{1.12}$$

where the momentum-change terms are the pressure gradient, local gravity, deviatoric stresses (τ is the stress tensor), the Coriolis and centrifugal forces due to the planet's

rotation, and the Lorentz force depending on the electrical current density $\mathbf{J}$ and on the magnetic field. The other equations governing the dynamo action are those stating the conservation of mass and energy together with the equations of state of the components of the dynamo-active layer.

The energy sources of the magnetic field are the kinetic energy associated to the rotation of the planet and the internal heat source that drives the convective motion of the active layer. The local rate of transfer from the kinetic to the magnetic energy is $-\mathbf{u}\cdot(\mathbf{J}\times\mathbf{B})$, that is, the opposite of the work done on the fluid by the Lorentz force (see equation 1.12). A rough criterion for determining if the magnetic field can be sustained by the dynamo action makes use of the dimensionless *magnetic Reynolds number*, which expresses the relative importance of induction (first right-hand-side term of equation 1.11) over diffusion (second right-hand-side term of equation 1.11) for the dynamics of the magnetic fields:

$$R_m = \mu\sigma_{\mathrm{DC}} u_{\mathrm{typ}} L_{\mathrm{typ}}, \tag{1.13}$$

where u_{typ} is a typical scale of the motion of the dynamo-active material and $L_{\mathrm{typ}} \sim \nabla^{-1}$ is the length scale of the gradients involved in equation 1.11, that is, a typical length scale of the motion of the material. Values of the magnetic Reynolds number $R_m \sim 40$ are believed to be generally sufficient to sustain a dynamo process [Olson and Christensen (2006)].

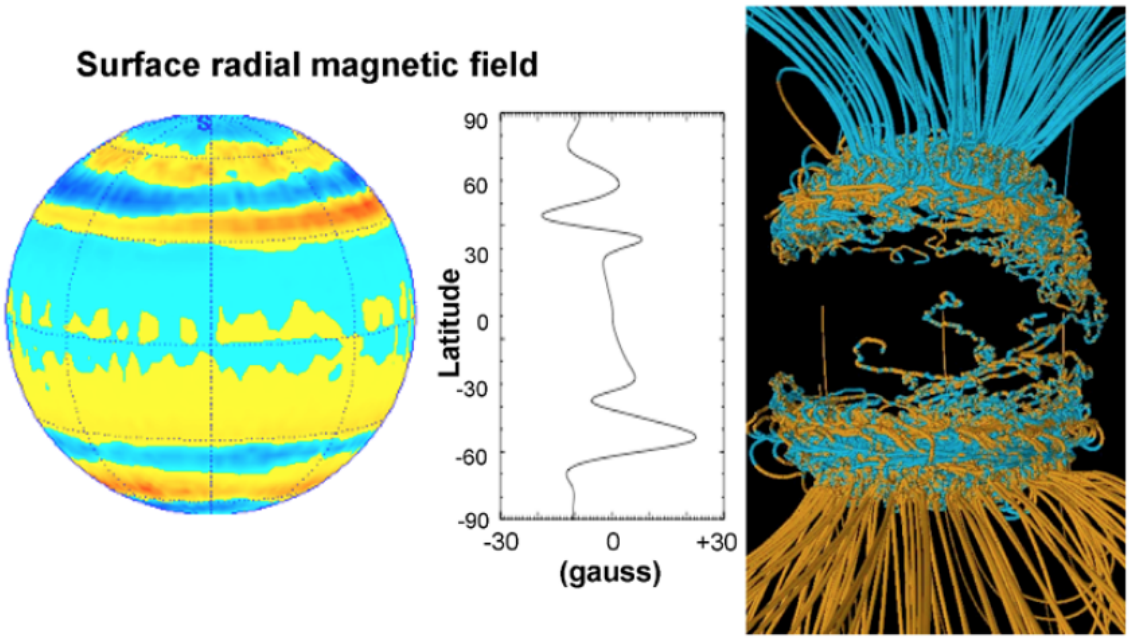

Figure 1.3 – Model of the magnetic field of Saturn. From left to right: the radial component of the magnetic field at the surface (warm colours: field directed outward; cool colours: inward); zonal average of the radial magnetic field as a function of latitude; three-dimensional field illustrated with lines of force (orange lines: outward directed; blue lines: inward). Adapted from Glatzmaier (2005).

Planetary dynamos are studied with the extensive use of numerical models. Such models must reproduce the measured magnetic field intensities and geometric structures (see Section 1.3.5). An example of output, relative to a three-dimensional numeric

model of the Saturn's magnetic field by Glatzmaier (2005), is provided in Figure 1.3. The knowledge of the equation of state and electrical conductivity of the materials composing the dynamo-active regions inside planets is essential for precise dynamo models. Indeed, a relation between density and pressure is needed to solve equation 1.12, whereas temperature intervenes in the energy equation. The electrical conductivity is a fundamental parameter for determining the importance of convection over diffusion (see equations 1.11 and 1.13) in each internal layer, determining in which region the magnetic field is generated.

1.2.3 Evolution

Terrestrial proto-planets, formed by undifferentiated silicates and metals, have grown through accretion. A combination of different processes heated them up: the decay of radioactive materials, gravitational compression, and the bombardment by meteorites. When the iron melting temperature was reached, a differentiation process began as iron, denser than silicates, sank due to gravity, forming a core. Silicate-rich materials, which were probably in the liquid state, forming a magma ocean, composed the mantle. Since, in the course of their histories, terrestrial planets have experienced thermodynamic conditions very different from the current ones, the characterisation of the relevant properties of their components at prior thermodynamic conditions (such as silicates in their liquid form) deserves a particular attention. Indeed, it provides essential benchmarks to the models describing the evolution of those planets. Within this context, an important goal is the precise determination of the melting curve of iron [Alfè et al. (2002); Zhang et al. (2015)].

Giant planets progressively contract and evolve from initial non-degenerate, high-entropy conditions towards a degenerate, low-entropy state. As described by the virial theorem linking the internal and potential (gravitational) energy inside giant planets, the energy gained by contraction is in part radiated away (constituting the planet's intrinsic luminosity), whereas the rest increases the internal energy of the planet, which is therefore heated.

Each planetary internal layer gives a contribution to the intrinsic luminosity L_{intr} via the decay of radioactive components (or, in massive enough giant planets, nuclear reactions) and as the effect of the contraction of the planet. Such contribution reads:

$$\frac{dL(r)}{dr} = 4\pi r^2 \rho(r) \left(\left.\frac{d\epsilon}{dt}\right|_{\text{reac}} - T\frac{\partial S}{\partial t} \right), \tag{1.14}$$

where $L(r)$ is the cumulated luminosity from the contribution from the internal layers up to a radius r, $d\epsilon/dt|_{\text{reac}}$ is the energy production rate of radioactive decay and nuclear reactions per unit mass, and S is the specific entropy per unit mass. The external boundary condition to equation 1.14 is $L_{\text{intr}} = L(R)$. The intrinsic luminosity, in its turn, can be linked to the global energy balance of the planet

$$\frac{\partial}{\partial t}\left(E_{int} + E_g\right) = M \left.\frac{d\epsilon}{dt}\right|_{\text{reac}} - L_{\text{intr}}, \tag{1.15}$$

where E_{int} and E_g are the total internal and gravitational energy of the planet, respectively. The intrinsic luminosity has thus a great importance in determining the

evolution of planets, providing information about its current stage. For instance, under simple hypotheses [Guillot (2005)], the luminosity of giant planets can be expressed in terms of a simple Kelvin-Helmholtz law:

$$L \propto \frac{GM^2}{R}\frac{1}{\tau_{pl}}, \tag{1.16}$$

where GM^2/R is a rough estimation of the planet's gravitational energy and τ_{pl} is the planet's age.

1.3 Measurement of planetary properties

For a long time, the only way to gain information about the structure of planets has been the characterisation of the planet on the surface of which we live, the Earth. As we have direct access to its surface and atmosphere, we can characterise their compositions, properties, and dynamics. Moreover, we can gain indirect information about its interior mainly via seismologic studies. Indeed, the velocity of seismic waves, which can measured from the delay between an earthquake and the arrival time of the wave to a distant seismologic station, encodes information about the properties of the planetary interiors along their path. Until a few decades ago, the study of the other Solar planets was only observational and limited to the planetary basic properties and to the distant study of the atmospheric layers. The space race between United States and Soviet Union in the second half of the 20$^{\text{th}}$ century, inaugurated in 1957 by the launch of the first artificial satellite, the *Sputnik 1*, has induced formidable breakthroughs not only for human technological capacities but also for our knowledge and understanding of our planetary system. Indeed, a huge number of space probes have been sent visiting all the major celestial bodies of the Solar System, either during a flyby or by landing on their surfaces. The last 30 years have witnessed the latest major breakthrough for planetary science: the discovery of a large number of extrasolar planets. Today, the discovery of about 4000 exoplanets belonging to more than 3000 different systems has been confirmed [`exoplanet.eu`]. The characterisation of these planets by distant observation is drastically limited if compared to Solar planets, and is essentially reduced to the determination of mass and size. For this reason, Solar planets are used as prototypes for the extrasolar ones, which are classified according to their similarities with the first. However, the latter exhibit a larger variability of conditions, as they encompass intermediate masses and sizes between Solar planets.

In this Section, we will review the main planetary properties that can be determined by observation or probing. Some basic properties are listed in Table 1.2 for an easier consultation.

1.3.1 Mass and size

The two most basic properties of a planet are its mass and size. Planetary masses (M) can be determined from the study of the motion of natural satellites or studying the effect of its gravitational field on the orbits of other planets. It can be inferred from gravity field data from space probe visiting the planet (see Section 1.3.2). Due to

Table 1.2 – Some basic properties of the Solar planets: mean orbital distance (in Astronomical Units; 1 AU = 149 597 870.7 km) equatorial radius, mass, mean density, rotational angular velocity, and axial tilt (the angle between the rotational axis of a planet and its orbital axis). The number of significative digits has been reduced for the sake of clarity – state-of-the-art measurements are more precise. Rotational angular velocity values in bold indicate that the motion is retrograde (that is, the axial tilt is $> 90°$).

Planet	D_{orb} (AU)	R_{eq} (10^3 km)	M (10^{24} kg)	$\bar{\rho}$ (g/cm^3)	Ω (10^{-6} rad/s)	Axial tilt (°)
Mercury	0.39	2.44	0.33	5.43	1.24	0
Venus	0.72	6.05	4.87	5.24	**0.30**	177
Earth	1	6.37	5.97	5.51	72.9	23
Mars	1.52	3.39	0.64	3.93	70.9	25
Jupiter	5.20	71.5	1900	1.33	176	3
Saturn	9.57	60.3	568	0.69	164	27
Uranus	19.2	25.0	86.8	1.32	**101**	98
Neptune	30.1	24.8	102	1.64	108	28

rotation (see Section 1.3.2), planets are not perfectly spherical but assume an oblate form: their equatorial radius R_{eq} becomes greater than the polar one R_{pol}. Both radii and the precise shape of planets are determined via distant observation or with the visit of space probes. The mass and equatorial radius of the Solar planets are provided in Table 1.2.

The knowledge of these basic properties, mass and radii, allows the determination of the first essential intensive property of the planet, the mean density

$$\bar{\rho} \simeq \frac{3}{4\pi} \frac{M}{R_{eq}^2 R_{pol}}. \tag{1.17}$$

The mean density (also provided in Table 1.2) is one of the key factors for inferring the composition of the planet and determining the conditions reached in its interior. The planets of the Solar System are classified as rocky planets, gas giants, and icy giants depending on their composition. The mean density values shown in Table 1.2 reflect their nature: terrestrial planets exhibit high values of $\bar{\rho} = 3.9 - 5.5$ g/cm^3; the gas giant Saturn has a low value (0.7 g/cm^3); the icy giants possess intermediate density values of $1.3 - 1.6$ g/cm^3. The only exception to this ordering is Jupiter, which has a high mean density of around 1.3 g/cm^3 despite being a gas giant. This anomaly is easily explained by the very high Jupiter mass (more than three times that of Saturn): the gases composing the interior of Jupiter are compressed much more than in Saturn. Also the trends in mass and radius follow the classification of planets: terrestrial planets have masses ranging from $0.3 - 6 \cdot 10^{24}$ kg, whereas giant planets exhibit much higher masses from $(90 - 560) \cdot 10^{24}$ kg (with the outlier of $1900 \cdot 10^{24}$ kg for Jupiter); the radii of the terrestrial planets – $(2.4 - 6.4) \cdot 10^3$ km – are also considerably lower than for giant planets – $(25 - 70) \cdot 10^3$ km).

1.3.2 Rotation and gravitational moments

All the Solar planets rotate around an axis while they orbit around the Sun. This feature can be exploited to gain an access to information about the density distribution inside the planets beyond the simple determination of the mean density. It can

be assumed that rocky planets essentially rotate as solid objects, so that their rotation angular velocity is a single value, at least for their surface and their solid layers. Differential rotation may be relevant in the liquid internal layers. Giant planets do not rigidly rotate but are subject to differential rotation depending on the depth and latitude. In this case, radio and magnetic-field data are mainly used for determining the internal rotation rate, whereas the angular velocity profile of the surface can be directly observed.

Table 1.3 – Some gravitational and rotational properties of Uranus and Neptune: second and fourth gravitational moments, rotation parameter, and dimensionless axial moment of inertia.

Planet	J_2 (10^{-2})	J_4 (10^{-4})	q (10^{-3})	C/MR_{eq}^2
Uranus	0.35160(32)	-0.354(41)	29.51(5)	0.230
Neptune	0.3539(10)	-0.28(22)	26.09(23)	0.241

All the Solar planets are "fast" rotators, with angular velocities of the order of 10^{-4} rad/s, with the exception of the two innermost planets, Mercury and Venus, which exhibit lower values around 10^{-6} rad/s (see Table 1.2). Mercury's rotation is locked by a 3:2 spin-orbit resonance (the planet rotates 3 times each 2 complete orbits around the Sun), whereas the origin of the slow rotation of Venus is unclear. Generally, Solar planets possess an axial tilt below 30° – that is, their rotational axis is close to their orbital axis – with the exception of Venus and Uranus which both exhibit values above 90°, meaning that their motion is retrograde. Uranus has an axial tilt close to 90°, meaning that it rotates near the Solar System plane, which affects the nature of seasons on its surface; Venus, on the contrary, has an axial tilt very close to 180°, meaning that its rotational axis is well aligned with the orbital axis but in the opposite sense.

Due to their rotation, planets assume an oblate form. This feature is described by the planetary *oblateness*:

$$\epsilon = \frac{R_{eq} - R_{pol}}{R_{eq}}, \tag{1.18}$$

whereas the importance of rotation is quantified by the *rotation parameter* q, defined as the ratio between the centrifugal acceleration and the gravitational acceleration at the equator:

$$q = \frac{\omega^2 R_{eq}^3}{GM}. \tag{1.19}$$

The determination of the polar moment of inertia C of a planet relative to its rotation axis is essential since it provides information on its mass distribution. Indeed,

$$C = \int r^2 \sin^2\theta \rho(r,\theta) d^3\mathbf{r} \tag{1.20}$$

where θ is the co-latitude.

A sphere with uniform density has a dimensionless (or reduced) moment of inertia $C/MR_{eq}^2 = 2/5$, whereas a sphere in which all the mass is concentrated in the center has $C/MR_{eq}^2 = 0$. In planetary interiors, the density increases with the depth because of the effect of hydrostatic pressure (see Section 1.2.1), so that planets exhibit reduced moments of inertia below 0.4: for instance, for Uranus and Neptune $C/MR_{eq}^2 = 0.23$

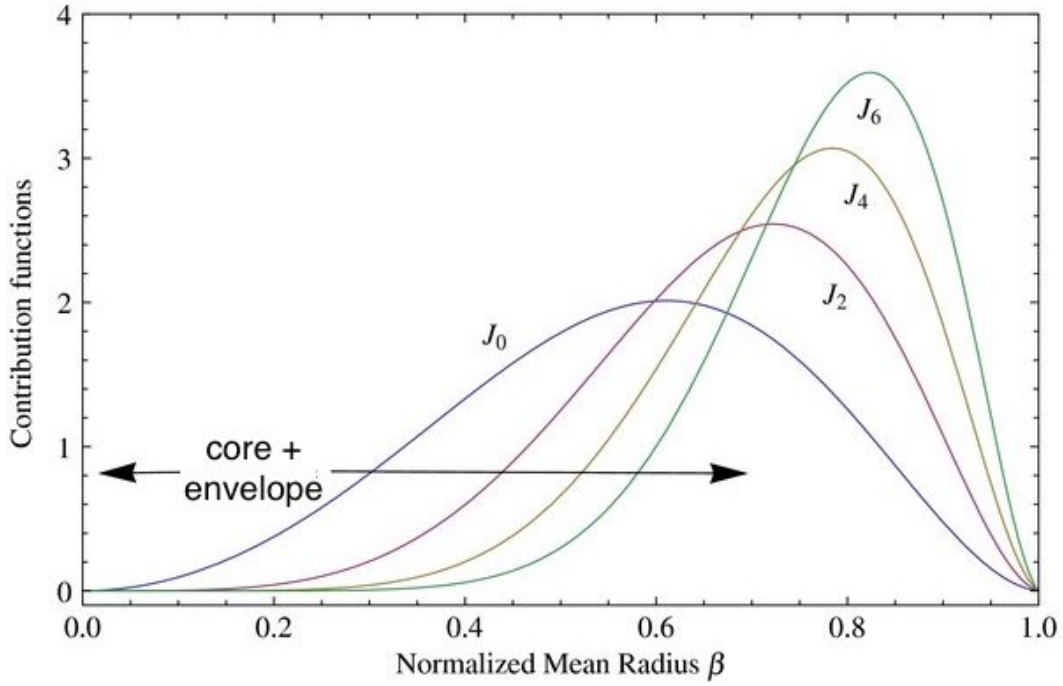

Figure 1.4 – Contribution of each layer to the gravitational moments J_0 (mass), J_2, J_4, and J_6 of Neptune according to an interior model by Helled et al. (2011) (see the integrand in equation 1.24). Moments of higher orders provide information principally about the density of outer layers. Adapted from the source.

and 0.24, respectively (see Table 1.3). The deviation of these values from the uniform-density value (0.4) indicates the importance of density gradients inside those planets. The moment of inertia can be determined from the oblateness ϵ and the rotation parameter q using the *Radau-Darwin approximation* [Zharkov and Trubitsyn (1978)], which is valid if rotation is slow enough that both parameters can be treated as small parameters:

$$\frac{C}{MR_{eq}^2} = \frac{2}{3}\left[1 - \frac{2}{5}\left(\frac{5q}{2\epsilon} - 1\right)^{1/2}\right]. \tag{1.21}$$

Rotation has an effect on the mass distribution of the planet. If we assume it to be axisymmetric, the general solution to the Laplace's equation for its external gravitational potential, $\nabla^2 U_g = 0$, is

$$U_g(r,\theta) = -\frac{GM}{r}\left[1 - \sum_{n=1}^{\infty}\left(\frac{R_{eq}}{r}\right)^{2n} J_{2n} P_{2n}(\cos\theta)\right], \tag{1.22}$$

where R_{eq} is the equatorial radius of the planet, J_{2n} are dimensionless coefficients expressing the relative importance of each term and are called *gravitational moments* of the planet, and $P_{2n}(\cos\theta)$ are Legendre polynomials. If there are no polar-equatorial asymmetries in the mass distribution of a planet, its external gravitational potential will simply be $U_g = -GM/r$ and all the J_{2n} will be zeros. Indeed, the terms with $J_{2n}P_{2n}(\cos\theta)$ express the different orders of asymmetry in the mass distribution from the equator to the poles. Only the even coefficients $2n$ appear since the odd ones

would represent a north-south pole asymmetry that would be incompatible with the assumption of hydrostatic equilibrium.

A space probe describing a polar or quasi-polar orbit around a planet can measure the gravitational field dependence on θ, which allows the determination of both the mass M and of the even gravitational moments J_{2n}. In general, because of the uncertainties in the measurements, only the first coefficients (J_2 and J_4) have already been determined with a high precision. The NASA's *Juno* space probe, which is currently orbiting Jupiter, is measuring its gravitational field allowing the determination of the even moments J_2-J_8 with considerably higher precision than previous probes [Folkner et al. (2017)]. As an example, Table 1.3 provides the measurements of the gravitational moments J_2 and J_4 for Uranus and Neptune, together with their rotation parameter and reduced moment of inertia. The error bars for J_2, J_4, and q are provided to give an idea of the precision of these measurements. Such measurements impose essential constraints on the mass distribution to be reproduced by planetary models. Indeed, the relations

$$M = \int \rho(r,\theta) d^3\mathbf{r} \tag{1.23}$$

$$J_{2n} = -\frac{1}{M R_{eq}^{2n}} \int \rho(r,\theta) r^{2n} P_{2n}(\cos\theta) d^3\mathbf{r} \tag{1.24}$$

connect M and J_{2n} to the internal density profile $\rho(r,\theta)$. However, as it is evident in Figure 1.4, due to the presence of a factor r^{2n} in equation 1.24, the higher the order gravitational momentum, the higher the contribution of outer layers to its value: the analysis of high-order moments does not bring significant information about the deep internal layers, whose characterisation remains elusive. Other methods have thus to be employed to characterise them, such as the measurement of the planetary magnetic field and luminosity.

1.3.3 Seismic waves

Studying the trajectories and velocities of seismic waves through a dense network of seismological stations has critically contributed to our knowledge of the interior structure of our Earth, of which we dispose today of a precise picture. We know that the Earth's interior consists of a central core (which is divided in a solid inner part and a liquid outer part), a solid mantle (further divided in a lower mantle, a transition zone, and an upper mantle), and a solid crust. A simplified sketch of the interior structure of our planet is provided in Figure 1.5.

Earthquakes produce seismic waves of various types, such as body waves and surface waves. The two main types of body waves – that are, waves that propagate through the Earth's interior – are primary (or P) waves, which are longitudinal, and secondary (or S) waves, which are transverse. Their definitions are due to the fact that P waves propagate faster than S waves and are thus observed sooner by seismologic stations. Figure 1.5 provides a simplified scheme of the path of seismic waves inside the Earth. While they propagate, seismic waves experience refraction as they encompass layers subject to different conditions of pressure and density. In particular, as their velocity increases with depth, they are refracted towards the surface until they re-emerge. The waves that penetrate enough inside the Earth eventually find a discontinuity in the

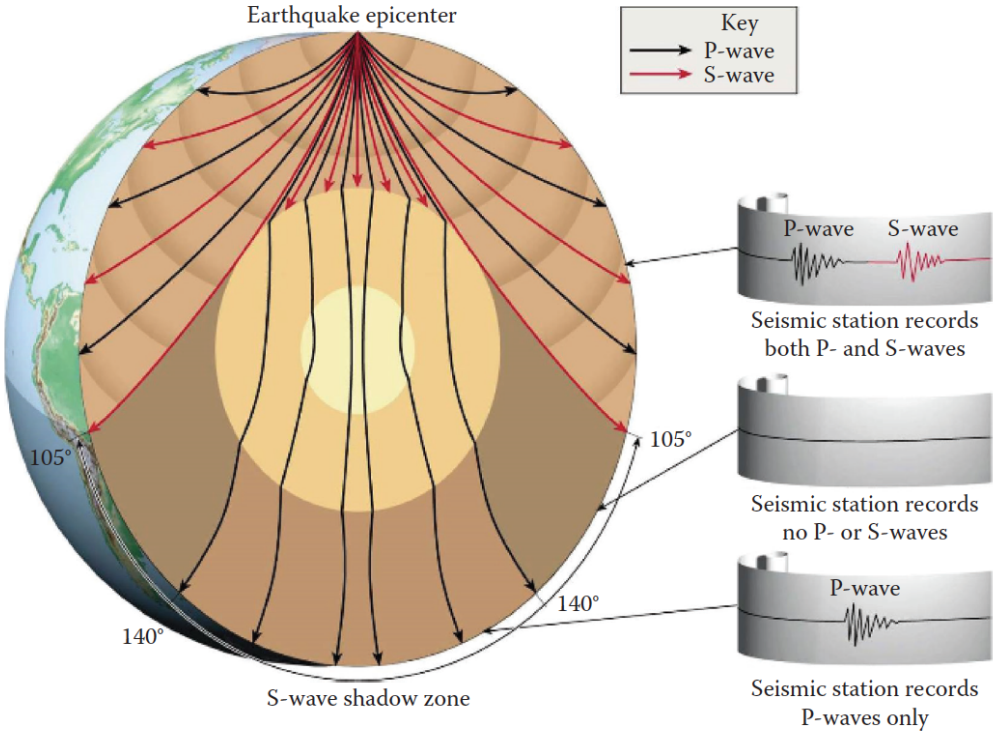

Figure 1.5 – Scheme of the Earth's interior and of the paths followed by P (black arrows) and S (red arrows) seismic waves through it. The different coloured layers are, from the interior: solid inner core, liquid outer core, mantle. For angular distances below 105°, both P and S waves are recorded. Between 105° and 140°, no waves are recorded. For angular distances above 140°, only P waves are recorded. From Boden (2016).

properties of the medium in which they propagate: it is the boundary between the lower mantle and the outer core. The velocity of P waves suddenly decreases, so that, because of refraction, they change their direction towards the center of the planet. They cross the outer core and re-emerge at the mantle experiencing another sudden refractive effect. When they re-emerge at the surface, because of the refractions they underwent, they can find themselves only at angular distances above 145° from their origin. When S waves cross the core-mantle boundary, they cannot propagate further: indeed, above 110° no S waves are detected. This proves that the outer core is liquid: indeed, transverse waves are not sustained by a medium without shear strength. Additionally, the arrival times of P and S waves as a function of the distance between the epicentre and the station encode essential information about the Earth's interior, as their velocities depend on the structural properties of its components.

Until recent times, our Earth has been the only planet for which we disposed of reliable seismological data. The situation changed when the NASA's *Apollo* missions in 1969–1972 deployed seismometers and seismic sources on the surface of the Moon. The first deployment of a seismometer on a planet followed in 1975 (*Viking Lander 2*). The mission *InSight* [mars.nasa.gov/insight], active from 2018, is the first one whose scientific goal is the combined measurement of the seismic activity and the internal heat flow of Mars, to elaborate models of the deep interiors and study the early geological evolution of the planet. To accomplish these tasks, the probe is equipped with a

seismometer (SEIS) and a self-penetrating heat flow probe (HP^3).

1.3.4 Luminosity

The measurement of the luminosities of planets allows to estimate the heat flux at their surfaces, which provides an indirect insight about their interior structure and their thermal evolution. Planets are irradiated by their host star. A fraction of the received radiation is reflected by the planet's surface or atmosphere, while the rest is absorbed, depending on the *optical properties* of the atmosphere's components (which have to be characterised along with the structural properties). The *Bond albedo* (a_{Bond}) of a planet is the fraction of the stellar radiation it reflects. The total absorbed energy depends on the distance from the star and on the albedo. Information about the absorbed energy is usually provided encoded in a planetary parameter called *equilibrium temperature* (T_{eql}). It is defined as the temperature of a black body that emits the same power than the planet absorbes from the star:

$$T_{\text{eql}} = \left[\frac{L_{\text{star}}(1 - a_{\text{Bond}})}{16\pi\sigma_{\text{S.-B.}} D_{\text{orb}}^2} \right]^{1/4}, \tag{1.25}$$

where L_{star} is the luminosity of the star, $\sigma_{\text{S.-B.}}$ is the Stefan-Boltzmann constant, and D_{orb} the mean distance from the star.

Table 1.4 – Some energy balance data for the giant planets: Bond albedo, equilibrium black-body temperature, effective black-body temperature, surface temperature at $P = 1$ bar.

Planet	a_{Bond}	T_{eql} (K)	T_{eff} (K)	$T_{\text{1-bar}}$ (K)
Jupiter	0.34	110	124	165
Saturn	0.34	81	95	135
Uranus	0.30	58	59	76
Neptune	0.29	47	59	72

Planets generally emit more energy than they receive from their host star, that is, they possess an *intrinsic luminosity* L_{intr}. Analogously to what has been done for the absorbed energy from the star, the information about the total energy emitted by the planet (including the intrinsic contribution) is translated into an *effective temperature*, defined as the temperature of a black body emitting the same power as the planet:

$$T_{\text{eff}} = \left[\frac{W_{em}}{\sigma_{\text{S.-B.}}} \right]^{1/4}, \tag{1.26}$$

where W_{em} is the emitted flux of energy from the planet's surface. If a planet is in thermal equilibrium with the radiation received from its host star, then $T_{\text{eql}} \simeq T_{\text{eff}}$. On the contrary, if $T_{\text{eff}} > T_{\text{eql}}$ then the planet possesses internal heat sources that generate more radiation.

Table 1.4 shows the radiation parameters of the Solar giant planets. Since they all exhibit similar albedos around 30%, according to equation 1.25 their equilibrium temperatures are ordered as their distances from the Sun (see Table 1.2). With the

striking exception of Uranus, all the giant planets have effective temperatures significantly higher than their equilibrium temperatures, indicating the presence of a consistent heat source. Neptune, for instance, emits $(T_{\text{eff}}/T_{\text{eql}})^4 \simeq 2.5$ times more energy than it receives from the Sun.

1.3.5 Magnetic field

In Section 1.2.2, we have seen that planetary magnetic fields are generated by a dynamo action of electric currents, due to the rotation and convection of internal conducting layers. The amplitude and geometric structure of a planetary magnetic field give essential insights about its interior structure and about the transport and electrical properties of its components. For these reasons, magnetometers are always part of the standard instrumentation onboard space probes. The magnetic fields of the Solar planets are thus measured by probes either executing flybys, which allow the measurement along the whole trajectory of the probe, or landing on the planet's surface – in this case the measurement is relative to a fixed point but is affected by lower uncertainties.

The global structure of the magnetic field can be inferred from measurements on a diverse range of positions. Outside the planet, in the absence of electrical currents, the magnetic field is irrotational ($\nabla \times \mathbf{B} = 0$) and can therefore be expressed as the gradient of a scalar potential: $\mathbf{B} = -\nabla\Phi$. The magnetic potential Φ is developed as a sum of harmonic terms:

$$\Phi(r,\theta,\phi) = R_{eq} \sum_{l=1}^{\infty} \left(\frac{R_{eq}}{r}\right)^{l+1} \sum_{m=-l}^{+l} P_l^m(\cos\theta) \left[g_l^m \cos m\phi + h_l^m \sin m\phi\right], \tag{1.27}$$

where P_l^m are associated Legendre polynomials of degree l and order m and g_l^m and h_l^m are coefficients indicating the magnitude of each specific term. The degree l indicates the contribution of the dipolar ($l = 1$), quadrupolar ($l = 2$), octupolar ($l = 3$), and higher multi-polar terms. The order m indicates the degree of non-axisymmetry of the field. The multi-polar development is made by taking the planet's center as geometrical origin. At this stage, modelling the magnetic field consists in finding the parameters g_l^m and h_l^m such that $-\nabla\Phi$ reproduces at best the measured magnetic field spatial profile. Once the parameters have been estimated, it is possible to calculate the power spectrum of the magnetic field, by determining the contribution of each term. The spectral power associated to each term (l, m) is proportional to $(2l+1)\,(|g_l^m|^2 + |h_l^m|^2)$. Two types of analysis can be made:

(i) The contribution of each multi-polar spectral term (dipole, quadrupole, etc.) to the magnetic field power can be calculated as the sum of the orders m associated to the same degree l. This analysis allows in particular to determine if the magnetic field can be viewed as essentially dipolar or the contribution of the higher orders is not negligible.

(ii) The degree of axisymmetry of the field can be estimated by comparing the contribution of the sum of the axisymmetric terms – the (l, m) terms with $m = 0$ – to the non-axisymmetric ones – those with non-zero values of m ($m = 1, 2, ...$).

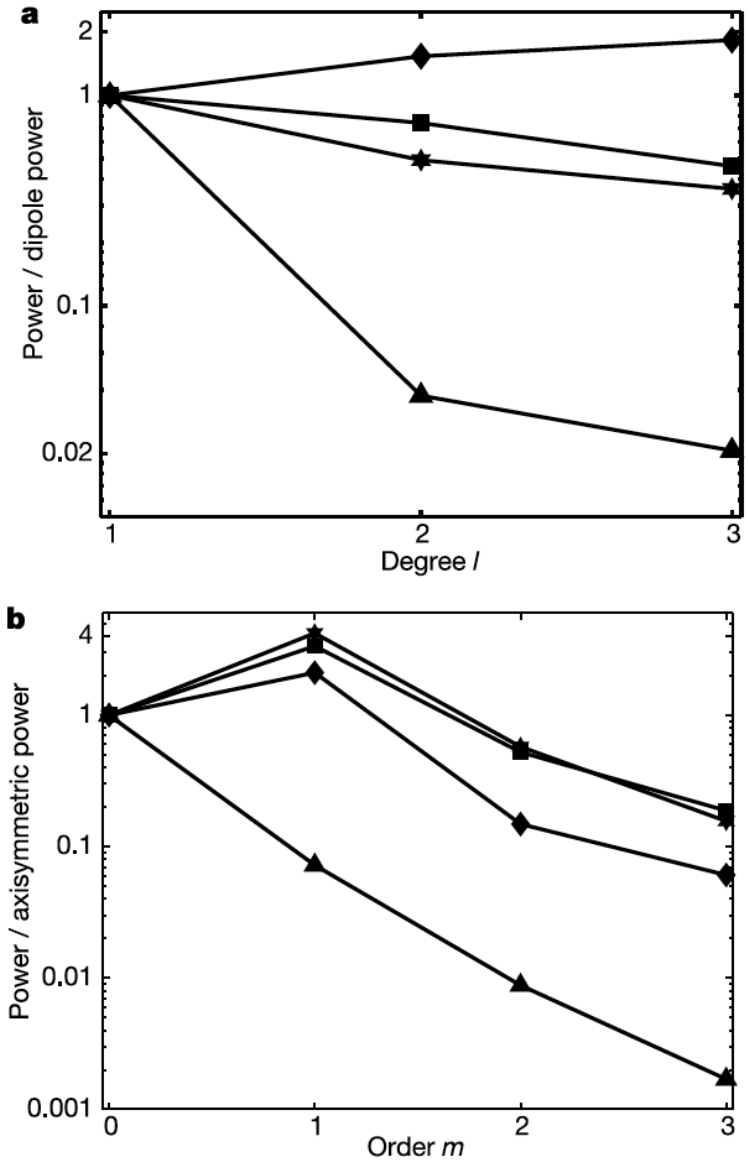

Figure 1.6 – Spectral analysis of the surface magnetic fields of the Earth (triangles), Uranus (squares), Neptune (diamonds), together with a numerical model (stars, see Section 1.2.2). **(a).** Spectral power of the dipolar ($l = 1$), quadrupolar ($l = 2$), and octupolar ($l = 3$) contributions to the field. **(b).** Spectral power of the axisymmetric terms $m = 0$ and the non-axisymmetric terms with $m = 1, 2, 3$. From Stanley and Bloxham (2004).

Terrestrial planets. The four terrestrial planets of our Solar System exhibit a diverse spectrum of magnetic field structures. The Earth has a mostly dipolar magnetic field (see Figure 1.6), tilted about 10° with respect to the rotation axis. It is generated by the convecting and rotating liquid iron in the outer core via a *dynamo* process (see Section 1.2.2). Mercury and Mars exhibit remnant crustal magnetic fields – as shown by the *Mariner 10* [Ness et al. (1975)] and the *Mars Global Surveyor* probes [Acuña et al. (1998)], respectively – probably the result of a dynamo action in their early history. Venus apparently does not exhibit neither an active dynamo nor a crustal field [Rus-

sell et al. (1979)], which is quite surprising considered its similarity with the Earth. Although the hypothesis that the heat flux is insufficient to produce strong enough convective currents has been advanced [Nimmo (2002)], a thorough explanation is still lacking.

Giant planets. All the giant planets of the Solar system exhibit active dynamos. Jupiter and Saturn, as shown by the *Pioneer 10* and 11 probes, respectively [Smith et al. (1974); Acuña and Ness (1980)], have mostly dipolar and axisymmetric fields. Saturn's filed, in particular, is remarkably highly axisymmetric – fact that has been confirmed by the later *Cassini* probe [Dougherty et al. (2005)]. The *Juno* probe is providing measurements of remarkably higher precision of the magnetic field of Jupiter [Connerney et al. (2017)], that will allow the determination of the spherical harmonic coefficients up to the 14^{th} order. Such a thorough characterisation should be sufficient to determine the depth and shape of the dynamo-active region, as in a recent complex dynamo model by Moore et al. (2018). Additionally, thanks to the long acquisition time, the secular variation of the magnetic field could be determined. Uranus and Neptune exhibit peculiar magnetic fields, as measured by the *Voyager 2* space probe [Ness et al. (1986); Ness et al. (1989)] – the only probe to visit the icy giants up to now. Figure 1.6 (a) and (b) show the spectral analysis (i) and (ii), respectively, on the magnetic fields of the Earth, Uranus, and Neptune. It is evident that the Earth possesses a mostly dipolar magnetic field [Figure 1.6 (a)], whereas the icy giants exhibit multipolar field without a dominant contribution of a specific term. Moreover, the terrestrial field is predominantly axisymmetric – that is, symmetrically oriented around the rotation axis – whereas the icy giants' fields are not.

Dynamo models should provide an unified framework to describe the magnetic field generation mechanism and an explanation for this diversity in the magnetic field presence and structure between terrestrial planets and between giant planets.

1.3.6 The case of exoplanets

We have seen that quite a lot of different data can be collected for all the Solar planets, including the outermost ones. For extrasolar planets the situation is obviously different: detecting them, rather than thoroughly characterising them, represents the challenge. Historically speaking, the first more common method used for detecting exoplanets has been the *radial velocity method*. It is based on the principle that a planet exercises a gravitational action on its host star, inducing a motion of the star around the center of mass of the system. Depending on the orientation of the planetary system's plane with respect to the axis towards the Earth, this motion may induce a periodic variation in the radial velocity. Such variation can be detected and quantified via the analysis of the star's spectral lines, which change as a function of the radial velocity due to the Doppler effect. Since the measured effect is due to the planet's gravitational field, this method allows the determination of the planet's mass. Figure 1.7 (top) shows the radial velocity of the star 51 Peg as measured by Mayor and Queloz (1995) – the first use of this method for detecting an exoplanet.

The launch of the *Kepler space telescope* in 2009 [`kepler.nasa.gov`] has been a game changer. *Kepler*, which has been active in the discovery of exoplanets until 2018, detected exoplanets using a different method, the *transit method*, that consists

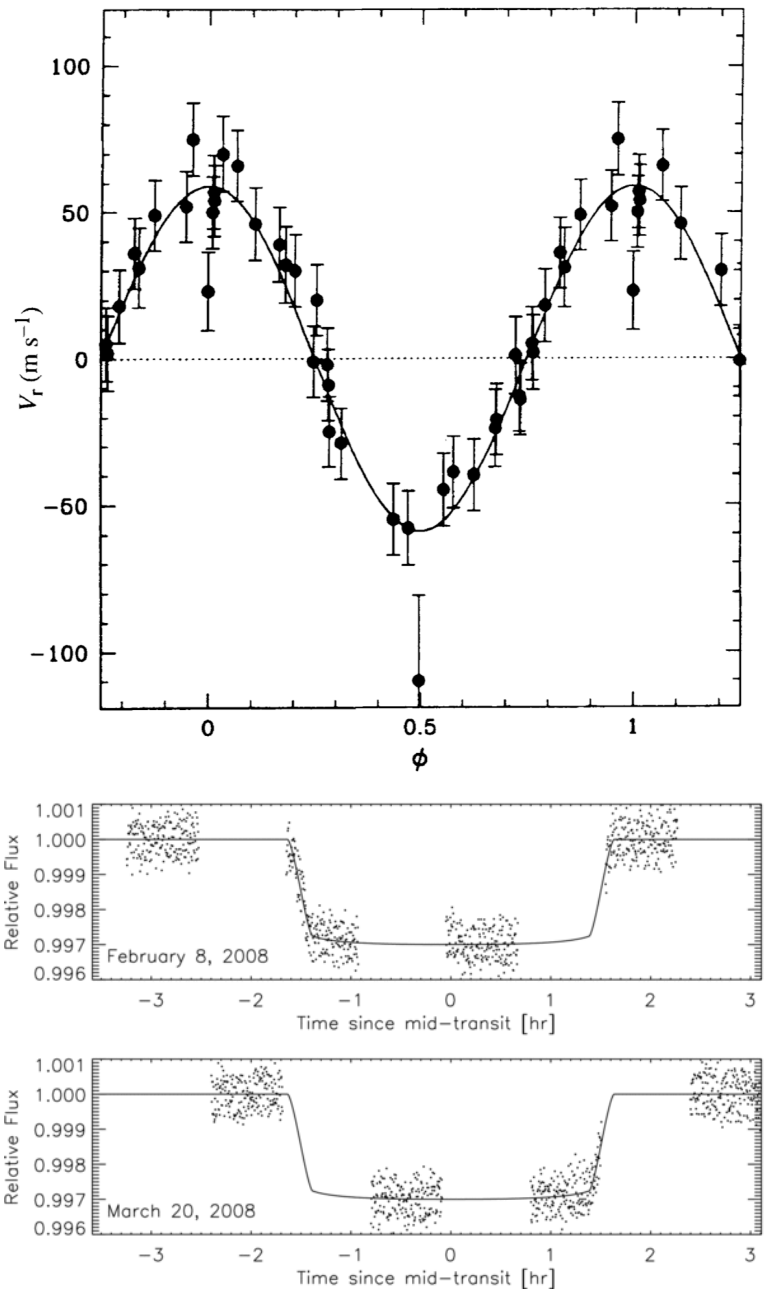

Figure 1.7 – Detection methods for exoplanets. **Top.** Radial velocity. Orbital motion (radial velocity *vs* phase) of 51 Peg. The solid line represents the computed motion. From Mayor and Queloz (1995). **Bottom.** Transit photometry. Infrared photometry by the *Hubble Space Telescope* [nasa.gov/hubble] of two transits of the exoplanet HD 149026b. Interruptions are due to Earth occultations. The solid curve is the best-fitting model. From Carter et al. (2009).

in detecting a drop in the observed brightness of the host star when the planet transits between the star and the observer. Figure 1.7 (bottom) shows the photometry of two transits of the exoplanet HD 149026b. Since the detected drop in the star's luminosity depends on the planet's size, the transit method can determine the planetary radius. The average number of planets of a given size for a main-sequence star determined

from re-elaborated *Kepler* data [Fressin et al. (2013)] is provided in Figure 1.8. It is evident that low-size planets, whose radius is between that of the Earth and Neptune, are the most common, whereas a significant drop in the average number happens at around 3 Earth radii.

The retirement of *Kepler* has not stopped the development of the field of space telescopes: *NASA*'s *TESS* (Transiting Exoplanet Survey Satellite) [`tess.mit.edu`], launched in 2018, is actively looking for small exoplanets using the transient method, and particularly rocky planets orbiting around their host star in the *habitable zone* (the zone of a planetary system compatible with a surface temperature which can host life as we know it). Conceived by a partnership between the *ESA* and the *Swiss Space Office*, *CHEOPS* (CHaracterising ExOPlanets Satellite) [`cheops.unibe.ch`] will be launched in Octobre/November 2019. It will characterise through the transient method the size of the exoplanets whose mass has already been measured, allowing the estimation of their mean density (via equation 1.17) and hence a rough determination of their type.

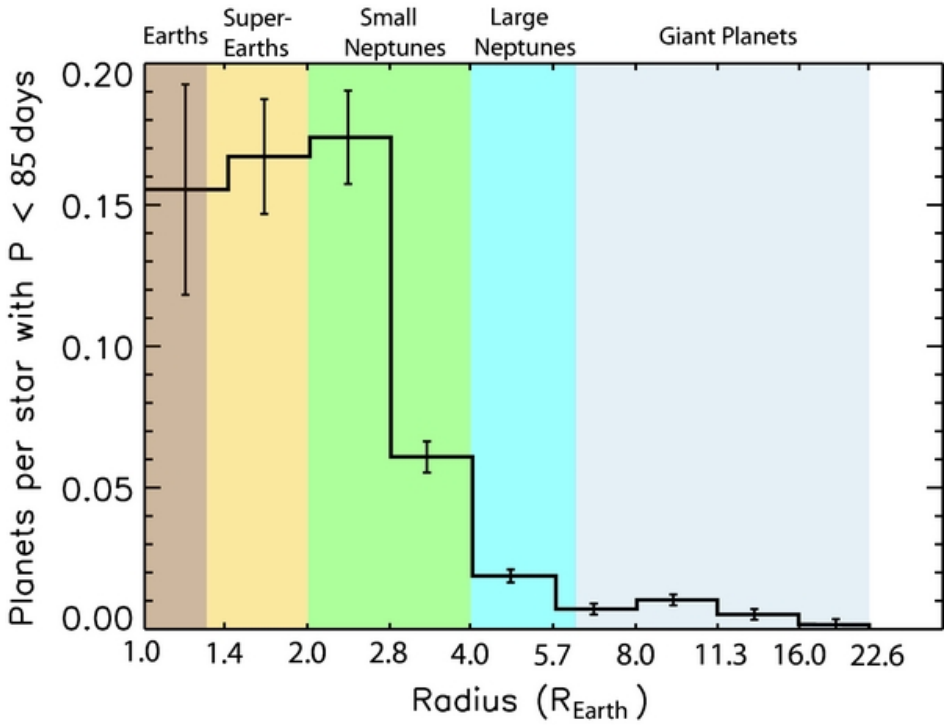

Figure 1.8 – Average number of planets per size bin for stars belonging to the main sequence. Size bins are named after their comparison with Solar planets' sizes, so that extrasolar planets are identified as Earth-like, super-Earths, small Neptunes, large Neptunes, and giant planets (similar to the Solar gas giants). These estimations have been determined from early *Kepler* data corrected by Fressin et al. (2013) for false positives and incompleteness. Only planets with orbital period shorter than 85 days have been considered, as longer periods lead to a dramatic increase in the uncertainties due to the drop in the transit probability and detection rate. Figure from the cited article.

Space telescopes are not limited to measure size and mass of exoplanets: other measurable parameters include colour and brightness, which encode information about about their atmospheres. Finally, essential insights about an exoplanet can be inferred by studying its host star and determining its luminosity, spectral category, age, and

metallicity [Baraffe et al. (2010)].

1.4 Current knowledge and limits

Our knowledge of the structure and evolution of planets derives from the elaboration of planetary models. Such models are built employing the characterised properties of planetary interiors, and in particular the equation of state, phase diagram, electrical conductivity, and transport properties, as we have seen in Section 1.2. Such models are constrained to reproduce the observable properties we presented in Section 1.3. In this Section, we will focus on our current knowledge of rocky and icy giant planets, whose interior components will be studied in the work presented in this Thesis. We will highlight the limits of our knowledge and the outstanding questions, outlining the investigations that are needed to provide a critical contribution to their solution.

1.4.1 Rocky planets

Our understanding of the interior structure of rocky planets strongly relies on the vast amount of collected data relative to our Earth. Rocky planets' interiors consist of three layers: crust, mantle, and core, as shown in Figure 1.9. Crusts terminate with solid surfaces, characterised by geological features such such as craters and mountains. Mantles are primarily composed by magnesium oxide – iron oxide – silica (MgO–FeO–SiO_2) systems. Cores are made of iron (Fe) and possibly nickel (Ni). Depending on the thermodynamic conditions experienced inside each layer and on its precise composition, transitions between sub-layers may occur. The locations of the boundaries between different sub-layers are primarily determined by the phase transitions of the major components, so that the precise determination of their phase diagram is essential for a consistent interior modelling. As an example, the Earth's core is divided in a solid inner core and a liquid outer core, and the boundary is determined by the melting curve of iron. Compositional gradients also contribute to create such transitions.

Melting. Melting is a fundamental process that has driven the evolution history of terrestrial planets, as the differentiation which followed the accretion process happened by gravitational separation of liquids. Melting processes give important contributions to the planetary energy balance. For instance, the latent heat of crystallisation of iron, released at the inner core boundary, is a major energy source for the convective motions that generate the magnetic field via a dynamo action. Melting is also critical to describe giant impacts scenarios, as such impacts caused the formation of a magma ocean whose consequent freezing and re-solidification may have driven the planet's thermal history [Stixrude (2014); Millot et al. (2015)]. For these reasons, the precise characterisation of the melting curves of the major components of terrestrial planets is essential for our understanding of such processes.

Magnetic fields. The four Solar rocky planets exhibit a fairly diverse spectrum concerning the presence and structure of a magnetic field. One of them (the Earth) currently possesses an active dynamo, which takes place in the liquid, iron-rich outer core; there are evidences that two others (Mercury and Mars) possessed one in their early

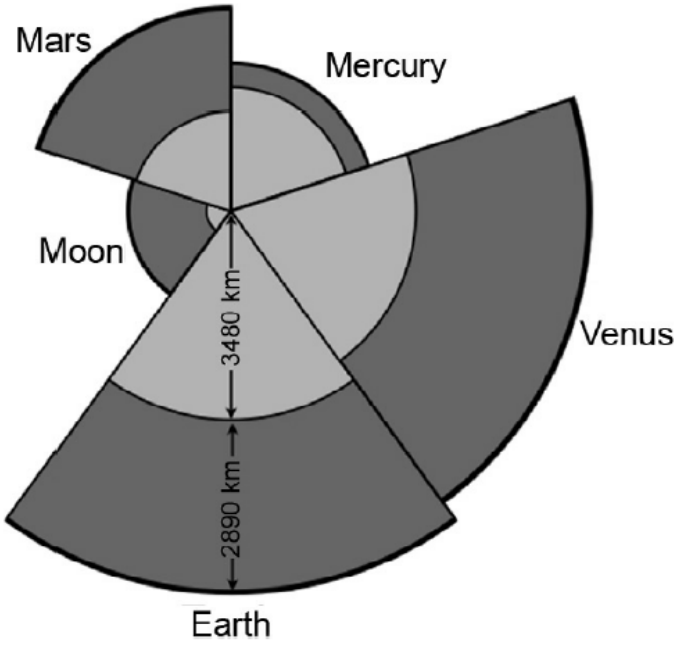

Figure 1.9 – Simplified internal structure of the four terrestrial planets and the Moon, consisting in an iron-rich core (light gray), a silicate mantle (dark gray), and a crust (black layer; not to scale). From Tosi et al. (2014).

history. As shown in Figure 1.6 and Figure 1.12 (a), the Earth exhibits a mostly dipolar and axisymmetric magnetic field. The dynamo-active region in the Earth interior is identified with the outer core, where iron is liquid and highly convecting [see Figure 1.12 (c)]. Therefore, our understanding of rocky planets' dynamos requires the thorough characterisation of the equation of state, transport properties, and electrical conductivity of warm dense iron. However, according to the current evolution models, the Earth (and, by extension, the other rocky planets) has experienced quite different conditions in the early stages of its life. The higher interior temperatures are compatible with the existence of a magma ocean, formed by molten silicate-rich minerals. Silicates, which are insulating at ambient conditions, undergo an insulating-to-conductor transition at megabar pressures and $\sim 10^3$ K temperatures, above their melting curves [Hicks et al. (2005); Millot et al. (2015); Bolis et al. (2016)]. Therefore, in the early stages of the Earth's life, a magnetic field could already exist, sustained by such conducting silicates [Soubiran and Militzer (2018)]. This hypothesis has to be confirmed via the study the conductivity of molten silicates at the thermodynamic conditions typical of the early Earth, which, up to now has been but poorly constrained. Such a study is essential not only with respect to our Earth, but also to understand if super-Earth exoplanets, which are more massive than the Earth and thus have hotter interiors, exhibit active dynamos with a magma ocean, rather than liquid iron, as dynamo-active component [Stanley and Glatzmaier (2010); Soubiran and Militzer (2018)].

Exoplanets. Many discovered exoplanets are rocky planets [Baraffe et al. (2008)]. The discovery of new exoplanets of this type is particularly exciting in the context of the quest for habitable planets. Within this context, a particular attention shall be

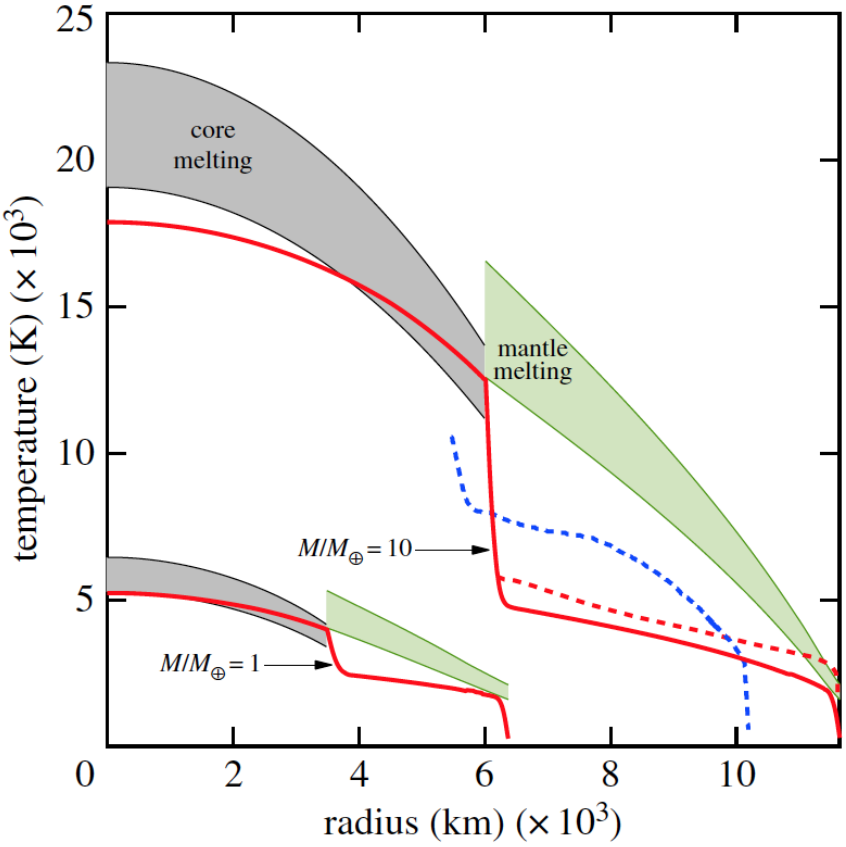

Figure 1.10 – Thermal models of super-Earth exoplanets. Temperature profiles (solid red) are compared to the silicate melting interval (green envelope), and the iron core melting interval (grey envelope). The Core-Mantle Boundary temperature is determined by the silicate melting curve. Also shown are results of simulations by Tackley et al. (2013) (10-Earth-masses exoplanet, red dashed curve) and by van den Berg et al. (2010) (8-Earth-masses exoplanet, blue dashed curve). From Stixrude (2014).

given to the identification of the conditions of habitability: we cite, between the many criteria, the presence of a magnetic field which acts as shield against harmful radiation, the presence of water on the surface, and surface temperature values compatible with the presence of liquid water. The existence of exoplanets with different thermodynamic conditions in their interiors induces the necessity of characterising the physical properties of their major components on a wider region of the phase diagram than that experienced inside Solar rocky planets. In particular, super-Earth exoplanets exhibit masses between $1-10$ Earth masses, so that their interiors experience higher pressures and temperatures. The melting curves of silicates are particularly important for the modelling of the thermal interior profile of super-Earths. Indeed, in such planets the Core–Mantle Boundary (CMB) temperature corresponds to the silicate melting temperature at the CMB pressure, as shown in Figure 1.10. In fact, the temperature jump at the CMB is much more steep than the silicate melting curve, but along a convecting zone, the temperature profile is adiabatic, less steep than the melting curve [Gaidos et al. (2010); Stixrude (2014)].

1.4.2 Icy giant planets

In our Solar System, the icy giant planets, Uranus and Neptune, are the last that have been visited by a space probe, the *Voyager 2*, which remains the only one to have done so – even if both NASA and ESA are studying the possibility of sending a second probe in the next years. The commonly assumed structure of icy giant planets includes an atmosphere (or envelope), an intermediate layer (the mantle), and possibly a rocky core. The atmospheres are primarily composed by hydrogen and helium in the gaseous form. The mantles contain mixtures of water (H_2O), methane (CH_4), and ammonia (NH_3) in the form of high-pressure "ices", mixed with hydrogen and helium. Though the precise composition of the mantles is not known, it is customarily assumed that carbon, nitrogen, and oxygen are present in their Solar abundance ratio C:N:O $\simeq$ 4:1:7 [Cameron (1973)], which gives a metallicity ratio $Z_{H_2O} : Z_{CH_4} : Z_{NH_3} \simeq 0.61{:}0.31{:}0.08$ [Bethkenhagen et al. (2013)]. The size and precise composition of the cores is difficult to infer, since the observable parameters, such as the gravitational moments J_2 and J_4 (see Table 1.3), provide information mainly on the external layers of the planets (see Figure 1.4).

Phase diagram of ices. The precise phase exhibited by icy mixtures in the mantle is still unclear, as their phase diagrams at the relevant thermodynamic conditions still has to be properly studied. As the behaviour of these mixtures is still far from having sufficiently been studied, interior models often use pure water as sole component [Redmer et al. (2011)]. Indeed, pure water has been thoroughly characterised at the relevant conditions [Knudson et al. (2012); Kimura et al. (2015); Millot et al. (2019)]. However, the validity and limits of this approximation depend on the role played by chemistry in determining the structural and transport properties of the icy mixtures. In particular, the presence of carbon and nitrogen atoms may strongly affect the phase diagram of the mixtures at moderate temperatures (a few 10^3 K) with respect to the phase diagram of pure water, by forming networks and clusters [Chau et al. (2011)]. Moreover, carbon- and nitrogen-bearing molecules have lower ionisation energies than water, which may affect the transport and electrical properties of the mixtures with respect to water. Therefore, investigating the accuracy of such an approximation requires the thorough study of the properties of the icy mixtures in the relevant range of thermodynamic conditions.

Thermal profiles. Uranus and Neptune possess analog structures but exhibit a dichotomy for what concerns their luminosities: indeed, Neptune's luminosity suggests an internal heat source, whereas the Uranus' low value indicates that it is essentially in thermal equilibrium with the radiation received from the Sun (see Table 1.4). The hypothesis that this dichotomy is due to giant impacts which occurred in the course of the history of the icy giants has been advanced [Podolak and Helled (2012)], which would also explain the strikingly high Uranus' axial tilt. In any case, the low luminosity exhibited by Uranus has questioned the validity of the general assumption that the planetary interior profiles are adiabatic. A non-adiabatic model including a thermal boundary layer (TBL) has been developed by Nettelmann et al. (2016) [see Figure 1.11) (b)] to fit the low luminosity value of Uranus. This model predicts temperatures 2 to 3 times higher than adiabatic models [Redmer et al. (2011); Bethkenhagen et al. (2017)]

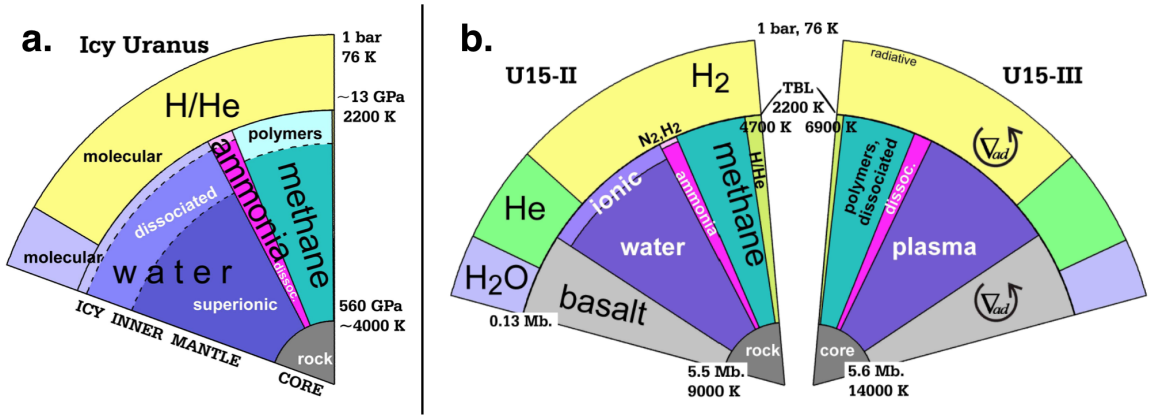

Figure 1.11 – Uranus interior models in comparison. **(a).** An adiabatic model by Bethkenhagen et al. (2017). **(b).** Two models by Nettelmann et al. (2016) including a thermal boundary layer between the mantle and the envelope to fit the available gravity and luminosity data. The temperature jumps are 2500 K and 4900 K for models U15-II and U15-III, respectively. Adapted from the sources.

in the deep interior of the planet: the predicted core temperatures reach $9000 - 14000$ K against the $4000 - 6000$ K in adiabatic profiles. As a consequence, there is a great uncertainty about the interior profile of Uranus. In particular, according to our knowledge of the phase diagram of water, methane, and ammonia, adiabatic models predict the mantle ices to be, depending on the depth, in the molecular, dissociated, and superionic phase – the latter being an exotic phase of water and ammonia in which oxygen or nitrogen atoms are arranged in a lattice whereas the hydrogen ions are free to diffuse between adjacent equilibrium positions. Models involving a TBL, on the contrary, predict that water exhibits mostly a plasma state in the mantles, whereas methane and ammonia are highly dissociated. As a consequence, the key properties of the icy mixtures shall be characterised on an extended range of conditions, encompassing a quite diverse set of phases (molecular, superionic, dissociated, plasma): this is one of the main challenges faced by the work presented in this Thesis.

Magnetic fields. Unlike the other Solar planets, the two icy giants exhibit non-dipolar, non-axisymmetric magnetic fields, as shown in Figure 1.12 (b). It is generally assumed that this peculiar structure is due to the fact that the dynamo-active region inside Uranus and Neptune is a thin outer shell. In particular, Stanley and Bloxham (2004) have proposed a dynamo model based on the geometry proposed by Podolak et al. (1991), according to which a thin dynamo-active shell consisting of conducting fluid "ices" surrounds a stably stratified internal layer in which convection is hindered by compositional gradients [see Figure 1.12 (d)]. Such a model was able to reproduce the field features (see Figure 1.6). An alternative picture has been provided by Nellis (2015, 2017). According to this picture, the dynamo-active shell is primarily made by hydrogen, the main component of the icy giants' atmospheres, which starts to exhibit an electrically conducting behaviour at around 100 GPa [at $r \simeq (0.8 - 0.9)R$, near the envelope-mantle boundary]. As in the model by Stanley and Bloxham (2004), the non-dipolar nature of the fields is explained by the fact that they originate in an outer shell. The non-axisymmetric geometry is probably explained by the fact

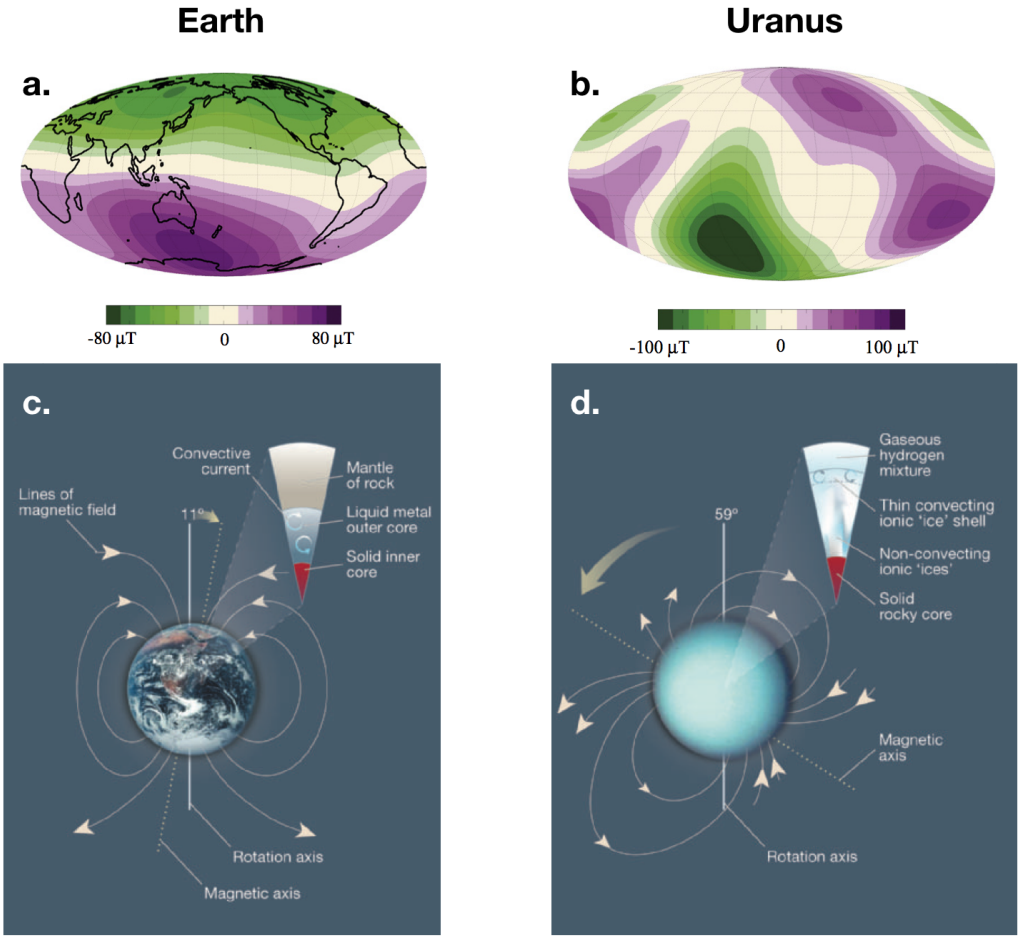

Figure 1.12 – Magnetic fields of the Earth and Uranus in comparison. **(a).** Radial magnetic field at the Earth surface. The colours represent field intensity; purple and green indicate the outward and inward direction, respectively. **(b).** Radial magnetic field at the 1-bar Uranus surface. **(c).** Field lines for the Earth magnetic field. The inset highlights the dynamo-active layer of the planetary interior: the liquid outer core. **(d).** Field lines for the Uranus magnetic field. The inset identifies a thin convecting icy shell as the dynamo-active layer in the planet's interior. (a) and (b) from Schubert and Soderlund (2011). (c) and (d) from Aurnou (2004). Magnetic field data shown in plot (a) are from Holme and Bloxham (1996). Those shown in plot (b) are elaborated by the working group *V-MOD: Geomagnetic Field Modeling* of the *International Association of Geomagnetism & Aeronomy* and are available online at `www.ngdc.noaa.gov/IAGA/vmod`.

that rotation and convection are but weakly coupled inside the icy giants, so that the dynamo action is free to "wander" with respect to the rotational axis. However, the relative contributions of metallic fluid hydrogen and of the water–methane–ammonia ices to the generation of a magnetic field are still unclear and the precise boundaries of such a dynamo-active shell still have to be determined. While the electrical properties of hydrogen have already been characterised at the conditions expected at the mantle-envelope boundary [Nellis (2017); Zaghoo and Silvera (2017); Celliers et al. (2018)], the behaviour of the electrical conductivity of the planetary ices in the mantles has to be studied on a wider range of conditions, encompassing the interior profiles predicted

by the different models.

Exoplanets. The study of the Solar icy giants is also useful to characterise similar discovered exoplanets. The latter can be included in the categories of mini-Neptunes (planets less massive than Neptune but with a similar, thick envelope made of H, He, and ices) and hot Neptunes (with a size similar to Neptune's, but orbiting closer to their stars) [Dong et al. (2018)]. As we have seen in Figure 1.8, exoplanets with a size close to Neptune's are fairly common. As a consequence, there is a need to characterise the physical properties of the icy mixtures on a wider set of conditions, in order to cover those typical of the interiors of those types of exoplanets.

1.5 Conclusions

In this Chapter we have summarised the observable data for Solar and extrasolar planets, presented the foundations of the models that describe their structure and evolution, and reviewed our current knowledge of the interiors of terrestrial and icy giant planets (the object of this Thesis). We explained how our Earth represents a fundamental prototype for planetary science, since we dispose of a huge amount of diverse data about its interior, and also how all the Solar planets – for which we are continuing to acquire fundamental data, including about their interiors – are used as prototype for exoplanets, for which we only dispose of very basic data.

We have seen that models of planetary interior structures, magnetic field generation, and evolution have to reproduce the measurements of the planetary properties and are based on our characterisation of the physical behaviour of the interiors' components. We have seen that the key components that still require to be characterised are, in particular, silica and silicate minerals for rocky planets, and mixtures of water, methane, and ammonia for icy giant planets. Moreover, we have shown that, in order to develop and improve planetary models, it is essential to gain the precise knowledge of:

(i) the equations of state and phase diagrams of the components of the planetary interiors at the thermodynamic conditions of interest – pressures of some megabar and temperatures of a few thousand Kelvin;

(ii) their transport properties, such as the thermal conductivity;

(iii) their optical and electrical properties, and in particular the electrical conductivity.

Studying these properties requires to reproduce, in simulations or in the laboratory, the extreme conditions experienced in planetary interiors and characterise the behaviour of matter at such conditions. In the next Chapter, we will overview the challenges faced in this approach and the techniques that can be employed.

Chapter 2

Generating and characterising extreme thermodynamic conditions

In Chapter 1, we have introduced the domain of planetary science and stressed how the study of the behaviour of the components of planetary interiors at the relevant thermodynamic conditions can give inputs that contribute to address outstanding questions concerning the formation, evolution, and structure of solar and extrasolar planets.

In this Chapter, we will describe how such extreme thermodynamic states – included in the domain called Warm Dense Matter (WDM) – can be reproduced and characterised in the laboratory. The fundamental tools employed in the work presented in this Thesis will be presented. First, we will explain why the study of WDM conditions is challenging. We will then introduce the experimental methods that can be employed to reach those conditions. We will focus on dynamic methods, with particular attention to the physics of shock waves, which is the method we mostly employed. We will then describe how shock waves can be generated using high-power lasers and how we can measure the equation of state of the sample under study using this methods. The typical diagnostics and tools used to this aim will be presented at the end of the Chapter.

Contents

2.1 A challenging regime

THE THERMODYNAMIC CONDITIONS existing in the planetary interiors belong to a peculiar regime called Warm Dense Matter (WDM) regime. The WDM domain, which encompasses densities from 10^{-2} to 10 g/cm^3 and temperatures from 10^3 to 10^5 Kelvin, is included in a more vast one, called High Energy Density (HED), that virtually includes all the thermodynamic conditions characterised by partial ionisation and by pressures above 10 GPa [Paul Drake (2006)].

WDM is really challenging to characterise from both a theoretical and an experimental point of view. Theoretical models are complicated by the fact that, at such conditions, densities are generally high enough for quantum degeneracy to play an important role, while temperatures are too high for a condensed matter description to be valid but, at the same time, too low to allow a classical plasma description. Additionally, for most of the molecular compounds of interest, a complex chemical behaviour occurs, due to the simultaneous effects of a high density and of an intermediate temperature. As a consequence, there is no well-established theory covering WDM conditions, which remain intermediate between the domains of classical plasmas and condensed matter. On the experimental point of view, the study of the WDM regime faces two major challenges: the generation of such extreme conditions in the laboratory and its characterisation with the proper diagnostics and techniques.

2.1.1 Quantum degeneracy

The behaviour of matter at sufficiently high densities and low temperatures is influenced by the effect of the Pauli exclusion principle on electrons. Indeed, since electrons are Fermions, they cannot occupy the same quantum state. As a consequence, if their quantum wavefunctions are significantly overlapped in space so that they share the same position, they are forced to occupy distinct energy states. Due to this quantum repulsion mechanism electrons can reach high energies even if temperature is very low. This scenario takes place when the thermal de Broglie wavelength of the electrons' wavefunctions (λ_{dB}, defined in equation 2.1) is comparable or greater than the distance between neighbouring electrons (d_e, defined in 2.2): $\lambda_{\mathrm{dB}} \geq d_n$. The de Broglie

wavelength and neighbour electron distance are defined as follows:

$$\lambda_{\mathrm{dB}} = \frac{h}{(2\pi m_e k_B T)^{1/2}}, \tag{2.1}$$

$$d_e = \left(\frac{3}{4\pi n_e}\right)^{1/3}, \tag{2.2}$$

where T is the temperature and n_e is the electronic density.

In the case $\lambda_{\mathrm{dB}} \geq d_e$, electrons pile from a zero-energy state up to a state of energy ϵ_F (the Fermi energy) expressed in equation 2.3 as a function of electron density. The electronic energy distribution is stepwise at $T = 0$ K; as temperature increases, it becomes smoother. With the increase of temperature, quantum effects become less important and eventually become negligible for $T \gg \epsilon_F/k_B$.

Quantum degeneracy is associated to a pressure p_F, described in equation 2.4, due to the fact that the energy of a degenerate system increases with compression, as it is evident by looking at equation 2.3. In the WDM regime, matter is typically strongly degenerate, so that the Fermi contribution to pressure is comparable or higher than the thermal one. Fermi energy and pressure are defined as follows:

$$\epsilon_F = \frac{h^2}{2m_e}\left(\frac{3}{8\pi}n_e\right)^{2/3}, \tag{2.3}$$

$$p_F = \frac{2}{5}n_e\epsilon_F \propto n_e^{5/3}. \tag{2.4}$$

An alternative and equivalent criterion to the geometric criterion $\lambda_{\mathrm{dB}} \gg d$ to define the quantum degeneracy of a state makes use of the temperature T and of the Fermi temperature defined as $T_F = \epsilon_F/k_B$. A *degeneracy parameter* is defined as $\theta = T/T_F$. According to such a criterion, matter is degenerate when $\theta \ll 1$.

2.1.2 Coupling

Charged particles in a plasma are subject at the same time to thermal motion and to Coulomb forces. For the ideal plasma theory to be valid, the first must dominate over the latter, so that the particle positions are essentially non correlated. On the contrary, if the Coulomb interaction is comparable to or dominates over thermal motion, the medium is partially or strongly *coupled* and the ideal plasma theory fails. For a quantitative determination of the behaviour, it is useful to compare the mean Coulomb potential $U_C \propto n^{-1/3}$ (where $n = n_e + n_i$ is the particle density of the plasma, treated for the sake of simplicity as a one-component medium instead of considering the electronic and ionic densities n_e and n_i) and the mean thermal energy $E_{\mathrm{th}} \propto T$ experienced by a particle. Their ratio

$$\Gamma = \frac{U_C}{E_{\mathrm{th}}} \propto n^{-1/3}T^{-1} \tag{2.5}$$

is called *coupling parameter* of the ionised medium. The condition for the validity of ideal plasma theory is $\Gamma \ll 1$ and is met at low densities and high temperatures. On the contrary, WDM states are typically partially ($\Gamma \sim 1$) or strongly ($\Gamma \gg 1$) coupled.

2.1.3 A complex phase diagram

We have seen that the typical scenario of a WDM state involves the simultaneous effect of quantum degeneracy and Coulomb coupling. This complexity is at the origin of the richness of the phase diagram of several materials in the WDM regime.

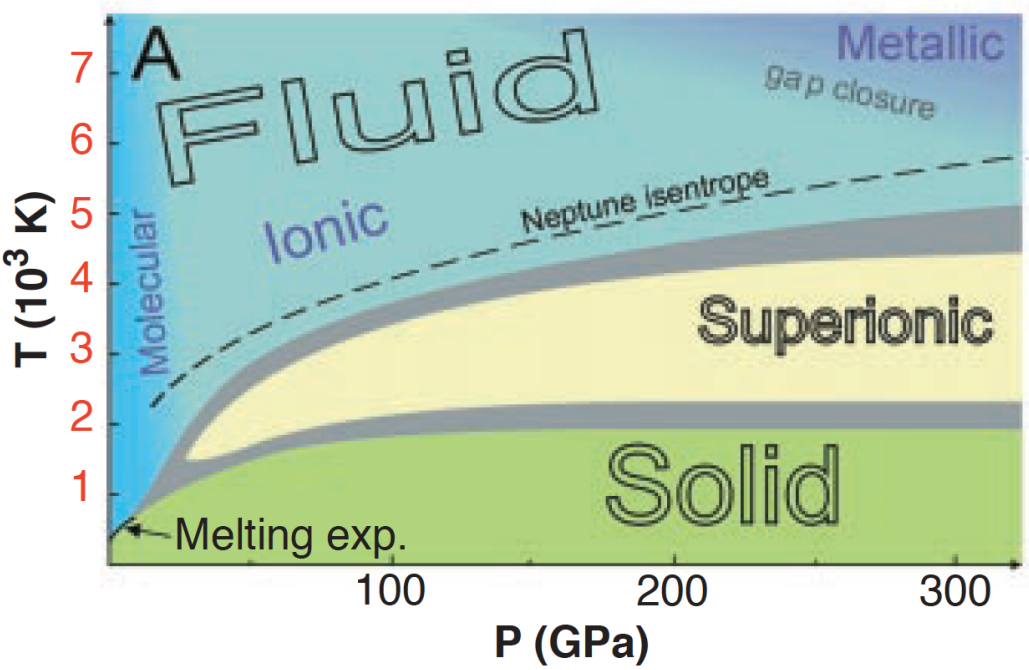

Figure 2.1 – Phase diagram of water at WDM conditions predicted in the pioneering work by Cavazzoni et al. (1999). Despite its stoichiometric simplicity, pure water exhibits a rich phase diagram including a superionic phase between 2000 and 4000 K, a dissociated ionic phase, and an electrically-conducting, metallic-like phase at temperatures around 6000 K. The gray regions indicate the conditions in which the stable phase was not clearly determined.

Complex bonding configurations are directly due to the characteristic temperatures of the order of some thousand Kelvin, high enough only for partial ionisation and dissociation. Therefore, one has to deal with the coexistence of lattices with different structures, clusters, molecules, atoms, and ions, present in different proportions at different thermodynamic conditions. A particular attention is to be paid to the electrical properties, both for the physical interest and because conductivity is a key parameter of the dynamo mechanism (see Chapter 1.2.2). Most materials of interest for planetary science, such as silica and water, are electrically insulating at standard conditions, but gradually become conducting with the increase of pressure and temperature [Millot et al. (2015); French and Redmer (2017)], as reported in the phase diagram of pure water predicted in the early work by Cavazzoni et al. (1999), shown in Figure 2.1. Moreover, an exotic superionic phase exists at high pressures and relatively low temperatures in water (see Figure 2.1), ammonia, and water–ammonia mixtures [Cavazzoni et al. (1999); Bethkenhagen et al. (2015)]. In this phase, the oxygen or nitrogen atoms, in the case of water or ammonia, respectively, are arranged in a lattice, whereas protons are free to diffuse by jumping between different sites in the lattice. The protonic contribution can therefore strongly influence the electrical conductivity.

2.2 How to generate Warm Dense Matter conditions

Warm Dense Matter (WDM) conditions can be generated in the laboratory via different approaches. The most common strategies to achieve high pressure conditions can be divided into two categories: *static* and *dynamic methods*.

2.2.1 Static methods

In static methods, a high pressure is obtained by constantly applying a compressional force, while temperature can be increased via a continuous heat source. The main advantage of static compression lies in the possibility of maintaining the WDM state for a considerably long time (some minutes to some hours), which allows long acquisition times for diagnostics. The static compression of a sample volume is achieved via an external mechanical force. A first possible approach involves the use of a press. An example of this approach is the *Paris-Edinburgh press*, which allows to compress a sample up to around 30 GPa (0.3 Mbar) [Loveday et al. (1996)].

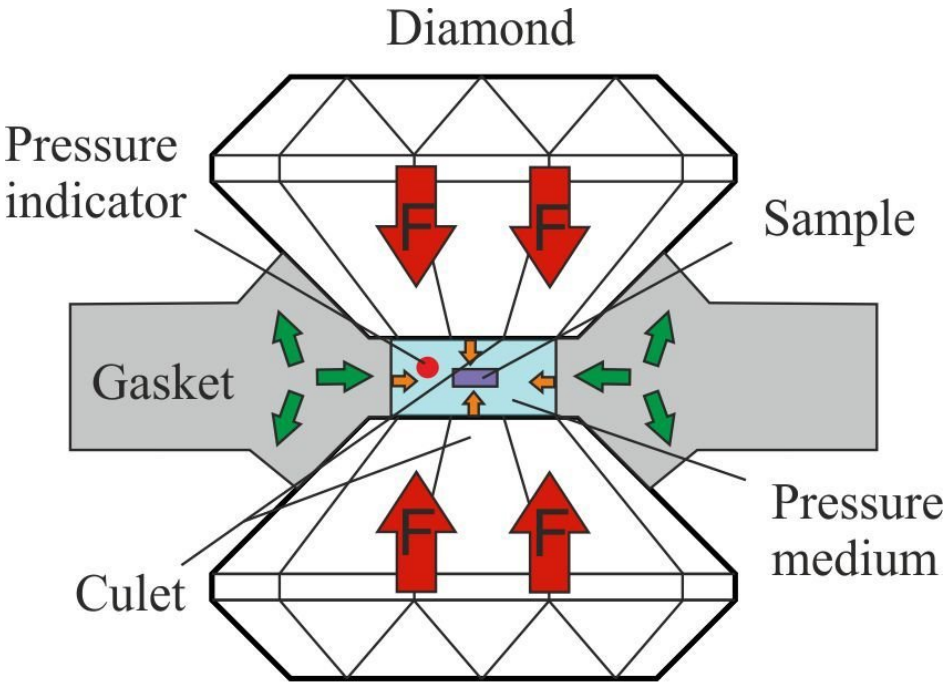

Figure 2.2 – Simplified scheme of a Diamond Anvil Cell (DAC). The coloured arrows indicate the directions in which the force of the corresponding element is exercised. Adapted from Waeselmann (2012).

An alternative approach to compress samples of a reduced volume up to higher pressures makes use of *Diamond Anvil Cells* (DAC), whose basic structure is sketched in Figure 2.2. The sample, contained in a pressure-transmitting medium, is placed between the culets of two opposite diamond anvils. A pierced gasket is also placed between the diamonds. A pressure witness may be placed next to the sample under

study. Ruby, whose fluorescence spectral profile depends on pressure and has been precisely calibrated [Mao et al. (1986); Rekhi et al. (1999)], is often used for this purpose. The cell is then mounted and placed in a membrane which pressurises it. Temperature can be increased up to a few thousand Kelvin by laser heating [Kimura et al. (2014)] or resistive heating [Ninet et al. (2012)]. Visible and X-ray diagnostics have access to the sample through the transparent diamond anvils and can probe it for long acquisition times, which represents a key advantage compared to dynamic methods, where the conditions to be probed are achieved for a short amount of time. However, static compression via a DAC is limited to pressures of a few megabar. Experiments over 4 Mbar are rare, even if a recent work by Jenei et al. (2018) managed to reach 5 Mbar at ambient temperature employing toroidal single-crystal diamond anvils. To obtain high-pressure / high-temperature conditions, the only possible approach is dynamic compression.

2.2.2 Dynamic methods

In dynamic methods, high pressures and temperatures are obtained by generating a compression wave which propagates through the sample. In most cases, this compression wave is a shock wave, *i.e.* a perturbation causing an abrupt change in the thermodynamic quantities and propagating at a supersonic velocity. Alternative techniques involve the generation of an adiabatic compression, without the formation of a shock. The lifetime of the generated WDM state is determined by the employed tool, varying from the nanosecond to the second scale. Dynamic methods represent the only possible approach to reach very high pressures well above 1 Mbar and very high temperatures up to 10^5 K. Nevertheless, the thermodynamic conditions created are transient, which may preclude the possibility of studying long-scale phenomena and limits the choice of diagnostics.

Several techniques have been developed allowing to span different pressure scales on a very diverse set of time scales, from the millisecond to the nanosecond range. This variability in the time scales allows to characterise a vast range of phenomena originating from the response of the sample to compression, such as elastic and plastic compression, phase transitions, and adiabatic releases after the shock loading. We will now overview the principles and the limits of each technique.

Explosions and gas-guns. Compression by explosion-generated shocks has been the first dynamic method employed in history. Explosions, which can have a chemical or nuclear source, generate a shock wave which propagates through a medium towards the sample. The typical time scale of the process is the microsecond range, even if longer scales up to the millisecond can be addressed. The maximum available pressure is up to several megabar for chemical explosives and considerably high values, up to a few gigabar, for nuclear explosives, which, however, have been banned in 1996 by the *Comprehensive Nuclear-Test-Ban Treaty* [www.ctbto.org]. The explosion-driven method has been improved with the use of a gas-gun. The detonation of an explosive actions a piston that compresses a gas chamber, which is separated by a valve from a metallic plate. When the gas pressure exceeds the breaking point of the valve, the plate is fired towards the target, and the impact generates a shock wave. Such an approach allows to precisely control the impact velocity, and thus the generated pressure, as well

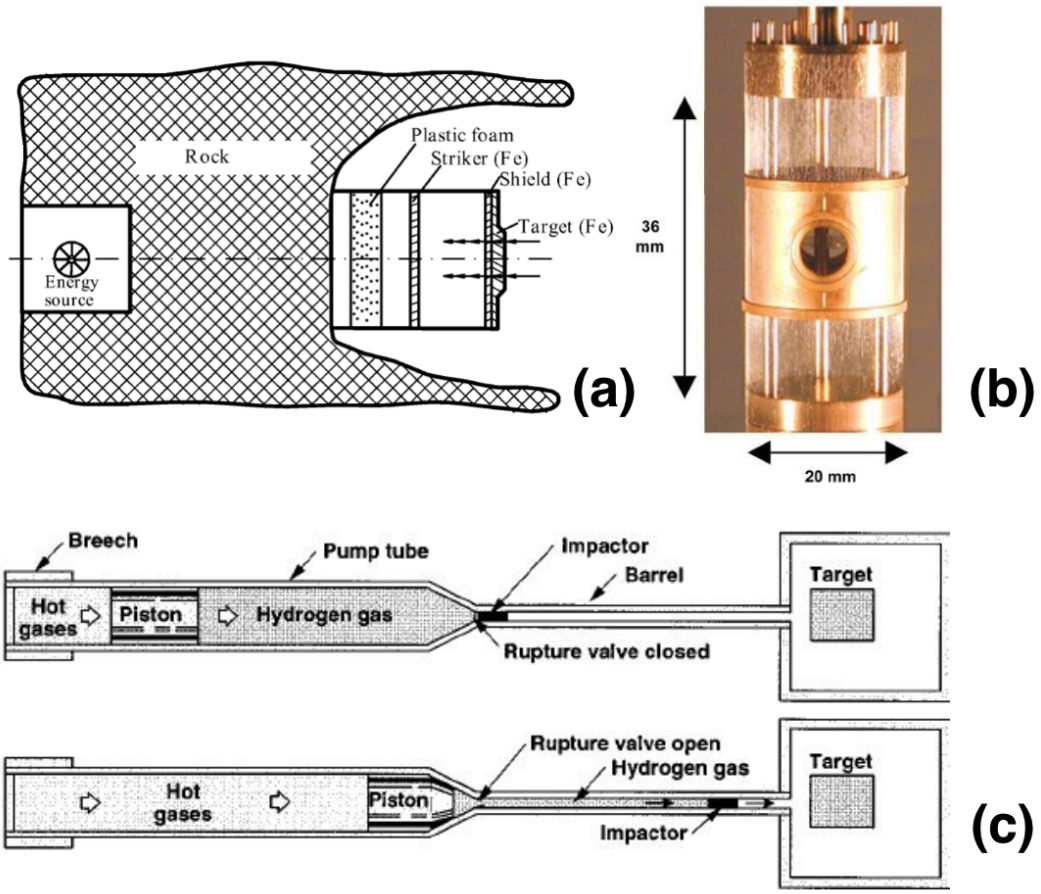

Figure 2.3 – Different methods for generating shock waves. **(a).** Scheme for compression of iron using a nuclear explosion. Adapted from Trunin (1994a). **(b).** Z-pinch target and wire array. Adapted from Cuneo et al. (2012). **(c).** Scheme of a gas-gun, showing the piston compressing the gas chamber (top) and the impactor flying towards the target (bottom). Adapted from Nellis et al. (1999).

as to channel the force generated by the explosion in a one-dimensional tube, which increases the maximum available pressures up to some tens of megabar. The time scale of the compression methods is also in the microsecond range.

Z pinches. High magnetic pressures can be obtained from very intense currents. In a Z machine, such that at the *Sandia National Laboratories (Albuquerque, New Mexico, USA)*, a very high electric current (20 MA at Sandia) is produced for some nanoseconds in a cylindrical array of metallic wires. The high magnetic field generated (10 MG at Sandia) can be used to fire a metal plate outwards at high velocity. The plate is directed with the target and the shock is generated by the impact [Lemke et al. (2005)]. An alternative approach consists in placing the target along the cylindrical axis. The high current ionises the metallic wires and the generated plasma is compressed towards the cylindrical axis by the Lorentz force (Z-pinch), reaching high pressures and temperatures and emitting hard X-rays which are absorbed by the target surface generating a shock. The interest of this method is due to the fact that the compression time scale is reduced with respect to explosion-based approaches – it is lower by an order of

magnitude, around 100 ns.

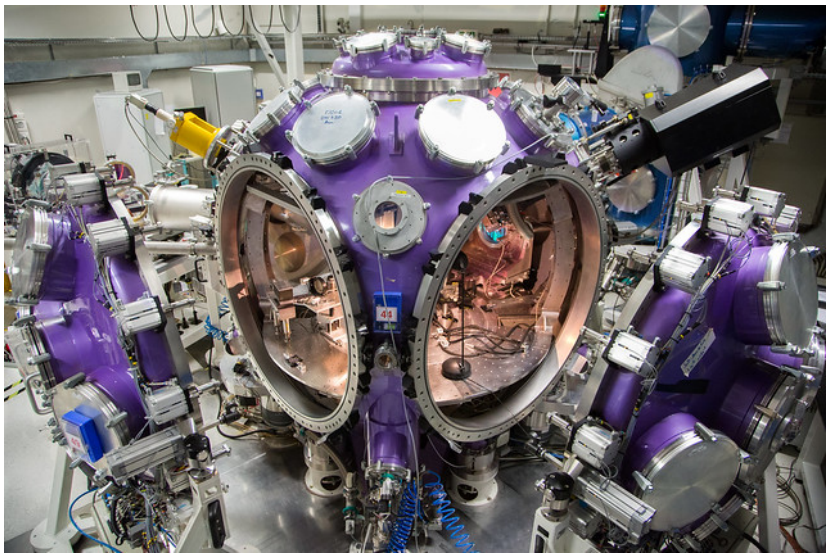

Figure 2.4 – Experimental hall and interaction chamber of the LULI2000 facility (Palaiseau, France). © *École polytechnique* – J.Barande.

High-power lasers. In the work described in this Thesis, shocks are generated using high-power lasers. Within this approach, a laser pulse delivering $10 - 10^6$ J in a nanosecond time scale is focused onto a multi-layered target and ionises its surface, which is ablated and generates a plasma corona, while a shock wave is generated and propagates through the sample (details are provided in Section 2.4). The scale of reachable pressures strongly depends on the laser intensity. Today, only a few facilities in the world, such as the Laser Mégajoule (LMJ – Le Barp, France) and the National Ignition Facility (NIF – Livermore, California, USA) can provide megajoule energies and are thus capable of compressing materials up to some hundreds of megabar. Mid-size facilities are more common but are able to deliver energies of some kilojoules, which is sufficient to compress matter up to some tenths of megabar. Examples of mid-size facilities are LULI2000 (Palaiseau, France) and GEKKO XII (Suita, Japan), which have both been used in the context of the experimental work of this Thesis. Figure 2.4 shows the experimental hall and interaction chamber of LULI2000. The compression time scale achieved by this technique is considerably lower than the other approaches: $1 - 10$ ns.

2.3 On shock waves

In the experimental work described in this Thesis, we have extensively made use of the shock-compression technique to generate the thermodynamic conditions of interest in the samples under study. In this Section, we will first describe how a shock wave forms from a non-linear hydrodynamic perturbation. We will then present the structure and properties of shock waves, introducing the fundamental laws by which they are governed: the Rankine–Hugoniot relations. Besides, we will explain how the equation

of state of the shocked sample can be measured and discuss the interest of allowing the propagation of sustained and decaying shocks.

2.3.1 Hydrodynamic perturbations

To describe the generation process of a shock wave, we begin by recalling the principles of linear hydrodynamics before introducing the concept of non-linear perturbations, which are at the base of the process of formation of a shock. The motion of a fluid is governed by the continuity equation (stating the conservation of mass) and the Euler's equation of motion (expressing the rate of change of momentum). We will consider one-dimensional motion for the sake of simplicity:

$$\frac{\partial \rho}{\partial t} + \frac{\partial}{\partial x}(\rho u) = 0, \tag{2.6}$$

$$\rho\left(\frac{\partial u}{\partial t} + u\frac{\partial u}{\partial x}\right) = -\frac{\partial P}{\partial x}, \tag{2.7}$$

where x and t are the space and time coordinates, respectively, ρ is the density of the fluid, u its velocity, and P its pressure.

The description of linear hydrodynamics is valid in the case perturbations to the equilibrium state are small and the variables can be thus written as:

$$u = 0 + u_1(x), \tag{2.8}$$

$$\rho = \rho_0 + \rho_1(x), \tag{2.9}$$

$$P = P_0 + P_1(x), \tag{2.10}$$

where $\rho_1(x) \ll \rho_0$, $P_1(x) \ll P_0$, and the fluid is taken at rest ($u_0 = 0$). $u_1(x)$ is small in a sense that will be clarified later. By applying the relations 2.8–2.10, equations 2.6 and 2.7 can be developed to the first order in the form:

$$\frac{\partial \rho_1}{\partial t} = -\rho_0 \frac{\partial u_1}{\partial x}, \tag{2.11}$$

$$\rho_0 \frac{\partial u_1}{\partial t} = -\frac{\partial P_1}{\partial x}. \tag{2.12}$$

Finally, a wave equation can be obtained composing equations 2.11 and 2.12:

$$\frac{\partial^2 \rho_1}{\partial t^2} = c_s^2 \frac{\partial^2 \rho_1}{\partial x^2}, \tag{2.13}$$

where c_s is the speed of sound in the material and depends to the pressure – density relation along an adiabatic path:

$$c_s = \left(\frac{\partial P}{\partial \rho}\right)_S^{1/2}. \tag{2.14}$$

Perturbations are considered as adiabatic since they are assumed to propagate faster than the typical time scale of heat conduction in the medium. Equation 2.13 introduces a velocity scale that allows us to clearly define what we meant when we required that velocity perturbations should be small: this condition now reads $u_1(x) \ll c_s$.

This means that the motion of the fluid mass is much slower than the propagation velocity of the disturbance. The general solution of equation 2.13 has the form $\rho_1 = f_+(x-c_s t)+f_-(x+c_s t)$. The functions $f_+(x-c_s t)$ and $f_-(x+c_s t)$ describe two arbitrary perturbations propagating at speed c_s towards the right and the left, respectively. It should be noticed that the perturbations propagate without changing their shape or amplitude.

What happens if perturbations are not small compared to the equilibrium state variables? In this case, neither the linear development of equations 2.6 and 2.7 nor the final result we obtained (that perturbations propagate without changing shape or amplitude) are valid anymore. A description of a perturbation of arbitrary, but finite, amplitude is thus needed. Let us continue to assume that the motion is isentropic, so that the adiabatic relation between pressure and density is still valid, and that there is a univocal relation between the mass motion u and the thermodynamic variables: $u = u(\rho)$. We want to study the trajectory of a point which keeps the same density over time, that is, we consider $\rho_i = \rho(x_i, t_i)$ and follow the motion of the point x_ρ in which $\rho = \rho_i$. Let us call $x_\rho(t; \rho_i)$ the law of this motion. Using the hypothesis we made, we can rewrite equation 2.6 as

$$\frac{\partial \rho}{\partial t} + \left(u + \rho \frac{\partial u}{\partial \rho} \right) \frac{\partial \rho}{\partial x} = 0. \tag{2.15}$$

This means that x_ρ moves with a velocity

$$c_\rho = u + \rho \frac{\partial u}{\partial \rho}. \tag{2.16}$$

An analogous treatment can be applied to equation 2.7 to study the motion of a point which keeps the same mass velocity over time (we consider $u_i = u(x_i, t_i)$ and follow the motion of x_u, the point in which $u = u_i$). In this case, we find that x_u moves with a velocity

$$c_u = u + \frac{1}{\rho} \frac{\partial P}{\partial u}. \tag{2.17}$$

Since we made the hypothesis that there is a univocal relation between mass velocity and density, x_ρ and x_u are in reality the same point, and we have thus the identity $c_\rho = c_u$, which, applied to equation 2.16 and 2.17 reads

$$\frac{\partial u}{\partial \rho} = \pm \frac{c_s(\rho)}{\rho}, \tag{2.18}$$

where

$$c_s(\rho) = \left[\frac{\partial P(\rho)}{\partial \rho} \right]_S^{1/2} \tag{2.19}$$

is the local speed of sound, which now, in the case of arbitrary perturbations, depends on density. This has the crucial consequence that the point x_ρ propagates with a velocity

$$c_\rho = u \pm c_s(\rho), \tag{2.20}$$

which means that the propagation velocity of a point keeping information on a certain density depends on the value of that density.

2.3.2 Formation and structure of a shock wave

Let us now consider the physical meaning of equation 2.20 and its consequences. To do this, we consider a spatial density profile $\rho(x)$, consisting in a finite perturbation to an equilibrium state ρ_0. We study the motion of two points, $x_\rho(t;\rho_A)$ and $x_\rho(t;\rho_B)$, initially at the positions x_A and x_B, carrying the position of the densities ρ_A and ρ_B, respectively. A schematic picture for $t = 0$ is provided in Figure 2.5.

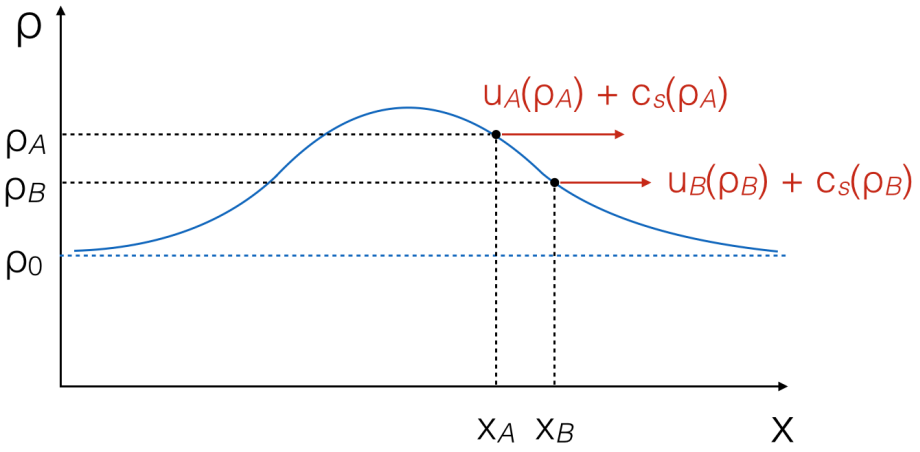

Figure 2.5 – Arbitrary finite-amplitude density perturbation to an equilibrium state ρ_0.

According to equation 2.20, if we make the hypothesis that the motion is exclusively towards the right, the points $x_\rho(t;\rho_A)$ and $x_\rho(t;\rho_B)$ will propagate with the velocities $c_\rho(\rho_A) = u_A(\rho_A) + c_s(\rho_A)$ and $c_\rho(\rho_B) = u_B(\rho_B) + c_s(\rho_B)$, respectively, which are in general different. For a density profile decreasing in x ($\rho_A > \rho_B$) and a perturbation propagating towards the right, as the case we are considering, there are two possibilities:

(i) if $c_\rho(\rho_A) < c_\rho(\rho_B)$, the spatial density profile becomes smoother over time;

(ii) if $c_\rho(\rho_A) > c_\rho(\rho_B)$, the spatial density profile steepens over time, until a time t_d such that $x_\rho(t_d;\rho_A) = x_\rho(t;\rho_B)$, where the theory predicts two different densities for a given position, which is physically impossible: in reality, a discontinuity in the state variable thus appears.

To discriminate between the two cases, we have to study the derivative of c_ρ with respect to ρ. Using equations 2.20 and 2.18, this reads

$$\frac{dc_\rho}{d\rho} = \frac{c_s}{\rho} + \frac{\partial c_s}{\partial \rho}. \tag{2.21}$$

Now, the first term on the right hand side of equation 2.21 is positive (as we assumed that the perturbation is propagating towards the right). The second term (thus the global sign of the derivative) depends on the material. In a perfect gas,

$$\frac{dc_\rho}{d\rho} = \frac{\gamma+1}{2}\frac{c_s}{\rho} > 0, \tag{2.22}$$

where $\gamma = (N+2)/N$ is the adiabatic index of the gas and $N = 3$, 5, or 6 for a monoatomic, diatomic, or polyatomic gas, respectively. Even in liquids and solids, the most common case is case (ii), in which a greater density propagates at greater velocity.

Case (ii) is depicted in Figure 2.6, which shows the evolution of the spatial density profile for three times. At $t = t_1$, the profile is the initial one, already shown in Figure 2.5. At $t = t_2$, the distance between the two points $x_\rho(t; \rho_A)$ and $x_\rho(t; \rho_B)$ has decreased, and the decreasing part of the density profile has become steeper. On the contrary, the increasing part (on the left) has become smoother for the same physical reason. At $t = t_3$, the two points occupy the same position: t_3 is the critical t_d for which the density discontinuity appears. When the density profile starts approaching the discontinuity, dissipation phenomena begin to play a non negligible role and the isentropic hypothesis is no longer valid. The physical scenario is the generation of a thin zone (of the order of some mean free paths) where density (as well as the other hydro- and thermodynamic variables) increases from the equilibrium value to a higher one. This phenomenon is called a *shock wave* and the thin transition zone is called a *shock front*.

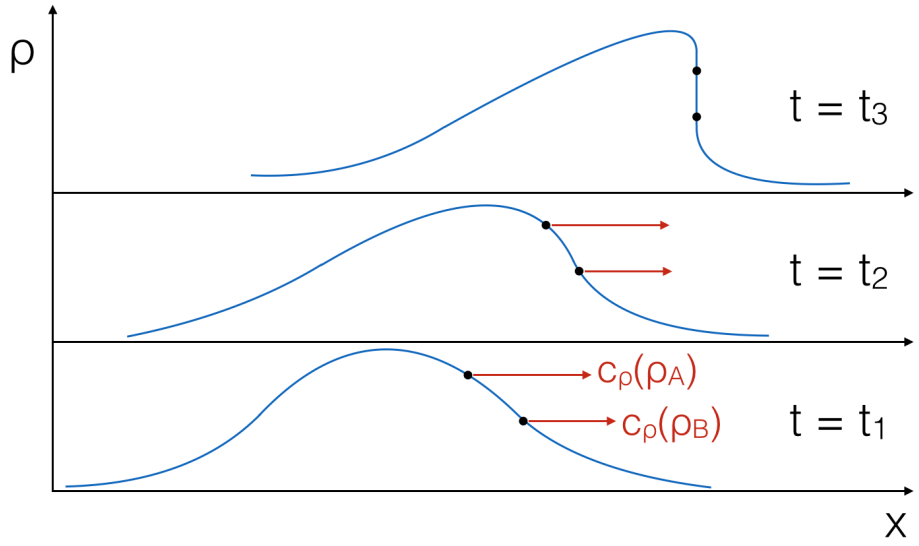

Figure 2.6 – Temporal evolution of the density perturbation depicted in Figure 2.5. The density profile at the times $t_1 < t_2 < t_3$ are shown.

2.3.3 The Rankine–Hugoniot relations

Now that we have seen how a shock wave forms in a medium, we want to know about the relation between the state variables before and after the medium has been loaded by a shock.

With this goal in mind, we consider a particular scenario in which a steady and plain shock wave loads a material at rest occupying a cylindrical volume. The volume is thus divided into an unperturbed region and a loaded region. Let U_s be the velocity of the shock front (or *shock velocity*). Because of mass conservation, if the shock loads the material to a higher density than the unperturbed one, then the loaded mass must have a non-zero material velocity. Until now, we have called u such a velocity. However, in the context of shock compression, the material velocity is called U_p as it is sometimes referred to as the *particle velocity*. From now on, we will use this notation. Figure 2.7

shows the scenario we just described of a shock wave loading a material contained in a cylindrical volume.

The density, pressure, and internal energy density of the shocked state (ρ_1, P_1, and e_1, respectively) are linked to those of the initial state (ρ_0, P_0, and e_0) by three equations stating the conservation of mass, momentum, and energy through the shock front. These equations are called Rankine–Hugoniot relations, to signify the importance of their work in building the foundations of the physics of shock waves[Rankine (1870); Hugoniot (1887)]. These relations can be written in the form:

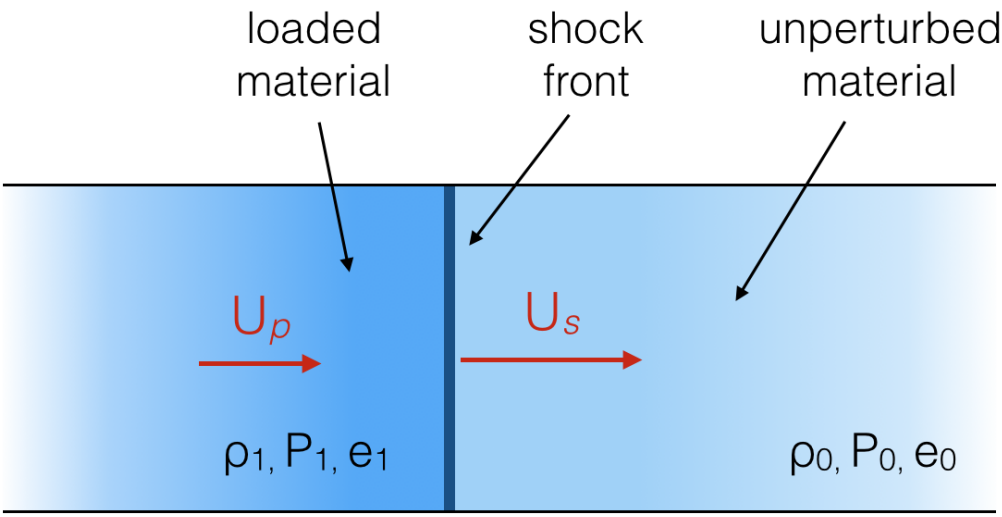

Figure 2.7 – Scheme of the propagation of a shock wave in the frame of reference of the unperturbed material. U_s is the shock velocity, U_p is the material velocity behind the shock.

$$\rho_1 = \rho_0 \frac{U_s}{U_s - U_p}, \tag{2.23}$$

$$P_1 = P_0 + \rho_0 U_s U_p, \tag{2.24}$$

$$e_1 = e_0 + \frac{1}{2}(P_1 + P_0)\left(\frac{1}{\rho_0} - \frac{1}{\rho_1}\right), \tag{2.25}$$

and depend on U_s and U_p.

Equations 2.23–2.25 have an important consequence: if a material in an initial state 0 is compressed through a single shock loading, the pressure reached will be uniquely determined by the density reached after compression and the initial state. This property can be expressed in the following form:

$$P = P_H(\rho; \rho_0, P_0), \tag{2.26}$$

where the function $P_H(\rho; \rho_0, P_0)$ – which can be alternatively written as $H(\rho, P; \rho_0, P_0) = 0$ – is called *Hugoniot curve* of the material for the initial state 0. It can be noticed that temperature, as a state variable, does not appear in equations 2.23–2.25. It should also be noticed that H is a function of only two out of the three state variables of the initial state, as the third depends on the other two via the *equation of state* of the material, in this case in the form $e = e(\rho, P)$.

To understand the physical meaning and the properties of the Hugoniot curve, it is useful to see some concrete examples. First, let us consider a perfect gas, whose equation of state has the very simple form

$$e(\rho, P) = \frac{1}{\gamma - 1}\frac{P}{\rho}. \tag{2.27}$$

It can be proved by inserting equation 2.27 into equation 2.25 that the Hugoniot curve of a perfect gas is

$$P_H(\rho; \rho_0, P_0) = P_0 \frac{(\gamma+1)\rho - (\gamma-1)\rho_0}{(\gamma+1)\rho_0 - (\gamma-1)\rho}. \tag{2.28}$$

The curve in equation 2.28 for a monoatomic gas is plotted in Figure 2.8 and compared to the adiabatic curve

$$P_{\mathrm{ad}}(\rho; \rho_0, P_0) = P_0 \left(\frac{\rho}{\rho_0}\right)^{\gamma}. \tag{2.29}$$

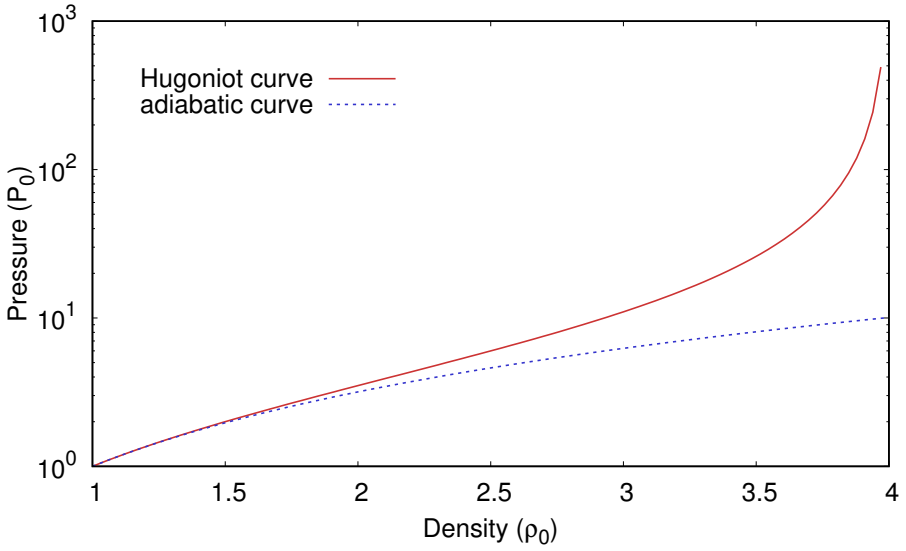

Figure 2.8 – Hugoniot and adiabatic curve for a perfect monoatomic gas. Pressure and density are expressed in units corresponding to the initial values P_0 and ρ_0, respectively.

By analysing equations 2.28 and 2.29 and looking at Figure 2.8, one can deduce several properties of the Hugoniot curves:

(i) for any $\rho > \rho_0$, the pressure along the Hugoniot curve is greater than along the adiabatic (this implies that the passage of two subsequent shocks cannot bring the material to a state which lies along the Hugoniot curve);

(ii) for $\rho \to \rho_0^+$, the Hugoniot and the adiabatic curve have the same slope (in fact, they also have the same second derivative; they start to differ at the third order in $d\rho$);

(iii) unlike the adiabatic, a certain *limit density* ρ_{lim} exists such that the pressure diverges when the density approaches this limit ($\rho_{\mathrm{lim}}/\rho_0$ is called *compression limit*).

For a perfect gas, the limit density can be written as

$$\rho_{\text{lim}} = \rho_0 \frac{\gamma + 1}{\gamma - 1}, \tag{2.30}$$

which assumes a value of 4 in the case of a monoatomic gas ($\gamma = 5/3$), like the one depicted in Figure 2.8.

Though the aforementioned properties are easier to demonstrate in the case of a perfect gas, it can be proved that they are universal. Nevertheless, even if the case of a perfect gas is a simple and useful example for describing the behaviour of matter under shock compression, it is quite different to the case of condensed materials (solids and liquids). Indeed, gases are much more compressible than matter in condensed states (*e.g.*, the compressibility of air is 10^4 times that of water at standard conditions). Therefore, let us now consider a solid material such as aluminum, which is – as already stated in the Introduction – a common standard material for the study of WDM. We extracted the Hugoniot curve and the adiabatic curve starting at room conditions ($\rho_0 = 2.70$ g/cm^3, $P_0 = 1$ bar) using the SESAME table 3720 for aluminum as equation of state, and plotted the two curves in Figure 2.9. A first thing to be noticed is that the pressure scale of Figure 2.9 is roughly six orders of magnitude higher than in Figure 2.8 whereas the shown density scales are almost identical, which is no surprise given the difference in compressibility between gases and solids. It should also be noticed that the properties of the Hugoniot curve stated above remain valid. The compression limit for aluminum according to the SESAME table 3720 is around 4.8.

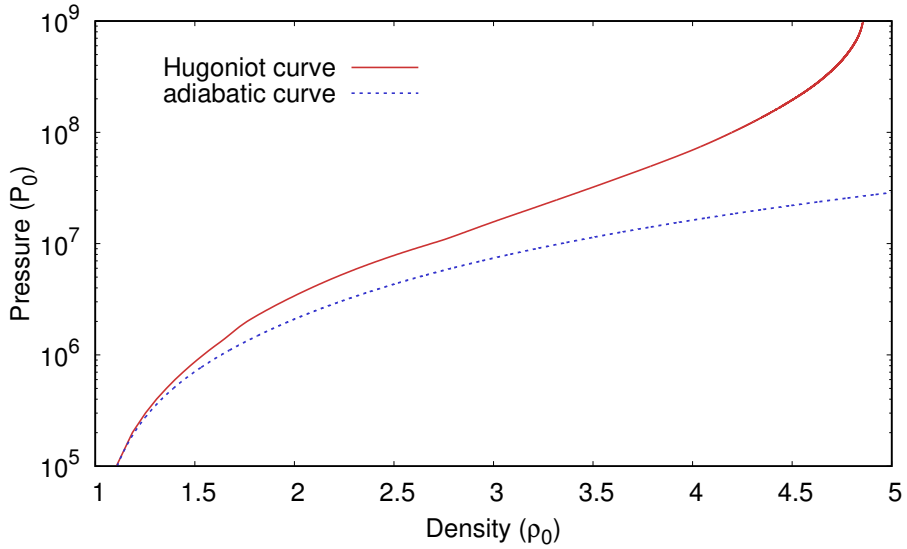

Figure 2.9 – Hugoniot and adiabatic curve for aluminum, represented by the SESAME EOS table 3720. Pressure and density are expressed in units corresponding to the initial values P_0 and ρ_0, respectively.

Entropy jump

When a sample is loaded by a shock wave, its specific entropy s increases. Such an increase is intimately linked to the structure of a shock wave, which consists of a

discontinuity of the thermodynamic variables of the sample. The propagation of a shock wave is thus necessarily an irreversible process associated to an entropy increase. This fact is evident by looking at the properties of the Hugoniot curve and at Figures 2.8 and 2.9. Indeed, a thermodynamic state belonging to the Hugoniot curve starting from a certain initial state has always a higher pressure than the state with the same density belonging to the adiabatic curve starting from the same initial state. However, the entropy increase associated to the shock loading – and thus the differentiation between the Hugoniot and the adiabatic curve – is very small for a small density increase. More precisely, the first and second derivatives of the entropy with respect to ρ are zeros. The first non-zero derivative is the third one, so that the entropy jump associated to shock loading can be written as

$$s - s_0 \simeq \frac{1}{6}\frac{\partial^3 s}{\partial \rho^3}\bigg|_{\rho_0, P_0} d\rho^3, \tag{2.31}$$

where the effect of the higher derivatives has been neglected. Even this property is visible in Figures 2.8 and 2.9: in the initial part of the curves, the Hugoniot and the adiabatic are almost superimposed; the Hugoniot then starts to exhibit a higher slope and eventually moves away from the adiabatic of several orders of magnitude in pressure when density further increases.

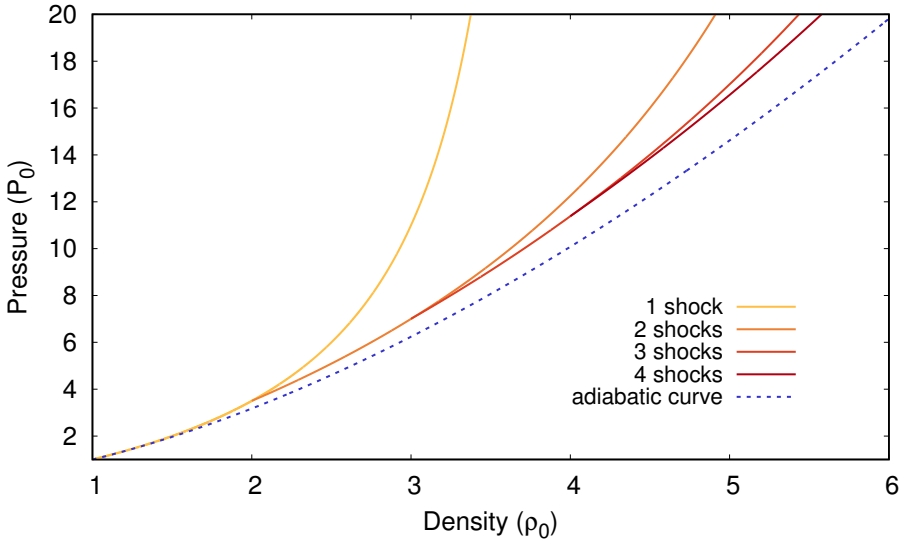

Figure 2.10 – Thermodynamic path in the pressure – density plane associated to compression by one, two, three, and four shocks compared to an adiabatic curve. Pressure and density are reduced, dimensionless variables. The initial pressure and density for the first Hugoniot curve and the adibatic curve are P_0 and ρ_0, respectively. The initial densities for the other Hugoniot curves are $2\rho_0$, $3\rho_0$, and $4\rho_0$.

The property highlighted in equation 2.31 has a fundamental consequence for the thermodynamics of shock compression: if a sample is compressed up to a given final density by a certain number of weak shocks, its final entropy will be lower than if it is compressed by a single, strong shock. Moreover, its final entropy will be a decreasing function of the number of shocks N: indeed, the entropy jump associated to a density

jump $\Delta\rho$ via a single shock loading can be expressed as $\Delta s_1 \propto \Delta\rho^3$. In the case of N weaker shocks,

$$\Delta s_N \propto N \left(\frac{\Delta\rho}{N}\right)^3 \propto \frac{\Delta s_1}{N^2}. \tag{2.32}$$

In the limit $N \to \infty$, the entropy jump is zero and the transformation is thus adiabatic. This means that an adiabatic transformation can be viewed as an infinite sequence of infinitesimally weak shocks. Such a concept has a fundamental role for the theoretical foundations of thermodynamics because it links the static and the dynamic interpretations of a reversible transformation: a reversible transformation produced in a finite amount of time can be viewed as a sequence of small shock waves collectively producing an infinitesimal amount of entropy.

From a more practical point of view, equation 2.32 tells us that a multiple-shock compression approach is suitable to experimentally probe low-entropy states characterised by high densities and moderate pressures and temperatures, such as states representative of planetary interiors (see Chapter 1). We will treat this aspect in detail later in Chapter 3. Here, we only show the application of such a multiple-shock compression approach to a perfect gas (Figure 2.10). The Hugoniot curve from an initial state eventually departs from the adiabatic curve starting from the same state. If a second shock loads the shocked sample, a secondary Hugoniot curve starts from a state belonging to the first one. This secondary Hugoniot has a lower slope than the first. Other two Hugoniot curves are iteratively sketched, each one exhibiting a lower slope than the precedent. The states belonging to the fourth Hugoniot curve within the limits of the plot are quite close to those belonging to the adiabatic curve.

2.3.4 Measuring the equation of state

Characterising a sample loaded to a WDM state by a shock wave requires in the first place the measurement of its equation of state (EOS). Such a measurement is possible by applying the Rankine–Hugoniot relations linking the pristine and the loaded states of the sample. Two approaches are possible: an *absolute* measurement of the EOS, which requires the measurement of two shocked-state parameters, and a *relative* measurement, which makes use of a standard material whose EOS is already well characterised and requires the measurement of a single shocked-state parameter for the sample under study and one for the standard.

Absolute measurement

The three Rankine–Hugoniot relations 2.23–2.25 contain five variables – three state variables of the shocked state 1 – ρ_1, P_1, and e_1 – and two hydrodynamic variables, U_s and U_p. The shock-compressed state 1 – identified by the three state variables ρ_1, P_1, and e_1 – can in principle be determined by measuring two out of the five aforementioned variables and by applying the Rankine–Hugoniot relations. This is called an *absolute measurement* of the EOS.

Figure 2.11 shows two possible approaches for an absolute EOS measurement. In Figure 2.11 (a), the two measured variables are U_p and U_s. The sample under study is designed with a step on its back surface. U_p is determined from the measurement of the free back surface velocity U_{fs} of the material by a velocimeter (for low shock

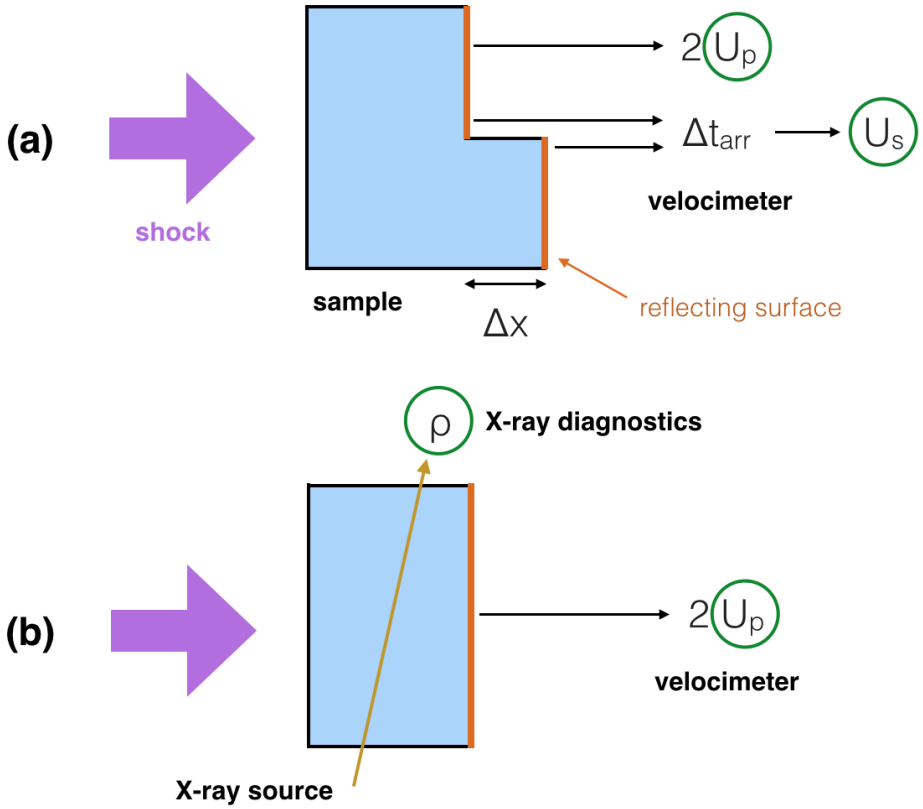

Figure 2.11 – Two methods for an absolute measurement of the EOS of a metallic sample. **(a).** The sample is designed with a step on its back surface. A reflecting layer is deposited in it to allow the measurement of the surface velocity by a velocimeter. The width of the step is Δx. The free-surface velocity is measured by a velocimeter when the shock arrives at the back surface of the material. The material velocity U_p is approximately 1/2 of the free-surface one. The velocimeter measures the arrival time of the shock at the upper and lower part of the back surface of the material. The arrival time difference Δt_{arr} is used to determine the shock velocity as $U_s = \Delta x / \Delta t_{\text{arr}}$. **(b).** The sample is designed with a flat back surface, with a reflecting layer deposited on it. The material velocity is measured as in (a). X-ray radiation (yellow arrow) is let crossing the shocked sample. An X-ray diagnostics (radiography or diffraction) acquires the transmitted signal, which is used to determine the shocked density ρ.

strengths, the approximation $U_p \simeq U_{fs}/2$ is valid); the second is determined from the difference between the arrival times of the shock to the two parts of the back surface. Other approaches are possible depending on the optical properties of the pristine and shocked sample (see Section 2.5.1). A rather different possibility is to include an X-ray diagnostics (such as radiography or diffraction) to probe the shocked density of the material. This approach is depicted in Figure 2.11 (b). However, the absolute measurement approach is generally quite complicated.

Relative measurement: impedance mismatch

Given the complications of the absolute measurement of the EOS, a *relative measurement* approach is often employed. In this scenario, a standard material (A), whose

EOS is already well known, can be placed before the sample to be studied (B), as depicted in Figure 2.12 (a). We will now see what happens when the shock wave sequentially loads the standard and the sample and how this can be exploited to infer the state reached in B.

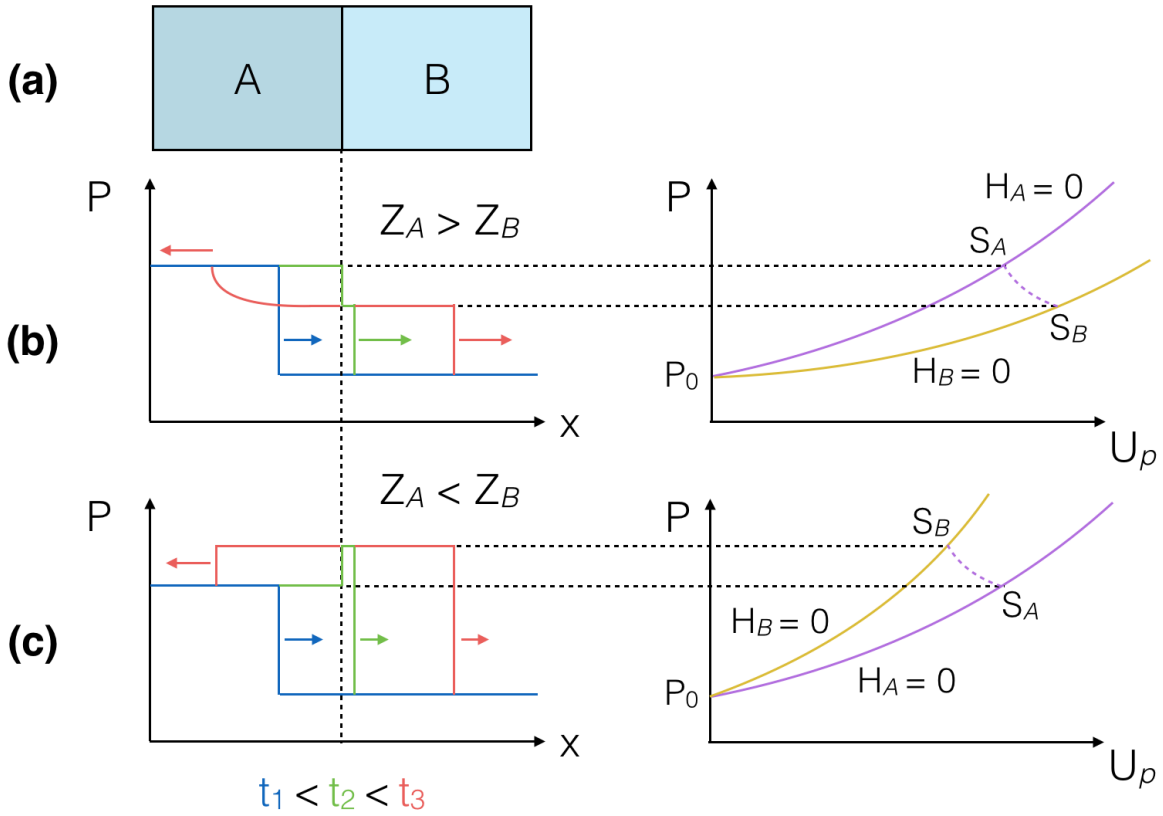

Figure 2.12 – Shock wave crossing an interface between a standard material A and a sample under study B. **(a).** Scheme of a target composed by a standard A and a sample B placed next to each other. **(b).** Case $Z_A > Z_B$. Left. Spatial profile of pressure for three times t_1, t_2, and t_3 (blue, green, and red lines, respectively). At $t = t_1$, the shock front propagates through the material A. At $t = t_2$, the shock front just entered the material B and loaded it to a lower pressure than that of A. At $t = t_3$, the shock front further propagates through B and an adiabatic release propagates backwards into A. Right. Pressure – material velocity conditions in the two materials after shock loading. The material A is compressed up to state S_A along its Hugoniot curve $H_A(U_p, P; P_0) = 0$ (violet curve) starting from P_0. The shock then compressed the material B up to state S_B along its Hugoniot $H_B(U_p, P; P_0) = 0$ (gold curve). After the shock has crossed the interface, A experiences an adiabatic release from S_A to S_B. The adiabatic curve is the dashed violet one. **(c).** Case $Z_A < Z_B$. Left. At $t = t_1$, the shock front propagates through the material A. At $t = t_2$, the shock front just entered the material B and loaded it to a higher pressure than that of A. At $t = t_3$, the shock front further propagates through B and a re-shock propagates backwards into A. Right. After the shock has crossed the interface, A experiences a re-shock from S_A to S_B. The re-shock Hugoniot curve is the dashed violet one.

Initially, the shock loads the standard A up to a state, characterised by a pressure P^A and a material velocity U_p^A, belonging to its Hugoniot curve starting from pressure P_0. The shock eventually crosses the interface between the standard A and the sample

B. When the shock subsequently enters the sample B, it loads it up to a state P^B, U_p^B belonging to its Hugoniot curve starting from pressure P_0. In general, the pressure and material velocity of the shocked material B will be different from those of A for a given shock strength. In particular:

(i) if the Hugoniot curve of B is lower than the Hugoniot of A in the $U_p - P$ plane, then $P^B < P^A$ – this case is depicted in Figure 2.12 (b);

(ii) in the opposite case where the Hugoniot curve of B is higher than that of A, then $P^B > P^A$ – this case is depicted in Figure 2.12 (c).

In case (i), the material B is said to have a lower *shock impedance* than A; in case (ii), a higher one. The shock impedance of a given material i is defined as $Z_i = \rho_0^i U_s^i$, where ρ_0^i is the unperturbed density of the material and U_s^i the shock velocity when the shock wave propagates in that material.

Right after the shock has crossed the A/B interface, a portion of the standard A in the state (U_p^A, P^A) and a portion of the sample B in the state (U_p^B, P^B) will coexist next to each other. However, this configuration is unstable as it is not at hydrodynamic equilibrium. Indeed, an equilibrium configuration requires the two sides of the interface to share the same pressure and material velocity:

$$P^A = P^B, \tag{2.33}$$

$$U_p^A = U_p^B. \tag{2.34}$$

The standard material A thus experiences a thermodynamic transformation that adapts its pressure and material velocity to those of the sample B to achieve hydrodynamic equilibrium. In the case $P^A > P^B$, this happens through an adiabatic release [see Figure 2.12 (b)]; in the opposite case, via the backward propagation of a reflected shock wave [see Figure 2.12 (c)].

The relative measurement of the EOS is based on the measurement of one hydrodynamic variable relative to the shocked sample and one relative to the shocked standard. The behaviour of the shock wave when it crosses the interface between the two layers is exploited to infer the state reached in the sample. Since this approach makes use of a standard material with a different impedance than the sample, it is called *impedance mismatch technique*. Let us consider the case in which the shock velocity is measured both in the standard A and in the sample B. Since the EOS of A is already well known, the Hugoniot curve in the $P - U_p$ plane can be extracted by inverting the Rankine–Hugoniot relations (equations 2.23–2.25). The Hugoniot curve provides a first constraint on the state reached after shock loading in A (S_A). The measurement of U_s^A gives another constraint through the Rayleigh line $P^A = (\rho_0^A U_s^A) U_p^A$. Both curves are shown in Figure 2.13. The intersection between the two curves gives the state S_A. The Hugoniot curve of the sample B is not known in advance. However, a first constraint on the state reached in B after shock compression, S_B, can be imposed using the measurement of U_s^B: S_B lies along the Rayleigh line $P^B = (\rho_0^B U_s^B) U_p^B$. If the Rayleigh line B is lower than S_A, then the standard A experiences an adiabatic release to adapt its pressure to that in B, as we have already seen. This is the case depicted in Figure 2.13. In the opposite case, A is loaded by a reflected shock wave. In both cases, the path taken by A – the release or re-shock – can be determined from the EOS, which

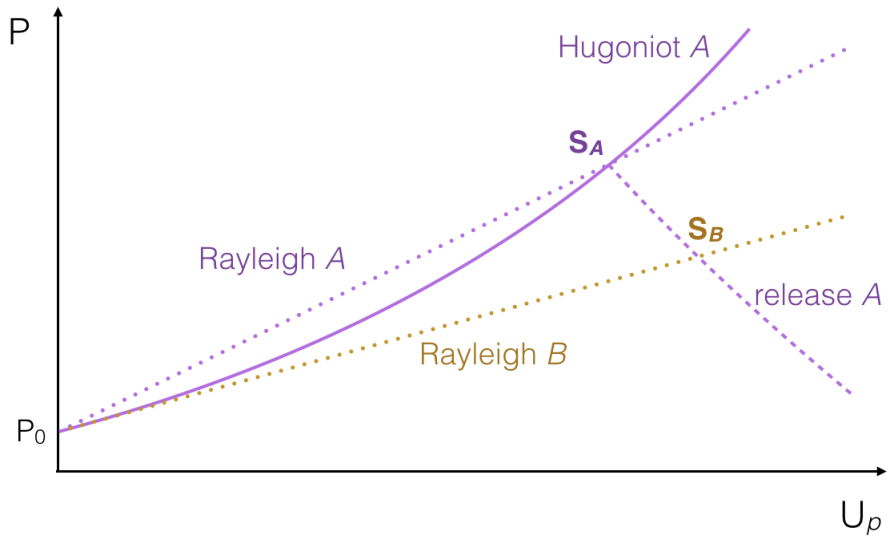

Figure 2.13 – Impedance mismatch technique using a standard A with a higher impedance than the sample B. The state S_A is determined as the intersection between the known Hugoniot curve of A and the Rayleigh line A, whose slope $\rho_0^A U_s^A$ is experimentally measured. The state S_B is then determined as the intersection between the Rayleigh line B and the release of A from S_A.

is already known. The release or re-shock of A provides the second constraint for the determination of S_B. S_B is indeed determined as the intersection between the Rayleigh line B and the release or re-shock of A, as depicted in Figure 2.13. After P_B and U_p^B have been determined, the other state variables ρ^B and e^B can be inferred using the Rankine–Hugoniot relations (equations 2.23–2.25).

In the context of the experimental work presented in this Thesis, we have routinely used α-quartz as standard material for the EOS measurements. This is a very common choice [Barrios et al. (2010); Celliers et al. (2010); Brygoo et al. (2015); Kimura et al. (2015); Sekine et al. (2016)], since the equation of state of quartz has been characterised along the principal Hugoniot curve [Hicks et al. (2005); Knudson and Desjarlais (2009); Millot et al. (2015)] as well as along adiabatic release paths [Knudson and Desjarlais (2013); Desjarlais et al. (2017)], which allows a precise determination of its behaviour and thus precise EOS measurements.

2.3.5 Sustained and decaying shocks

Up to now, we have made the implicit hypothesis that the material loaded by the shock conserves its pressure indefinitely in time and that the shock front conserves its velocity while propagating through the same material. This is in theory true if the shock is *sustained*, that is, if the external agent which applies the pressure generating the shock wave exercises its action indefinitely in time.

If the external application of pressure is interrupted at a certain moment, a release wave will start propagating inside the sample towards the shock front and will eventually catch it up. When this happens, the shock starts to load the sample at pressures decreasing in time, up to its complete extinction. This is the case of a *decaying* shock.

As the shock keeps loading the sample starting from the same initial conditions, immediately behind the shock front the sample state lies along the Hugoniot curve of that material. Figure 2.14 shows the pressure spatial profile and the pressure – material velocity evolution of the loaded sample in the case of a sustained and of a decaying shock.

In the context of shock-compression experiments, sustained or decaying shock can be employed. The main advantage of sustained shock is that the probed state is stationary, so that it can be diagnosed for the whole duration of the compression, allowing more precise measurements. However, with this approach, only one state can be explored for each shot. Depending on the number of available shots and on the target cost, this can be a major disadvantage. A possible solution consists in employing the decaying shock technique and exploring a whole range of conditions along the same Hugoniot curve with a single shot. This approach is quite interesting when one wants to detect phase transitions along the probed Hugoniot path. Indeed, when the Hugoniot curve crosses a phase boundary, a discontinuity in the probed state variables may appear, allowing to characterise the thermodynamic conditions of the boundary [Millot et al. (2015); Bolis et al. (2016)]. The major drawback for this approach is that the non-stationarity of the shocked conditions decreases the quality of the measurement, as the diagnostics have access to each different state for a very short amount of time.

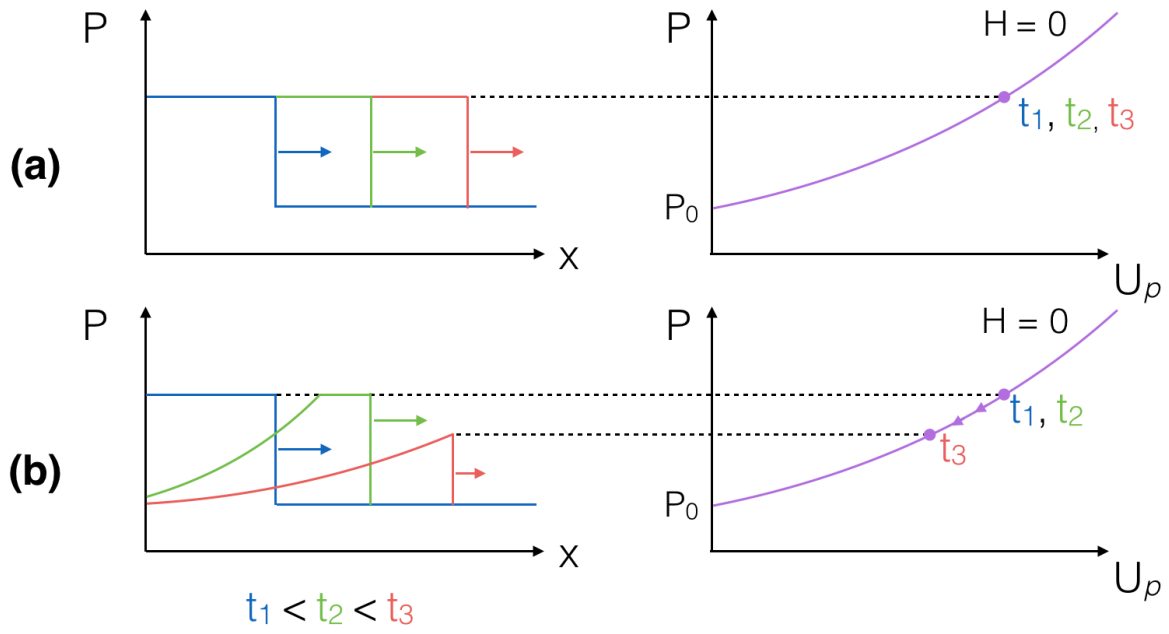

Figure 2.14 – Pressure spatial profile and pressure – material velocity evolution for a loaded sample in the case of a sustained (a) and a decaying (b) shock.

2.4 Generation of shock waves using high-power lasers

2.4.1 Principles of laser-matter interaction

The generation of a shock wave via a high-power laser [Kruer (1988); Paul Drake (2006)] is intimately related to the phenomenon of *laser ablation*. When a nanosecond laser pulse with an intensity $\geq 10^{12}$ W/cm^2 is focused onto a solid target, it rapidly creates a plasma near the target surface, as shown in Figure 2.15. Indeed, a few electrons are initially removed from their atoms by multi-photon ionisation and are subsequently accelerated by the laser electric field until they collide with other atoms, ionising them in an avalanche process, called laser ablation, which takes place in a picosecond time scale. The generated plasma, that expands into the vacuum, is characterised by a density gradient from values close to the solid density near the target surface to very low values at the expansion border (see Figure 2.15).

After the plasma is created, the propagation of the laser beam is affected by its presence. The dispersion relation of the laser inside the plasma

$$\omega^2(z) = \omega_{pe}^2(z) + c^2k^2(z), \tag{2.35}$$

where z is the propagation direction and

$$\omega_{pe}(z) = \frac{n_e(z)e^2}{\varepsilon_0 m_e} \tag{2.36}$$

is the local plasma frequency, tells us that the propagation of the beam is possible only for densities lower than a critical value $n_c(\omega) = \varepsilon_0 m_e \omega^2/e^2$, as depicted in Figure 2.15. At that boundary, the laser beam is reflected. The region where $n_e(z) < n_c$ is called *corona* or *interaction zone*, since the laser energy absorption by the plasma takes place in this zone. The region of the plasma characterised by $n_e(z) > n_c$ is called *conduction zone*. Its other limit is the *ablation front*, which can be defined as the plane where the plasma density is roughly equal to the solid one.

The ablation of the target is associated to a negative momentum p_{ablation}, as the plasma is ejected towards the direction of the laser source. The principle of momentum conservation dictates that a positive momentum is transmitted to the target. This transfer of momentum rapidly generates a shock wave, as seen in Section 2.3.2. The shock compresses the target up to a pressure P_a, called *ablation pressure*, that depends on the laser intensity I_L and wavelength λ_L, as well as on the target composition (and in particular its atomic mass number A and its atomic number Z). In the approximation of a self-similar and isothermal plasma expansion,

$$P_a[\text{Mbar}] \simeq 12 \cdot I_L[10^{14}\text{W/cm}^2]^{2/3} \cdot \lambda_L[\mu\text{m}]^{-2/3} \cdot \left(\frac{A}{2Z}\right)^{1/3}, \tag{2.37}$$

as shown by Fabbro (1982). According to this model, for a material with $A \simeq 2Z$, a typical laser intensity of 10^{13} W/cm^2 at 527 nm (as in the experiments at LULI2000 for this work) produces an ablation pressure of 4 Mbar.

Hereafter we will describe the energy absorption and transfer mechanisms which take place in the corona and the conduction zone, respectively.

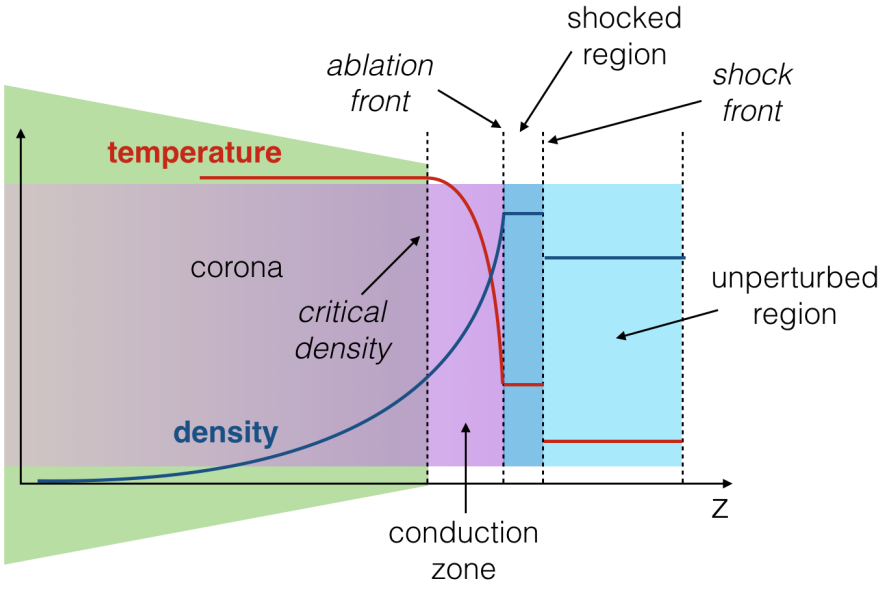

Figure 2.15 – Density and temperature spatial profiles during the ablation of a low-Z target by a high-intensity laser pulse. From left to right: corona, conduction zone, shocked region of the target, unperturbed region of the target.

Energy absorption and transport

The plasma electric permittivity has an imaginary part due to electron-ion collisions. This imaginary part is physically linked to the absorption of a fraction of the laser beam via the *inverse Bremsstrahlung* process, in which an electron absorbs a photon during a collision with an ion. Absorption takes place essentially when the electronic density approaches the critical density $[n_e(z) \simeq n_c]$, that is, near the conduction zone (see Figure 2.15).

The energy transport mechanism in the conduction zone strongly depends on the mean atomic number of the pristine target material (or, in the case of a multi-layered target, of the first-layer material, called *ablator*). For light materials ($Z < 10$), the main mechanism is electronic thermal transport. In the case the ablator is a heavy material ($Z > 10$), the main energy transport mechanism is not due to thermal electrons but rather to the XUV and X radiation. Such a mechanism risks to pre-heat the sample under study, changing its initial conditions and thus preventing a correct characterisation of the shocked state. For this reason, only low-Z materials such as hydrocarbon polymers (*e.g.* polystyrene) are used as ablators.

2.4.2 Laser-shock experiments

We have seen that a laser pulse providing energies of $10 - 10^6$ J in a few nanoseconds can be used to generate a shock wave inside a target via an ablation process. An usual requirement is the spatially uniformity of the shock wave, so that the shocked state can be precisely characterised by diagnostics. To ensure this conditions, the drive lasers must uniformly illuminate a wide area of the target. On the contrary, since laser radiation is characterised by a high degree of coherence, the spatial profile of a

drive laser beam is affected by strong non-uniformities and intensity spikes. An optical smoothing of the spatial profile is thus necessary, and usually obtained with the use of phase plates [Kato et al. (1984); Pepler and Paradowski (2006)]. Phase plates are transparent plates which induce a space-dependent phase shift on the incident beam, aimed at breaking the spatial coherence of the laser beam. The induced phase shift profile may consist of a lattice of square or hexagonal regions in which the shift is randomly taken as 0 or π (random phase plates), or may continuously vary (Kinoform phase plates). The far field generated by phase plates has a super-Gaussian profile, where intensity is almost uniform inside a desired area (usually, diameters span from $500 - 1000$ μm) and then exponentially drops outside it.

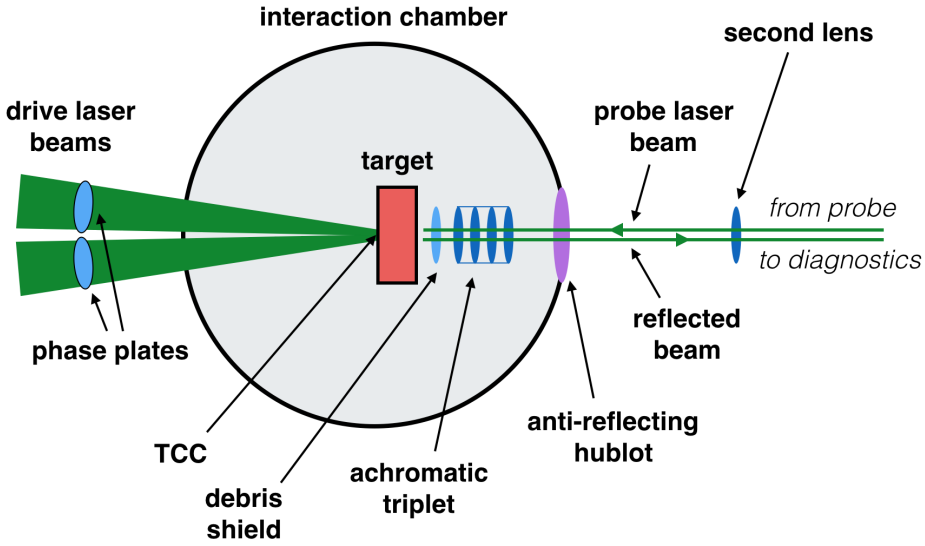

Figure 2.16 – Scheme of a typical target chamber setup in a laser-driven shock experiment. Two nanosecond drive laser beams are focused by phase plates onto a target positioned at the TCC. The chamber provides optical access to the drive lasers (left) and to the optical diagnostics (right, through an anti-reflecting hublot). A first image of the target is made by an achromatic triplet (protected by a debris shield from the ejection of material from the target) and collected by a second lens, which generates a collimated beam that is directed towards the diagnostics. A probe laser is focused onto the rear side of the target and is reflected. The object sizes are not scaled – the diameter of the interaction chamber is around 10 m, whereas the lateral size of the target is typically a few cm and its width between 100 μm and a few cm.

Given the high intensity of the drive lasers, it is necessary to place the target in a vacuum chamber, as depicted in Figure 2.16. The chamber generally has at least two optical accesses, one for the drive laser and one for the optical diagnostics. Supplementary accesses for alignment purposes may be provided. The Target Chamber Center (TCC) is the reference position for the alignment of the target and of the optical path to the diagnostics. Targets are pre-aligned on an alignment station outside the chamber, equipped with four cameras. All cameras are focused to a single point which reproduces the TCC in the station. Pre-aligned targets are then transferred to the vacuum chamber, where small corrections to the position are made if necessary.

On the diagnostics side, an image relay system is put in place from the rear side of the target to the optical diagnostics. An achromatic triplet is placed in the chamber

and makes the first image of the target rear side out of the chamber. That image is then collimated by a second lens. The collimated light beam is then split using dichroic mirrors and beam splitters, so that each resulting beam may be directed to a diagnostic. Some diagnostics collect the light emitted by the target; others measure the light reflected by the target. Probe laser beams are necessary to illuminate the rear side of the target for the diagnostics of the second type – this is the case shown in Figure 2.16.

2.5 Diagnostics

Optical diagnostics are aimed at measuring the thermodynamic state reached by the sample after being loaded by the shock. In particular, Doppler velocimetry – the most common diagnostics in the context of shock-compression – measures the shock or material velocity, that allows the determination of the shocked density and pressure (see Section 2.5.1). The last fundamental state variable – temperature – can be estimated from the measurement of the self-emission of the shocked sample. This is the working principle of optical pyrometry. After having introduced these two basic optical diagnostics, we will briefly explain how time-resolved measurements can be achieved with the use of streak cameras. Figure 2.17 shows the simplified scheme of a typical setup in the context of laser-driven shock-compression, including two Doppler velocimeters (VISARs) and an optical pyrometer (SOP), all employing streak cameras. In the experimental work described in this Thesis, we used variations of this setup.

As optical diagnostics can only probe the macroscopic variables, the microscopical structure remains elusive. We will thus introduce X-ray diagnostics – such as radiography, diffraction, and absorption – that allow to study the lattice structure in crystals, the structure factor in glasses and liquids, as well as the dynamics of phase transitions of shock-compressed samples.

2.5.1 Doppler velocimetry

Doppler velocimetry is the most routinely used diagnostics in the framework of shock compression. As we have seen in Section 2.5.1, the shock and material velocity are fundamental parameters to measure to have an access to the thermodynamic state of the shocked sample. In particular, via the Rankine–Hugoniot relations, one can determine the shocked density and pressure.

The principle of Doppler velocimetry diagnostics is to measure a velocity U_{obj} of a reflecting object by focusing a probe laser of wavelength λ_0 onto it and measuring the Doppler shift of the reflected beam wavelength λ_R, which is directly linked to the velocity of the object via

$$\lambda_R = \lambda_0 \frac{1 - U_{\text{obj}}/c}{1 + U_{\text{obj}}/c}. \tag{2.38}$$

In the non relativistic case $U_{\text{obj}} \ll c$, equation 2.38 can be approximated as

$$\lambda_R \simeq \lambda_0 \left(1 - 2\frac{U_{\text{obj}}}{c}\right). \tag{2.39}$$

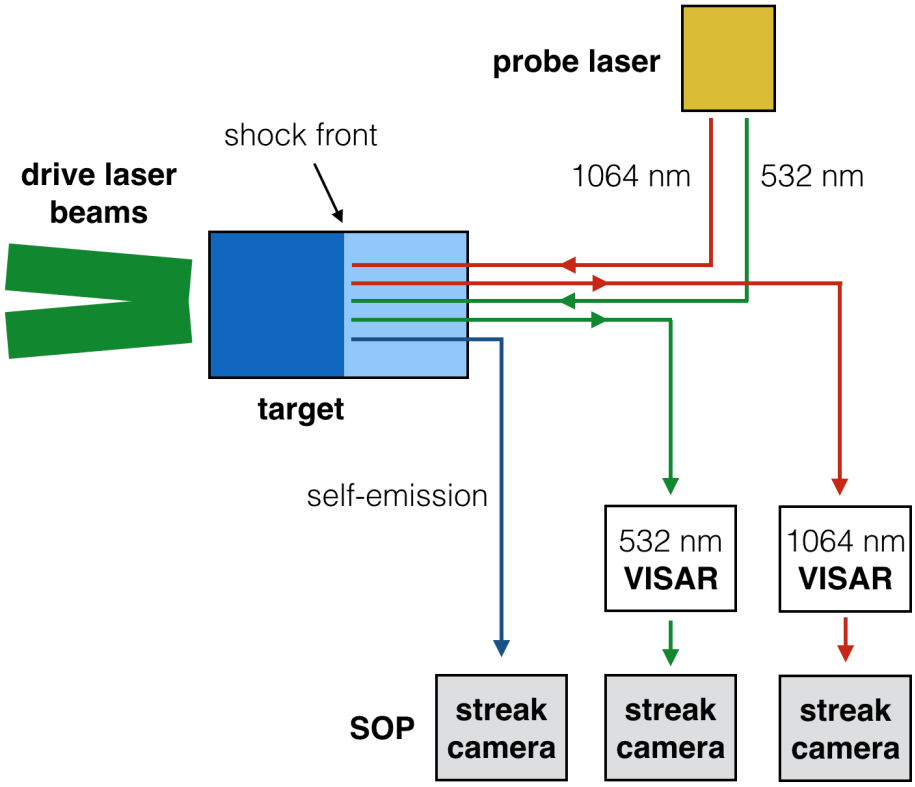

Figure 2.17 – Simplified scheme of a typical optical diagnostics setup in the context of laser-driven shock compression. A shock wave has been generated by the drive lasers and is propagating into the sample. Two probe laser beams, at 532 nm and 1064 nm, are focused onto the rear-side of the target and are reflected by the shock front. Each reflected beam is sent to the VISAR working at the corresponding wavelength, which measures the shock velocity from the Doppler shift. The thermal radiation emitted by the shocked sample is collected and measured by the SOP, allowing an estimation of the temperature. Each diagnostics acquires time-resolved data thanks to the use of streak cameras.

The Doppler velocimetry technique is commonly used in shock experiments by means of the Velocity Interferometric System for Any Reflector (VISAR). A VISAR is a Mach-Zehnder interferometer in which a transparent *etalon* has been inserted in one of the two arms with the aim of introducing a delay between them (see Figure 2.18). The *etalon* is placed right before the mirror of the corresponding arm.

Let l_{etalon} be the *etalon* thickness and $n_{\text{etalon}}(\lambda)$ its refractive index. If the two arms originally have the same optical length and a fringe system is formed at the exit beam-splitter, when the *etalon* is inserted the mirror of the arm which contains it must be moved backward of a length

$$\Delta l = l_{\text{etalon}} \left[1 - \frac{1}{n_{\text{etalon}}(\lambda_0)} \right] \tag{2.40}$$

to recover the imaging by taking into account the refraction due to the *etalon*, as depicted in Figure 2.19. Due to this backwards movement of the mirror, the arm containing the etalon becomes longer than the other. This introduces a geometrical

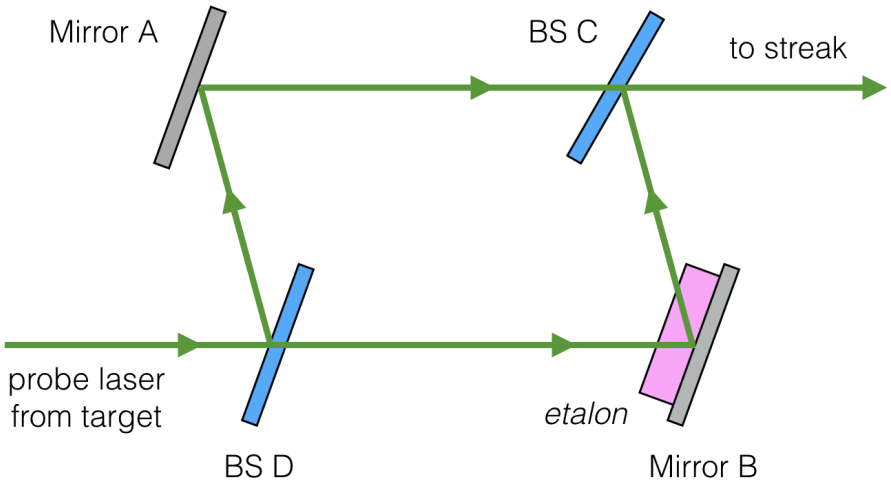

Figure 2.18 – Scheme of a VISAR. BS C and BS D are 50% beam-splitters. The incoming laser beam is split by BS D. The beam sent to the upper arm is just reflected by mirror A. The beam sent to the lower arm passes through an etalon before and after being reflected by mirror B. BS C then recomposes the two beams and sends them to the streak camera.

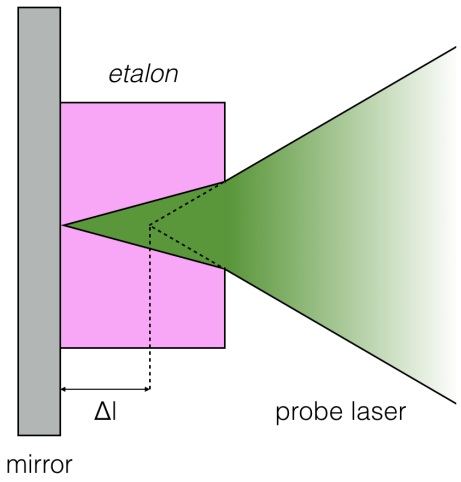

Figure 2.19 – Correction of the mirror position after the insertion of the *etalon* on one arm of the interferometer.

delay between the two beams inside the interferometer:

$$\tau_{\text{geom}} = \frac{\Delta l}{c}. \tag{2.41}$$

Additionally, when the reflected laser beam passes through the etalon, it experiences a delay with respect to the beam sent to the other arm of the interferometer due to the etalon refractive index. This delay introduced by the *etalon* is

$$\tau_{\text{etalon}} = \frac{2l_{\text{etalon}}}{c}\left[n_{\text{etalon}}(\lambda_R) - 1\right]. \tag{2.42}$$

The total delay between the two arms of the interferometer $\tau = \tau_{\text{geom}} + \tau_{\text{etalon}}$ is thus

$$\tau(\lambda_R) = \frac{2l_{\text{etalon}}}{c}\left[n_{\text{etalon}}(\lambda_R) - \frac{1}{n_{\text{etalon}}(\lambda_0)}\right]. \tag{2.43}$$

Equation 2.43 can be rewritten by isolating the wavelength dependence of the refractive index of the etalon from the constant part:

$$\tau(\lambda_R) = \tau_0\left(1 + 2\delta_{\text{etalon}}\frac{U_{\text{obj}}}{c}\right), \tag{2.44}$$

where

$$\tau_0 = \frac{2l_{\text{etalon}}}{c}\left[n_{\text{etalon}}(\lambda_0) - \frac{1}{n_{\text{etalon}}(\lambda_0)}\right] \tag{2.45}$$

is the constant part,

$$\delta = -\lambda_0\frac{n_0}{n_0^2 - 1}\frac{dn}{d\lambda}\bigg|_{\lambda_0} \tag{2.46}$$

is a correction parameter proposed by Barker and Schuler (1974) to take into account the dispersion of the etalon, and the approximation provided in equation 2.39 has been used to link the wavelength shift to the object velocity.

The recomposed laser beams exiting the VISAR produce a fringe system at the entrance of the streak camera. The delay τ therefore generates a phase shift $\Delta\phi$ on such a fringe system:

$$\Delta\phi = 2\pi\tau(\lambda_R)\left(\frac{1}{\lambda_R} - \frac{1}{\lambda_0}\right). \tag{2.47}$$

Equation 2.47 can be simplified using the approximation provided in equation 2.39 and the new expression for τ given by equation 2.44:

$$\Delta\phi = \frac{2\pi\tau_0}{\lambda_0}(1 + \delta)\frac{U_{\text{obj}}}{c}. \tag{2.48}$$

A linear relation thus exists between the phase shift of the fringe system and the velocity of the object. The velocity for which the fringe system is shifted of a a fringe ($\Delta\phi = 2\pi$) is called Velocity Per Fringe parameter (VPF) of the VISAR and indicates its sensitivity (a low VPF corresponds to a high sensitivity to small velocities). According to equation 2.47, it is

$$\text{VPF} = \frac{c\lambda_0}{2\tau_0(1 + \delta)}. \tag{2.49}$$

Using the VPF parameter defined in equation 2.49, equation 2.47 can be rewritten as

$$U_{\text{obj}} = \text{VPF}\frac{\Delta\phi}{2\pi}. \tag{2.50}$$

Up to now, we have considered a moving object with constant velocity. In the context of shock experiments, the velocity to be measured varies with time (*e.g.* in the case of decaying shocks). Resolution in time is guaranteed by sending the VISAR output signal to a streak camera (see Section 2.5.3) which acquires its horizontal lineout.

At this point, we stress that the treatment we made up to now and thus the final equation 2.50 are valid only in the case the object propagates into vacuum. If, on the

contrary, the object moves in a medium with a refractive index higher than 1, the left-hand side of equation 2.50 is not the actual velocity of the object but rather an *apparent* velocity (U_{app}). Hereafter we will treat this issue and specify which corrective factors must be introduced to obtain the real velocity of the reflecting object. In particular, we will treat the following cases, all of which have been encountered in the course of the work presented in this Thesis:

(i) a sample loaded by a strong shock wave, whose front is reflecting;

(ii) a sample that remains transparent after being loaded by the shock, but whose refractive index increases due to compression;

(iii) a sample that becomes opaque after being loaded by the shock, whose front is not reflecting.

The pristine sample will be always considered as transparent, with a real refractive index n_0. In all the cases treated hereafter, a target design will be considered in which a metallic layer is placed before the sample with the aim of reflecting the probe laser beam.

The shock front is reflecting

This is a common case when dealing with high-intensity shocks, which strongly compress and ionise the loaded sample so that the shock front becomes highly reflecting (in this work, this case is found in Chapters 4, 5, and 6). Indeed, according to the Fresnel's law, the shock-front reflectivity $R_{\text{s-f}}$ is

$$R_{\text{s-f}} = \frac{(n_1 - n_0)^2 + k_1^2}{(n_1 + n_0)^2 + k_1^2}, \tag{2.51}$$

so that a high reflectivity value is to be expected when the shocked material is highly compressed (high n_1) and ionised (high k_1). The shock velocity is easily linked to the apparent velocity measured by the VISAR:

$$U_s(t) = \frac{U_{\text{app}}(t)}{n_0}, \tag{2.52}$$

where the corrective factor $1/n_0$ takes into account the fact that the apparent velocity is higher than the actual one due to the higher optical path that the reflected probe laser undergoes.

In this case of a reflecting shock front, VISARs can also be used to measure the reflectivity. To do so, the intensity of the fringe system collected during the shock propagation is compared to that of a reference image taken prior to the shot.

In this Thesis, we used the methods described here to measure the shock velocity and shock-front reflectivity of pure water, pure liquid ammonia, and icy planetary mixtures in their optically reflecting regime, at pressures above or comparable to 1 Mbar, as described in Chapters 4 and 5. Moreover, we used these methods in the context of dynamical pre-compression experiments on pure water, icy mixtures (see Chapter 4), and α-quartz (see Chapter 6). An example of a VISAR output image, together with the extracted time-dependent shock velocity, is provided in Figure 2.20.

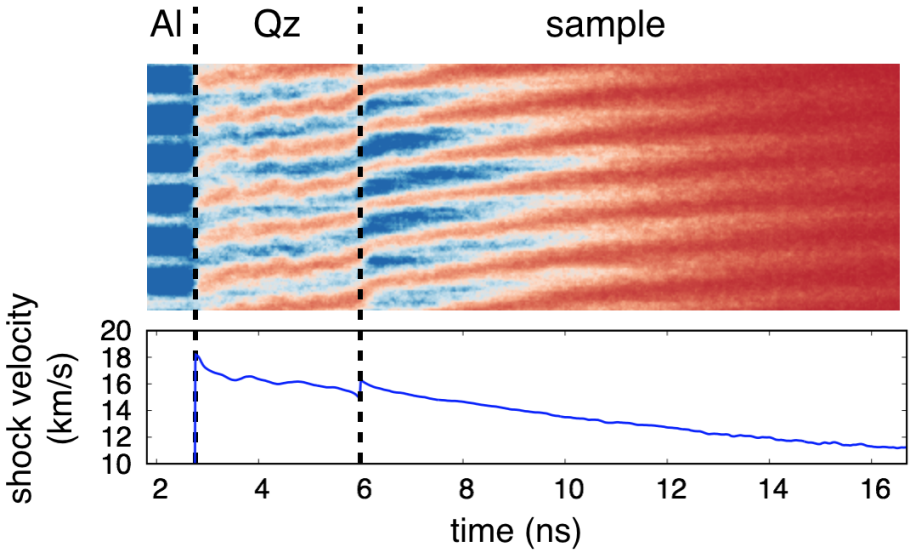

Figure 2.20 – VISAR measurement of the shock velocity in an optically reflecting shocked standard of α-quartz and in a sample of icy mixture of water, ethanol, and ammonia (see Chapter 4) under study. **Top.** VISAR output image. Two dotted lines indicate when the shock enters the quartz standard and the icy mixture sample. The three time intervals correspond to when the probe laser is reflected by a metallic (aluminum) layer placed before quartz, when it is reflected by the shock front inside quartz, and by the shock front inside the icy mixture sample. **Bottom.** Measured shock velocity as a function of time. The jump at the crossing of the interface between quartz and icy mixture is due to the lower shock impedance of the latter (see Section 2.3.4).

The loaded sample is transparent

In the experimental work presented in this Thesis, this can be found within the context of double-shock compression after the loading of the first weak shock (see Chapters 4 and 6). In general, this is the case when the shock is weak enough to leave the sample in a transparent state with a real refractive index $n_1 > n_0$, the VISAR can be used to measure not the shock velocity, but the material velocity of the shocked sample. Indeed, the probe laser will propagate through both the pristine and shocked volumes of the sample, reflect onto the metal-sample interface, and propagate backwards through the sample before exiting and reaching the diagnostics. The metal-sample interface propagates at the material velocity as it is in equilibrium with the shocked sample. The following relation, which can be calculated by analysing the optical path followed by the probe laser beam (sketched in Figure 2.21), links the apparent velocity measured by the VISAR, the shock velocity, and the material velocity:

$$U_{\text{app}} = n_1 U_p - (n_1 - n_0)\, U_s. \tag{2.53}$$

Equation 2.53 is valid only in the case of a sustained shock, with constant U_s and U_p and a spatially uniform index n_1 in the shocked portion of the sample. In the case of a decaying shock, an integral over the optical path followed by the probe laser must be calculated.

If the refractive index linearly depends on density, the material velocity and the

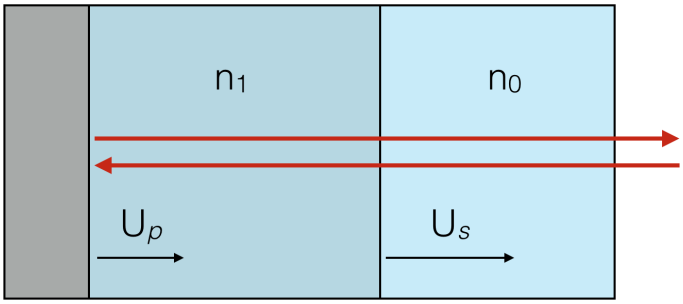

Figure 2.21 – Scheme of the optical path followed by the probe laser beam (red arrows) inside a sample which remains transparent after shock loading.

apparent velocity are bound by the linear relation

$$U_p = \frac{U_{\text{app}}}{n^\star}, \tag{2.54}$$

where

$$n^\star = n_0 - \rho_0 \left(\frac{dn}{d\rho}\right)_{\rho=\rho_0} \tag{2.55}$$

n_0 and ρ_0 are the initial refractive index at the probe laser wavelength and the initial density, respectively [Hardesty (1976), Setchell (1979)].

In this Thesis, we used the method described here to measure the material velocity of water, icy mixtures (see Chapter 4), and α-quartz (see Chapter 6) in the low-pressure, optically transparent regime of their principal Hugoniot curves, within the context of a dynamical pre-compression approach. Moreover, we employed equation 2.53 to estimate the shocked refractive index of α-quartz, which is a key parameter for the correct analysis of dynamic pre-compression data (see Chapter 6). In Figure 2.22, we provide an example of VISAR output image in the context of this investigation, together with the time-dependent profile of the apparent material velocity.

The loaded sample is opaque

If the shock loading the sample leaves an opaque state with a complex refractive index $\tilde{n}_1 = n_1 + ik_1$, as it is the case *e.g.* for water compressed to around 1 Mbar [Batani et al. (2015)], the probe laser will be partially absorbed when propagating back and forth into the sample. This allows the determination of the imaginary part of the shocked refractive index (k_1) from the measurement of the decay in time of the VISAR signal intensity. Indeed, the intensity dependence on time will be

$$I(t) = I(0) \exp\left[-\frac{4\pi k_1}{\lambda_0}\left(U_s - U_p\right)\left(t - t_{\text{arrival}}\right)\right], \tag{2.56}$$

where t_{arrival} is the arrival time of the shock wave in the sample and it has been assumed that the shock is sustained (*i.e.* that both U_s and U_p are constant in time and that k_1 is uniform in the shocked portion of the sample). If this is not the case, a spatial integral over the shocked portion must be calculated. An exponential fit on $I(t)$ allows

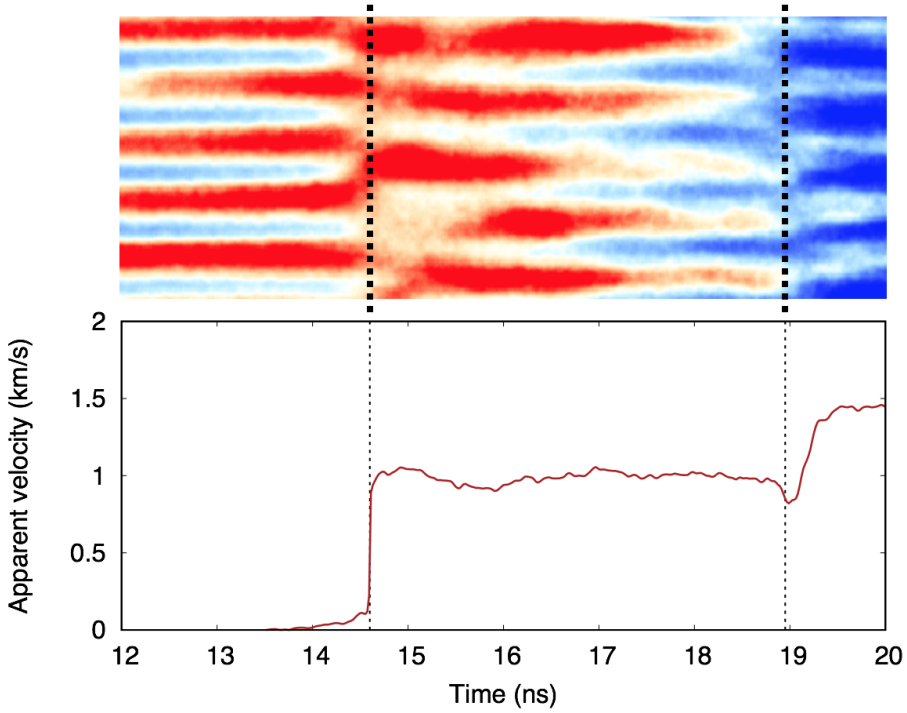

Figure 2.22 – VISAR measurement of the apparent material velocity in the case of a transparent shocked sample of α-quartz. **Top.** VISAR output image. **Bottom.** Apparent velocity as a function of time. The two dotted lines indicate the entrance of the shock wave in the quartz sample and its exit.

the determination of k_1 provided that U_s and U_p are known. U_p can be measured at the same time with the method we described when we treated the case of a transparent sample, at least in the time interval in which the fringe intensity is high enough to allow the estimation of the phase shift. U_s cannot be directly determined in general, so that the $U_s - U_p$ relation for the sample under study should be known in advance or characterised in other shots.

2.5.2 Optical pyrometry

We have seen that the use of VISARs allows to determine, via the Rankine–Hugoniot relations, the density and pressure of the shocked sample. Nevertheless, another critical parameter in the equation of state should be measured: the temperature T. The principle of optical pyrometry is to collect the thermal self-emission of the sample – heated by the shock loading – and estimate its temperature using Planck's law. According to this law, the spectral radiance of a black body is

$$B_\lambda(\lambda, T) = \frac{2hc^2}{\lambda^5} \frac{1}{\exp\left(\frac{hc}{k_B \lambda T}\right) - 1}, \tag{2.57}$$

where λ is the considered wavelength and T is the black body temperature. A physical body at temperature T exhibits a lower spectral radiance than a black body, that can be expressed as:

$$L_\lambda(\lambda, T) = \epsilon(\lambda, P, T) B_\lambda(\lambda, T), \tag{2.58}$$

where $\epsilon(\lambda, P, T)$ – the ratio between the radiance of the physical body and that of a black body, which depends on the thermodynamic state of the body – is called body *emissivity*.

In the context of shock experiments, a Streaked Optical Pyrometer (SOP) is generally used. Such a diagnostics is able to measure the time-resolved self-emission of the sample thanks to the use of a streak camera (see Section 2.5.3). A bi-dimensional output image is produced by a CCD placed after the streak: one of the two dimensions is the horizontal line out of the sample, the other one represents the temporal evolution of the signal. An example of SOP output is provided in Figure 2.23, which shows the SOP image and the time-dependent number of counts relative to a shot at the GEKKO XII facility on a target composed by an α-quartz standard and an icy mixture sample (see Chapter 4).

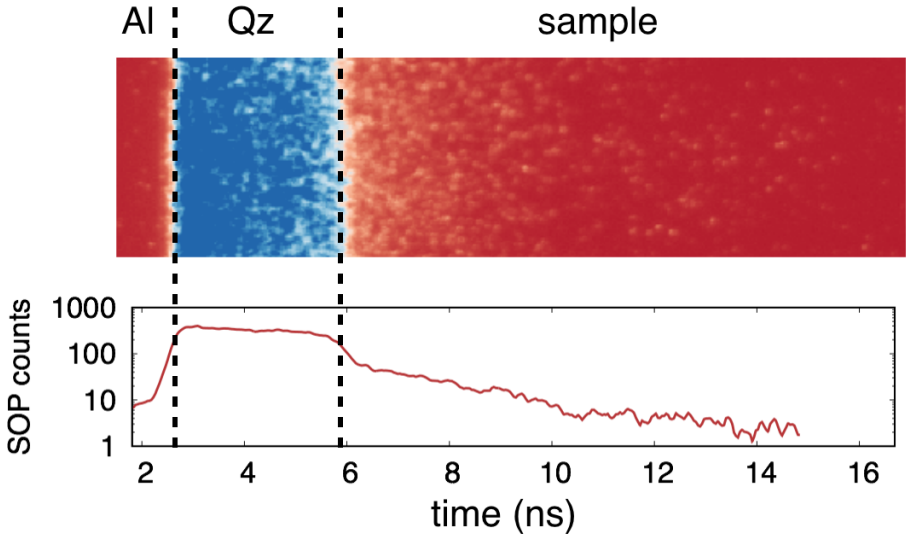

Figure 2.23 – SOP measurement of the self-emission of a multi-layered target (aluminum / α-quartz standard / icy mixture sample) at the GEKKO XII facility (see Chapter 4). The two dotted lines indicate the entrance of the shock wave in the quartz standard and in the icy mixture sample. **Top.** SOP output image. **Bottom.** Number of counts as a function of time. Prior to the shock arrival into the quartz standard, there are only a few counts (~ 10). When the shock enters into quartz, the signal becomes very high and slowly decaying in time as the shock is sustained by the drive laser pulse. When the shock enters in the sample, there is a sudden drop in the signal, which indicates that the shocked icy mixture emits less than quartz. The signal becomes decaying in time, as the shock is not sustained anymore by the laser pulse. It also becomes more noisy when the shocked-sample temperature approaches the detection limit of the SOP.

A combination of optical filters is placed at the entrance of the streak to select the spectral range of the collected emission. In fact, the self-emission can be linked to the temperature only if the emissivity $\epsilon(\lambda, P, T)$ is known all over the probed spectral range, but this parameter can be usually characterised only on a limited set of wavelengths. A common method to measure the emissivity of the shocked sample, which is extensively employed in the work presented in this Thesis, makes use of the shock-front reflectivity

$R_{sf}(\lambda, P, T)$ measured by the VISARs and applies Kirchhoff's law:

$$\epsilon(\lambda, P, T) = 1 - R_{sf}(\lambda, P, T). \tag{2.59}$$

This method allows the determination of the emissivity at the probe laser wavelengths (in this work, 532 nm and 1064 nm). However, the SOP has to work at a different spectral interval, as the one around the probe laser wavelengths is allocated to the VISARs and separated from the rest of the interval by the optical setup. Generally, the SOP working spectral interval is in the $300 - 500$ nm range. This choice, made to guarantee a maximum sensitivity to the self-emission of the sample, is dictated by the spectral efficiency of the streak camera and by the opportunity of working around the maximum spectral radiance of the sample, which is at 300 nm at typical probed temperatures around 10^4 K. A common approximation [Sano et al. (2011); Millot et al. (2015); Kimura et al. (2015)] consists in neglecting the spectral variation of the emissivity between the probe laser wavelength and the spectral interval of the SOP. This is called *grey-body approximation*, as it models the shocked sample as a grey body whose spectral radiance is a fixed fraction of that of a black body. Such approximation is justified by the fact that the working spectral interval of the SOP is near one of the two probe laser wavelengths (namely, 532 nm).

The relation between the self-emission of the body and the number of counts on the SOP output image depends on the path the emitted radiation undergoes before being finally acquired by the CCD. Depending on the F-number of the first diagnostics-side lens, a fraction of the emission is collected by the optical system, which globally has a spectral transmissivity $T_{\text{opt}}(\lambda)$ from the target to the entrance of the SOP (including the filters placed just before it). The spectral transmissivity affects the signal intensity and its spectral profile. The signal intensity is also affected by the magnification M of the optical system. The fraction of the signal which enters the streak camera is determined by the size of the slit, which can be regulated in the course of the experiment and is typically around 100 μm. Finally, the conversion efficiency of the streak camera and of the CCD have to be taken into account (see Section 2.5.3). This whole process can be condensed into a single formula linking the time-dependent number of counts on the output image $N_c(t)$ to the time-dependent self-emission of the source $L_\lambda(\lambda, T, t)$:

$$N_c(t) = \alpha \int_0^{+\infty} L_\lambda(\lambda, T, t) T_{\text{opt}}(\lambda) d\lambda, \tag{2.60}$$

Equation 2.60 provides a parametric formula which depends on a calibration factor α, which depends on the experimental setup. A useful approximation can be made to simplify equation 2.60 if the optical filter placed before the SOP has a narrow bandwidth, *i.e.* it has a non-zero transmittance only inside an interval $(\lambda_0 - \Delta\lambda, \lambda_0 + \Delta\lambda)$, with $\Delta\lambda \ll \lambda_0$. In this case, equation 2.60 can be easily inverted to

$$T = T_0 \left[\log\left(1 + \frac{A\epsilon}{N_c}\right) \right]^{-1}, \tag{2.61}$$

where $T_0 = hc/\lambda_0 k_B$ and A is a simplified calibration factor, linked to α by the formula

$$A = \left[\frac{4hc^2}{\lambda_0^5} T_{\text{opt}}(\lambda_0) \Delta\lambda \right] \alpha. \tag{2.62}$$

If the optical filter before the SOP is not narrow, there is no analytical inversion possible for equation 2.60 and temperature must be obtained from N_c via a numerical method.

Calibration

At this point, we have determined the formula linking the number of counts on the SOP to the temperature of the sample. This formula (equation 2.60) contains a parameter α, which has to be measured – by doing so, the SOP is calibrated. If the SOP optical filter has a narrow bandwidth, calibration consists in measuring the simplified parameter A in equation 2.61. To do so, in the experimental work presented in this Thesis we employed three methods: (i) calibration on dedicated shots, (ii) *in situ*, and (iii) using a spectral lamp.

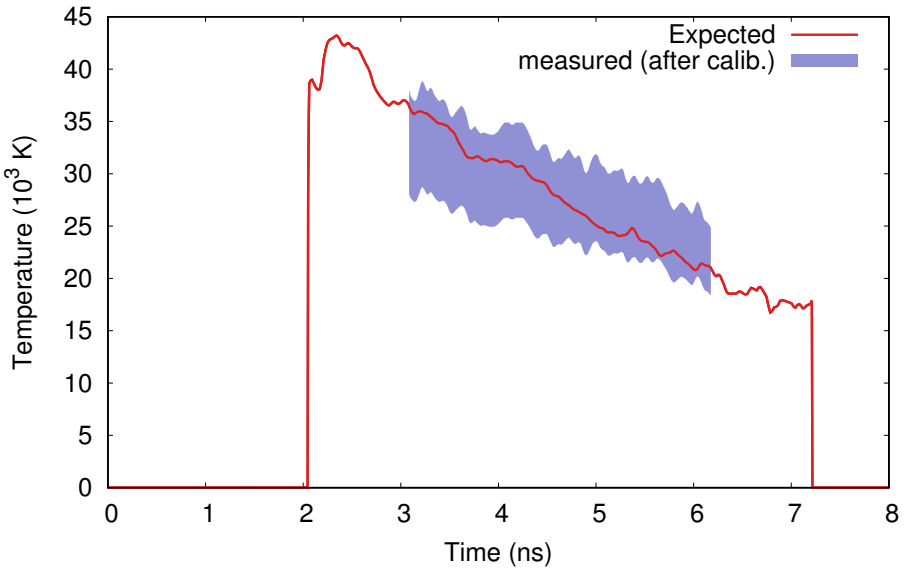

Figure 2.24 – SOP calibration with a dedicated shot on α-quartz during an experimental campaign at LULI2000. The red curve is the expected temperature of shocked α-quartz from the measurement of $U_s(t)$ using the $T - U_s$ relation from Millot et al. (2015). The blue area represents, within error bars, the temperature of shocked α-quartz obtained after calibrating the signal on the expected temperature profile. Only a central interval of the time window of the signal has been taken into account for a better precision.

Method (i) consists in performing, during an experimental campaign, a certain number of dedicated shots on targets which contain a standard material whose $T - U_s$ relation is well known. The shock velocity of the standard is measured by VISAR, so that the expected temperature is known from the $T - U_s$ relation. The calibration factor of the SOP α or A is then measured by linking the measured counts N_c to the expected temperature through equation 2.60 or equation 2.61, respectively. Within this context, a very common standard is α-quartz (which is also a common standard for the relative EOS measurements, as we have discussed in Section 2.3.4). Indeed, Millot et al. (2015) provided a robust $T - U_s$ fit along its principal Hugoniot curve. Moreover, the effect of static pre-compression on shock-compressed α-quartz properties, including temperature, has been studied by Brygoo et al. (2015). This last study is crucial in the context of shock-compression of statically pre-compressed samples (see Chapter 3), which is one of the techniques we used in this Thesis to characterise warm dense ammonia (see Chapter 5). For every experimental campaign at LULI2000, we dedicated some shots on targets with the following structure: polystyrene / aluminum /

α-quartz to calibrate the SOP. Figure 2.24 shows the comparison between the expected temperature profile in shocked quartz from the shock velocity measurement using the $T - U_s$ by Millot et al. (2015) and the measured temperature after calibration. The measured calibration factor was $A = (72^{+12}_{-7}) \cdot 10^3$ for the employed time window of 20 ns.

Method (ii) – *in-situ* calibration – can be seen as a variation of method (i) that consists in placing a standard material directly inside the target containing the sample under study. It can be placed before it or side by side. In both cases, the SOP collects the emission from both the standard and the sample.

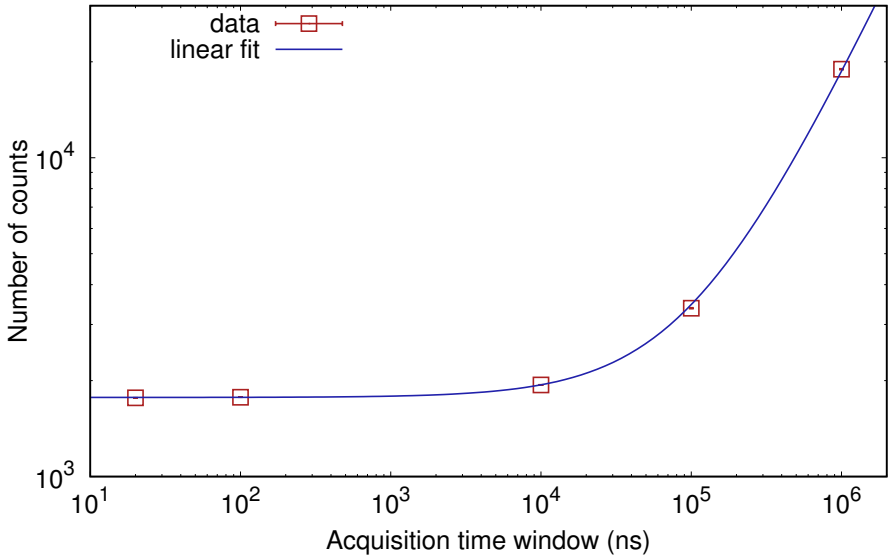

Figure 2.25 – SOP calibration with an Osram lamp after an experimental campaign at LULI2000.

Finally, the SOP can be calibrated placing at the TCC a lamp whose spectral emission is well known and measuring the SOP signal – this is method (iii). For some experimental campaigns at LULI2000 included in this work, an Osram WI 17/G lamp has been used, providing a black-body temperature of $T = 2611 \pm 11$ K. This value has been estimated by extrapolating the black-body values for other wavelengths provided in a previous calibration by Ruprechter (2000). Such temperature is below the detection limit of the SOP when the typical time window of 20 ns is employed. For this reason, the SOP signal was acquired for a set of acquisition time windows Δt_{acq}. A linear fit

$$N_c(\Delta t_{\mathrm{acq}}) = a \cdot \Delta t_{\mathrm{acq}} + b \tag{2.63}$$

was then performed, where b represents the background noise and $N_c^{\mathrm{calib}} = a \cdot \Delta t$ is the quantity to consider to calibrate the SOP for an acquisition time window Δt. Figure 2.25 shows the fit performed on the measurements acquired for different time windows after an experimental campaign at the LULI2000 facility. The SOP filter was centred around 450 μm and its spectral width was 20 μm. The best fit parameters were $a = 0.01692(30)$ and $b = 1.7706(34) \cdot 10^3$. The resulting calibration factor valid for the narrow bandwidth approximation was $A = (68.8 \pm 3.7) \cdot 10^3$ for an acquisition time window of 20 ns. This value has to be compared to that measured with method

(i) during a dedicated shot on the same campaign: $A = (72^{+12}_{-7}) \cdot 10^3$. The two values are compatible within error bars. The value found with method (iii) is affected by considerably lower uncertainties. Indeed, method (iii) is based on a huge series of acquisition runs.

Detection limit

The number of counts on the SOP image pixels has an exponential dependence on temperature because of Planck's law (see equation 2.57). For this reason, low temperatures generate very low signals, so that the signal-to-noise ratios are too low to allow a precise determination of temperature. This implies that the SOP diagnostics has a certain temperature detection limit. For a typical setup, this limit is around $4000 - 5000$ K. Different approaches can be considered to decrease this value:

(i) increase the solid angle of the collected sample emission;

(ii) increase the width of the working spectral interval of the SOP;

(iii) increase the time window of the SOP.

Approach (i) is technically challenging, as the solid angle of the collected radiation from the target is limited by the quality of the first triplet lens and by the necessity of placing a shield between the target and the lens.

Approach (ii) increases the SOP signal by allowing photons belonging to a larger wavelength spectrum to be transmitted to the streak camera. However, this affects the precision of the temperature measurement since the contribution of each wavelength depends on the emissivity of the shocked material, which is wavelength-dependent and, in general, not measured except at the probe laser wavelengths.

Approach (iii) does not increase the number of photons itself, but the number of photons whose signal is collected in a single pixel of the CCD. The main drawback of this approach is the partial losing of temporal resolution. This may be critical if a decaying shock technique is employed, which requires the precise determination of the time-dependency of the emission. On the contrary, this approach can be justified in the context of sustained shocks.

Optical depth

A critical aspect to be taken into account when analysing a SOP output is due to the optical depth of the shocked sample under study. If the optical depth is thin, meaning that the absorption coefficient of the sample in the shock-compressed state is high, the self-emission of the target corresponds to the Planck radiation from the layer immediately behind the shock front, whose thickness is comparable to the photon wavelength, in the $0.1 - 1$ μm interval. The radiation coming from all the further layers is absorbed before leaving the shocked region. In this case, the self-emission encodes information only about the temperature of the state immediately behind the shock front. This is the case when the material is compressed up to a highly conducting state by a strong shock. We have dealt with this case in all the experiments presented in this Thesis in which we have characterised the high-pressure behaviour of materials compressed by single shocks (see Chapters 4 and 5).

On the contrary, if the optical depth of the shocked state is high enough (typically, $\sim$ 10 μm), the self-emitted radiation escaping from the target comes not only from the layer immediately behind the shock front, but also from the further layers of the compressed sample. The thermodynamic states of these layers do not lie along the Hugoniot curve of the material, as heat transport and hydrodynamic unloading have modified temperature and pressure after the shock loading. In particular, if the shock is unsustained, after the shock loading the pressure decreases in time, so that the spatial profile for a given time is characterised by increasing values of pressures when approaching the shock front; if the shock is sustained, the pressure profile is uniform. In any case, after a layer of the sample has been loaded by the shock, it initially exhibits the Hugoniot temperature corresponding to its pressure, but it is subsequently heated by conduction from the neighbouring layers, so that, at later times, it exhibits a higher temperature. In our experimental work, we had to deal with the last case in the context of dynamic pre-compression experiments (see Chapters 4 and 6), when a first, weak shot was let propagating inside the sample before a second, stronger one. The sample compressed by the first shock was optically transparent but exhibited a finite optical depth, which decreased the acquired signal coming from the double-shocked volume.

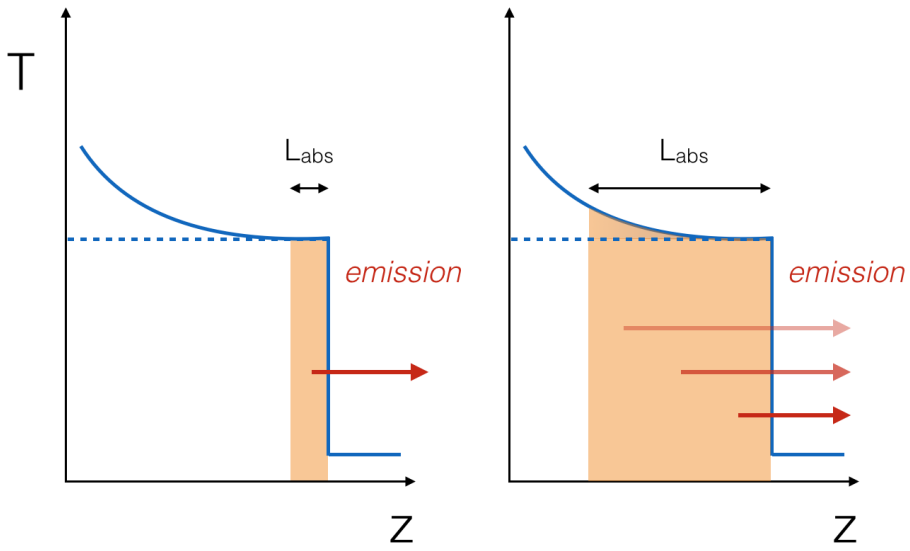

Figure 2.26 – Effect of the absorption length on the origin of the emitted radiation from a shocked sample. **Left**. The absorption length is smaller than the temperature gradient length scale and all the emitted radiation comes from a thin layer immediately behind the shock front. **Right.** The absorption length is greater than the temperature gradient length scale and the emitted radiation comes from different layers at different temperatures.

The general case is described by the radiation transport equation:

$$\frac{\partial I_\lambda(z)}{\partial z} = -k_\lambda(z) I_\lambda(z) + e_\lambda(z), \tag{2.64}$$

where $I_\lambda(z)$ is the local spectrally resolved radiation intensity crossing the layer positioned at z, $k(z)$ is the local spectrally resolved absorption coefficient, and $e(z)$ the local spectrally self-emission. From equation 2.64 a typical absorption length scale can be extracted: $L_{\text{abs}} \sim 1/k$, where k is the typical scale of the $k_\lambda(z)$ involved in the problem.

Let L_P and L_T be the typical pressure and temperature gradient lengths, respectively: $L_P \sim P/\partial_z P$, $L_T \sim T/\partial_z T$. If $L_{\text{abs}} \ll L_P$ and $L_{\text{abs}} \ll L_T$, all the self-emitted radiation can be considered as coming from a thin layer immediately behind the shock front, thus giving information only about the temperature of the Hugoniot state. In the opposite case, it will give information about all the off-Hugoniot states further behind, so that the data analysis becomes delicate and, often, impossible. Figure 2.26 depicts the first and second case on the left and right side, respectively.

2.5.3 Streak cameras

In shock experiments, a critical aspect to be considered is the time dependence of the properties of the shocked samples, given the fast temporal scales involved when WDM states are produced in the laboratory. The time scale of the studied phenomena is very short, typically of the order of 10 ns if high-power lasers are used to generate the shock, so that a high time resolution, in the picosecond regime, is needed to properly characterise them.

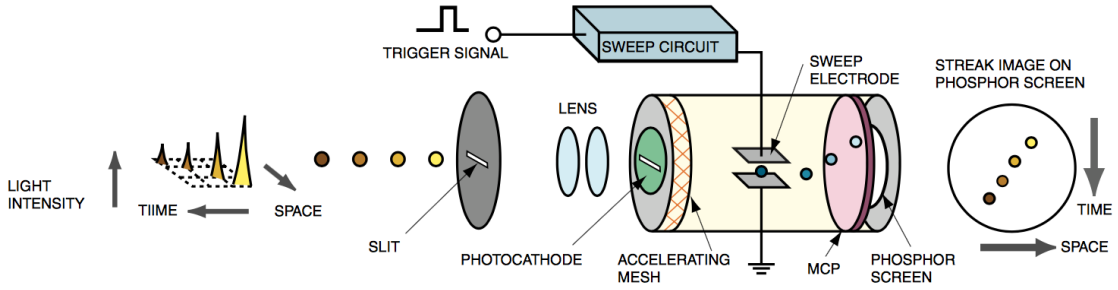

Figure 2.27 – Operating principle of a streak tube. Source: www.hamamatsu.com.

A streak camera is a device capable of diagnosing these fast phenomena. It delivers information about the intensity of a collected light signal as a function of time (over a window that can typically range from 1 ns to 1 ms) and of one spatial dimension (in shock experiments, this is usually the horizontal line-out of the target).

A streak tube, sketched in Figure 2.27, works as follows. The light signal passes through an entrance slit. A photocathode then converts the light signal into a proportional electronic signal. The produced electrons are accelerated along the tube axis. Inside the tube, the electrons pass through a capacitor (also called sweep electrode) whose voltage linearly varies in time over the acquisition time window of the streak. This means that electrons are accelerated (and thus deflected) towards the top depending on the time the pass through the capacitor. The vertical spatial axis is thus used as the arrow of time. After this stage, the electrons hit a micro-channel plate (MCP), which has a multiplying effect, and then impact against a phosphor screen, which has the function to convert the electron signal into a light signal, which is collected by a charge-coupled device (CCD), not shown in the Figure.

2.5.4 X-ray diagnostics

We have seen that, despite optical diagnostics such as velocimetry and pyrometry are essential tools for the characterisation of the thermodynamic state reached in the

shock-compressed sample, they are not capable of probing its microscopical behaviour. With this aim, X-ray diagnostics such as X-ray radiography, diffraction, and absorption have be to employed. Even if such diagnostics have not been used in the experimental work presented in this Thesis, one of the major perspectives of our work consists in the coupling of laser-driven shock compression of our materials of interest and these diagnostics, as we will detail later in the Thesis.

The basic principle of X-ray diagnostics is to probe the sample with photons whose wavelength is comparable to the length of the lattice parameters in crystals or to the distance between neighbour molecules in liquids and glasses. Within the context of shock compression, short-duration X-ray pulses are used to probe the structure of the sample volume under shock compression and during the subsequent release. Since the delay between the shock loading and the X-ray probe can be varied shot-by-shot, this diagnostics allows to characterise the kinetics of the transformation of the sample. In particular, the dynamics of shock-induced phase transitions can be investigated [Denoeud et al. (2016b); Hartley et al. (2019)]. X-ray diagnostics are generally coupled to the optical diagnostics, for a simultaneous determination of thermodynamic state and structural properties of the sample.

Experiments employing X-ray diagnostics in the context of shock-compression of materials have to respect several strict requirements: (i) the sources must have a high brilliance and monochromaticity; (ii) the X-ray pulse duration has to be short with respect to the dynamics of the shock compression; and (iii) a precise synchronisation between the mechanism producing the shock (such as the drive laser) and the X-ray probe has to be established to characterise the kinetics of the process under study.

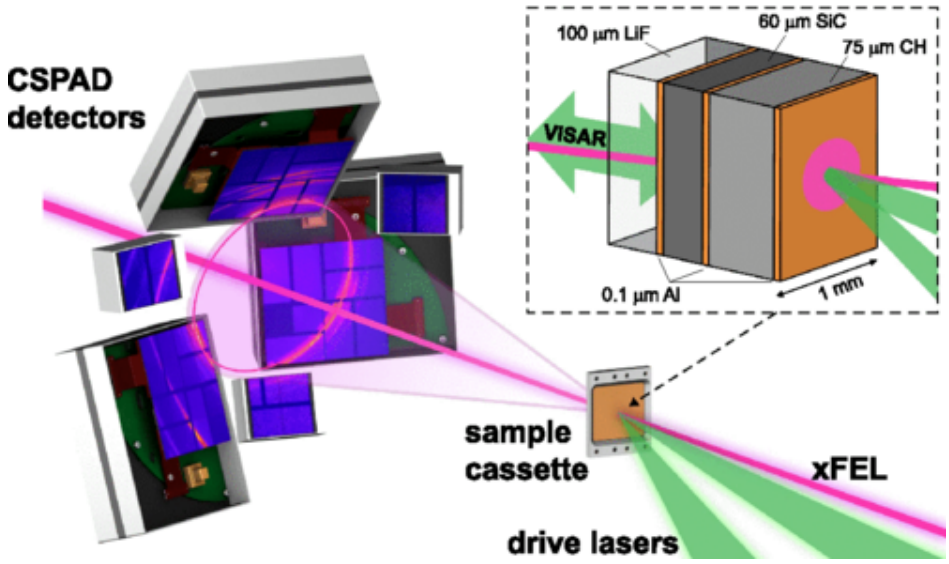

Figure 2.28 – Scheme of a typical setup for an X-ray diffraction experiment at the Matter in Extreme Conditions (MEC) instrument of SLAC–LCLS. The targets are encapsulated in a sample cassette which is moved and realigned after each shot. The two drive laser pulses are focused onto the target and generate a shock wave. VISARs are used to measure the shock velocity or the material velocity of the loaded sample. The XFEL beam is sent into the target. The scattered X-ray signal is acquired by the CSPADs (Cornell–SLAC pixel array detectors). Adapted from Tracy et al. (2019).

X-ray sources consist either of X-ray free electron lasers (XFEL) such as at SLAC–

LCLS (Menlo Park, California, USA), at the European XFEL (Schenefeld, Germany), and at SACLA (Sayo, Japan), or in synchrotrons, such as the ESRF (Grenoble, France). These sources are characterised by a high brilliance (around 10^{12} photons per pulse at LCLS) and energy resolution ($\Delta E_{\text{beam}}/E_{\text{beam}} \simeq 1.4 \cdot 10^{-4}$ at LCLS). The X-ray pulse durations (*e.g.* $\sim$ 100 ps at ESRF) are lower compared to the dynamics of shock-compression, so that the diffraction pattern effectively acquires a snapshot of the physical process in course. The sources are also tunable in energy, allowing to study processes with different spatial scales. In Figure 2.28 we show a scheme of a typical setup for an XRD experiment on shock-compressed matter at SLAC–LCLS. The quality of the acquired diffraction signal is evident, due to the use of dedicated detectors. However, only a few facilities in the world exist that can couple such high-quality X-ray beams to a setup for dynamic compression. Therefore, an approach to generate X-rays at high-power laser facilities has been developed. A possibility is to focus a picosecond-long laser beam onto a high-Z flag-shaped target, as it has been done at the LULI2000 facility [Antonelli et al. (2017)]. Within this approach, the brilliance and spectral quality of the X-ray beam are not comparable to those obtained by XFELs or synchrotrons. Nevertheless, this method allows to perform preliminary experimental campaigns to prepare a principal campaign on an X-ray facility.

2.6 Simulation tools

2.6.1 Hydrodynamic simulations

Hydrodynamic simulations are an essential tool that allows to anticipate the response of the target to the drive laser pulse and to the subsequent propagation of a shock wave. This is crucial for the design of the drive laser pulse parameters (energy, time shape, duration, and delay) and of the target, in order to avoid unwanted shock reverberations or pre-heating of the sample. It also allows to choose good diagnostics parameters (such as time window and delay). In the experimental work presented in this Thesis, we used the MULTI code, developed by Ramis et al. (1988) at the *Max-Planck-Institut für Quantenoptik (Garching, West Germany)*. The post-processing used in this work has been developed at LULI [Vinci (2006)]. We have performed hydrodynamic simulations to develop an alternative dynamic pre-compression method for the exploration of high-pressure / moderate-temperature states, presented in Chapter 3. Within this context, extensive simulation runs have been useful to understand the hydrodynamic path that a sample undergoes when it is compressed by a double-shock structure. They also allowed to design the laser pulse shapes and the target structures. Moreover, MULTI simulations have been performed in the context of single-shock compression to optimise the target structures, in particular for the high-energy shots on ammonia samples (see Chapter 5) that required a thin layer of gold as X-ray shield. Such a layer would generate a series of shock reverberations. Using hydrodynamic simulations we could design a target in which the reverberations did not modify the initial thermodynamic state of the ammonia sample.

We will now present the theoretical basis of the MULTI code. MULTI is a one-dimensional code. This means that it requires a reasonable computation time (in most cases, from a few tens of seconds to a few minutes on a typical laptop computer), but

the cost to pay is the complete loss of information about the spatial profile of the shock inside the target and its evolution over time. In particular, the transverse relaxation taking place at the boundaries of the shocked volume is not considered. This can be problematic especially in the case of a small drive-laser focal spot area and a thick target. In such case, two-dimensional codes may represent a better alternative, though they need a much higher computation time.

MULTI is a one-dimensional Lagrangian code, meaning that the target is decomposed in cells of constant mass and that the code follows their trajectories over time. Each cell i is identified by its initial position x_0^i, and each property F^i of the cell is represented as a function of the initial position x_0^i and of time t:

$$F^i = F(x_0^i, t), \tag{2.65}$$

in contrast with an Eulerian approach which uses the *current* position of the material cell:

$$F^i = F(x^i, t). \tag{2.66}$$

The Lagrangian picture is advantageous since it naturally rules out the flux of matter through two adjacent cells, hence reducing the computation time.

Shock compression can be generated by a mechanic force or by a high-power laser. In the first case, MULTI simulates a piston acting on one end of the target, and the piston velocity (which can vary over time) must be fixed by the user. In the second case, several laser pulses can be simulated, with the choice for each pulse of the wavelength, intensity, time shape (rectangular, Gaussian, triangular, with or without rise and fall times), and time delay. MULTI also allows the possibility of using the actual time profile of the drive laser to reproduce a shot already performed. The drive-laser beam is absorbed by the target via inverse Bremsstrahlung when it enters the corona and propagates up to the critical density (see Section 2.4.1), where it is reflected. Also the reflected beam loses energy via inverse Bremsstrahlung when it propagates backwards towards the source. The deposited power per length S is defined as the sum of the power per length lost by the incident beam and by the reflected beam (which is equivalent to the *difference* between the intensity gradients of the incident beam and the reflected beam).

Multi-layered targets can be easily treated with MULTI. Each material composing the target is divided in a mesh. The cell length Δx^i can be constant or can exponentially vary depending on the cell number:

$$\Delta x^i = k \cdot \Delta x^{(i-1)}, \tag{2.67}$$

with the parameter k (the geometrical ratio of the progression in equation 2.67) chosen by the user together with the number of cells of each material. As general rules, the target mesh should respect two conditions:

(i) the first cells on the drive-laser side must have a thickness which is at least 10 times smaller than the drive-laser wavelength, in order for the code to correctly simulate the laser energy deposition onto the target;

(ii) at each transition between two layers, the masses of the adjacent cells must not differ of more than 10%, to avoid non physical, mesh-related effects. An example of mesh is provided in Figure 2.29.

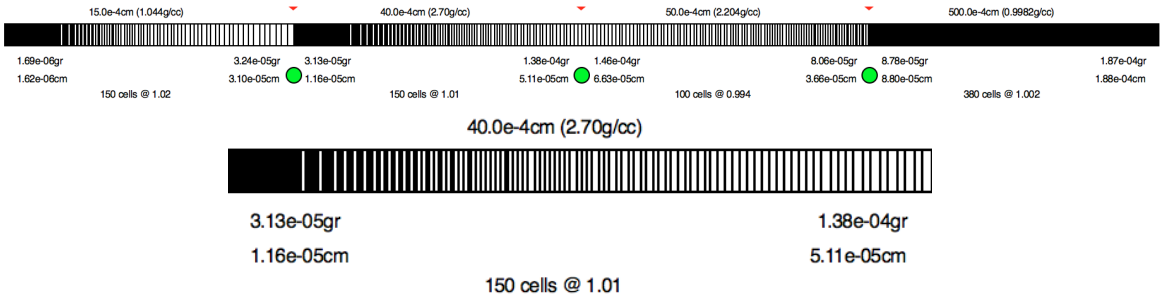

Figure 2.29 – **Top.** Screen capture of the user interface showing an example of mesh on a target composed by 15 μm of plastic, 40 μm of aluminum, 50 μm of quartz and 500 μm of water for a MULTI simulation. Each material has been divided in cells whose thickness varies exponentially as a function of the cell number. The cell mass and thickness are shown for the first and last cell of each material. The green circles indicate that the mass of the adjacent cells in a material transition zones differ of less than 10%. **Bottom.** Detail of the mesh of the aluminum layer. The layer thickness and the initial density of the material are shown on top. The number of cells and the parameter k of equation 2.67 are shown on bottom.

MULTI describes the shocked material as a single fluid with one or two temperatures depending on the user's choice. Using two temperatures becomes interesting when the dynamic under study is more rapid than the typical energy exchange time scale between the electronic and ionic populations. However, the one-temperature description is sufficient in most cases treated in this study, as the equilibration time between electrons and ions [Celliers et al. (1992); Basko et al. (1997)] is much lower ($\sim$ 10 ps) than the time scale of the shock-compression phenomenon ($\sim 1 - 10$ ns). The electronic heat flux q is simulated using the harmonic mean between the Spitzer-Harm flux and a free-streaming limit corrected by a limiting factor. This is done to take into account the effect of strong temperature gradients. The ionic heat flux is neglected. The details are presented in Ramis et al. (1988).

Radiation transfer effects can be taken into account depending on the user's choice. If this is the case, opacity tables must be provided to the code for each target layer. The opacity for each specified frequency interval is modelled using the Planck and Rosseland mean opacities. Including radiation effects considerably increases simulation times (from less than a minute to a few minutes) but is mandatory for an efficient target design in the case of high drive-laser intensities ($\sim 10^{13}$ W/cm^2), where the risk of unwanted sample pre-heating is high.

MULTI solves the three hydrodynamic equations that state the mass, momentum, and internal energy conservation. They are treated in the form:

$$\frac{\partial \rho}{\partial t} = -\rho^2 \frac{\partial u}{\partial m}, \tag{2.68}$$

$$\frac{\partial u}{\partial t} = -\frac{\partial \left(P_{\text{real}} + P_{\text{artif}}\right)}{\partial m}, \tag{2.69}$$

$$\frac{\partial e}{\partial t} = -\left(P_{\text{real}} + P_{\text{artif}}\right) \frac{\partial u}{\partial m} - \frac{\partial q}{\partial m} - \frac{Q}{\rho} + \frac{S}{\rho}, \tag{2.70}$$

where ρ, u, and e are the density, fluid velocity, and internal energy density, m is the Lagrangian coordinate (defined as the total mass at the left of the considered position),

P_{real} is the physical pressure, P_{artif} is a viscous-like artificial stabilising term, q is the thermal flux, Q is the radiated energy density, and S the energy density deposited by the laser. It should be noticed that m is a proper Lagrangian coordinate since the total mass at the left of a given cell position is invariant over time (there is no mass transfer between different cells). It is also worth noticing that temperature does not explicitly appear in the system of equations 2.68–2.70, but is implicitly included in the terms q and Q. In the case of a two-temperatures treatment, equation 2.70 must be separately written for each species (electrons and ions).

The system of equations 2.68–2.70 must be closed by providing an equation of state, in the form

$$P = P(e, T), \tag{2.71}$$

$$\rho = \rho(e, T). \tag{2.72}$$

The employed EOS must cover a quite wide range of thermodynamic conditions. Indeed, MULTI simulates the whole process of laser-target interaction, including laser ablation and the generation of a low-density, high-temperature corona and the response of the target to the shock loading and the subsequent release. Even if the EOS are not precise over the whole range of conditions, the output of the MULTI simulations nevertheless gives a rough anticipation of the response of the target to the drive laser and to the shock propagation. The EOS can be provided in an analytical form or as a table. In the last case, equations 2.71 and 2.72 are provided for a given set of e and T. In the case of two-temperatures treatment, separate electronic and ionic equations of state must be used. SESAME EOS tables are commonly used to run hydrodynamic simulations. They are developed and maintained by the Mechanics of Materials and Equation-of-State Group (T-1) of the Theoretical Division at the *Los Alamos National Laboratory (New Mexico, USA)* [Lyon and Johnson (1992); Johnson (1994)]. It has to be noticed that SESAME tables are in the form $P(\rho, T)$, $e(\rho, T)$, so that they have to be inverted to respect the form of equations 2.71 and 2.72. In the case where no SESAME table is available for a given material or for given conditions, one can build a quotidian equation of state (QEOS) [More et al. (1988)], which is less accurate and based on a Thomas-Fermi free electron gas model.

2.6.2 Ab initio simulations

Ab initio simulations are an essential tool for predicting the structural, transport, and optical-electrical properties of materials on a wide range of thermodynamic conditions, encompassing the Warm Dense Matter regime – which, as we have seen, is not covered by the well-established theories describing condensed matter or classical plasmas. As their name suggests, such simulations find solutions to the initial problem – the quantum many-body problem for a system of nuclei and electrons – that are based only upon the *first principles* of quantum mechanics. This means that no empiric parameter or model derived from experimental data is introduced in the process.

The experimental results of the work described in this Thesis have been compared to the predictions of supporting *ab initio* simulations performed by many collaborators. Therefore, we will not enter in details as we have done in the description of the diagnostics and tools we have directly used, but we will rather provide the fundamental

basis to understand the contribution given by this tool to our work and, more generally, to the study of WDM.

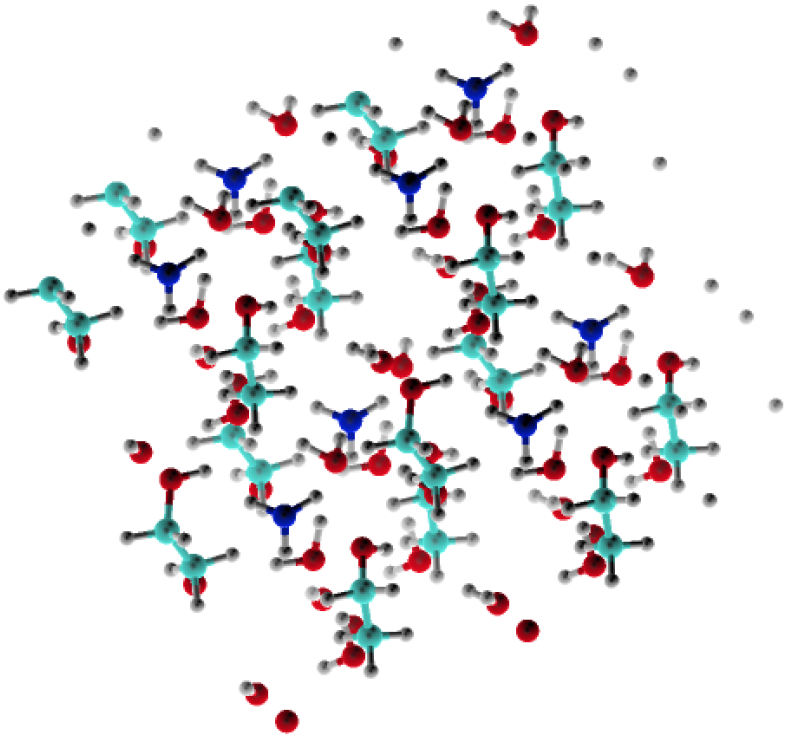

Figure 2.30 – Snapshot of a simulation by Mandy Bethkenhagen *(University of Rostock)* of a mixture of water, ethanol, and ammonia at ambient conditions. Hydrogen, carbon, nitrogen, and oxygen atoms are in grey, light blue, blue, and red, respectively. Water (H_2O), ethanol (C_2H_5OH), and ammonia (NH_3) molecules are visible, together with more complex structures and isolated hydrogen atoms. Simulations of water–ethanol(–ammonia) at ambient conditions and water–methane(–ammonia) mixtures along their Hugoniot curves have been conducted in support to our experimental results (see Chapter 4). Courtesy of the author.

The initial problem to be solved by simulations is the quantum many-body problem, which consists in finding the quantum wavefunction ψ that solves the Schrödinger equation $H\psi = E\psi$ where the Hamiltonian H describes a system of N_e interacting electrons and N_{nuc} atomic nuclei:

$$H = \sum_{i=1}^{N_{\text{nuc}}} \frac{P_i^2}{2M_i} + \sum_{i=1}^{N_{\text{nuc}}} \sum_{j \neq i} \frac{Z_i Z_j e^2}{|\mathbf{R}_i - \mathbf{R}_j|} + \sum_{i=1}^{N_e} \frac{p_i^2}{2m_e} + \sum_{i=1}^{N_e} \sum_{j \neq i} \frac{e^2}{|\mathbf{r}_i - \mathbf{r}_j|} + \sum_{i=1}^{N_{\text{nuc}}} \sum_{j=1}^{N_e} \frac{Z_i e^2}{|\mathbf{R}_i - \mathbf{r}_j|}, \tag{2.73}$$

where P_i and p_i are the momenta of the nucleus i and the electron i, respectively, M_i and m_e are the masses of the nucleus i and of the electron, respectively, Z_i is the electric charge of the nucleus i, and $\mathbf{R}_i$ and $\mathbf{r}_i$ are the positions of the nucleus i and of the electron i, respectively. The five terms of the Hamiltonian in equation 2.73 are the kinetic energy of the nuclei, the Coulomb interaction between the nuclei, the kinetic energy of the electrons, the Coulomb interaction between the electrons, and the Coulomb interaction between nuclei and electrons, respectively. The wavefunction

solving the Schrödinger equation is a function of the positions of the nuclei ($\mathbf{R}_i$) and of the electrons ($\mathbf{r}_i$): $\psi = \psi(\mathbf{R}_i, \mathbf{r}_i)$.

Even if *ab initio* simulations are not based on empirical parameters, they make use of different approximations that reduce the computational complexity of this initial problem. The first one is the Born–Oppenheimer approximation [Born and Oppenheimer (1927)], based on the fact that the electronic and nuclear motions happen at separated time scales, due to the much higher inertia M_{nuc} of a nucleus with respect to an electron (as $M_{\text{nuc}} \geq m_i \simeq 1840 m_e$). The nuclear and electronic motion are thus assumed to be decoupled, that is, the response of electrons to the movements of the nuclei is instantaneous. The wavefunction thus can be expressed as $\psi = \psi_{\text{nuc}}(\mathbf{R}_i)\psi_e(\mathbf{R}_i, \mathbf{r}_i)$, where $\psi_{\text{nuc}}(\mathbf{R}_i)$ is the wavefunction of the nuclei, that only depends on their positions, and $\psi_e(\mathbf{R}_i, \mathbf{r}_i)$, the electronic wavefunction, also depends on the positions of the nuclei as the electronic nebula follows their motion. The initial problem is separated into two parts: first, the electronic wavefunction has to be calculated for a given set of positions of the nuclei $\mathbf{R}_i$; second, the motion of the nuclei has to be calculated. This procedure is iterative as, once the new positons of the nuclei have been determined, the new electronic configuration has to be found and so on.

Electrons. In WDM conditions, electrons are degenerate (see Section 2.1.1). This means that a quantum description of their behaviour is mandatory. The problem to be solved is thus a quantum many-body problem for N_e electrons interacting with each other and with a given Coulomb external potential due to the presence of the nuclei, whose positions are known and which are considered as immobile in the framework of the Born–Oppenheimer approximation. Density Functional Theory (DFT), based upon the Hohenberg–Kohn theorems [Hohenberg and Kohn (1964)], provides a framework for reducing the initial problem (with $3N_e$ degrees of freedom) to the problem of determining the electronic density $n_e(\mathbf{r})$, a function of the 3 space coordinates, for the ground state of the system. Indeed, each observable of the system in its ground state can be expressed as a functional of $n_e(\mathbf{r})$. Such a drastic reduction of the degrees of freedom considerably reduces the computational cost of simulations, which maintain anyway a remarkable precision. However, the exact forms of the functionals are not known in general, implying that, at this point, some approximations have to be made. Kohn and Sham (1965) proposed to approximate the system of N_e interacting electrons with a fictitious system of N_e non-interacting electrons subject to an external potential that models the effect of the other electrons. The Kohn–Sham equations allow to iteratively determine the electronic density and thus to solve the initial problem. However, their theory does not provide the functional for the exchange–correlation (XC) term. To model this term, many functionals have been proposed. Between the most used in the context of WDM, we cite the Perdew–Burke–Ernzerhof (PBE) [Perdew et al. (1996)] and Heyd–Scuseria–Ernzerhof (HSE) [Heyd et al. (2003)] potentials.

Nuclei. As nuclei are much more massive than electrons, their de Broglie wavelength (see Section 2.1.1) is lower than their nearest-neighbour distance, so that the nuclear population is not affected by quantum degeneracy effects. This means that the motion of nuclei can be treated within a classical description. A Molecular Dynamics (MD) approach is thus suited, which consists in calculating the forces that act on the nu-

clei as the gradients of a potential (depending on the positions of the nuclei and on the electronic wavefunction) and updating their velocities and positions according to Newton's laws of motion.

2.7 Conclusions

In this Chapter, we have seen how WDM states can be generated and characterised in the laboratory. We have described different compression techniques, with particular attention to dynamic methods and to laser-driven shock loading, which is the approach employed in the experimental part of this Thesis. We have also introduced the optical diagnostics we have used in our work and that are common in the WDM domain: Doppler velocimetry and pyrometry. Finally, we have presented the simulation tools that have been essential for the anticipation and interpretation of our experimental results: hydrodynamic simulations and *ab initio* simulations.

The theoretical and experimental treatments of this Chapter were reduced to the case in which a single – sustained or decaying – shock is propagating inside the target. However, since shock loading generates very high temperatures, alternative compression techniques have to be developed to explore states closer to those typical of planetary interiors. Therefore, in the next Chapter we will treat the different methods which allow to probe lower temperatures. All these methods go beyond the single-shock compression technique by introducing some form of static or dynamic pre-compression of the sample.

Chapter 3

Going beyond single-shock compression

In Chapter 2, we described how to generate WDM states in the laboratory, with a particular attention to the shock-compression technique. Since the propagation of a shock wave is associated to a high entropy increase, compression via a single shock allows to characterise high-pressure / high-temperature ($10^4 - 10^5$ K) regimes. At high-pressure / moderate-temperature ($10^3 - 10^4$ K) conditions, closer to planetary interior profiles, the materials of interest for this Thesis possess variegated phase diagrams. Moreover, they all exhibit an insulator-to-conductor transition. Generating and probing such conditions requires alternative approaches based on the increase, via static or dynamic means, of the sample initial density, in order to decrease the shock-loading entropy jump. Static pre-compression usually consists of coupling a Diamond Anvil Cell and shock loading. Different dynamic pre-compression methods exist, including shock reverberation and the sequential generation of multiple shocks.

In this Chapter, we will first overview such techniques. We will then explore in more detail two strategies which have been used in this work: static pre-compression with Diamond Anvil Cells and dynamic pre-compression through double-shock loading. When addressing the latter we will present a method, which we have developed and applied, for directly characterising the thermodynamic state and optical properties of a double-shocked sample.

Contents

3.1 Context

3.1.1 The interest of moderate-temperature states

As we have seen in Chapter 2.2, today the most effective method for reaching high pressures up to tens of megabar is laser-driven shock compression. Within this context, the simplest possible approach consists in allowing the propagation of a shock through the sample which is initially at ambient conditions. The sample is thus compressed to a state belonging to the principal Hugoniot curve. Since the loading by a shock wave is a highly entropic phenomenon, for most materials of interest the principal Hugoniot spans very high temperatures ($10^4 - 10^5$ K) for pressures in the megabar range. In such a high-pressure / high-temperature regime, the materials of interest in the context of this Thesis – icy water–methane–ammonia mixtures, silica and silicate minerals – are for the most part in dense-plasma, electrically conducting states [Laudernet et al. (2004); Clerouin et al. (2005); French et al. (2010); McWilliams et al. (2012)].

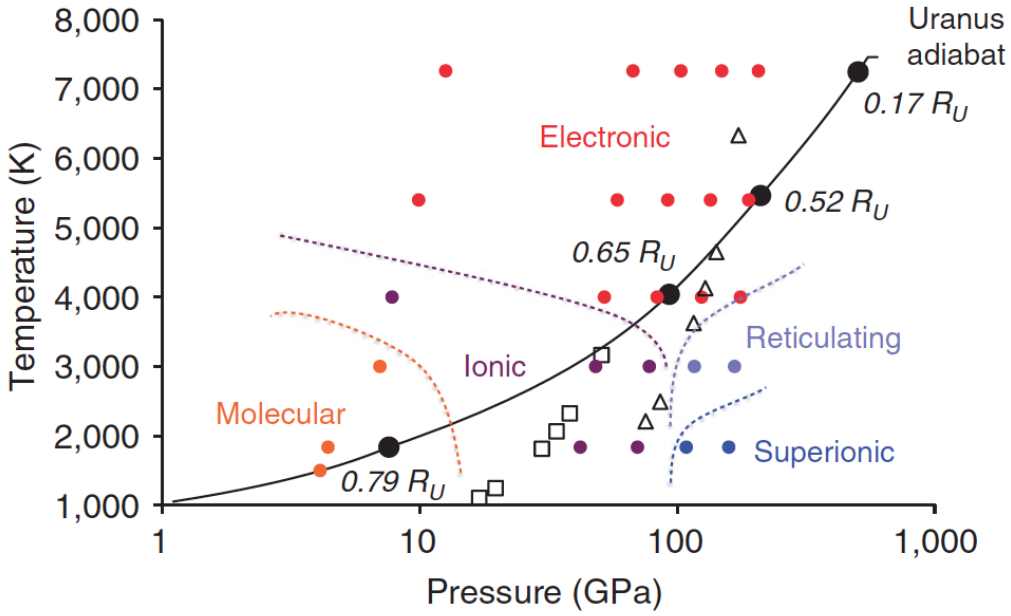

Figure 3.1 – Phase diagram of synthetic Uranus [Nellis et al. (1997)] in the temperature – pressure plane. The filled circles are results of *ab initio* calculations by Chau et al. (2011). Each colour corresponds to a stable phase. Open squares and triangles are experimentally obtained conditions after an initial shock and a reverberating shock, respectively. From Chau et al. (2011).

At lower temperatures ($10^3 - 10^4$ K), these materials undergo deep modifications of their structural and optical-electrical properties. Silica, for instance, melts at temperatures spanning from $4000 - 8000$ K at pressures between $1 - 5$ Mbar [Millot et al. (2015)]. At lower temperatures, it exhibits several stable phases, depending on pressure: between them, stishovite, $CaCl_2$, α-PbO_2, pyrite, cotunnite [Hicks et al. (2006)]. Above its melting curve, silica is in a fluid phase in which chemical bonds dominate;

melting is associated to a transition from an optically opaque, electrically insulating behaviour to a reflecting and conducting one [Millot et al. (2015)].

The same transition in the optical-electrical properties takes place in icy water–methane–ammonia mixtures and their end-members at temperatures of some 10^3 K. The onset of conductivity is primarily due to the generation of free electrons consequent to molecular dissociation with the increase of temperature. Besides, at temperatures of some 10^3 K, below the electronically conducting phase, a superionic phase has been predicted by *ab initio* calculations in pure water [Cavazzoni et al. (1999); Goldman et al. (2005); French et al. (2009); Hernandez and Caracas (2016, 2018)], pure ammonia [Cavazzoni et al. (1999); Bethkenhagen et al. (2013)], and water–ammonia mixtures [Bethkenhagen et al. (2015)]. In this peculiar state, oxygen or nitrogen atoms (for water and ammonia, respectively) are predicted to be organised in a crystalline lattice, whereas hydrogen atoms are free to diffuse by hopping between adjacent equilibrium positions in the lattice. This high ionic diffusivity affects the electrical conductivity. An experimental evidence of superionic water has been only recently found by Millot et al. (2018). The icy mixtures of water, alcohol, and ammonia, such as synthetic Uranus [Nellis et al. (1997)], exhibit a lot of chemistry-driven phenomena and stable phases. In particular, at moderate temperatures carbon and nitrogen atoms affect the structural properties of the mixtures by forming networks and lattices, as shown by the *ab initio* simulations by Chau et al. (2011). Figure 3.1 provides the phase diagram of synthetic Uranus in this moderate-temperature ($10^3 - 10^4$ K) regime.

Finally, characterising such high-pressure / moderate-temperature conditions is essential for planetary science. Indeed, planetary interior profiles are mostly adiabatic and span temperatures around $10^3 - 10^4$ K, as we have seen in Chapter 1.2.1. For all of these reasons, it is necessary to develop and apply alternative compression methods to the simple single-shock approach in order to probe such an interesting regime.

3.1.2 Increasing the initial density to probe lower temperatures

The entropy jump across a shock wave determines which fraction of the shock energy is used to compress the sample and which to heat it. Therefore, in order to decrease the temperature reached after shock loading, the entropy jump across the shock front has to be limited. The latter is controlled by the initial density of the sample: a higher initial density corresponds to a lower entropy jump. We have seen this principle at work in Chapter 2.3.3, when discussing the entropy jump associated to the compression by a series of shock waves: indeed, the action of each shock wave is to increase the density of the sample before the loading by the next shock, so that the global entropy jump is lower than in the case of the loading by a single shock wave.

Such behaviour of the entropy increase as a function of the initial density is general; however, for the sake of simplicity, we will only discuss it in the case the sample is an ideal gas. In this case, the jump in specific entropy across a shock front is

$$\Delta s_H(\rho_0, P_0; \rho) = k_B \left[\frac{3}{2} \log \left(\frac{e_H(\rho_0, P_0; \rho)}{e_0} \right) - \log \left(\frac{\rho}{\rho_0} \right) \right], \tag{3.1}$$

where ρ_0 and P_0 are the initial density and pressure of the sample, respectively, ρ is the final density, k_B is the Boltzmann constant, and $e_H(\rho_0, P_0; \rho)$ is the internal energy

density along the Hugoniot curve starting from ρ_0 and P_0 for the final pressure ρ, which can be written (using equations 2.27 and 2.23–2.25) as:

$$e_H(\rho_0, P_0; \rho) = \frac{P_0}{(\gamma-1)\rho_0}\left[\frac{(\gamma+1)-(\gamma-1)\rho_0/\rho}{(\gamma+1)-(\gamma-1)\rho/\rho_0}\right]. \tag{3.2}$$

In Figure 3.2 (top), we show the specific entropy jump across a shock front for different initial states of the sample. The effect of the initial density of the sample on the entropy jump function is evident. Figure 3.2 tells us that, by controlling the initial density, one can tune the final entropy for a given shock strength. As a consequence, the final temperature can be tuned, as shown in Figure 3.2 (bottom). As an example, an increase of 15% of the initial density allows to decrease the shocked temperature of 30% for a shock-compression factor of 3.

3.2 Different pre-compression techniques

The initial density of the sample can be increased through different techniques. A rather natural method to do it is to employ, if they exist, the different stable or metastable solid polymorphs of the sample material at ambient conditions. This has been done by Millot et al. (2015), who used three different initial phases of silica: fused silica ($\rho_0 = 2.20$ g/cm^3), α-quartz ($\rho_0 = 2.65$ g/cm^3), and stishovite ($\rho_0 = 4.29$ g/cm^3), exploring three distinct Hugoniot curves. Moreover, the sample may be pre-compressed statically (*e.g.* in a Diamond Anvil Cell) and maintained at high pressure prior to the shock [Loubeyre et al. (2004); Jeanloz et al. (2007)]. Similarly, the initial density can be increased dynamically. This can be done by placing a layer of a higher-density material next to the sample in order to obtain a shock reverberation [Nellis et al. (1999); Boehly et al. (2004); Knudson et al. (2012)] or using several laser pulses to sequentially produce multiple shocks [Benuzzi-Mounaix et al. (2004)].

Pre-compression techniques shall at the same time allow to reach high initial densities and to precisely characterise them. Indeed, the characterisation of the initial state is essential for determining the final conditions after the shock loading. Static pre-compressions with Diamond Anvil Cells allow very precise measurements of the reached state possible but are limited in the initial compression. Dynamic pre-compression methods generally allow to reach much lower temperatures than along the principal Hugoniot. However, the precise characterisation of the pre-compressed state is more challenging as it is obtained for a small amount of time. In this Section, we will review the different approaches and discuss their main advantages and limits.

3.2.1 Static method: Diamond Anvil Cells

The first possible approach to increase the initial density of the sample before shock loading is to compress it statically inside a Diamond Anvil Cell, which is also used within the framework of static compression studies (see Chapter 2.2.1). Within this approach, the DAC must be properly designed in order to maximise the initial compression of the sample and, at the same time, allow the coupling with a drive laser and the probing of the shocked state. Meeting such requirements involves real technical challenges. Indeed, the maximum achievable pre-compression is primarily determined

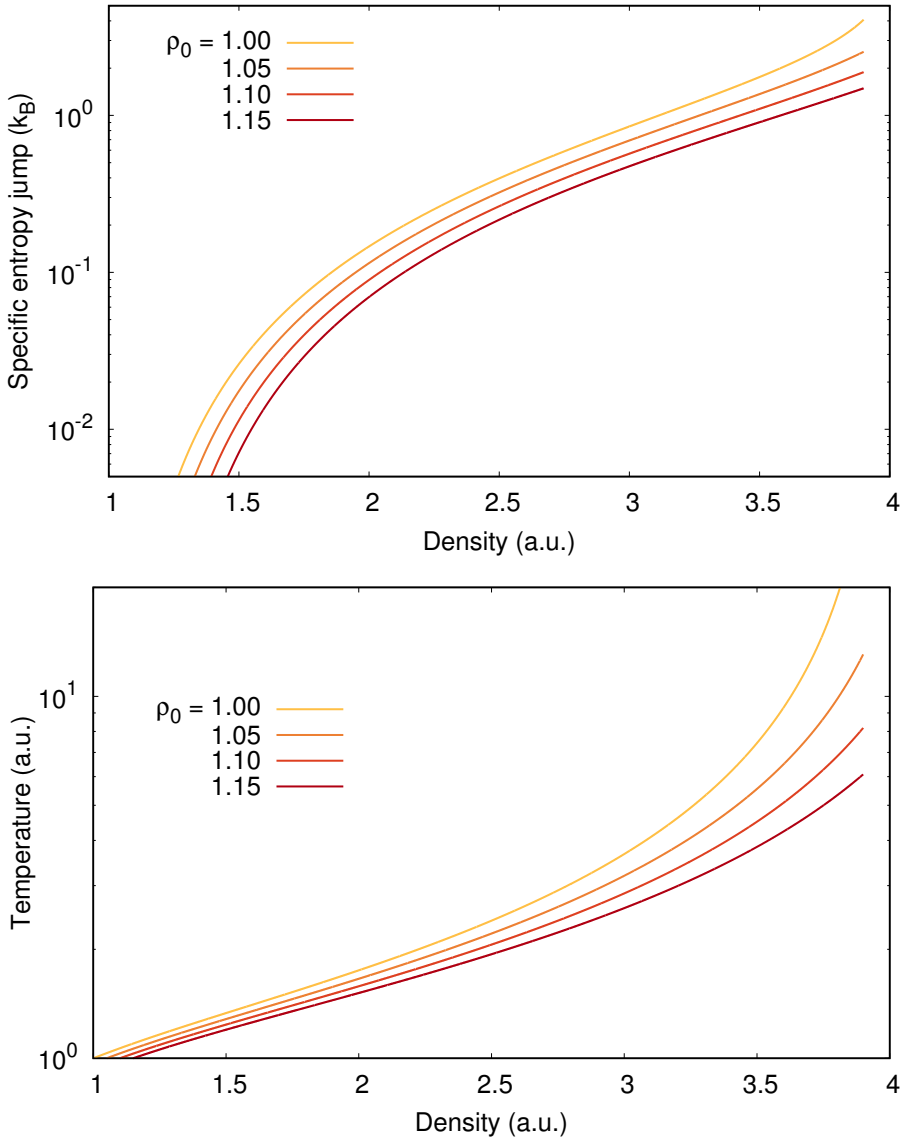

Figure 3.2 – **Top.** Specific entropy jump across a shock front as a function of the shocked density for a perfect monoatomic gas ($\gamma = 5/3$). **Bottom.** Shocked temperature as a function of the shocked density. Each curve in both plots corresponds to a different initial state ρ_0, P_0, T_0. The four initial states have the same temperature T_0 (hence $P_0 \propto \rho_0$). Density and temperature are expressed in arbitrary units.

by the shape and thickness of the diamond anvils [Loubeyre et al. (2004)]. However, the drive laser pulse has a limited energy and time duration, depending on the characteristics of the facility. Therefore, with the increase of the diamond thickness, a considerable fraction of the drive laser energy is employed in sustaining the shock while it propagates through the diamond layer. Moreover, if the laser pulse is not long enough, the lateral release of the shocked volume may affect the planarity of the shock wave before it enters the sample under study. To ensure shock planarity, the surface of the diamond anvil can be increased, so that its drive-laser side can be illuminated by a high-diameter pulse. However, the maximum initial pre-compression in the sample decreases if the diamond surface increases. As a consequence, designing a DAC

compatible with laser-driven shock implies a choice of compromise between the initial pre-compression (requiring high diamond thickness, low surface) and the final pressure after shock loading (requiring low thickness, high surface).

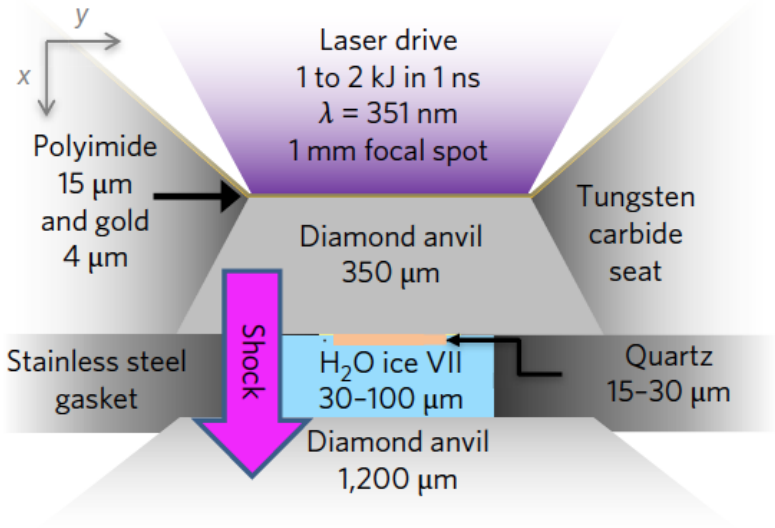

Figure 3.3 – Scheme of a Diamond Anvil Cell designed for laser-driven shock loading. A water sample is statically pre-compressed by two diamond anvils. A stainless steel gasket ensures the watertightness of the cell. A quartz layer is placed between water and the drive-laser-side diamond anvil as *in situ* standard. The drive-laser-side diamond anvil is 350 μm thick and is kept in place by a tungsten carbide seat. Its external side diameter is 1 mm. On the external side of the anvil and seat, a polyimide and a gold layers are deposited to act as ablator and X-ray shield, respectively. The rear-side diamond anvil is 1.2 mm thick. Adapted from Millot et al. (2018).

The maximum initial pressures achievable in a DAC designed to be coupled with laser-driven shock loading are of the order of some 100 kbar [Brygoo et al. (2015); Brygoo et al. (2017)]. This value is much lower than those achievable with a standard DAC, for which pressures beyond 5 Mbar have been achieved by Jenei et al. (2018) (see Chapter 2.2.1). It is also lower than the initial pressure values which can be obtained by dynamic pre-compression (see Section 3.2.2).

Figure 3.3 shows a scheme of a coupling between DAC and laser-driven shock loading realised by Millot et al. (2018) to study the Hugoniot curve of water starting from the ice VII ($\rho_0 \simeq 1.6$ g/cm^3) phase. The drive-laser side diamond anvil is 350 μm thick (usual thickness values are of some 100 μm), a compromise between the initial density and the compression reached by shock loading. The rear-side anvil is not subject to such compromise, but shall only allow the optical probing of the shocked sample. As a consequence, it can be much thicker (in this case, 1200 μm). The external diameter of the drive-laser side diamond is 1 mm, which corresponds to the diameter of the drive laser beam. Even this value is the result of a compromise between the laser intensity and the avoiding of a lateral release of the laser-driven shock while it propagates through the diamond anvil.

Despite the limits we discussed, the static pre-compression technique has a great potential for exploring a wide and interesting range of thermodynamic conditions. In-

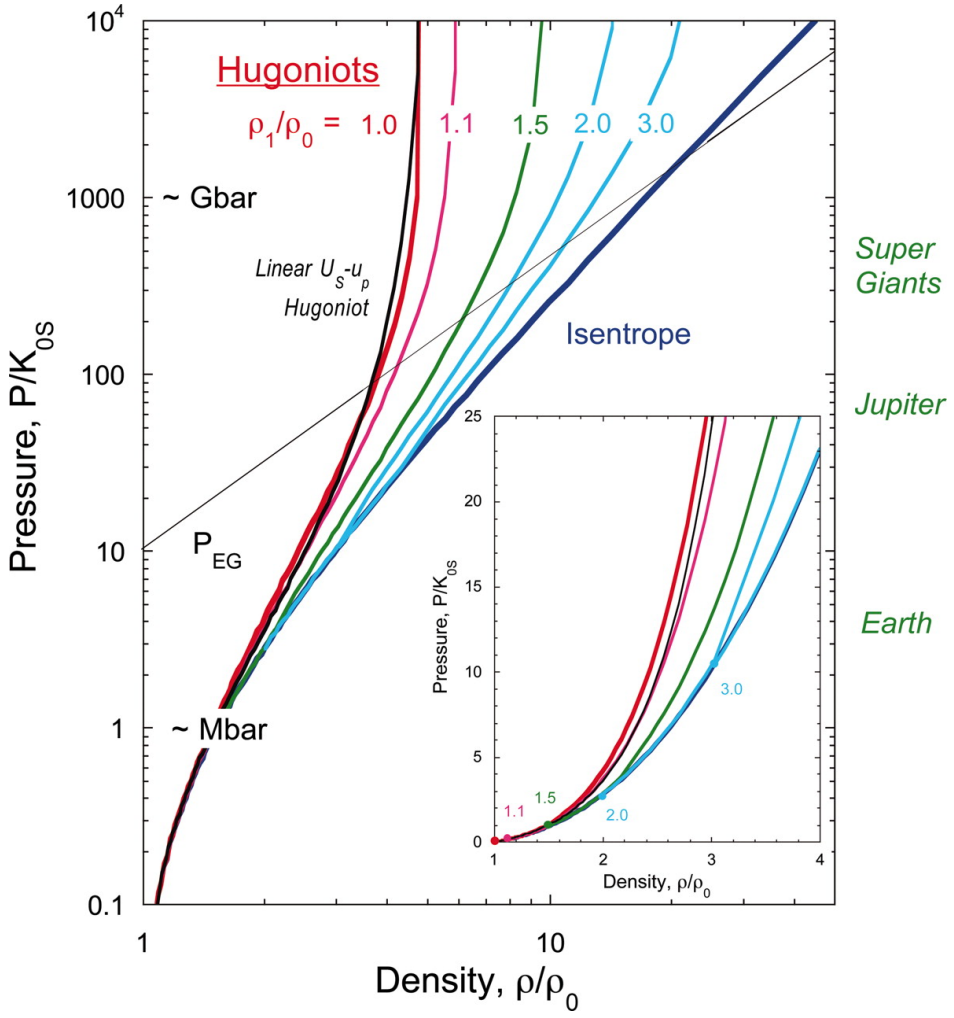

Figure 3.4 – Predicted pressure – density relations for generic condensed matter along an isentropic path (thick dark blue curve) and along different Hugoniot curves: the principal Hugoniot (thick red curve) and several statically pre-compressed Hugoniot for $\rho_1/\rho_0 = 1.1$, 1.5, 2.0, and 3.0 (thin coloured curves). Also the density dependence of the free-electron-gas pressure ($P \propto \rho^{5/3}$) is shown (thin grey curve). K_{0S} is the ambient-pressure bulk modulus. **Inset.** Zoom on low-density / low-pressure conditions. From Jeanloz et al. (2007).

deed, Jeanloz et al. (2007) considered a generic material of fixed ambient density ρ_0 and bulk modulus K_{0S} and calculated the Hugoniot curves for different pre-compressions using a Mie-Grüeneisen EOS model [Eliezer et al. (2002)]. These curves are shown in the pressure – density plane in Figure 3.4 and compared to the isentropic compression path starting from standard conditions. The Hugoniot curves starting from statically pre-compressed states occupy the intermediate region between the principal Hugoniot and the isentropic curve. In particular, an initial pre-compression limited to $\rho_1/\rho_0 < 2$ allows to span a considerably wide portion of the intermediate region between the principal Hugoniot and the isentropic curve.

The static pre-compression technique introduces the need of characterising standard materials for the initial conditions reached. A major contribution to this aspect has been given by Brygoo et al. (2015), who have extended the use of α-quartz as a standard material for the equation of state and reflectivity measurements to pre-

compressed states up to a pressure of 50 kbar (5 GPa). In the experimental work described in this Thesis, we employed Diamond Anvil Cells to statically pre-compress liquid ammonia samples (see Chapter 5). α-quartz has been used as *in situ* standard for impedance mismatch as well as for the determination of temperature and reflectivity in the ammonia sample.

3.2.2 Dynamic methods

Dynamic pre-compression methods are based upon the generation of a preliminary shock wave. This can be done by creating a reverberation or by directly generating multiple shock waves that will sequentially propagate inside the sample.

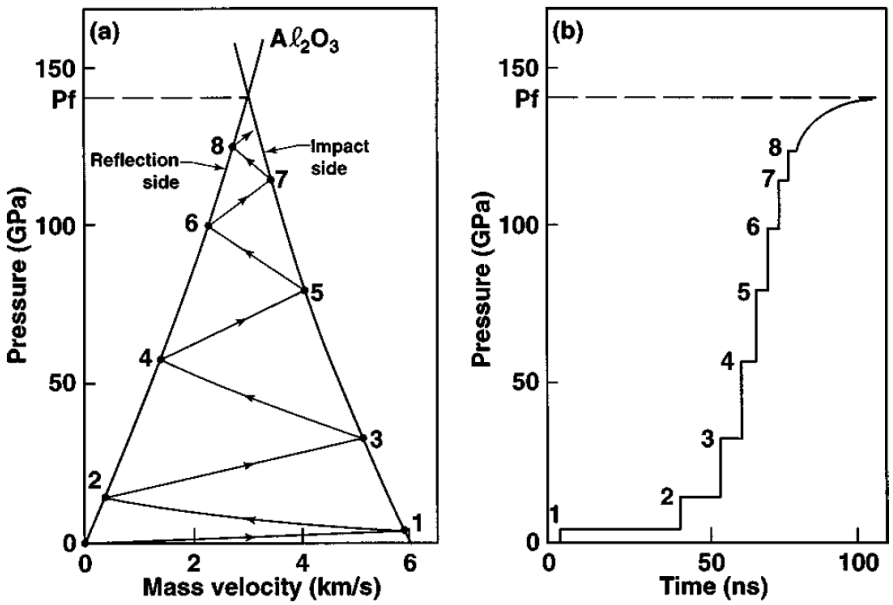

Figure 3.5 – Shock reverberation in hydrogen. The hydrogen sample is encapsulated between two sapphire (Al_2O_3) windows. **(a).** Compression path of hydrogen in the pressure – material velocity plane. up. State 1 is reached after the first shock in hydrogen; state 2 is reached when the first shock reflects off sapphire, etc. Even-numbered states lie on the Al_2O_3 principal Hugoniot; odd-numbered states lie on the mirror reflection of such Hugoniot. **(b).** Pressure as a function of time at midpoint of the hydrogen sample. The time duration of each pressure step shortens as hydrogen compresses. State 1 is a shocked state; states 2 and higher are very weak shocks and comprise a quasi-isentrope. P_f is the final pressure in hydrogen, equal to the incident pressure from sapphire. From Nellis et al. (1999).

Shock reverberations. As we have seen in Chapter 2.3.4, if a layer of a higher-density material B is placed after a layer of a material A in a target, when the shock propagates from A through B it will increase its loaded pressure; because the A/B interface is at mechanical equilibrium, this generates a reflected shock wave that propagates backwards through A (Figure 2.12). The state reached after this reflected shock is an off-Hugoniot state: indeed, the original shock wave has pre-compressed the sample A, and the reflected shock finds a sample off ambient conditions. This approach

has been employed by Boehly et al. (2004) and Knudson et al. (2012) for the study of deuterium and water, respectively. In both cases, a quartz window was placed after the sample. The double-shocked state in the sample was inferred via an impedance mismatch technique (see Chapter 2.3.4) from the measurement of the shock velocity in the sample and in the quartz layer.

A more complicated setup can be considered in which the reflection of the shock wave occurs multiple times. Indeed, if the sample under study is sandwiched between two higher-density materials, the shock wave will reverberate inside the sample as it will be reflected each time it arrives at the interface between the sample and the high-density layer. This technique has been applied by Nellis et al. (1999) and Denoeud et al. (2016a) for the study of hydrogen and silica, respectively. Nellis et al. (1999) placed the sample between two sapphire (Al_2O_3) layers and generated a shock wave using a two-stages gas-gun (see Chapter 2.2.2). The compression path of the sample in their experiment is shown Figure 3.5 (a) in the pressure – material velocity plane. The state reached in the sample reverberates between the principal Hugoniot curve of sapphire and its adiabatic release curve starting from the first shocked state of sapphire, until the pressure in the sample reaches the shocked pressure in sapphire (P_f). Pressure in hydrogen as a function of time is shown in Figure 3.5 (b).

Within a single-reverberation approach, the final state reached in the sample under study can be determined in a model-independent fashion [Boehly et al. (2004)]. Multiple-reverberation experiments, on the contrary, generally have to rely on hydrodynamic simulations (necessarily based on a modelled or tabulated EOS) to infer the reached conditions [Denoeud et al. (2016a)].

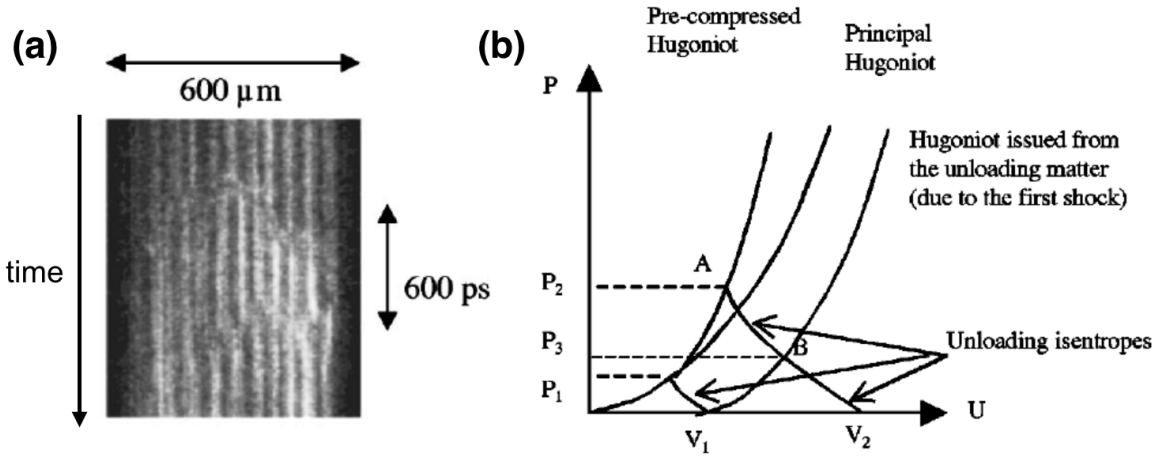

Figure 3.6 – Double-shock compression of an aluminum sample. **(a).** Free rear-side surface velocity of the sample measured on the VISAR image. A first fringe shift is visible when the first shock front reaches the rear side of the sample. This fringe shift is due to the movement of the free surface. A second shift appears when the second shock front reaches the free surface. **(b).** Determination of the state reached in double-shocked aluminum in the pressure – material velocity plane. P_1 and P_2 are the pressures reached after the first and second shock, respectively. V_1 and V_2 are the free-surface velocities experimentally. P_3 is the pressure after the second shock transmitted into the volume unloaded by the material velocity after the first shock. Adapted from Benuzzi-Mounaix et al. (2004).

Generation of multiple shocks. Another approach in the context of dynamic pre-compression is the generation of multiple shocks that sequentially propagate inside the sample, so that each shock finds a pre-compressed state after the action of the previous shocks. The last shock wave compresses the sample up to the high-pressure, moderate-temperature state of interest.

Benuzzi-Mounaix et al. (2004) proved the feasibility of this approach on the 6F laser facility at LULI (Palaiseau, France), generating a double-shock structure inside an aluminum sample. Since aluminum is metallic, the states reached in the sample were experimentally characterised with the measurement of the rear-side free-surface velocity by the VISARs, as shown in Figure 3.6 (a). The reached thermodynamic state was inferred using a tabulated EOS of aluminum. The hydrodynamic path of the sample under double-shock loading in the pressure – material velocity plane is provided in Figure 3.6 (b).

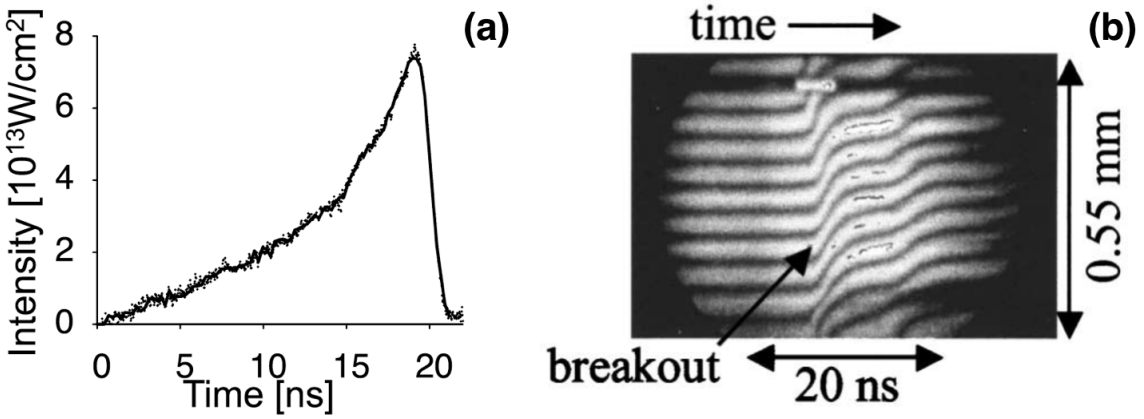

Figure 3.7 – Isentropic compression. **(a).** Ramped temporal profile of the drive-laser intensity. Adapted from Amadou et al. (2015). **(b).** VISAR image measuring the free-surface velocity of the rear side of a target. After the shock breakout, the fringe system shifts continuously as pressure gradually increases. Adapted from Edwards et al. (2004).

Isentropic and quasi-isentropic compression. Within the context of dynamic compression, an alternative method to probe moderate-temperature states is to compress the sample through an isentropic path [Swift and Johnson (2005); Smith et al. (2014)]. In this case, a compression wave is generated and let propagate through the sample, but the external force that sustains it (*e.g.* the drive laser) is carefully designed in order to avoid the formation of a shock within the interval during which the state is probed. In the case of laser-driven compression, this requires the generation of a ramped laser pulse. An example of such a laser ramp is provided in Figure 3.7 (a). As we have already discussed in Chapter 2.3.3, isentropic compression can be viewed as the limit for an infinite number of shocks of a multiple-shock compression approach.

Also a hybrid approach between shock and shock-less compression can be considered in which a weak initial shock wave is followed by an adiabatic compression wave. Such an approach allows to explore the adiabatic curve starting from the principal Hugoniot state reached after the first shock loading, characterised by slightly higher temperatures than the adiabatic starting from standard conditions. By designing the

laser pulse, one can control the strength of the initial shock and of the subsequent shock-less compression to control the thermodynamic path undertaken by the sample. This approach has been employed *e.g.* by Rothman et al. (2005) for the study of lead–antimony via magnetic compression and by Smith et al. (2014) for the study of diamond via indirect laser-driven compression.

Isentropic and quasi-isentropic compression experiments generally have to rely on the use of simulations to determine the reached set of states in the sample [Xue et al. (2018)]. However, an iterative Lagrangian analysis [Aidun and Gupta (1991)] can be employed to determine the reached pressure and density from a VISAR velocity measurement [Rothman et al. (2005); Smith et al. (2014)].

3.2.3 A thorough exploration of the phase diagram

The single-shock compression approach and the different pre-compression methods can be seen as complementary techniques that, when consistently applied to a material under study, allow to span a wide region of its phase diagram and to characterise different regimes. To prove this point, let us consider water, a key component of the interiors of the icy giant planets and also a paradigmatic material for the study of the WDM regime. The WDM phase diagram of water is shown in Figure 3.8, together with the interior profiles of Uranus predicted by different models.

Single shock. The principal Hugoniot of water (red curve in Figure 3.8) encompasses an ionic fluid phase, characterised by an electrically insulating behaviour, and, starting from around 6000 K, an electrically conducting fluid (plasma) regime. The principal Hugoniot crosses the adiabatic interior profiles of Uranus at around 0.4 Mbar, in the ionic regime, and the profiles including a Thermal Boundary Layer (TBL) at around 1.2 Mbar, in the plasma regime. Probing water via a single shock starting from ambient conditions is thus interesting for the characterisation of moderate-pressure / moderate-temperature states and high-temperature / high-pressure states.

DAC + shock. The set of conditions can be widened in the first place by coupling shock-compression with static pre-compression with the use of a DAC. This approach allows to span lower temperatures along a secondary Hugoniot whose slope is controlled by the initial pre-compression. In Figure 3.8, we show a secondary Hugoniot starting from an initial density of 1.25 g/cm^3 (blue curve). Such a curve enters in the stability domain of the superionic phase from 0.5 to 1.5 Mbar; at higher pressures and temperatures, it explores the plasma regime. It crosses the interior models of Uranus at considerably higher pressures than the principal Hugoniot ($0.8 - 0.9$ Mbar for the adiabatic, around 2.5 Mbar for the TBL models).

Double shock. Dynamic pre-compression can be employed by generating two shocks that sequentially propagate inside the sample. To allow an optical access to the double-shocked state, the first shock must leave water in a transparent state. If the first shock compresses water to 0.3 Mbar along the principal Hugoniot, the sample is still completely transparent, as water becomes opaque at around $0.5 - 0.6$ Mbar [Batani et al. (2015)]. We show in Figure 3.8 a secondary Hugoniot (green curve) starting

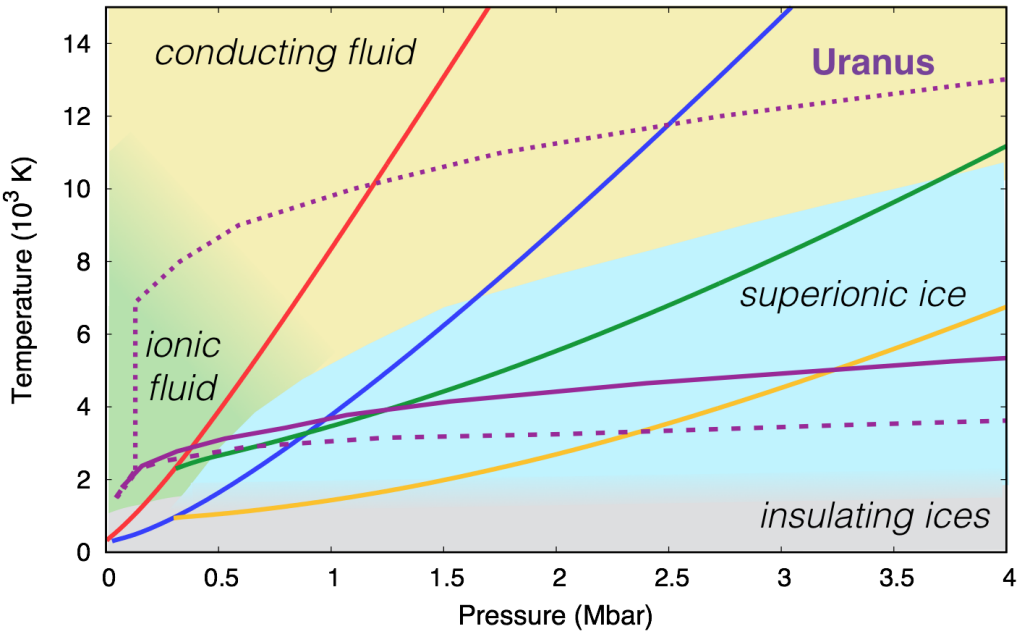

Figure 3.8 – Phase diagram of water in the WDM regime, in the temperature – pressure plane. The purple curves are the Uranus interior profiles as predicted by different models by Redmer et al. (2011) (water-only adiabatic interior, solid curve), Bethkenhagen et al. (2017) (icy adiabatic interior, dashed curve), and Nettelmann et al. (2016) (icy interior with a Thermal Boundary Layer, dotted curve). The other solid curves are the Hugoniot curves corresponding to different compression techniques: principal Hugoniot (single shock compression, red curve), statically pre-compressed Hugoniot (DAC + shock, blue curve), dynamically pre-compressed Hugoniot (double-shocks, green curve), statically + dynamically pre-compressed Hugoniot (DAC + double-shock, yellow curve). The Hugoniot curves have been extracted from the SESAME table 7154 for water. The initial conditions are: 1 bar, 300 K (red curve); 24 kbar, 300 K (blue curve); 0.3 Mbar, 2280 K (green curve); 0.3 Mbar, 1020 K (yellow curve). The water phase diagram has been taken from Millot et al. (2018).

from that point. Such Hugoniot is the locus of states that can be explored by the second shock. It is evident that, due to the higher initial compression, the slope of the double-shock Hugoniot is lower than the static pre-compression one. The double-shock Hugoniot crosses the interior profiles at $0.7 - 1.2$ Mbar (adiabatic models) and more than 4 Mbar (models including a TBL). Moreover, it probes a considerably extended portion of the superionic phase, from $0.4 - 3.7$ Mbar.

DAC + double shock. Finally, we can think of combining the static and dynamic pre-compression approaches to probe even lower temperature conditions. This is possible by generating two sequential shocks in a sample compressed in a Diamond Anvil Cell. Such sample would thus be statically pre-compressed, then dynamically loaded by two shocks. In Figure 3.8, we show a Hugoniot (yellow curve) starting from a state belonging to the statically pre-compressed Hugoniot (blue curve) at 0.3 Mbar (the same starting pressure of the green curve). The statically-and-dynamically pre-compressed Hugoniot curve has a slightly lower local slope than the double-shock Hugoniot but, due to its lower initial temperatures, probes lower temperature conditions. Such a Hugoniot

is in principle able to characterise the transition between the low-temperature insulating ices (which are stable up to around 1500 K) and the superionic phase. The lower boundary of the superionic phase should be studied with this method by controlling the static and dynamic pre-compression and thus tuning the pressure and temperature conditions reached after the second shock loading.

Table 3.1 – Application of different compression methods (single-shock compression, static pre-compression, and dynamic pre-compression) to the materials of interest in the context of this Thesis. **Legend.** p: applied in previous work; x: applied in the experimental work of this Thesis; n: still not applied in the literature.

Sample	**Single-shock c.**	**Static p.-c.**	**Dynamic p.-c.**
Water	px	p	px
Ammonia	x	x	p
Water–ethanol mix	x	n	n
Water–ethanol–ammonia mix	px	n	px
Silica	p	p	px

In the experimental work presented in this Thesis, we applied some of these techniques to each of the materials of interest, depending on the thermodynamic conditions we needed to probe. Static pre-compression is of particular interest for the study of the icy mixtures and their end-members, as the moderate pressure range ($\sim$ 1 Mbar) that can be achieved in mid-size laser facilities such as LULI2000 is sufficient to probe exotic phases (Figure 3.1) and conditions predicted inside icy giant planets (Figure 3.8). In Chapter 5, we will present our static pre-compression study of pure liquid ammonia.

Dynamic pre-compression has been applied to pure water and an icy water–ethanol–ammonia mixture to compare their optical properties on a wide set of thermodynamic conditions (see Chapter 4). An extensive application of the same technique to α-quartz samples has allowed to considerably extend the explored region of the phase diagram of silica. In Table 3.1 we summarise which techniques have been employed on the different materials of interest in this Thesis.

3.3 Directly probing dynamically pre-compressed samples

In the work presented in this Thesis, we have employed a double-shock compression technique on icy mixtures and silica. In particular, we have developed a method in which the thermodynamic state and optical reflectivity of double-shocked states can be *directly* probed using standard optical diagnostics, such as Doppler velocimetry and optical pyrometry.

The technique we developed, described in this Section, is based on the sequential propagation of two shocks inside the sample under study. A similar method has been demonstrated in a previous experiment by Benuzzi-Mounaix et al. (2004), as already mentioned in Section 3.2.2. In that case, the shocks were propagating inside a metallic sample so that the VISARs could only measure its free-surface velocity, as shown in Figure 3.6 (a). Our approach is different as it is aimed at directly probing the state

of interest instead of reconstructing it from indirect measurements using and EOS model. Our technique is thus relevant for transparent materials, such as silica and water–methane–ammonia mixtures, which are central in the work presented in this Thesis. Within our approach, the measurement of the thermodynamic state is based on a generalisation of the Rankine–Hugoniot relations already provided by Birnboim et al. (2010), who studied the propagation of double shocks in an astrophysical context concerning galaxy clusters. Our technique requires the knowledge of the principal Hugoniot of the sample and of its refractive index in the transparent portion of the Hugoniot curve. Moreover, if the compressed material exhibits a multiple-wave structure in the low-pressure region of the Hugoniot curve as a consequence of its elastic behaviour or of a phase transition [Zel'dovich and Raizer (1966)], the properties of the precursor wave should be accounted for. The properties whose knowledge are necessary to apply our method have been already characterised for many materials of planetary interest [Sano et al. (2011); Knudson et al. (2004); Kimura et al. (2015); Zha et al. (1994); Batani et al. (2015); Wackerle (1962)]. However, this requirement does not limit the application field of this technique since such properties can be measured in a preliminary part of a dedicated experimental campaign.

In our compression approach, the first shock brings the material to a uniformly-compressed, denser state. To allow a direct characterisation of such state, we require that the material remains transparent after being loaded by the first shock. To achieve uniform compression, it is essential that the first shock is stationary, so that it must be sustained by a fairly long ($\sim$ 10 ns) pulse. For the state to remain transparent, the pulse must be weak enough – its intensity should be around $\sim 10^{12}$ W/cm^2. The second shock aims at creating the high pressures conditions and is sustained by a much more intense ($\sim 10^{13}$ W/cm^2), but shorter ($\sim$ 2 ns) laser pulse. Since it loads a material with a higher density than the ambient one, it generates colder states with respect to those belonging to the principal Hugoniot. Given that the second shock is faster than the first, the two eventually merge inside the target. The merged shock brings back the sample to a state on the principal Hugoniot.

The density, pressure, and internal energy density of the double-shocked sample are measured via a "self impedance mismatch" technique, which is analogous to classical impedance mismatch (see Chapter 2.3.4) but employs the principal Hugoniot curve of the sample itself as standard instead of another material. The self impedance mismatch technique requires the experimental characterisation of the state reached after the first shock loading and after the merged-shocked loading, which both lie along the principal Hugoniot of the sample. The characterisation of the second-shock velocity is also essential.

As the characterisation of the double-shocked state is direct, our technique does not require the use of hydrodynamic simulations to infer it. Since, in our approach, the double-shock state can be directly probed, its optical properties can be characterised. In particular, it can be determined if such state is opaque or reflecting. In the latter case, the second-shock-front reflectivity can be measured exploiting the VISAR data. In general, our technique extends the possibility to investigate high-pressure / moderate-temperature states to a wide class of medium-size laser facilities including LULI2000.

3.3.1 Hydrodynamic path and measurement strategy

We present in detail the hydrodynamic path inside the sample and how the variables of interest can be measured. A synthesis of the situation inside the sample and the measurable variables for each phase of a double-shock compression shot is provided in Table 3.2. The space–time diagram of the path followed by the shock waves through the sample is shown in Figure 3.9. The target shown in the Figure consists of an ablator, an aluminum layer, and the transparent sample under study. The aluminum layer serves as reflector for the probe laser in the initial phases of the shot. Diagnostics (VISARs, SOP) are on the right side of the Figure. All the velocities are expressed in the laboratory frame.

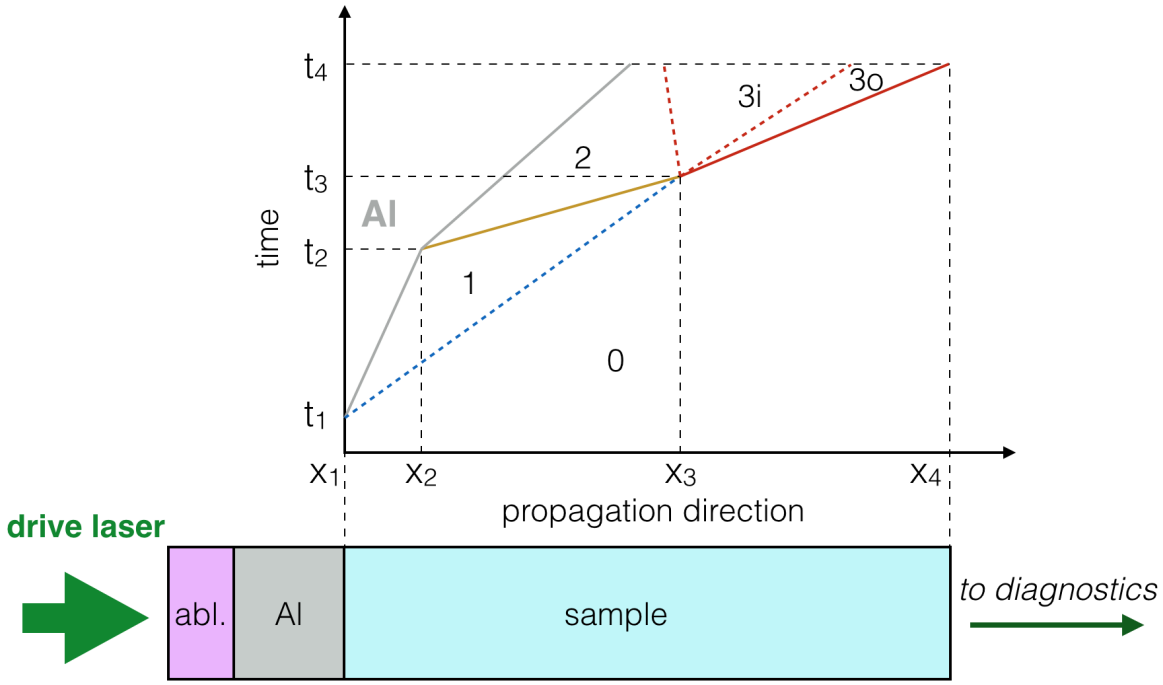

Figure 3.9 – **Top.** Shock propagation history inside the sample. x_1 and x_4 are the initial position of the aluminum/sample interface and of the rear side of the sample, respectively. The grey line is the path of the aluminum/sample interface. The blue dashed line is the first shock front. The yellow line is the path of the second shock front. The red solid line is the merged shock front. The two red dashed lines represent the adiabatic release (left) and the contact discontinuity (right). **Bottom.** Scheme of a typical laser target for double-shock compression.

First shock

At $t = t_1$, the first shock enters into the sample. The shock propagates at the velocity $U_s^0(t)$ (blue line in Figure 3.9). Due to the weakness of the first shock, the shocked state 1, which moves at the material velocity $U_p^1(t)$, remains optically transparent. As a consequence, the probe laser is reflected by the interface between the sample and the metal layer designedly placed before it. The interface is at mechanical equilibrium with the state 1 of the sample, so that it moves at its material velocity $U_p^1(t)$ (grey line).

Therefore, starting from $t = t_1$, the VISARs can measure that velocity. The first laser pulse must be properly designed to guarantee the stationarity of the first shock, so that the material velocity remains constant ($U_p^1(t) \simeq U_p^1$). The hydrodynamic configuration inside the sample while the first shock is propagating inside is shown in Figure 3.10 (a).

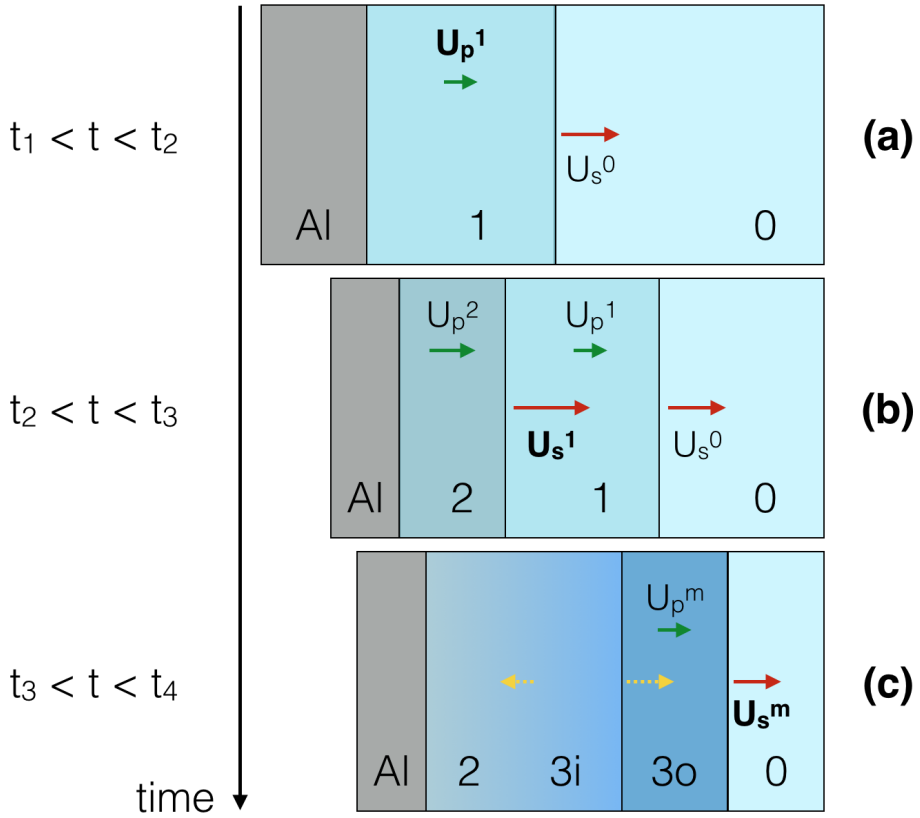

Figure 3.10 – Schematic picture of the shocked target for $t_1 < t < t_2$ (a), $t_2 < t < t_3$ (b), and $t_3 < t < t_4$ (c). *(a).* The first shock propagates with a velocity U_s^0, leaving a transparent shocked state 1 moving at the material velocity U_p^1. *(b).* The second shock propagates at U_s^1, leaving a double-shocked state 2 moving at U_p^2. *(c).* The merged shock propagates at U_s^m, leaving a shocked material in state 3o. A contact discontinuity, which moves towards the right, divides 3o and 3i. A gradual adiabatic transition, which connects the regions 2 and 3i, moves towards the left. The variables measured during each time window are in bold.

Second shock

At $t = t_2$, the second shock enters the sample and leaves it on a state 2. Such state is off the principal Hugoniot curve of the sample, as it is produced by a sequence of two shock-compressions, and is the state of interest for this technique. The second shock propagates with a velocity $U_s^1(t)$ (yellow line in Figure 3.9) which is supposed constant (U_s^1). Since the second shock is quite strong, state 2 cannot in general be transparent. Depending on the optical properties of state 2, the probe laser can be reflected by the second-shock front or absorbed while it propagates the region 2 of the sample. In the first case, the second-shock front velocity U_s^1 can be measured by the

VISARs. The thermal self-emission from the double-shocked state is generally intense enough to be measured by the SOP, so that an increase in its signal is visible at $t = t_2$. The hydrodynamic configuration inside the sample, while both the first and the second shock are propagating inside, is shown in Figure 3.10 (b).

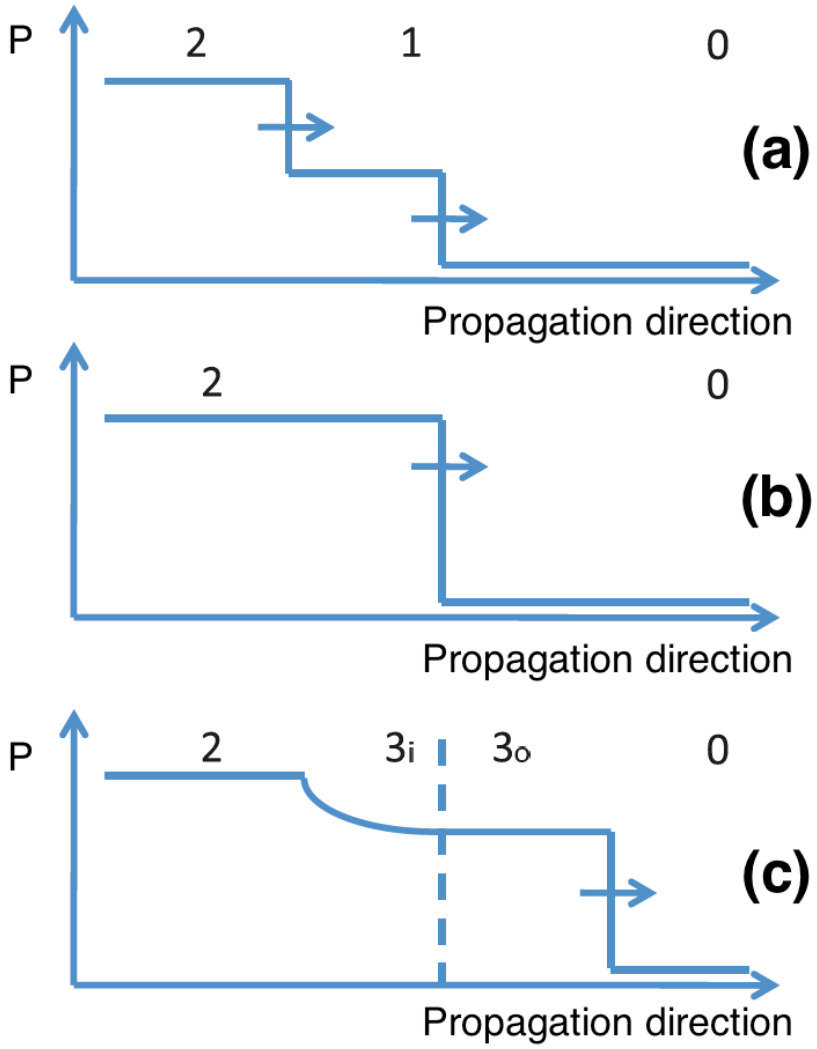

Figure 3.11 – Spatial profile of the pressure in the different stages of double-shock compression. **(a).** The two shocks propagate inside a sample with a pristine state 0. The first compresses the sample to a principal-Hugoniot state 1; the second to an off-Hugoniot state 2. **(b).** The two shocks have just merged, producing an inconsistent discontinuity between the pristine state 0 and the double-shocked state 2. **(c).** An adiabatic release between state 2 and a newly formed state 3i, which has a slightly lower pressure, takes place. State 3i is connected to state 3o by a contact discontinuity (dashed line). State 3o is a principal-Hugoniot state produced by the compression of state 0 by the merged shock. Adapted from Birnboim et al. (2010).

Merging of first and second shock

Since the second shock is faster than the first, the two will eventually merge and form a merged-shock which propagates at $U_s^m(t)$ (solid red line in Figure 3.9). This happens at $t = t_3$. In that moment, a discontinuity between the pristine state 0 and the double-shocked state 2 occurs. Now, this transition is not consistent with the Rankine–Hugoniot relations: indeed, the internal energy of the double-shocked state 2 is lower than that of a state at the same pressure but obtained through a single-shock compression. As a consequence, the configuration at $t = t_3$ is unstable. Stability is recovered when an adiabatic release takes place from the double-shocked region 2 to a newly formed region 3. The region 3 consists of two sub-regions 3i and 3o, separated by a contact discontinuity, across which density and internal energy are not continuous, while pressure and fluid velocity are. The sub-region 3i is the result of the adiabatic release from state 2, while 3o is consistent with the Rankine–Hugoniot relations from state 0 and therefore lies along the principal Hugoniot [Birnboim et al. (2010)]. The spatial profile of pressure in the process of merging of two shocks is provided in Figure 3.11.

Merged shock

The merged shock compresses the sample to state 3o, which lies along the principal Hugoniot curve. As a consequence, its temperature is considerably higher than that of state 2. A strong emission increase is thus observed by the SOP, which now acquires the self-emission signal from state 3. Indeed, the state behind the shock front lies along the principal Hugoniot. The pressure behind the merged shock is slightly lower than that of the second shock, as a consequence of the adiabatic release, but temperature is much higher and can typically be detected. Moreover, since high pressures are aimed for the state 2, at the only slightly lower pressure on the Hugoniot the shock front is typically optically reflecting and shock velocity measurements can also be achieved with the VISARs. The merged-shock front velocity decreases in time because the shock is generally no longer sustained by the laser pulse. As a consequence, also the emission fades in time. If the sample is thin enough, the merged shock exit can be seen at $t = t_4$ on the diagnostics, corresponding to an abrupt decrease on the VISAR and SOP intensity. The hydrodynamic configuration inside the sample after the two shocks have merged is shown in Figure 3.10 (c).

Table 3.2 – Synthesis of the situation inside the sample and of the measurable variables for each phase of a double-shock compression shot.

Time	**Situation**	**Measurement**
$t_1 < t < t_2$	First shock propagating.	Material velocity after the first shock.
$t_2 < t < t_3$	First and second shocks sequentially propagating.	Second-shock velocity (directly, if the shock front is reflecting; indirectly, from the measurement of the timings, otherwise); self-emission from double-shocked state; second-shock-front reflectivity (if reflecting).
$t_3 < t < t_4$	Merged shock propagating.	Merged-shock velocity and reflectivity; self-emission from merged-shocked state.

3.3.2 Analysis of diagnostics outputs

The double-shock compression technique we are describing has been developed for a diagnostics setup including VISARs and SOP. The diagnostics output images can be analysed to obtain the time-dependent fringe shift and fringe intensity (VISARs) and self-emission (SOP). Here we describe the analysis to be performed to extract information about shock and material velocities, temperatures, and reflectivities in the different phases of the shock propagation process.

Material velocity after the first shock

The material velocity of the first shocked state U_p^1 can be inferred from the apparent velocity measured by the VISARs U_{app}^1 in the $t_1 - t_2$ time interval with the method described in Chapter 2.5.1 for the case in which the shock leaves the material in a transparent state. The material velocity is found by solving the implicit equation

$$U_p^1 = \frac{U_{\text{app}}^1 + \left[n(U_p^1) - n(0)\right] U_s(U_p^1)}{n(U_p^1)}, \tag{3.3}$$

where $U_s(U_p)$ and $n(U_p)$ are the shock velocity and shocked refractive index as a function of the material velocity, respectively. Both relations have to be known in the transparent range of the principal Hugoniot of the sample under study.

Second-shock velocity

In the case the second shock is reflecting, its shock velocity is directly deduced from the VISAR fringe shift as in the classical case of strong reflecting shocks, using the refractive index after the first shock loading $n(U_p^1)$ as correction (see Chapter 2.5.1). Alternatively, including the situation in which the fringes are not of sufficient quality to allow a fringe-shift analysis, U_s^1 can be inferred from the measurement of the velocities U_p^1 and $U_s^m(t_3)$ and of the timings t_1, t_2, and t_3. Let the origin $x = 0$ correspond to the initial position of the metal/sample reflecting interface in the laboratory frame, x_2 be its position when the second shock enters the sample, and x_3 be the position of the two shock fronts when they merge (see Figure 3.9). It follows that

$$x_2 = U_p^1(t_2 - t_1) \tag{3.4}$$

$$x_3 = U_s^0(t_3 - t_1), \tag{3.5}$$

where U_s^0 (the first shock velocity) is given by the known $U_s - U_p$ relation in the sample. The second shock velocity U_s^1 can be found as follows:

$$U_s^1 = \frac{x_3 - x_2}{t_3 - t_2} \tag{3.6}$$

assuming that it is constant in time.

Merged-shock velocity

The time-dependent merged-shock velocity is measured from the VISAR fringe shift as in the classical case of strong reflecting shocks, using the unperturbed refractive index as correction (see Chapter 2.5.1). In practice, the interaction between the two shock fronts may affect the flatness of the resulting shock front. As a result the quality of the merged shock VISAR signal may decrease. To overcome this limitation, the SOP signal can be used to indirectly determine $U_s^m(t)$ if the $T - U_s$ relation along the principal Hugoniot is known.

If the thickness of the sample is low enough for the shot exit from the sample to be seen in the VISAR and SOP images, the mean merged-shock velocity

$$\langle U_s^m \rangle = \frac{1}{t_4 - t_3} \int_{t_3}^{t_4} U_s^m(t) dt = \frac{L - x_3}{t_4 - t_3} \tag{3.7}$$

can be measured from the VISAR and SOP timings t_3 and t_4, the calculated x_3 and the initial sample thickness L.

Shock-front reflectivities

The loading of a transparent material by a shock wave changes the real part of the material refractive index, n, due to the density increase. Moreover, if the shock compression is strong enough, the loaded sample becomes semi-conducting or conducting [Clerouin et al. (2005); French and Redmer (2011)], so that the imaginary part of its refractive index k cannot be neglected anymore. The global refractive index change makes the shock front reflecting according to Fresnel's law.

In the specific case of double-shock propagation, the second-shock front propagates through state 1 and its reflectivity R_2 will be

$$R_2 = \left| \frac{\tilde{n}_2 - \tilde{n}_1}{\tilde{n}_2 + \tilde{n}_1} \right|^2, \tag{3.8}$$

where $\tilde{n}_1$ and $\tilde{n}_2$ are the complex refractive indices of the region loaded by the first and second shock, respectively.

If the refractive index behaviour of the sample is known at the conditions reached in state 1, so is its refractive index, which is basically real as the material remains transparent: $\tilde{n}_1 \simeq n_1$. Therefore, the measurement of R_2 can be used to estimate $\tilde{n}_2$. The static electrical conductivity can be estimated via a Drude-Sommerfeld model, as done by Celliers et al. (2000), Celliers et al. (2010), and Millot et al. (2018), or with more complicated approaches. We will discuss in detail this problem in Chapters 4 and 6, when analysing double-shock reflectivity data of icy mixtures and silica, respectively.

If the probe laser is reflected by a shock front propagating into a transparent sample, shock-front reflectivity at the probe laser wavelength can be obtained as the ratio of the VISAR signal acquired during the shot to a reference one. In the framework of double-shock compression, the second and the merged shock front reflectivity can be measured. This procedure can fail in giving an absolute reflectivity measurement if the reference metallic layer is oxidised or contaminated in the gluing process. If the sample reflectivity is well characterised as a function of the shock velocity on the Hugoniot curve, the measured reflectivity of the merged shock front $R[U_s^m(t)]$ can be used as a calibration factor.

Temperatures

If the shock front is propagating in an ideally transparent material, *i.e.* without being partially absorbed, the temperature of the shocked sample can be evaluated from the SOP counts through an inverse Planck's law. The emissivity in the SOP working spectral range is estimated from the reflectivity at the probe wavelength measured by the VISARs (see Section 3.3.2) via a grey-body hypothesis (see Chapter 2.5.2).

As explained in Chapter 2.5.2, the SOP can be calibrated either with a lamp of known spectral emission, or with some dedicated shots on a standard material, or *in situ*, using the known temperature – shock velocity relation of a standard placed inside the target and the shock velocity measurements from the VISARs. The second method is possible in the framework of double-shock experiments if the $T(U_s)$ relation of the sample along the principal Hugoniot is known. In this case, in the $t > t_3$ time interval, $U_s^m(t)$ is measured from VISARs and a SOP calibration is obtained applying the $T[U_s^m(t)]$ relation. An alternative approach makes use of the mean merged shock velocity $\langle U_s^m \rangle$ measured using the timings t_3 and t_4 (see Section 3.3.2).

The temperature measurement of the double-shocked region must be carefully handled. Indeed, the second shock front propagates in a sample which has been pre-compressed by the first shock and may thus be partially absorbing. Defining μ_1 as the absorption coefficient of the sample loaded by the first shock, the time-dependent intensity collected by the SOP (proportional to the number of counts) $I_{\text{collected}}(t)$ will be

$$I_{\text{collected}}(t) = I_{\text{emitted}}(t) \exp\left[-\mu_1 l_1(t)\right], \tag{3.9}$$

where $I_{\text{emitted}}(t)$ is the time-dependent intensity emitted by the double-shocked sample and $l_1(t)$ is the width of the sample region already loaded by the first shock but not loaded by the second one yet.

From simple geometrical considerations in the propagation direction – time plane – see Figure 3.9 – one obtains:

$$l_1(t) = U_s^0(t - t_1) - U_s^1(t - t_2) - x_2. \tag{3.10}$$

An exponential fit on the SOP counts using equations 3.9 and 3.10 is performed to measure the emitted intensity and thus the temperature of the double-shocked sample. In principle, if the time resolution of the SOP is high enough, the fit will also provide a reliable measure of the absorption coefficient μ_1.

3.3.3 Self impedance mismatch

The analysis of the diagnostics output in a double-shock shot allows to determine the state reached after the first shock and merged shock loading. Additionally, the second-shock velocity can be directly or indirectly measured. Our goal is now to determine from these measurements the off-Hugoniot, moderate-temperature state reached after the second shock loading. To do so, we have developed an analysis we will denote as "self impedance mismatch".

The "classic" impedance mismatch technique, described in Chapter 2.3.4, is a common procedure in the context of shock compression for measuring the loaded state in an unknown material. A standard material, whose EOS is well known, is placed before

the sample and the shock velocity is measured in both layers. The state loaded in the sample under study is determined from that loaded in the standard material, after the conditions of mechanical equilibrium of the standard/sample interface have been imposed. In our framework, we use a similar approach to determine the double-shocked state 2. In this case, the mismatch is not applied to two different materials, but to different thermodynamic conditions of the sample under study: those reached after the first, second, and merged shock loading. This technique requires the knowledge of the properties of the principal Hugoniot of the sample.

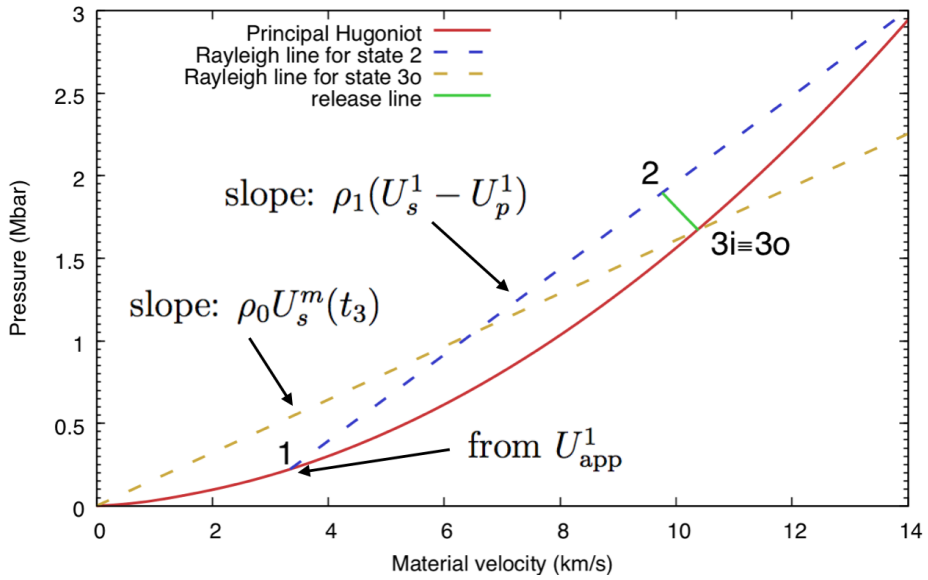

Figure 3.12 – Self impedance mismatch analysis in the (U_p, P) plane for the determination of the double-shocked state of the sample. The principal Hugoniot of the sample (solid red curve) is already known. State 1, along the principal Hugoniot, is experimentally determined from U_p^1, extracted from U_{app}^1. State 3o (which has the same P and U_p as state 3i), also along the principal Hugoniot, is experimentally determined from $U_s^m(t_3)$. Finally, state 2 is determined as the intersection between the Rayleigh line from state 1, which has a slope $\rho_1 \left(U_s^1 - U_p^1\right)$ (blue dashed curve) and the adiabatic re-shock curve from state 3i (green solid curve).

Figure 3.12 illustrates the procedure to determine the double-shocked state in the (U_p, P) plane. The solid red curve is the known principal Hugoniot of the sample. State 1, which lies along the principal Hugoniot as it is obtained by single-shock loading, is determined from the measurement of U_p^1 through the VISARs (see Section 3.3.2).

The second shock loads the sample in state 1 to a double-shocked state 2. Across the second-shock front, momentum is conserved, so that state 2 must lie along the Rayleigh line

$$P(U_p) = P_1 + \rho_1 \left(U_s^1 - U_p^1\right)\left(U_p - U_p^1\right), \tag{3.11}$$

where P_1 and ρ_1 are the pressure and density of the state 1, respectively. The second-shock velocity U_s^1 must be experimentally determined in order to trace this Rayleigh line. Equation 3.11 represents the first constraint for the determination of state 2.

The second constraint is dictated by the fact that state 3i lies along the adiabatic unloading path starting from state 2. In the pressure – material velocity plane, states

3i and 3o are identified, as they are separated by a contact discontinuity. State 3o is obtained by loading of the merged shock right after the merging. It is determined from the VISAR measurement of $U_s^m(t_3)$ (see Section 3.3.2) by intersecting the Rayleigh line

$$P(U_p) = \rho_0 U_s^m(t_3) U_p. \tag{3.12}$$

with the principal Hugoniot.

At this point, the adiabatic release from state 2 to state 3 is built starting from the final state, state 3, as state 2 is still unknown. An adiabatic release curve is traced from state 3 towards higher pressures and lower material velocities. If the adiabatic release line of the material crossing the state 3o is not known, a good approximation consists in taking the mirror reflection of the principal Hugoniot with respect to the vertical line $U_p = U_p^{3o}$ [Kimura et al. (2015)]. The intersection between the adiabatic curve from state 3 and the Rayleigh line from state 1 provided the material velocity and pressure of the double-shocked state 2.

Finally, the double-shocked density ρ_2 is determined via the generalised Rankine–Hugoniot equation stating mass conservation:

$$\rho_2 = \rho_1 \frac{U_s^1 - U_p^1}{U_s^1 - U_p^2}, \tag{3.13}$$

whereas the internal energy density e_2 is obtained using the Rankine–Hugoniot equation for energy conservation:

$$e_2 = e_1 + \frac{P_2 U_p^2 - P_1 U_p^1}{\rho_1 \left(U_s^1 - U_p^1\right)} + \frac{1}{2}\left[\left(U_p^1\right)^2 - \left(U_p^2\right)^2\right]. \tag{3.14}$$

All the state variables of the double-shocked state 2 can thus be determined via the self impedance mismatch technique. The only exception is temperature, which can nevertheless be directly measured with the SOP as our technique provides a direct optical access to state 2.

3.3.4 Simulations and experimental design

We performed hydrodynamical simulations with MULTI (see Chapter 2.6.1) to verify if the double-shock compression technique we described is feasible on a mid-size laser facility such as LULI2000. Simulations were aimed at optimising the drive-laser pulse profiles and the target structure in order to meet the several technical requirements of our technique. Here are the main requirements to be respected:

(i) the first shock must be weak enough to maintain the sample in a transparent state;

(ii) the first shock must be stationary;

(iii) the lifetime of the second-shock front must be long enough to allow optical probing;

(iv) the second shock must be stationary;

(v) the merging of the two shocks must take place before the first shock breakout from the sample;

(vi) no unwanted shock reverberations must occur, as they would affect the state reached by shock loading.

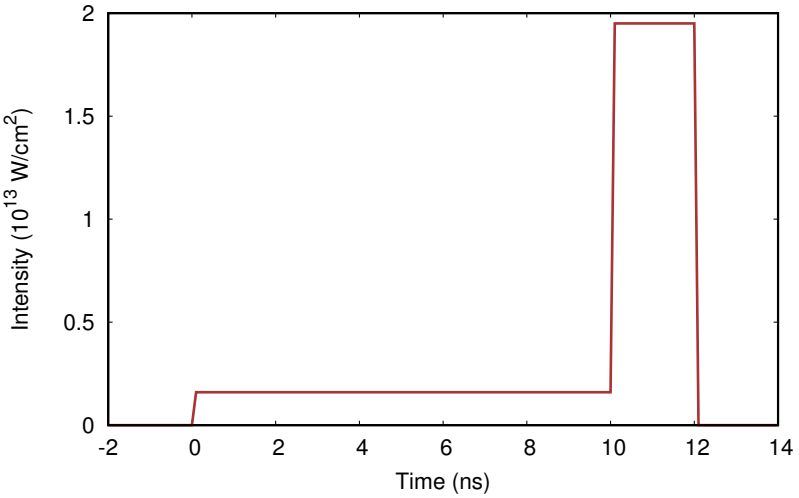

Figure 3.13 – Temporal profile of the drive laser intensity employed in the MULTI simulation. Two flat pulses have been simulated: the first is weak and long, the second is stronger and short. Each laser pulse drives a shock wave inside the sample.

A thorough set of simulations has been run with various laser pulse profiles and target structures, with the aim of reproducing a double-shocked state in a water sample belonging to the superionic phase. Here we present the results of a successful simulation in which a target composed by a polystyrene ablator, an aluminum buffer layer, and a sample of pure water has been employed. The aluminum layer allows both transmitting a controlled shock to the water sample and measuring its material velocity when in state 1 by reflecting the probe laser at the aluminum/water interface. We have generated two laser pulses, whose time profiles are shown in Figure 3.13. The basic parameters employed in the simulation are listed in Table 3.3.

Table 3.3 – Basic parameters used in the MULTI simulation of a double-shock compression shot on a water sample.

Laser pulses

No.	Beginning time (ns)	Duration (ns)	Rise & fall time (ns)	I (10^{13} W/cm^2)
1	0	10	0.3	0.16
2	10	2	0.3	1.95

Target layers

No.	Material	SESAME table	Thickness (μm)
1	Polystyrene (CH)	7592	10
2	Aluminum	3717	70
3	Water	7153	500

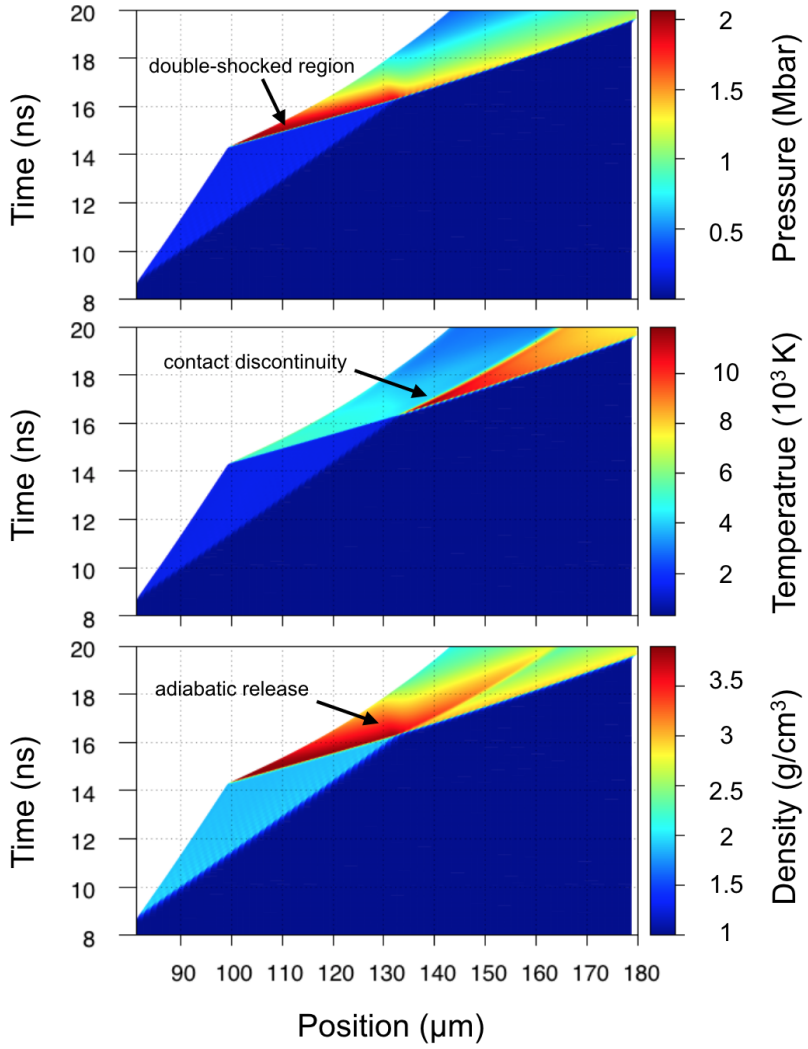

Figure 3.14 – From top to bottom: pressure, temperature, and density (in colour scale) history inside the water sample employed in the simulations. The drive laser comes from the left, diagnostics are on the right side.

The time-dependent pressure, temperature, and density profiles inside the water sample according to our simulation are shown in Figure 3.14. The x axis is the position in the laboratory frame. The white region on the left of the sample is occupied by aluminum, which has been excluded by the plots for clarity. The first shock enters the water sample at around 8 ns and starts propagating through it. The aluminum/water interface also starts moving. Both the shock velocity and the aluminum/water interface velocity appear as constant in time, as the shock is sustained by the first laser pulse. The stationarity criterion *(ii)* is thus respected. The second shock enters water at around 14 ns, engendering a sudden increase in the interface velocity. Between 14 and 16 ns, the second shock travels through a volume already pre-compressed by the first one. The second shock appears as stationary, meeting criterion *(iv)*. The two shocks merge at around 16 ns. The second-shock front has thus existed for around 2 ns, which is enough to allow the optical diagnostics of state 2, as imposed by criterion *(iii)*. The merging takes place well before the shock breakout from water, meeting criterion

(v). After the merging, an adiabatic release connects the double-shocked region to the region behind the merged shock. The release is localised at around 135 μm and can clearly be seen in the pressure and the density plot. A discontinuity in density and temperature is generated and propagates at the material velocity [Birnboim et al. (2010)]. This feature is observed as a discontinuity in the temperature and density plots, but it does not exist in the pressure profiles since pressure and material velocity are conserved. Over the whole relevant time window, no unwanted shock reverberations occur, so that criterion *(i)* is respected.

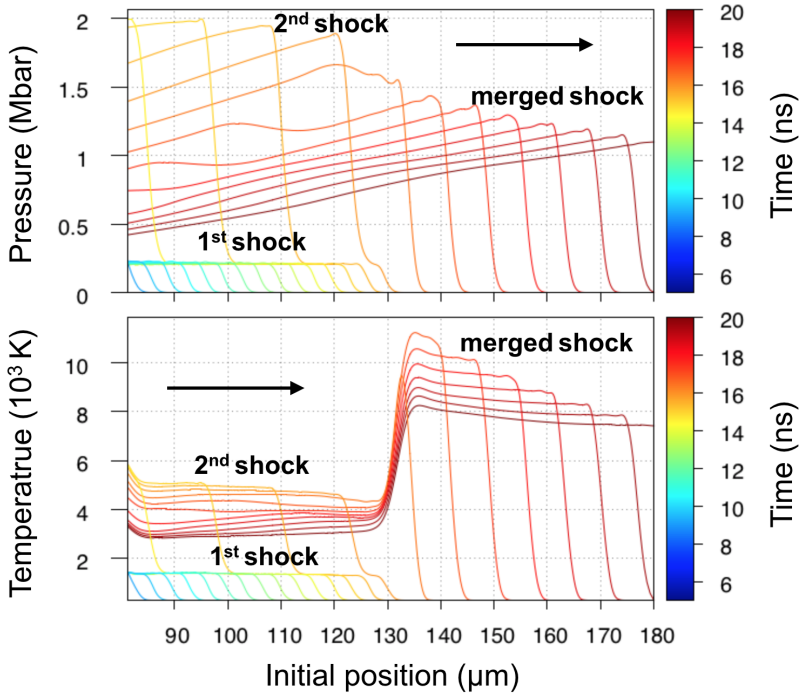

Figure 3.15 – From top to bottom: pressure and temperature profiles in a portion of the water sample as a function of time (in colour scale). The drive laser comes from the left, diagnostics are on the right side. The arrows indicate the shock propagation direction. The loading pressure behind the merged shock is slightly lower than behind the second shock. In contrast, temperature of portion loaded by the merged shock, which lies along the principal Hugoniot, is sensibly higher than the second-shock loaded region, which is an off-Hugoniot state.

The evolution of pressure and temperature in the first 100 μm of the sample are shown in Figure 3.15. The horizontal axis is the initial position (*i.e.* the Lagrangian position variable). In this representation we find the same salient stages as explained above for Figure 3.14. The first weak shock enters the sample at 8 ns and generates low-pressure / low-temperature uniform conditions. Pressure is around $0.20 - 0.25$ Mbar, well below the transparent-to-opaque optical transition along the principal Hugoniot of water, to meet criterion *(i)*. The first shock is followed by the second shock, which enters the water sample at 14 ns. The spatial profile of pressure and temperature starting from this time consists in two successive jumps, with the highest discontinuity pursuing the first slower one. Their merging at 16 ns is associated to a huge increase in temperature and a slight decrease in pressure. The fairly uniform pressure and

temperature conditions depicted in Figure 3.15 confirm that the stationarity of both shocks is guaranteed.

3.3.5 Presence of a precursor of the first shock wave

Elastic waves

Until now, when treating the response of the sample under study to the first, weak shock wave, we have implicitly assumed that it exhibited a simple plastic response. However, this behaviour is not universal but typical of liquid and amorphous materials. Materials with a crystalline structure, when solicited by a weak shock wave, may on the contrary exhibit a compression structure consisting of two distinct waves [Zel'dovich and Raizer (1966)]. The first wave compresses the material mainly along the shock-propagation axis. The lateral stresses are lower than the longitudinal one due to the material rigidity. This first wave compressed the material up to its elastic limit, that is, the maximum pressure that the material rigidity can resist before the structure is yielded. This wave is called *elastic precursor*. The second wave compresses the material up to the final pressure and yields its crystalline structure: it is thus called the *plastic wave*.

Between the materials of interest in the context of this Thesis, α-quartz exhibits an elastic–plastic response to weak shock waves up to around 600 kbar [Wackerle (1962)]. Here we treat how the analysis procedure has to be adapted to this case, which will be done in Chapter 6. The hydrodynamic path followed by the sample is shown in Figure 3.16. At $t = t_1$, when the first, weak compression wave enters the sample, two waves start propagating inside it: the elastic precursor, with a velocity U_{prec}, and the plastic wave, with the usual first-shock velocity U_s^0. The elastic precursor does not induce a significative change in the refractive index of the loaded sample. The standard method for transparent samples (see Chapter 2.5.1) thus remains valid to determine U_p^1. At $t = t_2$, the second shock enters the sample. Typically, this shock wave is strong enough for the crystalline sample to exhibit only a plastic response, as the plastic shock velocity is higher than the elastic velocity. At $t = t_3$, the second shock catches up the plastic wave of the first compression and a merged shock front is generated, as in the case of amorphous materials. The merged-shock velocity is in general higher than the velocity of the elastic wave of the first compression of the sample. As a result, the merged-shock front catches up the elastic precursor at $t = t_{3b} > t_3$. Since the momentum of the merged shock is in general much greater than that of the elastic precursor, the velocity change of the merged shock wave when it catches up the elastic precursor is negligible.

Phase transitions

Another source of wave-splitting behaviour is the existence of a phase transition in the thermodynamic path from the unperturbed to the shocked state [Zel'dovich and Raizer (1966)]. In this case, the shock wave may split in a precursor, which compresses the sample up to the Hugoniot pressure at the phase boundary, and a second wave, which induces the phase transition and brings the sample to the final state.

A phase-transformation-induced precursor may have a non negligible effect on the refractive index of the loaded sample. In such a case, the relation between real and

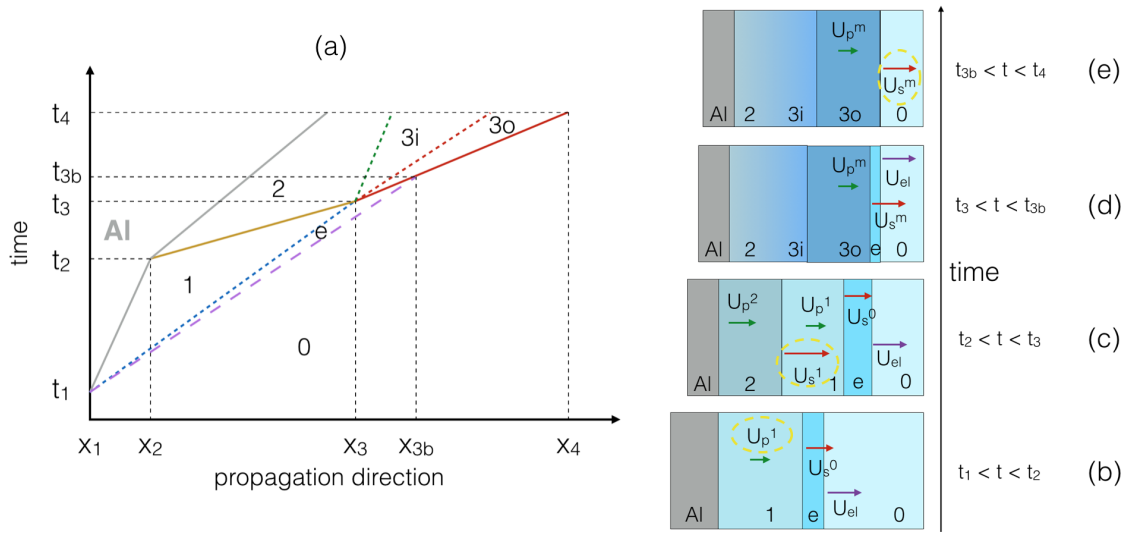

Figure 3.16 – Compression path for a sample exhibiting an elastic precursor. Drive lasers come from the left, diagnostics are on the right side. **Left.** The violet dashed line is the elastic precursor front. **Right.** Schematic picture of the shocked target for $t_1 < t < t_2$ (b), $t_2 < t < t_3$ (c), $t_3 < t < t_{3b}$ (d), and $t_{3b} < t < t_4$ (e). *(b).* The first shock propagates at U_s^0, leaving a transparent shocked state 1 moving at U_p^1. It is anticipated by an elastic precursor compressing the material to the state e. *(c).* The second shock propagates at U_s^1, leaving a double-shocked state 2 moving at U_p^2. *(d).* The merged shock propagates at U_s^m, leaving a shocked material in state 3o. State e still exist between the non-perturbed region and the merged shock front. A cold front divides 3o and 3i. A gradual adiabatic transition connects the regions 2 and 3i. *(e).* The merged shock has caught up the elastic precursor front. The dashed dark-yellow circles indicate the quantities measured during each time window. For the sake of simplicity, the effects of the pre-compression operated by the elastic precursor on further compressed states have been neglected.

apparent velocity reads

$$U_{\text{app}} = n_1 U_p^1 - (n_1 - n_{\text{prec}})\, U_s^0 - (n_{\text{prec}} - n_0)\, U_{\text{prec}}, \tag{3.15}$$

where n_{prec} is the refractive index after the precursor. The effect of the precursor on the refractive index should be taken into account for the determination of the double-shocked state temperature and reflectivity T_2 and R_2 as well.

Precursor velocity

The velocity of the precursor can be measured from the observation of t_{3b} on the diagnostics as

$$U_{\text{prec}} = \frac{1}{t_{3b} - t_1} \left(x_3 + \int_{t_3}^{t_{3b}} U_{sm}(t) dt \right). \tag{3.16}$$

If the elastic precursor velocity in the sample under study is already known, the measurement of U_{prec} allows to identify the observed precursor as an elastic wave if U_{prec} corresponds to the known value; the same is true in the case of a phase-transition-induced splitting.

3.4 Conclusions

In this Chapter, we have shown several approaches that allow to explore lower temperature states with respect to those which can be reached by single-shock compression (presented in Chapter 2). We have described two approaches that have been used in the experimental work of this Thesis: the coupling of Diamond Anvil Cells and shock compression and double-shock compression. In particular, we developed a technique which allows the direct characterisation of the double-shocked, off-Hugoniot state without the use of tabulated EOS or hydrodynamic simulations.

This Chapter concludes the Part I of this Thesis, which introduced the concepts and techniques employed in our work. In Parts II and III we will present our experimental investigations of the components of the interiors of icy giant and terrestrial planets, respectively.

Part II:

Experimental study of components of icy giant planets

> Praise him, ye heavens of heavens,
> and ye waters that be above the heavens.
>
> Psalms 148, 4

Chapter 4

Study of mixtures of water, ethanol, and ammonia

Mixtures of water, methane, and ammonia are key components of the interiors of icy giant planets. Studying their structural, transport, and optical-electrical properties at the relevant thermodynamic conditions is crucial to improve planetary models and, in perspective, to explain the peculiar magnetic fields and thermal histories of Uranus and Neptune.

In this Chapter, we will first overview the prior knowledge about the behaviour of pure water and the mixtures of various composition at Warm Dense Matter conditions. We will then present our experimental study of pure water, a water–ethanol mixture (WEM), and a water–ethanol–ammonia "synthetic planetary mixture" (SPM) compressed by laser-driven shocks. In a first investigation, the samples have been studied along their principal Hugoniot curves. Their thermodynamic state and shock-front reflectivity have been measured and compared. DFT-MD calculations have been performed by Mandy Bethkenhagen *et al. (University of Rostock)* to be compared to the experimental results. In a second investigation, pure water and the SPM have been compressed off their principal Hugoniot curves using a double-shock technique (described in Chapter 3.3), with the aim of extending the comparison of their equations of state and optical properties to a wider region of the phase plane, at temperatures closer than those expected inside the icy giants.

Contents

4.1 Context

Mixtures of water (H_2O), methane (CH_4), and ammonia (NH_3) constitute the major components of the interiors of the Solar icy giant planets, Uranus and Neptune (see Chapter 1.4.2). For this reason, they are also called "planetary ices", regardless of the actual phases they experience inside those planets. As pressure and temperature increase from the outer layers towards the core, icy mixtures are expected to abandon their original molecular nature and exhibit a wide range of different states such as atomic and molecular fluids, dissociated plasmas, and superionic phases [Cavazzoni et al. (1999); Chau et al. (2011)]. At pressures around $0.1 - 1$ Mbar and temperatures of some thousand Kelvin, such mixtures exhibit intriguing chemical and physical processes, involving complex bonding configurations.

As a consequence of the difficulty in characterising the complex behaviour of these mixtures at the relevant conditions, our understanding of icy giant planets suffers major limits. In particular, as we already discussed in Chapter 1.4.2, two outstanding puzzles need to be addressed:

(i) the dichotomy in the thermal histories of Uranus and Neptune – the latter has an internal heat source whereas the first is in thermal equilibrium with the radiation received from the Sun;

(ii) the origin of the highly non-dipolar, non-axisymmetric magnetic fields of Uranus and Neptune.

Solving these open questions is even more urgent today, as a considerable fraction of the discovered exoplanets exhibit masses and sizes similar to the icy giants and are therefore believed to have a similar composition and structure.

The attempts made to solve the open question (i) involved either a giant impact in the history of Uranus [Podolak and Helled (2012)] or structural interior models including a thermal boundary layer (TBL) predicting high interior temperatures but a low luminosity [Nettelmann et al. (2016)]. As a consequence, the interior temperatures predicted by different models differ a lot and there is the need of characterising the physical properties of the icy mixtures on a wide range of conditions.

Concerning the open question (ii), it is customarily assumed that the peculiar structure of Uranus' and Neptune's magnetic fields originates in the fact that they are produced in a thin outer shell of the planet's volume. However, it is not clear if the main contribution is given by hydrogen, which is present in the atmosphere and becomes conducting around 1 Mbar [Nellis (2015, 2017)], or by the icy mixtures [Stanley and Bloxham (2004)]. Identifying the origin of the magnetic fields and the relative importance of the icy mixtures with respect to hydrogen requires the study of their equations of state, electrical conductivity, and transport properties at planetary interior conditions.

Since water is believed to be the most abundant component of the icy mixtures, some planetary models use it as their sole representative [Nettelmann et al. (2010); Redmer et al. (2011)]. A natural question thus arises, if the water-only approximation is able to reproduce both the structural and electrical behaviour of the real planetary mixtures. In particular, the importance of chemical effects due to the presence of carbon and nitrogen atoms in determining such properties shall be addressed.

4.1.1 State of the art

Our knowledge of the behaviour of pure water and icy mixtures at WDM conditions relies on the one hand on *ab initio* calculations and, on the other hand, on static and dynamic compression experiments. Calculations have provided equations of state, phase diagrams, pair distribution functions, and bond autocorrelation functions of pure water [Cavazzoni et al. (1999); Goldman et al. (2005); Mattsson and Desjarlais (2006); Goldman et al. (2009); Schwegler et al. (2008)] and of the icy mixtures [Chau et al. (2011); Lee and Scandolo (2011); Meyer et al. (2015); Bethkenhagen et al. (2017)], allowing to deduce their structural properties, such as compressibility, and their transport properties, such as viscosity and electrical conductivity. These properties are essential building blocks for models describing the structure and evolution of icy giant planets and for the modelling of the planetary dynamo mechanism (see Chapter 1.2.2). In particular, both pure water [Chau et al. (2001)] and icy mixtures [Chau et al. (2011)] are expected to undergo an insulator-to-conductor transition with the increase of temperature along their principal Hugoniot curves, due to the increase of the free electron density driven by gradual ionisation. The precise determination of the onset conditions and, more generally, of the dependence of electrical conductivity on pressure and temperature is crucial for the modelling of dynamos. The stability of an exotic superionic phase is predicted for pure water [Cavazzoni et al. (1999); Goldman et al. (2005); French et al. (2009); Hernandez and Caracas (2016, 2018)], pure ammonia [Cavazzoni et al. (1999); Bethkenhagen et al. (2013)], and water–ammonia mixtures [Bethkenhagen et al. (2015)] at pressures of some megabar and relatively low temperatures of a few thousand Kelvin. In this peculiar state, the high proton diffusion implies a non-negligible contribution to the electrical conductivity, with possible consequences on the magnetic field structure in icy giant planets.

Experimental data are abundant for pure water but still scarce for icy mixtures. Indeed, water has been compressed up to pressures of several megabar with the use of a diverse set of compression methods, including single-shock loading starting from ambient conditions [Mitchell and Nellis (1982); Lyzenga et al. (1982); Celliers et al. (2004); Knudson et al. (2012); Henry (2003); Kimura et al. (2015)], single-shock loading from

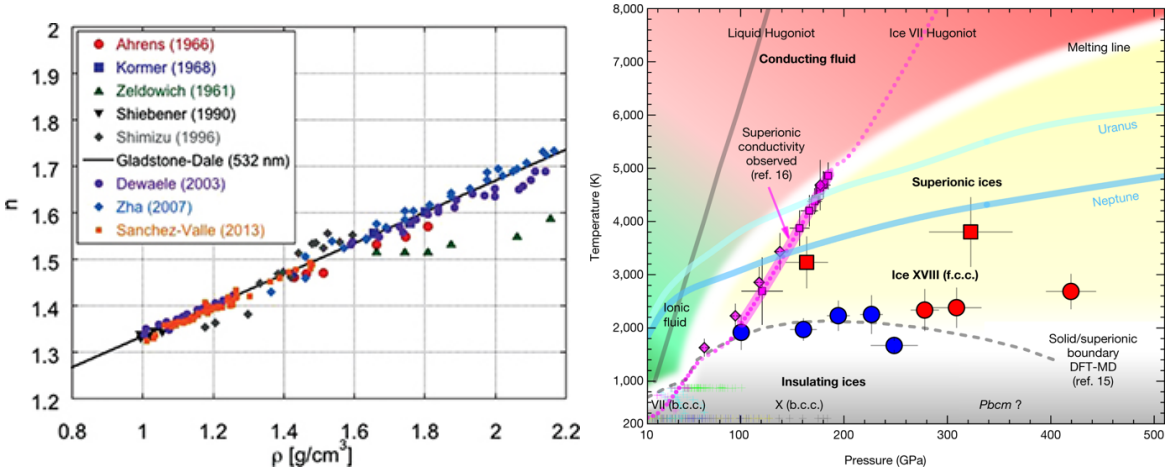

Figure 4.1 – **Left.** Water refractive index along the principal Hugoniot curve as a function of density. From Batani et al. (2015). **Right.** Water phase diagram in the WDM regime. From Millot et al. (2019).

statically pre-compressed conditions [Henry (2003); Kimura et al. (2015); Millot et al. (2018) and multiple shock loading [Mitchell and Nellis (1982); Knudson et al. (2012)]. The first experimental evidence of the superionic phase predicted by calculations has been reported by Millot et al. (2018), who applied shock compression to statically pre-compressed water in the ice VII phase to explore relatively low temperatures.

The refractive index of compressed water has been measured along the principal Hugoniot curve (and, partially, along statically pre-compressed Hugoniot curves) in the whole range of transparency [Batani et al. (2015)]. These measurements are crucial not only to access a thorough view of the optical-electrical properties of water, but also to enable VISAR measurements of the fluid velocity in dynamic pre-compression experiments (see Chapter 3.3). The water shock-front reflectivity has been measured in the conducting regime along the principal and statically pre-compressed Hugoniot curves. The available data cover the whole transition from the onset to the saturation at high values of reflectivity [Celliers et al. (2004); Knudson et al. (2012); Kimura et al. (2015); Millot et al. (2018)]. Figure 4.1 shows the refractive index of shocked water along the principal Hugoniot as a function of density (left) and a phase diagram of water in the WDM regime including the superionic phase, whose lower boundary has been recently determined via XRD by Millot et al. (2019).

The available experimental works on icy mixtures have primarily characterised their equation of state and electrical conductivity, using single-shock compression – thus exploring thermodynamic conditions along the principal Hugoniot curve [Radousky et al. (1990); Nellis et al. (1997)], or double-shock compression, which allowed to probe lower temperatures [Nellis et al. (1997); Chau et al. (2011)]. However, the existing experimental data are limited to 0.8 Mbar along the principal Hugoniot curve and 2.2 Mbar off the Hugoniot. In addition, they completely miss reflectivity measurements and almost completely miss temperature measurements. We report in Figure 4.2 the "synthetic Uranus" experimental data from Nellis et al. (1997) along the principal and secondary Hugoniot curves in the pressure-volume plane (left) and a phase diagram calculated by Chau et al. (2011) showing five different phases, including the superionic phase at low temperatures of $1000 - 2000$ K (right).

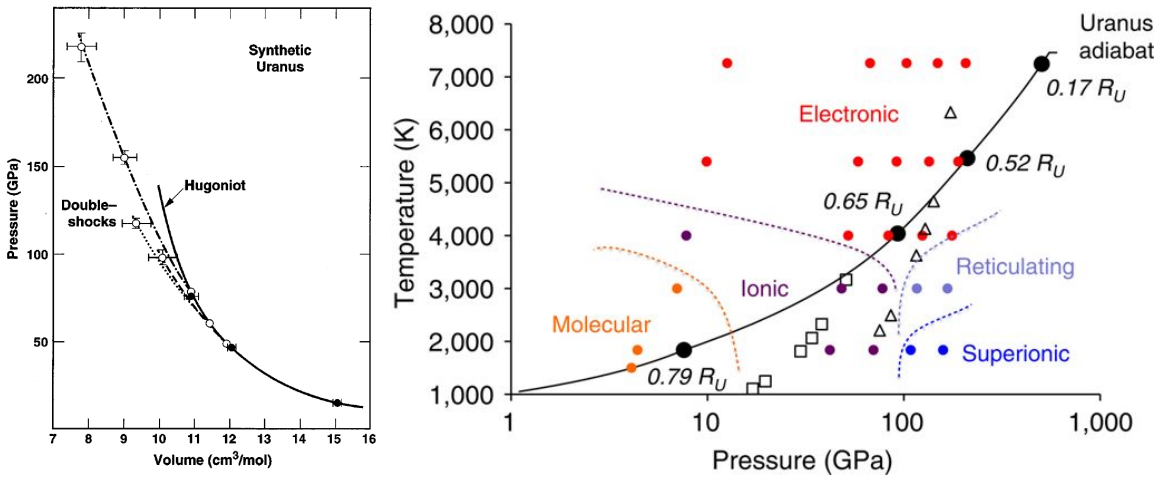

Figure 4.2 – **Left.** Principal and secondary Hugoniot curves of "synthetic Uranus" in the pressure – specific volume plane. From Nellis et al. (1997). **Right.** "Synthetic Uranus" phase diagram in the WDM regime. From Chau et al. (2011).

Within this context, it is crucial to know if and how the measured physical properties of the pure end-members – water, methane, ammonia – are transferred to their mixtures and contribute to define their structural and electrical behaviour. The dependence on the phase stability domains of the end-members of the phase diagram of the mixtures shall also be studied. Answering these questions requires in the first place to characterise the icy mixtures on a wide set of thermodynamic conditions.

4.1.2 This work

In the work presented in this Chapter, we have studied pure water, a water–ethanol mixture (WEM), and a water–ethanol–ammonia "synthetic planetary mixture" (SPM) – the latter being a representative of the interiors of Uranus and Neptune. The SPM is similar to the "synthetic Uranus" previously studied by Nellis et al. (1997).

In a first investigation, the samples have been compressed via decaying shocks along their principal Hugoniot curves. Their equations of state have been characterised and compared between them and with the results of the *ab initio* calculations by Mandy Bethkenhagen, Martin French, and Ronald Redmer *(University of Rostock)*. The reflectivity and conductivity of pure water and icy mixtures have been compared to question the validity of the use of pure water as a proxy for the actual icy mixtures by models of the dynamo mechanism.

A second study involved the compression of pure water and the SPM off their principal Hugoniot curves using a dynamic pre-compression technique, described in Chapter 3.3, to probe lower-temperature states in which chemistry plays a more important role and which are closer icy giant planets' interior profiles.

4.2 Experimental setup

4.2.1 Mixtures

Spectrometric-grade water samples have been employed for the study of pure water. The density at ambient conditions is $\rho_0^{\text{water}} = 0.998$ g/cm^3 and the refractive index at 532 nm and 1064 are 1.3337 and 1.3260, respectively [Hale and Querry (1973)]. The composition of the water–ethanol mixture (WEM) is 49.45% water, 50.55% ethanol in mass ratios, corresponding to the atomic abundance ratios of H:C:N:O = 22:4:0:7. The SPM has been prepared by adding up pure water, pure ethanol, and a liquid water/ammonia (28% wt.) mixture with the following mass ratios: 23.26% of water, 46.23% of ethanol, 30.51% of water/ammonia. The following atomic ratio has been obtained: H:C:N:O = 25:4:1:7, with the aim of reproducing the chemical composition of Uranus and Neptune's mantles. The C:N:O abundance ratios are comparable to those of the Solar System [Cameron (1973)]. Ethanol has been preferred over methane as component of the mixture to avoid demixing issues. The refractive index at 532 nm has been measured for both mixtures as $n_0^{\text{SPM, WEM}} = 1.36$. Values at 1064 nm have been extrapolated using the same water index refraction dependence on wavelength. The density of the mixtures at ambient conditions are $\rho_0^{\text{SPM}} = 0.889$ g/cm^3 and $\rho_0^{\text{WEM}} = 0.881$ g/cm^3. The atomic compositions of the mixtures are also reported in Table 4.1.

Table 4.1 – Initial density and atomic composition of the experimentally studied mixtures (WEM and SPM), of the water–methane and water–methane–ammonia mixtures studied with the Linear Mixing Approximation, and of the water–isopropanol–ammonia "synthetic Uranus" mixture [Nellis et al. (1997)], compared to pure water. The number of atoms of each type (N_{type}) in the chemical formula of the mixture and the percentage of its molar fraction ($\%_{\text{type}}$) are reported.

Mixture	ρ_0 (g/cm^3)	N_H	N_C	N_N	N_O	$\%_H$	$\%_C$	$\%_N$	$\%_O$
Pure water	0.9982	2	0	0	1	66.7	0	0	33.3
WEM	0.881	22	4	0	7	66.7	12.1	0	21.2
SPM	0.889	25	4	1	7	67.6	10.8	2.7	18.9
LMA H_2O-CH_4	0.7019	30	4	0	7	73.2	9.7	0	17.1
LMA H_2O-CH_4-NH_3	0.7301	33	4	1	7	73.3	8.9	2.2	15.6
synthetic Uranus	0.896	28	4	1	7	70.0	10.0	2.5	17.5

4.2.2 Target cells

The conception of target cells for laser-driven shock compression of liquids is delicate, as the sample cannot be simply glued to the ablator/pusher combination but must be confined in a volume next to it. The volume must be watertight under vacuum, as the target is placed in a vacuum chamber for the laser shot, and provide the diagnostics an optical access to the shocked state.

The target cells used in this work have been conceived at the *Observatoire de Paris* by Patrice Barroso. The cells are made of aluminum and consist in a parallelepiped body which measures 15 × 15 × 4 mm and two 3.5 mm thick aisles on the diagnostics side (see Figure 4.3). A cylindrical duct with a 2 mm diameter is carved through the body. Two lateral holes are carved to enable the filling of the cell. The cylindrical

Figure 4.3 – **Left.** Scheme of the target developed for the laser shock compression of liquid mixtures. **Right.** Photo of a target connected to plastic tubes to be filled with the liquid sample under study.

duct is plugged with the ablator/pusher combination on the drive laser side and with a transparent quartz window on the diagnostics side. Both windows are glued to the body of the cell. Two copper or aluminum capillaries are then plugged and glued to the lateral holes.

The filling of the cell with the sample under study (pure water or SPM) took place 1-2 hours before the shot. The capillaries were connected to plastic tubes – one is then put inside a beaker containing the liquid, the other one connected to an oil pump (GEKKO experiment) or to a plastic syringe (LULI experiments). The cell was then filled with the sample through the suction of the pump or syringe. Finally, the capillaries were cut with a pair of pliers, making the cell globally watertight and ready for the alignment.

4.2.3 Laser facilities and diagnostics

The experiments were performed at the GEKKO XII laser facility *(Institute of Laser Engineering, Osaka University, Japan)* [Ozaki et al. (2004)] and at the LULI2000 laser facility *(École Polytechnique, France)*. Rear-side optical diagnostics were employed to characterise the shocked state of the sample.

VISARs. The time-resolved shock velocity was measured by two VISARs. At GEKKO XII, VISARs were illuminated by a YAG probe laser at 532 nm with a full-width half-maximum pulse duration of $\sim$ 10 ns. A YAG at 532 and 1064 nm was used at LULI2000, with a full-width half-maximum pulse duration of $\sim$ 20 ns. The VPF parameters of the VISARs were 4.48 and 7.43 km/s at GEKKO XII, 15.94 and 6.08 km/s or 12.81 and 4.96 km/s at LULI2000. VISARs also measured the reflectivity at their working wavelength. The reflectivity at 532 nm was measured also by a VISAR-independent diagnostic, called "reflectometer" later in this Chapter.

SOP. The time-resolved self-emission of the shocked sample was measured by a streaked optical pyrometer (SOP) working in a variable spectral window, always comprised in the $300 - 500$ nm interval.

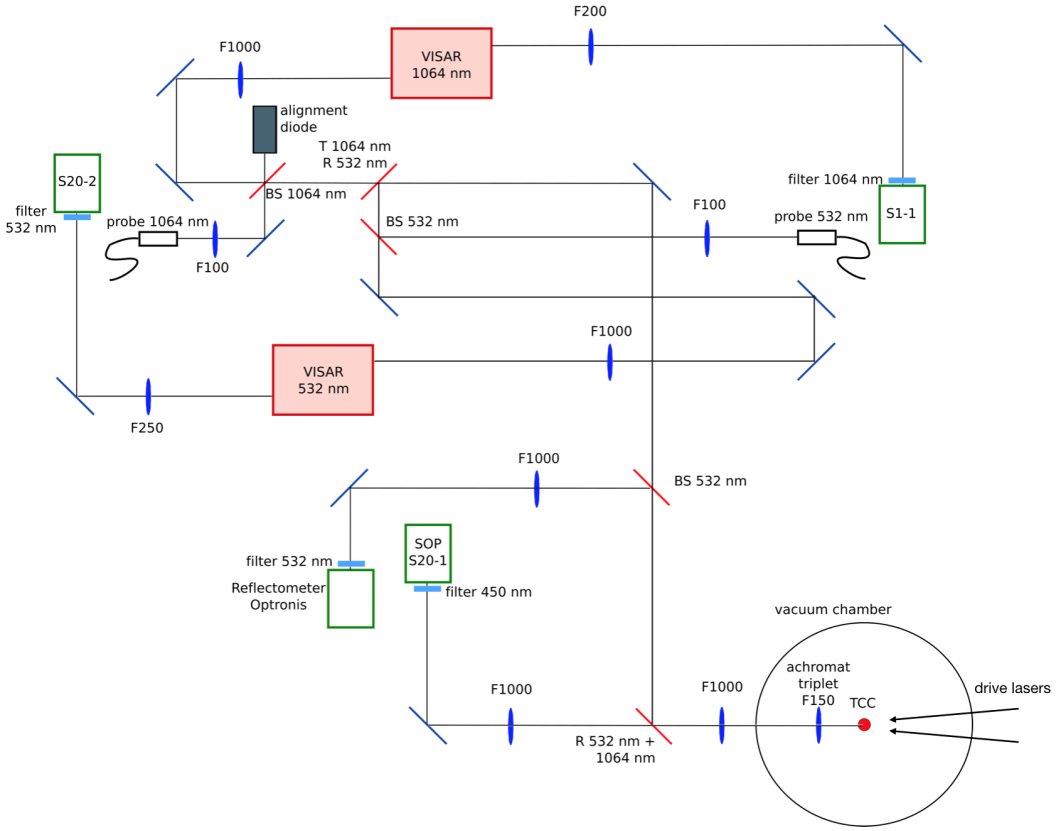

Figure 4.4 – Setup for a shock-compression experiment performed at the LULI2000 facility. Straight black lines are the optical axes. For each lens, the focal length is specified in millimeters (*e.g.* F200 means focal length of 200 mm). The boxes with a green frame are streak cameras. Common mirrors are in blue, beam splitters or dichroic mirrors are in red.

Reflectometer. A time-resolved VISAR-independent reflectivity measurement at 532 nm ("reflectometer") was included in the setup to corroborate the reflectivity measurements obtained from the VISARs, with the advantage of a pure intensity measurement without any fringe system.

The setup scheme of one of the experimental campaigns at LULI2000 is provided in Figure 4.4. An image relay system was put in place from the rear side of the target to the optical diagnostics. An achromatic lens placed in the chamber made the first image of the target rear side out of the chamber. That image was then collimated by a second lens. The collimated light beam was then split using dichroic mirrors and beam splitters, so that each resulting beam could be directed to a diagnostics.

4.3 Principal-Hugoniot study

In this first study, we characterised the structural and optical-electrical properties of water, the WEM, and the SPM along their principal Hugoniot curves. We employed a decaying shock technique (see Chapter 2.3.5) to probe a whole set of Hugoniot states within a single shot. In this approach, the laser pulse is designed to produce a strong

shock that decays in time. As the shock propagates in the sample, each successive layer is compressed at a different pressure-temperature condition on the principal Hugoniot curve. As long as the optical depth of the loaded state is lower than the temperature longitudinal gradient length scale, the collected self-emission can be considered as originating from a thin layer behind the shock front, thus allowing a temperature measure of the Hugoniot states loaded by the shock [Hicks et al. (2006); Bolis et al. (2016)].

4.3.1 Experiments

An experimental campaign at GEKKO XII (GK) and two campaigns at LULI2000 (L1 and L2) have been conducted. At GEKKO XII, three up to nine beams at 351 nm have been used, delivering energies from $120 - 440$ J on a focal spot with a diameter of 600 μm. At LULI2000, one or two beams at 527 nm delivered energies from $200 - 500$ J on a focal spot with a 500 μm diameter. In both cases, the laser pulse duration was 2.5 ns. Phase plates were used to obtain a uniform irradiation spot.

To optimise the target design and ensure there were no shock reverberations in the sample, the laser-target interaction and the shock loading into the cell have been simulated with the Lagrangian 1-D hydrodynamic code MULTI (see Chapter 2.6.1). The multi-layered target cells were composed by a $10 - 15$ μm thick polystyrene ablator, a 40 μm thick aluminum shield, a 50 μm thick α-quartz standard, the liquid sample (which was 4 mm thick), and a rear α-quartz window (200 μm thick). We also performed some high-intensity shots at GEKKO XII with 50 μm of polystyrene / 3 μm of gold / 5 μm of aluminum / 20 μm of α-quartz / 4 mm of sample / 200 μm of α-quartz targets. The gold layer served as X-ray shield to prevent any pre-heating of the sample.

The time-resolved reflectivity of the shock front has been measured with the VISARs and the reflectometer as the ratio between the shot signal and a reference signal reflected on the aluminum/quartz interface. The ratio has been normalised using the known relation between shock velocity and reflectivity for α-quartz at 532 nm [Millot et al. (2015)] and 1064 nm [Huser et al. (2015)].

The SOP has been calibrated (see Chapter 2.5.2) using quartz as *in situ* standard (GEKKO XII experiment) or using a calibration lamp with known emission temperature (LULI2000 experiments).

4.3.2 Diagnostics output

A typical VISAR and SOP output for the GEKKO XII (left) and the LULI2000 (right) experiments is shown in Figure 4.5, together with the extracted temporal profile of shock velocity and self-emission. Initially, a stationary fringe system is visible on the VISAR image, associated to the reflection of the probe laser by the aluminum / quartz interface; no signal appears in the SOP image, as the sample is initially cold. When the shock wave reaches the quartz standard, the shock front becomes reflecting as quartz is compressed to a metallic-like state. The VISAR fringe system thus moves according to the shock velocity. The SOP acquires the self-emission from shocked quartz. Both shock velocity and emission decrease in time as the shock is sustained only for a brief amount of time (2.5 ns). When the shock reaches the liquid sample, the shock velocity

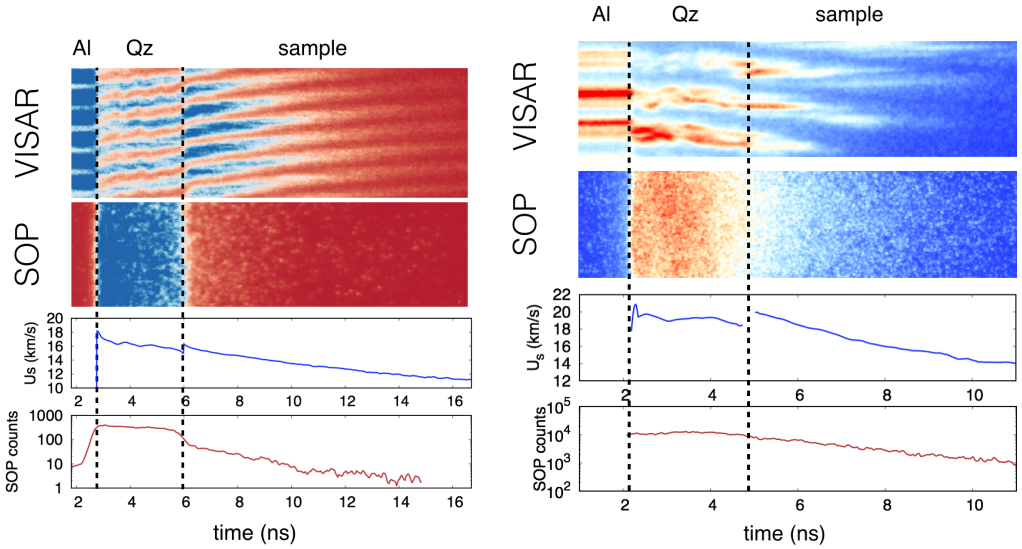

Figure 4.5 – Diagnostics output for a shot at GEKKO XII (left) and at LULI2000 (right). From top to bottom: VISAR image; SOP image; time-resolved shock velocity; time-resolved SOP counts. The three time intervals indicate when the probe laser is reflected by aluminum (Al), when a reflecting shock front is propagating through the quartz layer (Qz), and when the shock front is propagating through the mixture sample. The transverse target dimension is about 200 μm.

increases, as the sample has a lower impedance than quartz (see Chapter 2.3.4). Shock velocity and emission continue to decrease until the end of the diagnostics time window.

Table 4.2 – Experimental decaying-shock data on pure water, WEM and the SPM. The run prefixes GK, L1, and L2 identify the campaign at GEKKO XII and the first and second campaign at LULI2000, respectively. The $\rho - P - (e - e_0)$ data are relative to the sample under study, immediately after the shock has entered it.

Run–sample	U_s^{Qz} (km/s)	U_s^{sample} (km/s)	ρ (g/cm^3)	P (Mbar)	$e - e_0$ (kJ/g)
GK–H_2O	12.96 ± 0.27	13.91 ± 0.30	2.74 ± 0.18	1.23 ± 0.05	39.2 ± 2.7
L1–H_2O	18.19 ± 0.31	20.24 ± 0.35	3.00 ± 0.17	2.73 ± 0.07	91.± 4
GK–WEM	14.27 ± 0.26	15.80 ± 0.31	2.48 ± 0.15	1.42 ± 0.04	52 ± 3
GK–WEM	10.73 ± 0.27	11.75 ± 0.30	2.24 ± 0.20	0.74 ± 0.03	25.5 ± 2.0
GK–WEM	18.27 ± 0.26	20.82 ± 0.30	2.65 ± 0.13	2.55 ± 0.06	97 ± 4
GK–WEM	13.03 ± 0.26	14.60 ± 0.30	2.32 ± 0.14	1.16 ± 0.04	41 ± 3
GK–WEM	11.94 ± 0.26	12.99 ± 0.30	2.38 ± 0.22	0.94 ± 0.04	33.5 ± 2.7
L1–WEM	18.74 ± 0.27	20.93 ± 0.31	2.86 ± 0.19	2.67 ± 0.07	105 ± 5
L2 –WEM	18.65 ± 0.41	22.47 ± 0.48	2.37 ± 0.16	2.79 ± 0.11	100 ± 7
L2–WEM	15.72 ± 0.43	18.37 ± 0.47	2.31 ± 0.19	1.84 ± 0.08	65 ± 5
GK–SPM	15.49 ± 0.26	17.26 ± 0.30	2.56 ± 0.19	1.73 ± 0.06	64 ± 4
GK–SPM	15.07 ± 0.26	16.16 ± 0.30	2.78 ± 0.19	1.58 ± 0.05	60 ± 3
GK–SPM	18.46 ± 0.26	20.71 ± 0.31	2.79 ± 0.23	2.60 ± 0.08	99 ± 6
GK–SPM	9.72 ± 0.27	10.71 ± 0.30	2.14 ± 0.19	0.60 ± 0.03	19.5 ± 2.1
GK–SPM	10.20 ± 0.27	11.27 ± 0.30	2.18 ± 0.19	0.67 ± 0.03	22.3 ± 2.1
L2–SPM	14.94 ± 0.42	16.29 ± 0.47	2.65 ± 0.31	1.57 ± 0.09	58 ± 6
L2–SPM	16.58 ± 0.46	19.20 ± 0.52	2.44 ± 0.30	2.08 ± 0.10	74 ± 8

4.3.3 Equation of state

Pure water: shock and particle velocity

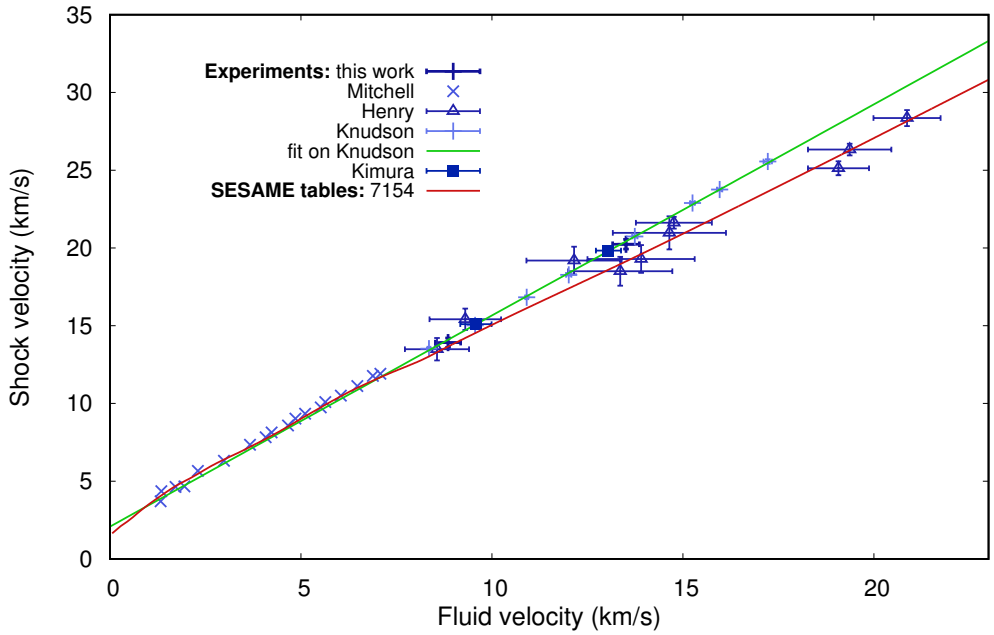

Figure 4.6 – Shock–fluid velocity relation for pure water. Our experimental results are relative to the state created immediately after the shock has entered the sample. They are compared to the SESAME table 7154 and to previous experimental studies [Mitchell and Nellis (1982); Henry (2003); Knudson et al. (2012); Kimura et al. (2015)]. A linear fit performed on the data from Knudson et al. (2012) is in agreement with our data set.

Two shots have been aimed at pure water samples (see Table 4.2). Figure 4.6 shows the resulting shock–fluid velocity ($U_s - U_p$) data, relative to the initial shocked state. The shock velocity has been directly measured by the VISARs, whereas the material velocity has been obtained by impedance mismatch (see Chapter 2.3.4) from the measurement of the shock velocity in the α-quartz standard and in the water sample, using the principal Hugoniot of α-quartz as modelled by Knudson and Desjarlais (2009). Our results are presented together with DFT-MD calculations by Mandy Bethkenhagen, the SESAME table 7154, and previous experimental results. It is to be noticed that, for $U_p > 7$ km/s, data in the literature do not universally agree, as the SESAME table 7154 and the work by Henry (2003) find a lower slope than more recent works [Knudson et al. (2012); Kimura et al. (2015)]. Though our low-pressure datum cannot discriminate between the two slopes, our high-pressure datum clearly agrees with a linear fit on data by Knudson et al. (2012) and is not compatible with the SESAME table. Overall, a remarkable agreement can be observed between the experimental data from the present work as well as from previous work [Mitchell and Nellis (1982); Knudson et al. (2012); Kimura et al. (2015)] and the present DFT-MD Hugoniot for water by Mandy Bethkenhagen.

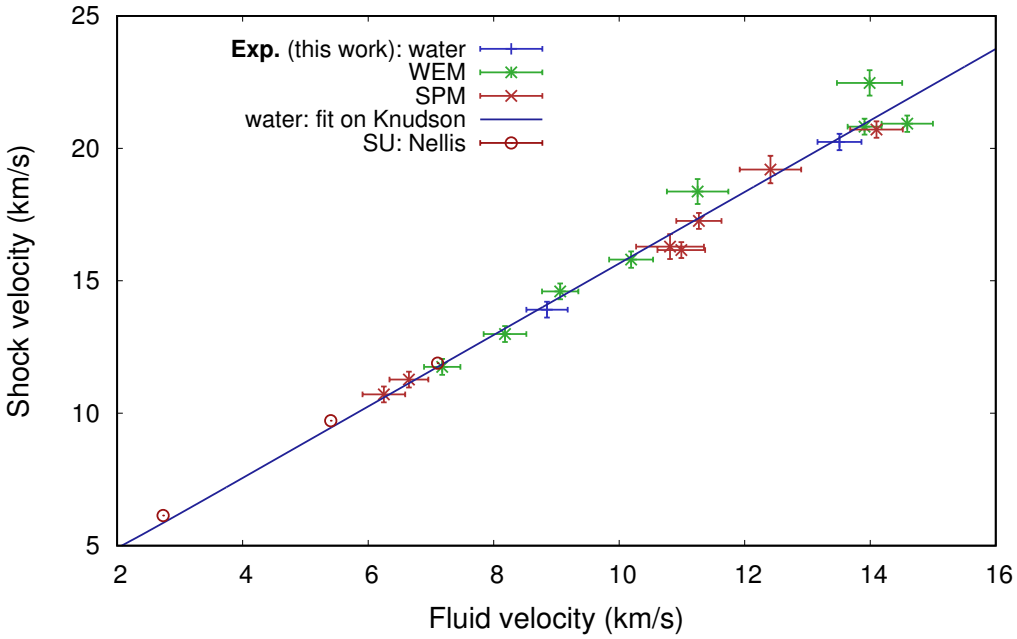

Figure 4.7 – Experimental data on water, WEM, and SPM, relative to the state created immediately after the shock has entered the sample. Our data are compared to previous experimental results on "synthetic Uranus" (similar to the SPM) by Nellis et al. (1997). The linear fit on water data by Knudson et al. (2012) is reported for comparison.

Mixtures: shock and particle velocity

Figure 4.7 shows the $U_s - U_p$ data for pure water, WEM and SPM, together with results on the similar "synthetic Uranus" [Nellis et al. (1997)]. A linear fit on previous water shock data Knudson et al. (2012), $U_s = (1.350 \pm 0.014)U_p + (2.16 \pm 0.15)$ km/s is also shown to compare the behaviour of the mixtures with that of pure water. The obtained SPM data are compatible within error bars with this linear fit. A satisfying agreement is also found for WEM except for two data points.

Density and pressure

For each shot, the pressure P in the sample immediately after the shock has entered it has been obtained together with the material velocity U_p by impedance mismatch. Using the Rankine–Hugoniot relations (equations 2.23–2.25), we extracted the density ρ and the internal energy density change $(e - e_0)$ in the sample immediately after the shock has entered it from the shock and particle velocity. Pressure as a function of the compression factor (ρ/ρ_0) is shown in Figure 4.8. Due to the non-linear nature of the Rankine–Hugoniot relations, the uncertainties on density are high, which complicates the comparison of data. Our two data points for pure water agree within error bars with the transposition to the $P-\rho/\rho_0$ plane of the linear U_s-U_p fit on data by Knudson et al. (2012). Although our results on the WEM and the SPM are highly scattered, a majority of data points agrees within error bars to the fit on water data, in analogy with the behaviour of previous low-pressure data on the similar "synthetic Uranus" by Radousky et al. (1990) and Nellis et al. (1997).

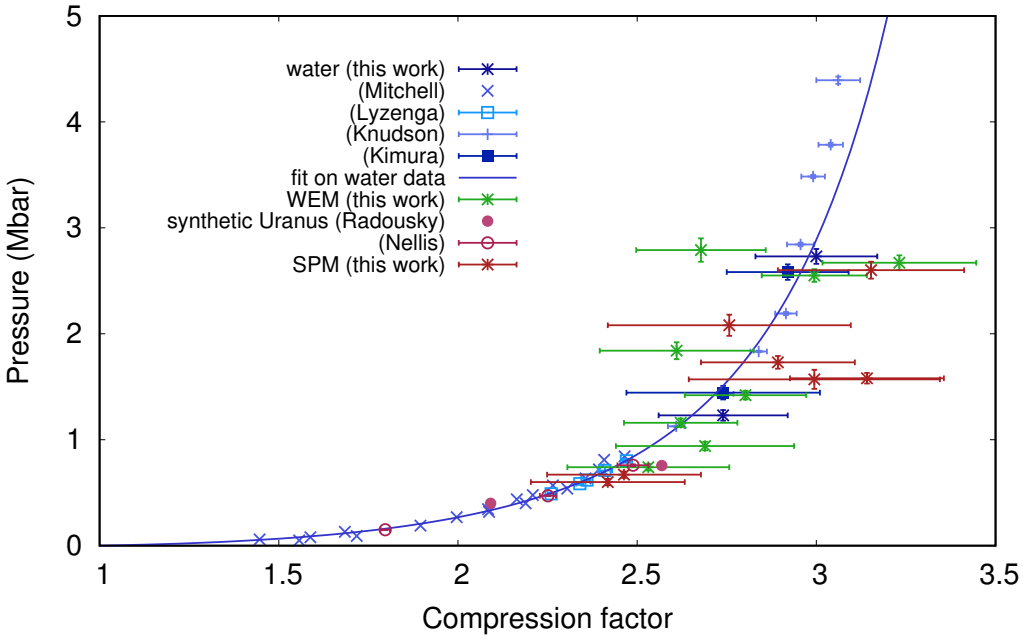

Figure 4.8 – Pressure as a function of the compression factor (ρ/ρ_0) along the Hugoniot curve of water, WEM, and SPM. Our data are relative to the state created immediately after the shock has entered the sample. Previous data for water [Mitchell and Nellis (1982); Lyzenga et al. (1982); Knudson et al. (2012); Kimura et al. (2015)] and for "synthetic Uranus" [Radousky et al. (1990); Nellis et al. (1997)] are also shown. The transposition on the $P-\rho/\rho_0$ plane of a linear fit on the $U_s - U_p$ data from Knudson et al. (2012) is provided as a guide for the eye.

Temperature

The time-resolved temperature was measured by the SOP. To obtain a temperature – pressure relation, the time-resolved shock velocity has been converted to pressure using the $P-U_s$ relations extracted from an experimental EOS by Knudson et al. (2012) for water and from our EOS data for SPM and WEM.

Figure 4.9 (top) shows the temperature – pressure ($T-P$) relation of pure water, including our experimental data, two SESAME tables for pure water, previous calculations and previous experimental studies. Figure 4.9 (bottom) shows the same relation for the WEM and SPM. Also different internal profiles of Uranus are shown as comparison [Redmer et al. (2011); Nettelmann et al. (2016); Bethkenhagen et al. (2017)]. The set of water data has been fitted with a quadratic function $T(P) = T_{\mathrm{amb}} + c_1 P + c_2 P^2$ (with $T_{\mathrm{amb}} = 300$ K). Such a function has been selected in order to reproduce the slightly non-linear behaviour of the experimental $T-P$ relation. A low-pressure extrapolation of our fit on the mixtures is compatible with previous gas-gun data by Lyzenga et al. (1982). While our data agree within the errors with recent laser shock results [Kimura et al. (2015)], our temperatures are higher than those given by *ab initio* molecular dynamics simulations [French et al. (2009)], although the discrepancy is reduced when quantum corrections from molecular vibrations are taken into account [French and Redmer (2009), dashed brass curve in Figure 4.9 (top)]: indeed, the predicted temperatures increase of $\simeq$ 700 K The data sets for the WEM and the SPM,

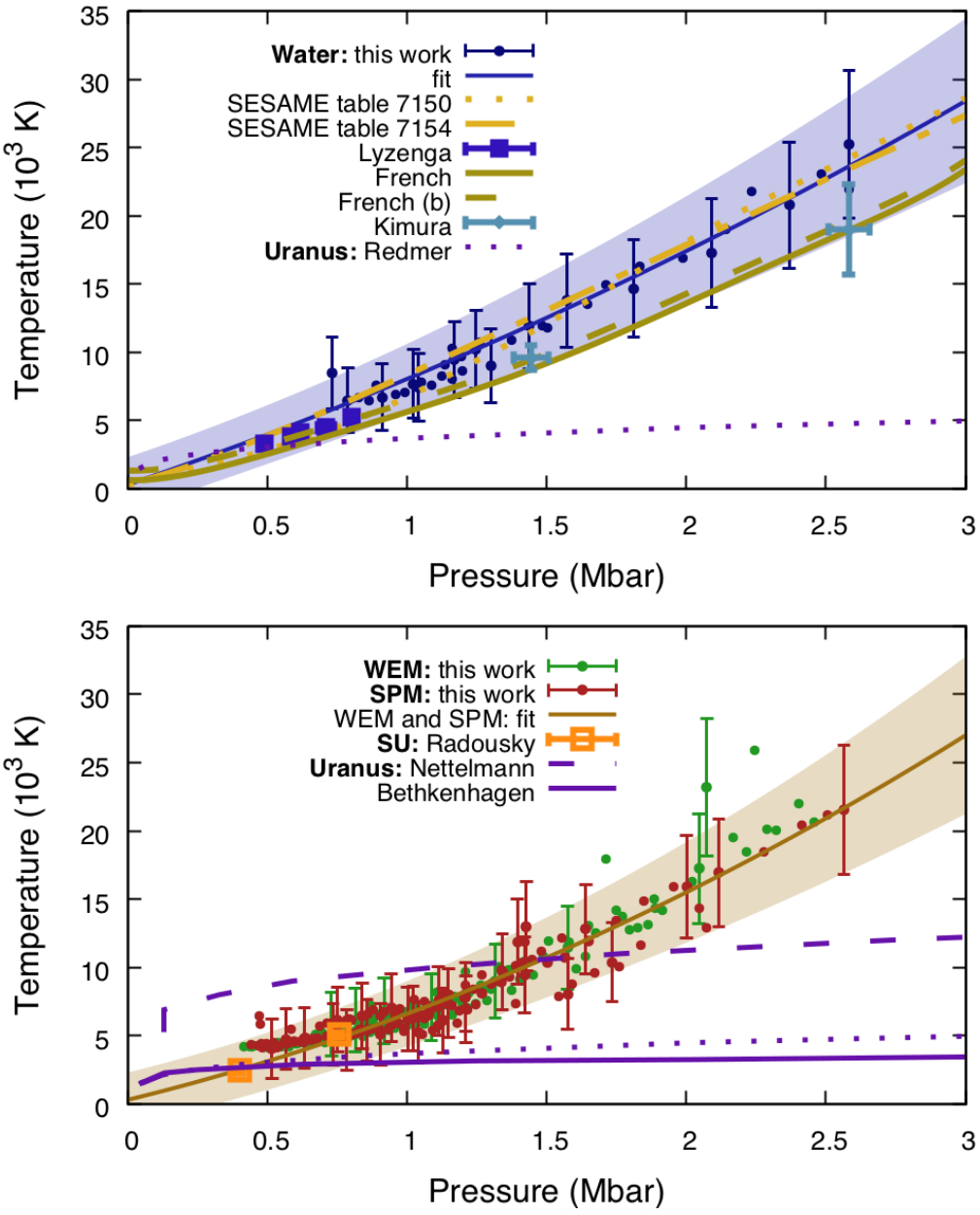

Figure 4.9 – Temperature – pressure relations for the samples under study. Each filled circle is a time-resolved measure during a decaying shock propagation. The colour-filled areas correspond to the fits within errors bars. Uranus interior models are taken from Redmer et al. (2011), Nettelmann et al. (2016), and Bethkenhagen et al. (2017). **Top.** $T-P$ relation for pure water along the principal Hugoniot curve. Also shown are the SESAME tables 7150 and 7154, previous experimental data [Lyzenga et al. (1982); Kimura et al. (2015)], and previous calculations [French et al. (2009); French and Redmer (2009)]. **Bottom.** $T-P$ relation for the WEM and the SPM. Also shown are previous experimental data by Radousky et al. (1990).

which mostly overlap, have been fitted together using the same function type. Our SPM data agree with a previous low-pressure experimental study of the similar "synthetic Uranus" mixture [Radousky et al. (1990)].

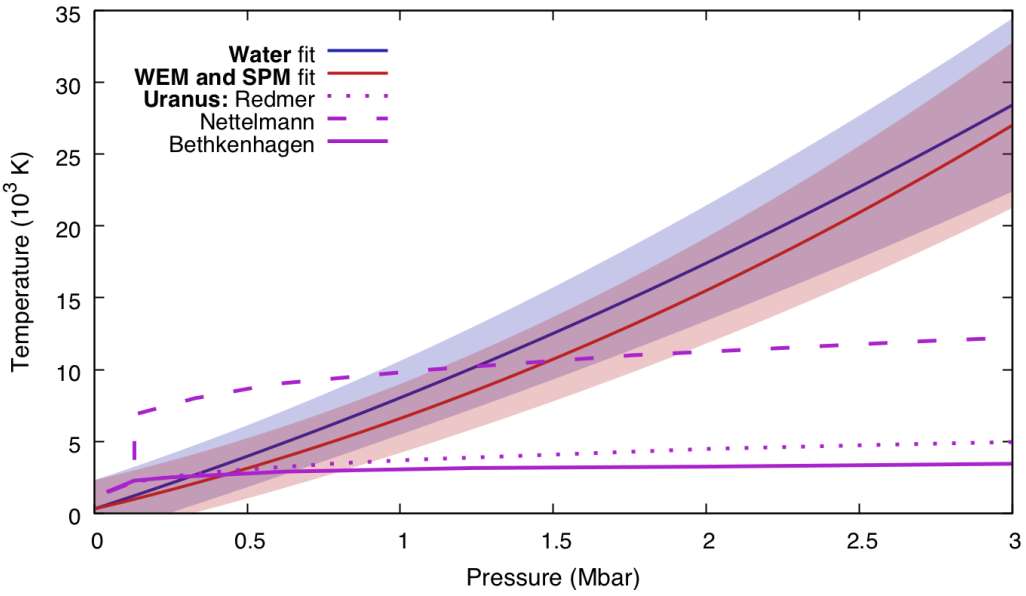

Figure 4.10 – Temperature – pressure relations for pure water and for the WEM and the SPM as determined by fitting our data sets. Uranus interior models are taken from Redmer et al. (2011), Nettelmann et al. (2016), and Bethkenhagen et al. (2017).

Although the relatively high error bars on temperature make difficult to point out possible discrepancies, the $T - P$ relations on the principal Hugoniot curves of pure water and of the mixtures (WEM and SPM) are comparable, as shown in Figure 4.10.

The similar $U_s - U_p$ and $T - P$ relations shared by water and mixtures can be interpreted in light of previous *ab initio* molecular dynamics simulations [Chau et al. (2011)], which identify the regime explored in this experiment as an electronic conducting phase. At these temperatures, carbon-carbon and carbon-nitrogen bond lifetimes are predicted to be very short [Meyer et al. (2015)]. Therefore phenomena like polymerisation and clustering are not expected to occur and the presence of carbon and nitrogen atoms should not influence the $U_s - U_p$ and $T - P$ relation of the SPM with respect to that of pure water. However, potentially existing chemical processes in the compressed bulk could not be observed in this study, relying on surface measurements of the shock front.

4.3.4 Shock-front reflectivity

Pure water, the WEM, and the SPM are transparent at ambient conditions. With the increase of pressure and temperature, their optical properties change: the real part of the refractive index increases due to compression, whereas the imaginary part eventually becomes non-negligible due to ionisation and dissociation. Water has been observed to exhibit an opaque regime starting from $4000-5000$ K [Batani et al. (2015)]. This regime is characterised by a high imaginary part of the refractive index which leads to strong absorption. Starting from pressures around 1 Mbar [Knudson et al. (2012)] and temperatures around 7000 K [Batani et al. (2015)], shocked water becomes optically reflecting due to the Fresnel's law, as both the real and imaginary parts of the refractive index considerably increase [Batani et al. (2015)]. In the thermodynamic

regime explored in this investigation, both water and the mixture exhibit a reflecting, metallic-like behaviour: while the shock propagates through the sample, the probe laser is reflected onto it. The analysis of the VISAR and reflectometer images (see Chapter 2.5.1) thus allows the determination of the shock-front optical reflectivity.

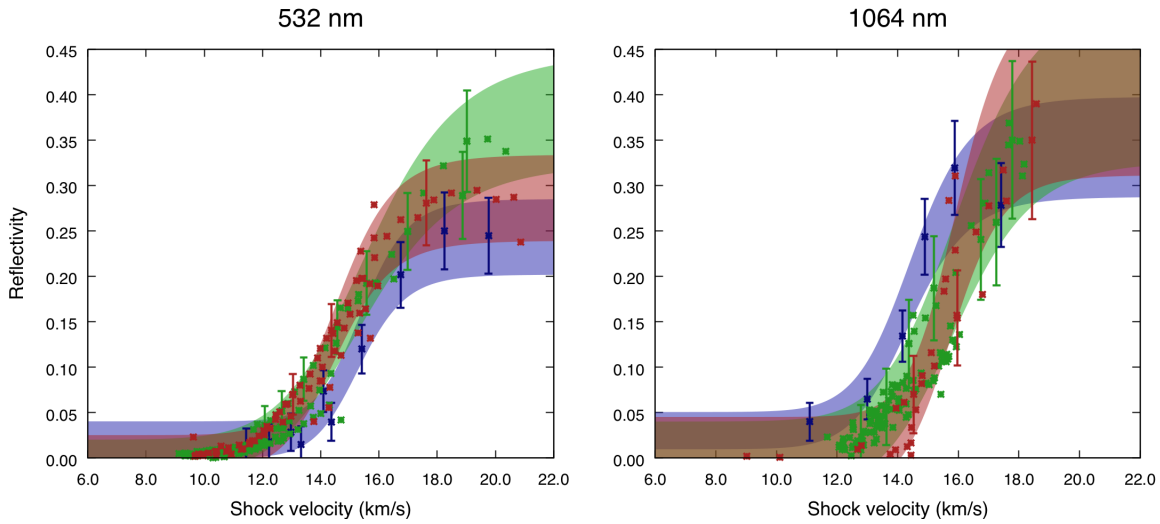

Figure 4.11 – Reflectivity dependence on shock velocity for water, the WEM, and the SPM at 532 nm (left) and 1064 nm (right) along their principal Hugoniot curves. Blue, green, and red areas correspond to the fit on our data on pure water, WEM, and SPM within the error bars, respectively. Crosses are time-resolved measures during decaying shock propagation. Error bars at 1064 nm are larger because of the limited number of available shots.

The reflectivity R for water, WEM and SPM at 532 nm (left) and 1064 nm (right) as a function of the shock velocity U_s is shown in Figure 4.11. These are the first reflectivity data for this type of mixtures; moreover, no calculations of shock-compressed icy mixtures reflectivity exist in the literature. For all the studied samples, the gradual increase of reflectivity, from a low initial value of a few percent up to a saturation value of some ten percent, along the principal Hugoniot curve indicates a smooth transition from an insulating to an electronically conducting (metallic-like) state with the increase of density, pressure, and temperature.

We performed a fit on each $R - U_s$ relation using a Hill function

$$R(U_s) = R_0 + (R_{sat} - R_0) \cdot \frac{U_s^k}{U_s^k + U_0^k}, \tag{4.1}$$

which is suitable to model this gradual transition.

In analogy with what has been done to extract the temperature – pressure dependence, the $R - U_s$ functions have been rescaled to model the pressure dependency of reflectivity by using an experimental EOS for water by Knudson et al. (2012) and our EOS data for SPM and WEM to link pressure and shock velocity. The reflectivity of water, WEM and SPM at 532 nm (left) and 1064 nm (right) as a function of pressure (top) and temperature (bottom) is shown in Figure 4.12. Strong differences between the reflectivities of the samples are observed in particular at 532 nm. The main one concerns the onset of reflectivity occurring in water at $1.1 - 1.2$ Mbar, while in SPM

and WEM it is observed at lower pressures, around 0.8 Mbar. The saturation values are also different (22% for water against 28% in SPM and even higher in WEM). Concerning water, our 532 nm reflectivity data are in quantitative agreement with previous experiments [Knudson et al. (2012); Kimura et al. (2015)].

When compared with existing calculations by French and Redmer (2011), at 532 nm, our reflectivity data suggests that HSE exchange functionals are more accurate over PBE, confirming what observed in Knudson et al. (2012). At 1064 nm, the differences are less important indicating a complex behaviour of optical conductivity to be investigated with ad hoc calculations. We note that saturation values of reflectivity at 1064 nm for both liquids are greater than those at 532 nm. Water data at 1064 nm are in qualitative agreement with the calculations. Reflectivity data are also presented as function of temperature showing the same trend.

The fact that the onset pressure of the SPM and the WEM reflectivity at 532 nm occurs at pressures around 26% lower than in water can not be fully explained by the 12% difference between their initial densities. The higher reflectivity of the mixtures may be due to a higher free electron density at the same thermodynamic conditions, as the ionisation energy of carbon-bearing molecules (*e.g.* 10.5 eV for ethanol) is lower than that of water (12.6 eV) [Meot-Ner (Mautner) and Lias (2018)]. This hypothesis seems to be corroborated by the reflectivity saturation values at 532 nm. Indeed they are 35% for the WEM, 29% for the SPM, and 24% for water, consistently ordered by carbon concentration.

4.3.5 Error estimation

The error on the measured fringe shift on each VISAR output has been estimated, quite conservatively, as 1/10 of a fringe. The error on velocity thus depends on the number of the 2π shifts added to the measured shift to superimpose the two VISAR signals. A typical error on U_s was 3%.

A Monte-Carlo routine has been implemented to propagate the errors through the impedance mismatching analysis. The analysis has been repeated 1000 times, each time using variable inputs extracted from Gaussian distribution whose mean was the measured value and whose deviation was the associated uncertainty. Variable inputs were U_s^{Qz} and U_s^{mix} (whose errors come from the VISAR measurement and from the linear fit) and the quartz Hugoniot curve [whose uncertainties are specified in the fit by Knudson and Desjarlais (2013)]. Figure 4.13 shows the output of a fraction of the repeated analysis in the mixture pressure – fluid velocity plane.

The error on reflectivity has different sources. The main one depends on the calibration method. For decaying shock shots, the fit operated on the quartz measurements has a typical relative error of about 15%. Another source derives from the background estimation of the reference and the shot image. An uncertainty of the background value propagates when background is subtracted from the value extracted from the VISAR image. This introduces a typical absolute error of about 2%, weakly depending on the reflectivity value.

The main error sources for temperature are the SOP calibration factor, the error on the number of SOP counts, and the error on the measured reflectivity. The use of the emission to determine the temperature induces the existence of a detection limit (see Chapter 2.5.2). Typical detection limit temperatures are about 4000 K. Typical

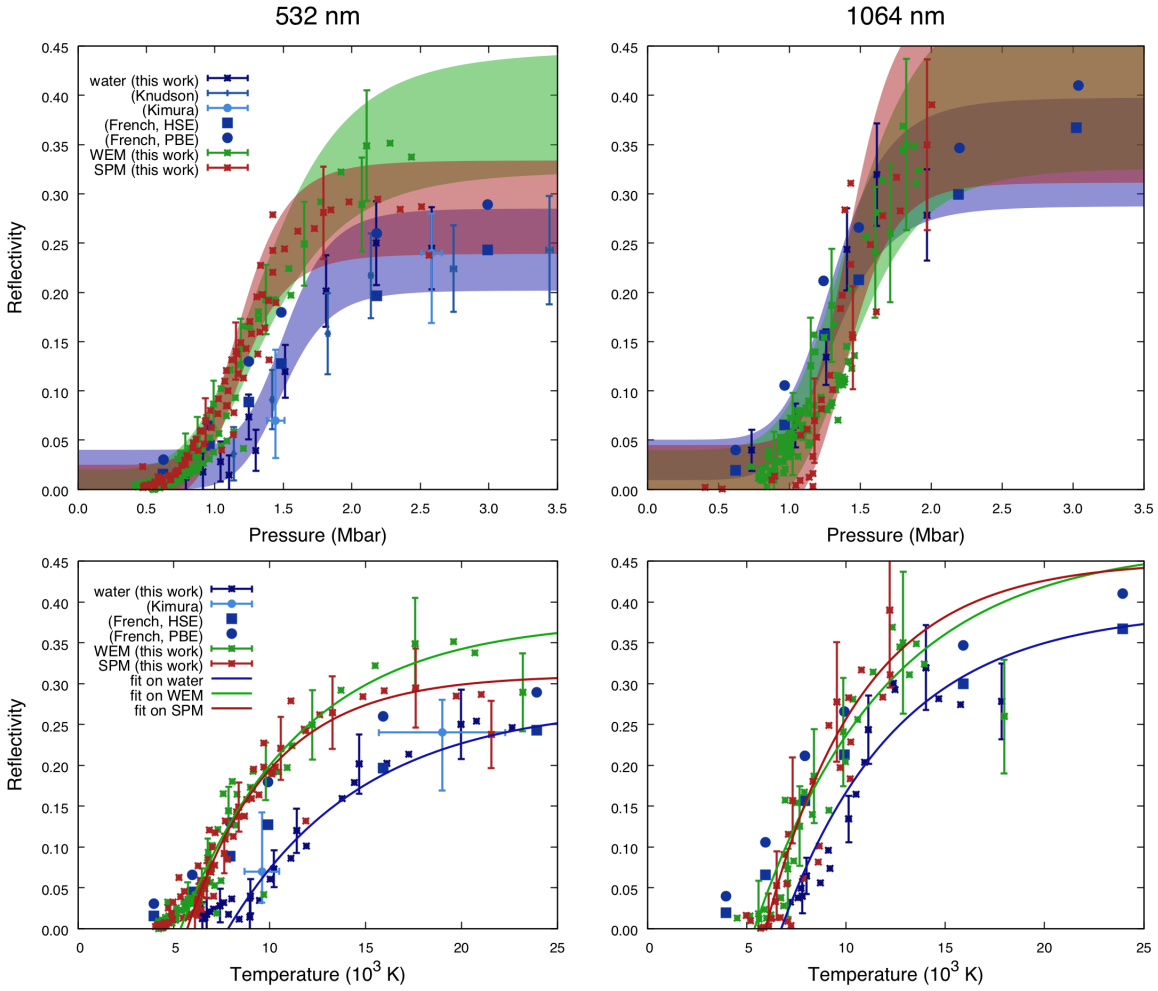

Figure 4.12 – Reflectivity behaviour of water, the WEM, and the SPM at 532 nm (left) and 1064 nm (right) as a function of pressure (top) and of temperature (bottom) along their principal Hugoniot curves. The experimental data for water from Knudson et al. (2012) and Kimura et al. (2015) are also shown. **Top.** Reflectivity *vs* pressure data. Blue, green, and red areas correspond to the fit on our data on pure water, WEM, and SPM within the error bars, respectively. Crosses are time-resolved measures during decaying shock propagation. Filled squares or circles correspond to DFT / Kubo–Greenwood reflectivity calculations by French and Redmer (2011) using the HSE or PBE exchange–correlation functionals, respectively. Error bars at 1064 nm are larger because of the limited number of available shots. **Bottom.** Reflectivity *vs* temperature data. Solid lines are guides for the eyes.

relative errors on the temperature are about 15%, when far enough from the detection limit.

4.3.6 Ab initio calculations

As we have already discussed in Section 4.1, the experimental data about planetary mixtures at the relevant thermodynamic conditions for planets' interiors are scarce. *Ab initio* simulations, on their side, are drastically complicated by the composition of the mixtures, as different molecules are initially present which undergo different transitions,

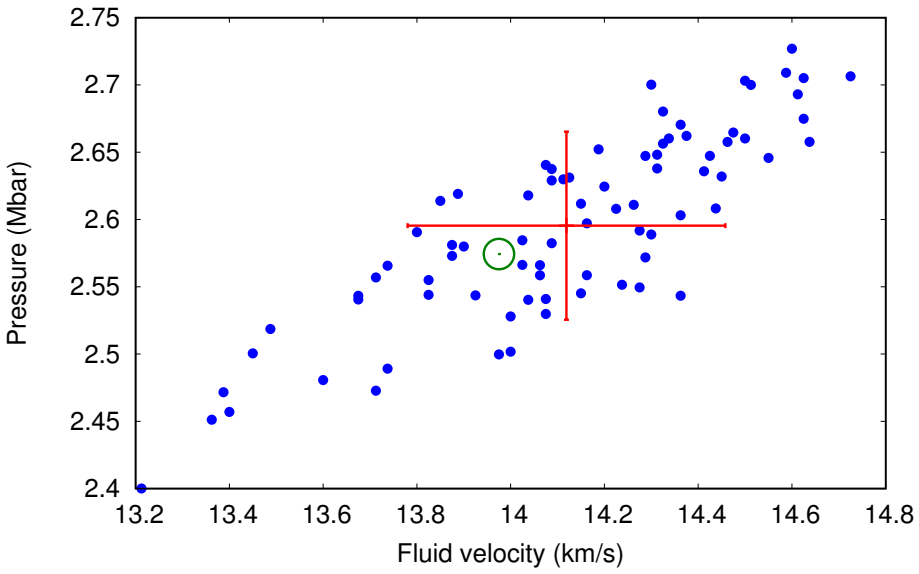

Figure 4.13 – Monte-Carlo error analysis in the (U_p, P) plane for the mixture state. Each blue circle is the result of a single run of the analysis, in which U_s^{Qz} and U_s^{mix} were varied around a central value. Only a fraction of the runs is shown to increase the figure readability. The red cross with error bars represents the mean values with their standard deviations. The green circle is the result obtained from the central value of the measure.

their products interacting with each other. As a consequence, the input data for planetary models are affected by serious uncertainties. For this reason, the equations of state and other physical properties of planetary mixtures are usually built from those of the pure end-members (hydrogen, helium, water, methane, ammonia, etc.) using a Linear Mixing Approximation (LMA) [Danel and Kazandjian (2015); Soubiran and Militzer (2016)]. Such a procedure consists in linearly adding up the relative volumes $V_i = 1/\rho_i$ and specific internal energies e_i of the end-members i weighted by their mass fractions x_i to predict the relative volume $V = 1/\rho$ and specific internal energy e of the mixture at given conditions of pressure (P) and temperature (T):

$$V(P,T) = \sum_i x_i V_i(P,T), \tag{4.2}$$

$$e(P,T) = \sum_i x_i e_i(P,T). \tag{4.3}$$

The validity of such a useful but drastic approximation for planetary ices has already been investigated by Bethkenhagen et al. (2017), who found small deviations around 4% for the equations of state.

In the context of the present work, the experimentally determined Hugoniot curves of the WEM and SPM have been reproduced by DFT-MD calculations (see Chapter 2.6.2) of icy mixtures performed by Mandy Bethkenhagen, Martin French, and Ronald Redmer *(University of Rostock)* using the North-German Supercomputing Alliance (HLRN) facilities and the IT- and Media Center of the *University of Rostock*. The goal was to test the validity of the LMA on icy mixtures using actual experimental data about the icy mixtures instead of simulations as already done by Bethkenhagen et al. (2017).

The LMA-based equations of state of the icy mixtures have been calculated via equations 4.2-4.3 from the simulated EOS of pure water, methane, and ammonia as discussed in Bethkenhagen et al. (2017). In particular, the WEM has been modelled by a 7:4 water–methane mixture [atomic composition displayed in Figure 4.14 (d)], while the SPM has been represented by a 7:4:1 water–methane–ammonia mixture [Figure 4.14 (e)]. The atomic compositions of the mixtures employed in the simulations are also reported in Table 4.1 together with the compositions of the experimentally studied mixtures. A quantum correction to the internal energies has been added as discussed in French and Redmer (2009), since this correction typically yields much better agreement between simulation and experiment along the Hugoniot as has been shown for pure ammonia [Bethkenhagen et al. (2013)].

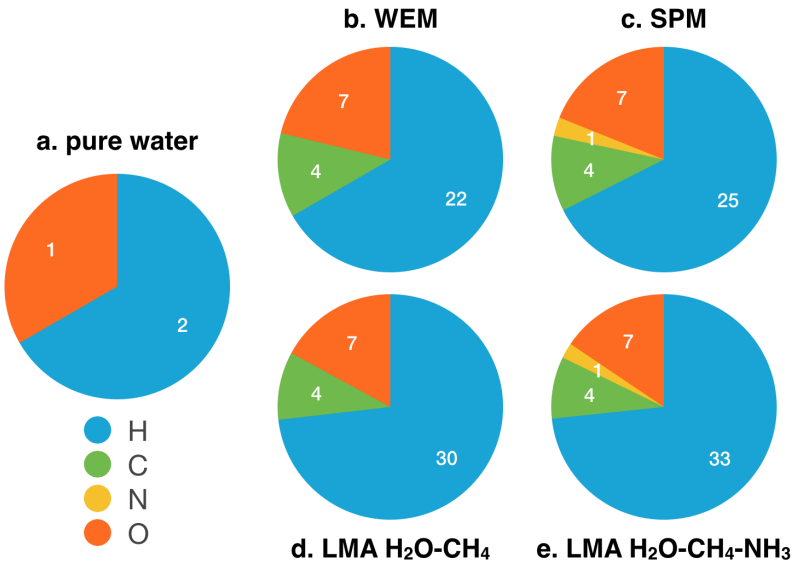

Figure 4.14 – Pie charts of the atomic compositions of the mixtures experimentally studied in this work and of the mixtures reproduced via LMA-based calculations, compared to pure water. The white numbers on the charts are the number of atoms of each type in the chemical formula of the considered mixture (see Table 4.1). **(a).** Pure water. **(b).** Water–ethanol mixture. **(c).** "Synthetic planetary mixture" (water–ethanol–ammonia). **(d).** LMA-based water–methane mixture. **(e).** LMA-based water–methane–ammonia mixture.

The compositions of the simulated mixtures in the simulations slightly differ from those of the experimentally studied mixtures (see Figure 4.14). This is due to the fact that the mixtures realised in the laboratory are mixtures of water, ethanol (C_2H_5OH, preferred to methane to avoid demixing issues), and ammonia. As a consequence, the molar fractions of hydrogen atoms in the experimental mixtures are lower than in the LMA mixtures ($67 - 68\%$ instead of 73% – see Table 4.1), whereas the C:N:O molar ratios coincide (4:0:7 for binary mixtures, 4:1:7 for ternary mixtures).

Comparison with the experimental data

Our experimental results on the icy mixtures – the WEM and the SPM – have to be compared with the equations of state of a water–methane mixture and a water–methane–ammonia mixture determined by the LMA-based calculations. First, we com-

pare in Figure 4.15 the $U_s - U_p$ relations experimentally determined for the WEM and the SPM with the LMA-based relations for the water–methane and water–methane–ammonia mixtures. At low fluid velocities ($6 - 8$ km/s), there is a good agreement between experiments and LMA-based calculations. At higher U_p, LMA-based data systematically exhibit lower U_s values than experimental data, although almost all the latter agree with the first within error bars.

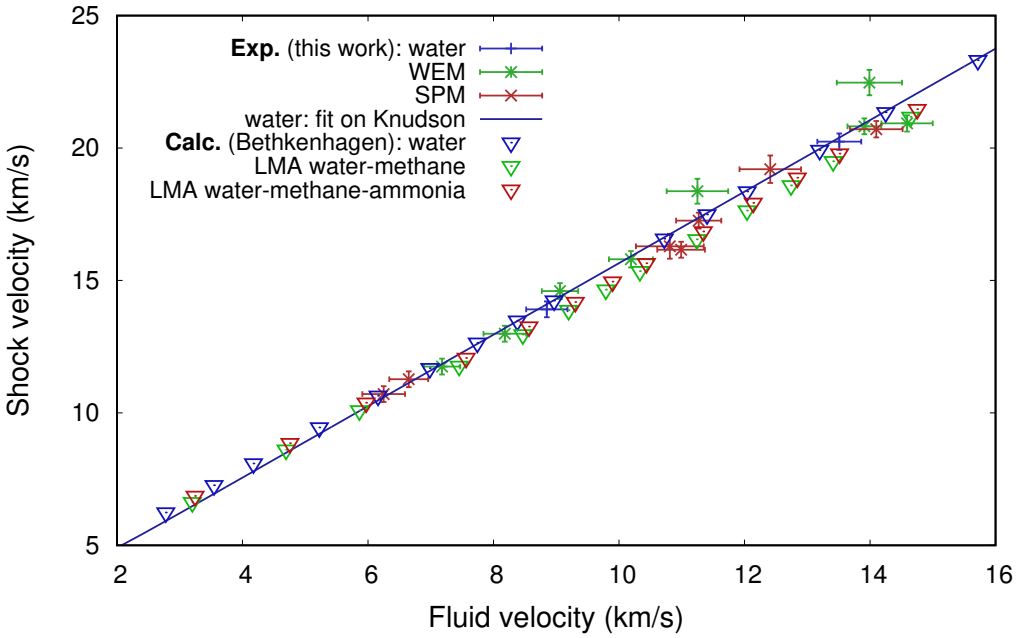

Figure 4.15 – Experimental shock–fluid velocity data on water, WEM, and SPM (points with error bars) compared $U_s - U_p$ data on a water–methane mixture and a water–methane–ammonia mixture obtained by Mandy Bethkenhagen from DFT-MD simulations of their end-members via a Linear Mixing Approximation.

It is interesting to translate the $U_s - U_p$ data into pressure – density relations. Figure 4.16 shows the adjusted pressure P/ρ_0 over the compression factor ρ/ρ_0 along the measured and LMA-based Hugoniot curves of water and the different mixtures. The scaling of both axes with the initial densities ρ_0 has been performed to account for the different compositions of the various mixtures. Indeed, the initial densities of the Hugoniot curves derived from DFT-MD are only 0.7301 g/cm^3 for the water–methane–ammonia mixture, and 0.7019 g/cm^3 for the water–methane mixture at a initial temperature of 298 K, against 0.889 g/cm^3 and 0.881 g/cm^3 for the SPM and the WEM, respectively.

If, on the one hand, DFT-MD calculations of water agree with experimental data on the whole set of explored conditions, there are discrepancies between experimental data on the mixtures and the LMA-based data. The latter predict compression ratios similar to that of water up to an adjusted pressure of 0.8 Mbar cm^3/g. For adjusted pressures beyond this point, the DFT-MD Hugoniots predict significantly higher compression factors compared to pure water. In this range, the compression ratio calculated for the water–methane mixture is found slightly higher compared to the ternary water–methane–ammonia mixture. This difference between experiments and calculations is most likely due to the slightly different hydrogen ratios considered in the mixtures in

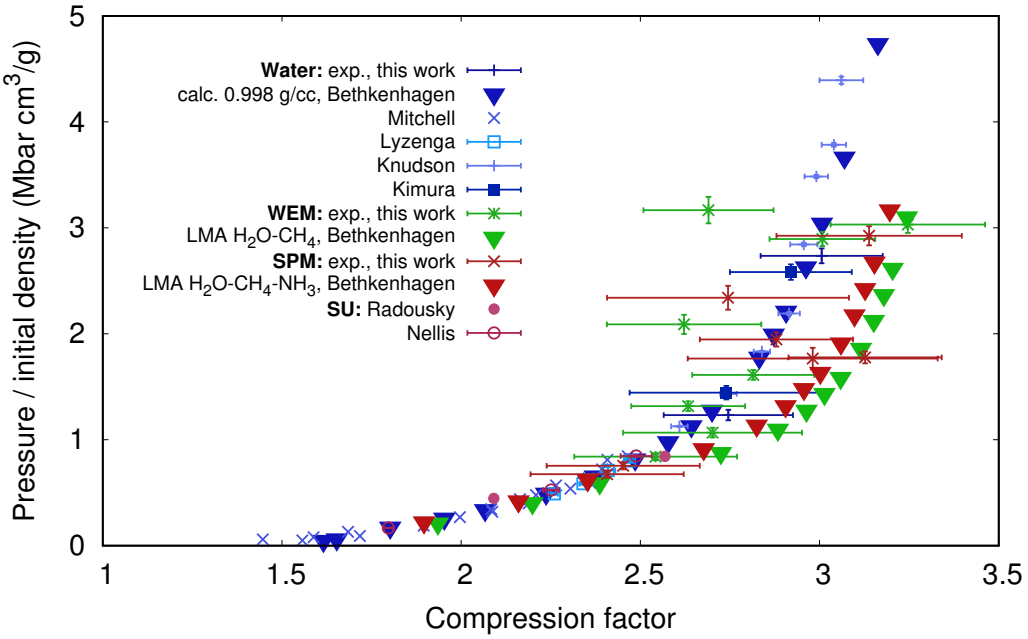

Figure 4.16 – Pressure – initial density ratio (P/ρ_0) as a function of the compression factor (ρ/ρ_0) along the Hugoniot curve of water, WEM, and SPM. The experimental data of this work and the DFT-MD simulations by M. Bethkenhagen are compared. Previous experimental data are shown for comparison.

the calculations (see Figure 4.14 and Table 4.1). Indeed, the hydrogen compression ratios are significantly higher at a given pressure. Since the LMA water–methane mixture is rich in hydrogen compared to the experimentally investigated water–ethanol mixture, the simulations systematically predict too high compression ratios. If the calculated Hugoniot curves were based on a less hydrogen-rich mixture, the calculated mixture points in Figure 4.16 would shift to lower compression ratios. The calculations containing methane instead of ethanol give thus an upper bound of the discrepancies between real mixtures and the LMA.

Finally, we compare the experimentally measured temperatures with the temperatures determined from DFT-MD simulations using the LMA. We provide in Figure 4.17 the experimental temperature – pressure data for the WEM and the SPM, together with the best-fit function, compared to the LMA-based data for the water–methane and the water–methane–ammonia mixtures. Experimental data agree with LMA-based calculations well within error bars. In particular, up to pressures of 1.5 Mbar the best-fit function and the LMA-based data are almost superimposed. The latter – and in particular the water–methane mixture data – start to exhibit higher temperatures at 1.5 Mbar, always remaining inside the uncertainty area of the best-fit function. This small difference in temperature can be attributed to the lower initial densities of the water–methane and water–methane–ammonia mixtures compared to the WEM and the SPM. Unlike what happened for pressure – density relations, the difference in hydrogen content between the experimentally studied mixtures and the LMA-calculated ones seems to have only a small effect on the pressure – temperature relation.

In summary, all over the studied range of conditions, our $U_s - U_p$ and $T - P$ data show a fair agreement with LMA-based calculations which suggests the use of this

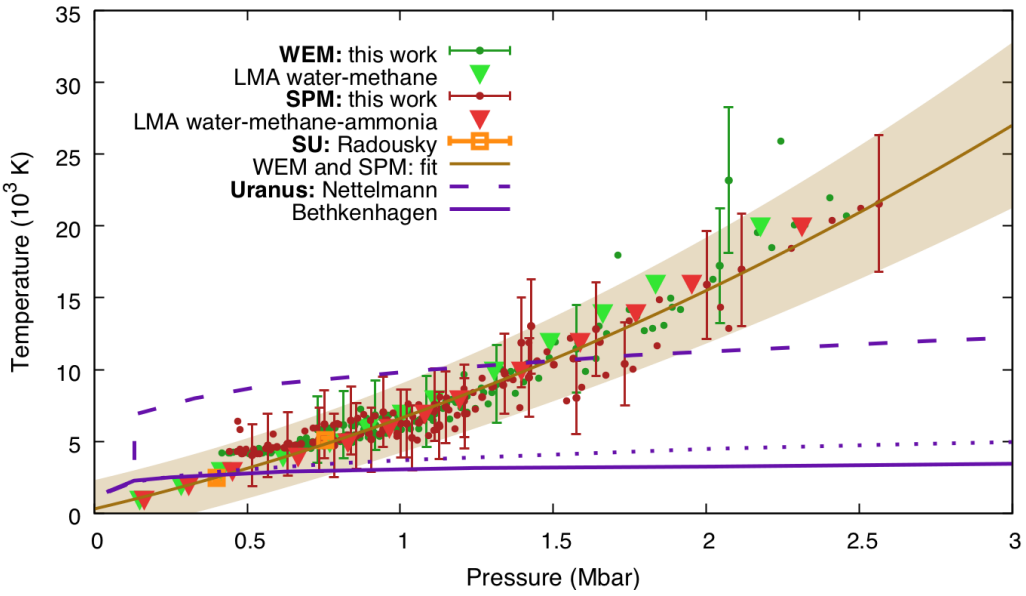

Figure 4.17 – Experimentally determined temperature – pressure relations for the WEM and the SPM along their principal Hugoniot curves compared to the temperature – pressure relations of a 7:4 water–methane mixture and a 7:4:1 water–methane–ammonia mixture determined from DFT-MD simulations using the Linear Mixing Approximation. Uranus interior models are taken from Redmer et al. (2011), Nettelmann et al. (2016), and Bethkenhagen et al. (2017).

approximation to model the behaviour of icy mixtures at planetary interior conditions.

4.3.7 Electrical conductivity

Electrical conductivity is one of the key parameters for the modelling of planetary magnetic fields. Indeed, a planetary dynamo can be sustained if magnetic induction dominates over diffusion, as discussed in Chapter 1.2.2.

In gas-gun shock experiments, the static electrical conductivity σ_{DC} can be directly measured using electrodes. This approach cannot be applied to laser shock experiments. In this case, the real part of the conductivity at a given frequency, $\Re[\tilde{\sigma}(\omega)]$, can be estimated from the measurement of the complex refractive index of the shocked sample $\tilde{n}(\omega) = n(\omega) + ik(\omega)$ at the same frequency via the wave solution of Maxwell's equations:

$$\Re[\tilde{\sigma}(\omega)] = 2\epsilon_0 n(\omega) k(\omega) \omega. \tag{4.4}$$

The evaluation is straightforward in the case both the absorption coefficient $\alpha(\omega)$ and the reflectivity $R(\omega)$ can be simultaneously measured, as done *e.g.* by Millot et al. (2018). Indeed, in such a case $n(\omega)$ and $k(\omega)$ can be determined by inverting

$$\alpha(\omega) = \frac{2\omega k(\omega)}{c}, \tag{4.5}$$

$$R(\omega) = \frac{[n(\omega) - n_0(\omega)]^2 + k^2(\omega)}{[n(\omega) + n_0(\omega)]^2 + k^2(\omega)}, \tag{4.6}$$

where n_0 is the real part of the pristine refractive index and its imaginary part k_0 is zero, as is the case for initially transparent materials. Nevertheless, this approach is very delicate and remains restricted to few experiments and conditions: the reflectivity must be high enough to be measurable by VISARs, whereas the absorption coefficient, which is extracted from a Lambert–Beer fit on the time-resolved self-emission measurement on the SOP, should be such that the time scale of the exponential increase of the signal is compatible with the time window of the SOP and is neither too long, nor too short to be measurable. In most cases, in laser-shock experiments only reflectivity is measured, at one or two probe laser wavelengths (often in the green, at 532 nm, and sometimes in the near-IR, at 1064 nm). In this case, a model has to be considered in order to infer the complex refractive index and thus the electrical conductivity.

A common approach consists in assuming that the medium under study is homogeneous and that a local constitutive equation links the current density $\mathbf{J}$ and the electric field $\mathbf{E}$ inside the medium. These assumptions imply that the following relation is valid:

$$\tilde{\mathbf{J}}_\omega(\mathbf{r}) = \tilde{\sigma}(\omega)\tilde{\mathbf{E}}_\omega(\mathbf{r}), \tag{4.7}$$

where $\tilde{\mathbf{J}}_\omega(\mathbf{r})$ and $\tilde{\mathbf{E}}_\omega(\mathbf{r})$ are the spectral local current density and electric field at the position $\mathbf{r}$ inside the medium at the frequency ω, respectively, whereas $\tilde{\sigma}(\omega)$ is the complex electrical conductivity at that frequency. Equation 4.7 states that the current density at a given point inside the medium under study is proportional to the electric field at the same position. For this reason, the regime it describes is called *local-response regime*. It can be proved [Grosso and Pastori Parravicini (2000)] that, given these assumptions, the complex refractive index at a given frequency can be linked to the complex electrical conductivity at the same frequency via:

$$\tilde{n}(\omega) = \left[\tilde{n}_b^2(\omega) + \frac{i\tilde{\sigma}(\omega)}{\epsilon_0\omega}\right]^{1/2}, \tag{4.8}$$

where $\tilde{n}_b(\omega)$ is the contribution of the bound electrons to the refractive index at the probe laser frequency and $\tilde{\sigma}(\omega)$ is the complex electrical conductivity at that frequency. The solution with a positive imaginary part has to be selected as the only one with a physical meaning – the other one would allow solutions involving exponentially increasing electric fields.

In the context of laser-driven shock experiments, the DC conductivity $\sigma_{\mathrm{DC}} = \sigma(0)$ is often [Celliers et al. (2004); McWilliams et al. (2012); Millot et al. (2015); Millot et al. (2018)] extracted from reflectivity data assuming that the studied material follows a Drude behaviour. The Drude model [Drude (1900a,b)] assumes that free electrons respond to the local electric field with a linearly accelerated motion until they collide with an ion. After a collision, the electron keeps no memory of its previous motion and randomly re-starts it. The Drude-like frequency dependency of the conductivity can be written as

$$\tilde{\sigma}(\omega) = \frac{1}{1 - i\omega\tau}\sigma(0), \tag{4.9}$$

where τ is the electron-ion scattering time, which represents a new unknown which has to be estimated depending on the probed thermodynamic conditions.

By taking the real part of equation 4.9, one obtains

$$\Re[\tilde{\sigma}(\omega)] = \frac{1}{1 + \omega^2\tau^2}\sigma(0), \tag{4.10}$$

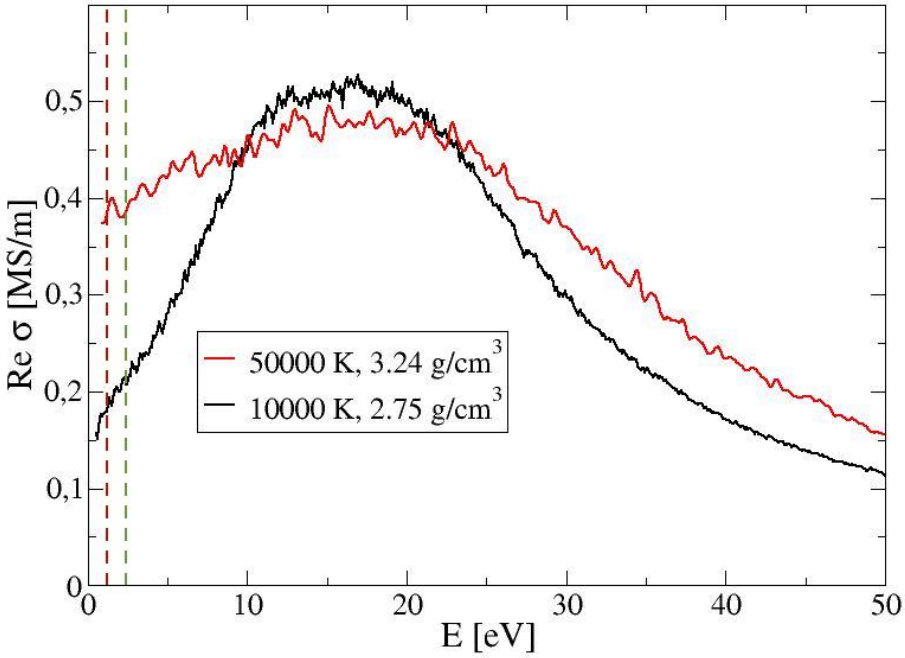

Figure 4.18 – Real part of the electrical conductivity of pure water as a function of photon energy for two principal-Hugoniot conditions: at 10 kK (black curve) and at 50 kK (red curve). At 10 kK, the behaviour is clearly not Drude-like, as the slope is initially positive and the curve reaches a maximum at around 15 eV. The ratio between the zero-energy and the maximum value is around 29%. Even at 50 kK, the initial slope is slightly positive revealing a non-Drude-like behaviour. However the ratio becomes closer to 1 (about 79%). Personal communication by Martin French *(University of Rostock)*. The energies corresponding to the wavelengths of 1064 nm and 532 nm (1.17 eV and 2.33 eV, respectively) are highlighted by the red and green dashed lines, respectively.

which describes a function with a maximum at $\omega = 0$, an initial plateau and then a decreasing behaviour, which becomes $\propto \omega^{-2}$ in the high-frequency limit.

Now, the assumptions of the Drude model, such as the independence of the motion after a collision from the velocity before it and the linearly accelerated motion of a free electron between two collisions, are too simplistic to describe the actual behaviour of electrons in a WDM state. Studies on warm dense silica [Laudernet et al. (2004)] and on warm dense copper [Clerouin et al. (2005)] have shown that a Drude-like behaviour is unlikely to be followed, at least for temperatures lower than some 10 kK. For this reason, attempts to modify it to take into account the effects of persistence of velocity for an electron after a collision with an ion have been done [Smith (2001)], but the cost to pay is to introduce other unknowns to the system of equations. Unsurprisingly – even if no *ab initio* calculations of the frequency dependence of the conductivity are available in the literature for water or planetary mixtures – calculated $\Re[\tilde{\sigma}(\omega)]$ curves personally communicated by Martin French *(University of Rostock)* show that pure water does not follow a Drude-like behaviour, even at considerably high temperatures of 50 kK (see Figure 4.18).

Our estimation

Given the impossibility of using a Drude approach to model the energy dependency of the conductivity, we made instead the assumption that the real part of the conductivity $\Re[\tilde{\sigma}(\omega)]$ is approximately constant from zero-frequency to the near-IR and visible range covering our probe laser wavelengths, whereas the imaginary part $\Im[\tilde{\sigma}(\omega)]$ can be neglected in the same range:

$$\Re[\tilde{\sigma}(\omega)] \simeq \sigma(0), \tag{4.11}$$

$$\Im[\tilde{\sigma}(\omega)] \ll \sigma(0). \tag{4.12}$$

The assumption of equations 4.11–4.12 are supported by the personal communication by M. French (see Figure 4.18) which show that, even at low temperatures of 10 kK, where the initial slope of the $\Re[\tilde{\sigma}(\omega)]$ curve is relatively high, the relative difference of the conductivity values between 0 eV and 2.33 eV (corresponding to the probe laser wavelength of 532 nm) does not exceed a value of 20%, whereas it is essentially negligible at 50 kK. To model the bound electrons' contribution to the refractive index n_b for the explored thermodynamic conditions, we supposed that it remains real $[\tilde{n}_b(\omega) = n_b(\omega)]$ and that it can be expressed by extrapolating a Gladstone–Dale model valid for water in the visible range [Batani et al. (2015)]. We also neglected the wavelength dependence of n_b between 532 nm and 1064 nm, which induces a negligible error in the conductivity estimation since, at sufficiently high ionisation rates, the complex refractive index value is mainly driven by the complex conductivity and n_b has a very low effect (see equation 4.8). Even if this model suffers major limitations, it can nonetheless be used to compare our data with previous data obtained with a similar approach.

In Figure 4.19 the estimated DC conductivities of water and of the SPM are shown as a function of temperature and compared to previous results. The conductivity of water appears to increase with temperature and reach a plateau around $15 \cdot 10^3$ K. The estimated profile of the SPM is available only starting near the plateau. At $20 \cdot 10^3$ K, conductivity values are $\sim 2.2 \cdot 10^3$ S/cm and $\sim 3.4 \cdot 10^3$ S/cm for water and the SPM, respectively. The estimated conductivity of the SPM is greater than that of water in the entire explored temperature range.

An opposite behaviour of the conductivity of planetary mixtures with respect to water was observed in previous experiments on "synthetic Uranus" by Nellis et al. (1997) and Chau et al. (2011). Nellis et al. (1997) explored low-pressure conditions up to around 0.75 Mbar via single-shock compression, whereas Chau et al. (2011) employed a multiple-shock compression technique to probe higher pressures between 0.7 and 1.9 Mbar and moderate temperatures between $(2.2 - 6.3) \cdot 10^3$ K. Such temperatures differ from the original paper: they have been obtained after applying a correction following a re-analysis by Millot et al. (2018) on a similar data set [Chau et al. (2001)]. The discrepancy between the conductivity ordering found by previous studies and in this investigation can be attributed to the different importance of the ionic and electronic contributions in the regime explored by each study. Indeed, at the moderate temperatures probed by Nellis et al. (1997) and Chau et al. (2011), the main contribution to the conductivity is due to H^+ ions generated by the breaking of molecular bonds. Moreover, in those studies the *total* conductivity was measured. In our study, we probed higher temperatures above 10^4 K, where, according to Chau et al. (2011), the dominant contribution is due to free electrons and is thus thermally-activated and

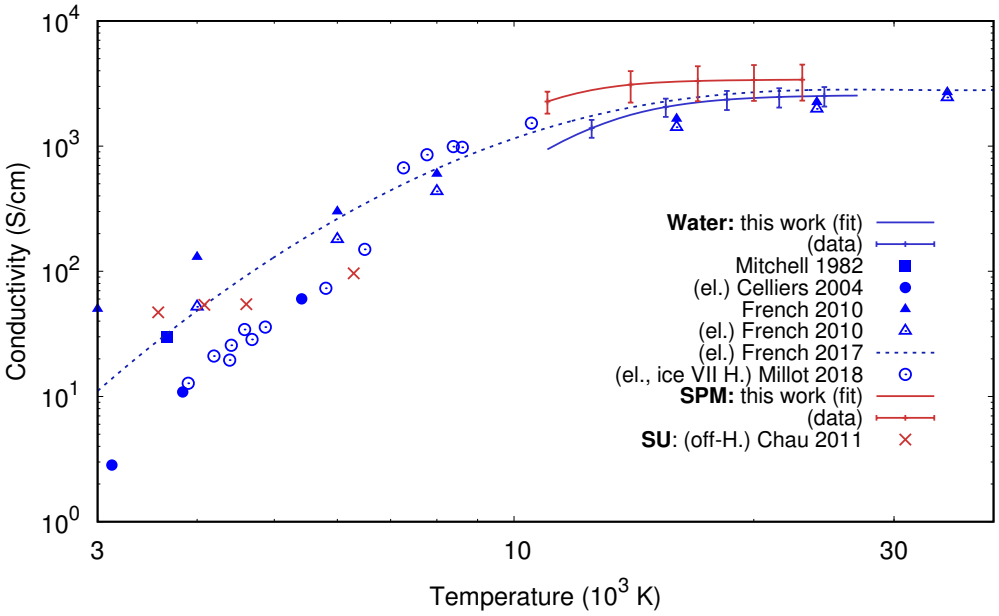

Figure 4.19 – Estimated DC electrical conductivity of water and the SPM as a function of temperature. Data in the literature for water [Mitchell and Nellis (1982); Celliers et al. (2004); French et al. (2010); French and Redmer (2017); Millot et al. (2018)] and of "synthetic Uranus" [Chau et al. (2011)], similar to the SPM, are shown for comparison. All data are relative to the principal Hugoniot curve of the material, except when explicitly marked ("ice VII H." means that the data are along the water Hugoniot starting from ice VII at $\rho_0 = 1.6$ g/cm^3; "off H." means that data are off the principal Hugoniot since the conditions have been obtained via multiple shocks). The data show total (electronic + ionic) conductivity, unless explicitly marked ("el." means that only the electronic contribution is shown). The temperature data of Chau et al. (2011) have been corrected according to are-analysis by Millot et al. (2018) to a data set obtained using the same methods [Chau et al. (2001)].

temperature-dependent. Besides, due to the fact that we estimated the conductivity from the optical properties in the visible and near-infrared frequencies, we could probe only the electronic contribution, as ions, due to their huge inertia, do not respond to such high frequencies. In analogy with the explanation of the difference in their reflectivity behaviours, the ordering between the electronic contribution to the conductivity of SPM and pure water can be explained with the fact that the ionisation energy of carbon-bearing molecules (*e.g.* 10.5 eV for ethanol) is lower than that of water (12.6 eV) [Meot-Ner (Mautner) and Lias (2018)]. At the same temperature, the SPM thus experiences a higher concentration of free electrons than water.

4.4 Off-Hugoniot study

The second investigation presented in this Chapter extended the comparison of the structural and optical properties of water and the SPM to a range of high-pressure / moderate-temperature conditions, colder than along the principal Hugoniot curves. To reach such states, we applied the double-shock compression technique that we have already described in Chapter 3.3.

We recall here the principle of the technique: a first, weak shock is generated to dynamically pre-compress the sample, so that a second, stronger shock can compress it up to the desired pressure generating a lower entropy jump due to the pre-compression of the first. This allows to explore colder conditions than by single-shock compression, which is associated to high entropy jumps across the shock front. In order to allow a direct characterisation to the double-shocked state, it is essential that the sample under study initially be transparent and that it remains so after being loaded by the first shock. This limits the maximum possible intensity of the first shock.

4.4.1 Experiments

Three double-shock experiments, which will be referred to as experiments A, B, and C later in this Section, have been performed at the LULI2000 facility. Two distinct laser pulses operating at 527 nm, obtained with the North and South chains of the facility, have been used to generate two subsequent shocks inside the sample under study. The first pulse was 10 ns long and of weak, constant intensity ($\sim 10^{12}$ W/cm^2). The second pulse, delivered right after the end of the first one, was $1.5-2$ ns long and much more intense ($\sim 10^{13}$ W/cm^2). Two phase plates were used to irradiate the target with uniform intensity on a focal diameter of 500 μm. Figure 4.20 shows the time profile of the drive-laser intensity for a shot on water.

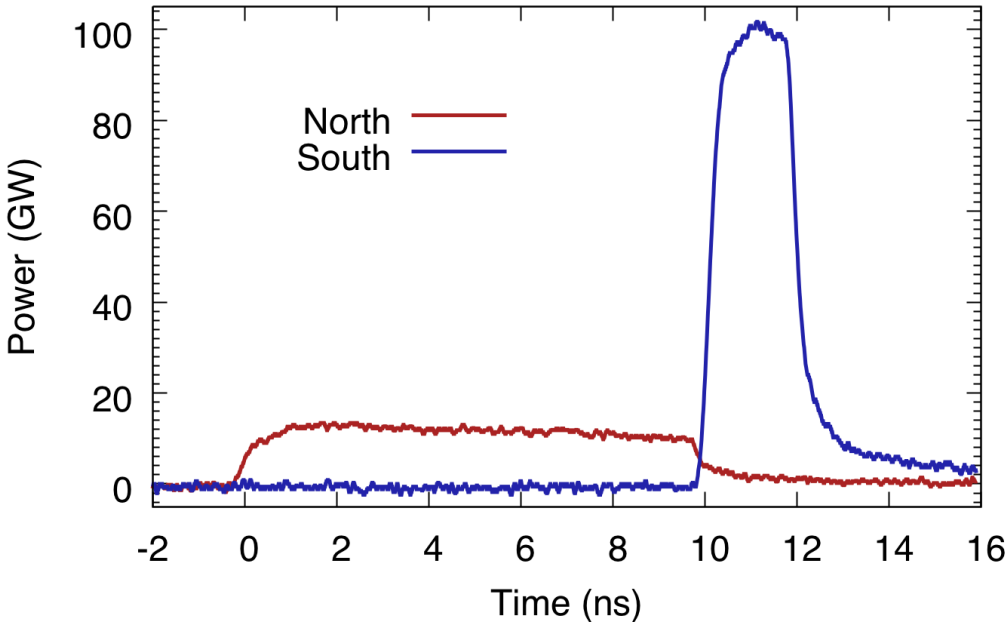

Figure 4.20 – Time profile of the power emitted by the North and South laser chains for a shot on pure water.

The target structure complied with the design optimised via hydrodynamic simulations as discussed in Chapter 3.3.4. The ablator / pusher combination consisted of 10 μm of polystyrene and 70 μm of aluminum.

The second-shock-front reflectivity has been calibrated by multiplying the merged-shock-front reflectivity of pure water or the SPM to a constant parameter to match the

$R - U_s$ relation along the principal Hugoniot curve obtained in the study presented in Section 4.3.

In experiment A, the SOP has been calibrated (see Chapter 2.5.2) externally, using a lamp of known emission temperature. In experiments B and C, the SOP calibration was done *in situ* for each shot. The known $T - U_s$ relations for water and the SPM along their principal Hugoniot curves, as determined in Section 4.3, have been used to calibrate the signal. The signal was calibrated in the merged-shock time interval using the self-emission, measured by the SOP, as a function of the shock velocity, measured by the VISARs (see Chapter 3.3.2 for the details). The *in situ* calibration in experiments B and C has been validated by comparison with an external calibration on some dedicated shots on α-quartz samples.

As we already explained in Chapter 3.3, the knowledge of the behaviour of the refractive index along the principal Hugoniot curve of the sample in the transparent regime is crucial for the analysis of double-shock data. For pure water, we used a non-linear model elaborated by Henry (2003), valid for water in the visible range. For the SPM, in the absence of previous studies of the refractive index along the Hugoniot curve, we used the same model that for water, changing the initial value to match the experimentally determined refractive index of that mixture. Such a solution is valid only for a preliminary analysis of the double-shock data: characterising the refractive index dependence on density for the SPM remains necessary for a correct analysis.

4.4.2 Diagnostics output

The output of a VISAR image and of the SOP image for a shot on pure water is shown in Figure 4.21. The time profile of the first material velocity and of the merged shock velocity [$U_p^1(t)$ and $U_s^m(t)$, respectively] and of the SOP counts are also shown. The red dotted lines correspond to the timings t_1, t_2, and t_3 defined in Chapter 3.3.1. Given the important thickness of the water sample, the timing t_4 was outside the time window of the optical diagnostics.

Four time intervals are distinguishable on the output images. Hereafter, we will describe the output for each of these intervals.

(i) Before t_1, the probe laser is reflected onto the aluminum/sample interface, as the unperturbed sample is transparent. The fringe system is constant in time since the reflecting interface remains immobile. No signal is detected by the SOP as the sample is at ambient temperature.

(ii) In the $t_1 - t_2$ time window, the first shock is propagating into the sample, leaving it in a transparent state. The probe laser is thus reflected by the aluminum/sample moving interface and Doppler-shifted according to $U_p^1(t)$. VISAR fringes are indeed shifted with respect to the unperturbed position and are fairly constant in time, indicating that the first material velocity does not vary with time. As the first shock is weak, the temperature of the shocked sample remains low and the SOP signal is also very low ($\sim$ 10 counts) and noisy.

(iii) From t_2 to t_3, the second shock, stronger and more rapid than the first, loads the sample. The fringe system disappears as the second shock brings the sample to

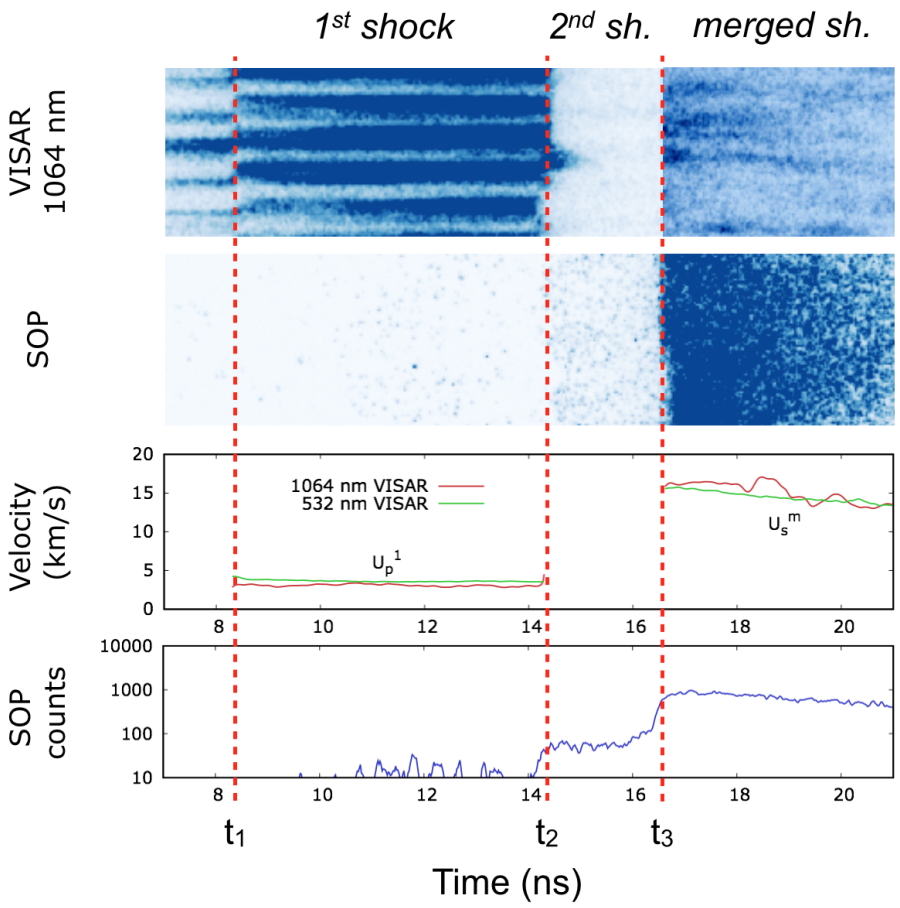

Figure 4.21 – Output image of the 1064 nm VISAR (first item) and of the SOP (second item) for a typical shot. $U_p^1(t)$ and $U_s^m(t)$, measured using the two VISARs, are shown in the third item. Time-dependent SOP counts are shown in the fourth item. The colour scale of the VISAR image has been changed for $t > t_3$ for a better readability.

an opaque state. The SOP signal gradually increases around t_2 and stabilises for the duration of the second shock.

(iv) At $t = t_3$, the two shocks merge forming a single shock loading the sample to a state belonging to the principal Hugoniot curve. Since this principal Hugoniot state is much hotter than the double-shocked state, the sample becomes optically reflecting: a fringe system re-appears on the VISARs. Fringes move in time in the $t > t_3$ time window, since the merged shock is unsustained by the laser pulse and thus decaying in time. Around $t = t_3$, an important increase is also noticeable in the SOP counts, due to the fact that the emitting sample now lies along the principal Hugoniot. The SOP counts then decay in time since the shock is losing its energy.

The colour scale of the VISAR image in Figure 4.21 has been changed for $t > t_3$ to increase readability. Indeed, fringes in the $t_1 - t_2$ window are the result of a reflection on a metallic surface, while from $t > t_3$ their intensity is much lower since they are the result of a shock-front reflection.

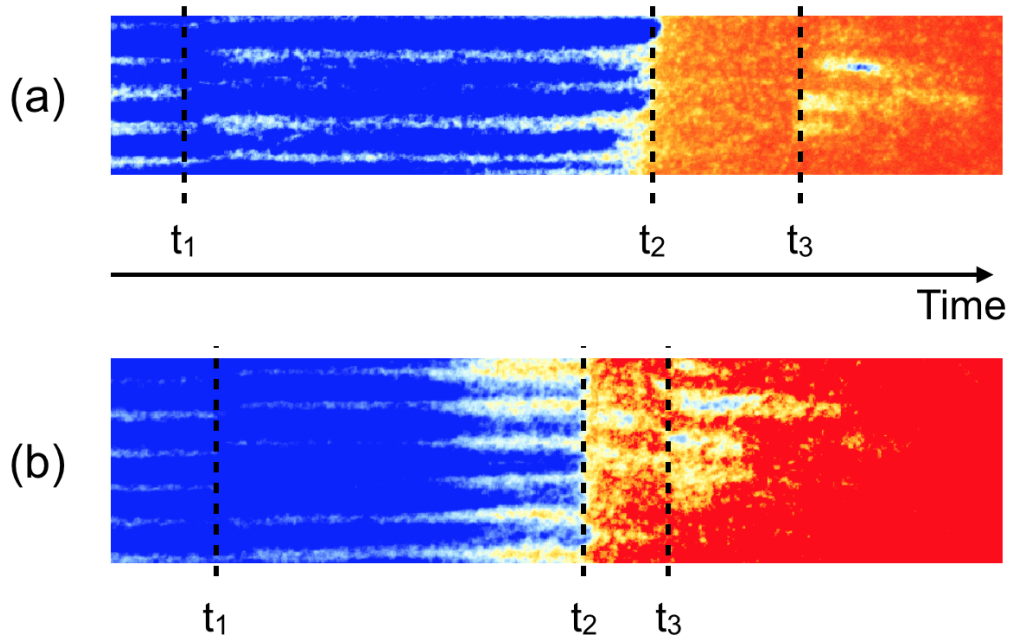

Figure 4.22 – VISAR output of two double-shock shots on the SPM. **(a).** The double-shocked state is opaque. No fringe shift is visible in the $t_2 - t_3$ interval. **(b).** The double-shocked state is reflecting. A fringe system is visible in the $t_2 - t_3$ interval, although only two fringes are clearly distinguishable.

Depending on the conditions probed, the double-shocked state can exhibit different optical properties. If it is opaque, the fringe system will disappear from t_2 to t_3 as the probe laser will be absorbed by the double-shocked sample volume. If it is reflecting, a fringe shift will happen at $t = t_2$ as, from t_2 to t_3, the VISAR will receive the probe laser reflected by the second shock front and will thus measure its velocity. Figure 4.22 shows these two cases. The VISAR output of two different shots on the SPM is provided. The image on the top shows a shot for which the double-shocked state is opaque (fringes are not visible in the correspondent time interval). The image on the bottom is that of a shot where the double-shocked state is reflecting (a fringe system in visible, and two fringes are clearly distinguishable). The VISAR diagnostics is thus useful to identify the optical properties of the double-shocked state and, in the case it is reflecting, to measure its reflectivity.

4.4.3 Thermodynamic states

By applying the double-shock compression technique on water and SPM samples, we have been able to reach pressures up to more than 5 Mbar and temperatures considerably lower than along the respective Hugoniot curves at the same pressures: the ratios between the probed temperatures and the principal Hugoniot temperatures were down to around 30%.

Figure 4.23 shows the $T - P$ conditions reached, compared to those of the principal Hugoniot curves. The water superionic phase boundary (SIPB) calculated by Redmer

Table 4.3 – Experimental double-shock data on pure water and the SPM. The run prefixes A, B, and C indicate in chronological order the experimental campaigns at LULI2000. Pressure and temperature values are relative to the double-shocked state. Reflectivity values at 532 nm and 1064 nm are relative to the second shock front.

Run-shot–sample	P (Mbar)	T (10^3 K)	R (532 nm)	R (1064 nm)
A-37–H_2O	2.02 ± 0.22	7.2 ± 1.7	13.9 ± 4.9	17.2 ± 5.3
A-48–H_2O	3.18 ± 0.35	9.7 ± 1.9	15.6 ± 5.1	19.9 ± 5.6
B-99–H_2O	4.63 ± 0.51	12.6 ± 2.1	16.9 ± 5.2	25.3 ± 6.5
B-114–H_2O	2.57 ± 0.28	9.1 ± 1.9	6.9 ± 4.2	12.7 ± 4.7
B-116–H_2O	5.60 ± 0.62	18.7 ± 2.7	22.4 ± 6.0	27.8 ± 6.8
B-118–H_2O	1.73 ± 0.19	6.0 ± 1.7	*opaque*	*opaque*
B-120–H_2O	5.31 ± 0.58	16.9 ± 2.5	17.0 ± 5.2	21.6 ± 5.9
B-122–H_2O	4.32 ± 0.48	14.2 ± 2.3	15.6 ± 5.1	26.9 ± 6.7
C–63–H_2O	1.54 ± 0.17	6.3 ± 1.7	*opaque*	*opaque*
C–64–H_2O	1.95 ± 0.21	6.1 ± 1.7	*opaque*	*opaque*
C–65–H_2O	1.90 ± 0.21	6.3 ± 1.7	*opaque*	*opaque*
C–73–H_2O	2.82 ± 0.31	9.2 ± 1.9	9.4 ± 4.4	18.5 ± 5.4
B-110–SPM	3.55 ± 0.39	13.4 ± 2.2	22.4 ± 6.0	24.1 ± 6.3
B-115–SPM	2.62 ± 0.29	7.9 ± 1.8	13.3 ± 4.8	9.2 ± 4.4
B-119–SPM	1.56 ± 0.17	5.3 ± 1.6	*opaque*	*opaque*
B-121–SPM	3.22 ± 0.35	11.6 ± 2.0	15.2 ± 5.0	28.7 ± 7.0
C-27–SPM	2.48 ± 0.27	6.5 ± 1.7	11.7 ± 4.6	12.2 ± 4.7
C-28–SPM	2.17 ± 0.24	6.0 ± 1.7	11.3 ± 4.6	13.6 ± 4.8
C-31–SPM	2.78 ± 0.31	7.0 ± 1.7	9.2 ± 4.4	9.5 ± 4.4
C-36–SPM	3.38 ± 0.37	9.9 ± 1.9	13.4 ± 4.8	20.0 ± 5.7
C-50–SPM	1.35 ± 0.15	3.9 ± 1.6	*opaque*	*opaque*

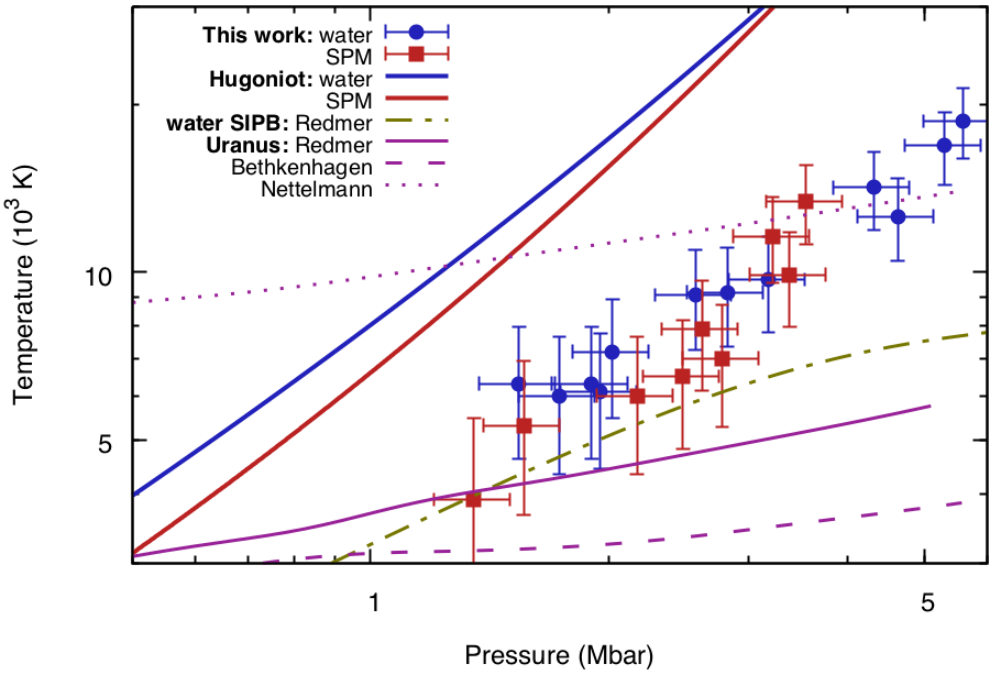

Figure 4.23 – Temperature and pressure conditions reached via double-shock compression of pure water (blue) and SPM (red) samples compared to the principal Hugoniot curves determined by decaying-shock compression (see Section 4.3).

et al. (2011) and three Uranus interior profiles by Redmer et al. (2011), Bethkenhagen et al. (2017), and Nettelmann et al. (2016) are shown for comparison, highlighting the fact that the conditions we explored are relevant both for the study of the phase diagram of water and mixtures and for planetary interior models. Such off-Hugoniot conditions are particularly challenging to reach. Only one recent study [Millot et al. (2018)] achieved similar conditions in pure water by coupling static pre-compression with Diamond Anvil Cells and laser-driven dynamic compression (see Chapter 3.2.1).

4.4.4 Reflectivity

The reflectivity at 532 nm (top) and 1064 nm (bottom) of double-shocked pure water and the SPM are shown in Figure 4.24. The Hill fits for the reflectivity along their Hugoniot curves (see Section 4.3.4) are also shown as a reference. At the lowest probed pressures and temperatures, we observe that the double-shocked state is optically opaque in both pure water and SPM samples. In particular, we observe opaque water in four shots, all around a temperature of 6000 K, and opaque SPM in two shots, at lower temperatures of around 4000 and 5000 K. The lowest-temperature reflecting state is at 7200 K for water and at only 6000 K for the SPM. We therefore conclude that the transition from the opaque to the reflecting region takes place at around 7000 K in pure water and around 6000 K in the SPM. Batani et al. (2015) predict the opaque–reflecting transition at temperatures between $6000 - 8000$ K along the principal Hugoniot, at pressures around 1.1 Mbar, lower than those probed in this work (around $1.5 - 2.0$ Mbar). The fact that the transition temperature seems to be independent from pressure indicates that the opaque–reflecting transition is primarily thermally-driven, with pressure playing only a secondary role. Moreover, the comparison between the opaque–reflecting transition temperatures of pure water and SPM off their principal Hugoniot curves confirms what has been found along the Hugoniot: the SPM becomes reflecting at lower temperatures. These results tend to validate the hypothesis that the transition from an optically opaque to an optically reflecting regime is primarily thermally-driven.

At the other end of the set of the reached conditions, we look for an evidence of the saturation of the reflectivity value, indicating that molecular dissociation – the driver of the free electronic population – is essentially complete. This phenomenon is commonly observed along Hugoniot curves and should be expected also along a dynamically pre-compressed path. The highest available pressure and temperature data concern pure water. In four shots, temperatures higher than 10 kK have been reached, corresponding to pressures around 5 Mbar. Three out of four shots exhibit a reflectivity of around 17% at 532 nm, which may be an indication of a saturation to this value. The highest-temperature point corresponds to a reflectivity of 22%, which is however compatible within the error bars with the other measurements. Along the principal Hugoniot, the water reflectivity at 532 nm saturates at a value around 25%. Saturation takes place at temperatures comparable with the highest temperatures reached in this study, around 20 kK. At 1064 nm, three out of four shots exhibit a reflectivity value around $25 - 28\%$, to be compared to the saturation value of around 34% along the principal Hugoniot. We can conclude that the measured high-temperatures reflectivity values, which can be viewed as inferior limits to the saturation values, are slightly lower than the reflectivity saturation values along the water principal Hugoniot curve.

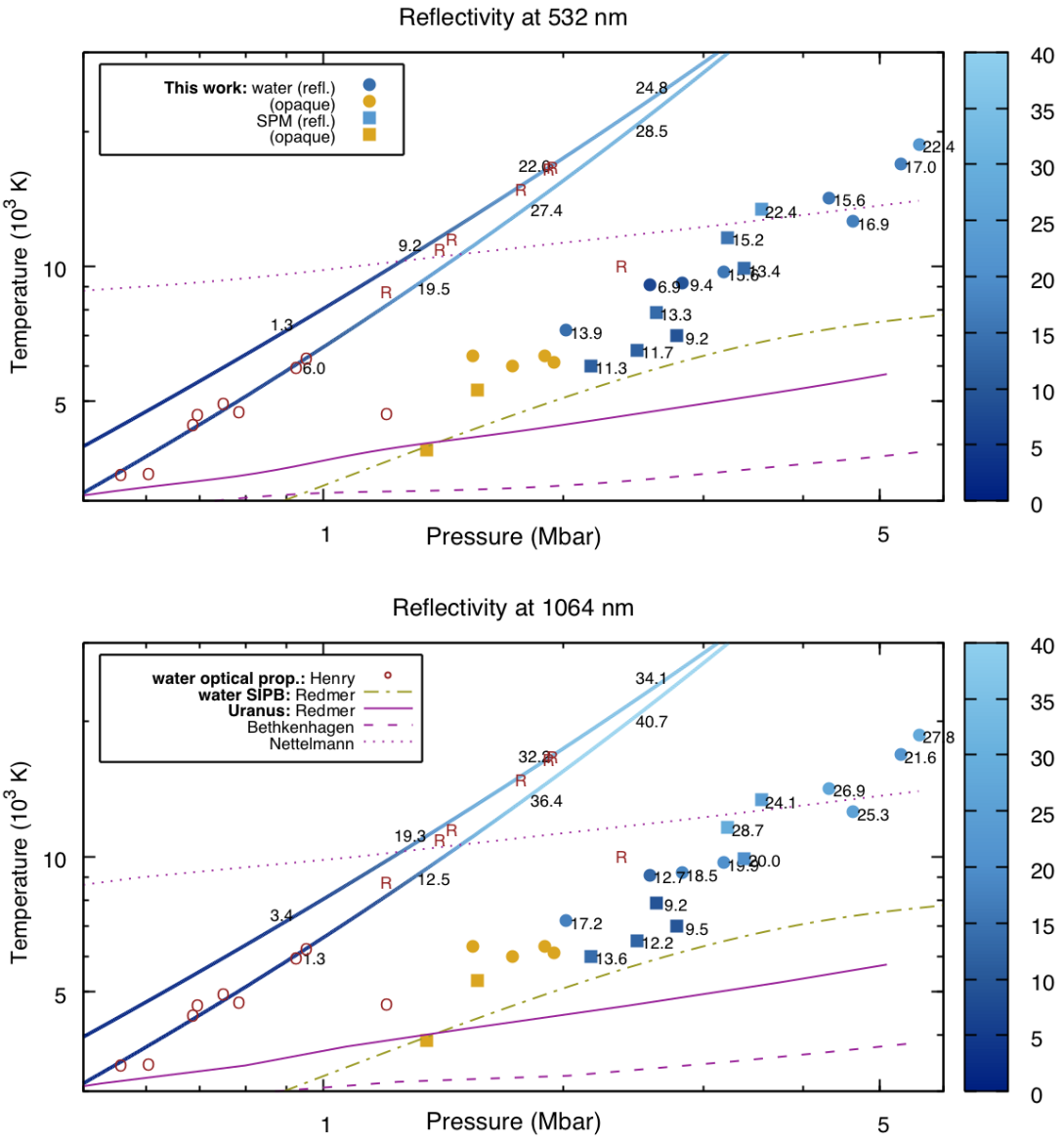

Figure 4.24 – Second-shock-front reflectivity at 532 nm (top) and 1064 nm (bottom) in pure water (circles) and SPM (squares). Each double-shock shot is shown in goldenrod if the double-shocked state was opaque or in the colour scale if it was reflecting, the colour depending on the reflectivity value. In the second case, the reflectivity value in percent is shown on the right of the symbol. The principal Hugoniot curve of water and the SPM are shown as comparison in colour scale depending on the reflectivity value. The optical properties of shock-compressed water from the work of Batani et al. (2015) are also shown in red capital letters (R for a reflecting state, O for an opaque state).

For the SPM, we dispose of just two shots reaching temperatures higher than 10000 K, corresponding to lower pressures than water (3 – 4 Mbar). Therefore, we have no evidence that the measured reflectivity values (15% and 22% at 532 nm, 29% and 24% at 1064 nm) correspond, nor are close to, saturation values. The latter are 29% and 41% along the SPM Hugoniot curve, much higher than the measured off-Hugoniot values. However, it should be noticed that reflectivity values measured via single and

double-shock compression are not immediately comparable. In fact, the shock-front reflectivity is related to the upstream and downstream refractive indices with respect to the shock front, $\tilde{n}_U$ and $\tilde{n}_D$, respectively, by:

$$R = \left| \frac{\tilde{n}_D - \tilde{n}_U}{\tilde{n}_D + \tilde{n}_U} \right|^2 . \tag{4.13}$$

In the case of single-shock compression, $\tilde{n}_U = n_U$ is just the pristine refractive index of the sample, whereas in double-shock compression it is determined by the state reached after the first shock loading. This means that the same reflectivity value may correspond to a lower downstream refractive index in a double-shock experiment compared to the single-shock case. To quantify this discrepancy, an off-Hugoniot reflectivity of 17% such as that exhibited in shot B-120 on pure water (see Table 4.3) may correspond to a reflectivity around 19.5% if the shocked sample was placed next to a pristine sample as in a single-shock scenario.

4.4.5 Error estimation

The error propagation to the density and pressure of the double-shocked state through the self impedance mismatch analysis (see Chapter 3.3.3) have been estimated through a Monte-Carlo routine, in analogy with what has been done for decaying-shock compression in Section 4.3. The varying inputs were the timings t_1, t_2, and t_3, the VISAR-measured velocities U_p^1 and U_s^m, and the $P - U_p$ relation along the principal Hugoniot curves of the samples. Errors on timings have estimated as 0.1 ns. The errors on U_p^1 and U_s^m have been determined as 1/10 of a fringe on each $P - U_p$ relations have been experimentally determined in Section 4.3.

The error on the second-shock-front reflectivity mainly depends on the uncertainty associated to calibration, which is done comparing the known Hugoniot $R - U_s$ relation of water and SPM to the experimental merged-shock-front reflectivity – merged-shock velocity relation. Other important sources are the spatial non-uniformities and the noise on the VISAR and reflectometer signals.

Like the reflectivity, temperature is principally affected by the error associated to calibration, which is done by comparing the known Hugoniot $T - U_s$ relation of water and SPM to the experimentally measured temperature of the sample loaded by the merged shock as a function of the merged-shock velocity. Spatial non-uniformities and noise issues also contribute to the total uncertainty.

4.4.6 Optical properties along quasi-isothermal lines

The combined variation of the energy of the first and second laser pulses allowed us to probe a set of states with different pressures but similar temperatures, as it is evident by looking at Figure 4.23. This opened the possibility to study the pressure dependence of the optical properties – and, in the reflecting region, of the reflectivity values – along quasi-isothermal lines. We thus extracted three of such lines, at around 6.3 kK, 9.4 kK, and 12.6 kK which encompass data points relative to both pure water and SPM, as shown in Figure 4.25.

For each quasi-isothermal line, we report in Figure 4.25 the reflectivity at 532 nm (green) and 1064 nm (red) as a function of pressure, including the double-shock shots

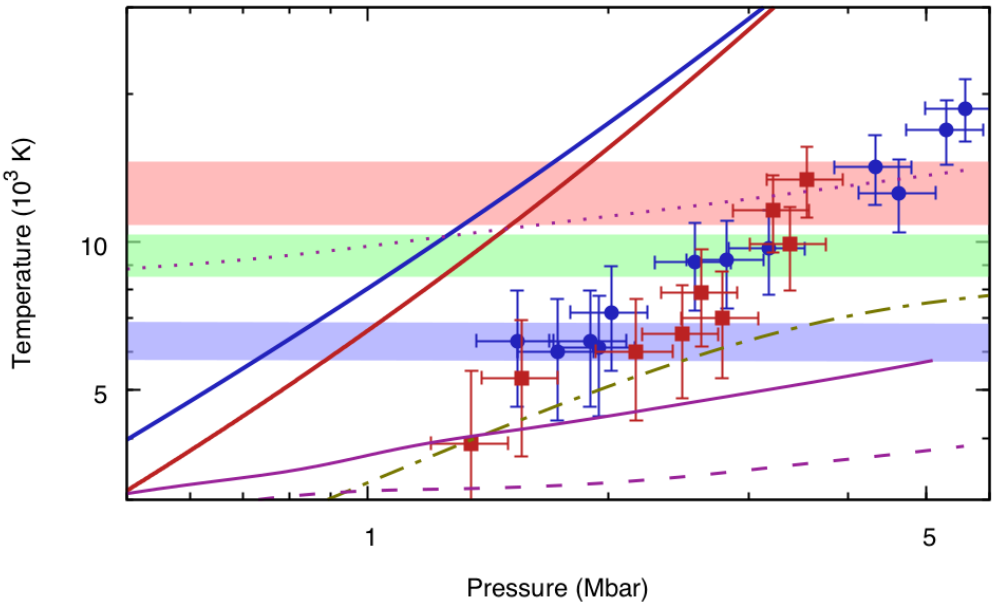

Figure 4.25 – The three quasi-isothermal lines along which the data sets have been extracted are shown as coloured areas: blue (6300 K), green (9400 K), and red (12600 K). Legend as in Figure 4.24.

in this work and also the Hill fits along the principal Hugoniot curves of pure water and the SPM. Hereafter we discuss the results for each quasi-isothermal line.

(i) At around 6300 K, pure water is still in the opaque regime whereas the SPM already exhibits a reflecting behaviour.

(ii) At around 9400 K, both pure water and the SPM are reflecting, both along their principal Hugoniot curves and at the off-Hugoniot conditions obtained via double-shock. We calculated the mean values of the reflectivity at 532 nm and 1064 nm for pure water and the SPM considering both the principal Hugoniot fits and the double-shock data. The mean values show that the SPM exhibits higher reflectivity values (15.6% at 532 nm and 17.0% at 1064 nm) than water (5.7% and 13.2%).

(iii) Around 12600 K, the mean reflectivity value for the SPM is 19.2% at 532 nm (against 15.1% for water) and 27.8% at 1064 nm (against 25.6%): even along this line, the SPM exhibits higher reflectivity values than water at both wavelengths.

These results indicate that the shock-front reflectivity of SPM is higher than that of water on a wide set of off-Hugoniot conditions. Such an ordering confirms the findings reported in Section 4.3 along the principal Hugoniot curves of water and SPM. This ordering will likely be transposed to the conductivity, which will be estimated from the reflectivity data in the near future. It is to be recalled that such a conductivity estimation from a reflectivity measurement in the visible and near-IR spectrum necessarily includes only the electronic contribution, ruling out any ionic contribution in this high-frequency spectrum due to the high inertia of ions. At high temperatures, the dominant contribution to the conductivity is electronic [Chau et al. (2011)], so that

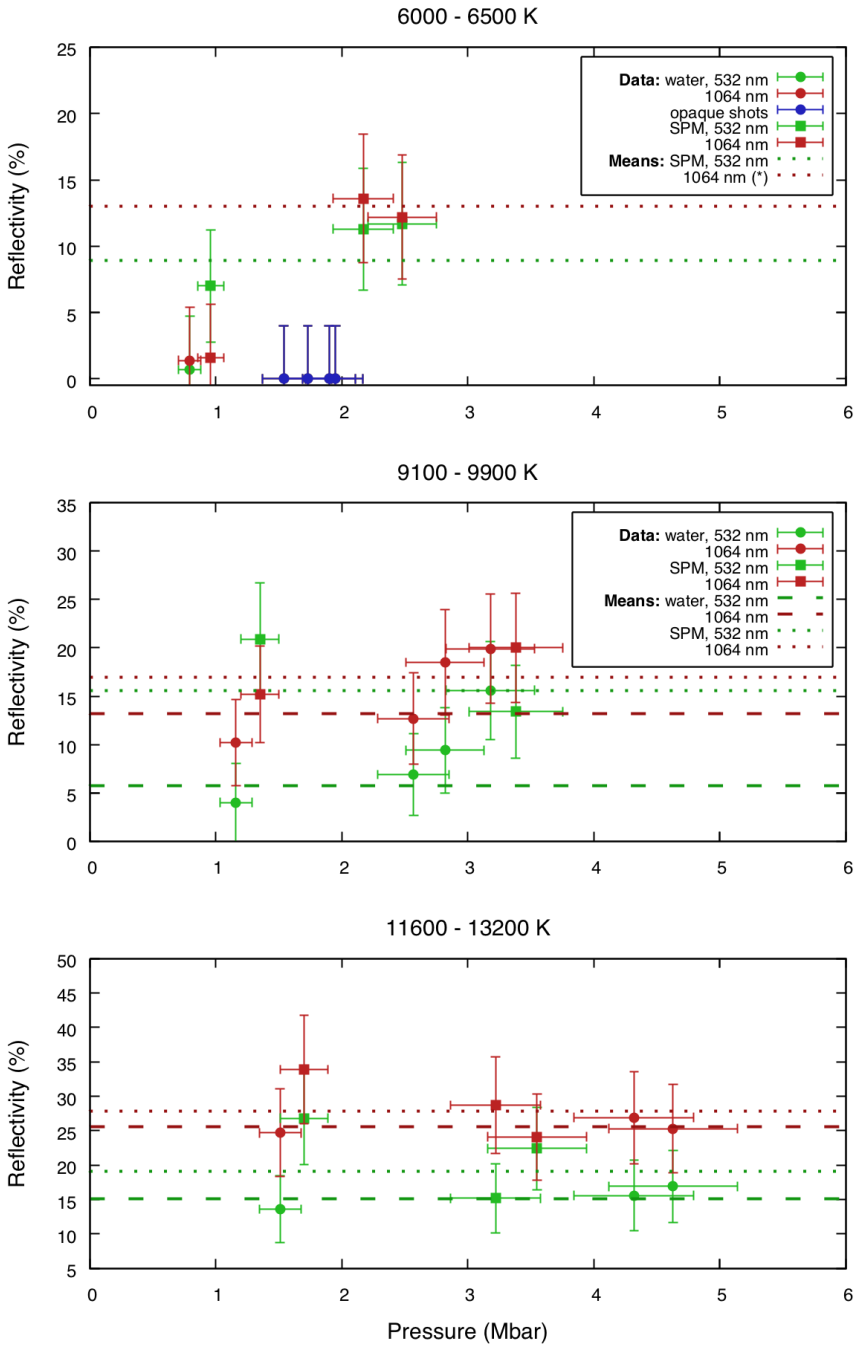

Figure 4.26 – From top to bottom: optical reflectivity at 532 nm (green) and 1064 nm (red) of pure water (circles) and the SPM (squares) as a function of pressure along quasi-isothermal lines at around 6300 K, 9400 K, and 12600 K. Experimental data using double-shocks and Hill fits along the principal Hugoniot curves are shown. In the first plot, opaque states of water are reported as zero-reflectivity measurements in blue. For each sample type and wavelength, a mean over all the double-shock data and the principal Hugoniot datum is shown as a dashed (pure water) or dotted (SPM) line. In the top plot, given the abundance of opaque states, the mean values for water have not been calculated. In the same plot, the mean value for the 1064 nm reflectivity of the SPM has been calculated considering only double-shock data.

this will not be an actual limitation. For such conditions, we can confirm the claim already done in Section 4.3 that the use of pure water as a proxy for the actual icy mixtures is not correct in the context of a dynamo modelling, as the mixtures exhibit a higher conductivity. At lower temperatures ($T \leq 6000$ K), determining the ionic contribution or measuring the total conductivity will remain essential to have a full picture of the conductivity behaviour. At such conditions our results are not sufficient to claim consequences on models of the dynamo mechanism.

Our reflectivity data suggest that the onset and behaviour of reflectivity is thermally-driven, with pressure playing only a secondary role. This is coherent with the prediction of Chau et al. (2011) about the behaviour of the electronic contribution to the electrical conductivity on the "synthetic Uranus", similar to the SPM. However, a comparison with the "synthetic Uranus" conductivity data of Chau et al. (2011) and, at lower temperatures, of Nellis et al. (1997) remains impossible until the electronic contribution to conductivity has been estimated from our reflectivity data. In any case, considering only our reflectivity data, we can preliminarily suggest that the electronic contribution to the conductivity in the SPM is systematically higher than in water, on a wide set of thermodynamic conditions. This is in contrast with the findings of Nellis et al. (1997) and Chau et al. (2011) about the *total* conductivity (including both the electronic and ionic contributions): they observed that, up to around 6000 K, the conductivity of the "synthetic Uranus" is lower than that of water. However, this contrast is only apparent as they probed low-temperature conditions in which the dominant contribution is the ionic one [Chau et al. (2011)].

In perspective, the estimation of the electronic contribution to conductivity from the reflectivity data reported in this study will clarify the relative importance of the electronic and ionic contributions in a high-pressure / moderate-temperature regime, encompassing thermodynamic conditions similar to those expected in the interiors of icy giant planets.

4.5 Conclusions and perspectives

4.5.1 Conclusions

In this work, we have characterised the equations of state and optical-electrical properties of pure water and mixtures of water, ethanol, and ammonia representing the interior of icy giant planets in the Warm Dense Matter regime. In particular, in order to isolate the contribution of each end-member to the behaviour of the mixtures, we studied a water–ethanol mixture (WEM) and a water–ethanol–ammonia "synthetic planetary mixture" (SPM).

With the aim of probing a wide set of thermodynamic conditions encompassing the predicted interior profiles of the icy giant planets, we employed two compression techniques:

(i) single decaying shocks allowed us to explore high-pressure / high-temperature states along the principal Hugoniot curves of the samples, close to the planetary interior conditions predicted by models including a Thermal Boundary Layer [Nettelmann et al. (2016)] and, possibly, to the interior profiles of extrasolar "hot Neptunes" [Dong et al. (2018)];

(ii) using double-shocks, we could probe off-Hugoniot, high-pressure / moderate-temperature conditions, closer to the interior conditions predicted by adiabatic models [Redmer et al. (2011); Bethkenhagen et al. (2017)].

Our data sets about the icy mixtures considerably extended the range of probed conditions (up to 2.8 Mbar along the principal Hugoniot and to 3.6 Mbar off-Hugoniot) and properties (EOS, reflectivity at two different wavelengths), as previous experimental investigations were limited in pressure and did not include neither temperature nor reflectivity data. On the contrary, we could characterise the reached thermodynamic state and the reflectivity of the shock front at two different wavelengths (532 nm and 1064 nm). This allowed us to obtain a full picture of the optical properties of pure water and icy mixtures.

Equations of state

Along their principal Hugoniot curves, the shock–fluid velocity relations for water, the WEM, and the SPM are comparable within error bars. Their temperature – pressure relations are also comparable, although possible small discrepancies could not be distinguished due to the error bars on the best-fit functions. These results imply that the use of pure water as a proxy of the actual icy mixtures in structural models of the interiors of the icy giant planets is reasonable.

Our experimental data along the principal Hugoniot have been compared to supporting calculations of the Hugoniot curves of a water–methane mixture and a water–methane–ammonia mixture made by Mandy Bethkenhagen *et al. (University of Rostock)* employing a Linear Mixing Approximation (LMA). Such an approximation is a very useful tool for planetary interior models since it allows to determine the equation of state of complex mixtures simply from the EOS of their end-members. The validity of the LMA was to be tested for the thermodynamic conditions we experimentally explored. The experimental and calculated shock–fluid velocity relations are compatible within error bars, together with the temperature – pressure relations. Important deviations have been observed in pressure – density relations, that have been explained by the difference in the composition of the mixtures employed in the experiments and in the calculations. In particular, the latter are more hydrogen-rich, which may contribute to increase their compressibility. That said, our experimental data validate the use of a LMA for the determination of the equation of state of icy mixtures in the explored range of thermodynamic conditions.

Optical-electrical properties

We measured the shock-front reflectivity, at two different wavelengths (532 nm and 1064 nm), of water, the WEM, and the SPM along their principal Hugoniot curves and of water and the SPM at off-Hugoniot conditions. The transition from an electrically insulating, optically opaque state to an electrically conducting, optically reflecting state has been observed in all the studied samples. The shock-front reflectivity, starting from a low value at low pressures and temperatures, undergoes a gradual increase up to a saturation regime at high pressures and temperatures.

Our results show that pure water and the mixtures (WEM and SPM) exhibit different shock-front reflectivity behaviours. In particular, along their principal Hugoniot

curves, the pressure onsets of reflectivity for the WEM and the SPM are lower than for water. Moreover, the reflectivity saturation values are higher for the SPM and WEM than for water. The off-Hugoniot data obtained via double-shock compression confirm this trend, showing that the SPM has a lower onset temperature for reflectivity and, globally, exhibits higher reflectivity values than water at similar temperatures. We have interpreted this discrepancy in the reflectivity behaviour as a signature of the fact that carbon-rich mixtures such as the WEM and the SPM dissociate at lower temperatures than pure water, given their lower ionisation energies.

Finally, we could estimate the electronic contribution to conductivity for pure water and the SPM along their principal Hugoniot curves. In the whole range of temperatures at which the conductivity has been estimated (between around 12000 K and 22000 K), we found that the SPM exhibits a higher conductivity value than pure water. This result is in stark contrast with previous studies at lower temperatures [Nellis et al. (1997); Chau et al. (2011)]. However, at the high-temperature conditions probed in our study, the dominant contribution to conductivity is electronic. This contribution is also the only one that can be estimated from visible and near-infrared measurements, which is our case. Previous studies explored a moderate-temperature regime in which the ionic contribution is dominant or comparable to the electronic one. Our results suggest that, in this range of thermodynamic conditions, the electrical properties pure water cannot be used as a proxy for those of the actual icy mixtures for the modelling of the dynamo mechanism generating a magnetic field inside icy giant planets. This may have direct repercussions on planetary models including a thermal boundary layer [Nettelmann et al. (2016)], which predict high interior temperatures corresponding to a regime in which the electronic contribution is dominant with respect to the ionic one.

The forthcoming estimation of the electronic contribution to conductivity at the conditions probed via double-shock compression will provide, in its turn, an insight about the behaviour of conductivity at moderate temperatures, closer to the interior profiles predicted by adiabatic models. However, such an insight will only be partial as, at these conditions, the ionic contribution cannot be ruled out and has thus to be characterised.

4.5.2 Perspectives

We propose three complementary axes for future work about the characterisation of the icy mixtures at WDM conditions.

(i) The assessment of the validity of the LMA along the principal Hugoniot curves of water, WEM, and SPM has given very promising results and shall therefore be extended to the off-Hugoniot conditions explored via double-shock compression, closer to those expected in the interiors of icy giant planets according to adiabatic models.

(ii) The contribution of each single end-member (water, methane/ethanol, ammonia) to the structural and optical-electrical properties of the icy mixtures has to be more precisely assessed. For this reason, the study presented in this Chapter shall be extended to other compositions, such as water–ammonia mixtures, ethanol-ammonia mixtures, etc.

(iii) Finally, future experimental work shall include X-ray diffraction studies to probe the bulk structures of the icy mixtures, as recently done for water by Millot et al. (2019), to overcome the limitations of shock-front measurements.

Chapter 5

Study of pure liquid ammonia

In Chapter 4, we studied mixtures of water, ethanol, and ammonia along their principal and dynamically pre-compressed Hugoniot curves. Their behaviours have been compared with that of pure water, with the aim of isolating the contribution of each end-member of the deep interiors of icy giant planets to their structural and electrical properties.

In this Chapter, we will expand this study of the components of icy giants' interiors by characterising pure liquid ammonia – an end-member of the icy giants' interiors together with water and methane – along Hugoniot curves from different initial conditions. Since a condensed initial state is necessary for an efficient shock compression, we developed and realised, after continuous efforts, a cell able to sustain laser-driven shock compression of a liquid ammonia sample at around 15 bar at ambient temperature, which will be referred to as Liquid Ammonia Cell (LAC) later in this Chapter. We also adapted Diamond Anvil Cells (DAC) to laser-driven shock compression of condensed ammonia samples. The equation of state and optical properties of warm dense ammonia will be presented and discussed.

Contents

5.1 Context

Ammonia (NH_3) is, together with water (H_2O) and methane (CH_4), an end-member of the icy mixtures which are believed to compose the interiors of icy giant planets (see Chapter 1.4.2). Characterising its equation of state, phase diagram, and electrical conductivity at pressures of several megabar and temperatures of a few thousand Kelvin is thus essential in order to build precise planetary models.

The study of ammonia is not only interesting for planetary science: indeed, its simple stoichiometry and its hydrogen-bonding structure make it an excellent case study for the physical and chemical behaviour of the WDM regime, as it is the case for water, which shares its polar nature and hydrogen-bonding structure. Moreover, the phase diagram of warm dense ammonia presents heavy similarities with that of water: like water, ammonia exhibits a superionic phase, first predicted by Cavazzoni et al. (1999), which features a crystalline ordering of nitrogen atoms and a large proton diffusivity, hence an important protonic contribution to the electrical conductivity, whereas, at the same time, electrons exhibit an insulating behaviour.

Besides, the study of the end-members of icy mixtures is essential to understand their contribution to the properties of the mixtures. For instance, the upper boundary of the superionic phase in a water-ammonia mixture is intermediate between the boundaries for pure water and pure ammonia [Bethkenhagen et al. (2015)]. Another critical aspect is the determination of the contribution of each end-member to the electrical conductivity of the icy mixtures, which is essential for modelling the generation of a magnetic field inside icy giant planets via a dynamo action (see Chapter 1.2.2).

5.1.1 State of the art

Warm dense ammonia has been simulated via *ab initio* methods [Cavazzoni et al. (1999); Ojwang et al. (2012); Bethkenhagen et al. (2013); Li et al. (2013, 2017)] and using a thermodynamical code [Mulford et al. (2014)]. Simulations have predicted the equation of state, phase diagram, transport properties, including the electrical conductivity and optical properties. The phase diagram reported by Bethkenhagen et al. (2013) at Warm Dense Matter conditions, shown in Figure 5.1, consists of five different phases: a face-centred cubic (fcc) solid phase (present at $10-50$ GPa and around 1000 K), the already mentioned superionic phase (occurring at pressure higher than 40 GPa and temperatures lower than 3000 K), and a fluid regime consisting in a molecular NH_3 phase (stable at low pressures and up to 3000 K), a molecular N_2+$3H_2$ phase (only present at low pressures and around $3000-4000$ K), and a dissociated phase which dominates the WDM regime, basically stable at all pressures for temperatures higher than 3000 K. According to this diagram, which is in good qualitative agreement with the previous one by Cavazzoni et al. (1999), superionic ammonia is quite unlikely to exist inside Uranus and Neptune, wherein it rather dissociates. The gradual dissociation behaviour pointed out by the phase diagram from Bethkenhagen et al. (2013) has been reproduced by calculations from Li et al. (2017) along the Hugoniot curve starting from 0.6933 g/cm^3 and 230 K. From the calculated diffusivity and viscosity, three regimes have been identified: a molecular (NH_3) fluid regime, where hydrogen and nitrogen atoms share a similar diffusivity, a mixture regime, where the ionic coupling becomes

stronger and the viscosity decreases and reaches a minimum, and a plasma regime [corresponding to the dissociated regime of Bethkenhagen et al. (2013)], characterised by high proton diffusivity and very short molecular lifetimes.

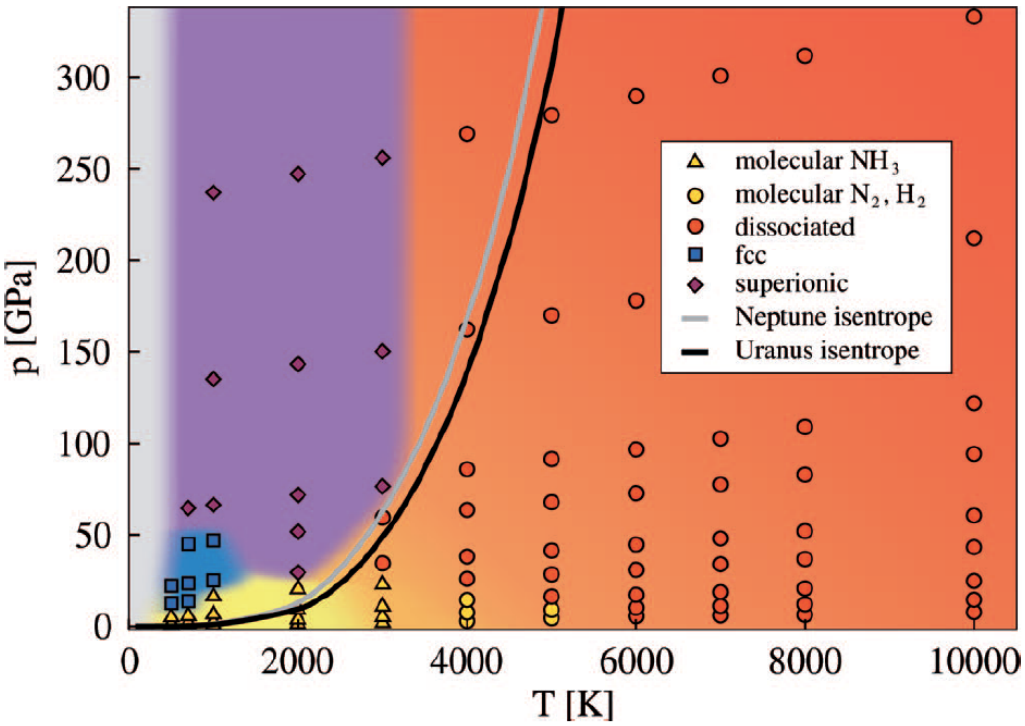

Figure 5.1 – Phase diagram of warm dense ammonia according to the DFT-MD calculations by Bethkenhagen et al. (2013). At low pressures (below 50 GPa) and low temperatures (below 3000 K), the standard molecular phase and a solid fcc phase are present. At higher temperatures (up to 5000 K) and low pressures a molecular N_2+$3H_2$ phase is stable. At pressures above 20 GPa and temperatures above 3000 K, the diagram is dominated by a dissociated phase. In the low-temperature (below 3000 K) and high-pressure region the superionic phase is stable. The Uranus and Neptune isentropes proposed by Redmer et al. (2011) are shown for comparison as black and grey solid lines, respectively.

On the experimental side, at high pressures and temperatures ammonia is much less studied than water. Most of the experimental investigations are conducted using static compression in Diamond Anvil Cells (DAC). Static compression studies [Ninet and Datchi (2008); Li et al. (2009); Ninet et al. (2012)] characterised the equation of state and phase diagram of ammonia up to 1 Mbar and 700 K. Other key parameters such as the sound velocity (which allows to estimate the bulk modulus) and the refractive index (which is critical for the analysis of shock experiments' data) have also been measured along four isothermal lines up to $1-2$ GPa [Li et al. (2009)]. The first experimental evidence for a superionic phase in ammonia has been provided by Ninet et al. (2012) using Raman spectroscopy and XRD on samples of ammonia inside resistive-heated Diamond Anvil Cells. Studies employing dynamic compression methods [Kovel (1973); Dick (1981); Mitchell and Nellis (1982); Nellis et al. (1988); Radousky et al. (1990); Nellis et al. (1997)] are very scarce and all involve explosives or gas-guns (see Chapter 2.2.2) limited to pressures of 0.7 Mbar along the liquid Hugoniot starting from 0.69 g/cm^3 and 230 K. Neither temperature – except two data points at 48 and 61 GPa

from Radousky et al. (1990) – nor shock-front reflectivity data are provided.

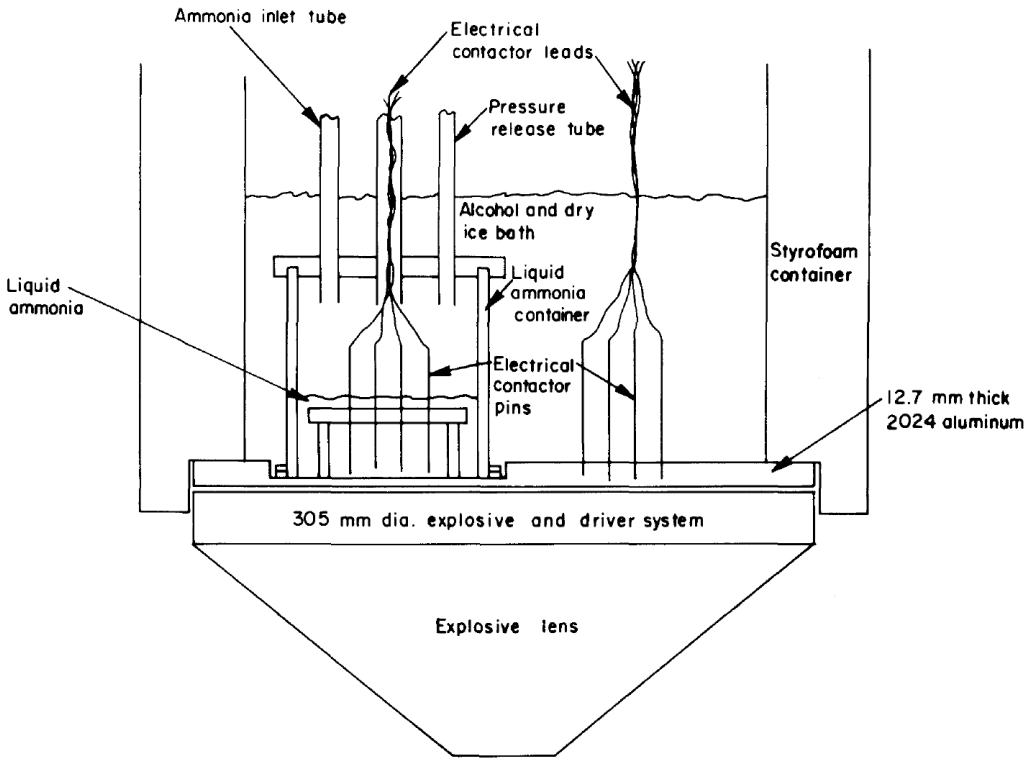

Figure 5.2 – Target for explosive-driven shock compression study of liquid ammonia, from Dick (1981). The design of a cell apt to shock-compression of liquid ammonia is necessarily complex.

Differently from pure water and other liquid samples, there are no works employing laser-based shock-compression techniques for the study of ammonia. A major reason for this is the difficulty in the target conception and fabrication. Indeed, the target shall satisfy very stringent requirements in order to simultaneously apply laser-driven compression, reach the relevant temperature and pressure conditions, and allow an optical access of the diagnostics to the shocked sample. A first technical challenge for the study of compressed ammonia is due to the fact that ammonia is gaseous at ambient conditions, whereas a condensed initial state is required for shock compression to attain high pressures and densities, as we explained in Chapter 3.1.2. Indeed, the Hugoniot curve starting from a gas spans very high temperatures, outside the range of interest for the modelling of icy giant planets, and is limited by a low maximum compression factor. Another issue resides in the chemical aggressiveness of liquid ammonia. This highly complicates the target design and assembling. For instance, it hinders the possibility of glueing the cell windows, as ammonia reacts with almost every type of glue. Because of these limitations, complicated target designs are necessary. As an example, Figure 5.2 shows the experimental apparatus used by Dick (1981) for the explosive-driven shock compression of a liquid ammonia sample. The gaseous ammonia, injected in a container via a tube, was cooled and liquefied thanks to an alcohol / dry ice bath around the container. Dick (1981), as well as the other studies, shock-compressed ammonia starting from ambient pressure and a cryostat temperature of around 230 K.

5.1.2 Present work

In this work, we have taken on this challenge and, with continuous effort, we have succeeded in realising a cell – called Liquid Ammonia Cell (LAC) later in this Chapter – able at the same time to sustain the propagation of a laser-driven decaying shock and allow an optical probing of the shocked sample through a transparent rear-side window. An α-quartz window was placed before the ammonia sample as standard for EOS and reflectivity measurements. Unlike the setup of Dick (1981) and other studies, where liquid ammonia was loaded in a cryostat cell, our setup consists in filling the cell with slightly pre-compressed ammonia (15 bar) at ambient temperature. This choice allowed us to avoid the technical problem of including a cryostat system in the laser interaction chamber and deliver a target which can be used on different facilities including high-power lasers coupled to X-ray sources such as XFEL and synchrotrons. The LAC has been conceived and built with the fundamental aid of the LULI support teams, and in particular Frédéric Lefevre. The development of the filling system of the LAC has been done in collaboration with Sandra Ninet and Frédéric Datchi from the Institut de Minéralogie, de Physique des Matériaux et de Cosmochimie (IMPMC) – *Sorbonne Université*, and will be detailed in Section 5.2.

We performed two experimental campaigns (denoted A and B later in this Chapter) on the LULI2000 laser facility, in which we compressed liquid ammonia in the LACs using decaying shocks, probing the equation of state and optical properties of ammonia along the Hugoniot curve starting from ambient temperature and 15 bar of pressure. Mandy Bethkenhagen *(University of Rostock)* provided us *ab initio* calculations of the equation of state of warm dense ammonia to be compared to our results.

During the two experimental campaigns, we also employed Diamond Anvil Cells (DAC) to statically pre-compress condensed ammonia samples prior to shock loading. With static pre-compression up to 31 kbar, we started from higher liquid densities and also solid phases, which allowed us to span lower temperature conditions, more relevant for planetary interiors. The DAC have been adapted and prepared by Jean-Alexis Hernandez (LULI). This study is presented in Section 5.3.

5.2 Study of the Hugoniot curve starting from 15 bar

5.2.1 Liquid Ammonia Cells

Liquid Ammonia Cells (LAC) have been conceived in collaboration with the Mechanical Design Office of the LULI laboratory. They are made of stainless steel and composed by a central body, two lateral washers, and two plugs. The scheme of the central body is provided in Figure 5.3. The central body has a central cylindrical duct and a lateral filling duct connected to a capillary. The capillary connects the LAC to a valve [Figure 5.4 (a)] used to isolate the cell once filled (see Section 5.2.2). Each washer has an inner and an outer side. The inner side is placed against the central body during the assembly procedure. Each side has a seat for a toroidal gasket. The LAC is assembled in order to make the central duct watertight. This is done by placing a z-cut α-quartz window on the inner side of each washer, which is then screwed to the central body via

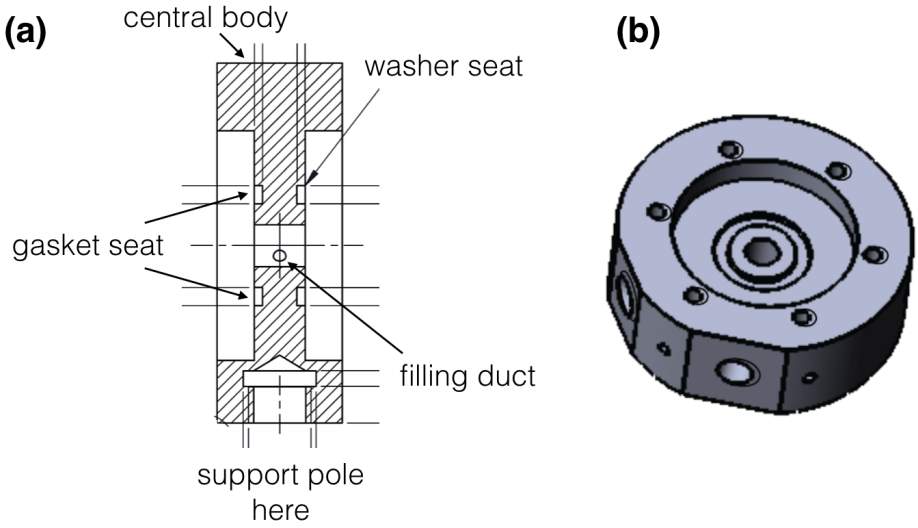

Figure 5.3 – **(a).** Lateral view of the central body of the LAC. The central cylindrical duct communicates with the two seats for the lateral washers. The toroidal seats of the EPDM gaskets for the connection between washers and central body are visible. At the bottom, a thread for the supporting rod is carved. On the center of the central duct, the opening to the filling duct is visible. **(b).** Three-dimensional view of the central body. The seat for the EPDM gasket, the six threads to screw the plug, the thread to screw the nut connected to the capillary, and the thread for the supporting rod are visible. Adapted from the design by the Mechanical Design Office of the LULI laboratory.

the plug. The quartz window on the drive-laser side also serves as *in situ* standard for shock-compression measurements (see Chapter 2.3.4). The rear-side quartz window is used as a mere transparent window to provide the diagnostics an optical access to the sample.

A multi-layered ablator / pusher combination is glued to the drive-laser side quartz window, isolated from the ammonia sample. Several combinations have been used. For the majority of shots, the following combination was employed:

$$10\ \mu\text{m of CH (polystyrene) / } 40\ \mu\text{m of Al / } 52 \text{ or } 112\ \mu\text{m of } \alpha\text{-quartz.}$$

For some high-energy shots, a gold layer has been used to avoid X-ray pre-heating. The combination was as follows:

$$10\ \mu\text{m of CH / } 5\ \mu\text{m of Au / } 52 \text{ or } 112\ \mu\text{m of } \alpha\text{-quartz.}$$

For one low-energy shot in the transparent regime of ammonia, the ablator / pusher was instead made of:

$$10\ \mu\text{m of CH / } 20\ \mu\text{m of Al / } 52\ \mu\text{m of } \alpha\text{-quartz / } 0.15\ \mu\text{m of Au.}$$

The very thin layer of gold after the quartz window allowed the measure of the pusher / ammonia interface velocity.

The assembly procedure of the LAC has been developed by Frédéric Lefevre (LULI). It consists of several stages. First, the different layers of the ablator / pusher combination are glued together and to the quartz window [Figure 5.4 (b)]. A toroidal gasket

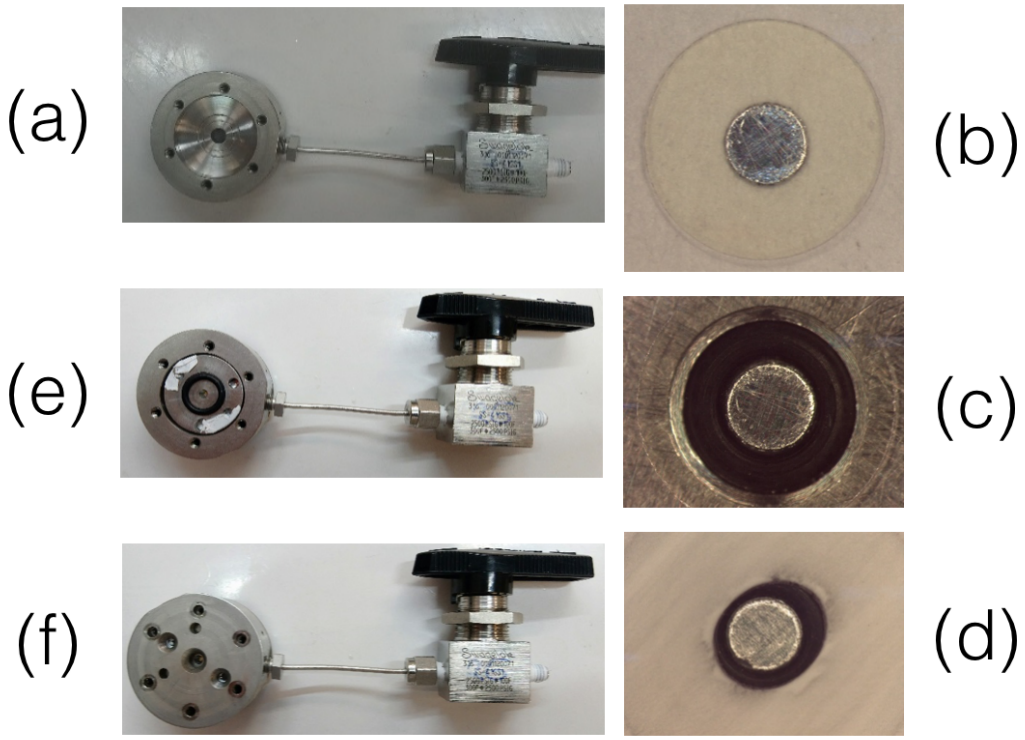

Figure 5.4 – Photos of the different phases of the mounting procedure of the LACs. **(a).** The central body connected to the valve by a capillary. **(b).** The ablator / pusher combination glued to the quartz window. **(c).** The EPDM rubber gasket placed in its seat in the inner side of the drive-laser-side washer. **(d).** The teflon tape is placed on the quartz window to keep it in place. **(e).** The drive-laser-side washer has been positioned on the central body and the EPDM gasket has been put on the external side of the washer. **(f).** The drive-laser-side plug has been placed and screwed to the central body and the corresponding washer. Photos are courtesy of F. Lefevre (LULI).

in EPDM (ethylene propylene diene monomer) rubber is then placed in its seat around the corresponding hole in the inner side of the drive-laser-side washer [Figure 5.4 (c)]. The quartz window, glued to the ablator / pusher combination, is positioned on the washer and let adhere to the gasket. A teflon tape, in which a hole has been pierced around the center, is placed to the quartz window and let adhere to the washer with some drops of alcohol [Figure 5.4 (d)]. Its function is to keep the quartz window in position without the use of any glue (which would be aggressed by liquid ammonia and hence contaminate the sample) when the filling system is vacuumed. The same procedure is applied to the diagnostics-side washer. On each side of the central body, an EPDM rubber gasket is put in its seat around the central cylindrical duct and the corresponding washer (drive-laser-side or diagnostics-side) is placed. At this point, an EPDM rubber gasket is put in its seat in the outer side of each washer [Figure 5.4 (e)] and the corresponding plug is placed on the washer and screwed directly to the central body via six screws. Two supplementary screws connect each plug to the corresponding washer [Figure 5.4 (f)]. After the mounting, the valve–cell system is filled with 6 bar of gaseous nitrogen to test its airtightness and keep the windows in place. The valve is closed and the system is brought to the filling station.

5.2.2 Filling procedure of the cryo-cells

LACs were filled with liquid ammonia according to the following procedure. First, the cell was connected to the hydraulic system. The whole system was tested at 30 bar with gaseous nitrogen for possible leakages. Once tested, it was filled with gaseous ammonia at room temperature from a reservoir. The final part of the system, including the cell, then cooled down to $-30°$ to allow the condensation of ammonia. This part was then isolated from the rest of the circuit by closing a valve and the temperature was slowly increased up to the room value. Liquid ammonia was therefore trapped into the last part of the circuit. To avoid the pressure to increase above the break limit of the cell windows, we kept it at around 15 bar by controlling with a valve the release of a fraction of the liquid volume inside the final part of the system. At the end of the process, liquid ammonia was obtained at $P_0^{\mathrm{NH_3}} = 15$ bar at ambient temperature. The cell–capillary system was finally isolated from the rest of the circuit, with the closure of a valve next to the capillary, and disassembled. A scheme of the thermodynamic path undertaken by ammonia inside the circuit in the course of the filling procedure is provided in Figure 5.5.

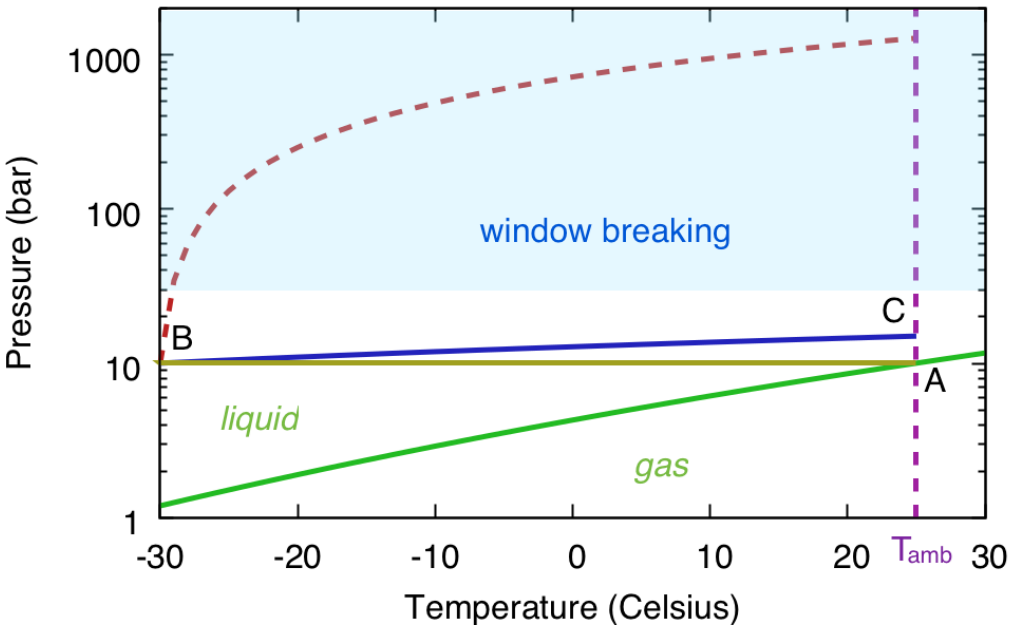

Figure 5.5 – Thermodynamic path, in the temperature-pressure plane, undertaken by ammonia inside the hydraulic system. The green solid line is the boundary layer between the gas and liquid phase. The solid lion line indicates the isobaric path from state A (ambient temperature, solid-gas equilibrium pressure) to state B (cryostat-controlled temperature). The red dashed line indicates the isochore path from state B. The blue solid line is the controlled path undertaken by ammonia when the amount of trapped liquid is controlled by the valves. State C is the final state (ambient temperature, pressure of around 15 bar). The light blue shaded area indicates pressures above the estimated breaking limit of the cell windows.

Filling system

A scheme of the hydraulic system used to fill the LACs with liquid ammonia is provided in Figure 5.6. The cell is connected to the circuit by the valve V1. The final part of

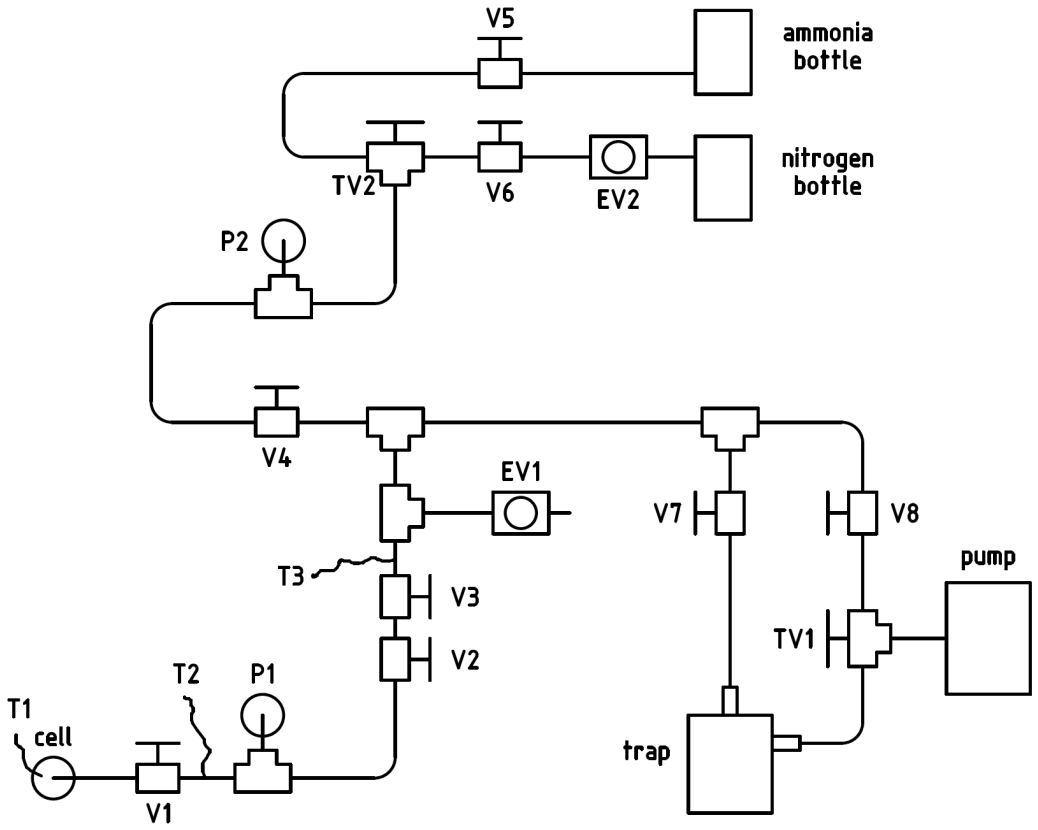

Figure 5.6 – Scheme of the filling system. T: thermocouple; P: manometer; V: standard valve (with open and close modes); EV: expansion valve (with controlled flow); TV: T-valve (with close, open-left, open-right modes).

the circuit consists of a manometer (P1) and a couple of valves (V2 and V3), after which an expansion valve (EV1) is placed. A T-junction then connects the final part of the system to the ammonia and nitrogen reservoirs (top of Figure 5.6) and to the pump-trap system (bottom right of Figure 5.6). The reservoirs are connected to the system via a valve (V5 for ammonia, V6 for nitrogen). Between V6 and the nitrogen bottle, an expansion valve (EV2) is placed to control the nitrogen pressure and allow a gradual increase. The pump is connected to the system via a T-valve (TV1). This allows two functioning modes, (a) and (b). In mode (a), TV1 connects the trap to the pump. This implies that, when the pump is turned on, the flow will pass inside the trap. This operation mode is mandatory when the circuit is filled with gaseous or liquid ammonia, which should not exit through the pump. The trap is a common glass cold trap immersed in a Dewar flask filled with liquid nitrogen. In mode (b), the pump is directly connected to the rest of the circuit. This operation mode is possible when the circuit is filled with air or with gaseous nitrogen, so that there is no need of the trap.

Three thermocouples allow to measure the temperature on the cell (T1), in the last

part of the system, between V1 and P1 (T2), and right above the couple of valves V2 and V3 (T3). Other thermocouples can be momentarily attached to other zones to monitor the temperature uniformity in the system.

The whole circuit is placed inside a laboratory fume hood to avoid intoxication or asphyxiation risks due to ammonia and nitrogen, respectively. Another important risk is the explosion of the cell windows, whose fragment may be directed to the eyes of the user. A security protocol has been put in place, according to which wearing goggles and gloves is mandatory when manipulating the system.

Cooling system

The system employed for cooling the filling circuit in order to condense ammonia has evolved over time. The first method, used during the experimental campaign A, consisted in placing the final portion of the circuit, from the valve V3 to the cell, in a tub filled with ice. Liquid nitrogen was then gradually added to the ice to cool down the thermal bath. The circuit was wrapped in a plastic case to avoid possible damage due to the direct contact with ice and liquid nitrogen. This method had several limits. First, the thermal coupling between the system and the bath was far from being ideal, because of the plastic case and the insulating role of ice with respect to the liquid nitrogen. For this reason, the condensation of ammonia required a huge amount of time (around 45 minutes). Second, the temperature of the bath was not easily controllable. The addition of a little bit of liquid nitrogen could decrease the temperature a lot, and no protocol was in place to reverse the effect. The only solution was to remove the tube from the bath for some minutes. This procedure was risky because it required to break the glass, exposing the circuit and, most importantly, the cell to strong mechanic solicitations.

To solve these issues, the cooling system has been improved after the first experimental run (campaign A). The new version, used in experiment B, makes use of copper capillaries coiled around the tube, in which liquid nitrogen is let flow. This method avoids the use of ice, significantly increases the thermal coupling (thus reducing the waiting time for the ammonia condensation), and allows a better control on the temperature.

Two copper capillaries are coiled around the final part of the filling system, one starting from the lower part (around V1), the other starting from the higher part (around V3). The coils are shown in Figure 5.7 (top). The use of two coils going to opposite directions allows to obtain a more uniform temperature in the whole part of the circuit. Each capillary is then connected to a T-junction together with a long plastic tube plugged onto a vacuum pump. The plastic tube is long enough (some meters) to let liquid nitrogen become gaseous while it propagates inside it, to avoid damages to the pump. An expansion valve is placed before the pump to control the flow. The free end of both capillaries is placed in a beaker filled with liquid nitrogen. A thermally insulating sleeve is wrapped around the portion of the filling circuit coiled with the capillaries. The setup at work is shown in Figure 5.7 (bottom). The flow is controlled with the expansion valve to obtain a uniform temperature in the whole part of the circuit.

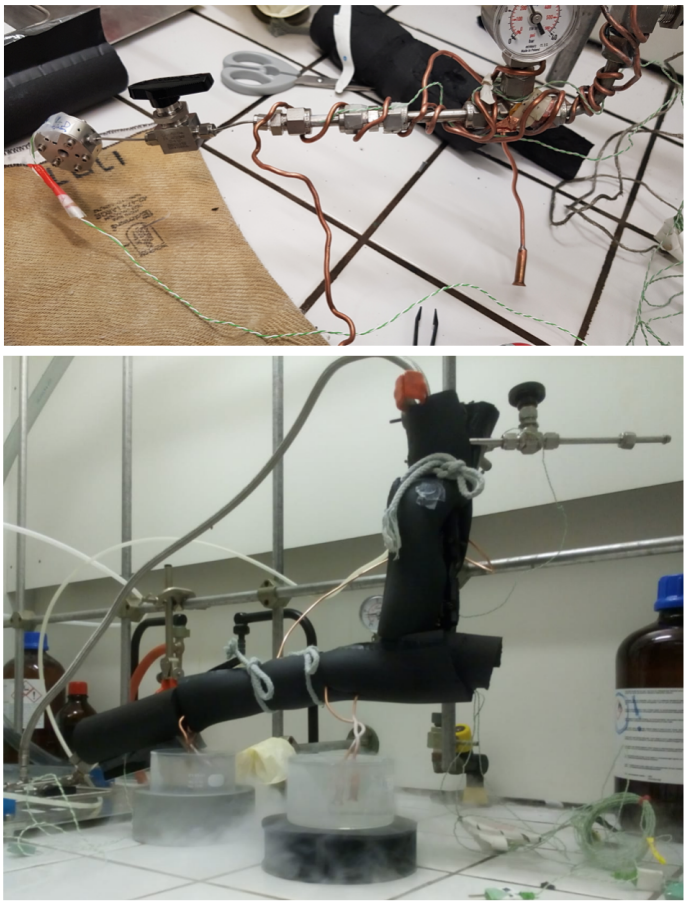

Figure 5.7 – Cooling system of the last part of the filling circuit used in experiment B. **Top.** Two copper capillaries are coiled around the final portion of the system. The white-green wires are the thermocouples permitting the measurement of the temperature in different portions of the system during the filling procedure. **Bottom.** The final portion of the system is thermally isolated by a sleeve wrapped around it and secured. The free ends of the two copper capillaries are immersed in a beaker filled with liquid nitrogen.

5.2.3 Simulations

Hydrodynamic simulations with MULTI (see Chapter 2.6.1) have been performed to choose the ablator / pusher combination and the drive laser pulse profile in order to avoid re-shocks in the ammonia sample. Figure 5.8 shows pressure (in colour bar) as a function of the initial position (*i.e* the Lagrangian coordinate) and time for a simulation of a high-intensity shot on the target including the gold layer. The thin pre-heating gold layer causes multiple shock reverberations. With the help of simulations, we chose a pusher design optimised in such a way that reverberations catch up in the quartz layer, and a single shock wave is transmitted to the ammonia sample.

5.2.4 Experimental setup

Drive laser pulses delivering $100 - 800$ J at the wavelength of 527 nm have provided by the two chains (North and South) of the LULI2000 facility, in two distinct experimental campaigns (A and B). The pulses were constant in intensity for a duration of 1.5, 2.5,

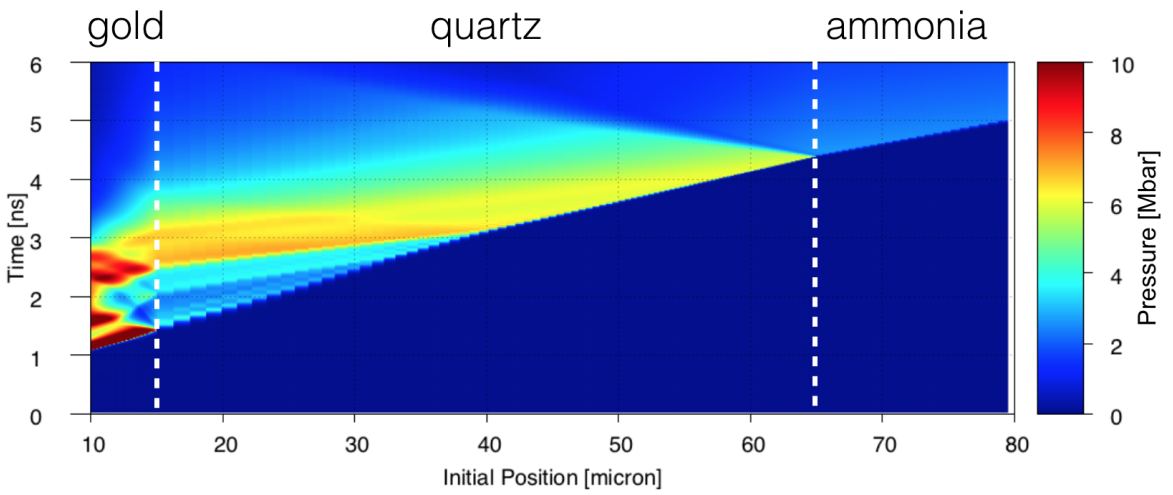

Figure 5.8 – Pressure (colour bar) as a function of the Lagrangian coordinate and time according to a MULTI hydrodynamic simulation of a shot on a target composed by 10 μm of CH, 5 μm of Au, 50 μm of α-quartz, and the ammonia sample. The drive laser pulse was 1.5 ns long. An initial loading pressure of 2.7 Mbar has been obtained in ammonia.

4, 5, or 10 ns. Phase plates guaranteed a uniform irradiation on the target on a focal spot of 500 μm.

The experimental setup was the same as the one presented in Chapter 4.2. Different spectral ranges have been employed for the SOP during experiment A: 420 ± 5 nm, 430 ± 30, 450 ± 20 nm. The spectral width of the filter was a key factor in determining the sensitivity of the SOP (see Chapter 2.5.2). For experiment B, since colder states were probed, several combinations of filters have been employed corresponding to wider spectral windows in the $300 - 500$ nm which guaranteed guaranteeing a higher SOP sensitivity. The time windows of VISARs, SOP, and reflectometer streak cameras were fixed to 20 ns in both experimental campaigns, in order to follow the propagation of the shock inside the ammonia sample during a substantial amount of time without losing too much resolution in time (as would have happened if windows of 50 ns had been chosen).

5.2.5 Results and discussion

Diagnostics output

Figure 5.9 shows a typical output image of a VISAR and the SOP, as well as the time-resolved shock velocity (from both VISARs), reflectivity (collected by both VISARs and the independent reflectivity measure streak) and self-emission (from the SOP). In the α-quartz window, the shock is almost steady, as it is evident from the time profile of the shock velocity, reflectivities, and self-emission. As a consequence, the state reached in shocked quartz can be precisely determined, which is crucial for a precise measurement of the state reached in the ammonia sample via impedance mismatch. In ammonia, the shock decays in time: the shock velocity drops to 14 km/s from the initial value of 22 km/s. The reflectivities and self-emission decay accordingly. This means that a whole portion of the $T(P)$ and $R(P)$ curves can be explored within a

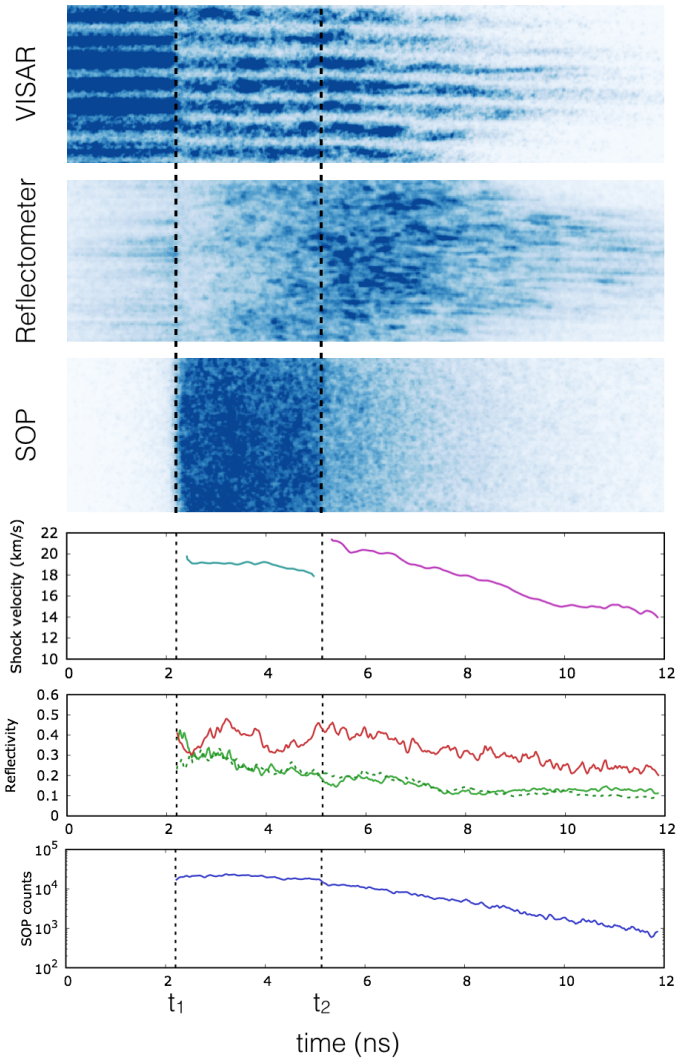

Figure 5.9 – Diagnostics outputs for shot A-107. From top to bottom: output images of VISAR at 1064 nm, reflectometer at 532 nm, and SOP; time-resolved shock velocity (in α-quartz, dark cyan line, and in ammonia, strong magenta line), shock-front reflectivity (from the VISAR at 1064 nm, solid red line, the VISAR at 532 nm, solid green line, and the reflectometer at 532 nm, dashed green line), and SOP counts. $t = 0$ is the beginning of the drive laser pulse. t_1 and t_2 are the shock arrival times in α-quartz and ammonia, respectively.

single shot.

Shock and fluid velocity

The shock and fluid velocities in ammonia are provided in Table 5.1. Velocity data are also shown in Figure 5.10, where they are compared to previous experimental data and simulation results corresponding to a different initial state ($\rho_0 = 0.69$ g/cm^3, $T_0 = 230$ K).

In order to better characterise the behaviour highlighted by previous experimental data, we performed a linear fit on the data from Kovel (1973), in the form

$$U_s = S' U_p + c'_s. \tag{5.1}$$

Table 5.1 – Shock velocity data for the shots including a quartz standard (all but B-66). Target types correspond to the following ablator / pusher combinations: (a) 10 CH / 40 Al / 52 SiO_2; (b) 10 CH / 40 Al / 112 SiO_2; (c) 10 CH / 5 Au / 112 SiO_2; (d) 10 CH / 5 Au / 52 SiO_2.

Shot #	Target type	U_s (Qz)	U_s (NH_3)	U_p (NH_3)
A-89	(a)	18.93 ± 0.72	21.58 ± 0.81	15.7 ± 1.0
A-107	(a)	18.23 ± 0.72	21.20 ± 0.84	14.88 ± 0.93
A-124	(b)	19.45 ± 0.74	21.97 ± 0.83	16.27 ± 0.71
A-125	(a)	10.66 ± 0.75	11.76 ± 0.82	7.66 ± 0.86
A-126	(a)	19.76 ± 0.73	21.97 ± 0.81	16.66 ± 0.95
A-127	(a)	12.81 ± 0.93	14.19 ± 0.81	9.6 ± 1.1
B-2	(a)	18.32 ± 0.58	21.25 ± 0.66	14.99 ± 0.68
B-3	(a)	16.44 ± 0.58	18.57 ± 0.65	13.10 ± 0.55
B-8	(a)	12.75 ± 0.58	14.30 ± 0.66	9.54 ± 0.65
B-10	(a)	14.98 ± 0.58	16.18 ± 0.65	11.72 ± 0.71
B-13	(a)	9.81 ± 0.65	11.60 ± 0.65	6.79 ± 0.86
B-16	(a)	9.94 ± 0.59	12.02 ± 0.65	6.88 ± 0.64
B-24	(a)	8.84 ± 0.61	9.57 ± 0.67	6.03 ± 0.54
B-38	(c)	22.42 ± 0.59	24.69 ± 0.65	19.70 ± 0.78
B-43	(c)	22.23 ± 0.64	23.96 ± 0.65	19.54 ± 0.89
B-48	(d)	19.87 ± 0.63	21.29 ± 0.67	16.89 ± 0.87
B-57	(d)	22.11 ± 0.61	24.89 ± 0.67	19.26 ± 0.71

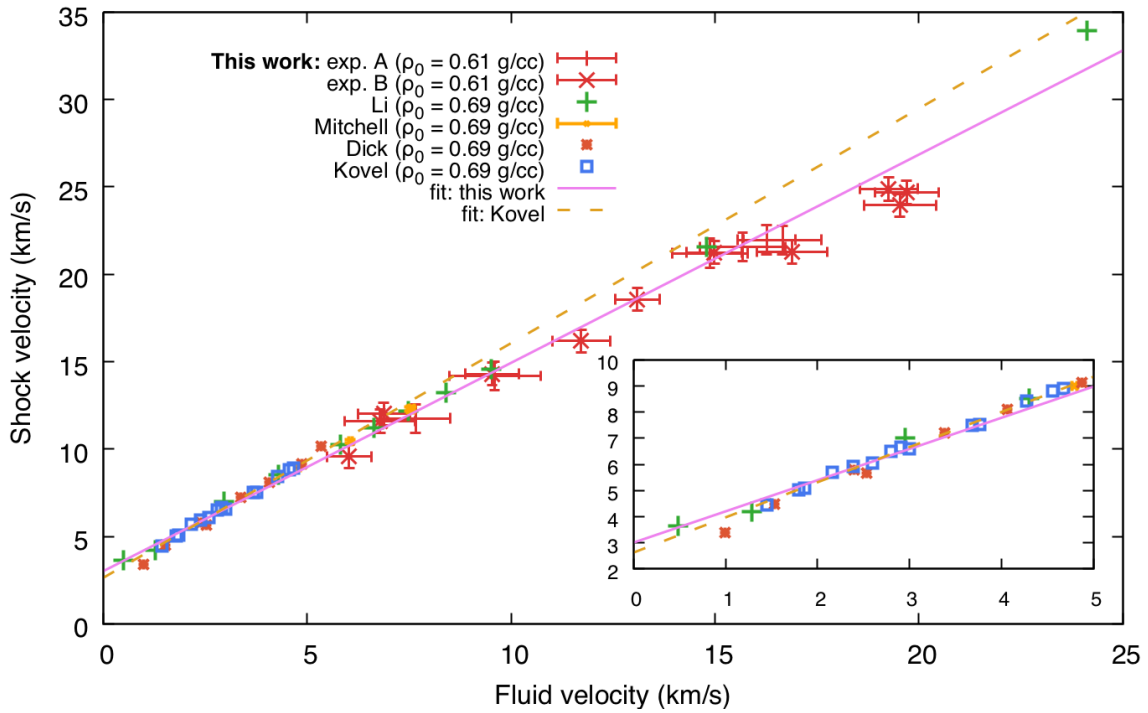

Figure 5.10 – Shock – fluid velocity relation for shocked liquid ammonia. Data from this work are in red. Previous experimental data [Kovel (1973); Dick (1981); Mitchell and Nellis (1982)] and *ab initio* calculations [Li et al. (2013)] for the Hugoniot starting from 0.69 g/cm^3 and 230 K are also shown for comparison. A linear $U_s - U_p$ fit has been performed on data from Kovel (1973) (dashed line) and on the data of this work up to a fluid velocity of 15 km/s (solid line). The inset on the bottom right highlights low-pressure results.

A linear function has been chosen since linear $U_s - U_p$ relations are very common in high-pressure materials [Zel'dovich and Raizer (1966)], in the absence of first-order phase transitions. The parameter S' gives the compression limit $\rho/\rho_0 = S'/(S'-1)$ if the linear fit is extrapolated to $P \to +\infty$ (see equation 2.23), whereas c'_s can be interpreted as the sound velocity at the initial conditions if the linear fit is extrapolated to $U_p = 0$. The best parameters are $S' = 1.343 \pm 0.026$ and $c'_s = (2.631 \pm 0.082)$ km/s. This linear fit predicts higher shock velocities at high pressures compared to the calculations by Li et al. (2013) – the latter suggest that the compressibility of warm dense ammonia increases with pressure.

Our data set is compatible within error bars to all previous experimental data, which span fluid velocities up to 8 km/s. At higher fluid velocities, we can only compare our data to two points obtained with *ab initio* calculations by Li et al. (2013), at $U_p = 10$ km/s and 15 km/s (green crosses in Figure 5.10). Both data points by Li et al. (2013) are in remarkably good agreement with our data, despite the different initial density. Up to a material velocity around 15 km/s, our $U_s - U_p$ data exhibit a linear trend. With the aim of comparing them to the data in the literature, we performed a linear fit on our data, with the form $U_s = SU_p + c_s$. The best fit gives $S = 1.192 \pm 0.052$ and $c_s = 3.01 \pm 0.58$ km/s. Only the data points with a material velocity lower than 15 km/s have been fitted: indeed, at higher material velocities our data move away from the linear trend and exhibit lower shock velocities than those predicted by the fit.

The sound velocity obtained with our fit is higher than that from the fit on higher initial density data, whereas the contrary should be true [the speed of sound has a positive dependence on density according to Li et al. (2009)]. However, the two speeds of sound are compatible within error bars. It is also to be noticed that an extrapolation to higher pressures of the fit on Kovel (1973) would give a quite low compressibility limit. However, simulations by Li et al. (2013) starting from the same density report lower shock velocities, even compatible with our data for fluid velocities around 15 km/s, meaning that the true compressibility limit is higher than that given by a simple linear fit.

Pressure and density

The pressure and density data of this work, obtained from the $U_s - U_p$ data with the procedure already detailed in Chapter 4.3.3, are provided in Table 5.2 and shown in Figure 5.11. Our low-pressure data ($P < 1$ Mbar) are in agreement with previous experimental results and *ab initio* calculations, which are also shown for comparison. The Hugoniot curve explored in our study exhibit higher pressures at the same density, since our initial density was lower: 0.61 g/cm^3 against 0.69 g/cm^3. However, due to the non-linear form of the Rankine–Hugoniot relations (see Chapter 2.3.3), our error bars on density are too high for this behaviour to be clearly highlighted by the data. At intermediate pressures ($1 - 2$ Mbar), there are no previous experimental works to compare with our data but two calculated points by Li et al. (2013). We explored five states in this range, all compatible within error bars with the curve interpolating the two calculated points. Our data tend to lie on the left side of that curve, compatible with the fact that our initial density was lower. At high pressures above 2 Mbar, our densities, although affected by large error bars and thus almost always compatible with the simulations by Li et al. (2013), are substantially higher, spanning from $2.3 - 3.3$

Table 5.2 – Equation of state data for shocked ammonia. Temperatures for shot B-38, B-43, and B-57 are not available because the SOP image was saturated. The low-intensity shot B-66 is not shown here, for it has been analysed using a different approach.

Shot #	Density (g/cm^3)	Pressure (Mbar)	Energy density incr. (kJ/g)	Temperature (kK)
A-89	2.20 ± 0.53	2.05 ± 0.16	121 ± 17	24.4 ± 5.4
A-107	2.01 ± 0.77	1.91 ± 0.13	109 ± 14	20.9 ± 4.8
A-124	2.32 ± 0.39	2.17 ± 0.12	131 ± 11	25.5 ± 5.6
A-125	1.75 ± 0.85	0.55 ± 0.06	29.4 ± 6.5	4.3 ± 2.5
A-126	2.49 ± 0.74	2.22 ± 0.16	138 ± 16	24.4 ± 5.4
A-127	1.80 ± 0.52	0.81 ± 0.09	44 ± 9	7.7 ± 2.8
B-2	2.04 ± 0.30	1.93 ± 0.10	111 ± 10	22.0 ± 5.0
B-3	2.02 ± 0.29	1.47 ± 0.07	84 ± 7	14.2 ± 3.7
B-8	1.76 ± 0.40	0.81 ± 0.06	44 ± 6	7.5 ± 2.8
B-10	2.13 ± 0.50	1.14 ± 0.09	67 ± 8	11.5 ± 3.3
B-13	1.47 ± 0.47	0.48 ± 0.06	23.0 ± 6.1	4.5 ± 2.5
B-16	1.43 ± 0.27	0.50 ± 0.05	23.6 ± 4.4	4.8 ± 2.5
B-24	1.65 ± 0.45	0.35 ± 0.04	18.2 ± 3.3	n.a.
B-38	2.98 ± 0.60	2.96 ± 0.13	193 ± 15	n.a.
B-43	3.26 ± 0.97	2.85 ± 0.16	190 ± 17	39.5 ± 8.2
B-48	2.9 ± 1.1	2.19 ± 0.11	142 ± 15	22.4 ± 5.0
B-57	2.67 ± 0.75	2.91 ± 0.13	184 ± 14	n.a.

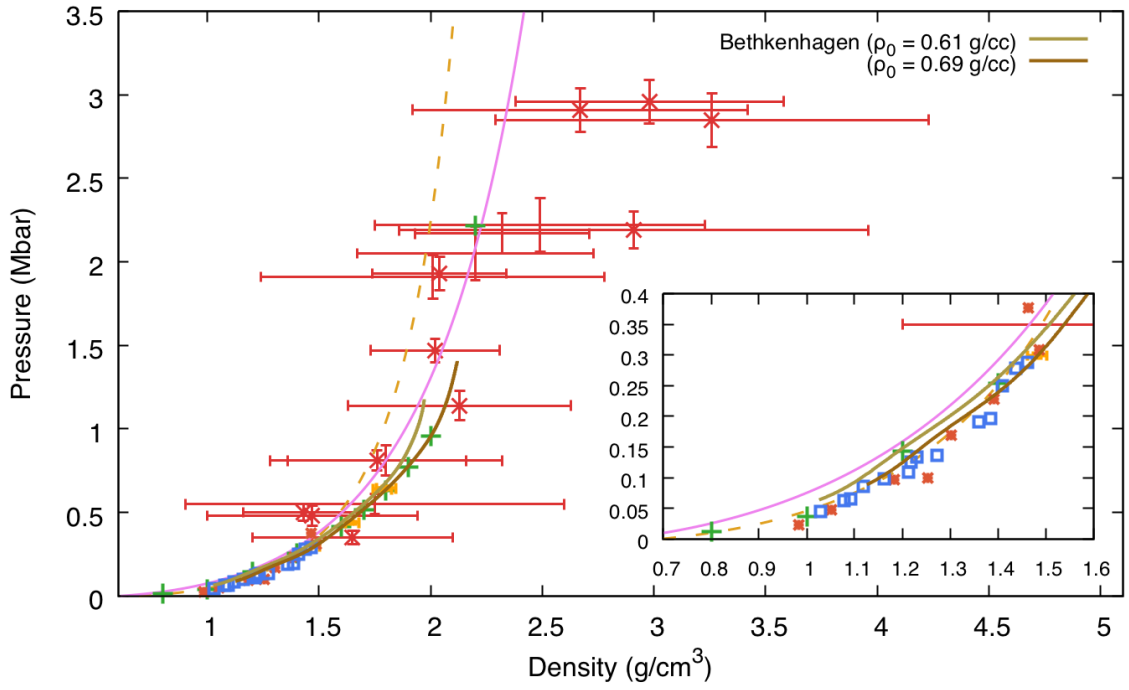

Figure 5.11 – Pressure – density relation for shocked liquid ammonia. Legend as in Figure 5.10. Two Hugoniot curves, starting from 0.61 and 0.69 g/cm^3, extracted from the *ab initio* calculations of the equation of state of ammonia by Bethkenhagen et al. (2013) are also shown. The inset on the bottom right highlights low-compression data.

g/cm^3 against predicted values around 2.2 – 2.3 g/cm^3. Moreover, the slope of the pressure – density curve probed in our work increases quite abruptly. Such a discontinuity in the slope is not explained by any phase transition: at such high temperatures,

ammonia is already expected to be dissociated. As we will discuss later, this point must be clarified in future experimental work.

Temperature

Temperature of shocked ammonia as a function of pressure is shown in Figure 5.12. For each shot, we show both a single temperature – pressure point where pressure is obtained with impedance mismatch at the interface with α-quartz, and a series of points, from the decaying-shock data. Temperature has been measured using the time-resolved SOP signal. Pressure has been extracted from the time-resolved shock velocity measurement with the procedure already described in Chapter 4.3.3.

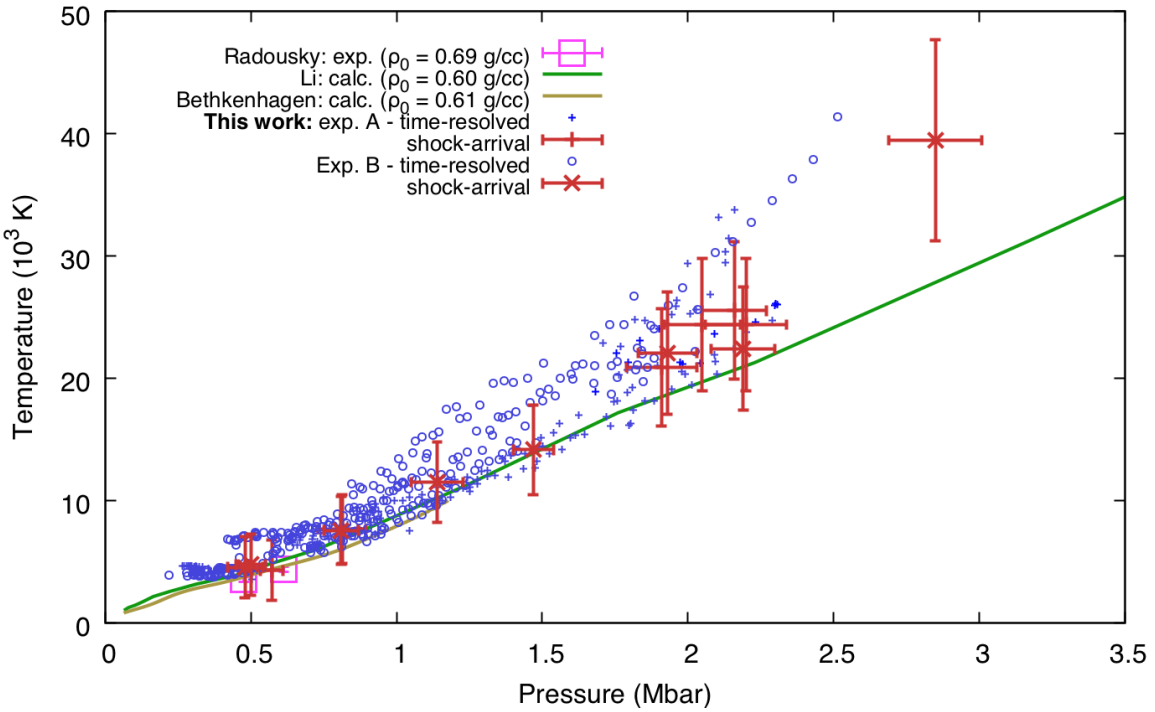

Figure 5.12 – Temperature – pressure relation in shocked liquid ammonia. Shock-arrival data from this work are in red Time-resolved data are in blue. Previous experimental data from Radousky et al. (1990) (starting from 0.69 g/cm^3 and 230 K) and calculations from Li et al. (2013) and Bethkenhagen et al. (2013) are also shown.

The data of this work are compatible within error bars with previous DFT-MD simulations by Li et al. (2013) at a similar initial density of 0.60 g/cm^3 and with those by Bethkenhagen et al. (2013) at the same initial density of 0.61 g/cm^3 (limited to 1.2 Mbar). At pressures around 2 Mbar, we measured generally higher, but still compatible, temperatures than those expected by simulations. Only our highest-intensity shot does not agree with the simulation, but exhibits a much higher temperature.

Figure 5.12 also shows the only previous experimental results by Radousky et al. (1990), corresponding to an initial density of 0.69 g/cm^3. The two data points at $0.4 - 0.6$ Mbar are compatible with our data but shifted downwards, as expected starting from a denser state (see Chapter 3.1.2).

EOS: comparison with ad hoc ab initio simulations

The $\rho - P - T - e$ equation of state of warm dense ammonia has been calculated by Mandy Bethkenhagen *(University of Rostock)* up to 40 kK and 15 Mbar via DFT-MD simulations. These calculations considerably extend the conditions explored in a previous work [Bethkenhagen et al. (2013)], which were limited to 10 kK and 3 Mbar. The methods employed have already been presented in the previous work, including the correction taken into account for quantum effects of the ionic motion. The Hugoniot curve starting from the initial conditions of our experiments (0.61 g/cm^3 and 300 K) has been extracted from the computed EOS table using the Rankine–Hugoniot relations (equations 2.23–2.25) to be compared with our experimental data.

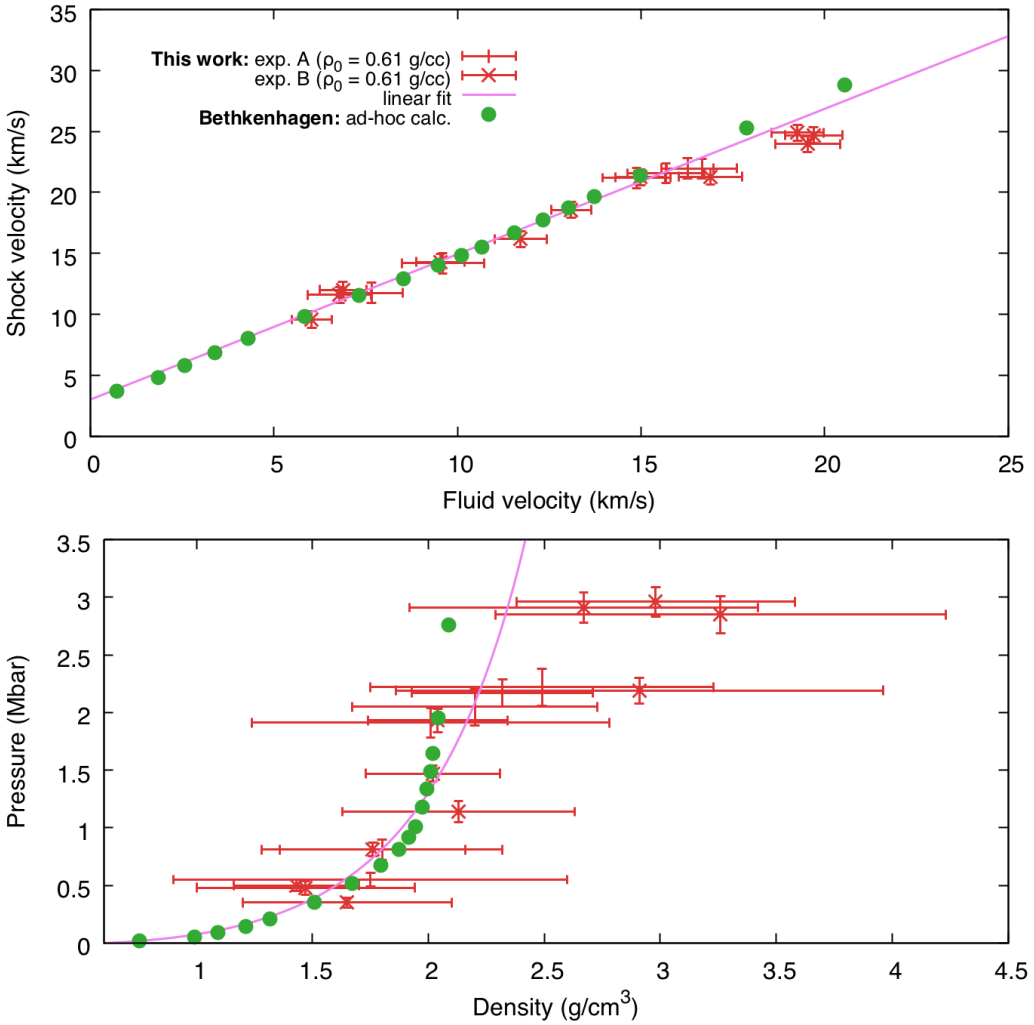

Figure 5.13 – Comparison between experimental data of this work and calculations by Mandy Bethkenhagen along the Hugoniot of ammonia starting from 0.61 g/cm^3 and 300 K. **(a).** Shock – material velocity relation. **(b).** Pressure – density relation.

In Figure 5.13 (a) and (b) we show the calculated Hugoniot curve in the shock – material velocity and in the pressure – density plane, respectively, compared with our results. The comparison between our experimental data and the simulation results is easier in the $U_s - U_p$ than in the $P - \rho$ plane, as our error bars on density are very

important due to the non-linearity of the Rankine–Hugoniot relations. At low and intermediate material velocities ($6 - 15$ km/s), we observe a remarkable agreement between simulations and experiments. All the calculated points fall along, or very close to, the linear fit on our experimental data. At very low material velocities, below 6 km/s, below our data sets, the calculated points follow the extrapolation of our linear fit. On the contrary, at high fluid velocities, above 15 km/s, our data are not compatible with the simulations and do not follow the linear behaviour of the rest of our data set, exhibiting lower shock velocities than the values predicted by both the simulations and our linear fit. This behaviour is reproduced in the pressure – density plane [Figure 5.13 (b)], where, for pressures higher than 2 Mbar, our data set starts to derive towards higher densities than the ones predicted by the simulations. Out of seven shots in which a pressure higher than 2 Mbar was reached, all exhibit a higher density than the simulations; five are compatible within error bars, whereas two are clearly incompatible. Our high-pressure data do not follow the trend of the rest of the data set. This can be unlikely linked to a phase transition, as no transitions are predicted by simulations in this high-temperature regime. Moreover, no discontinuities are visible in the $T(U_s)$ curves. The reason must thus be found elsewhere: it can be linked to a systematic issue in the experimental procedure (including the eventuality of the contamination of the ammonia sample) and must be checked in future experimental work.

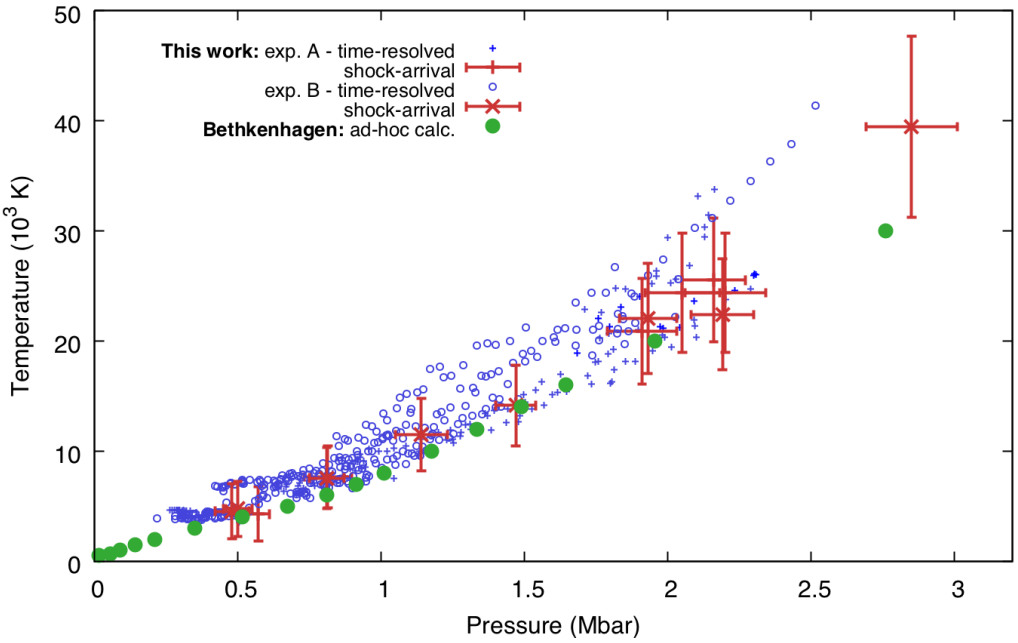

Figure 5.14 – Comparison between experimental data of this work and calculations by Mandy Bethkenhagen along the Hugoniot of ammonia starting from 0.61 g/cm^3 and 300 K in the temperature – pressure plane.

In Figure 5.14, we compare our experimental data with the results of the simulations in the temperature – pressure plane. Up to a pressure of 2 Mbar, our results are well in agreement with the simulations. In particular, our shock-arrival data are almost superimposed to the simulations; our time-resolved data are slightly higher than the simulations, but still compatible within error bars. For pressures above 2 Mbar, we only

dispose of a single datum from the simulations, at 2.76 Mbar. Our shock-arrival data between $2-2.3$ Mbar are compatible with a linear interpolation of the two highest data points of the simulations. Our highest-pressure datum, at 2.85 ± 0.16 Mbar, exhibits a much higher temperature than the simulation point at 2.8 Mbar [$(39.5 \pm 8.2) \cdot 10^3$ K against $30 \cdot 10^3$ K]. To solve this question, more high-intensity shots on ammonia samples are needed. An experiment is already scheduled for December 2019.

Optical properties

The optical properties of shocked ammonia were inferred from the VISAR and reflectometer output images.

Liquid ammonia is transparent at ambient temperature. When loaded by a shock wave, its optical properties change: the real part of the refractive index increases due to compression, whereas the imaginary part of the index eventually becomes non-negligible, as a function of the shock strength, due to shock-induced dissociation and ionisation processes. As we have seen in Chapter 2.5.1, after the shock loading of a transparent ammonia sample there are three possibilities concerning its optical properties:

(i) ammonia stays transparent, since the shock is weak and does not considerably dissociate and ionise it, and the probe laser can propagate into the shocked sample;

(ii) ammonia becomes opaque due to the increase of the imaginary part of the refractive index, and the probe laser is absorbed;

(iii) the shock front becomes considerably reflecting due to the strong increase of the real and imaginary parts of the refractive index (Fresnel's law).

If the target structure is such that a reflecting layer is placed immediately before the ammonia sample, then in case (i) the probe laser will be reflected by such layer. If, on the contrary, a quartz standard is placed between the reflecting layer and the ammonia sample, then in case (i) the probe laser will not be necessarily reflected by the metallic layer, depending on the optical properties of shocked quartz. Indeed, if shocked quartz becomes opaque, even if shocked ammonia remains transparent the probe laser will be absorbed inside the quartz layer and no signal will be visible on the VISAR image.

In the target of shot B-66, the ammonia sample was placed immediately next to a reflecting layer. As detailed in Section 5.2.1, the target was structured as follows:

$$\text{polystyrene / aluminum / } \alpha\text{-quartz / gold / ammonia,}$$

so that the probe laser could be reflected by the gold layer after propagating into the transparent ammonia sample. We used a long (10 ns) and relatively weak (87 J) drive laser pulse to generate a weak shock wave with the aim of studying the low-pressure optical behaviour of ammonia. The VISAR signal at 532 nm is provided in Figure 5.15 (a). After the shock enters in the ammonia sample, the intensity of the fringe system roughly remains the same, which indicates that the probe laser is still reflected by the gold layer: shocked ammonia exhibits a transparent state.

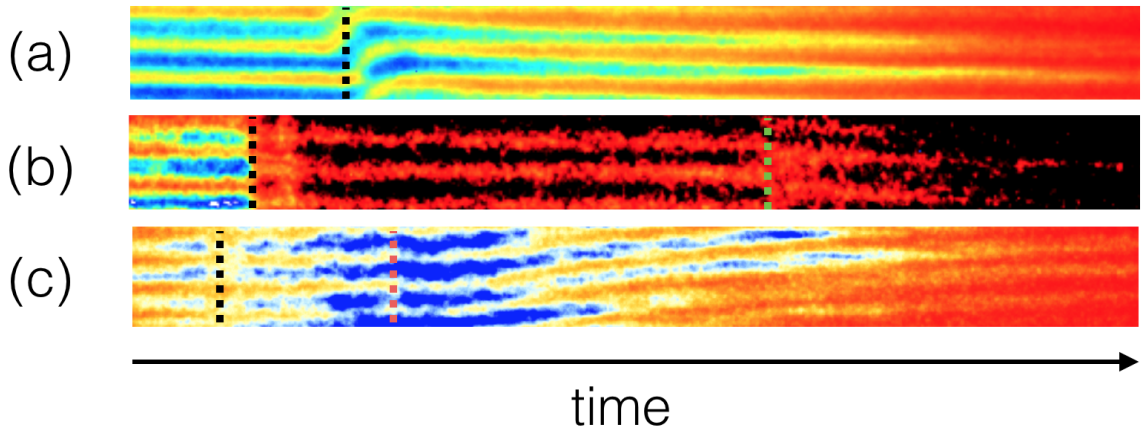

Figure 5.15 – Optical properties of shocked ammonia: output of the VISAR at 532 nm for shot B-66 **(a)**, B-24 **(b)**, and A-126 **(c)**, showing different regimes. The target of shot B-66 has no quartz standard layer. Shocked ammonia exhibits a transparent state. Shot B-24 exhibits a very low shock-front reflectivity in both the α-quartz standard and the ammonia sample. In shot A-126, the shock-front reflectivity is high in both quartz and ammonia. The dashed vertical lines correspond to the instants when the shock front enters quartz (only in shots B-24 and A-126) and ammonia.

To estimate the pressure reached in shocked ammonia, we first measured the apparent gold / ammonia interface velocity from the VISAR images: $U_{\text{app}} = 5.0 \pm 0.3$ km/s. The real interface velocity (and thus the ammonia fluid velocity) could not be determined using a refractive index correction (see Chapter 2.5.1), since the refractive index behaviour along the Hugoniot curve is not known, whereas the only study about the refractive index of compressed liquid ammonia, by Li et al. (2009), uses static compression up to less than 2 GPa along an isotherm. In the absence of a refractive index measurement, a simplistic possibility consists in supposing that the index follows the Gladstone–Dale relation:

$$n(\rho) = 1 + (n_0 - 1)\frac{\rho}{\rho_0}. \tag{5.2}$$

In this case, $U_p = U_{\text{app}}$ and the pressure, according to our $U_s - U_p$ fit, is around 0.27 Mbar. Another possible approach makes use of the scaling law between ablation pressure and drive laser intensity (equation 2.37). Supposing that the loading pressure in ammonia is proportional to the ablation pressure, the ammonia pressure in shot B-66 is

$$P_{\text{B-66}} = P_{\text{B-24}} \cdot \left(\frac{I_{\text{B-66}}}{I_{\text{B-24}}}\right)^{2/3} \simeq 0.23 \text{ Mbar}. \tag{5.3}$$

We will therefore assume that the loading pressure of ammonia in shot B-66 is 0.25 ± 0.04 Mbar, by taking the mean of the two results and, very conservatively, the double of their difference as error bar.

The other shots we performed in our experimental campaigns were on targets with the following structure:

polystyrene / aluminum / α-quartz / ammonia.

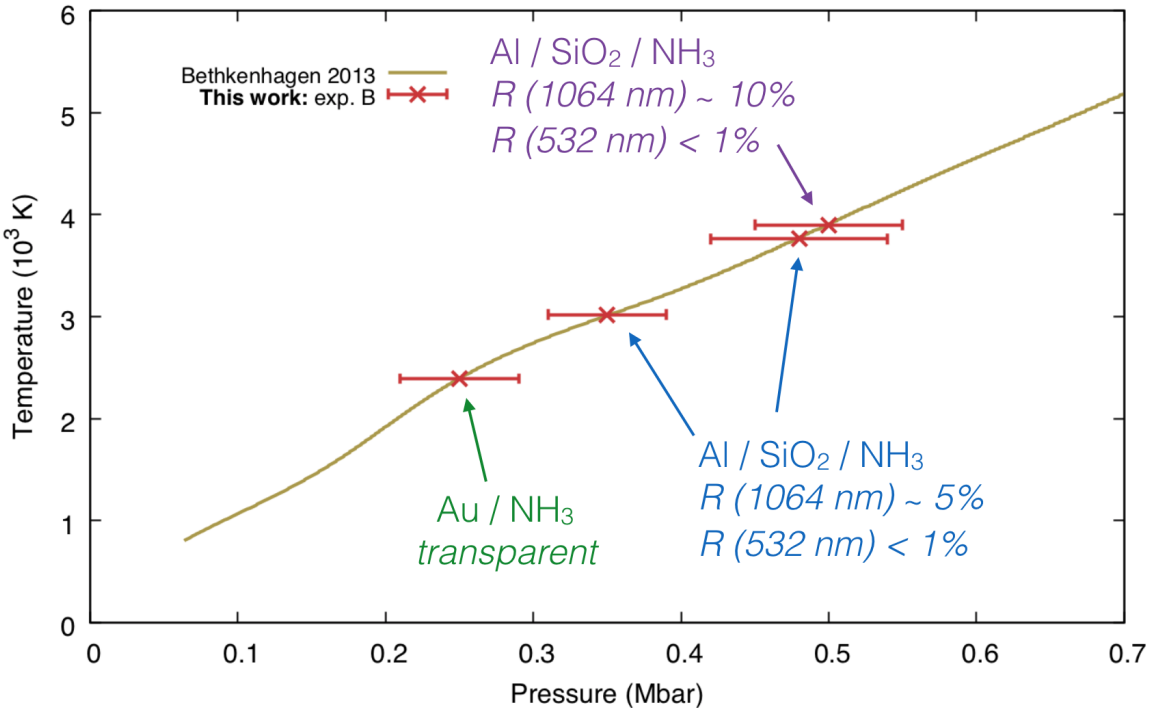

Figure 5.16 – Thermodynamic conditions reached in the low-energy shots on liquid ammonia using the temperature – pressure curve calculated by Bethkenhagen et al. (2013). For each shot, the target structure (Au / NH_3 or Al / SiO_2 / NH_3) and the observed optical properties (transparent or reflecting) are specified.

Ammonia always exhibited a reflecting state. We could thus extract the shock-front reflectivity at 532 nm (from both the corresponding VISAR and the independent reflectometer) and 1064 nm (only from the corresponding VISAR), in both α-quartz and ammonia. An example of VISAR output image for a low-reflectivity (B-24) and high-reflectivity (A-126) shot are provided in Figure 5.15 (b) and (c), respectively. Moreover, the low-pressure data relative to the target type including a quartz standard (shots B-24, B-13, B-16) are shown in Figure 5.16. They all highlight a very low reflectivity at 532 nm (around 1%) and a higher value at 1064 nm (5% to 10%). Figure 5.16 shows that shocked liquid ammonia remains transparent at least up to 0.25 Mbar along the Hugoniot. More experimental work is needed to characterise the low-pressure optical properties of shocked ammonia and probe the upper limit of the transparency range, which is crucial to employ a double-shock compression technique (see Chapter 3.3).

Since, for every shot except shot B-66, we could measure both the time-resolved reflectivity and shock velocity, the dependence of the ammonia reflectivity on shock velocity could be determined, as done in Chapter 4.3.4. Such dependence is shown in Figure 5.17. As we have already done for the $T - P$ data, we converted the time-resolved shock velocity to shock-compressed pressure using the $U_s - U_p$ fit on our data and the Rayleigh equation ($P = \rho_0 U_s U_p$) to provide the dependence on pressure of reflectivity, which is shown in Figure 5.18.

Our data, available from a pressure of 0.2 Mbar, display a smooth transition from a low-reflectivity to a high-reflectivity behaviour. This transition starts at about 0.5 Mbar and is essentially complete at 1.2 Mbar. At higher pressures, reflectivity is almost

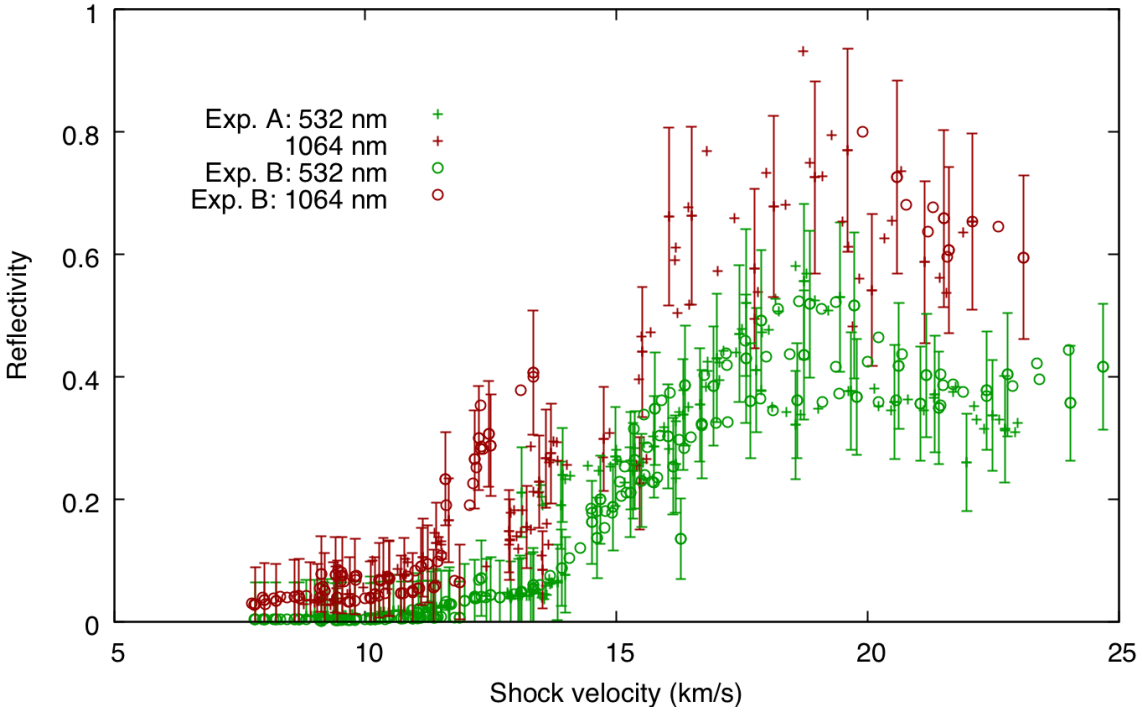

Figure 5.17 – Shock-front reflectivity at 532 nm and 1064 nm as a function of shock velocity along the ammonia Hugoniot curve starting from 0.61 g/cm^3 and ambient temperature.

constant, with a slightly decreasing trend. We fitted our data at both wavelengths using a modified Hill function:

$$R(P) = R_0 + (R_{sat} - R_0) \cdot \frac{P^\gamma}{P^\gamma + P_0^\gamma} - \alpha \frac{P^2}{P + P_1}, \tag{5.4}$$

expressing the smooth transition (whose onset and width are given by the fitting parameters P_0 and γ) from an initial value R_0 to a saturation value R_{sat}. The function includes a negative correction which becomes relevant only at pressures higher than, or comparable to, the fitting parameter P_1: this term models the quasi-saturation behaviour.

Our reflectivity data are the first experimental results ever on shocked condensed ammonia. They can only be compared to previous DFT-MD calculations by Li et al. (2013) along the Hugoniot curve starting from a density of 0.6933 g/cm^3 and a temperature of 230 K (see Figure 5.18). Our results at 532 nm are not compatible within errors with the calculations in the low-pressure region: for instance, at 0.5 Mbar we measured $R(532\text{ nm}) = 1.9^{+5.5}_{-1.9}\%$, considerably lower than the value of 21% obtained by Li et al. (2013). However, between $0.5 - 0.8$ Mbar, the slope of our best-fit function at 532 nm, $dR(532\text{ nm}, P)/dP$, is comparable to that predicted by simulations: both are around 0.7 Mbar^{-1}. Then, around 0.8 Mbar, the slope of the calculated reflectivity – pressure curve considerably decreases, whereas our reflectivity function almost linearly increases with pressure up to $1.1 - 1.2$ Mbar. For pressures higher than 1 Mbar, our 532 nm data become compatible within error bars with those calculated by Li et al. (2013). At 2.2 Mbar, in our quasi-saturation regime, we measured $(46 \pm 11)\%$, compatible with the 51% calculated value. The discrepancy between our 532 nm data and

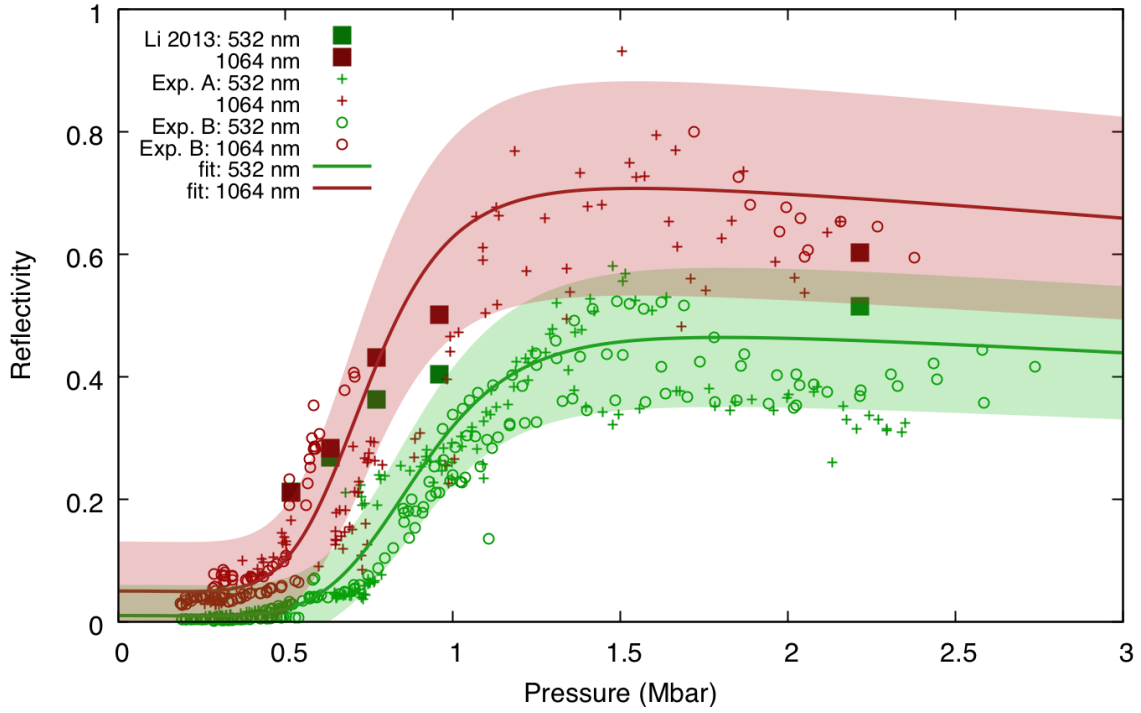

Figure 5.18 – Shock-front reflectivity at 532 nm and 1064 nm in liquid ammonia along the Hugoniot curve. Data from this work start from 0.61 g/cm^3 and ambient temperature. Calculations by Li et al. (2013), which are also shown, start from 0.69 g/cm^3 and 230 K.

the calculations of Li et al. (2013) at low pressures may be explained by a failure of the functional employed in the simulations to reproduce the actual behaviour of ammonia in that regime.

At 1064 nm, our experimental results agree with the calculated data by Li et al. (2013) in the whole pressure range. However, between $0.5 - 1.0$ Mbar we measured a higher slope $dR(1064\text{ nm}, P)/dP$ than the calculations. As a consequence, our reflectivity function $R(1064\text{ nm}, P)$, which was slightly below the calculated value at 0.5 Mbar, overcomes the calculated profile at around 0.8 Mbar. In all the high-pressure, quasi-saturation regime, our data are higher than the calculated ones, though compatible with them within error bars. At 2.2 Mbar, we measured $(69 \pm 17)\%$, compatible within error bars with the calculated value of 60%.

Our results can be interpreted in light of the work by Li et al. (2013) and Li et al. (2017), who identify three regimes along the Hugoniot curve of ammonia (see Section 5.1): molecular (up to 25 GPa), mixture (up to 96 GPa), and plasma (at higher pressures). Our data show that ammonia is likely to maintain a transparent behaviour up to $\sim$ 25 GPa. This is coherent with the predicted low dissociation fraction at this pressure. We then observe a steady increase of the shock-front reflectivity from 50 GPa to 100 GPa (pseudo-saturation at 1064 nm) or 120 GPa (pseudo-saturation at 532 nm). We might interpret this regime to be the mixture regime described by Li et al. (2013, 2017), as the high slope of $R(P)$ indicates that the dissociation fraction is very sensitive to pressure, which is a signature of a transient behaviour. Our pseudo-saturation region could correspond to the plasma regime, where dissociation is essentially complete and only short-lifetime bonds exist. It is to be noticed that Li et al. (2013) predict a slightly

negative dependence on density (hence on pressure) of both dissociation fraction and static electrical conductivity in the plasma regime. Although the link to reflectivity is not direct, that prediction may be confirmed by our observation of slightly decreasing reflectivity at pseudo-saturation conditions.

5.3 Study of Hugoniot curves starting from higher pressures

In this Section we present the shock-compression study of ammonia statically pre-compressed inside Diamond Anvil Cells, primarily led by Jean-Alexis Hernandez (LULI). The coupling of shock-compression and static pre-compression with DACs allows to probe lower temperatures with respect to the approach used in Section 5.2, as explained in Chapter 3.2.1.

5.3.1 Diamond Anvil Cells

The DAC design which has been employed in this work has been adapted from the original one by Paul Loubeyre, with the help of Florian Occelli *(CEA, France)*. The diamond design has changed between experimental campaigns A and B. A first design allowed to obtain low initial pressures up to 0.3 GPa. In experiment B, an alternative diamond design by Boehler and De Hantsetters (2004) has been adopted in order to increase the initial pressure and hence explore colder states. A maximum initial pressure of 3.15 GPa has been obtained. This second design is provided in Figure 5.19. In our Diamond Anvil Cells, static pre-compression is achieved by means of a diamond and a sapphire anvils, placed onto support plates made of tungsten carbide. The diamond anvil is placed in its seat in the support plate on the laser side. On the diagnostics side, a 3 mm thick sapphire anvil is placed on the respective support plate. A 0.20 mm thick circular stainless steel gasket, with a central hole with a $0.5-0.6$ mm diameter, is placed between the diamond and sapphire anvils. After the cell has been filled, the ammonia sample will occupy the volume carved by the central hole.

As we explained in Chapter 3.2.1, the thickness of the drive-laser-side diamond anvil must be carefully chosen, as a function of the available laser energy, as a compromise between the needs for a limited shocked-state temperature (requiring a high initial pressure) and a high shocked-state pressure. Indeed, on the one side, the maximum initial pressure which can be reached increases with the diamond thickness. On the other side, an increased diamond thickness implies that the laser-driven shock wave will lose a higher fraction of its energy during its propagation of the anvil. Longer laser pulses are also necessary to sustain the shock until its arrival in the ammonia sample. This requires a considerable laser energy – this is the reason why this technique is usually limited to the largest laser facility such as NIF and LMJ. For the icy mixtures and their components, including ammonia, the interesting processes and the relevant conditions for planetary modelling are at limited pressures around $1-2$ Mbar, which motivates the use of static pre-compression on a mid-sized facility such as LULI2000. Extensive hydrodynamic simulations with MULTI have been performed to optimise the thickness of the diamond anvil. A thickness of 200 μm has been chosen for the first

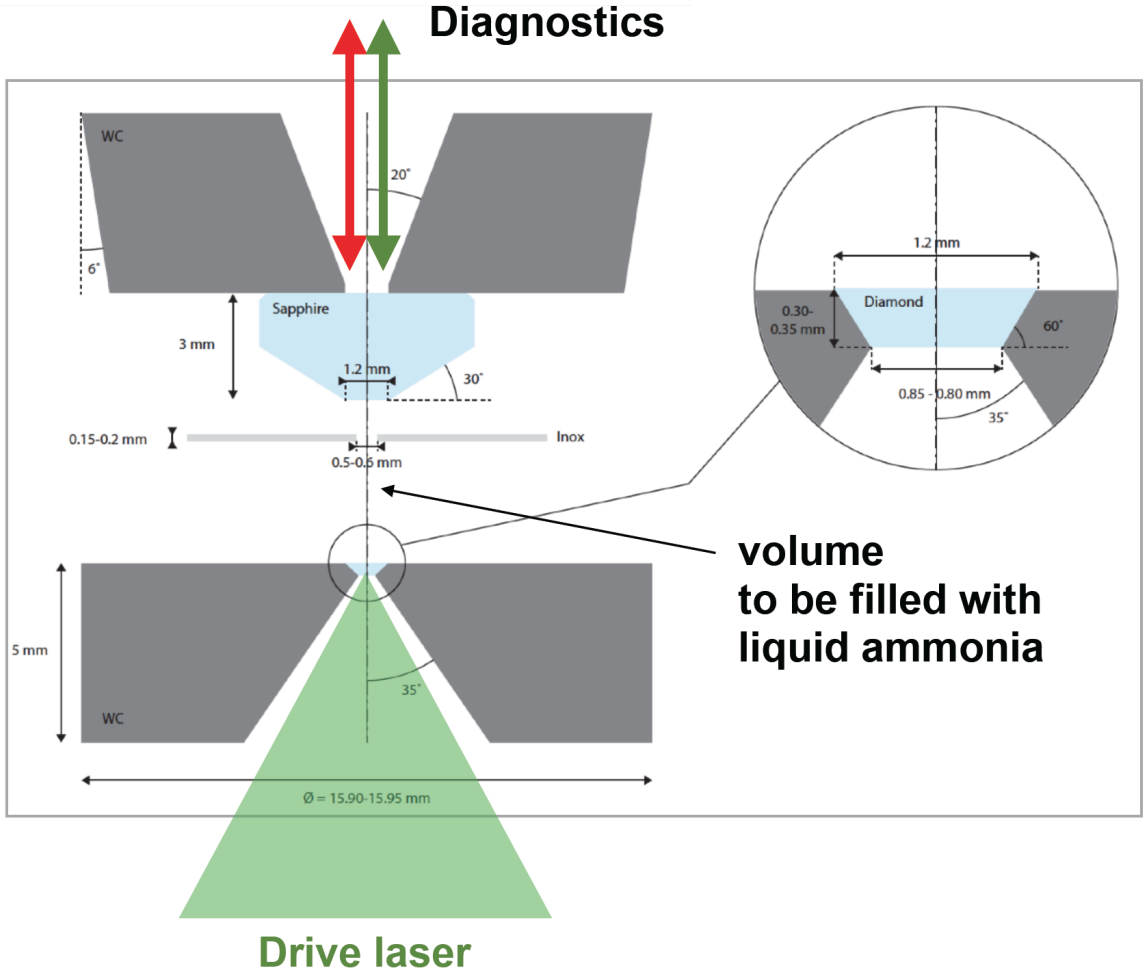

Figure 5.19 – Scheme of the DAC with the Boehler design. The optical axis is vertical; the drive laser comes from the bottom, diagnostics are on top. The support plates are in dark gray; the gasket is in light gray; the diamond and sapphire anvils are in light blue. The inset on the right focuses on the drive-laser-side diamond anvil seat. The figure has been adapted from a scheme by J.A. Hernandez (LULI).

DAC design. For the Boehler design, the lowest thickness available, of $300 - 350$ μm, has been used. Another important parameter to optimise is the area of the outer face of the carbide hole. In this case, the compromise is between the maximum available initial pressure (which decreases with increasing area, at constant thickness) and the necessity of transmitting a spatially uniform shock wave to the ammonia sample. Indeed, on such important thicknesses of several hundreds micrometer, lateral release could introduce two-dimensional effects in the shock propagation. The diameter of the carbide hole has been varied between $600 - 800$ μm.

A $20-30$ μm thick α-quartz standard has been used as *in situ* standard for the EOS and reflectivity measurements, coated with 0.2 μm of gold as reflecting layer for the initial VISAR signal. On the external side of the diamond anvil, an ablator consisting of 10 μm of polystyrene has been coated. A 3 μ thick gold shield was coated between ablator and diamond.

The filling procedure of Diamond Anvil Cells with liquid ammonia was the same as

in previous static compression work and is described by Datchi et al. (2006) and Ninet et al. (2006).

5.3.2 Experimental setup

The same experimental setup as that described in Section 5.2.4 for the LACs has been used for the shock-compression of DACs. Only the drive laser parameters changed. In the experimental campaign A, during which the first DAC design adapted from the *CEA* has been used, the two chains available at LULI2000 synchronously fired a maximum amount of energy (some 500 J at 527 nm) with a 2.5 or 5 ns long flat pulse.

5.3.3 Results and discussion

Laser-driven shock compression on Diamond Anvil Cells allowed us to explore Hugoniot curves starting from different conditions. The data set obtained in this way thus expands the one obtained by compressing ammonia starting from 15 bar, detailed in Section 5.2. Initial pressures of $0.2 - 0.3$ GPa have been reached with the first DAC design. The second design (Boehler), using a thicker diamond anvil and of a different shape, permitted to obtain higher initial pressures ($0.75 - 3.15$ GPa). The highest pressures reached by static pre-compression correspond to an orientationally-disordered cubic phase called phase III [Ninet and Datchi (2008)].

A typical VISAR and SOP output is provided in Figure 5.20 (a) and (b), respectively. Prior to the shock entering the quartz layer, the probe laser is reflected by the (immobile) gold layer placed before the quartz standard, so that a static fringe system is visible on the VISAR image [Figure 5.20 (a)]. When the shock front enters the quartz layer, the intensity of the fringe system drops, as the probe laser is now reflected by the shock front which is propagating in the standard. The VISAR clearly shows the shock entrance and its propagation through the quartz layer. At around 16 ns the shock is transferred to the ammonia sample and its propagation can be clearly followed. Shocked ammonia becomes reflecting and exhibits a reflectivity slightly lower than shocked quartz. As ammonia has a lower impedance than quartz, the shock velocity increases from 14 km/s to 17 km/s, as it is visible on the velocity output [Figure 5.20 (c)]. The SOP signal decreases a lot: shock ammonia emits far less radiation than shocked quartz. While the shock propagates inside the sample, it decays in strength. The decrease in shock velocity, shock-front reflectivity, and emission is visible on the diagnostics output images. At 22 ns, the shock front reaches the interface between the ammonia sample and the sapphire.

Figure 5.21 shows the final thermodynamic states reached in shocked ammonia in the temperature – pressure plane. Pressure has been obtained via impedance mismatch with the α-quartz standard, using the statically pre-compressed Hugoniot curve proposed by Brygoo et al. (2015) (see Chapter 3.2.1). Temperature has been measured from the SOP signal. The pre-compressed α-quartz layer could be used as *in situ* standard, exploiting the temperature – shock velocity relation from Brygoo et al. (2015). This analysis is preliminary and a further treatment of the data is ongoing.

The combined use of different static pre-compressions and dynamic compressions permitted us to span a wide region of the phase diagram. According to the phase diagram proposed by Bethkenhagen et al. (2013), all the states we reached are in the

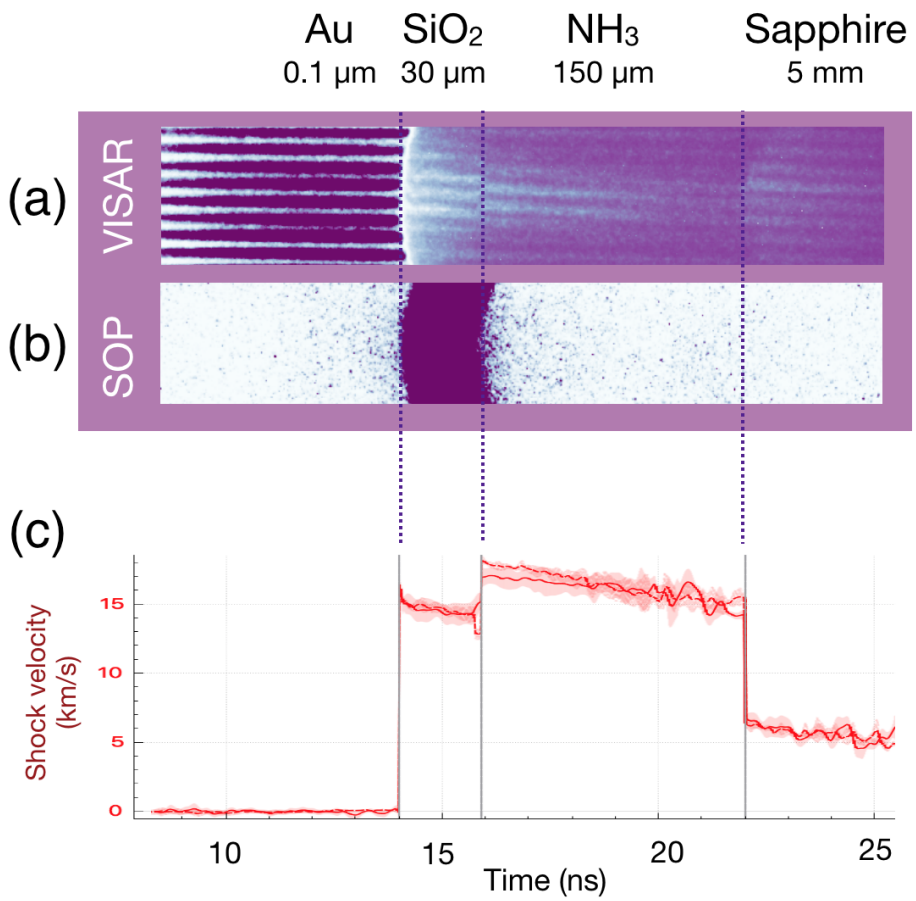

Figure 5.20 – **Top.** Output of a VISAR and of the SOP for a shot on a DAC. In the first time interval, the probe laser is reflected onto the Au/SiO_2 interface. At around 14 ns after the beginning of the laser pulse, the shock front enters the SiO_2 sample. The probe laser is thus reflected by the shock front. At around 16 ns, the shock enters the ammonia sample. At 22 ns, the shock exits the ammonia sample under study and enters the rear-side sapphire anvil. No emission is registered by the SOP while the shock front is behind the gold layer. A very high signal is acquired while the shock front crosses quartz. A signal considerably lower and decaying in time is then collected while the shock front propagates inside the ammonia sample. **Bottom.** Shock velocity as a function of time as measured by the two VISARs. The shock decays in time in quartz, then its velocity jumps upwards when it enters less dense liquid ammonia. The shock then continues to decay in time during the crossing of the ammonia sample. Finally, an important downward jump of the shock velocity takes place when the shock enters the considerably denser sapphire anvil. Adapted from a figure courtesy of A. Ravasio (LULI).

liquid dissociated phase. However, the lowest explored temperatures ($3000 - 4000$ K) are quite close to the superionic phase. A comparison between the measured thermodynamic states and the Hugoniot curves extracted from the equation of state calculated by Bethkenhagen et al. (2013) shows a remarkably good agreement. The high static pre-compressions allowed us to provide planetary models with a lot of data spanning diverse thermodynamic conditions, reaching low temperature typical of adiabatic interior profiles of icy giant planets [Redmer et al. (2011); Bethkenhagen et al. (2017)] at

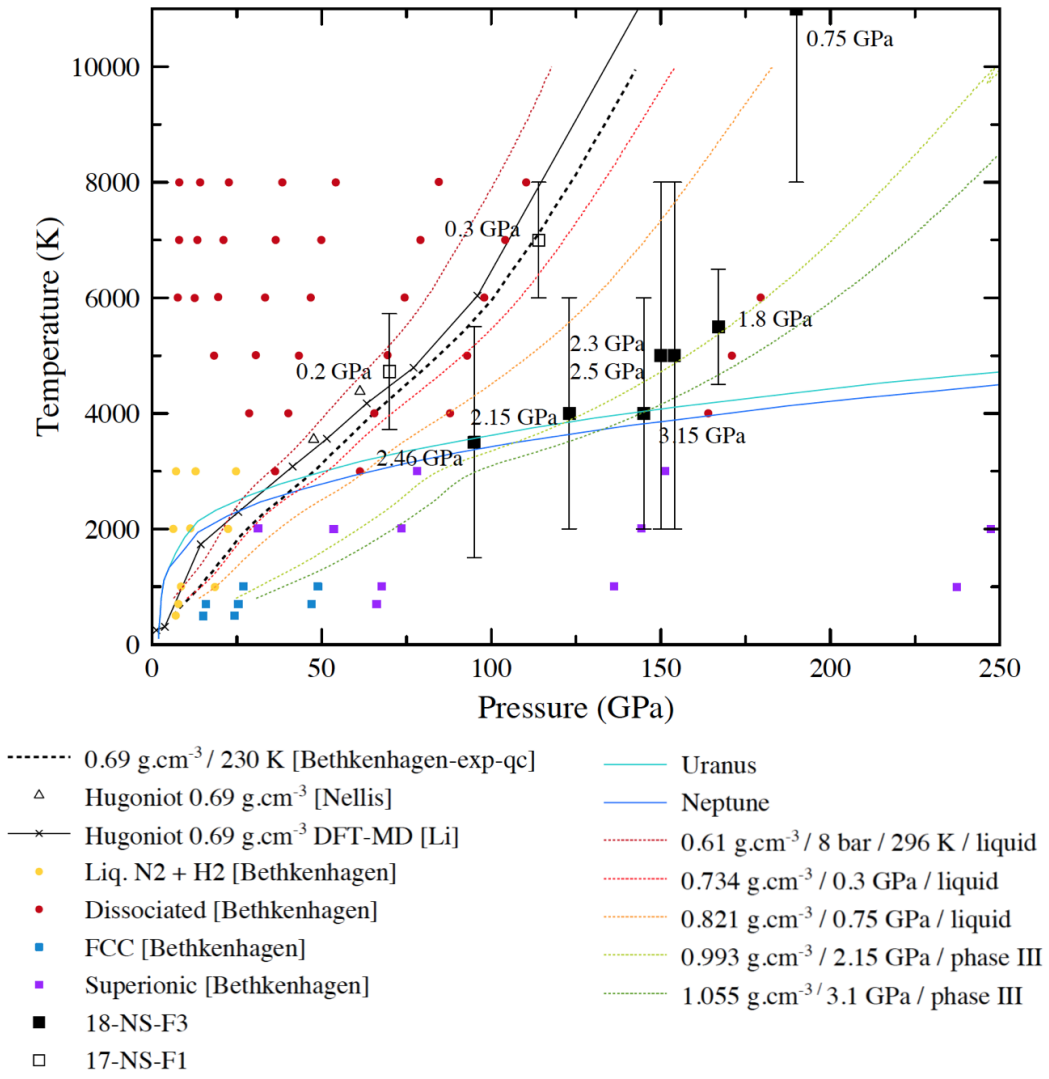

Figure 5.21 – Final states obtained in liquid ammonia with laser-shock compression on DAC in the temperature-pressure plane. Open squares are data from the first experimental campaign, using the DAC design by P. Loubeyre. Filled squares are from the second campaign, using the Boehler design. The coloured circles and squares correspond to the different phases predicted by Bethkenhagen et al. (2013) (liquid N_2+3H_2, liquid dissociated, fcc solid, superionic). The coloured dashed curves are the ammonia Hugoniot curves extracted from the equation of state provided by Bethkenhagen et al. (2013) for the different initial pressures obtained in the DAC. The Uranus and Neptune isentropic internal profiles according to Redmer et al. (2011) are also shown for comparison. Adapted from a figure courtesy of J.A. Hernandez (LULI).

remarkably high pressures between $1-1.5$ Mbar. As a comparison, the Hugoniot curve of ammonia starting from 15 bar (explored by compression of LAC targets) crosses the same profiles only at around 0.25 Mbar.

Thanks to the use of the decaying shock technique (see Chapter 2.3.5), not only the initial pressure and temperature in shocked ammonia could be determined for each shot, but also the time-resolved shock velocity and self-emission, which can be used to estimate the time-resolved pressure and temperature, respectively. This means that,

in addition to the shock-arrival data presented in Figure 5.21, decaying-shock data will be available continuously covering a portion of the Hugoniot curve. This analysis is currently ongoing. Moreover, for each shot, the time-resolved shock-front reflectivity at 532 nm and 1064 nm could be measured, meaning that the reached states for all the shots were optically reflecting (hence electrically conducting). Also this analysis of the reflectivity as a function of shock velocity, pressure, and temperature is still ongoing.

Combination of LAC and DAC data

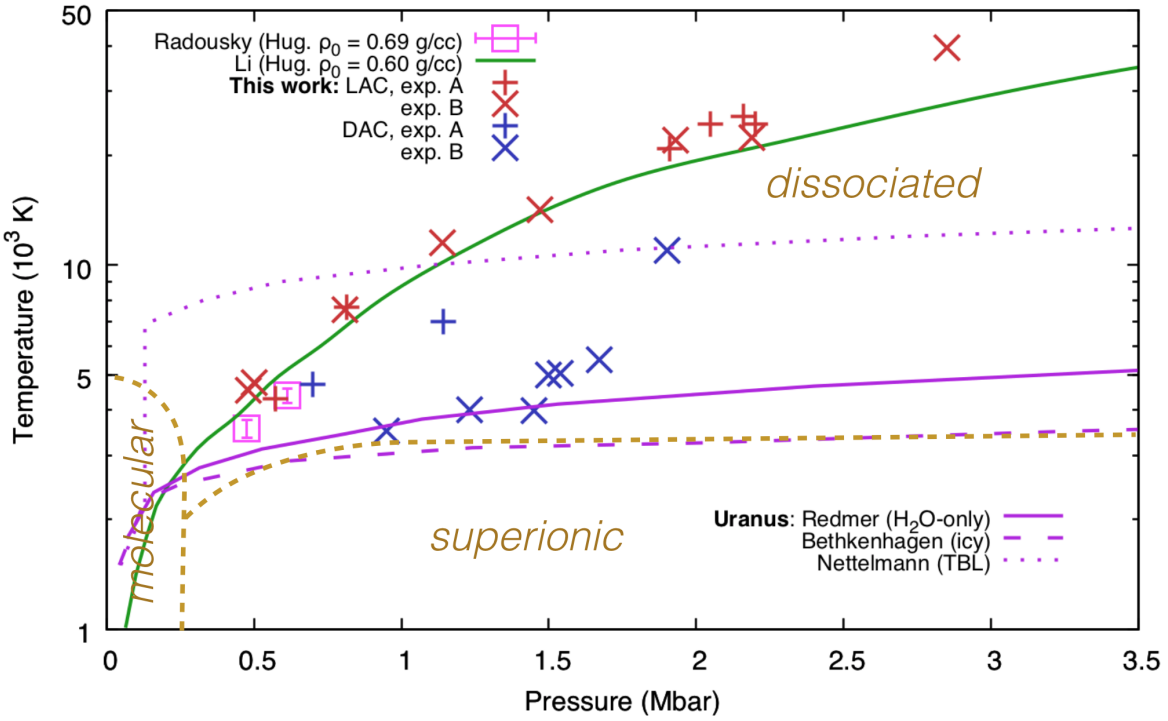

Figure 5.22 – Temperature – pressure diagram showing the conditions reached by laser-driven shock compression of Liquid Ammonia Cells (red crosses) and Diamond Anvil Cells (blue crosses) in this work. The Hugoniot curve of ammonia starting from 0.60 g/cm^3, calculated by Li et al. (2013), is shown for comparison with our LAC data. The phase diagram of warm dense ammonia calculated by Bethkenhagen et al. (2013) is also shown (the phase boundaries are the dashed, straw-coloured curves). Finally, some Uranus interior profiles predicted by different models by Redmer et al. (2011) (water-only interior), Bethkenhagen et al. (2017) (interior with icy mixtures), and Nettelmann et al. (2016) (interior with icy mixtures, including a Thermal Boundary Layer) are shown for comparison with the experimentally explored conditions.

By combining Hugoniot data from 15 bar, obtained by shock-compression of LACs, and Hugoniot data from higher pre-compressions ($2 - 31$ kbar) obtained with the use of DACs, we explored a wide region of the phase diagram of warm dense ammonia, as shown in Figure 5.22. All the explored conditions appear to belong to the dissociated phase according to calculations by Bethkenhagen et al. (2013), although, as we already said, we probed conditions very close to the upper superionic phase boundary by shock-compression of DACs. Figure 5.22 shows that we explored conditions similar to the

internal profiles of Uranus as predicted by different models. In particular, our LAC and DAC data are closed to the Uranus interior profile from Nettelmann et al. (2016) from $0.8 - 1.9$ Mbar, whereas the interior profile predicted by Redmer et al. (2011) is probed by our DAC data from $0.9 - 1.7$ Mbar. The combination of LAC and DAC data will also allow to characterise the pressure and temperature dependence of the optical properties of warm dense ammonia along quasi-isothermal and quasi-isobar lines, as it is evident by looking at Figure 5.22. For instance, LAC and DAC data span the isothermal line at 5 kK from $0.5 - 1.7$ Mbar and the line at 10 kK from $1.2 - 1.9$ Mbar. Such study is analog to what has already been done on pure water and icy mixtures (see Chapter 4.4.6) but is still ongoing, as more data are needed.

5.4 Conclusions and perspectives

In this Chapter we have described the work we have initiated about the study of warm dense ammonia using laser-based compression techniques. In particular, we have developed a Liquid Ammonia Cell (LAC) and a filling system which allows to obtain a liquid ammonia sample inside the cell at 15 bar and ambient temperature. The LAC is compatible with laser-driven shock loading and allows the optical probing of the shocked sample. The system we developed is portable, so that it can be employed in experimental campaigns on other high-power laser facilities, especially those coupled with X-ray sources such as XFELs and synchrotrons. Liquid ammonia in the LAC has been compressed along the Hugoniot curve by laser-driven decaying shocks up to pressures around 3 Mbar. The equation of state and the shock-front reflectivity at two different wavelengths, 532 nm and 1064 nm, have been measured. We provide the first data at such high pressures, which enlarge the range of probed conditions which was previously limited to 0.6 Mbar. Moreover, our experimental study is the first one employing laser-driven shock compression and providing shock-front reflectivity data. It represents the first experimental evidence of an optically reflecting, metallic-like behaviour in warm dense ammonia.

Our thermodynamic data are compatible with previous calculations by Li et al. (2013) and with those recently provided by Mandy Bethkenhagen up to 2.5 Mbar. This work has therefore initiated the validation of the available *ab initio* studies in this hardly accessible region of the phase diagram, though lower error bars are needed to complete the validation in future experimental work. We measured reflectivity values compatible with the predictions in the high-pressure saturation region, but our data are considerably lower up to 1 Mbar, particularly at 532 nm. More experimental and simulation work is needed to understand the optical properties of ammonia and thus to precisely assess the contribution of ammonia to the electrical properties of the mixtures composing the icy giants' interiors.

With the aim of probing lower-temperature conditions, we coupled laser-driven shock compression and static pre-compression using Diamond Anvil Cells. We were able to pre-compress condensed ammonia samples up to more than 30 kbar, starting from a solid phase. For shocked pressures between $1 - 1.5$ Mbar, we explored remarkably low temperatures between $3000 - 5000$ K (almost 50% lower than along the 15 bar liquid Hugoniot curve). Such conditions are compatible with those of the interior profiles of Uranus and Neptune and not far from the upper boundary of the superionic phase

as predicted by calculations. We also measured the optical properties of the shocked samples, and in particular the shock-front reflectivity, but these data are still under analysis. It is possible that the domain of the superionic phase has been probed by decaying shock compression. Moreover, the electrical conductivity of shocked ammonia shall be estimated from both the 15-bar and the DAC data sets, either in analogy to what has been done in Chapter 4.3.7 for pure water and water–ethanol–ammonia mixtures or with the use of *ab initio* calculations as we will describe later in Chapter 6.

Future experimental work shall make use of dynamic pre-compression methods (*e.g.* with laser pulse shaping) to explore colder states and characterise the properties of the superionic phase and its boundaries. To achieve this goal, a thorough study of the equation of state and optical properties of the low-pressure (up to $0.3 - 0.4$ Mbar) region of the Hugoniot curve shall be performed. A preliminary study of the optical properties in this regime has already been conducted in this work. Moreover, the techniques used in this work will be useful not only for future work on pure ammonia. Indeed, cells and cryostat filling system similar to those used here shall be employed to obtain liquid methane in target cells apt to laser-driven shock compression. The characterisation of warm dense liquid methane would be the last link in the chain of the end-members composing the deep interiors of the icy giants (H_2O, NH_3, and CH_4).

Icy giant planets' components: general discussion

The Second Part of this Thesis was devoted to the study of samples representative of the components of the interiors of icy giant planets, in their pure and mixed form. In this Discussion we take stock of the state of the art before and after our work, highlighting its contribution to planetary science and to the more general study of the WDM regime.

Before this work

Before this Thesis, on one hand warm dense water had already been extensively studied from modest compressions up to extreme conditions. Its phase diagram, equation of state, and optical properties (transparent, opaque, and reflecting regions, and shock-front reflectivity in the latter) were already well known along diverse thermodynamic paths: the principal Hugoniot and several statically pre-compressed Hugoniot (from the liquid state and from the ice VII state). On the other hand, all the other samples investigated in this work had been experimentally characterised only up to modest pressures and temperatures. Data sets were sparse, especially those concerning temperature measurements, and the study of the optical properties was even totally absent. The scenario before this Thesis is summarised in the top part of Table 5.3, which specifies the limits of the pressure – density, temperature, and reflectivity studies for each sample.

The lack of high-pressure experimental data about the components of icy giant planets represents a major hindrance to the validation and improvement of models describing their evolution and structure. In particular, the thermodynamic interior profiles are but loosely constrained. Adiabatic profiles using water as sole component of the deep interiors [Redmer et al. (2011)] or water–methane–ammonia mixtures [Bethkenhagen et al. (2017)] predict quite low temperatures, between $1.5 - 5.8$ kK. However, some models [Nettelmann et al. (2016)] explain Uranus' low luminosity by considering that the heat flow is inhibited between the light H/He-rich atmosphere and the icy interiors. This originates a Thermal Boundary Layer which leads to the prediction of much higher temperatures up to 14 kK. As a consequence of such uncertainty in the thermodynamic conditions reached in the interiors icy giants, the origin of the dichotomy in Uranus' and Neptune's luminosity is far from being understood. Moreover, although there is general consensus on the fact that the non-dipolar, non-axisymmetric

magnetic fields of Uranus and Neptune are generated in a thin outer dynamo-active shell, the relative contributions of metallic fluid hydrogen (present in the atmosphere) and of the water, methane, and ammonia ices are not precisely known, due to the lack of data about the electrical properties of the ices.

The contribution of this work

Table 5.3 – State of the art of the experimental study in the WDM regime of pure water (H_2O), pure liquid ammonia (NH_3), water–ethanol mixture (WEM), and ternary mixtures (synthetic Uranus, SU, and synthetic planetary mixture, SPM) before and after this Thesis (first and second line, respectively). Pressure – density ($P-\rho$), temperature (T), and reflectivity (R) data are considered.
Abbreviations: Hug. = Hugoniot curve; pr. Hug. = principal Hugoniot curve; stat. prec. Hug. = statically pre-compressed Hugoniot curve; dyn. prec. Hug. = dynamically pre-compressed Hugoniot curve; sat. = (reflectivity) saturation.

$P-\rho$ **data**	T **data**	R **data**
	H_2O	
up to 10 Mbar (pr. Hug.) / up to 3.5 Mbar (ice VII Hug.)	sparse, up to 19 kK (pr. Hug.) / up to 10 kK (ice VII Hug.)	532 nm: up to saturation (pr. Hug.) / sparse data, up to 1.8 Mbar (stat. prec. Hug.); 1064 nm: none
same + up to 5.6 Mbar (dyn. prec. Hug.)	continuous, up to 25 kK (liquid Hug.) / 7-19 kK (dyn. prec. Hug.)	532+1064 nm: up to sat. (pr. Hug.) / up to 5.6 Mbar, 19 kK (dyn. prec. Hug.)
	NH_3	
up to 0.6 Mbar (0.69 g/cm^3 Hug.)	only 2 points: 3.5 and 4.4 kK (0.69 g/cm^3 Hug.)	none
up to 2.1 Mbar (0.61 g/cm^3 Hug.) / 2 Mbar (stat. prec. Hug.)	up to 24 kK (0.61 g/cm^3 Hug.) / $3-11$ kK (stat. prec. Hug.)	532+1064 nm: up to sat. (0.61 g/cm^3 Hug.) / *ongoing analysis (stat. prec. Hug.)*
	WEM	
none	none	none
up to 2.7 Mbar (pr. Hug.)	up to 20 kK (pr. Hug.)	532+1064 nm, almost up to sat.
	SU/SPM	
up to 0.8 Mbar (pr. Hug.) / 2.2 Mbar (off pr. Hug.)	only 2 points: 2.4 and 5.1 kK	none
up to 2.6 Mbar (pr. Hug.) / up to 3.6 Mbar (dyn. prec. Hug.)	up to 20 kK (pr. Hug.) / $6-13$ kK (dyn. prec. Hug.)	532+1064 nm: up to sat. (pr. Hug.), up to 3.5 Mbar, 13 kK (dyn. prec. Hug.)

In the work described in Chapters 4 and 5, we characterised the thermodynamical and optical properties of pure water, pure ammonia, a water–ethanol mixture (WEM), and a water–ethanol–ammonia synthetic planetary mixture (SPM) in the WDM regime. The experimental techniques employed allowed us to reach two complementary technical goals:

(i) reproducing extreme thermodynamic conditions (pressures of a few megabar, temperatures of several thousand Kelvin);

(ii) spanning a set of conditions as wide as possible, *i.e.* limiting the heating of the sample as much as possible while maximising the compression.

High-pressure / high-temperature states were attained by single-shock compression of samples starting from standard conditions. High-pressure / moderate-temperature states, which are technically more difficult to achieve, have been reproduced by shock-compression of statically or dynamically pre-compressed samples (using DACs or double-shocks, respectively). The situation after this work is summarised in the bottom part of Table 5.3.

Principal Hugoniot curves

Since all four samples have been characterised by single shock from standard conditions, their behaviours along their principal Hugoniot curves can be compared. The shock–particle velocity relations for water, ammonia, the WEM, and the SPM are shown in Figure 5.23. The $U_s - U_p$ relations for water, the WEM, and the SPM are comparable within error bars. The experimentally observed similarity in those relations, together with the ancillary *ab initio* calculations performed in the work described in Chapter 4, validate the hypothesis according to which the thermodynamic properties of the mixtures can be satisfactorily predicted using the Linear Mixing Approximation. This work has thus confirmed the *ab initio* results by Bethkenhagen et al. (2017). Liquid ammonia, along the Hugoniot starting from 0.61 g/cm^3, exhibits a higher initial sound velocity and a higher maximum compressibility than water and mixtures.

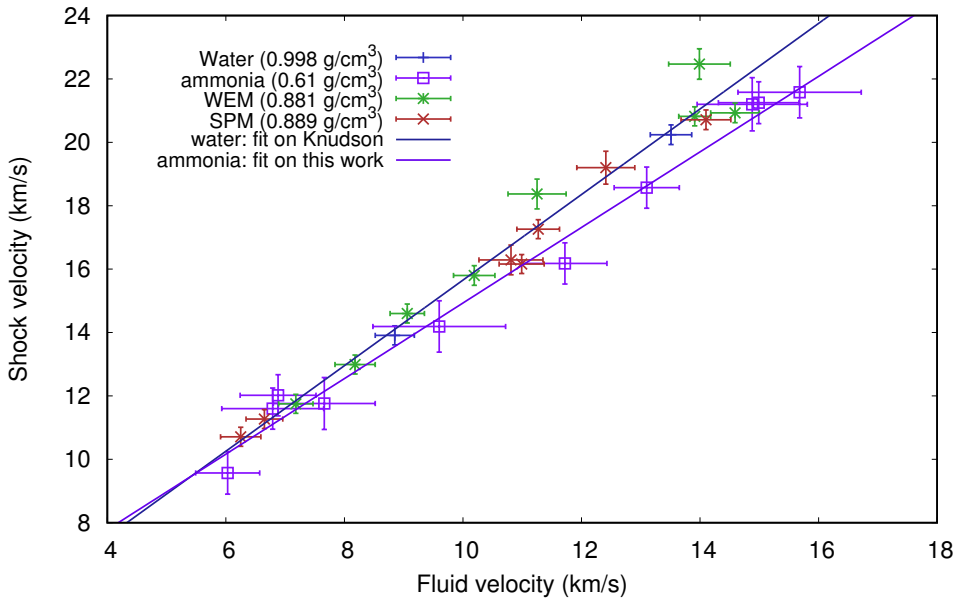

Figure 5.23 – Shock–particle velocity relation along the principal Hugoniot curves of water, WEM, and SPM and along the Hugoniot curve starting from 15 bar and ambient temperature of liquid ammonia. The dark blue line is a linear fit operated on previous water data by Knudson et al. (2012).

The temperature – pressure relations of the studied samples (shown in Figure 5.24) are also comparable, although the high error bars, typical of self-emission measurements, do not allow to identify small discrepancies. However, shock-compressed ammonia along the Hugoniot starting from 0.61 g/cm^3 exhibits higher temperatures than water and mixtures at comparable pressures. This is probably due to the very different initial density (0.998 for water, around $0.88 - 0.89$ for the mixtures) rather than to a different response of the material to shock-compression.

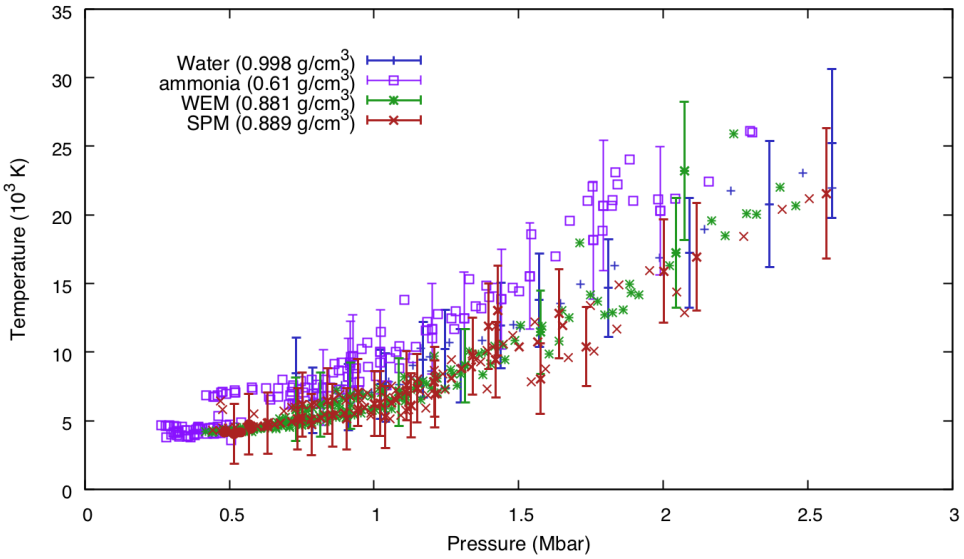

Figure 5.24 – Temperature – pressure relation along the principal Hugoniot curves of water, WEM, and SPM and along the Hugoniot curve starting from 15 bar and ambient temperature of liquid ammonia.

The same behaviour is much more evident if the shock-front reflectivity dependence on pressure (shown in Figure 5.25 at 532 nm) is investigated. Indeed, the onset pressures of reflectivity and the saturation values are clearly ordered depending on the initial density: the lower the initial density, the lower the onset pressure and the higher the saturation value. This ordering is also in part a consequence of the ordering of the molecular ionisation energies of the samples' end-members: 12.6 eV for water, 10.5 eV for ethanol, and 10.1 eV for ammonia [Meot-Ner (Mautner) and Lias (2018)]. A major difference exists between water and ethanol–ammonia, which may imply that ammonia and the mixtures dissociate at lower pressures and temperatures than pure water.

Secondary Hugoniot curves

The characterisation off the principal Hugoniot has only been done by employing a double-shock technique on water and on the SPM, and by employing static precompression with DACs on ammonia. Moreover, the study of the off-Hugoniot optical properties of ammonia is still ongoing. A comparison of the different samples at these conditions would therefore be premature. However, double-shock compression studies of water and SPM have shown that their reflectivities (hence conductivities) are almost constant along isothermal lines, and that along all the explored conditions the SPM exhibits higher reflectivity (hence conductivity) values than water.

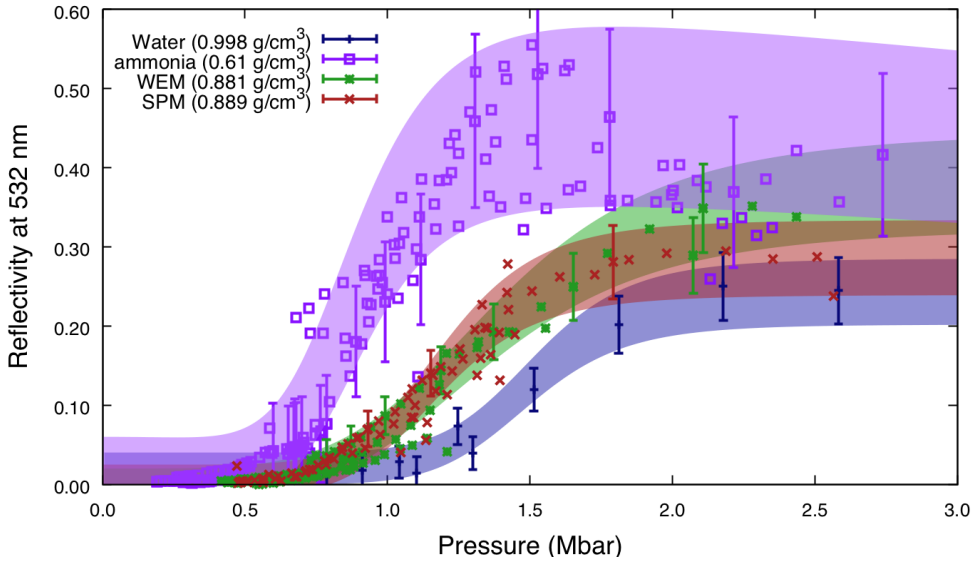

Figure 5.25 – Shock-front reflectivity at 532 nm as a function of pressure along the principal Hugoniot curves of water, WEM, and SPM and along the Hugoniot curve starting from 15 bar and ambient temperature of liquid ammonia. Shaded areas represent fits on experimental data within error bars.

Interest for planetary interior models

The results of this work have not only direct repercussions on the study of the WDM regime, but can also be useful for models describing the evolution and structure of the icy giant planets. In particular, we provided EOS data of the relevant samples up to unprecedentedly extreme conditions of pressure and temperature and wide ranges of thermodynamic states. High-pressure / high-temperature data are immediately useful for planetary models if a Thermal Boundary Layer exists. High-pressure / moderate-temperature data, which were very scarce before this work, are closer to the adiabatic profiles. Additionally, all the produced data will be useful to the *ab initio* community as a testbed for simulations, which in their turn represent a critical factor for the improvement of planetary models.

Moreover, we have qualitatively characterised the optical properties and, in the reflecting regime, quantitatively studied the shock-front reflectivity of the relevant samples at two different wavelengths. In some cases (mixtures, ammonia), our reflectivity data have been the first ever. For water, previous data only included one wavelength. We have observed that the SPM exhibits higher reflectivities than pure water both along and off the principal Hugoniot curve, indicating that planetary models using water as the sole component of the deep interiors may undervalue their contribution to the magnetic field. All the collected reflectivity data can be immediately compared with those obtained from conductivity predictions by *ab initio* calculations. In particular, the study at two different wavelengths represents not only a more precise data set for the validation of calculations, but also a first attempt in characterising the spectral dependence of the optical-electrical properties of the warm dense samples, which has been proven to be far from being trivial [Laudernet et al. (2004); Clerouin et al. (2005)]. The validation of *ab initio* calculations will drastically improve the models of planetary

dynamos, clarifying the relative contribution of the icy mixtures with respect to that of metallic hydrogen.

Perspectives

The work conducted in this Part of the Thesis and its limits chart a rather clear path to be followed by future investigation. Hereafter we propose a plan of action consisting in three axes.

(i) Most urgently, all the pre-compression techniques employed here shall be applied to all samples. We could not do it in our work principally because of the limited available beam-time on laser facilities. This first track is therefore a natural and obvious prosecution of the work described here, requiring little to no technical improvements. Doing so will allow to extend the conditions at which the behaviours of the samples under study can be compared. This extension should also include methane, the last end-member of the icy mixtures. Liquid methane can be obtained and shock-compressed by adapting the target and filling procedure presented in Chapter 5.

(ii) Furthermore, the thermodynamic and reflectivity data for all the samples should be used to estimate the electrical conductivity. Indeed, conductivity, rather than reflectivity, is the property of interest for the modelling of planetary dynamos. As already pointed out in Chapter 4, this estimation is quite delicate, as calculations clearly show that the behaviour of conductivity at WDM conditions is far from being described by a simple Drude model. On the contrary, it requires the precise knowledge of hardly achievable properties such as the behaviour of bound electrons and the frequency dependence of the complex refractive index. A possible strategy, which will be employed on silica in Chapter 6 of this Thesis, consistently employs both experimental data and *ab initio* calculations.

(iii) Last, once the basic thermodynamic and optical properties of the materials of interest have been extensively characterised, diagnostics allowing the microscopical probing of the shock-compressed samples, such as X-ray diffraction, should be employed to probe their bulk structures and phase transitions, whereas the optical diagnostics employed in this work only allowed the characterisation of a thin layer right behind the shock front. This has recently been done for pure water by Millot et al. (2019).

Part III:

Experimental study of components of rocky planets

In his hand are the deep places of the earth:
the strength of the hills is his also.

Psalms 95, 4

Chapter 6

Optical and electrical properties of warm dense silica

Experimentally characterising the equation of state, phase diagram, and opto-electrical properties of silica and silicate minerals at Warm Dense Matter conditions is essential not only to globally deepen our knowledge of this regime, but also to benchmark *ab initio* calculations and to improve interior models of super-Earth and giant exoplanets. In particular, the study of conductivity is crucial to understand if silicates can sustain magnetic dynamos inside super-Earth exoplanets.

In this Chapter, we present our experimental study of warm dense silica via double-shock compression of α-quartz samples. The theoretical concepts of this method have been provided in Chapter 3.3. After having discussed the state of the art of the study of warm dense silica and placed our work in its scientific context, we will describe two preliminary studies which are essential to the principal investigation: the modelling of the principal Hugoniot of α-quartz and the study of the refractive index along the principal Hugoniot of α-quartz in the transparent regime. We will then present the principal study of this Chapter: double-shock compression of warm dense silica. In the analysis we will include the description of the approach we have used to estimate the electrical conductivity from the reflectivity measurement using *ab initio* calculations to go beyond simplistic models. Finally, we will report the observation of an elastic precursor of the first shock wave in some shots and infer the precursor velocity.

Contents

6.1 Context

Silica (SiO_2) is a material of major importance for several scientific domains, such as the physics of shock compression and planetary science. On one hand, it represents a common standard material for shock experiments; on the other hand, it is an end-member of MgO–FeO–SiO_2 systems, which are key components of proto-planets [Guillot (1999)] and super-Earth extrasolar planets [Stixrude (2014)].

The precise characterisation of shock-compressed silica is crucial for the measurement of the EOS and reflectivity of the samples under study when silica (often starting from the α-quartz phase) is used as *in situ* standard [Barrios et al. (2010); Celliers et al. (2010); Brygoo et al. (2015); Kimura et al. (2015); Sekine et al. (2016)]. Indeed, the $U_p - P$ equation of state of silica is needed for the impedance mismatch technique (see Chapter 2.3.4), whereas the temperature – shock velocity and reflectivity – shock velocity relations are used for the calibration of temperature and reflectivity measurements in the sample under study.

The equation of state and phase diagram of silica and silicate minerals at planetary interiors conditions are necessary to constrain formation, evolution, and structure models of rocky and giant planets [Guillot (2005); Baraffe et al. (2010); Swift et al. (2012)] (see Chapter 1.4.1). Of particular interest are the determination of the phase boundaries determining the transitions between different layers in planetary interiors and that of the role played by impacts with astronomical objects of various size in the planetary evolution history. Moreover, silica and silicate minerals, which are optically transparent and electrically insulating at ambient conditions, become reflecting and conducting in the liquid phase [Hicks et al. (2006); Spaulding et al. (2012); Sekine et al. (2016)]. Characterising their electrical conductivity is therefore crucial to understand if they are capable of sustaining a planetary dynamo in Super-Earth exoplanets, inside which convecting magma oceans are expected to exist [Stanley and Glatzmaier (2010); Soubiran and Militzer (2018)]. In addition, the complex behaviour of conductivity at these extreme conditions [Laudernet et al. (2004); Soubiran and Militzer (2018)] is interesting on its own and should be studied with the aim of deepening our knowledge of the Warm Dense Matter (WDM) regime.

6.1.1 State of the art

The planetary interest of silica and its role as prototype material for the WDM have motivated several *ab initio* [Laudernet et al. (2004); Mazevet et al. (2015); Qi et al. (2015); Denoeud et al. (2016a); Scipioni et al. (2017); Soubiran and Militzer (2018)] and experimental [Lyzenga and Ahrens (1980); Lyzenga et al. (1983); Boslough (1988); Trunin (2001); Luo et al. (2004); Hicks et al. (2005); Hicks et al. (2006); Knudson and Desjarlais (2009); Millot et al. (2015)] studies of its equation of state, phase diagram, structural, optical, and electrical properties. Shock-compression experiments have extensively studied the principal Hugoniot associated to different initial phases (fused silica, α-quartz, and stishovite), up to remarkably high pressures around 20 Mbar. In particular, the α-quartz Hugoniot curve has been very well explored. In Figure 6.1 (right) we provide the pressure – density relation along it as determined by experiments until the work of Knudson and Desjarlais (2009). However, the experimental studies of silica are not limited to the Hugoniot curves. Indeed, the α-quartz adiabatic release [Knudson and Desjarlais (2013); Desjarlais et al. (2017)], the sound velocity of silica [McCoy et al. (2016)], and the effect of static pre-compression on α-quartz properties [Brygoo et al. (2015)] have been characterised, providing essential insights to widen our understanding of this material off the Hugoniot conditions. A XANES (X-ray Absorption Near-Edge Spectroscopy) study by Denoeud et al. (2016a) could characterise the structural properties of silica off the α-quartz Hugoniot using shock reverberation (for higher densities) and release (for lower densities).

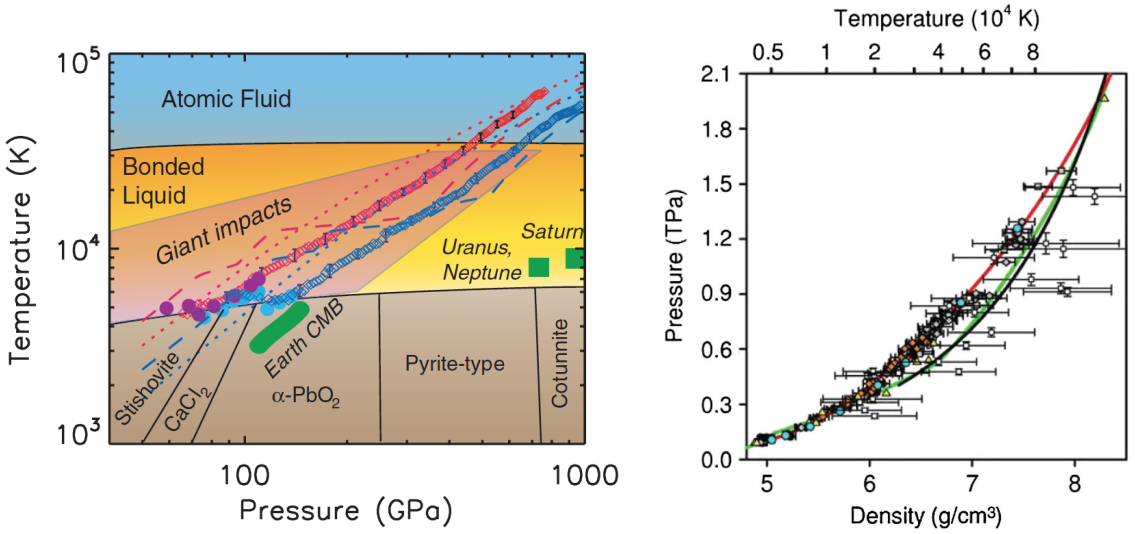

Figure 6.1 – **Left.** Phase diagram of warm dense silica as proposed by Hicks et al. (2006). Experimentally determined (diamonds) and model-extracted (dotted lines) $T - P$ profiles along the principal Hugoniot curves of α-quartz (blue) and fused silica (red) are shown, together with previous data from Lyzenga et al. (1983) (fused silica: purple dots; α-quartz: light blue dots). **Right.** Pressure – density relation along the principal Hugoniot curve of α-quartz from Knudson and Desjarlais (2009), showing all the available data at the time. The solid green, black, and red lines are the Hugoniot curve from the SESAME table 7360, a fit from Hicks et al. (2005), and a fit from Knudson and Desjarlais (2009), respectively.

The phase diagram of warm dense silica proposed by Hicks et al. (2006) is shown

in Figure 6.1 (left). Several low-temperature phases are shown, including stishovite. At around $4000 - 6000$ K, depending on pressure, all these phases melt and silica assumes the status of bonded liquid. At around 30 kK, the structural role of chemical bonds becomes negligible and silica becomes an atomic fluid. The determination of the melting curve of warm dense silica is necessary on the one hand for our understanding of the melting mechanism in the WDM regime and, on the other hand, to determine the evolution and structure of rocky Solar and extrasolar planets. Indeed, as we discussed in Chapter 1.4.1, melting is a key process in driving the differentiation of planets into a core and a mantle. Besides, melting can be caused by giant impacts during the history of a planet, generating a magma ocean whose gradual solidification drastically changes the subsequent thermal history of that planet. Millot et al. (2015) probed the melting curve of silica at different pressure conditions via the decaying-shock compression of samples of fused silica, α-quartz, and stishovite. Kinks in the $T - P$ profiles along the principal Hugoniot curves of fused silica and α-quartz were associated to the latent heat of solidification. Along the stishovite principal Hugoniot, a quasi-plateau in the $T - P$ profile has been observed at around 5 Mbar and interpreted as melting. Mazevet et al. (2015) and González-Cataldo et al. (2016) calculated the melting curve of warm dense silica with *ab initio* simulations. The different predicted and measured melting curves differ of some thousand Kelvin, so that the precise determination of the temperature – pressure profile of such curve is still missing and represents a key priority for future work.

6.1.2 Present work

In our work, we employed a double-shock compression technique (see Chapter 3.3) to explore a wide region of the phase diagram of silica with the possibility of characterising the temperature and pressure dependence of its properties along isobaric and isothermal lines, respectively. In particular, we probed an intermediate region between the principal Hugoniot curves of α-quartz and stishovite.

We ran three experimental campaigns (denoted experiments A, B, and D later in this Chapter) at the LULI2000 laser facility. Besides, an ancillary campaign (C) has been run to measure the refractive index of α-quartz in its transparent regime up to 0.3 Mbar along the principal Hugoniot. This study was required for the analysis of the double-shock data. Standard rear-side optical diagnostics have been used to probe the shocked sample: two VISARs, one working at 532 nm (2.331 eV) and the other one at 1064 nm (1.165 eV), and a streaked optical pyrometer (SOP) working at different wavelength intervals in the $300-500$ nm interval. In double-shock experiments, the first shock compressed the sample up to $0.2-0.6$ Mbar, where α-quartz remains transparent along its principal Hugoniot. In this pressure interval, the α-quartz Hugoniot lies in the stishovite phase region: the second shock thus loaded hot stishovite and brought it to a high-pressure state. Some shots exhibited the signature of the presence of an elastic precursor of the first plastic shock wave, as expected in α-quartz at those pressures [Wackerle (1962)]. Conductivity has been inferred from reflectivity data employing *ab initio* simulations of the optical and electrical properties of silica performed by François Soubiran of the ENS Lyon – who reproduced thermodynamic conditions similar to those experimentally explored in this work – and by Laudernet et al. (2004).

6.2 Properties along the α-quartz Hugoniot

Double-shock compression of z-cut α-quartz samples allows to explore conditions otherwise difficult to reach. However, the data analysis procedure of double-shock experiments requires the precise knowledge of the properties of the sample under study along its principal Hugoniot curve, as presented in Chapter 3.3.

(i) The ambient density value of α-quartz has to be known in order to apply the Rankine–Hugoniot relations (equations 2.23–2.25) for the determination of the different reached states. Such value is well known [Sosman (1927)]: $\rho_0 = 2.648$ g/cm^3.

(ii) In order to ensure a direct optical access to the double-shocked state, the first shock leaves the loaded sample in a transparent state. Therefore, the apparent velocity measured by the VISARs has to be linked to U_p^1 through a relation including the $U_s - U_p$ dependence and the behaviour of the shocked refractive index $n(\rho)$ (see Chapter 2.5.1). Those properties have thus to be known in the low-pressure, transparent regime of the principal Hugoniot of α-quartz.

(iii) The state loaded by the merged shock is determined via the Rankine–Hugoniot relations (equations 2.23–2.25) from the measurement of the merged-shock velocity U_s^m. Such state lies along the principal Hugoniot of α-quartz and, given the shock strength, is generally situated in the high-pressure, optically reflecting regime, were the $U_s - U_p$ relation along the Hugoniot must thus be known also in this regime is well characterised by a fit from Knudson and Desjarlais (2009).

(iv) The $T - U_s$ relation in the high-pressure regime is crucial to calibrate the SOP, if an *in situ* calibration method is used, in order to obtain the double-shocked state temperature T_2. Such relation has been experimentally studied by Millot et al. (2015).

The Hugoniot properties whose knowledge is necessary for the analysis of double-shock data are summarised in Table 6.1.

In this Section, we will present a fit of the $U_s - U_p$ relation at low pressures. Besides, we will present our study of the behaviour of the shocked refractive index in the transparent regime along the α-quartz principal Hugoniot. After this work, we will dispose of all the necessary knowledge of the behaviour of α-quartz to perform and analyse the results of double-shock experiments.

6.2.1 Shock – material velocity relation at low pressures

In the pressure range from $0.9 - 16$ Mbar, the $U_s - U_p$ relation along the principal Hugoniot α-quartz is very well expressed by a fit by Knudson and Desjarlais (2009). For pressures lower than the validity range of the fit, we built an interval-defined linear function to match the experimental data in the literature [Adadurov et al. (1962); L. V. Al'tshuler (1965); Trunin et al. (1971); Pavlovskii (1976); van Thiel (1977); Marsh (1980); Trunin (1994a)]. When shock-compressed up to very low material velocities ($U_p < 0.8$ km/s), α-quartz remains in the initial phase and the $U_s - U_p$ relation is

Table 6.1 – Properties along the principal Hugoniot of α-quartz that are necessary for the analysis of double-shock compression data.

Property	**Necessary for determining:**
ρ_0	ρ and P of states 1, 2, and 3o
$U_s(U_p)$	ρ and P of states 1 and 3o
$n(\rho)$	ρ_1 and P_1
$T(U_s)$	SOP *in situ* calibration; T_2 and T_{3o}

linear with a positive slope. At $U_p < 0.6$ km/s, due to the effects of the material strength, α-quartz exhibits a composite wave structure, with an elastic precursor wave and a subsequent plastic compression wave. Such effects have not been considered in this fit and will be treated afterwards in Section 6.5.

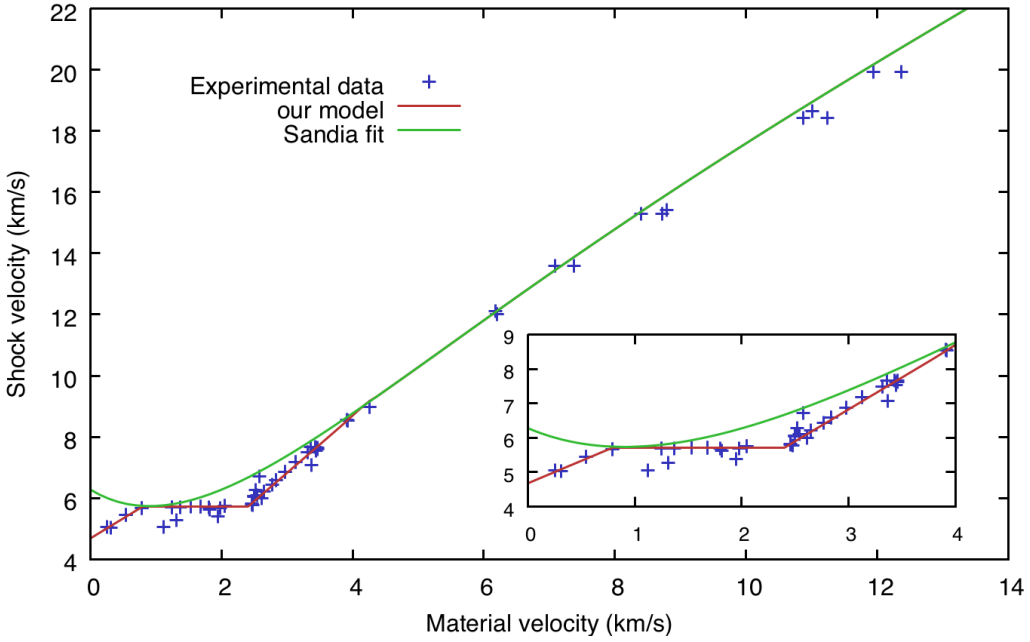

Figure 6.2 – Shock – material velocity relation for α-quartz showing experimental data [Adadurov et al. (1962); L. V. Al'tshuler (1965); Trunin et al. (1971); Pavlovskii (1976); van Thiel (1977); Marsh (1980); Trunin (1994b)], the fit done at the Sandia facility by Knudson and Desjarlais (2009), and our fit, which differs from the Sandia fit at low pressures. **Inset.** Zoom of the same plot at low-pressure conditions, to highlight the features of our fit and its divergence from that by Knudson and Desjarlais (2009).

Consistently with the analysis by Boettger (1992), in the interval 0.8 km/s $< U_p <$ 2.4 km/s shock-compressed quartz exhibits a mixed phase, as a direct α-quartz $\rightarrow$ stishovite phase transition is taking place. In this region, the shock velocity displays a constant value, around 5.7 km/s. For higher $U_p > 2.4$ km/s, the phase transition is complete and the phase of the shocked sample is stishovite. The slope of the $U_s - U_p$

relation is positive again. Figure 6.2 shows our fit of the $U_s - U_p$ relation as well as the high-pressure fit performed by Knudson and Desjarlais (2009) compared to the experimental data.

6.2.2 Refractive index

In double-shock experiments, we want the first shock to leave the sample in an optically transparent state so that we can directly probe the double-shocked volume. We have thus the necessity of characterising the state loaded by the first shock (state 1) as starting point for the action of the second shock front. Since state 1 is transparent, we can measure with the VISARs the velocity of the interface between the sample under study and a metallic layer placed before it. As such interface moves at the same speed as the shocked material, the material velocity U_p^1 can be measured. However, as we explained in Chapter 2.5.1, the VISARs do not directly measure such velocity: instead, they measure an apparent velocity U_{app}^1, which is linked to the actual material velocity through a relation including the first-shock velocity, U_s^0, the pristine refractive index n_0, and the refractive index of the state loaded by the first shock, n_1:

$$U_{\text{app}}^1 = n_1 U_p^1 - (n_1 - n_0) U_s^0. \tag{6.1}$$

Solving equation 6.1 requires the knowledge of the $U_s(U_p)$ dependency, so that U_s^0 and U_p^1 can be linked [as $U_s^0 = U_s(U_p^1)$], and the knowledge of the behaviour of the shocked refractive index as a function of the material velocity, $n(U_p)$ [so that $n_1 = n(U_p^1)$]. The refractive index can also be expressed as a function of another variable, *e.g.* the density, provided that such variable can be determined from U_p. After these relations have been applied, equation 6.1 becomes an implicit equation for U_p^1 and can be solved.

Present knowledge and our work

The α-quartz ordinary refractive indices at ambient pressure (1.5469 and 1.5341 at 532 nm and 1064 nm, respectively) are well known [Ghosh (1999)]. Very precise refractive index measurements up to 60 kbar are available [Jones and Gupta (2000); Jensen et al. (2007)], showing a linear relation between refractive index and density. However, the action of the first shock in our double-shock compression method brings the sample to considerably higher pressures of some 100 kbar, spanning the whole transparency range of the principal Hugoniot curve of α-quartz. At such conditions, no refractive index data were available at the beginning of this work.

In order to extend the range along the Hugoniot in which the refractive index of quartz is known, we performed an ancillary experimental campaign at the LULI2000 facility. We generated a uniform, transparent shocked state in an α-quartz sample by focusing a 10 ns long, weak ($\sim 10^{12}$ W/cm^2) laser pulse on a multi-layer target. The ablator / pusher combination was 10 μm CH / 40 μm Al or 2 μm Ti / 50 μm CH / 40 μm Al. On one half of the rear-side of the Al layer, we glued a 200 μm thick α-quartz window with a thin layer of formvar resin, in order to minimise the effect on the optical properties of the interface. This target type is denoted as target type (a) later in this Chapter. For some shots, a 100 μm LiF window was glued (also with formvar) on the other half of the Al surface [target type (b)]. Both target schemes are provided in Figure 6.3. We employed two different target types with the aim of

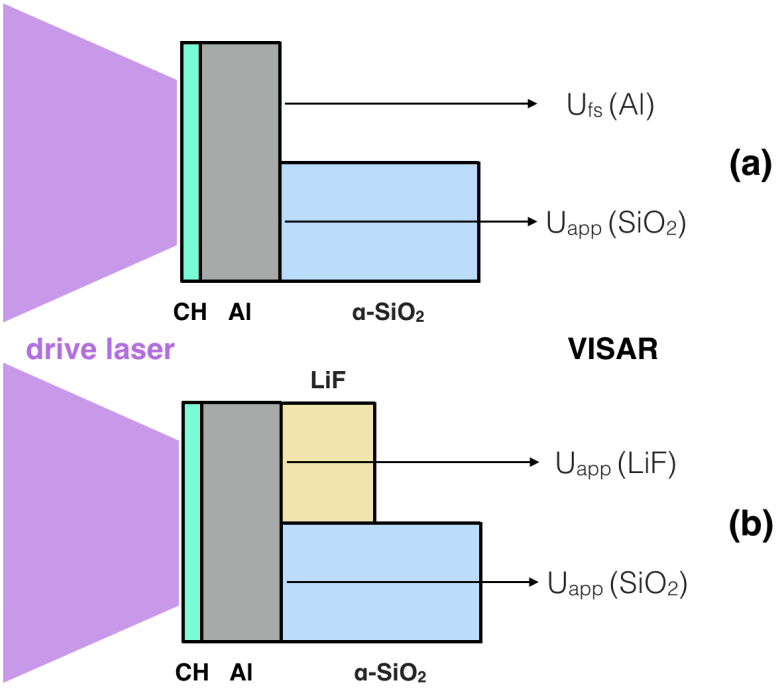

Figure 6.3 – Scheme of the target types **(a)** and **(b)** for the measurement of the quartz refractive index. The target type **(a)** allows the simultaneous measure of the free-surface velocity of aluminum and of the apparent velocity of the aluminum-quartz interface (that is, the apparent material velocity in quartz). The target type **(b)**, instead of the free-surface velocity of aluminum, allow the measure of the apparent velocity of the Al-LiF interface (that is, the apparent material velocity in lithium fluoride).

reducing systematic errors due to the use of tabulated EOS of the standard materials (Al, LiF) in the determination of the shocked state in α-quartz. Diagnostics included two VISARs, one at 532 nm and the other at 1064 nm. The thermodynamic state and the actual material velocity reached in the α-quartz sample have been obtained through an impedance mismatch analysis (see Chapter 2.3.4) with the aluminum layer and, for target type (b), the lithium fluoride sample. The refractive index has then been determined from the relation between the real and apparent material velocity in the α-quartz sample.

Data analysis

Target type (a): quartz + free-aluminum.

At the shock arrival at the rear-side aluminum surface, the free-surface velocity of aluminum U_{fs}(Al) and the apparent material velocity of the aluminum/α-quartz interface $U_{\text{app}}(\text{SiO}_2)$ have been measured. The material velocity in aluminum has been estimated from the measurement of U_{fs}(Al) by approximating the adiabatic release from the shocked state to the free-surface state ($P_{fs} = 0$) using the mirrored Hugoniot curve, that is, the symmetric curve with respect to the vertical line $U_p = U_p(Al)$. Such approximation, employed as no adiabatic release data are available in this region, is justified by the fact that the entropy increase along the Hugoniot at low pressures is negligible. The approximation gives $U_p(Al) = U_{fs}(Al)/2$. From $U_p(Al)$, the other

variables of the Hugoniot state reached in aluminum have been then obtained using the SESAME table 3713, which has been reproduced quite precisely by experimental studies [Knudson et al. (2003)]. As the shock impedance of quartz is lower than in aluminum, when the shock crosses the aluminum/quartz interface an adiabatic release takes place in the aluminum layer. The mirrored aluminum Hugoniot curve in the (P, U_p) plane has been used to approximate such release in aluminum towards state reached in α-quartz. The α-quartz Hugoniot curve from our fit (see Section 6.2.1) has been used. The intersection between the aluminum release and the quartz Hugoniot gave the reached (P, U_p) point in shocked quartz. A scheme of the impedance mismatch analysis is provided in Figure 6.4 (a). The refractive index of shocked quartz has then been extracted using the inverted equation 6.1:

$$n = \frac{U_{\text{app}} - U_s n_0}{U_p - U_s}. \tag{6.2}$$

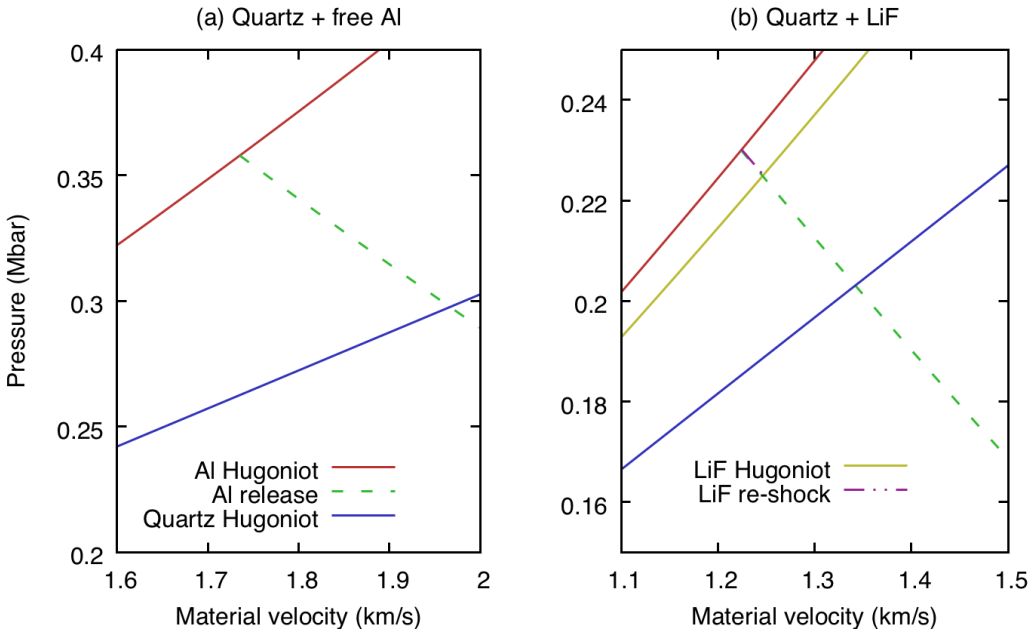

Figure 6.4 – Example of impedance mismatch analysis for a shot on a quartz + free-aluminum target **(a)** and on a quartz + lithium fluoride target **(b)** for the determination of the shocked quartz state in the context of the measurement of the quartz refractive index.

Target type (b): quartz + lithium fluoride.

For this type of target, we measure the apparent material velocity of the aluminum / LiF and of the aluminum / α-quartz interface, $U_{\text{app}}(\text{LiF})$ and $U_{\text{app}}(\text{SiO}_2)$, respectively, at the shock arrival at the rear-side aluminum surface. The principal Hugoniot and shocked refractive index of LiF are known [SESAME table 7270 and Rigg et al. (2014), respectively] and have been used to estimate the true material velocity in LiF $U_p(\text{LiF})$ and thus the reached pressure $P(\text{LiF})$. The state reached in aluminum has been determined through an impedance mismatch analysis between aluminum and LiF, using the mirrored Hugoniot of Al to approximate its adiabatic release towards the conditions reached in LiF. Finally, the (U_p, P) state reached in quartz has been measured

via an impedance mismatch analysis between aluminum and quartz. A scheme of the analysis is provided in Figure 6.4 (b). The refractive index of shocked-quartz has been measured using equation 6.2.

Table 6.2 – α-quartz refractive index shots. Targets of type (a) allow the simultaneous measurement of the apparent velocity in quartz and of the aluminum free-surface velocity. Targets of type (b) allow the measurement of the apparent velocity in lithium fluoride instead that of the aluminum free-surface.

Shot #	Target type	Density (g/cm^3)	Pressure (Mbar)	Refractive index
C-39	(b)	4.01 ± 0.08	0.292 ± 0.012	1.76 ± 0.04
C-46	(a)	4.22 ± 0.06	0.320 ± 0.008	1.81 ± 0.03
C-48	(a)	3.10 ± 0.03	0.124 ± 0.007	1.62 ± 0.02
C-51	(b)	3.47 ± 0.06	0.203 ± 0.011	1.68 ± 0.03
C-55	(a)	4.05 ± 0.06	0.298 ± 0.008	1.81 ± 0.03

Results

Our results (provided in Table 6.2) show that the α-quartz refractive index dependence on density can be reasonably assumed to be linear up to 4.2 g/cm^3 (320 kbar). Figure 6.5 shows the experimental results of this work together with previous low-compression data from Jones and Gupta (2000) and Jensen et al. (2007). The linear fits performed on the data from Jones and Gupta (2000) and on the results of this work, both forced to reproduce the known refractive index value at initial density, exhibit surprisingly similar slopes.

Error estimation

Errors in the refractive index measurements (appearing in Table 6.2) depend on the apparent material velocity measurement done with the VISARs and on the equation of state measurement done through impedance mismatch. A Monte-Carlo routine has been used to estimate the error on density and pressure of the reached state and on its refractive index. The data analysis code has been run 1000 times by varying the apparent material velocity in quartz and either the aluminum free-surface velocity [target type (a)] or the apparent material velocity in LiF [target type (b)]. Each input was extracted from a Gaussian distribution whose mean and standard deviation correspond to the measured value and its estimated uncertainty, respectively. The uncertainties on density, pressure, and refractive index have been estimated as the standard deviations of the output population.

6.3 Double-shock compression experiments

Once we have characterised the low-pressure behaviour of α-quartz along its principal Hugoniot, we are ready to apply the double-shock compression technique to α-quartz samples to explore high-pressure / moderate-temperature conditions.

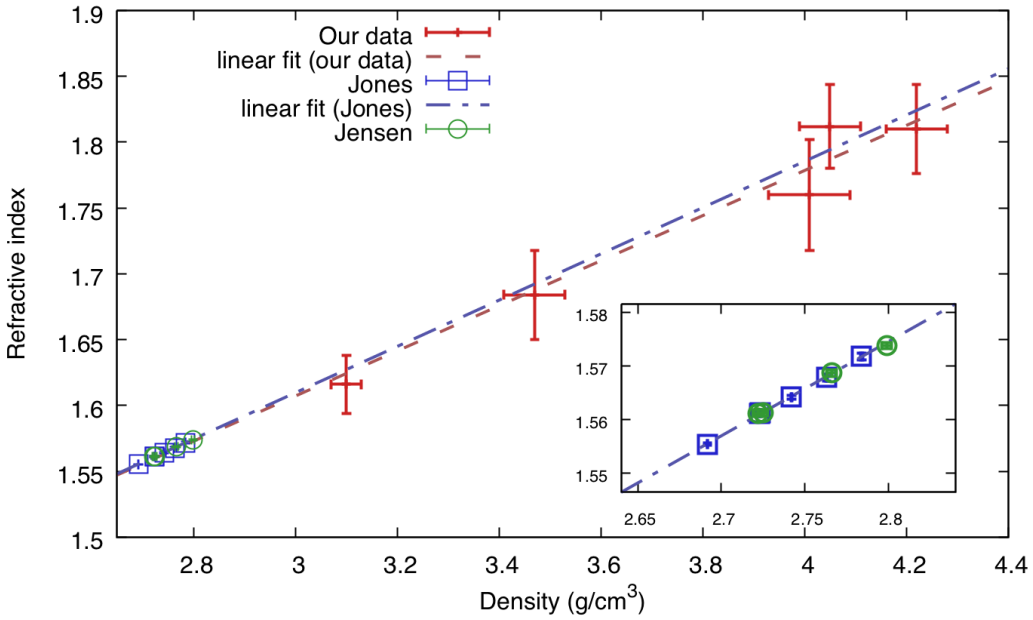

Figure 6.5 – Refractive index *vs* density for z-cut α-quartz. Our data (also shown in Table 6.2) are at 532 nm. Data from Jones and Gupta (2000) and Jensen et al. (2007) (highlighted on the inset) are at 514.5 nm and 532 nm, respectively. Both linear fits are forced to reproduce the known refractive index value at standard conditions.

6.3.1 Setup

Drive laser pulses at 527 nm were delivered by the North and South chains of the LULI2000 facility. The first pulse delivered $70 - 130$ J within a duration of 10 ns; the second one delivered $300 - 500$ J in 1.5 or 2 ns. Phase plates guaranteed a uniform illumination of the target on a circle with a 500 μm diameter. A time-profile plot of the two laser pulses for shot A-40 is provided in Figure 6.6 (top). Such profile has been optimised using MULTI simulations to ensure the stationarity of the first and second shock, that no unwanted reverberations occur, etc., as detailed in Chapter 3.3.4. The targets were mounted on cone-shaped plastic washers. Also the target structure has been optimised with the use of MULTI simulations. Targets were composed by a 10 μm thick polystyrene ablator, a 70 μm thick aluminum buffer layer, and 110 or 210 μm thick z-cut α-quartz samples. A scheme of the target is shown in Figure 6.6 (bottom).

Diagnostics included two VISARs, one working at 532 nm and the other at 1064 nm. VISARs were illuminated by a probe laser whose FWHM duration was $\sim$ 20 ns at 532 nm and $\sim$ 10 ns at 1064 nm. The VISAR velocity-per-fringe (VPF) parameters were 3.31 or 6.11 km/s (experiment A), 6.11 km/s (experiment B) and 4.96 km/s (experiment D) at 532 nm; 15.94 km/s (experiments A and B) and 12.81 km/s (experiment D) at 1064 nm. The couples of VPF values were chosen in order to measure both relatively low velocities (the apparent material velocity after the first shock compression) and relatively high velocity (the merged-shock velocity). A SOP collected the self-emission of the shocked target in a spectral range of 455 ± 10 nm (experiments A, B and D) or in a wider spectral range obtained by composition of different filters, in the 300-500 nm range (experiment D).

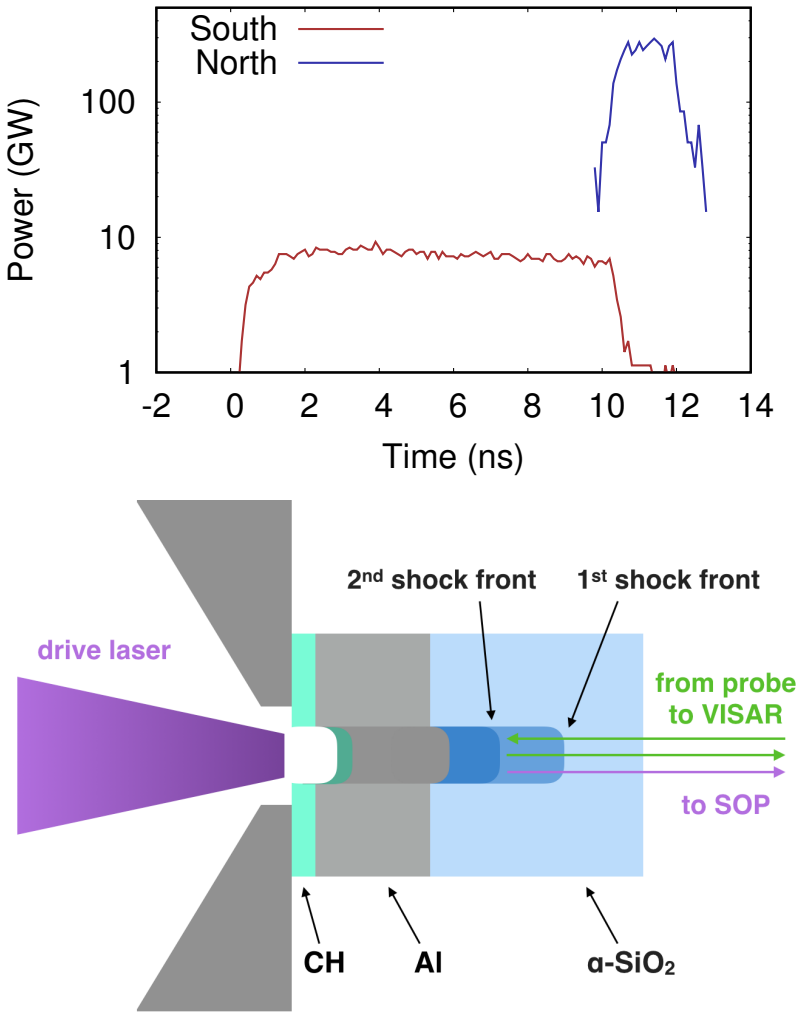

Figure 6.6 – **Top.** Time profile of the drive laser pulses for shot A-40. **Bottom.** Schematic picture of the target during the propagation of the two shock fronts inside the α-quartz sample. The focal spot is 500 μm, while the initial target thickness is 180 μm.

6.3.2 Diagnostics output

A typical VISAR and SOP output is shown in Figure 6.7. Also shown are the temporal profiles of the velocities – the material velocity for the state reached after the first shock, the shock velocity for the merged state – and of the thermal self-emission.

(i) At around 9 ns, the first shock enters the α-quartz sample. From around $9-13.5$ ns, the fringe system on the VISAR image, which measures the material velocity, is shifted. Its shift remains constant in time, since the first shock is stationary: this means that a key criterion for our double-shock compression technique – that of the stability of the first shock, which guarantees the spatial uniformity of the volume shocked by that shock – has been respected. No signal is detected by the SOP due to the weakness of this shock.

(ii) From around $13.5-14.5$ ns, the intensity of the VISAR signal drops and the fringe system is shifted again: the second shock has entered the sample, changing its

optical properties. The sample becomes absorbing or reflecting depending on the conditions reached. In Figure 6.7, the case of a reflecting double-shocked sample is shown: the probe laser is thus reflected onto the second shock front. The SOP displays a signal, since the second shock is strong enough to considerably heat the sample.

(iii) At 14.5 ns and 15 ns, the second shock merges with the first shock and with its elastic precursor, respectively. This causes an increase of the SOP signal, since the shock merging brings the shocked sample to a principal Hugoniot state. The VISAR measures the shock velocity of the merged shock. Since this merged shock is not sustained by the drive laser pulse, it decays in time.

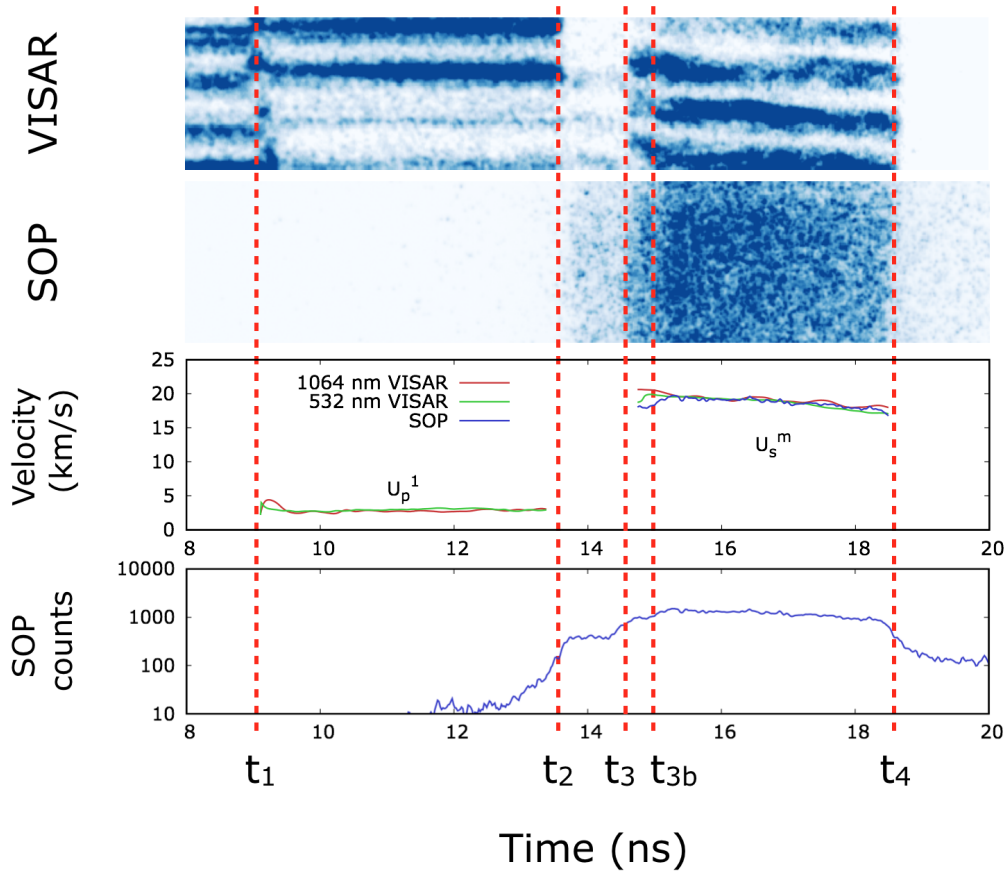

Figure 6.7 – From top to bottom: **(i).** output image example of the 1064 nm VISAR; **(ii).** output image example of the SOP; **(iii).** time profile of the measured material velocity after the first shock and merged shock velocity; **(iv).** time profile of the measured SOP counts. Timings t_1, t_2, t_3, t_{3b}, and t_4 represent the arrival time of the first shock into the sample, the arrival of the second shock into the sample, the catch-up time of the first shock by the second one, the catch-up time of the elastic precursor by the merged shock, and the exit time from the sample of the merged shock. In item (iii), we provide a merged shock velocity measurement which uses the temperature measured by the SOP and a temperature – shock velocity relation provided by Millot et al. (2015).

6.3.3 Thermodynamic states

Determining the probed thermodynamic state from the diagnostics output

As detailed in Chapter 3.3, the thermodynamic state reached after the loading of the first and merged shock (from now on, states 1 and 3, respectively) lie along the principal Hugoniot of α-quartz. State 1 belongs to the low-pressure, optically transparent regime. It has been determined from the measurement of the material velocity U_p^1. State 3 belongs to the high-temperature, optically reflecting regime. It has been obtained from the measurement of the merged-shock velocity. As the merged shock is decaying in time, state 3 has to be determined from the measurement of the merged shock velocity right after the merging, $U_s^m(t_3)$. A linear fit of the measured $U_s^m(t)$ is employed to determine the initial value. The fit of the principal Hugoniot of α-quartz used to determine states 1 and 3 from the experimental measurements is the one presented in Section 6.2.1.

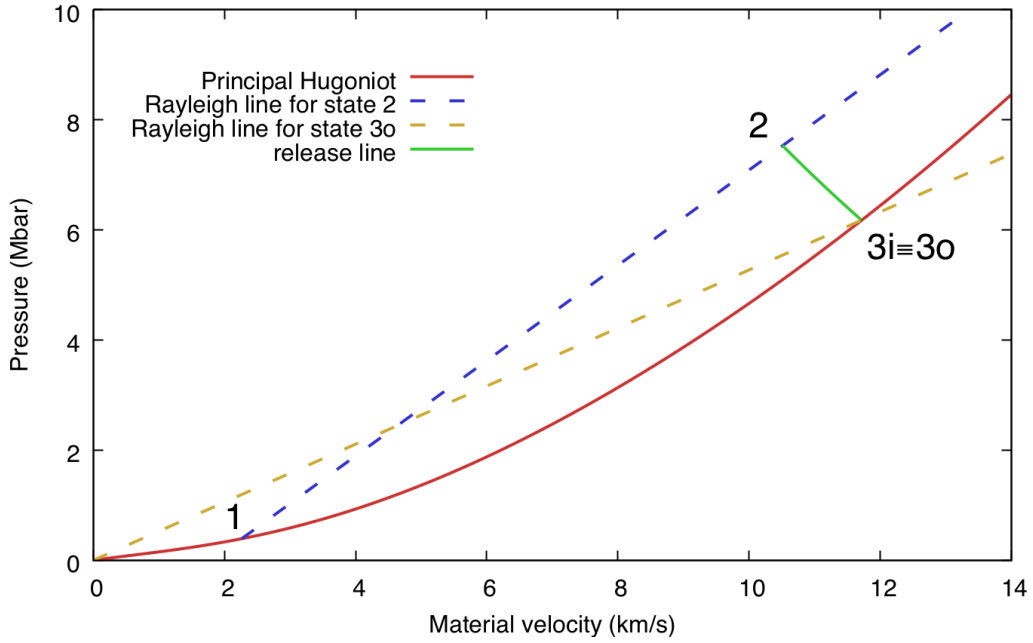

Figure 6.8 – Application of the self impedance mismatch, as detailed in Chapter 3.3.3, for the determination of state 2 for shot A-40. States 1 and 3 are identified along the principal Hugoniot of α-quartz. State 3 identifies two different states, 3o and 3i, with the same material velocity and pressure. A Rayleigh line is traced from state 1, with a slope depending on the measurement of the second-shock velocity. An adiabatic compression curve is traced from state 3, using the mirror-Hugoniot approximation. State 2 is identified as the intersection of the two curves.

The U_p and P conditions of the double-shocked state have been determined using a self-impedance mismatch analysis, as shown in Figure 6.8. Like standard impedance mismatch (see Chapter 2.3.4), this method is based on the modelling of the thermodynamic transition produced when a shock front crosses the interface between two materials with different impedances. However, in this case one does not deal with two materials but with different portions of the same sample: the state reached after first-shock loading and that reached after the merged-shock loading. The U_p and P

conditions of the double-shocked state are determined as the intersection between a Rayleigh line starting from state 1 (blue dashed line in Figure 6.8) and the adiabatic compression curve starting from state 3 (solid green curve in Figure 6.8). The Rayleigh line expresses the conservation of momentum across the second shock front. Its slope is $\rho_1 \left(U_s^1 - U_p^1\right)$. It can be calculated from the determination of state 1 (hence of ρ_1 and U_p^1) and from the measurement of the second-shock velocity U_s^1. The adiabatic curve describes the release from state 2 to state 3 after the merging of the two shocks.

The temperatures of states 2 and 3 have been estimated from the SOP self-emission measurement. For the measurement of the self-emission from state 2, the opacity of state 1 has been taken into account with the method described in Chapter 3.3.2. As shown in Figure 6.7, from the time-resolved temperature measurement with the SOP in the $t_3 - t_4$ interval, the merged-shock velocity can be extracted using the $T - U_s$ relation along the α-quartz principal Hugoniot curve provided by Millot et al. (2015). This measurement increases the redundancy already guaranteed by the use of two VISARs and may be useful in case of partial diagnostics failure.

Table 6.3 – Thermodynamic conditions reached in the double-shocked state and reflectivities of the second shock front. The frequencies Ω and 2Ω correspond to the probe laser wavelengths of 1064 nm and 532 nm, respectively. For shot B-98, the reflectivity at 1064 nm could not be determined due to partial diagnostics failure. For shot D-49, the reflectivity at both wavelengths could be estimated but are affected by high error bars due to the low quality of the VISAR output images.

Shot #	ρ_2 (g/cm^3)	P_2 (Mbar)	T_2 (10^3 K)	$R_2(2\Omega)$ (%)	$R_2(\Omega)$ (%)
A-15	$6.34^{+0.64}_{-0.15}$	$5.25^{+0.74}_{-0.62}$	11.6 ± 1.7	4.4 ± 0.9	7.3 ± 1.5
A-40	$7.4^{+1.6}_{-0.4}$	$7.75^{+0.88}_{-0.81}$	16.2 ± 2.4	12.9 ± 2.6	16.3 ± 3.2
A-49	$8.9^{+4.7}_{-1.4}$	$6.40^{+0.82}_{-0.79}$	27.9 ± 4.2	22.0 ± 4.4	32.8 ± 6.6
A-51	$7.6^{+2.8}_{-0.3}$	$10.7^{+1.1}_{-1.4}$	32.5 ± 4.9	29.5 ± 5.9	40.3 ± 8.1
A-53	$7.6^{+5.1}_{-0.4}$	$8.6^{+0.9}_{-1.1}$	36.0 ± 5.4	23.2 ± 4.7	32.8 ± 6.6
B-93	$7.3^{+1.5}_{-0.3}$	$8.21^{+0.90}_{-0.96}$	17.4 ± 2.6	8.0 ± 1.6	13.1 ± 2.6
B-98	$6.43^{+0.54}_{-0.31}$	$3.96^{+0.56}_{-0.48}$	7.9 ± 1.2	4.2 ± 0.8	n.a.
B-103	$6.80^{+0.96}_{-0.26}$	$6.22^{+0.77}_{-0.74}$	12.8 ± 1.9	5.0 ± 1.0	9.7 ± 1.9
B-109	$7.7^{+1.8}_{-0.4}$	$9.2^{+1.1}_{-1.0}$	19.7 ± 4.0	19.7 ± 3.9	35.9 ± 7.2
B-111	$7.0^{+1.1}_{-0.3}$	$7.31^{+0.88}_{-0.85}$	16.6 ± 2.5	12.6 ± 2.5	22.4 ± 4.5
D-49	$8.1^{+2.0}_{-0.8}$	$7.42^{+0.90}_{-0.80}$	16.0 ± 2.4	*4.0 ± 3.4*	*11.0 ± 7.1*
D-54	$7.24^{+0.97}_{-0.32}$	$7.53^{+0.88}_{-0.86}$	12.0 ± 1.8	6.9 ± 1.4	10.4 ± 2.1

The explored conditions

The thermodynamic states reached via double-shock compression span pressures from $4-11$ Mbar and temperatures from $8{\cdot}10^3$ K to $36{\cdot}10^3$ K. They are provided in Table 6.3 and shown, in the temperature – pressure plane, in Figure 6.9, where they are compared to the principal Hugoniot curves starting from fused silica, α-quartz, and stishovite. As shown in Figure 6.9, we probed intermediate states between the Hugoniot curves

of α-quartz and stishovite; in particular, we could explore temperatures up to three times lower than along the α-quartz Hugoniot at the same pressure. Such conditions are very difficult to reach with other methods, as they are distant from the different principal Hugoniot curves.

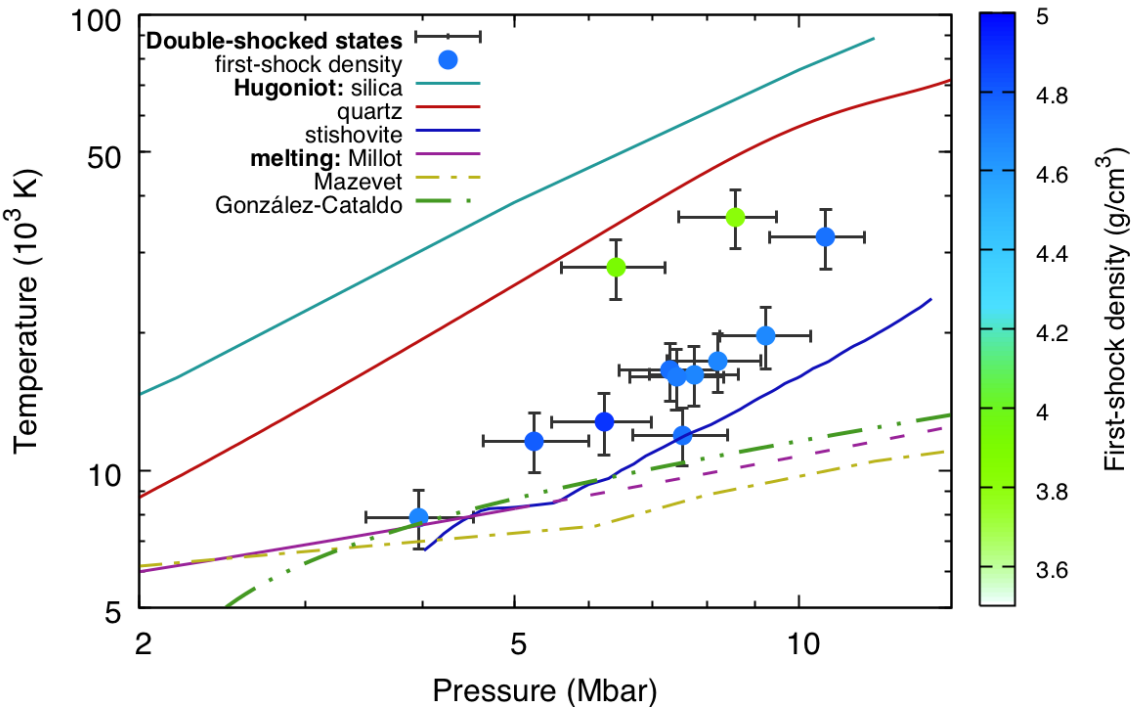

Figure 6.9 – Temperature and pressure conditions reached in the double-shocked state in our experiments. The colour scale indicates the density reached after the first-shock loading. The Hugoniot curves starting from fused silica [Mazevet et al. (2015)], α-quartz (see Section 6.2.1), and stishovite [Millot et al. (2015)] are shown for comparison. The different calculations of the melting curve of silica are from Millot et al. (2015), Mazevet et al. (2015), and González-Cataldo et al. (2016).

Figure 6.9 also shows the dynamic pre-compression obtained after the loading of the first shock. For two shots, the state loaded by the first shock had a lower density around $3.8 - 3.9$ g/cm^3. For all the other shots, this value was higher, between 4.6 and 4.8 g/cm^3. Such difference in the initial compression generated a clear differentiation in the conditions reached after the second shock loading. Indeed, the two shots with a low initial compression exhibited higher double-shocked state temperatures, closer to the principal Hugoniot of α-quartz, whereas for the other shots the double-shocked state is closer to the stishovite principal Hugoniot. This result proves how, in the context of double-shock compression, one can probe a wide set of conditions by varying the energy of the two drive laser pulses.

Error estimation

Errors on density and pressure have been estimated through a Monte-Carlo routine. The principles of Monte-Carlo routines have already been described in Section 6.2.2. The analysis has been run 1000 times changing the following inputs: the thickness of

the quartz sample ($1-2$ μm, indicated by the supplier), the timings t_1, t_2, t_3, t_{3b}, and t_4, and the velocities U_p^1 and $U_s^m(t_{3b})$. The errors on the timings depend on the VISARs and SOP time resolution and on the planarity of the shock profiles. In a typical case, uncertainties were about 5 pixels, or about 100 ps. Velocities directly measured by the VISARs (U_p^1 and U_s^m) are affected by an error due to the uncertainty on the fringe shift measure. We estimated it as 1/10 of a fringe. In the case of a material velocity measure, such as U_p^1, also the low-pressure $U_s - U_p$ relation and the shocked refractive index are error sources. A Taylor expansion of the $U_s - U_p$ relation thus gives the correct error estimation. The measurement of the merged shock velocity right after the merging, $U_s^m(t_3)$, is also affected by the uncertainty associated to the linear fit on $U_s^m(t)$ to extract that value. The indirect measurement of the second-shock velocity U_s^1 (see equation 3.6) was affected by the uncertainties on the material velocity U_p^1 and the timings t_1, t_2, and t_3. Errors on temperature have multiple sources: uncertainty on the SOP calibration parameter, on the measurement of the counts on the SOP image, on the measurement of reflectivity. Typical relative errors were of about 20%.

6.3.4 Shock-front reflectivities

The time-resolved intensity of the reflected probe lasers at 532 nm and 1064 nm have been measured by the VISAR working at the corresponding wavelength, allowing the extraction of the second-shock front reflectivities.

Data analysis

At first, the time-resolved reflectivity measurements have been calibrated using a reference image taken prior to the shock. Calibration has been then refined by considering the $R - U_s$ relations along the α-quartz Hugoniot measured by Millot et al. (2015) (at 532 nm) and Huser et al. (2015) (at 1064 nm). The merged-shock front reflectivity from t_3 to t_4 has been predicted from our measurement of $U_s^m(t)$ using such relations. The predicted reflectivity has been compared to the measured one, which has been rescaled to adhere to the prediction.

Figure 6.10 shows the time-resolved reflectivity measurements for shot D-54 (light green and red curves for the 532 nm and the 1064 nm VISAR, respectively) and the merged-shock front reflectivity profiles predicted by applying the models by Millot et al. (2015) (dark green curve) and Huser et al. (2015) (dark red curve) to our merged-shock measurements. During the time interval $t_2 - t_3$, in which the second shock propagates through the sample, the reflectivities at both wavelengths remain roughly constant (they slightly decrease in time). The time dependence of the merged-shock front reflectivities in the interval $t_3 - t_4$ qualitatively reproduce the behaviour predicted by the $R - U_s$ models.

Results

The optical reflectivities of the second-shock front at 532 nm and 1064 nm are shown in Figure 6.11, as a function of the measured temperature and pressure. They are also listed in Table 6.3. Previous measurements of reflectivity on the principal Hugoniot curves of α-quartz and stishovite are also shown. Intermediate states between the

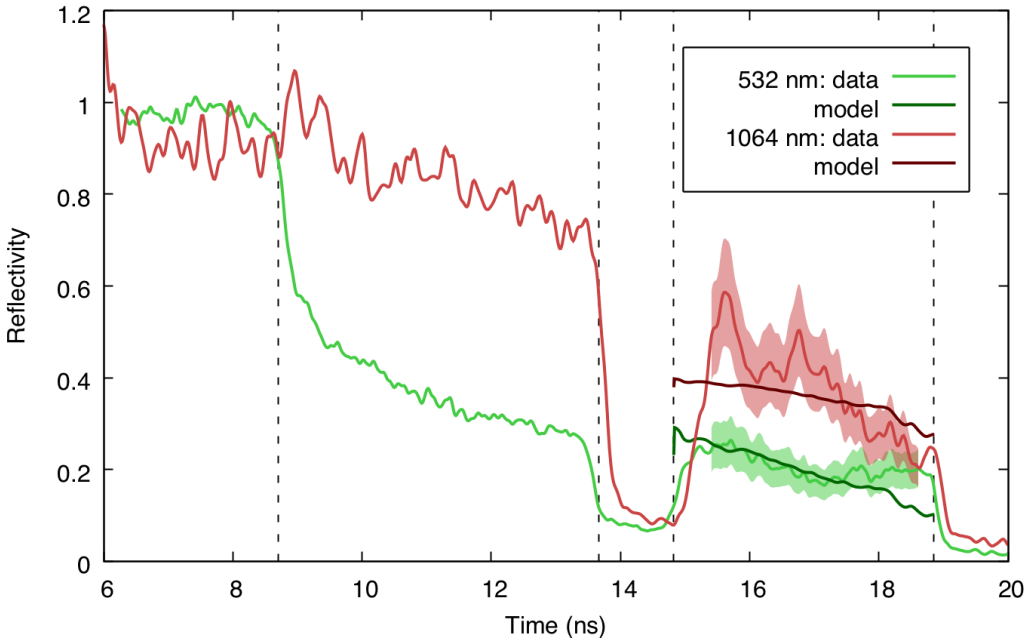

Figure 6.10 – Time-resolved reflectivity measured by the VISARs at 532 nm (green) and 1064 nm (red) for shot D-54. The timings t_1, t_2, t_3, and t_4 are indicated by dashed vertical lines. Before t_1, the reflectivity signals, which are relative to the aluminum/quartz interface and are calibrated using a reference image prior to the shock, are ~ 1, meaning that the reference value is reproduced. At $t = t_1$, the reflectivity signals, always relative to the aluminum/quartz interface start to slowly decrease at 1064 and abruptly decrease at 532 nm, under the action of the first shock loading. At $t = t_2$, the measured reflectivities start to be relative to the second-shock front. Both values are almost constant in time. In the interval $t_3 - t_4$, the measured values are relative to the merged shock front. Higher values than in the $t_2 - t_3$ interval are acquired, since the merged state is hotter and more reflecting. In this interval, the time-resolved reflectivities of α-quartz extracted from the VISAR measurement of U_s using the $R - U_s$ relations from Millot et al. (2015) (at 532 nm) and Huser et al. (2015) (at 1064 nm) are shown. Our measurements in the $t_2 - t_3$ and $t_3 - t_4$ intervals are calibrated using the aforementioned predictions.

principal Hugoniot curves of α-quartz and stishovite have been reached. At 532 nm, our reflectivity measurements span from 4.2% at the low temperature value of $8 \cdot 10^3$ K, near the melting curve, to 29% at $32 \cdot 10^3$ K, where silica is predicted to become an atomic fluid [Hicks et al. (2006)]. The 1064 nm reflectivity at the lowest probed temperature is not available due to partial diagnostics failure. The available data span from 7.3% at $12 \cdot 10^3$ K to 40% at the high temperature of $32 \cdot 10^3$ K, in the atomic-fluid phase.

Two of our data points (shots A-49 and A-53) are close in temperature and pressure to the α-quartz principal Hugoniot. In that region, the α-quartz reflectivity at 1064 nm is around $38 - 39\%$, near its saturation value. At 532 nm, it is still increasing with temperature and pressure. Near our data points, it is around $25 - 27\%$. Our data points exhibit slightly lower reflectivities than the Hugoniot profiles: around 33% at 1064 nm and $22 - 23\%$ at 532 nm. Such a discrepancy can be explained with the fact that single-shock and double-shock compression are not immediately comparable, as we discussed

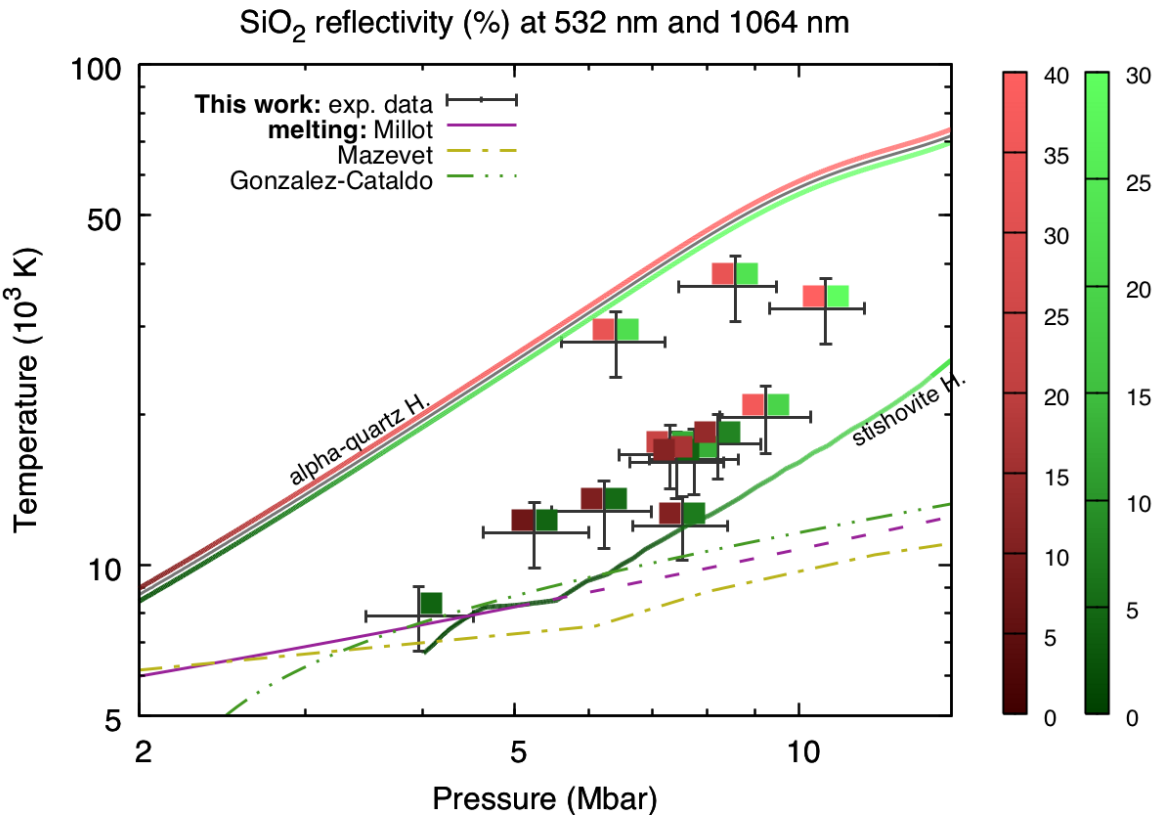

Figure 6.11 – Shock-front reflectivity of silica at 532 nm and 1064 nm as a function of pressure and temperature. The experimental data of this work are shown. Crosses indicate the thermodynamic conditions. Squares are coloured in red and green according to the reflectivity at 1064 nm and 532 nm, respectively. The α-quartz $T-P$ relation and reflectivity at 532 nm (green colour scale of the curve) along the Hugoniot are from Millot et al. (2015). Reflectivity data at 1064 nm (red colour scale) along the α-quartz Hugoniot curve are from Huser et al. (2015). The stishovite Hugoniot curve has been calculated using data from Millot et al. (2015), which also includes reflectivity at 532 nm (green colour scale of the curve). The melting curves of silica are the same as in Figure 6.9.

in Chapter 4.4.4. In double-shock data, the reflecting surface is the interface between the sample shocked by the first shock (characterised by a higher refractive index than the initial one) and the sample shocked by the second shock. Single-shock data, on their side, are relative to the interface between the pristine and the shocked state. As a consequence, the same shocked state generates a lower shock-front reflectivity within our approach than within a single-shock compression approach, as it is the case. We can also compare the reflectivity in shot D-54 to that along the principal Hugoniot of stishovite, as we probed conditions very close to that curve. Along the stishovite Hugoniot, we dispose only of the reflectivity at 532 nm [Millot et al. (2015)]. At that wavelength, we measured a value around 6.9%, to be compared with an interval, centred around 4.5%, from $0.5 - 8.5\%$ spanned along the stishovite Hugoniot at the pressures compatible with our datum within error bars. In general, we can say that our data points close to conditions already explored are compatible with the previous measurements of reflectivity.

Another aspect that shall be studied is the dependence on pressure and temperature of the optical reflectivities. Experiments probing the principal Hugoniot cannot discriminate between the two state variables but only study the reflectivity as a function of both variables along that curve. As we already said, a critical advantage of the double-shock technique is the possibility of tuning both pressure and temperature by controlling the intensity of the two shock waves that sequentially bring the sample to the desired state. As a consequence, the effects of pressure and temperature can be considered separately. In our experimental data, we can clearly distinguish that clusters of conditions at similar temperatures exhibit roughly the same reflectivity:

(i) from $(8-13)\cdot 10^3$ K, reflectivity values are low ($4-7\%$ at 532 nm, $7-10\%$ at 1064 nm);

(ii) between $(16-17)\cdot 10^3$ K, intermediate values ($8-13\%$ at 532 nm, $13-22\%$ at 1064 nm) are observed;

(iii) finally, at high temperatures $30\cdot 10^3$ K, the highest reflectivity values are measured ($22-30\%$ at 532 nm, $33-40\%$ at 1064 nm).

In particular, our lowest-temperature datum (shot B-98) is very close to the melting curve of silica as predicted by calculations [Mazevet et al. (2015); González-Cataldo et al. (2016)] and obtained in shock experiments [Millot et al. (2015)]. Its very low reflectivity at 532 nm (4.2%) indicates that, at the explored conditions, silica is still electrically insulating, as the shock-front reflectivity is mainly due to the increase of the real part of the refractive index due to shock-compression. The behaviour of reflectivity appears to be primarily driven by temperature; only slight changes are associated to the increase of pressure. We interpret this behaviour as the consequence of the fact that the onset of conductivity (hence of reflectivity) is primarily driven by thermally-activated ionisation.

Error estimation

Uncertainties on the second-shock front reflectivity are mainly due to calibration. Other sources of error include the noise in the VISAR output and the spatial non-uniformity of the shock fronts. Typical relative error bars are of about 20%.

6.4 Study of the electrical conductivity

The optical reflectivity of the second-shock front encodes essential information about the electrical conductivity of the double-shocked state. However, the relation between reflectivity and conductivity is far from being straightforward. To infer the second from the first, assumptions about the electrical behaviour of the sample have to be made. Simplistic approaches such as the Drude and Drude-Smith models are often used, but generally fail in reproducing the actual behaviour of the conductivity in Warm Dense Matter, as discussed in Chapter 4.3.7. Therefore, we developed and employed an alternative approach based on the insights from *ab initio* calculations from Laudernet et al. (2004) and F. Soubiran about the conductivity behaviour of warm dense silica. We estimated the electrical conductivities at 532 nm and 1064 nm from the measured

shock-front reflectivities at the same wavelengths. The optical conductivities were then used to estimate the static conductivity.

6.4.1 Ab initio calculations

Ad hoc ab initio calculations of the electrical conductivity and complex refractive index of warm dense silica along or near the principal Hugoniot curve of stishovite have been performed by F. Soubiran. Six thermodynamic states have been simulated – four along the stishovite Hugoniot and two at lower pressures. The probed conditions are shown in the temperature – pressure plane in Figure 6.12 together with similar calculations from Laudernet et al. (2004).

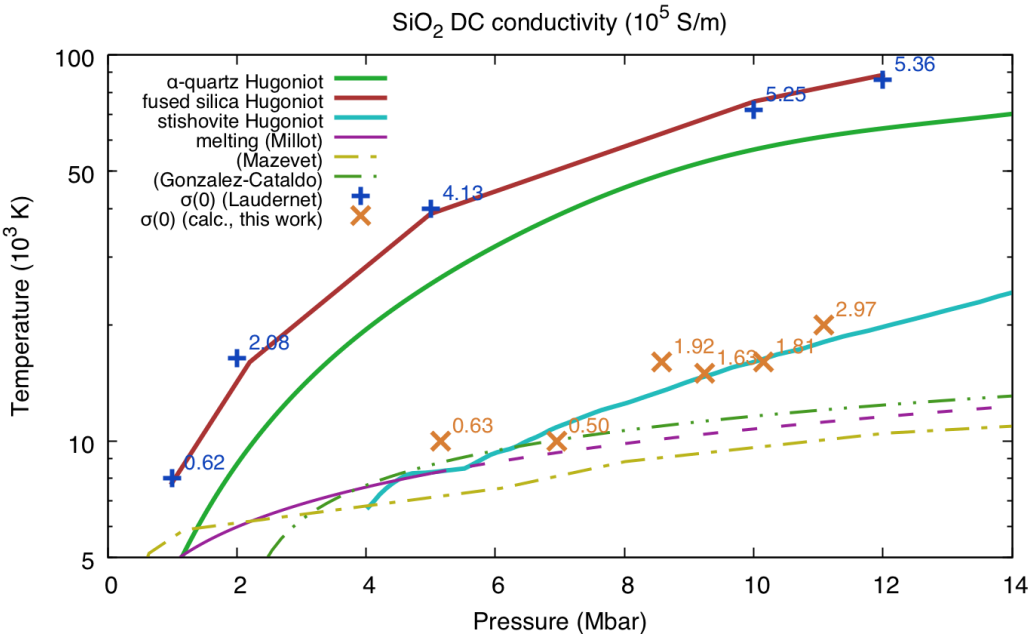

Figure 6.12 – Static electrical conductivity of silica according to calculations from Laudernet et al. (2004) (blue crosses) and performed by F. Soubiran (orange xs). The α-quartz and stishovite Hugoniot curves are from Millot et al. (2015). The fused silica Hugoniot curve is from Mazevet et al. (2015). The melting curves of silica are the same as in Figure 6.9.

The optical reflectivities at 532 nm and 1064 nm have been calculated from the simulated complex refractive indices using Fresnel's law. The reflectivities of the states along the stishovite principal Hugoniot have been calculated using the pristine refractive index of stishovite $n_{0,\text{stishovite}} = 1.799$ [Sclar et al. (1962)] as index before the shock loading. For the states off the stishovite Hugoniot, the shocked refractive index of α-quartz corresponding to the initial compression needed to reach those conditions via a double-shock technique has been used as index before the shock loading ($n_{1,\alpha\text{-quartz}} = 1.89$ and 1.91 for the high-pressure and low-pressure datum, respectively).

The reflectivities calculated with this approach have been compared to our experimental reflectivity data, as shown in Figure 6.13. Since the calculated and experimentally achieved thermodynamic states are close, a comparison between the reflectivity data sets can be made. The calculated and experimental reflectivity behaviours exhibit

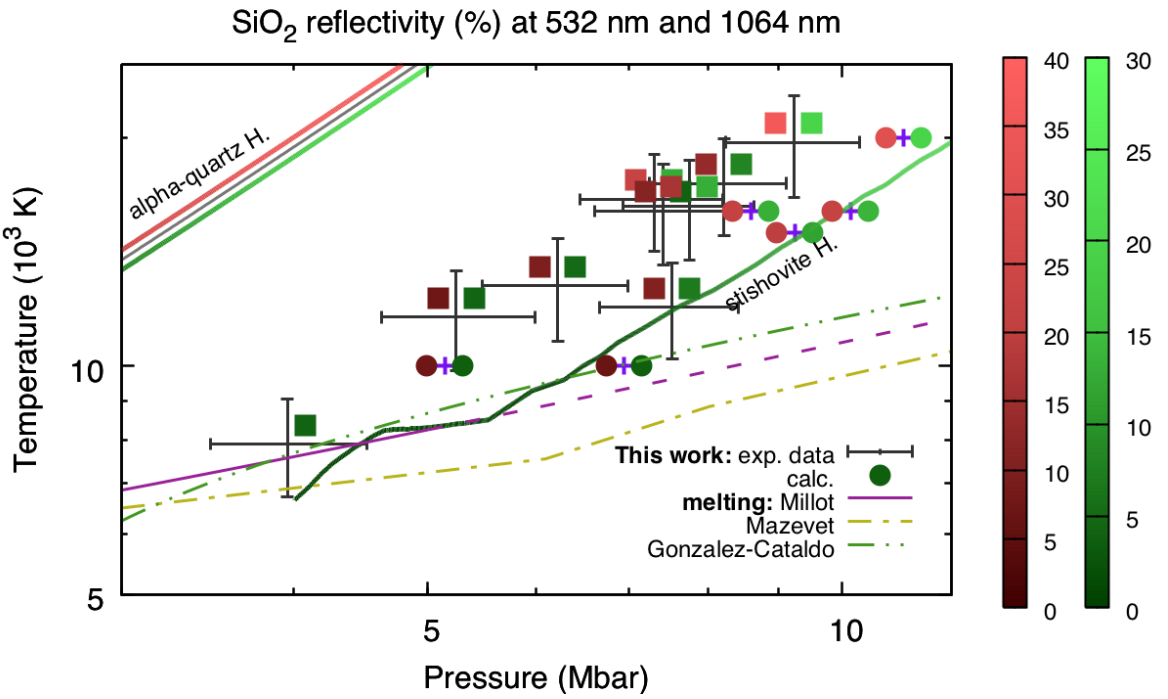

Figure 6.13 – Shock-front reflectivity at 1064 nm and 532 nm of warm dense silica. Grey crosses are the conditions experimentally explored via double-shocks; violet crosses are the conditions simulated by F. Soubiran. Coloured squares (experimental data) and circles (calculations) on the left and right side of the crosses express the reflectivity at 1064 nm and 532 nm, respectively, according to the colour scale. The melting curves of silica are the same as in Figure 6.9.

a remarkable agreement. The calculated values at 10 kK are slightly lower than the experimental values at around 12 kK. The experimental values at around $16-17$ kK are comparable to, but slightly lower than, the calculated values at $15-16$ kK. Finally, our experimental datum at 20 kK agrees within its error bars with the calculated datum at the same temperature. Our experimental data at higher temperatures cannot be compared to the calculations, which reach a maximum temperature of 20 kK. However, it should be noticed, as we did in Section 6.3.4, that the shock-front reflectivity in the case of single-shock and double-shock compression are not immediately comparable.

Given the fair agreement between our reflectivity data and the predictions of these simulations, the latter have been employed, together with the results from Laudernet et al. (2004) (also shown in Figure 6.12), to build a model of the conductivity behaviour of warm dense silica as a function of pressure and temperature. Such model has been used, as it will be explained later in Section 6.4.2, to estimate the conductivity from the measured reflectivity without recurring to a simplistic Drude approach, which is not representative of the real frequency dependence of the conductivity of silica. Indeed, the Drude model predicts a maximum at zero-energy and a negative monotonic slope for positive energies. This behaviour is far from that predicted by simulations, which is shown in Figure 6.14. The slopes of the curves describing real parts of the conductivity are positive up to a global maximum whose position shifts towards the right with the increase of temperature (from around 19 to 20 eV). After the maximum, the slopes of

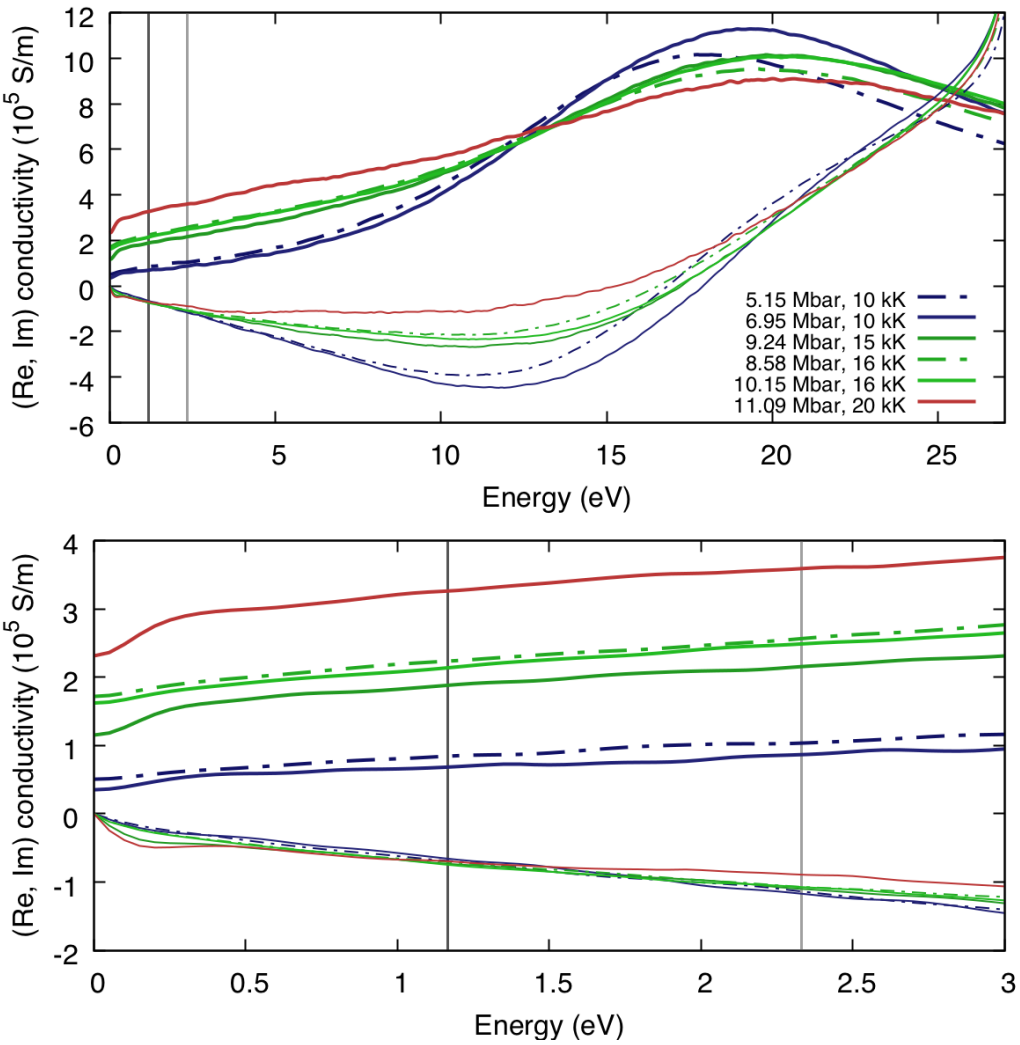

Figure 6.14 – **Top.** Real and imaginary part of the electrical conductivity of silica as a function of photon energy according to the calculations performed by F. Soubiran. Each thick (thin) curve represents the real (imaginary) part of the conductivity for a given thermodynamic state. The dark and light grey vertical lines correspond to the photon wavelengths of 1064 nm and 532 nm, respectively, at which the optical reflectivity has been measured in our experiments. **Bottom.** Zoom of the plot at low photon energies. The low-energy conductivity is not well computed due to the finite size of the computation cell [Soubiran and Militzer (2018)].

the curves become negative. The imaginary parts of the conductivity are zero at zero energy, as imposed by the Kramers–Kronig relations, then decrease assuming negative values up to a minimum at around $10 - 11$ eV. At higher energies, they increase and eventually assume positive values. In the high-frequency limit, the imaginary parts become much higher than the real parts of the conductivity – the electric current is in phase quadrature with the electric field. The bottom of Figure 6.14 shows a zoom on the low-energy part of the conductivity – photon energy plot. The energies corresponding to the probe lasers employed in our experiments are shown as grey vertical lines. In this low-energy range, calculations predict an almost linear energy dependence of the real part of the conductivity. The slope changes at very low energies below 0.3 eV.

This behaviour is not physical but is due to the finite size of the cells employed in the simulations. As a consequence, the static conductivity has to be computed by extrapolating a linear fit of the low-energy portion of the curve [Soubiran and Militzer (2018)].

6.4.2 Optical conductivities

The measurement of the shock-front reflectivities at 532 nm and 1064 nm allows us to estimate the electrical conductivities at the same wavelengths. In our method, the relation between the real and imaginary part of the conductivity, which is a key factor for the determination of the complex conductivity from a reflectivity measurement, has been estimated using the results of *ab initio* calculations instead of employing a simplistic Drude model.

From the reflectivity to the optical conductivity

In Chapter 4.3.7, we have already presented the relation, for a given wavelength, between the measured reflectivity of a shock front, the refractive index of the shocked sample, and its electrical conductivity in the case of a material exhibiting a local-response behaviour. Such discussion was reduced to the case of single-shock compression. Within the framework of double-shock compression, the reflectivity of the first shock front was negligible ($\leq 1\%$), due to the low change in the refractive index in the first compression. We could therefore assume that we essentially measure the second-shock front reflectivity $R_2(\omega)$ at the two probe laser frequencies $\omega = \Omega,\ 2\Omega$ (corresponding to the wavelengths of 1064 nm and 532 nm, respectively).

$R_2(\omega)$ can be linked to the refractive indices of states 1 and 2 at the same frequency, $\tilde{n}_1(\omega)$ and $\tilde{n}_2(\omega)$, respectively, via the Fresnel's equation:

$$R_2(\omega) = \left| \frac{\tilde{n}_2(\omega) - \tilde{n}_1(\omega)}{\tilde{n}_2(\omega) + \tilde{n}_1(\omega)} \right|^2 , \tag{6.3}$$

where $\tilde{n}_1(\omega)$ was determined from the measurement of the thermodynamic state 1.

In the same way as for the discussion of the conductivity of water and the SPM along their principal Hugoniot curves (see Chapter 4.3.7), we recall that the complex refractive index of the double-shocked state 2 can be linked to its complex electrical conductivity via

$$\tilde{n}_2(\omega) = \left[\left(n_2^b(\omega) \right)^2 + \frac{i\tilde{\sigma}_2(\omega)}{\epsilon_0 \omega} \right]^{1/2} , \tag{6.4}$$

where $n^b(\omega)$ is the contribution of the bound electrons to the refractive index at the frequency ω. To estimate $n^b(\omega)$, we used the linear dependence on density of the total refractive index of shocked α-quartz, as measured in Section 6.2.2, and extrapolated it up to the conditions reached by double-shock compression. Such approximation does not introduce large uncertainties since, as discussed in Chapter 4.3.7, in the electrically conducting regime we explored the dependence of $\tilde{n}_2(\omega)$ on $n^b(\omega)$ is low. The dominant contribution to $\tilde{n}_2(\omega)$ is the given by the conductivity term instead.

At this point, the complex optical conductivity of state 2, $\tilde{\sigma}_2(\omega)$, cannot be univocally determined without further assumptions. Indeed, the system to be solved is

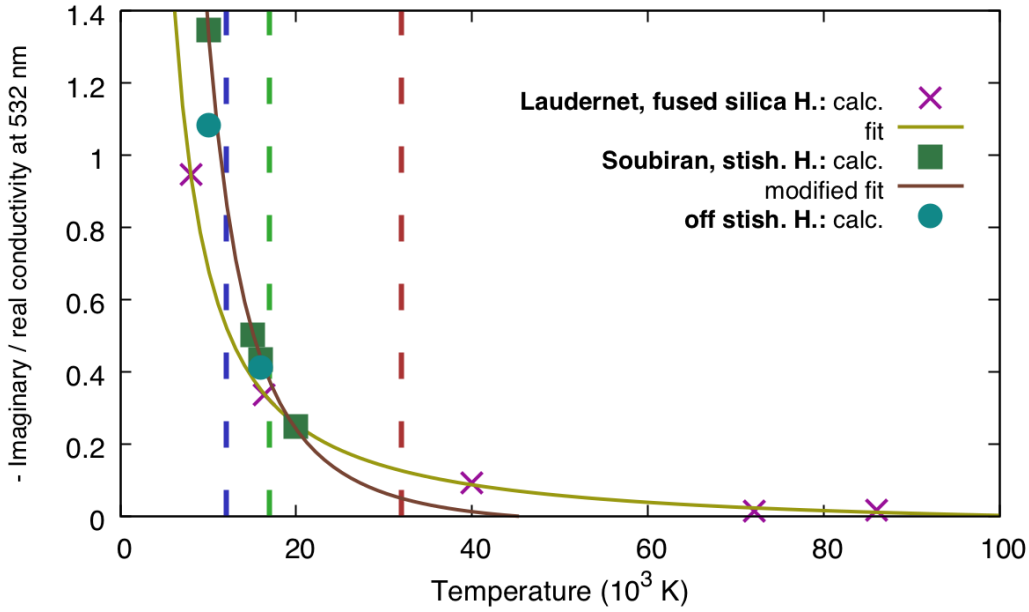

Figure 6.15 – Opposite of the ratio between the imaginary and real parts of the conductivity at 532 nm ($-\Im[\tilde{\sigma}(2\Omega)]/\Re[\tilde{\sigma}(2\Omega)]$) according to calculations from Laudernet et al. (2004) and by F. Soubiran, as a function of temperature. The three dashed vertical lines indicate the temperatures of the isotherms considered in this study (12 kK, 17 kK, and 32 kK).

composed only by one equation linking the measured reflectivity to the complex optical conductivity, but has two unknowns, $\Re[\tilde{\sigma}_2(\omega)]$ and $\Im[\tilde{\sigma}_2(\omega)]$. Therefore, an additional relation including the unknowns must be considered. In the Drude model, such relation is implicitly provided by the functional form of $\tilde{\sigma}(\omega)$, provided in equation 4.9. In our case, we wanted to find a more significative relation $\Re[\tilde{\sigma}_2(\omega)]$ and $\Im[\tilde{\sigma}_2(\omega)]$ at both probe laser frequencies ($\omega = \Omega$, 2Ω) without the use of the simplistic Drude approach. First, we have interpolated the ratio between $\Re[\tilde{\sigma}_2(\omega)]$ and $\Im[\tilde{\sigma}_2(\omega)]$ along the fused silica and stishovite Hugoniot conditions explored by the *ab initio* simulations from Laudernet et al. (2004) and F. Soubiran, respectively (see Figure 6.12), which we have previously validated by comparing our reflectivity data with their predictions. The calculated ratios are shown in Figure 6.15 as a function of temperature. We performed a fit on both datasets with the function

$$r(\omega, T) = a(\omega) + \frac{b(\omega)}{T} + \frac{c(\omega)}{T^2}, \tag{6.5}$$

where

$$r(\omega, T) = -\frac{\Im[\tilde{\sigma}(\omega, T)]}{\Re[\tilde{\sigma}(\omega, T)]} \tag{6.6}$$

is the opposite of the ratio between the imaginary and real part of the conductivity at a given probe laser frequency.

To estimate $r(\omega)$ to our conditions, which are off both the fused silica and the stishovite Hugoniot, we considered their pressure and temperature dependence. In particular, the effect of pressure on $r(\omega)$ appears to be weak. Therefore, we operate a linear interpolation between the values from Laudernet et al. (2004) and F. Soubiran

along isothermal lines:

$$r^m(\omega, P, T) = r^L(\omega, T)\frac{P_{\text{stishovite}}(T) - P}{P_{\text{stishovite}}(T) - P_{\text{fused}}(T)} + r^S(\omega, T)\frac{P - P_{\text{fused}}(T)}{P_{\text{stishovite}}(T) - P_{\text{fused}}(T)}, \tag{6.7}$$

where $r^m(\omega, P, T)$ is the estimated ratio at a certain frequency for a pressure P and a temperature T, $r^L(\omega, T)$ and $r^S(\omega, T)$ are the ratios given by the fit on data from Laudernet et al. (2004) and from the calculations by F. Soubiran, respectively, and $P_{\text{stishovite}}(T)$ and $P_{\text{fused}}(T)$ are the Hugoniot pressure of stishovite and fused silica at the temperature T, respectively. This interpolation has physical meaning for $P_{\text{fused}}(T) < P < P_{\text{stishovite}}(T)$, which is always the case for our data.

Table 6.4 – Conductivity data for double-shocked α-quartz. Ω indicates a wavelength of 1064 nm, 2Ω a wavelength of 532 nm. The real part of the conductivity at each wavelength is shown together with its positive and negative error bar. Conductivity values are expressed in 10^5 S/m. For shot D-49, the error bars on conductivity are not available due to the high uncertainties of the reflectivity measurements. Conductivity data are provided as estimations.

Shot #	$\Re[\tilde{\sigma}_2(2\Omega)]$	Δ_+	Δ_-	$\Re[\tilde{\sigma}_2(\Omega)]$	Δ_+	Δ_-	$\sigma_2(0)$	Δ_+	Δ_-
A-15	0.93	0.24	0.22	0.78	0.17	0.16	0.60	0.10	0.09
A-40	2.75	0.61	0.63	1.75	0.38	0.44	1.72	0.28	0.30
A-49	4.4	1.3	1.4	3.9	1.3	1.8	3.7	0.8	1.0
A-51	7.3	2.1	3.0	6.3	2.4	4.1	6.6	1.5	2.4
A-53	4.5	1.3	1.5	3.6	1.2	1.7	3.9	0.8	1.1
B-93	1.74	0.41	0.37	1.40	0.29	0.31	1.27	0.20	0.20
B-98	0.46	0.16	0.21	n.a.	n.a.	n.a.	n.a.	n.a.	n.a.
B-103	1.09	0.29	0.26	1.05	0.22	0.22	0.78	0.13	0.12
B-109	4.4	1.0	1.2	5.3	1.8	2.8	3.9	0.9	1.4
B-111	2.73	0.56	0.59	2.62	0.64	0.81	2.13	0.35	0.41
D-49	*0.75*	n.a.	n.a.	*1.15*	n.a.	n.a.	*0.75*	n.a.	n.a.
D-54	1.22	0.36	0.35	1.02	0.25	0.25	0.80	0.15	0.15

Results

Using the procedure we have detailed to determine the ratio between real and imaginary part of the conductivity, we could write the latter as

$$\tilde{\sigma}_2(\omega) = \Re[\tilde{\sigma}_2(\omega)][1 - i \cdot r^m(\omega, P_2, T_2)], \tag{6.8}$$

where P_2 and T_2 are the measured pressure and temperature of the double-shocked state, respectively. Equation 6.8 has been substituted into equation 6.4 and then into equation 6.3 to infer the real part of the conductivity at $\omega = \Omega$, 2Ω from the measurement of the second-shock front reflectivity at the same frequency.

The electrical conductivity values at 532 nm and 1064 nm of the double-shocked states found in such a way are provided in Table 6.4. They are also shown in Figure 6.16, where they are compared with the values calculated by F. Soubiran. At low temperatures [$(10 - 12) \cdot 10^3$ K], the calculated and experimental conductivities are compatible. At intermediate temperatures [$(15 - 17) \cdot 10^3$ K], our experimental values

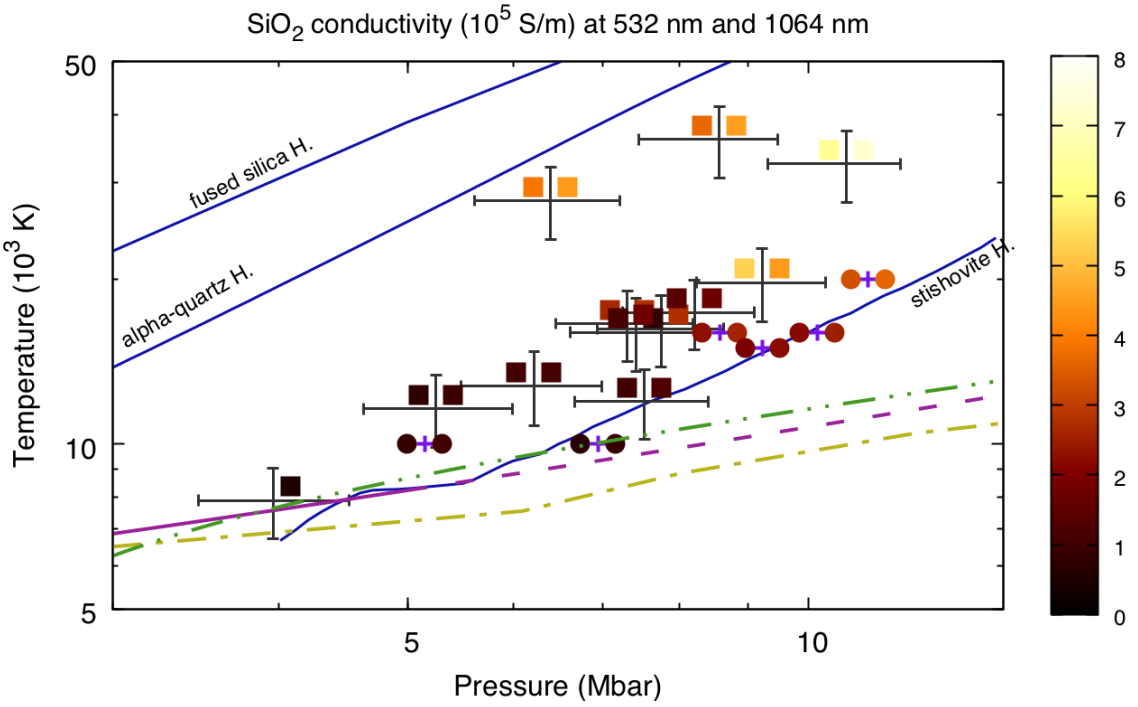

Figure 6.16 – Optical conductivities of warm dense silica. Grey crosses are the conditions experimentally explored via double-shocks; violet crosses are the conditions simulated by F. Soubiran. Coloured squares (experimental data) and circles (calculations) on the left and right side of the crosses express the conductivity at 1064 nm and 532 nm, respectively, according to the colour scale. The melting curves of silica are the same as in Figure 6.9.

are slightly lower than the calculated ones, following the same ordering as for the reflectivities (see Section 6.3.4). Finally, our experimental datum at $20 \cdot 10^3$ K exhibits higher conductivities than the calculated one: 4.4 and 5.3 $\cdot 10^5$ S/m at 532 nm and 1064 nm, respectively, against 3.6 and $3.2 \cdot 10^5$ S/m. However, due to the high error bars associated to our datum, the two are compatible.

Error estimation

The estimation of the optical conductivity values is delicate and depends on several parameters. The most important error source for $\sigma(\omega)$ is the second-shock reflectivity measure at the same wavelength, $R_2(\omega)$. Other error sources are the double-shocked density (which influences the estimated contribution of the bound electrons to the refractive index, n_b), and the double-shocked state pressure and temperature (which influence the estimation of the ratio between imaginary and real part of the conductivity, as detailed in Section 6.4.2).

The errors on electrical conductivity have been estimated using a Monte-Carlo routine. The routine repeated the analysis 5000 times varying the following inputs: ρ_2, T_2, P_2, $R_2(\Omega)$, $R_2(2\Omega)$. Figure 6.17 shows a subset of the conductivity output data as a function of the reflectivity input.

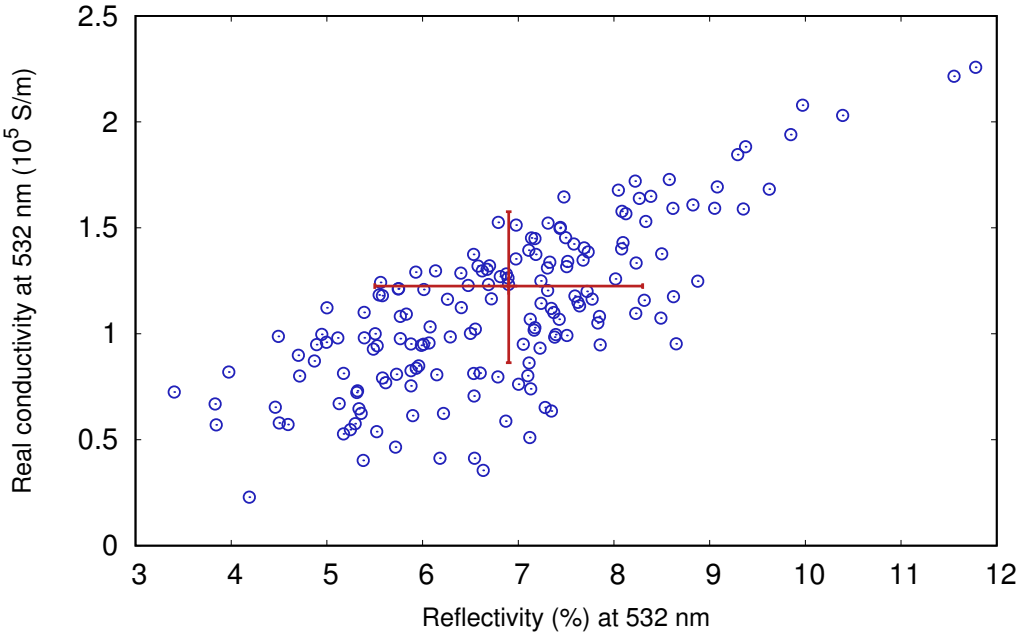

Figure 6.17 – Monte-Carlo error estimation of the double-shocked conductivity for shot D-54. The real part of the optical conductivity at 532 is shown against the reflectivity. Each blue circle represents the result of a single run of the Monte-Carlo routine. Only a fraction of the 5000 total runs is shown, to increase the readability of the Figure. A strong correlation between the reflectivity and the associated conductivity is evident. The red cross indicates the central value with the error bars associated to $R(2\Omega)$ and $\Re[\tilde{\sigma}(2\Omega)]$.

6.4.3 Static conductivity

Up to now we have characterised the optical conductivities of warm dense silica. Such properties have an immediate interest as benchmark values for the *ab initio* simulations of the frequency dependency of the conductivity and, more generally, for the study of the electrical properties of materials in the WDM regime. However, only the study of the static conductivity $\sigma(0)$ is relevant for planetary science, given the very low-frequency nature of the dynamo action inside planets (see Chapter 1.2.2).

From the optical to the static conductivity

We can keep using the previous approach to estimate the static conductivity of the double-shocked state $\sigma_2(0)$. We can notice that, according to the calculations by Laudernet et al. (2004) and F. Soubiran, the slope of the real part of the conductivity as a function of frequency is independent on the temperature or pressure in the low-frequency range (around $0 - 3$ eV), which covers our probe laser frequencies Ω and 2Ω (see Figure 6.14). Besides, this observation holds for different DFT exchange–correlation functionals (see Chapter 2.6.2) since the slope is unchanged when using a HSE functional, as in Scipioni et al. (2017), or a PBE, as in the simulations by F. Soubiran. We thus determined the DC value of the conductivity $\sigma(0)$ and the real part of the values at 1.165 eV and 2.33 eV ($\Re[\tilde{\sigma}(\Omega)]$ and $\Re[\tilde{\sigma}(2\Omega)]$, respectively) directly from a linear fit on the data in the visible range. Our approach consists in determining the ratio between static and optical values of the conductivity from the *ab initio*

simulations and then search for the static conductivity value that reproduces, via the aforementioned ratio, the optical values as close as possible to those we estimated in Section 6.4.2.

Therefore, for each state simulated by Laudernet et al. (2004) or F. Soubiran, we extracted the ratio between the static conductivity and the real part of the conductivity at $\omega = \Omega$ and $\omega = 2\Omega$:

$$s(\omega, T) = \frac{\sigma(0, T)}{\Re[\tilde{\sigma}(\omega, T)]}. \tag{6.9}$$

In order to determine the temperature dependency of such ratio, we fitted the datasets of Laudernet et al. (2004) and F. Soubiran with a properly designed function

$$s(\omega, T) = s^{\text{in}}(\omega) + \left[s^{\text{sat}}(\omega) - s^{\text{in}}(\omega)\right] \left[1 - \exp\left(-\frac{T}{T^{\text{sc}}(\omega)}\right)\right]. \tag{6.10}$$

The free parameters of the fit are $s^{\text{in}}(\omega)$, $s^{\text{sat}}(\omega)$, and $T^{\text{sc}}(\omega)$. From now on, the best fits on the datasets of Laudernet et al. (2004) and F. Soubiran will be called $s^L(\omega, T)$ and $s^S(\omega, T)$, respectively. The datasets and the corresponding fitting functions are provided in Figure 6.18.

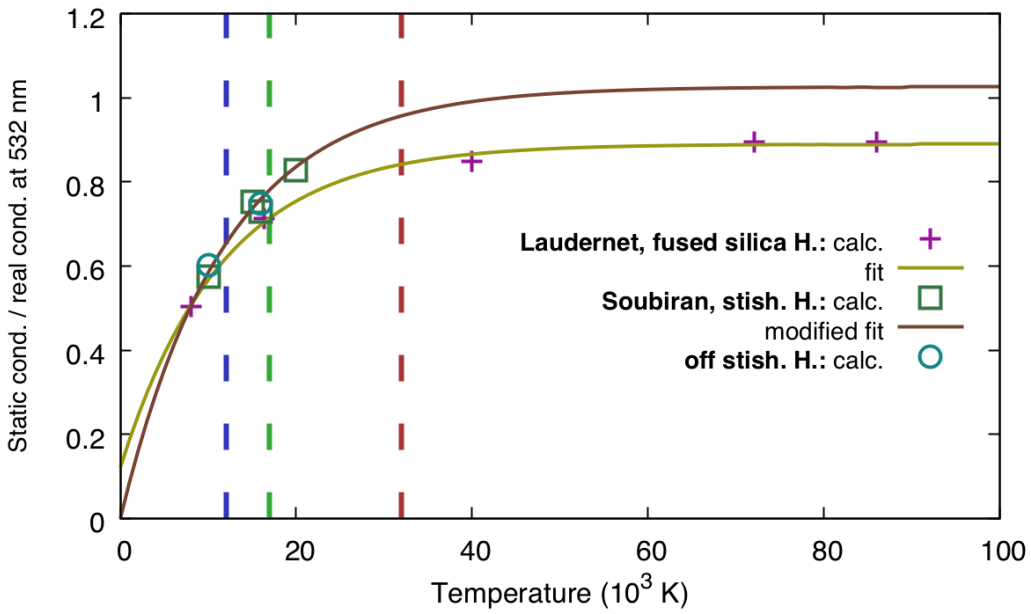

Figure 6.18 – Ratio between the static conductivity and the real part of the conductivity at 532 nm ($\sigma(0)/\Re[\tilde{\sigma}(2\Omega)]$) according to calculations from Laudernet et al. (2004) and by F. Soubiran, as a function of temperature. The three dashed vertical lines indicate the temperatures of the isotherms considered in this study (12 kK, 17 kK, and 32 kK).

The functions $s^L(\omega, T)$ and $s^S(\omega, T)$ assume fairly close values at similar temperatures, despite being relative to much different pressure values: the pressure dependence appears to be much weaker than the temperature one. Therefore, in analogy with what we have done in Section 6.4.2, we supposed that the pressure dependence of the ratio $s^{\text{m}}(\omega, P, T)$ can be approximated by a linear interpolation of the values $s^L(\omega, T)$ and

$s^S(\omega, T)$:

$$s^{\mathrm{m}}(\omega, P, T) = s^L(\omega, T)\frac{P_{\mathrm{stishovite}}(T) - P}{P_{\mathrm{stishovite}}(T) - P_{\mathrm{fused}}(T)} + s^S(\omega, T)\frac{P - P_{\mathrm{fused}}(T)}{P_{\mathrm{stishovite}}(T) - P_{\mathrm{fused}}(T)}. \tag{6.11}$$

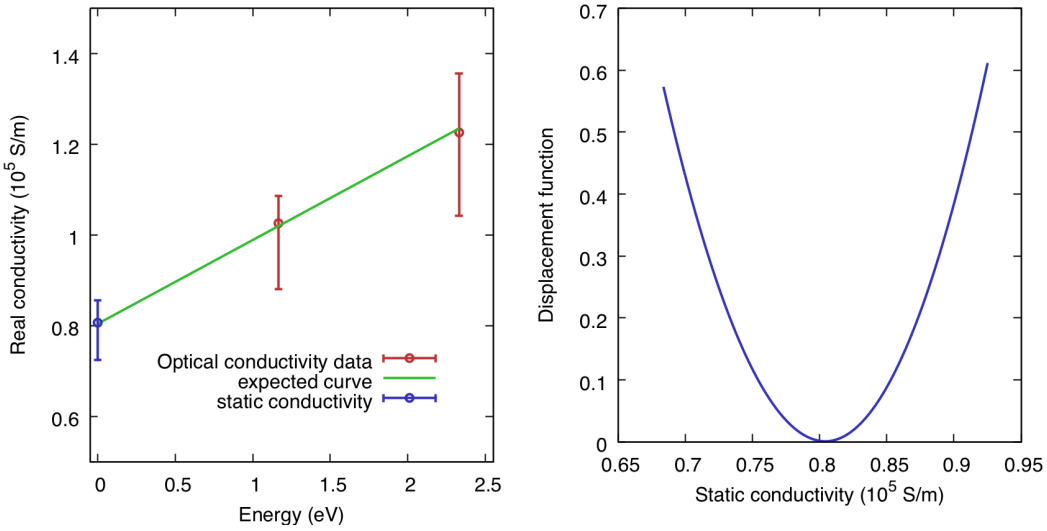

Figure 6.19 – Determination of the static conductivity of the double-shocked state in shot D-54. **Left.** Real part of the conductivity as a function of the photon energy. An energy of 1.165 eV (2.331 eV) corresponds to a wavelength of 1064 nm (532 nm). **Right.** Displacement function (introduced in equation 6.14 against tentative static conductivity values. A local minimum is found for a conductivity value of $0.804 \cdot 10^5$ S/m.

At this point, we had determined the ratios between the static conductivity and the real part of the conductivity Ω and 2Ω to employ to infer the first from the second. The problem was thus to find the static conductivity that produced, via the aforementioned ratios, the closest optical conductivity values to the values obtained from the experimental data. To do so, we considered a free parameter $\sigma^{\mathrm{m}}(0)$ representing the static conductivity and calculated the corresponding optical values for each value of that parameter:

$$\sigma^{\mathrm{m}}(\Omega) = \sigma^{\mathrm{m}}(0)/s^{\mathrm{m}}(\Omega, P, T) \tag{6.12}$$
$$\sigma^{\mathrm{m}}(2\Omega) = \sigma^{\mathrm{m}}(0)/s^{\mathrm{m}}(2\Omega, P, T). \tag{6.13}$$

Then, we searched for the value of $\sigma^{\mathrm{m}}(0)$ that minimised a displacement function $D[\sigma^{\mathrm{m}}(0)]$, defined as the sum of the squares of the displacement between the optical conductivity predicted by the model and that estimated from the experimental data, rescaled with the uncertainty associated to the latter:

$$D[\sigma^{\mathrm{m}}(0)] = \left[\frac{\sigma^{\mathrm{m}}(\Omega) - \sigma(\Omega)}{\Delta_{\pm}\sigma(\Omega)}\right]^2 + \left[\frac{\sigma^{\mathrm{m}}(2\Omega) - \sigma(2\Omega)}{\Delta_{\pm}\sigma(2\Omega)}\right]^2. \tag{6.14}$$

Since the error bars on $\sigma(\omega)$ are asymmetric, the upper and lower values $\Delta_+\sigma(\omega)$ and $\Delta_-\sigma(\omega)$ have been considered if the predicted optical conductivity value $\sigma^{\mathrm{m}}(\omega)$ was respectively higher or lower than the value estimated from the experimental data $\sigma(\omega)$.

In Figure 6.19 (left), we show the estimated static conductivity of the double-shocked state for a given shot, together with the optical values at Ω and 2Ω and the linear dependency on energy given by the model. We provide on the right of Figure 6.19 the displacement function D against the varying static conductivity $\sigma^{\mathrm{m}}(0)$ for shot D-54.

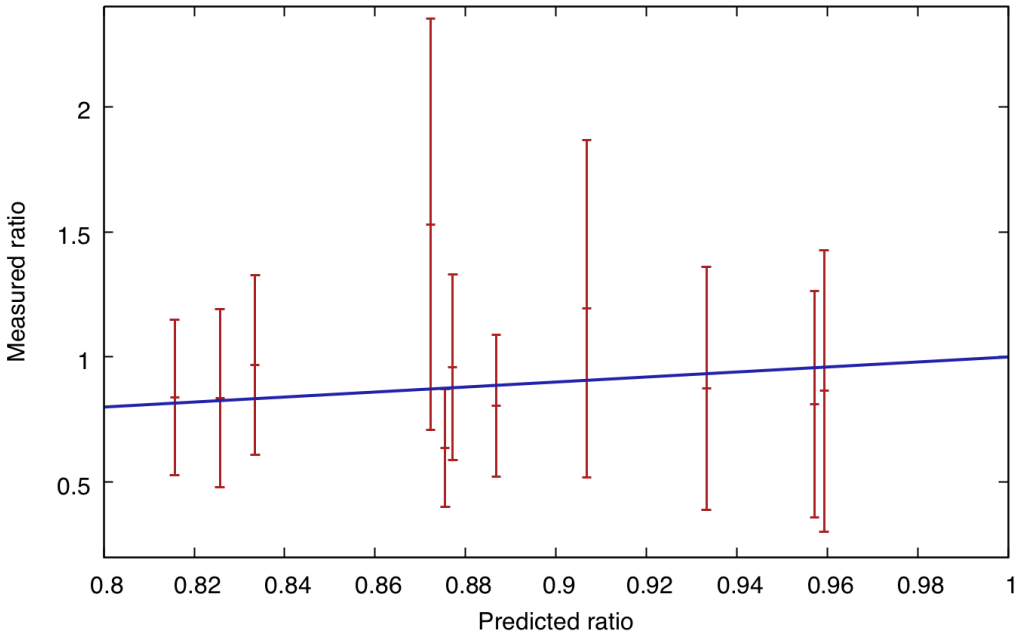

Figure 6.20 – Ratio between the $\Re[\tilde{\sigma}(\Omega)]$ and $\Re[\tilde{\sigma}(2\Omega)]$ values estimated from the measured reflectivities as a function of the same ratio predicted by interpolating the results of *ab initio* calculations. The blue line is the identity (predicted ratio = measured ratio). All data except two are compatible with the identity well within their error bars; two data points exhibit discrepancies comparable to, but still lower than, their error bars.

In order to test the consistency of our results, we can compare the ratio between the real part of the conductivity at 1064 nm and at 532 nm ($\Re[\tilde{\sigma}(\Omega)]/\Re[\tilde{\sigma}(2\Omega)]$) obtained from the *ab initio* calculations and the same ratio of the conductivity values we have independently estimated from the reflectivity measurements. We show in Figure 6.20 the two ratios for each shot. The deviation between predicted and measured value is satisfactorily lower than the error bar for all the shots except two, for which the deviations and the error bars are comparable. Globally, these results seem to support the hypothesis that the method used to estimate the optical conductivities is consistent.

Results

The static electrical conductivities of the double-shocked states as a function of temperature and pressure found by the method we just described are provided in Table 6.4 and shown in Figure 6.21 (colour bar). In this Figure we also show the *ab initio* calculations of the static conductivity from Mazevet et al. (2015) and Scipioni et al. (2017) as well as the *ad hoc ab initio* calculations from F. Soubiran. Along the α-quartz Hugoniot curve, the static conductivity has been estimated by applying the

same method described in this Section to the available EOS and reflectivity data by Millot et al. (2015) (at 532 nm) and Huser et al. (2015) (at 1064 nm).

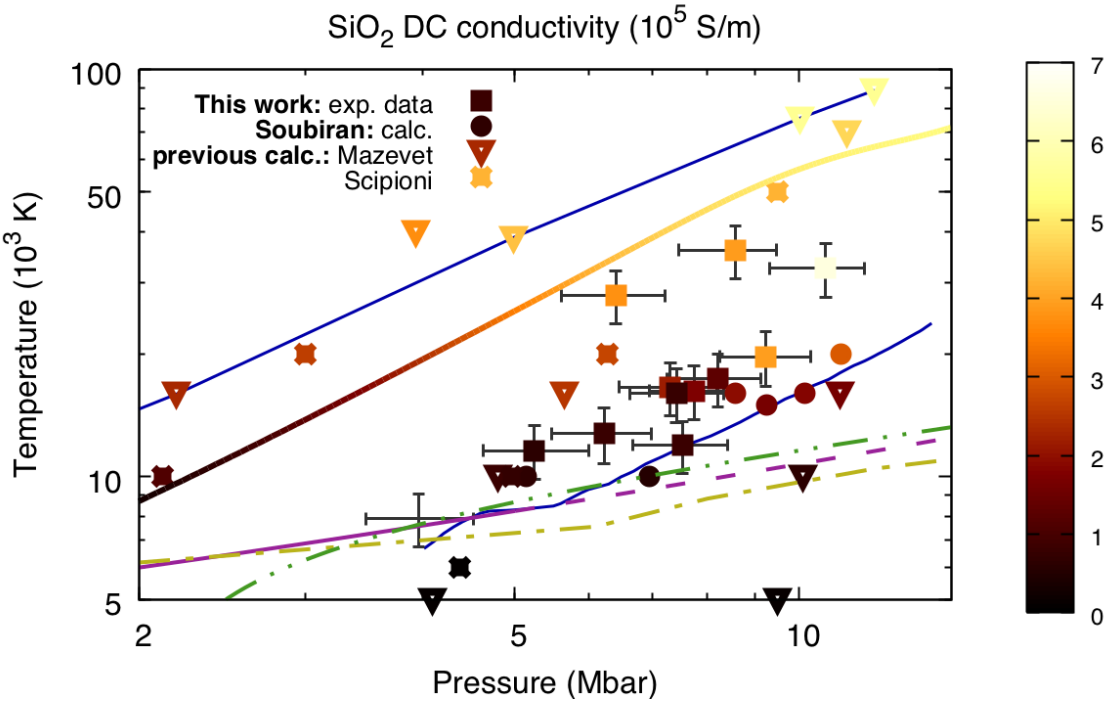

Figure 6.21 – Static electrical conductivity of silica as a function of pressure and temperature. The double-shock experimental data from this work are shown in colour scale inside the squares. Calculations from F. Soubiran are provided in colour scale inside the circles. Previous calculations from Mazevet et al. (2015) and Scipioni et al. (2017) are also shown (colour scale inside reversed triangles and crosses, respectively). The static conductivity along the α-quartz Hugoniot (colour scale of the corresponding curve) has been estimated by applying the same method presented in this Section to the reflectivity and equation-of-state data in the literature [Millot et al. (2015); Huser et al. (2015)]. The melting curves of silica are the same as in Figure 6.9.

The behaviour of the static conductivity of warm dense silica as a function of pressure and temperature, as it appears from our data and from the results of *ab initio* calculations, is analogous to that of the optical conductivities, shown in Figure 6.16. In general, our data are in fair agreement with the results of *ab initio* simulations.

The wide set of thermodynamic conditions we covered via double-shock compression allowed us to independently study the pressure and temperature dependence of the static conductivity. Conductivity appeared to be primarily driven by temperature. We studied the pressure dependence along extracted three quasi-isothermal lines extracted from our data, as shown in Figure 6.22:

(i) at $12 \cdot 10^3$ K: shots A-15 and B-103, D-54;

(ii) at $17 \cdot 10^3$ K: shots A-40, B-93, and B-111 (shot D-49 has been excluded from the analysis due to the high error bars on reflectivity);

(iii) and at $32 \cdot 10^3$ K: shots A-49, A-51, and A-53.

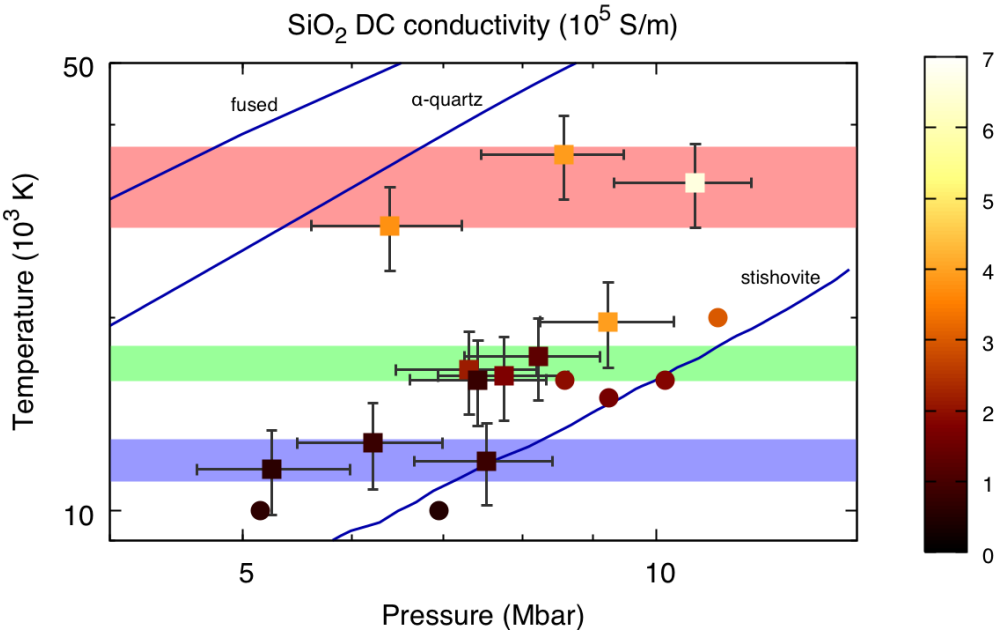

Figure 6.22 – Quasi-isothermal lines extracted from our double-shock data to study the pressure dependence of conductivity at constant temperature. The blue, green, and red areas correspond to the conditions covered by the quasi-isothermal lines centred around $12 \cdot 10^3$ K, $17 \cdot 10^3$ K, and $32 \cdot 10^3$ K, respectively. The solid blue lines are, from top to bottom, the fused silica, α-quartz, and stishovite principal Hugoniot curves. Only our static conductivity data and the static conductivity calculated by F. Soubiran are shown. Legend as in Figure 6.21.

The pressure dependence of $\sigma(0)$ along such quasi-isothermal lines is provided in Figure 6.23, where we can notice a non-monotonic behaviour. We also compare our data to *ab initio* simulations by Mazevet et al. (2015), Scipioni et al. (2017), and F. Soubiran. Simulations by Mazevet et al. (2015) and Scipioni et al. (2017) observed a non-trivial behaviour of the electrical conductivity of silica. Indeed, both studies have found that, for temperatures below $20 \cdot 10^3$ K, the static conductivity is not monotonically dependent on pressure along isothermal paths, but rather increases at low pressures, exhibits a maximum, then decreases. The decrease of conductivity with the increase of pressure (or density) has been interpreted either as the consequence of a change in the Si–O coordination with pressure [Mazevet et al. (2015)] or as the result of a high-pressure charge-ordering breaking mechanism [Scipioni et al. (2017)]. Mazevet et al. (2015) have shown that the increase of pressure induces an increase of the Si–O coordination number from 4 (typical of α-quartz) to 9 (typical of high-pressure phases such as cotunnite). By analysing the pressure dependence of the electronic density of states and occupied density of states, they noticed that this increase opens a pseudo-gap and decreases the density of states near the Fermi energy. They interpret this effect as an increase of the ionic character of silica (that is, an increase in the electronic localisation on the Si or O atom). The deepening of the pseudo-gap with compression has been confirmed by Scipioni et al. (2017), who attribute this feature to a compression mechanism breaking the charge ordering in silica. Indeed, at low pressures, an O atom is surrounded only by Si first neighbours, and by other O atoms only as second neighbours. At high pressures, this ordering breaks down as O atoms

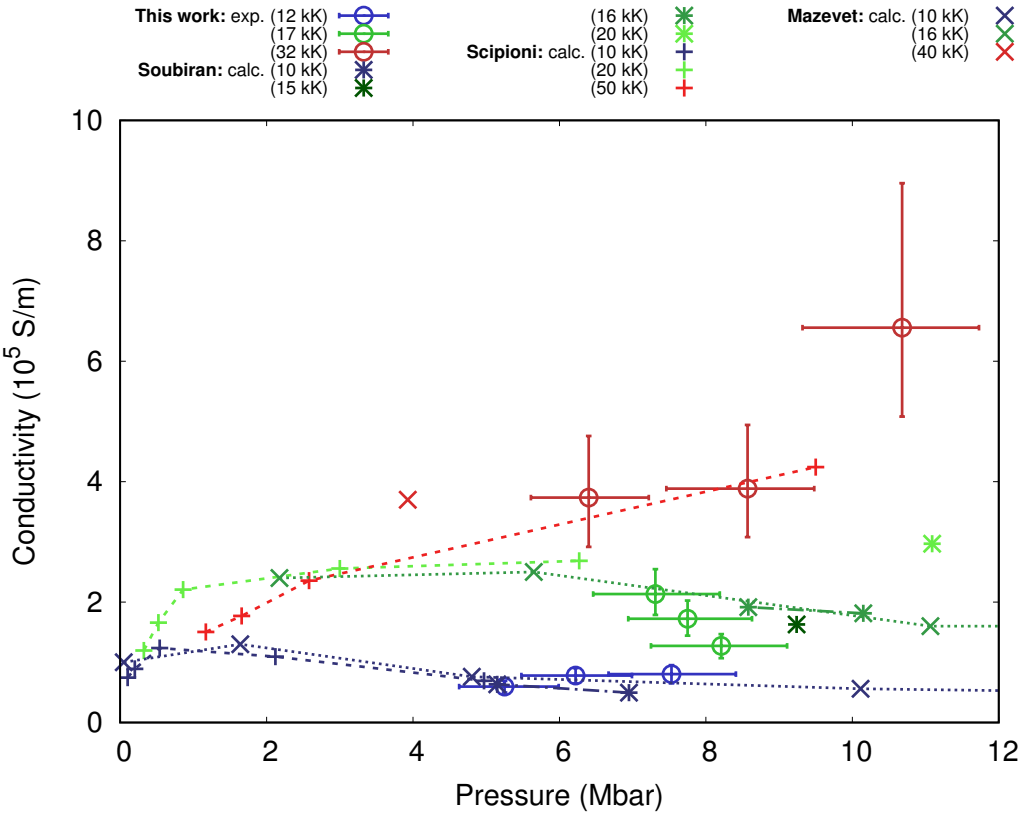

Figure 6.23 – Electrical conductivity of silica as a function of pressure along different isothermal lines. The static conductivity values extracted from the experimental data in this work are shown together with the *ad hoc* calculations performed by F. Soubiran *(ENS Lyon)*. Previous calculations from Mazevet et al. (2015) and Scipioni et al. (2017) (personal communication of the pressure values) are also shown.

are surrounded by both Si and O atoms, and the O–O and Si–O mean distances become comparable. This new charge-disordered configuration strongly influences the electronic structure and hence the electrical conductivity. At the beginning of the present work, this evidence lacked of experimental confirmations.

Our data at 12 kK show an almost constant behaviour of conductivity with the increase of pressure, in agreement with data from Scipioni et al. (2017) and Mazevet et al. (2015) at the similar temperature of 10 kK. At 17 kK our data points exhibit a rapid decrease of conductivity for increasing pressures. Data from Mazevet et al. (2015) at 16 kK highlight a slower decrease in conductivity with the increase of pressure, while data from Scipioni et al. (2017) at 20 kK are limited to 6 Mbar, below our explored range. At 32 kK, our three data points follow a positive slope, in agreement with the clearly monotonic behaviour of conductivity along the isothermal at 50 kK obtained by Scipioni et al. (2017).

Since we only employed optical diagnostics in our experiments, our results only include macroscopic quantities, that do not allow us to discriminate between the two different interpretations of the structural origin of the non-monotonic behaviour of the conductivity given by Mazevet et al. (2015) and Scipioni et al. (2017). Further experimental work shall include X-ray diagnostics to directly probe the microscopic mechanism at the base of such a dependence.

Error estimation

The same Monte-Carlo routine employed for the determination of the uncertainties on the optical conductivity values has been used to calculate the error bars on $\sigma(0)$. They are reported in Table 6.4.

6.5 Elastic precursor

When loaded by a weak shock wave, a solid material undergoes a one-dimensional strain along the longitudinal axis of propagation of the shock. Due to the rigidity of the material, the stresses along the lateral directions are lower than the longitudinal one. In this case, as the wave loading the material does not overcome its rigidity, it is called an elastic wave. By increasing the strength of the shock wave, a limit (called Hugoniot elastic limit) is eventually found, when the rigidity of the material can no longer support the difference between longitudinal and lateral stresses and the yield of the solid structure occurs. For higher shock strengths, the yielded solid is hydrostatically compressed by a plastic wave [Zel'dovich and Raizer (1966); Wackerle (1962)].

The transition from elastic to plastic behaviour produces a discontinuity in the first derivative of the Hugoniot curve in the pressure – specific volume plane, as shown in Figure 6.24 (top) for the case of α-quartz. As a consequence, the Rankine–Hugoniot relations have multiple solutions for a range of shock strengths. Indeed, depending on the slope of the Rayleigh line (expressing the conservation of momentum through the shock front), the Hugoniot and the Rayleigh may cross once or twice.

(i) For a sufficiently high shock strength (*i.e.* slope of the Rayleigh), there is only one solution. The physical consequence is that the compression only produces a plastic wave. This corresponds to the right portion of Figure 6.24 (bottom), which shows the elastic precursor velocity U_{prec} and the shock velocity U_s as functions of the material velocity U_p.

(ii) For intermediate shock strengths, there are two solutions. The physical meaning is that both an elastic and a plastic wave are produced, and the first is faster than the second since the Rayleigh line reaching the apical point of the elastic portion of the Hugoniot has a higher slope than the Rayleigh line considered in that case. In this regime, an elastic precursor compresses the sample up to the Hugoniot elastic limit, then a plastic wave compresses it up to the final state given by the highest-pressure solution of the Rankine–Hugoniot relations. This is shown in Figure 6.24 (bottom), in the zone in which the $U_s - U_p$ curve is solid and the $U_{\text{prec}} - U_p$ curve is dashed. In this zone, U_{prec} is constant.

(iii) For very low shock strengths, there is only one solution as only an elastic wave is produced. In Figure 6.24 (bottom), this regime corresponds to the zone in which the $U_s - U_p$ curve is dotted and the $U_{\text{prec}} - U_p$ curve is solid. In this zone, U_{prec} varies as a function of the shock strength.

Examples of Rayleigh lines for cases (i) and (ii) are provided in Figure 6.24 (top) and denoted Rayleigh line 1 and 2, respectively.

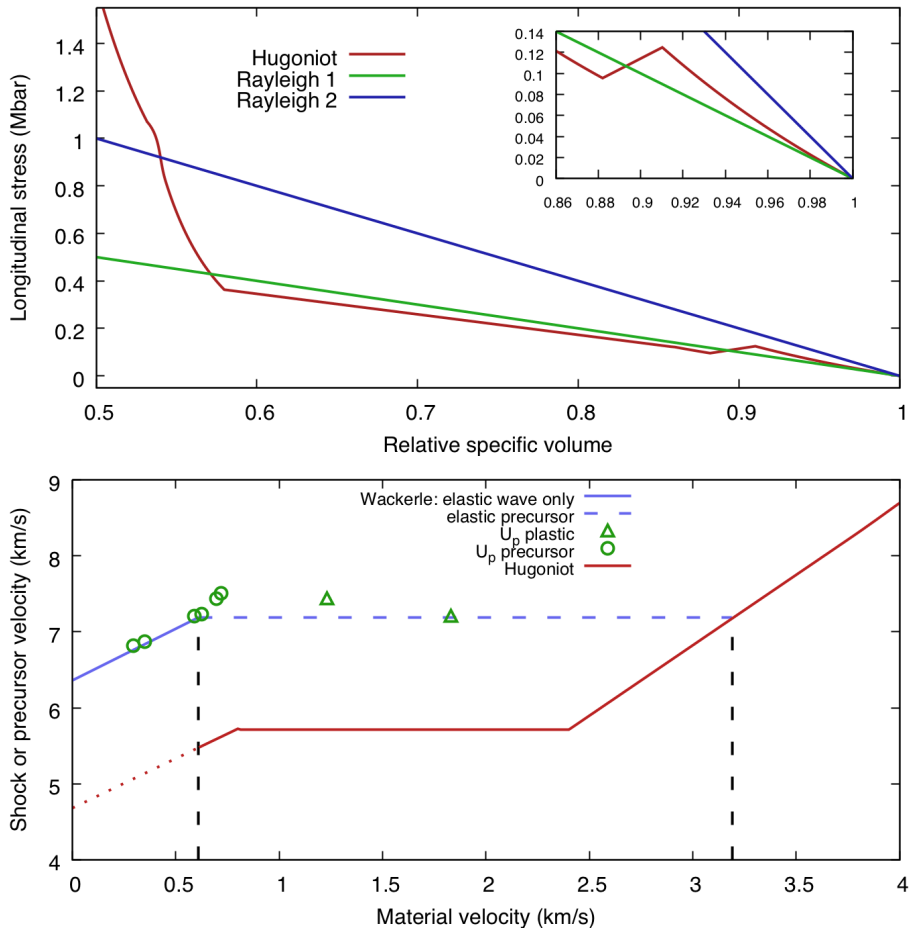

Figure 6.24 – **Top.** Conditions for the existence of an elastic precursor in α-quartz. The Hugoniot curve (red curve) is taken from our model described in Section 6.2.1, modified at low pressures to include the elastic behaviour of z-cut α-quartz as modelled by Wackerle (1962). The green and blue lines are two examples of Rayleigh curves, the first crossing the Hugoniot twice, hence producing an elastic–plastic wave structure, the second crossing it once, hence producing only a plastic wave. *Inset. Zoom on the low-pressure region. The apical point of the elastic portion of the Hugoniot is evident.* **Bottom.** Shock velocity as a function of the material velocity according to our fit (red curve) and elastic precursor velocity as a function of the material velocity according to Wackerle (1962) (blue curve) along the principal Hugoniot of z-cut α-quartz. Up to $U_p \simeq 0.6$ km/s, quartz exhibits only an elastic wave (solid blue curve). From $0.6 - 3.2$ km/s, an elastic precursor and a plastic wave sequentially propagate. For material velocities higher than around 3.2 km/s, only the plastic wave propagates, as its velocity is higher than that of the elastic wave.

Quartz is predicted to exhibit an elastic-plastic wave structure [case (ii)] when compressed up to a pressure range from $100-600$ kbar [Wackerle (1962)]. Such pressure range is compatible with the conditions reached after the first shock loading in this work. For very low material velocities $U_p < 0.61$ km/s, quartz only exhibits an elastic wave [case (iii)]. Finally, at high material velocities ($U_p > 3.34$ km/s), the plastic wave immediately catches up the elastic one [case (i)].

6.5.1 Determination of the precursor velocity from the diagnostics outputs

In some shots of this work, the VISAR and SOP outputs have clearly shown signatures of the presence of an elastic precursor. This case is depicted in Figure 6.7, where the second shock is seen catching up the plastic wave of the first compression at $t = t_3$, then the elastic precursor at $t = t_{3b} > t_3$. As already anticipated in Chapter 3.3.5, the analysis of the timings can be employed to measure the elastic precursor velocity. Here I recall that the shock velocity of the first shock is indirectly determined from the material velocity measurement, and the shock velocity of the second shock is determined from the timings t_2 and t_3. Therefore, the velocity of the elastic precursor can be measured using the timing t_{3b} by imposing that the distance covered in the sample by the elastic precursor from t_1 to t_{3b} equals that covered by the first shock from t_1 to t_2 plus that covered by the second shock from t_3 to t_{3b}.

Table 6.5 – Material velocity of the plastic compression wave (U_p^1) and elastic precursor velocity (U_{prec}) for the shots in which z-cut α-quartz compressed by the first shock exhibits an elastic-plastic behaviour.

Shot #	U_p^1 (km/s)	U_{prec} (km/s)
A-15	3.30 ± 0.41	7.90 ± 0.76
A-40	2.75 ± 0.15	7.31 ± 0.40
B-93	2.77 ± 0.27	7.27 ± 0.53
B-98	2.77 ± 0.09	6.99 ± 0.24
B-109	2.74 ± 0.15	7.34 ± 0.42
D-54	3.04 ± 0.09	7.62 ± 0.32

6.5.2 Results

We had evidence of the existence of an elastic precursor for 6 shots, for first-shock material velocities U_p^1 between $2.7 - 3.3$ km/s, as shown in Table 6.5. Figure 6.25 shows the measured velocity of the elastic precursor as a function of the material velocity of the precursor itself ($U_p < 0.61$ km/s) and of the plastic wave (0.61 km/s $< U_p <$ 3.34 km/s). The model of the precursor velocity dependence on U_p and the experimental data by Wackerle (1962), which reach material velocities up to 1.8 km/s, are also shown for comparison. All the 6 data points from this work are compatible within error bars with the model by Wackerle (1962). Moreover, the mean value for this work (red dotted line) is compatible within error bars with both the mean value of the two data points by Wackerle (1962) (dashed blue line) and the value given by their model (solid blue line).

In conclusion, we extended the explored range of conditions of the study of elastic precursors in α-quartz up to the higher limit of their existence domain (material velocity of around 3.4 km/s). Our data confirm the model by Wackerle (1962) predicting a constant elastic precursor velocity of around 7.3 km/s in the whole range in which quartz exhibits an elastic-plastic response.

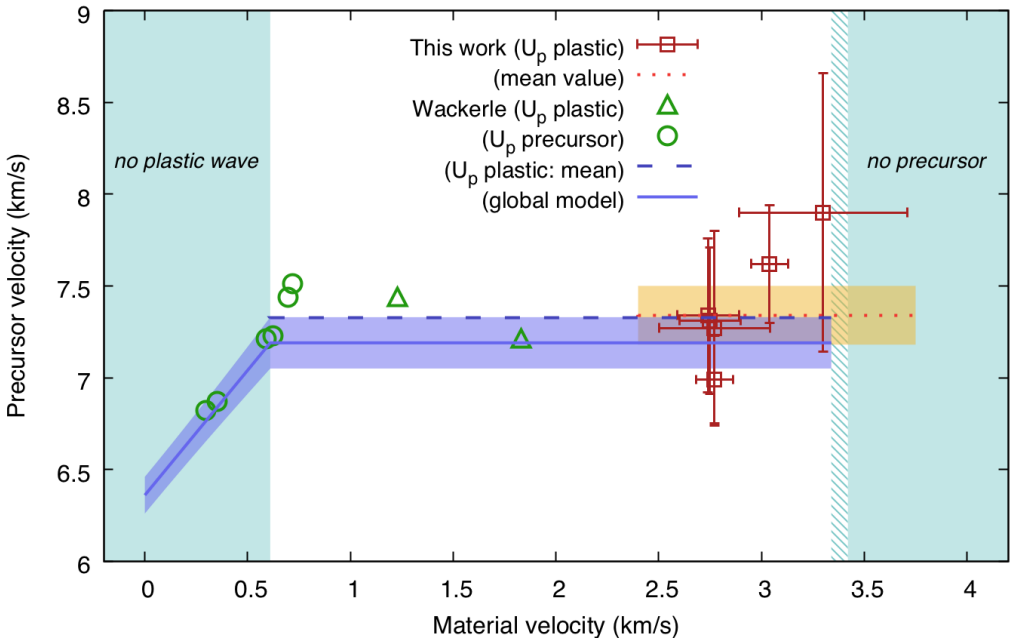

Figure 6.25 – Elastic precursor velocity as a function of material velocity for z-cut α-quartz. Elastic-wave velocity data from Wackerle (1962) are shown both as a function of the elastic-wave material velocity (circles) and of the plastic-wave material velocity (triangles). The shaded area on the left indicates the region where no plastic wave was observed by Wackerle (1962). The shaded area on the right shows the conditions for which Wackerle (1962) did not observe an elastic precursor. The dashed area indicates the region where their model predicts no precursor.

6.5.3 Error estimation

The Monte-Carlo routine employed to determine the uncertainties on densities and pressures (cf. Section 6.3.3) has also been used to estimate the error associated to the measurement of the elastic precursor velocity, when the signature of the precursor was visible. The relevant variables were t_1, t_2, t_3, t_{3b}, U_p^1, and U_s^1.

6.6 Conclusions and perspectives

In this Chapter, we have presented the study of the thermodynamic properties, reflectivity, and electrical conductivity of warm dense silica in a range of pressure and temperature conditions up to now unexplored. Extreme conditions up to 11 Mbar and $36 \cdot 10^3$ K were obtained via the compression of α-quartz samples with a double-shock technique. Those conditions were challenging to achieve since they do not belong to the principal Hugoniot curves starting from the stable low-pressure phases of silica. In particular, temperatures up to three times lower than along the principal Hugoniot curve were probed, so that a wider region of the phase diagram of silica could be characterised. This work has not only provided new insights on the properties of silica, but also demonstrated the interest of using the dynamic pre-compression technique presented in Chapter 3.3 for exploring high-pressure / moderate-temperature states.

Preliminary studies necessary for the characterisation of the state reached after the

first shock loading, which is essential for a correct analysis of double-shock experimental data, have been conducted on α-quartz. To this aim, an existing model of the shock – material velocity relation along the principal Hugoniot has been extended to low-pressure conditions. Moreover, the study of the refractive index along the Hugoniot has been extended up to 320 kbar during a dedicated campaign.

A novel approach for the determination of the optical and static conductivity from the measurements of shock-front reflectivity and equation of state has been presented. This approach is hybrid, using both experimental data and *ab initio* calculations – the latter for the estimation of the energy dependence of conductivity and the relation between real and imaginary part. Within this context, *ad hoc ab initio* calculations have been performed by F. Soubiran *(ENS Lyon)* which have been used together with already available calculations to build the models necessary for the aforementioned method. The approach used in this work allows to get rid of simplistic assumptions on the behaviour of conductivity, such as Drude or Drude-Smith models, and consistently gains in robustness because of its simultaneous use of experimental data and calculations. It can be employed for the study of the electrical properties of other materials in the warm dense regime, in the context of shock-compression experiments.

A large ensemble of thermodynamic conditions could be probed by varying the intensity of the two drive laser pulses, hence of the two shocks. This opened the possibility of studying the behaviour of silica along quasi-isothermal curves. In particular, the dependence on pressure of the electrical conductivity of silica has been studied along three quasi-isothermal lines, which we have extracted by considering data points at similar temperatures. We found that conductivity does not increase with pressure along isothermal lines at moderate temperatures, but is almost constant at around $12 \cdot 10^3$ K and decreasing at around $17 \cdot 10^3$ K. On the contrary, it is clearly increasing with pressure along the isothermal at $32 \cdot 10^3$ K. These findings are the first experimental confirmation of previous *ab initio* simulations. The latter provide insights about the atomic structure of warm dense silica and its compression mechanisms which are crucial for the modelling of the interiors of super-Earth and giant exoplanets.

Finally, for some shots, a signature of the presence of an elastic precursor of the first shock wave in double-shock experiments on α-quartz has been observed in this work. The precursor was visible when the state loaded by the first shock was compressed up to around 550 kbar. We could infer the elastic precursor velocity from the measurement of the timings of the different phases of double-shock loading. Our velocity measurements confirm previous experimental results, which were limited to lower pressures. We confirm that, in the whole pressure range from the elastic limit to the disappearing of the elastic precursor, the precursor velocity is constant, around 7.3 km/s.

Future work should apply the double-shock compression technique used in this Chapter to samples of different phases of silica, and in particular to stishovite, to achieve even lower temperature states, more interesting for the study of super-Earth exoplanets. Another research line consists in applying *in situ* X-ray diffraction to shock-compressed silica and silicate minerals to directly probe their microscopical structure at thermodynamic conditions comparable to those explored in this work. This study shall be done along the Hugoniot, using single-shock compression, and, in a second stage, off the Hugoniot, using the double-shock compression technique employed in this work or similar approaches.

Rocky planets' components: general discussion

The Third Part of this Thesis was devoted to the experimental study of the optical and electrical properties of silica, a key component of the mantles of rocky planets. The investigation of silicate minerals has been the object of an additional study, involving an experimental campaign at SLAC–LCLS to which I participated but which is not included in this Thesis. In this Discussion we summarise the state of the art before this Thesis and specify the contribution of this work to planetary science and, more generally, to the study of the Warm Dense Matter regime.

Before this work

Before the beginning of this Thesis, almost all the major components of the mantles of rocky planets – MgO–FeO–SiO_2 systems – had already been the object of several theoretical and experimental studies. Such studies covered, if not the exact thermodynamic conditions reached in the planetary interiors, leastwise a wide set of Hugoniot and off-Hugoniot states in the Warm Dense Matter regime. This situation was quite different from the state of the art for the water–methane–ammonia mixtures (cfr. Chapters 4 and 5) composing the interiors of icy giant planets, which lacked even a characterisation of their basic properties. Hereafter we briefly summarise the state of the art for silica and silicate minerals prior to our work.

Silica. The silica (SiO_2) end-member, whose knowledge prior to this Thesis has been detailed in Chapter 6, has been the object of a particular interest not only for its planetary relevance (as a key component of proto-planets and of rocky and giant planets), but also because of its role as *in situ* standard for shock-compression experiments and as a formidable prototype material for the study of WDM. The numerous calculations of equation of state, phase diagram, optical, electrical, and transport properties cover a very wide region of the WDM regime. The principal Hugoniot of α-quartz has been remarkably well characterised and experimental data are also available for the fused silica and stishovite Hugoniot curves. Many off-Hugoniot studies exist on the behaviour of statically pre-compressed quartz, adiabatic release, speed of sound. However, at the beginning of this work the experimental characterisation of off-Hugoniot states left important gaps in the high-pressure region, especially at intermediate conditions between

the α-quartz and stishovite Hugoniot curves.

Magnesium oxide. The thermodynamic properties and phase diagram of the magnesium oxide (MgO) end-member have been quite extensively characterised by simulations [between the most recent: Cebulla and Redmer (2014), Miyanishi et al. (2015), and Soubiran and Militzer (2018)] and shock-compression experiments [Coppari et al. (2013); Bolis et al. (2016)]. Whether some phase transitions – such as the solid-solid B1-B2 transition and melting – occur in a dynamic compression context and at which thermodynamic conditions is still questioned, with consequences on our current knowledge of the properties of super-Earth's mantles and dynamo action in terrestrial planets.

Magnesium oxide – silica systems. MgO–SiO_2 systems, such as $MgSiO_3$ and Mg_2SiO_4, in both their glass and crystalline forms, are still far from being satisfactorily studied, especially at high pressures above 2 Mbar, and a debate on the occurrence of different phase transitions along the Hugoniot curves is currently ongoing [Spaulding et al. (2012); Bolis et al. (2016)]. Moreover, materials including both Fe and Mg essentially still need to be characterised.

The contribution of this work

In the work described in Chapter 6, we studied the thermodynamic, optical, and electrical properties of warm dense silica employing a double-shock compression technique on α-quartz samples, which allowed us to probe off-Hugoniot states challenging to attain. We have also performed ancillary studies such as the measurement of the refractive index and of the elastic precursor velocity in the transparent region of the α-quartz Hugoniot curve.

The experimental work conducted at the SLAC–LCLS facility, although not presented in this Thesis, is a fully-fledged part of the wider scientific project in which this work is inscribed. Several materials of interest, such as silica (starting from the α-quartz and fused phases), $MgSiO_3$ (starting from the glass and the enstatite phases), and Mg_2SiO_4 (forsterite phase) have been laser-driven shock compressed up to 3 Mbar. Their microscopical structures have been probed via X-ray diffraction using the LCLS XFEL beam, allowing the study of the thermodynamic and kinetic features of phase transitions in the nanosecond time scale.

Hereafter we detail the significance of the results of the work described in Chapter 6 for both the general study of the WDM regime and planetary science.

Principal Hugoniot curve

We have conducted different ancillary studies on the low-pressure region of the principal Hugoniot of α-quartz, where a precise characterisation was missing. These studies have been motivated by their importance for a correct analysis of double-shock experimental data.

(i) We modelled the $U_s - U_p$ relation at low pressures after previous experimental data, thus extending a relation, valid from 0.9 Mbar, provided by Knudson and

Desjarlais (2009). In particular, our extension covers the α-quartz $\rightarrow$ stishovite phase transition which takes place at around $0.1-0.4$ Mbar and that is expressed by a mixed-phase region in which U_s assumes a constant value. Our model agrees with that given by the model of Boettger (1992) which covers pressures from $0.06-0.7$ Mbar.

(ii) We extended up to 0.32 Mbar the refractive index measurement in the transparent region of the Hugoniot, showing that the linear behaviour of the refractive index as a function of density is valid not only at very low compressions, as found by Jones and Gupta (2000) and Jensen et al. (2007), but also in our explored range, although our error bars are too high to rule out minor discrepancies.

(iii) In our double-shock experiments we have observed the signature of the existence of an elastic precursor of the first shock wave (hence along the principal Hugoniot) at around $0.45-0.65$ Mbar, near the upper boundary of its predicted existence domain. Our velocity measurements are compatible with previous sparse results by Wackerle (1962) and extend the range of study.

A brief stock of the situation before and after this Thesis is provided in Table 6.6.

Table 6.6 – State of the art of the study of the U_s-U_p relation, refractive index, and elastic precursor before this work and contribution given by this study.

Property	**Study**	
	Before this work	In this work
U_s-U_p **relation**	2 studies: $0.06-0.7$; $0.9-16$ Mbar	unified model
Refractive index	2 studies, up to 0.035 Mbar	5 data pts, $0.12-0.32$ Mbar
Elastic precursor	up to 0.27 Mbar	6 data pts, $0.45-0.65$ Mbar

Off-Hugoniot conditions

Employing a double-shock compression technique, we explored a set of intermediate conditions between the principal Hugoniot curves of α-quartz and stishovite, as shown in Figure 6.26. The attained thermodynamic conditions have been determined using the procedure presented in Chapter 3. The obtained $\rho-P-T$ EOS data in this region so challenging to reach represent a useful benchmarking tool for future *ab initio* simulations of warm dense silica. Figure 6.26 also shows the interior profiles of several planets to be compared to the range explored in our work. On the one hand, it is evident that our data, even if colder than along the α-quartz principal Hugoniot, are still too hot to be of immediate interest for super-Earth exoplanets. On the other hand, silica may be a key component of the cores of giant planets. It is therefore interesting to compare the conditions we reached with the profiles of those planets. In particular, Jupiter and a Jupiter-mass hot Jupiter are shown in the Figure. In this case, the experimentally attained conditions are much closer to the interior profiles, so that the collected data represent a more direct contribution to the interior models of those planets.

In our double-shock experiments, we measured the shock-front reflectivity at two different wavelengths (532 nm and 1064 nm). This multi-wavelength setup has proved to be essential for the subsequent study of the electrical properties of warm dense silica. Indeed, from our reflectivity measurements we estimated the optical electrical conductivities at the corresponding wavelengths as well as the static value. Instead than classical Drude or Drude–Smith models, which fail in describing the actual frequency dependence of conductivity, we employed an hybrid approach based on both experimental data and *ab initio* calculations.

What has been said about the scientific value of the off-Hugoniot EOS data for benchmarking *ab initio* calculations is even more valid for these conductivity data, as the electrical properties are generally elusive in shock-compression experiments. In addition, our data represent the first experimental confirmation of the recent *ab initio* investigations of the conductivity of warm dense silica by Scipioni et al. (2017) and Soubiran and Militzer (2018). Our results strengthen their conclusions, according to which a dynamo action could take place in magma oceans inside super-Earth exoplanets and could also have taken place in the early history of the Earth, when magma oceans are expected to have existed.

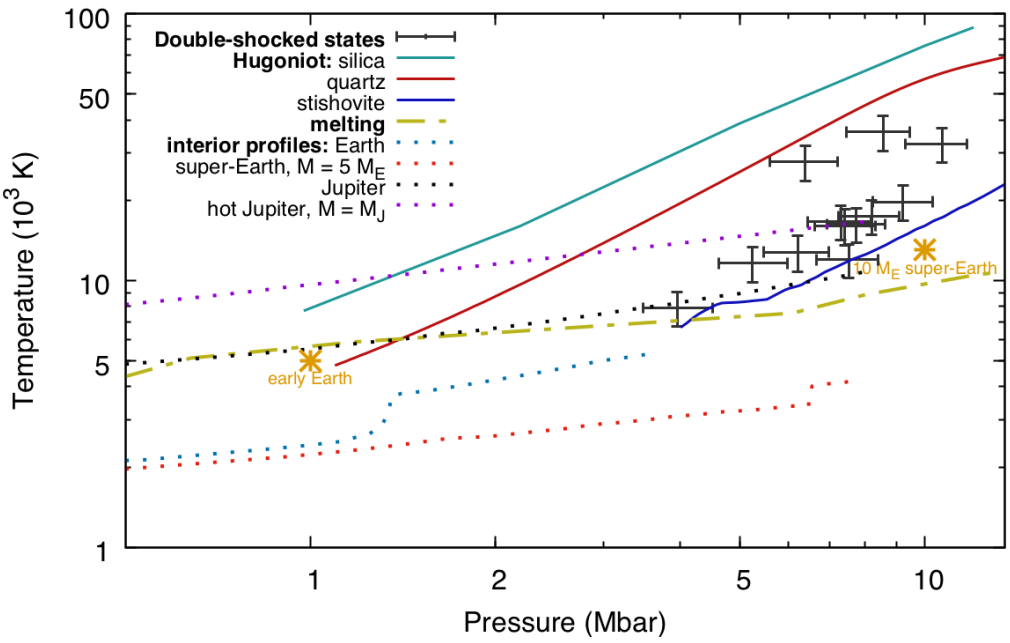

Figure 6.26 – Comparison between the phase diagram of silica and the internal profiles of different planets. The thermodynamic states attained in this work by double-shock compression are shown together with the principal Hugoniot curves starting from fused silica [Mazevet et al. (2015)], α-quartz [Millot et al. (2015)], and stishovite (*ibid.*). The silica melting line proposed by Mazevet et al. (2015) is also shown. The internal profiles of the Earth [Tateno et al. (2010)], a super-Earth with $M = 5M_E$ [Valencia et al. (2006)], Jupiter [Guillot (2005)], and a Jupiter-mass hot Jupiter [Baraffe et al. (2008)] are provided to be compared to the conditions achievable by shock-compression. Two $T - P$ points roughly representative of the conditions of early Earth and of a super-Earth with $M = 10M_E$ [Scipioni et al. (2017)] are also shown.

Perspectives

At the end of this Third Part of the Thesis, we propose a multi-faceted path to be undertaken in future investigations. The following research axes shall be interpreted as independent and simultaneously feasible rather than as different stages of a single project.

(i) Notwithstanding the common assumption that the principal Hugoniot of α-quartz has been satisfactorily characterised for the purpose of using quartz as *in situ* calibrant in shock-compression experiments, the work done in this Part has highlighted two critical gaps that shall be urgently bridged: (a) as the multi-wavelength setup concept has started to catch on in the community, additional and more precise studies of the shock-front reflectivity at 1064 nm should be done (only one study by Huser et al. (2015) is currently available, with high error bars in the saturation region); (b) the refractive index shall be better characterised along the whole transparent region of the α-quartz principal Hugoniot, and the transparent $\rightarrow$ opaque transition shall be accurately determined.

(ii) Since this work has proven the feasibility of double-shock compression of solid transparent samples, we propose that this technique shall be extensively applied to other materials. As it is evident by looking at Figure 6.26, the application on stishovite samples would allow to probe very low temperatures compared to basic compression approaches, and thus the characterisation of the silica melting curve at high pressures around 10 Mbar and of interesting conditions for massive super-Earth planets. Moreover, silicate minerals shall be studied at off-Hugoniot conditions using this technique following the research line which has already been undertaken for silica.

(iii) The X-ray diffraction study of silica and silicate minerals shock-compressed along the principal Hugoniot curves is already on track in the community, and the SLAC–LCLS experiment – conducted as part of the wider project to which this Thesis belongs – fits into this path. A natural step forward, which has already been started, is the thorough application of alternative compression techniques allowing to reach high-pressure, moderate-temperature states in experiments involving X-ray diagnostics. This would allow the characterisation of the microscopic structure of the compressed samples on a wider range of conditions, including the study of wide portions of phase boundary curves and of the pressure dependence of the structural properties along isothermal lines. Within this context, we propose the use of the double-shock compression technique employed in our work, which has the advantage of permitting the optical access to the probed state and therefore to couple more easily the output of optical and X-ray diagnostics.

General conclusions and perspectives

> Then I looked on all the works that my hands had wrought, and on the labour that I had laboured to do: and, behold, all was vanity and vexation of spirit, and there was no profit under the sun.
>
> Ecclesiastes 2, 11

Conclusions

In the work presented in this Thesis we have experimentally characterised several key representatives of the interiors of icy giant (pure water, pure ammonia, water–alcohol–ammonia mixtures) and rocky planets (silica). Extreme conditions of pressure ($0.1 - 10$ Mbar) and temperature ($10^3 - 10^4$ K), belonging to the Warm Dense Matter regime, have been obtained in the laboratory by means of laser-driven shock compression. The experimental campaigns presented in this work have been conducted at the GEKKO XII and LULI2000 facilities. On both facilities, a standard diagnostics setup has been employed consisting of two Doppler velocity interferometers (VISARs) and a streaked optical pyrometer (SOP), permitting the measurement of time-resolved shock velocity, shock-front reflectivity, and thermal self-emission of the shock-loaded sample. The reached thermodynamic state variables (density, pressure, and temperature) have been determined together with the optical properties at those conditions, so that a thorough description of the macroscopic properties of the sample could be given. In an experimental campaign at SLAC–LCLS, to which I participated but which is not presented in this Thesis, laser-driven compression was coupled to X-ray diffraction (XRD) to allow an *in-situ* probing of the microscopic features of silicate samples.

Target cells. At the beginning of this work, the experimental study of some key components of icy giant planets, such as methane and ammonia, was drastically limited. A major reason of the limitedness of the studies on methane and ammonia is that such compounds are gaseous at ambient conditions, whereas an efficient shock compression requires the initial state to be liquid or solid (cfr. Chapter 2). Therefore, we have conceived and employed a target cell apt to be filled with mildly pre-compressed ($P_0 \simeq 15$ bar) liquid samples and compatible with laser-driven shock compression (cfr.

Chapter 5). We also conceived a cryostat-based filling circuit for these cells. These methods have permitted us to study shock-compressed liquid ammonia up to unprecedented pressures of 2.9 Mbar and to observe for the first time the electrically conducting ("metallic-like") regime of warm dense ammonia. The cell we developed and its filling system shall be adapted in future work to study methane and other materials that are gaseous at ambient conditions. The portability of the filling system guarantees that it can be used for experiments in other facilities.

Compression methods. A cardinal aspect of the work presented in this Thesis has been the use of complementary compression approaches in order to span a wide region of the phase diagram of the materials under study: in particular, high-pressure / high-temperature states along the principal Hugoniot curves have been attained by single-shock compression, whereas high-pressure / moderate-temperature states, more difficult to achieve but also more relevant for planetary science, have been reached with the use of static or dynamic pre-compression methods prior to the shock loading.

The thermodynamic and optical properties of pure water, water–ethanol and water–ethanol–ammonia mixtures, and pure ammonia have been studied and compared along their principal Hugoniot curves (cfr. Chapter 4). On the one hand, their temperature – pressure relations are all comparable within error bars, with ammonia exhibiting slightly higher temperatures. On the other hand, for what concerns the reflectivity behaviour, there is a clear ordering in the onset pressure and in the saturation values. Such ordering may depend on the different initial densities of the samples as well as on their different molecular ionisation energies. As a consequence, models using water as sole representative of the components of the icy interiors of icy giants may underestimate their contribution to the generation of a magnetic field via a dynamo action.

Pre-compression of samples has been achieved statically, with the use of Diamond Anvil Cells adapted to laser-driven shock compression, and dynamically, via a double-shock compression technique employing two different drive laser pulses. In particular, a complete framework for double-shock compression has been conceived (cfr. Chapter 3), tested, and applied to several materials (cfr. Chapters 4 and 6) in this Thesis. In our approach, a direct optical access to the state of interest is guaranteed, which allows a data analysis routine to determine such state without the use of hydrodynamic or *ab initio* simulations. Via the application of this method, the optical and electrical properties of water, the water–ethanol–ammonia mixture, and silica have been probed on a wide set of conditions. We could in particular study the behaviour of such properties along quasi-isothermal lines extracted from the data sets. Our results on liquid samples show that the water–ethanol–ammonia mixture exhibits a lower onset temperature for reflectivity and higher reflectivity value than water in the whole set of characterised conditions. This confirms our results along their principal Hugoniot curves.

Ab initio calculations. During the work presented in this Thesis, we could establish fruitful collaborations with the *ab initio* community. Supporting *ab initio* calculations have represented an invaluable aid for the interpretation of our experimental results. More specifically, the Linear Mixing Approximation calculations provided by M. Bethkenhagen and co-workers *(Rostock University)* have been compared to our exper-

imental data on pure water, a water–ethanol, and a water–ethanol–ammonia mixtures (cfr. Chapter 4). The good agreement between experimental data and calculations sustains the hypothesis that linear mixing well describes the behaviour of those mixtures in the investigated thermodynamic range.

Moreover, the electrical conductivity of warm dense silica calculated by means of *ab initio* calculations by Laudernet et al. (2004) and F. Soubiran *(ENS Lyon)* has allowed us to build a model of the behaviour of the frequency-dependent conductivity as a function of pressure and temperature. This model has been essential for the conception of a novel hybrid approach for determining static and optical conductivity values from experimental shock-front reflectivity measurements (cfr. Chapter 6). Such an approach, after being conveniently adapted, could be employed for the estimation of conductivity from the reflectivity measurement in other materials for which several *ab initio* studies are available. In this work, the static conductivity dependence on pressure and temperature extracted with the use of the aforementioned method has permitted the first experimental verification of previous calculations by Mazevet et al. (2015) and Scipioni et al. (2017). Those calculations predicted that, at temperatures below around 20 kK, the conductivity of silica is not monotonically dependent on pressure along isothermal lines, due to the effects of compression on the electronic structure. Moreover, having experimentally found similar conductivity values to those calculated by Scipioni et al. (2017) and Soubiran and Militzer (2018), our work supports their conclusions that magma oceans can sustain a dynamo-generated magnetic field inside super-Earth exoplanets and possibly the same could be true in the early Earth.

Perspectives

The study presented in this Thesis and its technical and scientific limits open a rather clear path for future investigations. The use of pre-compression methods has allowed us to characterise previously uncharted regions of the phase diagram of several materials (including pure water, pure ammonia, the water–ethanol–ammonia mixture, and quartz) and to provide fresh data for the benchmarking of *ab initio* calculations. However, the set of probed conditions has to be expanded in order to encompass the interior profiles predicted by different models, take into account the evolution history of the planetary objects and also the great diversity of the exoplanets' population. As a consequence, a first axis of future work consists in the further development of pre-compression techniques and in the effort to couple static and dynamic pre-compressions within a single shot, that is, compressing a sample inside a Diamond Anvil Cell via a double-shock. A proposed experimental campaign at LULI2000, whose scientific goals include a preliminary test of this approach on liquid ammonia samples, has been accepted and is scheduled for December 2019. Other experimental campaigns at facilities where higher-energy laser pulses are available shall be programmed to further enlarge the set of explored conditions.

The measurement of the thermodynamic and optical properties of materials by means of standard optical diagnostics is undoubtedly crucial for the advancement of both our knowledge of the Warm Dense Matter regime and of planetary models as it allows to probe the macroscopic properties of the sample. A natural continuation of the characterisation work consists in making use of X-ray diagnostics to directly

probe the microscopic properties of the materials under study. If, on the one hand, the X-ray study of shock-compressed liquid mixtures still seems premature, as a lot of work shall be done in the first place to unveil their macroscopic properties, on the other hand water, silica and silicate minerals, whose equations of state have already been sufficiently characterised, are currently being the object of several X-ray studies. For water, we want to cite the very recent work by Millot et al. (2019), where the insulating and superionic ice states have been probed by X-ray diffraction. Silica, on its part, has recently been the object of K-edge X-ray absorption spectroscopy [Denoeud et al. (2016a)] and X-ray diffraction studies [Tracy et al. (2018)]. The experimental campaign at SLAC–LCLS is inscribed in this logic, as its scientific goal was the X-ray diffraction study of silica and silicate minerals. The results of this campaign suggest that the influence of the temporal scale of the material compression on the occurrence of phase transitions and the conditions at which they take place should be further investigated. Such a study, which shall be conducted by comparing the behaviour of materials at the same thermodynamic conditions but obtained via compression methods involving different time scales (dynamic Diamond Anvil Cells, gas-guns, high-power lasers) would enlighten the kinetic effects in phase transitions and strongly contribute to the understanding of the planetary relevance of dynamic compression experiments.

Bibliography

Acuña, M., Connerney, J., Wasilewski, P. a., Lin, R., Anderson, K., Carlson, C., McFadden, J., Curtis, D., Mitchell, D., Reme, H., et al. (1998). Magnetic field and plasma observations at Mars: Initial results of the Mars Global Surveyor mission. *Science*, 279(5357):1676–1680.

Acuña, M. H. and Ness, N. F. (1980). The magnetic field of Saturn: Pioneer 11 observations. *Science*, 207(4429):444–446.

Adadurov, G., Dremin, A., Pershin, S., Rodionov, V., and Ryabinin, Y. N. (1962). Shock compression of quartz. *Zh. Prikl. Mekh. Tekhn. Fiz.*, 4:81–89.

Aidun, J. B. and Gupta, Y. (1991). Analysis of Lagrangian gauge measurements of simple and nonsimple plane waves. *Journal of applied physics*, 69(10):6998–7014.

Alfè, D., Gillan, M., and Price, G. (2007). Temperature and composition of the Earth's core. *Contemporary Physics*, 48(2):63–80.

Alfè, D., Price, G. D., and Gillan, M. J. (2002). Iron under Earth's core conditions: Liquid-state thermodynamics and high-pressure melting curve from ab initio calculations. *Phys. Rev. B*, 65:165118.

Amadou, N., Brambrink, E., Vinci, T., Benuzzi-Mounaix, A., Huser, G., Brygoo, S., Morard, G., Guyot, F., de Resseguier, T., Mazevet, S., Miyanishi, K., Ozaki, N., Kodama, R., Henry, O., Raffestin, D., Boehly, T., and Koenig, M. (2015). Probing iron at Super-Earth core conditions. *Physics of Plasmas*, 22(2):022705.

Anglada-Escudé, G., Amado, P. J., Barnes, J., Berdiñas, Z. M., Butler, R. P., Coleman, G. A. L., de La Cueva, I., Dreizler, S., Endl, M., Giesers, B., Jeffers, S. V., Jenkins, J. S., Jones, H. R. A., Kiraga, M., Kürster, M., López-González, M. J., Marvin, C. J., Morales, N., Morin, J., Nelson, R. P., Ortiz, J. L., Ofir, A., Paardekooper, S.-J., Reiners, A., Rodríguez, E., Rodríguez-López, C., Sarmiento, L. F., Strachan, J. P., Tsapras, Y., Tuomi, M., and Zechmeister, M. (2016). A terrestrial planet candidate in a temperate orbit around Proxima Centauri. *Nature*, 536:437–440.

Antonelli, L., Atzeni, S., Schiavi, A., Baton, S. D., Brambrink, E., Koenig, M., Rousseaux, C., Richetta, M., Batani, D., Forestier-Colleoni, P., Le Bel, E., Maheut, Y., Nguyen-Bui, T., Ribeyre, X., and Trela, J. (2017). Laser-driven shock waves studied by x-ray radiography. *Phys. Rev. E*, 95:063205.

Anzellini, S., Dewaele, A., Mezouar, M., Loubeyre, P., and Morard, G. (2013). Melting of iron at Earth's inner core boundary based on fast X-ray diffraction. *Science*, 340(6131):464–466.

Aquilanti, G., Trapananti, A., Karandikar, A., Kantor, I., Marini, C., Mathon, O., Pascarelli, S., and Boehler, R. (2015). Melting of iron determined by X-ray absorption spectroscopy to 100 GPa. *Proceedings of the National Academy of Sciences*, 112(39):12042–12045.

Aurnou, J. (2004). Planetary science: Secrets of the deep. *Nature*, 428(6979):134.

Baraffe, I., Chabrier, G., and Barman, T. (2008). Structure and evolution of super-Earth to super-Jupiter exoplanets - I. Heavy element enrichment in the interior. *Astronomy & Astrophysics*, 482(1):315–332.

Baraffe, I., Chabrier, G., and Barman, T. (2010). The physical properties of extra-solar planets. *Reports on Progress in Physics*, 73(1):016901.

Barker, L. M. and Schuler, K. W. (1974). Correction to the velocity-per-fringe relationship for the VISAR interferometer. *Journal of Applied Physics*, 45(8):3692–3693.

Barrios, M. A., Hicks, D. G., Boehly, T. R., Fratanduono, D. E., Eggert, J. H., Celliers, P. M., Collins, G. W., and Meyerhofer, D. D. (2010). High-precision measurements of the equation of state of hydrocarbons at 1-10 Mbar using laser-driven shock waves. *Physics of Plasmas*, 17(5):056307.

Basko, M., Löwer, T., Kondrashov, V., Kendl, A., Sigel, R., and Meyer-ter Vehn, J. (1997). Optical probing of laser-induced indirectly driven shock waves in aluminum. *Physical Review E*, 56(1):1019.

Batani, D., Jakubowska, K., Benuzzi-Mounaix, A., Cavazzoni, C., Danson, C., Hall, T., Kimpel, M., Neely, D., Pasley, J., Gloahec, M. R. L., and Telaro, B. (2015). Refraction index of shock compressed water in the megabar pressure range. *Europhysics Letters*, 112(3):36001.

Benuzzi-Mounaix, A., Koenig, M., Huser, G., Faral, B., Grandjouan, N., Batani, D., Henry, E., Tomasini, M., Hall, T. A., and Guyot, F. (2004). Generation of a double shock driven by laser. *Physical Review E*, 70(4):045401.

Bethkenhagen, M., Cebulla, D., Redmer, R., and Hamel, S. (2015). Superionic phases of the 1:1 water-ammonia mixture. *The Journal of Physical Chemistry A*, 119(42):10582–10588.

Bethkenhagen, M., French, M., and Redmer, R. (2013). Equation of state and phase diagram of ammonia at high pressures from ab initio simulations. *Journal of Chemical Physics*, 138(23).

Bethkenhagen, M., Meyer, E. R., Hamel, S., Nettelmann, N., French, M., Scheibe, L., Ticknor, C., Collins, L. A., Kress, J. D., Fortney, J. J., and Redmer, R. (2017). Planetary ices and the linear mixing approximation. *The Astrophysical Journal*, 848(1):67.

Birnboim, Y., Keshet, U., and Hernquist, L. (2010). Cold fronts by merging of shocks. *Monthly Notices of the Royal Astronomical Society*, 408:199–212.

Boates, B. and Bonev, S. (2013). Demixing instability in dense molten $MgSiO_3$ and the high-pressure phase diagram of MgO. In *APS Meeting Abstracts*, volume 1, page 39006.

Boden, D. R. (2016). *Geology and Heat Architecture of the Earth's Interior*. CRC Press.

Boehler, R. (1993). Temperatures in the Earth's core from melting-point measurements of iron at high static pressures. *Nature*, 363(6429):534.

Boehler, R. and De Hantsetters, K. (2004). New anvil designs in diamond-cells. *High Pressure Research*, 24(3):391–396.

Boehly, T. R., Hicks, D. G., Celliers, P. M., Collins, T. J. B., Earley, R., Eggert, J. H., Jacobs-Perkins, D., Moon, S. J., Vianello, E., Meyerhofer, D. D., and Collins, G. W. (2004). Properties of fluid deuterium under double-shock compression to several Mbar. *Physics of Plasmas*, 11(9):L49–L52.

Boettger, J. C. (1992). New model for the shock-induced α-quartz $\rightarrow$ stishovite phase transition in silica. *Journal of Applied Physics*, 72(11):5500–5508.

Bolis, R. M., Morard, G., Vinci, T., Ravasio, A., Bambrink, E., Guarguaglini, M., Koenig, M., Musella, R., Remus, F., Bouchet, J., Ozaki, N., Miyanishi, K., Sekine, T., Sakawa, Y., Sano, T., Kodama, R., Guyot, F., and Benuzzi-Mounaix, A. (2016). Decaying shock studies of phase transitions in MgO-SiO_2 systems: Implications for the super-Earths' interiors. *Geophysical Research Letters*, 43(18):9475–9483.

Born, M. and Oppenheimer, R. (1927). Zur quantentheorie der molekeln. *Annalen der Physik*, 389(20):457–484.

Boslough, M. B. (1988). Postshock temperatures in silica. *Journal of Geophysical Research: Solid Earth*, 93(B6):6477–6484.

Brown, J. M. and McQueen, R. G. (1986). Phase transitions, grüneisen parameter, and elasticity for shocked iron between 77 GPa and 400 GPa. *Journal of Geophysical Research: Solid Earth*, 91(B7):7485–7494.

Bruno, G. (1584). *De l'infinito, universo e mondi*.

Brygoo, S., Millot, M., Loubeyre, P., Celliers, P., Collins, G., Eggert, J., Rygg, R., Swift, D., and Jeanloz, R. (2017). Double shocks on precompressed deuterium near the plasma phase transition. In *APS Shock Compression of Condensed Matter Meeting Abstracts*, page J6.003.

Brygoo, S., Millot, M., Loubeyre, P., Lazicki, A. E., Hamel, S., Qi, T., Celliers, P. M., Coppari, F., Eggert, J. H., Fratanduono, D. E., Hicks, D. G., Rygg, J. R., Smith, R. F., Swift, D. C., Collins, G. W., and Jeanloz, R. (2015). Analysis of laser shock experiments on precompressed samples using a quartz reference and application to warm dense hydrogen and helium. *Journal of Applied Physics*, 118(19):195901.

Cameron, A. G. W. (1973). Abundances of the Elements in the Solar System. *Space Science Reviews*, 15:121–146.

Carter, J. A., Winn, J. N., Gilliland, R., and Holman, M. J. (2009). Near-infrared transit photometry of the exoplanet HD 149026b. *The Astrophysical Journal*, 696(1):241.

Cassan, A., Kubas, D., Beaulieu, J.-P., Dominik, M., Horne, K., Greenhill, J., Wambsganss, J., Menzies, J., Williams, A., Jørgensen, U. G., et al. (2012). One or more bound planets per Milky Way star from microlensing observations. *Nature*, 481(7380):167.

Cavazzoni, C., Chiarotti, G., Scandolo, S., Tosatti, E., Bernasconi, M., and Parrinello, M. (1999). Superionic and metallic states of water and ammonia at giant planet conditions. *Science*, 283:44–46.

Cebulla, D. and Redmer, R. (2014). Ab initio simulations of MgO under extreme conditions. *Physical Review B*, 89(13):134107.

Celliers, P., Ng, A., Xu, G., and Forsman, A. (1992). Thermal equilibration in a shock wave. *Phys. Rev. Lett.*, 68:2305–2308.

Celliers, P. M., Collins, G. W., Da Silva, L. B., Gold, D. M., Cauble, R., Wallace, R. J., Foord, M. E., and Hammel, B. A. (2000). Shock-induced transformation of liquid deuterium into a metallic fluid. *Phys. Rev. Lett.*, 84:5564–5567.

Celliers, P. M., Collins, G. W., Hicks, D. G., Koenig, M., Henry, E., Benuzzi-Mounaix, A., Batani, D., Bradley, D. K., Silva, L. B. D., Wallace, R. J., Moon, S. J., Eggert, J. H., Lee, K. K. M., Benedetti, L. R., Jeanloz, R., Masclet, I., Dague, N., Marchet, B., Gloahec, M. R. L., Reverdin, C., Pasley, J., Willi, O., Neely, D., and Danson, C. (2004). Electronic conduction in shock-compressed water. *Physics of Plasmas*, 11(8):L41.

Celliers, P. M., Loubeyre, P., Eggert, J. H., Brygoo, S., McWilliams, R. S., Hicks, D. G., Boehly, T. R., Jeanloz, R., and Collins, G. W. (2010). Insulator-to-conducting transition in dense fluid helium. *Phys. Rev. Lett.*, 104:184503.

Celliers, P. M., Millot, M., Brygoo, S., McWilliams, R. S., Fratanduono, D. E., Rygg, J. R., Goncharov, A. F., Loubeyre, P., Eggert, J. H., Peterson, J. L., et al. (2018). Insulator-metal transition in dense fluid deuterium. *Science*, 361(6403):677–682.

Chau, R., Hamel, S., and Nellis, W. (2011). Chemical processes in the deep interior of Uranus. *Nature Communications*, 2(203).

Chau, R., Mitchell, A. C., Minich, R. W., and Nellis, W. J. (2001). Electrical conductivity of water compressed dynamically to pressures of 70 - 180 GPa (0.7 - 1.8 Mbar). *The Journal of Chemical Physics*, 114(3):1361–1365.

Clerouin, J., Renaudin, P., Laudernet, Y., Noiret, P., and Desjarlais, M. P. (2005). Electrical conductivity and equation-of-state study of warm dense copper: Measurements and quantum molecular dynamics calculations. *Phys. Rev. B*, 71:064203.

Connerney, J. E. P., Benn, M., Bjarno, J. B., Denver, T., Espley, J., Jorgensen, J. L., Jorgensen, P. S., Lawton, P., Malinnikova, A., Merayo, J. M., Murphy, S., Odom, J., Oliversen, R., Schnurr, R., Sheppard, D., and Smith, E. J. (2017). The Juno magnetic field investigation. *Space Science Reviews*, 213(1):39–138.

Coppari, F., Smith, R., Eggert, J., Wang, J., Rygg, J., Lazicki, A., Hawreliak, J., Collins, G., and Duffy, T. S. (2013). Experimental evidence for a phase transition in magnesium oxide at exoplanet pressures. *Nature Geoscience*, 6(11):926.

Cuneo, M. E., Herrmann, M. C., Sinars, D. B., Slutz, S. A., Stygar, W. A., Vesey, R. A., Sefkow, A. B., Rochau, G. A., Chandler, G. A., Bailey, J. E., Porter, J. L., McBride, R. D., Rovang, D. C., Mazarakis, M. G., Yu, E. P., Lamppa, D. C., Peterson, K. J., Nakhleh, C., Hansen, S. B., Lopez, A. J., Savage, M. E., Jennings, C. A., Martin, M. R., Lemke, R. W., Atherton, B. W., Smith, I. C., Rambo, P. K., Jones, M., Lopez, M. R.,

Christenson, P. J., Sweeney, M. A., Jones, B., McPherson, L. A., Harding, E., Gomez, M. R., Knapp, P. F., Awe, T. J., Leeper, R. J., Ruiz, C. L., Cooper, G. W., Hahn, K. D., McKenney, J., Owen, A. C., McKee, G. R., Leifeste, G. T., Ampleford, D. J., Waisman, E. M., Harvey-Thompson, A., Kaye, R. J., Hess, M. H., Rosenthal, S. E., and Matzen, M. K. (2012). Magnetically driven implosions for inertial confinement fusion at Sandia National Laboratories. *IEEE Transactions on Plasma Science*, 40(12):3222–3245.

Danel, J.-F. and Kazandjian, L. (2015). Equation of state of a dense plasma by orbital-free and quantum molecular dynamics: Examination of two isothermal-isobaric mixing rules. *Physical Review E*, 91(1):013103.

Datchi, F., Ninet, S., Gauthier, M., Saitta, A. M., Canny, B., and Decremps, F. (2006). Solid ammonia at high pressure: A single-crystal x-ray diffraction study to 123 GPa. *Phys. Rev. B*, 73:174111.

Denoeud, A., Mazevet, S., Guyot, F., Dorchies, F., Gaudin, J., Ravasio, A., Brambrink, E., and Benuzzi-Mounaix, A. (2016a). High-pressure structural changes in liquid silica. *Phys. Rev. E*, 94:031201.

Denoeud, A., Ozaki, N., Benuzzi-Mounaix, A., Uranishi, H., Kondo, Y., Kodama, R., Brambrink, E., Ravasio, A., Bocoum, M., Boudenne, J.-M., Harmand, M., Guyot, F., Mazevet, S., Riley, D., Makita, M., Sano, T., Sakawa, Y., Inubushi, Y., Gregori, G., Koenig, M., and Morard, G. (2016b). Dynamic X-ray diffraction observation of shocked solid iron up to 170 GPa. *Proceedings of the National Academy of Sciences*, 113(28):7745–7749.

Desjarlais, M. P., Knudson, M. D., and Cochrane, K. R. (2017). Extension of the Hugoniot and analytical release model of α-quartz to 0.2-3 TPa. *Journal of Applied Physics*, 122(3):035903.

Dick, R. D. (1981). Shock compression data for liquids. III. substituted methane compounds, ethylene glycol, glycerol, and ammonia. *The Journal of Chemical Physics*, 74(7):4053–4061.

Dong, S., Xie, J.-W., Zhou, J.-L., Zheng, Z., and Luo, A. (2018). LAMOST telescope reveals that Neptunian cousins of hot Jupiters are mostly single offspring of stars that are rich in heavy elements. *Proceedings of the National Academy of Sciences*, 115(2):266–271.

Dougherty, M. K., Achilleos, N., Andre, N., Arridge, C. S., Balogh, A., Bertucci, C., Burton, M. E., Cowley, S. W. H., Erdos, G., Giampieri, G., Glassmeier, K.-H., Khurana, K. K., Leisner, J., Neubauer, F. M., Russell, C. T., Smith, E. J., Southwood, D. J., and Tsurutani, B. T. (2005). Cassini magnetometer observations during Saturn orbit insertion. *Science*, 307(5713):1266–1270.

Drude, P. (1900a). Zur Elektronentheorie der Metalle. *Annalen der Physik*, 306(3):566–613.

Drude, P. (1900b). Zur Elektronentheorie der Metalle; II. Teil. Galvanomagnetische und thermomagnetische Effecte. *Annalen der Physik*, 308(11):369–402.

Eales, S. (2009). *Planets and Planetary Systems*. John Wiley & Sons, Ltd.

Edwards, J., Lorenz, K., Remington, B., Pollaine, S., Colvin, J., Braun, D., Lasinski, B., Reisman, D., McNaney, J., Greenough, J., R.Wallace, Louis, H., and Kalantar, D. (2004). Laser-driven plasma loader for shockless compression and acceleration of samples in the solid state. *Physical review letters*, 92(7):075002.

Eggert, J., Brygoo, S., Loubeyre, P., McWilliams, R. S., Celliers, P. M., Hicks, D. G., Boehly, T. R., Jeanloz, R., and Collins, G. W. (2008). Hugoniot data for helium in the ionization regime. *Phys. Rev. Lett.*, 100:124503.

Eliezer, S., Ghatak, A., and Hora, H. (2002). *Fundamentals of Equations of State*. World Scientific Publishing Company.

Fabbro, R. (1982). *Thèse d'État*. PhD thesis, Université de Paris Sud.

Folkner, W., Iess, L., Anderson, J., Asmar, S., Buccino, D., Durante, D., Feldman, M., Casajus, L. G., Gregnanin, M., Milani, A., et al. (2017). Jupiter gravity field estimated from the first two Juno orbits. *Geophysical Research Letters*, 44(10):4694–4700.

Fortov, V. E., Ternovoi, V. Y., Zhernokletov, M. V., Mochalov, M. A., Mikhailov, A. L., Filimonov, A. S., Pyalling, A. A., Mintsev, V. B., Gryaznov, V. K., and Iosilevskii, I. L. (2003). Pressure-produced ionization of nonideal plasma in a megabar range of dynamic pressures. *Journal of Experimental and Theoretical Physics*, 97(2):259–278.

French, M., Becker, A., Lorenzen, W., Nettelmann, N., Bethkenhagen, M., Wicht, J., and Redmer, R. (2012). Ab Initio Simulations for Material Properties along the Jupiter Adiabat. *The Astrophysical Journal Supplement Series*, 202:5.

French, M., Mattsson, T., Nettelmann, N., and Redmer, R. (2009). Equation of state and phase diagram of water at ultrahigh pressures as in planetary interiors. *Physical Review B*, 79:054107.

French, M., Mattsson, T. R., and Redmer, R. (2010). Diffusion and electrical conductivity in water at ultrahigh pressures. *Physical Review B*, 82(17):174108.

French, M. and Redmer, R. (2009). Estimating the quantum effects from molecular vibrations of water under high pressures and temperatures. *Journal of Physics Condensed Matter*, 21:375101.

French, M. and Redmer, R. (2011). Optical properties of water at high temperature. *Physics of Plasmas*, 18(4):043301.

French, M. and Redmer, R. (2017). Electronic transport in partially ionized water plasmas. *Physics of Plasmas*, 24(9):092306.

Fressin, F., Torres, G., Charbonneau, D., Bryson, S. T., Christiansen, J., Dressing, C. D., Jenkins, J. M., Walkowicz, L. M., and Batalha, N. M. (2013). The false positive rate of Kepler and the occurrence of planets. *The Astrophysical Journal*, 766(2):81.

Gaidos, E., Conrad, C. P., Manga, M., and Hernlund, J. (2010). Thermodynamic limits on magnetodynamos in rocky exoplanets. *The Astrophysical Journal*, 718(2):596.

Ghosh, G. (1999). Dispersion-equation coefficients for the refractive index and birefringence of calcite and quartz crystals. *Optics Communications*, 163:95–102.

Glatzmaier, G. (2005). A Saturnian dynamo simulation. *American Geophysical Union Fall Meeting 2005, San Francisco, CA*.

Goldman, N., Fried, L. E., Kuo, I.-F. W., and Mundy, C. J. (2005). Bonding in the superionic phase of water. *Phys. Rev. Lett.*, 94:217801.

Goldman, N., Reed, E. J., Kuo, I.-F. W., Fried, L. E., Mundy, C. J., and Curioni, A. (2009). Ab initio simulation of the equation of state and kinetics of shocked water. *The Journal of Chemical Physics*, 130(12):124517.

González-Cataldo, F., Davis, S., and Gutiérrez, G. (2016). Melting curve of SiO_2 at multimegabar pressures: implications for gas giants and super-Earths. *Scientific Reports*, 6:26537.

Grosso, G. and Pastori Parravicini, G. (2000). *Solid State Physics*. Academic Press.

Guillot, T. (1999). Interiors of giant planets inside and outside the solar system. *Science*, 286(5437):72–77.

Guillot, T. (2005). The interiors of giant planets: models and outstanding questions. *Annu. Rev. Earth Planet Sci.*, 33:493–530.

Hale, G. M. and Querry, M. R. (1973). Optical constants of water in the 200-nm to 200-μm wavelength region. *Appl. Opt.*, 12(3):555–563.

Hardesty, D. R. (1976). On the index of refraction of shock-compressed liquid nitromethane. *Journal of Applied Physics*, 47(5):1994–1998.

Harmand, M., Ravasio, A., Mazevet, S., Bouchet, J., Denoeud, A., Dorchies, F., Feng, Y., Fourment, C., Galtier, E., Gaudin, J., Guyot, F., Kodama, R., Koenig, M., Lee, H. J., Miyanishi, K., Morard, G., Musella, R., Nagler, B., Nakatsutsumi, M., Ozaki, N., Recoules, V., Toleikis, S., Vinci, T., Zastrau, U., Zhu, D., and Benuzzi-Mounaix, A. (2015). X-ray absorption spectroscopy of iron at multimegabar pressures in laser shock experiments. *Phys. Rev. B*, 92:024108.

Hartley, N., Brown, S., Cowan, T., Cunningham, E., Döppner, T., Falcone, R., Fletcher, L., Frydrych, S., Galtier, E., Gamboa, E., et al. (2019). Evidence for crystalline structure in dynamically-compressed polyethylene up to 200 GPa. *Scientific Reports*, 9(1):4196.

Helled, R., Anderson, J. D., Podolak, M., and Schubert, G. (2011). Interior Models of Uranus and Neptune. *Astrophysical Journal*, 726.

Henry, E. (2003). *Équation d'état et métallisation de l'eau comprimée par choc laser*. PhD thesis, École Polytechnique.

Hernandez, J.-A. and Caracas, R. (2016). Superionic-Superionic Phase Transitions in Body-Centered Cubic H_2O Ice. *Physical Review Letters*, 117:135503.

Hernandez, J. A. and Caracas, R. (2018). Proton dynamics and the phase diagram of dense water ice. *Journal of Chemical Physics*, 148:214501.

Heyd, J., Scuseria, G. E., and Ernzerhof, M. (2003). Hybrid functionals based on a screened Coulomb potential. *The Journal of Chemical Physics*, 118(18):8207–8215.

Hicks, D. G., Boehly, T. R., Celliers, P. M., Eggert, J. H., Vianello, E., Meyerhofer, D. D., and Collins, G. W. (2005). Shock compression of quartz in the high-pressure fluid regime. *Physics of Plasmas*, 12(8):082702.

Hicks, D. G., Boehly, T. R., Eggert, J. H., Miller, J. E., Celliers, P. M., and Collins, G. W. (2006). Dissociation of Liquid Silica at High Pressures and Temperatures. *Physical Review Letters*, 97(2):025502.

Hohenberg, P. and Kohn, W. (1964). Inhomogeneous electron gas. *Phys. Rev.*, 136:B864–B871.

Holme, R. and Bloxham, J. (1996). The magnetic fields of Uranus and Neptune: Methods and models. *Journal of Geophysical Research: Planets*, 101(E1):2177–2200.

Hugoniot, H. (1887). Mémoire sur la propagation des mouvements dans les corps et spécialement dans les gaz parfaits (première partie). *Journal de l'École Polytechnique*, 57:3–97.

Huser, G., Koenig, M., Benuzzi-Mounaix, A., Henry, E., Vinci, T., Faral, B., Tomasini, M., Telaro, B., and Batani, D. (2005). Temperature and melting of laser-shocked iron releasing into an LiF window. *Physics of Plasmas*, 12(6):060701.

Huser, G., Recoules, V., Ozaki, N., Sano, T., Sakawa, Y., Salin, G., Albertazzi, B., Miyanishi, K., and Kodama, R. (2015). Experimental and ab initio investigations of microscopic properties of laser-shocked Ge-doped ablator. *Phys. Rev. E*, 92:063108.

IAU (2006). International Astronomical Union 2006 General Assembly: Resolutions 5 and 6.

Jakubowska, K., Batani, D., Clerouin, J., and Siberchicot, B. (2019). Theoretical and experimental refraction index of shock compressed and pre-compressed water in the megabar pressure range. *EPL (Europhysics Letters)*, 126(5):56001.

Jarmakani, H., Bringa, E., Erhart, P., Remington, B., Wang, Y., Vo, N., and Meyers, M. (2008). Molecular dynamics simulations of shock compression of nickel: From monocrystals to nanocrystals. *Acta Materialia*, 56(19):5584–5604.

Jeanloz, R., Celliers, P. M., Collins, G. W., Eggert, J. H., Lee, K. K. M., McWilliams, R. S., Brygoo, S., and Loubeyre, P. (2007). Achieving high-density states through shock-wave loading of precompressed samples. *Proceedings of the National Academy of Sciences*, 104(22):9172–9177.

Jenei, Z., O'Bannon, E. F., Weir, S. T., Cynn, H., Lipp, M. J., and Evans, W. J. (2018). Single crystal toroidal diamond anvils for high pressure experiments beyond 5 megabar. *Nature Communications*, 9:3563.

Jensen, B. J., Holtkamp, D. B., Rigg, P. A., and Dolan, D. H. (2007). Accuracy limits and window corrections for photon Doppler velocimetry. *Journal of Applied Physics*, 101(1):013523.

Johnson, J. (1994). National Technical Information Service Document DE94-011699.

Jones, S. C. and Gupta, Y. M. (2000). Refractive index and elastic properties of z-cut quartz shocked to 60 kbar. *Journal of Applied Physics*, 88:5671–5679.

Kato, Y., Mima, K., Miyanaga, N., Arinaga, S., Kitagawa, Y., Nakatsuka, M., and Yamanaka, C. (1984). Random phasing of high-power lasers for uniform target acceleration and plasma-instability suppression. *Phys. Rev. Lett.*, 53:1057–1060.

Kietzmann, A., Holst, B., Redmer, R., Desjarlais, M. P., and Mattsson, T. R. (2007). Quantum molecular dynamics simulations for the nonmetal-to-metal transition in fluid helium. *Phys. Rev. Lett.*, 98:190602.

Kimura, T., Kuwayama, Y., and Yagi, T. (2014). Melting temperatures of H_2O up to 72 GPa measured in a diamond anvil cell using CO_2 laser heating technique. *Journal of Chemical Physics*, 140(074501).

Kimura, T., Ozaki, N., Sano, T., Okuchi, T., Sano, T., Shimizu, K., Miyanishi, K., Terai, T., Kakeshita, T., Sakawa, Y., and Kodama, R. (2015). P-ρ-T measurements of H_2O up to 260 GPa under laser-driven shock loading. *Journal of Chemical Physics*, 142(16):164504.

Knudson, M., Desjarlais, M. P., Lemke, R., Mattsson, T. R., French, M., Nettelmann, N., and Redmer, R. (2012). Probing the interiors of the ice giants: Shock compression of water to 700 GPa and 3.8 g/cm^3. *Physical Review Letters*, 108:091102.

Knudson, M. D. and Desjarlais, M. P. (2009). Shock Compression of Quartz to 1.6 TPa: Redefining a Pressure Standard. *Physical Review Letters*, 103(22):225501.

Knudson, M. D. and Desjarlais, M. P. (2013). Adiabatic release measurements in α-quartz between 300 and 1200 GPa: Characterization of α-quartz as a shock standard in the multimegabar regime. *Physical Review B*, 88(18):184107.

Knudson, M. D., Hanson, D. L., Bailey, J. E., Hall, C. A., Asay, J. R., and Deeney, C. (2004). Principal Hugoniot, reverberating wave, and mechanical reshock measurements of liquid deuterium to 400 GPa using plate impact techniques. *Phys. Rev. B*, 69:144209.

Knudson, M. D., Lemke, R. W., Hayes, D. B., Hall, C. A., Deeney, C., and Asay, J. R. (2003). Near-absolute Hugoniot measurements in aluminum to 500 GPa using a magnetically accelerated flyer plate technique. *Journal of Applied Physics*, 94(7):4420–4431.

Kohn, W. and Sham, L. J. (1965). Self-consistent equations including exchange and correlation effects. *Phys. Rev.*, 140.

Kopernikus, N. (1543). *De revolutionibus orbium coelestium.* Petrejus, J.

Kovel, I. (1973). PhD thesis, Lawrence Livermore National Laboratory.

Kruer, W. (1988). *The physics of Laser Plasma Interactions.* Addison-Wesley.

L. V. Al'tshuler, R. F. Trunin, G. V. S. (1965). Shock compression of periclase and quartz and composition of low Earth's mantle. *Izv. Akad. Nauk. SSSR Fiz. Zemli*, 10:1–6.

Laudernet, Y., Clérouin, J., and Mazevet, S. (2004). Ab initio simulations of the electrical and optical properties of shock-compressed SiO2. *Phys. Rev. B*, 70:165108.

Lee, M. and Scandolo, S. (2011). Mixtures of planetary ices at extreme conditions. *Nature communications*, 2:185.

Lee, R. W., Kalantar, D., and Molitoris, J. (2004). Warm Dense Matter: An overview. Lawrence Livermore National Laboratory Report UCRL-TR-203844. Technical report, LLNL.

Lemke, R. W., Knudson, M. D., Bliss, D. E., Cochrane, K., Davis, J.-P., Giunta, A. A., Harjes, H. C., and Slutz, S. A. (2005). Magnetically accelerated, ultrahigh velocity flyer plates for shock wave experiments. *Journal of Applied Physics*, 98(7):073530.

Li, D., Wang, C., Yan, J., Fu, Z.-G., and Zhang, P. (2017). Structural and transport properties of ammonia along the principal Hugoniot. *Scientific Reports*, 7:12338.

Li, D., Zhang, P., and Yan, J. (2013). Quantum molecular dynamics simulations of the thermophysical properties of shocked liquid ammonia for pressures up to 1.3 TPa. *Journal of Chemical Physics*, 139(134505).

Li, F., Li, M., Cui, Q., Cui, T., He, Z., Zhou, Q., and Zou, G. (2009). The velocity, refractive index, and equation of state of liquid ammonia at high temperatures and high pressures. *The Journal of Chemical Physics*, 131(13):134502.

Loubeyre, P., Celliers, P. M., Hicks, D. G., Henry, E., Dewaele, A., Pasley, J., Eggert, J., Koenig, M., Occelli, F., Lee, K. M., Jeanloz, R., Neely, D., Benuzzi-Mounaix, A., Bradley, D., Bastea, M., Moon, S., and Collins, G. W. (2004). Coupling static and dynamic compressions: first measurements in dense hydrogen. *High Pressure Research*, 24(1):25–31.

Loubeyre, P., Occelli, F., and Dumas, P. (2019). Observation of a first order phase transition to metal hydrogen near 425 GPa. *arXiv preprint arXiv:1906.05634*.

Loveday, J. S., Nelmes, R. J., Marshall, W. G., Besson, J. M., Klotz, S., Hamel, G., and Hull, S. (1996). High pressure neutron diffraction studies using the Paris-Edinburgh cell. *High Pressure Research*, 14(4-6):303–309.

Luo, S.-N., Akins, J. A., Ahrens, T. J., and Asimow, P. D. (2004). Shock-compressed $MgSiO_3$ glass, enstatite, olivine, and quartz: Optical emission, temperatures, and melting. *Journal of Geophysical Research: Solid Earth*, 109(B5):B05205.

Lyon, S. and Johnson, J. (1992). *Los Alamos technical report LA-UR-92-3407*.

Lyzenga, G. A. and Ahrens, T. J. (1980). Shock temperature measurements in Mg_2SiO_4 and SiO_2 at high pressures. *Geophysical Research Letters*, 7(2):141–144.

Lyzenga, G. A., Ahrens, T. J., and Mitchell, A. C. (1983). Shock temperatures of SiO_2 and their geophysical implications. *Journal of Geophysical Research: Solid Earth*, 88(B3):2431–2444.

Lyzenga, G. A., Ahrens, T. J., Nellis, W. J., and Mitchell, A. C. (1982). The temperature of shock-compressed water. *Journal of Chemical Physics*, 76:6282–6286.

Mao, H. K., Xu, J., and Bell, P. M. (1986). Calibration of the ruby pressure gauge to 800 kbar under quasi-hydrostatic conditions. *Journal of Geophysical Research: Solid Earth*, 91(B5):4673–4676.

Marsh, S. P. (1980). *LASL Shock Hugoniot Data*. Univ. California Press.

Mattsson, T. R. and Desjarlais, M. P. (2006). Phase diagram and electrical conductivity of high energy-density water from density functional theory. *Phys. Rev. Lett.*, 97:017801.

Mayor, M. and Queloz, D. (1995). A Jupiter-mass companion to a solar-type star. *Nature*, 378(6555):355.

Mazevet, S., Tsuchiya, T., Taniuchi, T., Benuzzi-Mounaix, A., and Guyot, F. (2015). Melting and metallization of silica in the cores of gas giants, ice giants, and super Earths. *Physical Review B*, 92(1):014105.

McCoy, C. A., Gregor, M. C., Polsin, D. N., Fratanduono, D. E., Celliers, P. M., Boehly, T. R., and Meyerhofer, D. D. (2016). Measurements of the sound velocity of shock-compressed liquid silica to 1100 GPa. *Journal of Applied Physics*, 120(23):235901.

McQueen, R. G. and Marsh, S. P. (1966). Shock-wave compression of iron-nickel alloys and the Earth's core. *Journal of Geophysical Research*, 71(6):1751–1756.

McWilliams, R. S., Spaulding, D. K., Eggert, J. H., Celliers, P. M., Hicks, D. G., Smith, R. F., Collins, G. W., and Jeanloz, R. (2012). Phase transformations and metallization of magnesium oxide at high pressure and temperature. *Science*, 338(6112):1330–1333.

Meot-Ner (Mautner), M. M. and Lias, S. G. (2018). Binding energies between ions and molecules, and the thermochemistry of cluster ions. In Linstrom, P. and Mallard, W., editors, *NIST Standard Reference Database Number 69*. National Institute of Standards and Technology, Gaithersburg MD, 20899.

Meyer, E. R., Ticknor, C., Bethkenhagen, M., Hamel, S., Redmer, R., Kress, J. D., and Collins, L. A. (2015). Bonding and structure in dense multi-component molecular mixtures. *The Journal of Chemical Physics*, 143(16):164513.

Militzer, B. (2013). Ab initio investigation of a possible liquid - liquid phase transition in $MgSiO_3$ at megabar pressures. *High Energy Density Physics*, 9(1):152–157.

Millot, M., Coppari, F., Rygg, J. R., Correa Barrios, A., Hamel, S., Swift, D. C., and Eggert, J. H. (2019). Nanosecond X-ray diffraction of shock-compressed superionic water ice. *Nature*, 569:251–255.

Millot, M., Dubrovinskaia, N., Černok, A., Blaha, S., Dubrovinsky, L., Braun, D. G., Celliers, P. M., Collins, G. W., Eggert, J. H., and Jeanloz, R. (2015). Shock compression of stishovite and melting of silica at planetary interior conditions. *Science*, 347:418–420.

Millot, M., Hamel, S., Rygg, J. R., Celliers, P. M., Collins, G. W., Coppari, F., Fratanduono, D. E., Jeanloz, R., Swift, D. C., and Eggert, J. H. (2018). Experimental evidence for superionic water ice using shock compression. *Nature Physics*, 14(3):297–302.

Mitchell, A. and Nellis, W. (1982). Equation of state and electrical conductivity of water and ammonia shocked to the 100 GPa (1 Mbar) pressure range. *Journal of Chemical Physics*, 76(12):6273–6281.

Miyanishi, K., Tange, Y., Ozaki, N., Kimura, T., Sano, T., Sakawa, Y., Tsuchiya, T., and Kodama, R. (2015). Laser-shock compression of magnesium oxide in the warm-dense-matter regime. *Physical Review E*, 92(2):023103.

Moore, K. M., Yadav, R. K., Kulowski, L., Cao, H., Bloxham, J., Connerney, J. E., Kotsiaros, S., Jørgensen, J. L., Merayo, J. M., Stevenson, D. J., et al. (2018). A complex dynamo inferred from the hemispheric dichotomy of Jupiter's magnetic field. *Nature*, 561(7721):76.

More, R. M., Warren, K. H., Young, D. A., and Zimmerman, G. B. (1988). A new quotidian equation of state (QEOS) for hot dense matter. *The Physics of Fluids*, 31(10):3059–3078.

Mulford, R., Swift, D. C., and Hamel, S. (2014). Equation of state of ammonia. *Journal of Physics: Conference Series*, 500(7):072001.

Musella, R., Mazevet, S., and Guyot, F. (2019). Physical properties of MgO at deep planetary conditions. *Phys. Rev. B*, 99:064110.

Nellis, W. (2015). The unusual magnetic fields of Uranus and Neptune. *Modern Physics Letters B*, 29(1).

Nellis, W., Holmes, N., Mitchell, A., Hamilton, D., and Nicol, M. (1997). Equation of state and electrical conductivity of synthetic Uranus, a mixture of water, ammonia, and isopropanol, at shock pressures up to 200 GPa. *J. Chem. Phys.*, 107(21):9096–9100.

Nellis, W., Holmes, N., Mitchell, A., Trainor, R., Governo, G., Ross, M., and Young, D. (1984). Shock compression of liquid helium to 56 GPa (560 kbar). *Physical Review Letters*, 53(13):1248.

Nellis, W. J. (2017). Magnetic fields of Uranus and Neptune: Metallic fluid hydrogen. *AIP Conference Proceedings*, 1793:090002.

Nellis, W. J., Hamilton, D. C., Holmes, N. C., Radousky, H. B., Ree, F. H., Mitchell, A. C., and Nicol, M. (1988). The nature of the interior of Uranus based on studies of planetary ices at high dynamic pressure. *Science*, 240(4853):779–781.

Nellis, W. J., Hamilton, D. C., and Mitchell, A. C. (2001). Electrical conductivities of methane, benzene, and polybutene shock compressed to 60 GPa (600 kbar). *The Journal of Chemical Physics*, 115(2):1015–1019.

Nellis, W. J., Weir, S. T., and Mitchell, A. C. (1999). Minimum metallic conductivity of fluid hydrogen at 140 GPa (1.4 Mbar). *Phys. Rev. B*, 59:3434–3449.

Ness, N., Behannon, K., Lepping, R., and Whang, Y. (1975). The magnetic field of Mercury, 1. *Journal of Geophysical Research*, 80(19):2708–2716.

Ness, N. F., Acuña, M. H., Burlaga, L. F., Connerney, J. E. P., and Lepping, R. P. (1989). Magnetic fields at Neptune. *Science*, 246.

Ness, N. F., Acuña, M. H., Behannon, K. W., Burlaga, L. F., Connerney, J. E. P., Lepping, R. P., and Neubauer, F. M. (1986). Magnetic fields at Uranus. *Science*, 233(4759):85–89.

Nettelmann, N., Kramm, U., Redmer, R., and Neuhauser, R. (2010). Interior structure models of GJ436b. *Astronomy & Astrophysics*, 523:A26.

Nettelmann, N., Wang, K., Fortney, J., Hamel, S., Yellamilli, S., Bethkenhagen, M., and Redmer, R. (2016). Uranus evolution models with simple thermal boundary layers. *Icarus*, 275:107–116.

Nguyen, J. H. and Holmes, N. C. (2004). Melting of iron at the physical conditions of the Earth's core. *Nature*, 427(6972):339.

Nimmo, F. (2002). Why does Venus lack a magnetic field? *Geology*, 30(11):987–990.

Ninet, S. and Datchi, F. (2008). High pressure – high temperature phase diagram of ammonia. *The Journal of Chemical Physics*, 128(15):154508.

Ninet, S., Datchi, F., and Saitta, A. M. (2012). Proton disorder and superionicity in hot dense ammonia ice. *Phys. Rev. Lett.*, 108:165702.

Ninet, S., Datchi, F., Saitta, A. M., Lazzeri, M., and Canny, B. (2006). Raman spectrum of ammonia IV. *Phys. Rev. B*, 74:104101.

Nolet, G. (2008). *A Breviary of Seismic Tomography: Imaging the Interior of the Earth and Sun*. Cambridge University Press.

Ojwang, J. G. O., Stewart McWilliams, R., Ke, X., and Goncharov, A. F. (2012). Melting and dissociation of ammonia at high pressure and high temperature. *The Journal of Chemical Physics*, 137(6):064507.

Olson, P. and Christensen, U. R. (2006). Dipole moment scaling for convection-driven planetary dynamos. *Earth and Planetary Science Letters*, 250(3):561–571.

Owen, T. C. (2019). Solar system. *Encyclopaedia Britannica*.

Ozaki, N., Tanaka, K. A., Ono, T., Shigemori, K., Nakai, M., Azechi, H., Yamanaka, T., Wakabayashi, K., Yoshida, M., Nagao, H., and Kondo, K. (2004). GEKKO/HIPER-driven shock waves and equation-of-state measurements at ultrahigh pressures. *Physics of Plasmas*, 11:1600–1608.

Paul Drake, R. (2006). *High-Energy-Density Physics*. Springer Nature.

Pavlovskii, M. N. (1976). Measurements of sound velocity in quartzite, dolomite, anhydrite, sodium cloride, paraffin, plexiglas, polyethilene, and fluoroplast-4 under shock compression. *Zh. Prikl. Mekh. Tekhn. Fiz.*, 5:136–139.

Pepler, D. and Paradowski, S. (2006). Central Laser Facility Annual Report 2005-06. Section 7 - Instrumentation. Technical report.

Perdew, J. P., Burke, K., and Ernzerhof, M. (1996). Generalized gradient approximation made simple. *Phys. Rev. Lett.*, 77:3865–3868.

Podolak, M. and Helled, R. (2012). What do we really know about Uranus and Neptune? *Astrophysical Journal Letters*, 759:L32(2).

Podolak, M., Hubbard, W. B., and Stevenson, D. J. (1991). Model of Uranus' interior and magnetic field. In Bergstralh, J. T., Miner, E. D., and Matthews, M. S., editors, *Uranus*, pages 29–61. Univ. Arizona Press, Tucson.

Qi, T., Millot, M., Kraus, R. G., Root, S., and Hamel, S. (2015). Optical and transport properties of dense liquid silica. *Physics of Plasmas*, 22(6):062706.

Radousky, H., Mitchell, A., and Nellis, W. (1990). Shock temperature measurements of planetary ices: NH_3, CH_4, and synthetic Uranus. *Journal of Chemical Physics*, 93(11):8235–8239.

Ramis, R., Schmalz, R., and Meyer-Ter-Vehn, J. (1988). MULTI: A computer code for one-dimensional multigroup radiation hydrodynamics. *Computer Physics Communications*, 49(3):475–505.

Rankine, W. M. (1870). On the thermodynamic theory of waves of finite longitudinal disturbance. *Philosophical Transactions of the Royal Society of London*, 160:277–288.

Redmer, R., Mattsson, T., Nettelmann, N., and French, M. (2011). The phase diagram of water and the magnetic fields of Uranus and Neptune. *Icarus*, 211(1):798–803.

Reeves, R. (1994). *The Superpower Space Race: An Explosive Rivalry through the Solar System*. Plenum Press.

Rekhi, S., Dubrovinsky, L., and Saxena, S. (1999). Temperature-induced ruby fluorescence shifts up to a pressure of 15 GPa in an externally heated diamond anvil cell. *High Temperatures - High Pressures*, 31(3):299–305.

Rigg, P. A., Knudson, M. D., Scharff, R. J., and Hixson, R. S. (2014). Determining the refractive index of shocked [100] lithium fluoride to the limit of transmissibility. *Journal of Applied Physics*, 116(3):033515.

Root, S., Shulenburger, L., Lemke, R. W., Dolan, D. H., Mattsson, T. R., and Desjarlais, M. P. (2015). Shock response and phase transitions of MgO at planetary impact conditions. *Phys. Rev. Lett.*, 115:198501.

Rothman, S., Davis, J., Maw, J., Robinson, C., Parker, K., and Palmer, J. (2005). Measurement of the principal isentropes of lead and lead–antimony alloy to 400 kbar by quasi-isentropic compression. *Journal of Physics D: Applied Physics*, 38(5):733.

Ruprechter, J. (2000). Entwicklung und Kalibration eines Submikrosekunden-Pyrometers. Diplomarbeit, Institut für Experimentalphysik der Technischen Universität Graz.

Russell, C., Elphic, R., and Slavin, J. (1979). Initial Pioneer Venus magnetic field results: Dayside observations. *Science*, 203(4382):745–748.

Sano, T., Ozaki, N., Sakaiya, T., Shigemori, K., Ikoma, M., Kimura, T., Miyanishi, K., Endo, T., Shiroshita, A., Takahashi, H., Jitsui, T., Hori, Y., Hironaka, Y., Iwamoto, A., Kadono, T., Nakai, M., Okuchi, T., Otani, K., Shimizu, K., Kondo, T., Kodama, R., and Mima, K. (2011). Laser-shock compression and Hugoniot measurements of liquid hydrogen to 55 GPa. *Phys. Rev. B*, 83:054117.

Schubert, G. and Soderlund, K. (2011). Planetary magnetic fields: Observations and models. *Physics of the Earth and Planetary Interiors*, 187(3):92–108. Special Issue: Planetary Magnetism, Dynamo and Dynamics.

Schwegler, E., Sharma, M., Gygi, F., and Galli, G. (2008). Melting of ice under pressure. *Proceedings of the National Academy of Sciences*, 105(39):14779–14783.

Scipioni, R., Stixrude, L., and Desjarlais, M. P. (2017). Electrical conductivity of SiO_2 at extreme conditions and planetary dynamos. *Proceedings of the National Academy of Science*, 114:9009–9013.

Sclar, C. B., Young, A. P., Carrison, L. C., and Schwartz, C. M. (1962). Synthesis and optical crystallography, of stishovite, a very high pressure polymorph of SiO_2. *Journal of Geophysical Research (1896-1977)*, 67(10):4049–4054.

Seager, S., Kuchner, M., Hier-Majumder, C., and Militzer, B. (2007). Mass-radius relationships for solid exoplanets. *The Astrophysical Journal*, 669(2):1279.

Sekine, T., Ozaki, N., Miyanishi, K., Asaumi, Y., Kimura, T., Albertazzi, B., Sato, Y., Sakawa, Y., Sano, T., Sugita, S., Matsui, T., and Kodama, R. (2016). Shock compression response of forsterite above 250 GPa. *Science Advances*, 2(8):1600157.

Setchell, R. E. (1979). Index of refraction of shock-compressed fused silica and sapphire. *Journal of Applied Physics*, 50(12):8186–8192.

Sherman, B. L., Wilson, H. F., Weeraratne, D., and Militzer, B. (2012). Ab initio simulations of hot dense methane during shock experiments. *Phys. Rev. B*, 86:224113.

Smith, E. J., Davis Jr., L., Jones, D. E., Coleman Jr., P. J., Colburn, D. S., Dyal, P., Sonett, C. P., and Frandsen, A. M. A. (1974). The planetary magnetic field and magnetosphere of Jupiter: Pioneer 10. *Journal of Geophysical Research*, 79(25):3501–3513.

Smith, N. V. (2001). Classical generalization of the Drude formula for the optical conductivity. *Physical Review B*, 64(15):155106.

Smith, R. F., Eggert, J. H., Jeanloz, R., Duffy, T. S., Braun, D. G., Patterson, J. R., Rudd, R. E., Biener, J., Lazicki, A. E., Hamza, A. V., Wang, J., Braun, T., Benedict, L. X., Celliers, P. M., and Collins, G. W. (2014). Ramp compression of diamond to five terapascals. *Nature*, 511:330–333.

Sosman, R. B. (1927). *The Properties of Silica*. Chemical Catalog Co.

Soubiran, F., Mazevet, S., Winisdoerffer, C., and Chabrier, G. (2012). Helium gap in the warm dense matter regime and experimental reflectivity measurements. *Phys. Rev. B*, 86:115102.

Soubiran, F. and Militzer, B. (2016). The Properties of Heavy Elements in Giant Planet Envelopes. *The Astrophysical Journal*, 829:14.

Soubiran, F. and Militzer, B. (2018). Electrical conductivity and magnetic dynamos in magma oceans of Super-Earths. *Nat. Comm.*, 9:3883.

Spaulding, D., McWilliams, R., Jeanloz, R., Eggert, J., Celliers, P., Hicks, D., Collins, G., and Smith, R. (2012). Evidence for a phase transition in silicate melt at extreme pressure and temperature conditions. *Physical Review Letters*, 108(6):065701.

Stanley, S. and Bloxham, J. (2004). Convective-region geometry as the cause of Uranus and Neptune unusual magnetic fields. *Nature*, 428:151–153.

Stanley, S. and Glatzmaier, G. A. (2010). Dynamo models for planets other than Earth. *Space Science Reviews*, 152(1):617–649.

Stevenson, D. J. (1982). Interiors of the giant planets. *Annual Review of Earth and Planetary Sciences*, 10:257.

Stixrude, L. (2014). Melting in super-Earths. *Philosophical Transactions of the Royal Society of London A: Mathematical, Physical and Engineering Sciences*, 372:20130076.

Sun, T., Brodholt, J. P., Li, Y., and Vočadlo, L. (2018). Melting properties from ab initio free energy calculations: Iron at the Earth's inner-core boundary. *Phys. Rev. B*, 98:224301.

Swift, D. C., Eggert, J. H., Hicks, D. G., Hamel, S., Caspersen, K., Schwegler, E., Collins, G. W., Nettelmann, N., and Ackland, G. J. (2012). Mass-radius relationships for exoplanets. *The Astrophysical Journal*, 744(1):59.

Swift, D. C. and Johnson, R. P. (2005). Quasi-isentropic compression by ablative laser loading: Response of materials to dynamic loading on nanosecond time scales. *Phys. Rev. E*, 71:066401.

Tackley, P., Ammann, M., Brodholt, J., Dobson, D., and Valencia, D. (2013). Mantle dynamics in super-Earths: Post-perovskite rheology and self-regulation of viscosity. *Icarus*, 225(1):50–61.

Tateno, S., Hirose, K., Ohishi, Y., and Tatsumi, Y. (2010). The structure of iron in Earth's inner core. *Science*, 330(6002):359–361.

Tosi, N., Breuer, D., and Spohn, T. (2014). Evolution of planetary interiors. In Spohn, T., Breuer, D., and Johnson, T. V., editors, *Encyclopedia of the Solar System*. Elsevier, Amsterdam.

Tracy, S. J., Smith, R. F., Wicks, J. K., Fratanduono, D. E., Gleason, A. E., Bolme, C. A., Prakapenka, V. B., Speziale, S., Appel, K., Fernandez-Pañella, A., Lee, H. J., MacKinnon, A., Tavella, F., Eggert, J. H., and Duffy, T. S. (2019). *In situ* observation of a phase transition in silicon carbide under shock compression using pulsed x-ray diffraction. *Phys. Rev. B*, 99:214106.

Tracy, S. J., Turneaure, S. J., and Duffy, T. S. (2018). In situ X-ray diffraction of shock-compressed fused silica. *Physical Review Letters*, 120(13):135702.

Trunin, R. (1994a). Shock compressibility of condensed materials in strong shock waves generated by underground nuclear explosions. *Physics - Uspekhi*, 37(11):1123–1146.

Trunin, R. F. (1994b). Shock compressibility of condensed matters in strong shock waves caused by underground nuclear explosions. *Usp. Fiz. Nauk.*, 164(11):1215–1237.

Trunin, R. F. (2001). *Experimental data on shock compression and adiabatic expansion of condensed matter*. RFNC-VNIIEF.

Trunin, R. F., Simakov, G. V., Podurets, M.A. andMoiseev, B. N., and Popov, L. (1971). Dynamical compressibility of quartz and quartzite at high pressures. *Izv. Akad. Nauk. SSSR Fiz. Zemli*, 1:13–20.

Valencia, D., O'Connell, R. J., and Sasselov, D. (2006). Internal structure of massive terrestrial planets. *Icarus*, 181(2):545–554.

van den Berg, A., Yuen, D., Beebe, G., and Christiansen, M. (2010). The dynamical impact of electronic thermal conductivity on deep mantle convection of exosolar planets. *Physics of the Earth and Planetary Interiors*, 178(3):136–154.

van Thiel, M. (1977). Compendium of shock wave data. *Lawrence Livermore Laboratory Report*, UCRL-50108:373–376.

Vinci, T. (2006). *Les chocs radiatifs générés par les lasers à haute énergie: une opportunité pour l'astrophysique de laboratoire*. PhD thesis, École Polytechnique.

Wackerle, J. (1962). Shock-wave compression of quartz. *Journal of Applied Physics*, 33(3):922–937.

Waeselmann, N. (2012). *Structural transformations in complex perovskite-type relaxor and relaxor-based ferroelectrics at high pressures and temperatures*. PhD thesis, Universität Hamburg.

Wagner, F. (2014). *The Physical State of Rocky Exoplanet Interiors*. PhD thesis, Westfälische Wilhelms-Universität Münster.

Williams, Q., Jeanloz, R., Bass, J., Svendsen, B., and Ahrens, T. J. (1987). The melting curve of iron to 250 gigapascals: A constraint on the temperature at Earth's center. *Science*, 236(4798):181–182.

Wolszczan, A. (1994). Confirmation of Earth-mass planets orbiting the millisecond pulsar PSR B1257 + 12. *Science*, 264(5158):538–542.

Xue, Q., Jiang, S., Wang, Z., Wang, F., Zhao, X., and Ding, Y. (2018). Laser pulse shape design for laser-indirect-driven quasi-isentropic compression experiments. *AIP Advances*, 8(2):025202.

Yoo, C., Holmes, N., Ross, M., Webb, D. J., and Pike, C. (1993). Shock temperatures and melting of iron at Earth core conditions. *Physical Review Letters*, 70(25):3931.

Zaghoo, M. and Silvera, I. F. (2017). Conductivity and dissociation in liquid metallic hydrogen and implications for planetary interiors. *Proceedings of the National Academy of Sciences*, 114(45):11873–11877.

Zel'dovich, Y. B. and Raizer, Y. P. (1966). *Physics of Shock Waves and High-Temperature Hydrodynamic Phenomena*. Academic Press Inc., New York.

Zha, C.-S., Hemley, R. J., Mao, H.-K., Duffy, T. S., and Meade, C. (1994). Acoustic velocities and refractive index of SiO_2 glass to 57.5 GPa by Brillouin scattering. *Phys. Rev. B*, 50:13105–13112.

Zhang, W.-J., Liu, Z.-Y., Liu, Z.-L., and Cai, L.-C. (2015). Melting curves and entropy of melting of iron under Earth's core conditions. *Physics of the Earth and Planetary Interiors*, 244:69–77.

Zharkov, V. N. and Trubitsyn, V. P. (1978). *Physics of planetary interiors*. Astronomy and Astrophysics Series: Tucson, AZ: Pachart.

Outreach

The work presented in this Thesis has been the object of two published articles, one submitted article (currently under review), and two articles currently in preparation. The author also presented it in five oral contributions. Articles and oral presentations are listed here below.

Articles

- Guarguaglini, M., Hernandez, J.-A., Benuzzi-Mounaix, A., Bolis, R., Brambrink, E., Vinci, T., and Ravasio, A. (2019). Characterizing equation of state and optical properties of dynamically pre-compressed materials. *Physics of Plasmas,* 26(4):042704.

- Guarguaglini, M., Hernandez, J.-A., Okuchi, T., Barroso, P., Benuzzi-Mounaix, A., Bethkenhagen, M., Bolis, R., Brambrink, E., French, M., Fujimoto, Y., Kodama, R., Koenig, M., Lefevre, F., Miyanishi, K., Ozaki, N., Redmer, R., Sano, T., Umeda, Y., Vinci, T., and Ravasio, A. (2019). Laser-driven shock compression of "synthetic planetary mixtures" of water, ethanol, and ammonia. *Scientific Reports,* 9:10155.

- Hernandez, J.-A., Morard, G., Guarguaglini, M., Alonso-Mori, R., Benuzzi-Mounaix, A., Bolis, R., Fiquet, G., Galtier, E., Gleason, A., Glenzer, S., Guyot, F., Ko, B. K., Lee, H. J., Mao, W. L., Nagler, B., Ozaki, N., Schuster, A., Shim, S. H., Vinci, T., and Ravasio, A. Direct observation of shock-induced amorphization of enstatite. *Submitted to Nature Communications.*

- Morard, G., Hernandez, J.-A., Guarguaglini, M., Bolis, R., Benuzzi-Mounaix, A., Vinci, T., Fiquet, G., Baron, M. A., Shim, S. H., Ko, B. K., Gleason, A. E., Mao, W., Alonso-Mori, R., Lee, H. H., Nagler, B., Galtier, E., Andrault, D., Garbarino, G., Mezouar, M., Schuster, A., and Ravasio, A. X-ray diffraction of silicate liquids and glasses under dynamic and static compression over megabar pressure. *Submitted to Proceedings of the National Academy of Science of the USA.*

- Guarguaglini, M., Soubiran, F., Hernandez, J.-A., Benuzzi-Mounaix, A., Bolis, R., Brambrink, E., Vinci, T., and Ravasio, A. Electrical conductivity of dynamically pre-compressed warm dense silica. *In preparation.*

Oral contributions

- *École Doctorale Ondes et Matière – SciDays*, Palaiseau (France), February 2018.
- *Forum Interaction Laser Plasma*, Saint-Pierre d'Oléron (France), June 2018.
- *Plas@Par – Young Researcher Conference on Plasma Physics and applications*, Paris (France), June 2018.
- *Joint Workshop on High Pressure, Planetary and Plasma Physics*, Berlin (Germany), October 2018.
- *International Workshop on Warm-Dense-Matter*, Travemünde (Germany), May 2019.

List of acronyms

EACH ACRONYM employed in this Thesis has been defined leastwise at its first use. However, in order to facilitate the reading of the Thesis, here we provide the complete lists of the scientific and technical acronyms and of the acronyms relative to institutions and facilities.

Scientific and technical

bcc	body-centred cubic (crystal system)
BS	Beam-Splitter
CCD	Charge-Coupled Device
CMB	Core-Mantle Boundary
CSPAD	Cornell–SLAC Pixel Array Detector
DAC	Diamond Anvil Cell
DC	Direct Current
DFT	Density Functional Theory
EOS	Equation Of State
EPDM	Ethylene Propylene Diene Monomer
fcc	face-centred cubic (crystal system)
hcp	hexagonal close packed (crystal system)
HSE	Heyd–Scuseria–Ernzerhof exchange–correlation functional
ICB	Inner Core Boundary
IR	InfraRed
LAC	Liquid Ammonia Cell
LMA	Linear Mixing Approximation
MCP	Micro-Channel Plate
MD	Molecular Dynamics
PBE	Perdew–Burke–Ernzerhof exchange–correlation functional
QEOS	Quotidian Equation Of State
SOP	Streak Optical Pyrometer
SIPB	SuperIonic Phase Boundary
SPM	Synthetic Planetary Mixture
TBL	Thermal Boundary Layer
TCC	Target Chamber Center

UV	UltraViolet
VPF	Velocity Per Fringe
VISAR	Velocity Interferometry System for Any Reflector
WDM	Warm Dense Matter
WEM	Water–Ethanol Mixture
XANES	X-ray Absorption Near-Edge Spectroscopy
XC	exchange–correlation
XFEL	X-ray Free Electron Laser
XRD	X-Ray Diffraction
YAG	Yttrium Aluminum Garnet ($Y_3Al_5O_{12}$)

Institutions and facilities

6F	Six faisceaux (former laser facility at LULI)
CEA	Commissariat à l'Énergie Atomique et aux Énergies Alternatives
CTBTO	(Preparatory Commission for the) Comprehensive Nuclear-Test-Ban Treaty Organization
ENS	École Normale Supérieure
ESA	European Space Agency
ESRF	European Synchrotron Radiation Facility
HLRN	Norddeutsche Verbund zur Förderung des Hoch- und Höchstleistungsrechnens
HP^3	Heat Flow and Physical Properties Package *(InSight probe)*
IMPMC	Institut de Minéralogie, de Physique des Matériaux et de Cosmochimie
JPL	Jet Propulsion Laboratory
LANL	Los Alamos National Laboratory
LCLS	Linac Coherent Light Source
LMJ	Laser MégaJoule
LULI	Laboratoire pour l'Utilisation des Lasers Intenses
MEC	Matter in Extreme Conditions *(LCLS end-station)*
NASA	National Aeronautics and Space Administration
NIF	National Ignition Facility
RISE	Rotation and Interior Structure Experiment *(InSight probe)*
SACLA	SPring-8 Angstrom Compact free electron LAser
SEIS	Seismic Experiment for Interior Structure *(InSight probe)*
SLAC	Stanford Linear Accelerator Center
SNL	Sandia National Laboratories

Résumé en langue française

Contexte

L'intérêt des intérieurs planétaires

La fascination pluri-millénaire de l'être humain pour les corps célestes "errants" – les *planètes* – a été récemment renouée avec la découverte d'un grand nombre de planètes extrasolaires (ou *exoplanètes*) : aujourd'hui, environ trente ans après la première découverte, l'existence de plus de 4000 exoplanètes appartenant à plus de 3000 systèmes stellaires à été confirmée. La Terre représente un point de départ naturel pour l'observation des propriétés planétaires, notamment grâce à l'investigation des ondes sismiques, qui nous permet de sonder la structure de l'intérieur, autrement inaccessible. Notre connaissance des autres planètes solaires est basée sur l'observation astronomique ainsi que sur l'envoi de sondes spatiales, capables de mesurer nombre de quantités, comme le champ gravitationnel et magnétique ainsi que la composition de l'atmosphère et de la surface. Pour les planètes extrasolaires, nous devons nous contenter de l'observation lointaine, limitée à des propriétés de base comme la masse et le rayon. Pour cette raison, les planètes solaires sont utilisées comme paradigme pour l'étude des exoplanètes.

L'exploration et l'observation des planètes sont aujourd'hui limitées à l'atmosphère et à la surface. Cependant, les modèles d'évolution et structure des planètes sont fortement basés sur les intérieurs, qui échappent à une caractérisation directe. Dans les intérieurs, la matière est soumise à des pressions et températures extrêmes : plusieurs millions d'atmosphères (ou mégabar) et quelques milliers de Kelvin, respectivement. Ce régime thermodynamique est appelé Matière Dense et Tiède (MDT). Située au carrefour entre la matière condensée et les plasmas classiques, la MDT, partiellement couplée d'un point de vue quantique et partiellement ionisée, est particulièrement difficile à modéliser et demande l'emploi de simulations *ab initio*, très coûteuses en termes de temps de calcul. Parmi les propriétés d'intérêt pour l'étude des intérieurs planétaires, l'équation d'état – une relation fondamentale entre densité, pression et température pour un matériau donné – et le diagramme de phase sont fondamentaux pour pouvoir prédire le profil thermodynamique précis des intérieurs. Par ailleurs, la conductivité électrique est un paramètre-clé pour la modélisation de la génération d'un champ magnétique via un processus *dynamo*.

Obtenir et caractériser des conditions extrêmes en laboratoire

Obtenir en laboratoire des états relevants du domaine de la MDT représente un défi, étant données les conditions extrêmes de température et pression associées. Ceci peut être fait via deux types d'approche : statique et dynamique. L'approche statique consiste à exercer une force sur un échantillon. Dans ce contexte, l'utilisation d'une Cellule à Enclumes de Diamant (CED) est très courante. Les approches dynamiques se basent sur la création et la propagation d'une onde de compression (souvent, une onde de choc). Dans ce travail, l'onde de choc a été générée par effet fusée en focalisant une impulsion laser puissante sur une cible multi-couche. La caractérisation de l'état obtenu est faite par des diagnostics adaptées à la technique. Dans le cadre de la compression par choc généré par laser, nous avons employé deux diagnostics de routine : l'interférométrie Doppler et la pyrométrie. L'utilisation combinée de ces deux diagnostics permettent de caractériser l'état thermodynamique atteint (densité, pression, température) et ses propriétés optique (réflectance du front de choc, coefficient d'absorption de l'état choqué).

La compression par choc d'un échantillon se trouvant dans des conditions initiales ambiantes permet d'explorer des hautes températures, mais le caractère hautement irréversible du processus de propagation d'un choc limite les états qui peuvent être reproduits à une courbe, dite *courbe d'Hugoniot principale*, qui explore un domaine de haute température et pression modérée. La nécessité d'explorer un domaine thermodynamique plus vaste demande de développer des techniques de compression alternatives capables de générer des états à haute pression et température limitée, plus proches des conditions attendues dans les intérieurs planétaires. Ceci peut se faire en pré-comprimant l'échantillon, afin de limiter le saut d'entropie lors du passage de l'onde de choc, ce qui permet d'atteindre un état appartenant à une *courbe d'Hugoniot secondaire*. La pré-compression peut avoir un caractère statique (on parle alors de couplage entre Cellules à Enclumes de Diamant et compression par choc) ou dynamique (il s'agit ici de générer un premier choc qui pré-comprime l'échantillon, avant l'arrivée d'un deuxième qui le porte à l'état final souhaité). Dans le cadre de ce travail, nous avons développé une technique de compression par double choc capable de garantir un accès optique direct à l'état doublement choqué et une mesure de ses variables d'état et propriétés optiques indépendantes des modèles et de l'emploi de simulations hydrodynamiques.

Objectifs de ce travail

Ce travail porte sur l'étude expérimentale des composantes des intérieurs planétaires dans des conditions extrêmes de température et pression. Il se développe sur deux axes principaux.

(i) Les planètes géantes de glace de notre système solaire (Uranus et Neptune) sont encore loin d'être décrites par des modèles fiables de structure et évolution, ce qui représente une limite majeure pour l'étude des exoplanètes du même type. Par conséquent, le premier axe de notre travail concerne la caractérisation expérimentale de l'équation d'état et des propriétés optiques des composantes des intérieurs de ces planètes : eau, méthane, ammoniac, dans leur forme pure et mélangée.

(ii) Le second axe de travail porte sur l'étude de la silice, composante-clé des intérieurs des planètes terrestres. La silice a déjà été l'objet de nombre d'études, qui ont caractérisé son équation d'état et propriétés optiques notamment le long des courbes d'Hugoniot de différents phases initiales (silice fondue, α-quartz, stishovite). Notre objectif consiste à caractériser le comportement optique et électrique dans des conditions jamais explorées appartenant au régime MDT, en employant une technique de compression par double choc. Nous voulons vérifier des calculs *ab initio* qui prédisent un comportement non trivial de la conductivité ; par ailleurs, nous voulons comprendre si, dans des exoplanètes terrestres de grosse taille, la silice dans un état liquide peut générer un champ magnétique en soutenant une action dynamo.

Étude des composantes des intérieurs planétaires

Les mélanges planétaires, composantes des géantes de glace

Afin d'explorer un domaine très vaste de conditions thermodynamiques et de reproduire les conditions atteintes non seulement dans Uranus et Neptune mais aussi dans les géants de glace extrasolaires, nous avons utilisé des chocs simples décroissants pour étudier des conditions de haute température et haute pression et des méthodes de pré-compression (couplage CED et choc laser, double choc) pour explorer des états à température plus modérée. Certaines composantes pures (eau, ammoniac) ainsi que certains mélanges (eau-éthanol, eau-éthanol-ammoniac) ont été étudiés afin d'isoler la contribution de chaque composante aux propriétés des intérieurs planétaires. Plusieurs campagnes expérimentales on eu lieu sur les installations GEKKO XII (Japon) et LULI2000 (France). Comme l'ammoniac est gazeuse à conditions ambiantes alors que un état initial condensé est nécessaire pour obtenir des conditions de MDT par choc, nous avons conçu des cellules adaptées à la compression par choc laser d'échantillons liquides ainsi qu'une procédure de remplissage avec l'ammoniac pur à l'état liquide.

Les relations vitesse de choc - vitesse fluide et température - pression expérimentalement déterminées pour l'eau pure et pour les mélanges eau-éthanol et eau-éthanol-ammoniac comprimés par choc sont similaires. Nos résultats confirment l'hypothèse selon laquelle l'équation d'état des mélanges liquides peut être construite avec une approximation dite de mélange linéaire. Des calculs *ab initio*, utilisant cette approximation et effectués par Mandy Bethkenhagen *et al.* (Université de Rostock) sont en effet en bon accord avec nos données. En revanche, les mélanges deviennent réfléchissants (donc conducteurs électriques) à des pressions plus basses que l'eau, et ont une réflectance (donc une conductivité) plus importante à haute pression. Les données de réflectance des mélanges sont les premières disponibles. L'ammoniac pur a été étudié expérimentalement pour la première fois à des hautes pressions (2.8 Mbar). La courbe température-pression de l'ammoniac pur comprimé par choc valide les résultats des simulations existantes. En outre, l'ammoniac a été observé devenir réfléchissant à des pressions plus basses que les mélanges. Tous ces résultats montrent que les manteaux des géantes de glace peuvent être électriquement conducteurs et contribuer ainsi à la génération des champs magnétiques de ces planètes.

La silice, composante-clé des planètes terrestres

Des échantillons d'α-quartz ont été comprimés par double choc pendant des campagnes conduites sur l'installation LULI2000. L'état thermodynamique atteint et la réflectance du front du deuxième choc pour deux longueurs d'onde différentes (532 nm et 1064 nm) ont été directement mesurés.

Les conductivités électriques optiques (à 532 nm et 1064 nm) de l'état doublement choqué ont été estimées à partir de ces mesures en appliquant la loi de Fresnel et en employant un modèle de réponse locale du courant au champ électrique. Comme la conductivité est une quantité complexe, une simple mesure de réflectance (une quantité réelle) n'est pas suffisante pour remonter à la précédente. Notre stratégie a été d'employer des prédictions des calculs *ab initio* de la conductivité électrique de la silice dense et tiède pour estimer la relation entre la partie réelle et imaginaire de la conductivité. Une démarche similaire a été adoptée pour estimer la conductivité statique à partir des valeurs optiques. Cette approche mixte, employant à la fois des résultats expérimentaux et des calculs, s'avère très promettante pour pouvoir remonter aux propriétés électriques à partir d'une mesure des propriétés optiques dans le cadre de la compression par choc. Les résultats ont confirmé les prédictions de plusieurs calculs *ab initio*, selon lesquelles la conductivité de la silice en fonction de la pression n'est pas monotone le long d'une isotherme pour des températures inférieures à 20000 K.

Par ailleurs, des calculs *ab initio* réalisés par François Soubiran (ENS Lyon) dans le cadre d'une collaboration avec notre équipe confirment ce comportement de la conductivité. Dans des conditions thermodynamiques proches de celles attendues dans les planètes terrestres de grosse taille (les super-Terres), les conductivités prédites par nos expériences et ces calculs sont assez hautes pour que la silice puisse générer un champ magnétique via un mécanisme dynamo dans ces planètes. Les super-Terres pourraient donc disposer d'un champ magnétique (condition indispensable pour le développement de la vie comme nous la connaissons) même dans le cas où le noyau de fer serait complètement solide et donc magnétiquement inactif.

Conclusions et perspectives

Dans ce travail, nous avons étudié l'équation d'état et les propriétés optiques et électriques de plusieurs composantes des intérieurs des planètes terrestres et géantes de glace, comprimées jusqu'à des conditions thermodynamiques extrêmes par choc généré par laser de puissance.

Nous avons employé différentes techniques de compression (choc simple, couplage CED–choc, double choc) afin d'explorer une région la plus vaste possible du diagramme de phase. Dans ce contexte, nous avons développé une technique de compression par double choc qui permet un accès direct à l'état d'intérêt. Par ailleurs, un effort considérable a été déployé pour le design de cellules compatibles avec la compression par choc laser d'échantillons liquides. Un système de remplissage de ces cellules permettant d'obtenir l'ammoniac pur dans un état liquide à température ambiante, développé dans ce travail, pourra être employé pour l'étude d'autres matériaux d'intérêt. Enfin, ce travail a été marqué par une interaction constante avec la communauté des calculs *ab initio*, afin de soutenir de façon réciproque nos résultats expérimentaux et les calculs

eux-mêmes.

Dans une perspective à court terme, les différentes techniques de compression devront être systématiquement appliquées aux matériaux étudiés ainsi qu'à un ensemble plus vaste de matériaux, comme le méthane (composant des géantes de glace) et les systèmes oxyde de magnésium – silice (d'intérêt pour les planètes terrestres). À plus long terme, un couplage entre la compression par choc laser et les diagnostics à rayons X (diffraction, absorption, ...), capables de sonder la structure microscopique de l'état choqué, permettra la caractérisation directe du diagramme de phase des échantillons ainsi que l'étude de la cinétique des transitions de phase conséquentes à la compression par choc.

Titre : Compression de mélanges liquides et silice par chocs générés par laser jusqu'à des conditions thermodynamiques extrêmes d'intérêt pour les modèles des intérieurs planétaires

Mots clés : intérieurs planétaires, lasers à haute puissance, ondes de choc, matière dense et tiède, équations d'état, conductivité électrique

Résumé : L'étude du comportement des composantes des intérieurs planétaires dans des conditions extrêmes de pression (megabar) et température (milliers de Kelvin) est essentielle afin de construire des modèles fiables décrivant l'évolution et la structure des planètes. Dans ce travail, nous avons étudié plusieurs composantes par compression par choc laser sur les installations LULI2000 (France) et GEKKO XII (Japon). Nous avons employé des chocs décroissants pour étudier des conditions de haute-pression / haute-température. Afin d'accéder à des conditions de température modérée, nous avons utilisé des techniques de pre-compression statique (couplage compression par choc – cellules à enclumes de diamant) et dynamique (génération de doubles chocs). Nous avons étudié l'équation d'état des mélanges eau-ethanol-ammoniac et de l'eau et ammoniac purs, d'intérêt pour la description des intérieurs des planètes géantes de glace. L'étude de l'ammoniac a été particulièrement délicate en raison de sa forte réactivité et donc de la complexité du design des cibles ; nous présentons les premières données obtenues par choc laser, dans un domaine de pression jamais exploré. Les données des mélanges confirment des calculs ab initio récents basés sur une approximation de mélange linéaire. Nous avons également mesuré la réflectivité des mélanges liquides et de la silice, une composante-clé des intérieurs des planètes terrestres. Nous avons ensuite estimé la conductivité électrique – un paramètre crucial pour modéliser la génération des champs magnétiques planétaires dans les intérieurs via un mécanisme dynamo – de ces composantes. Eau, ammoniac et mélanges eau-ethanol-ammoniac affichent des réflectivités différentes, ce qui suggère que l'eau pure ne peut pas être considérée comme représentative des mélanges planétaires dans les modèles dynamo. Par ailleurs, nous avons apporté une confirmation expérimentale de calculs ab initio récents selon lesquels la conductivité de la silice n'est pas monotone le long d'une ligne isotherme pour des températures modérées. Nos données supportent des calculs qui prédisent qu'une dynamo peut avoir lieu dans les océans de magma dans des super-Terres ainsi que dans la jeune Terre.

Title: Laser-driven shock compression of liquid mixtures and silica up to extreme thermodynamic conditions of interest for planetary interior models

Keywords: planetary interiors, high-power lasers, shock waves, warm dense matter, equations of state, electrical conductivity

Abstract: Characterising the behaviour of planetary interiors' components at extreme conditions (megabar pressures, temperatures of a few thousand Kelvin) is essential to build reliable models describing the evolution and structure of planets. In this thesis, we investigated various components on a wide set of conditions using laser-driven shock compression techniques at the LULI2000 (France) and GEKKO XII (Japan) facilities. Single decaying shocks were employed to study high-pressure / high-temperature states. To reach moderate-temperature conditions, closer to planetary interior profiles, we employed static and dynamic pre-compression techniques coupling Diamond Anvil Cells to shock compression and generating double shocks, respectively. We studied the equation of state of water-ethanol-ammonia mixtures and of pure liquid water and ammonia, of interest for icy giant structure models. Pure ammonia measurements have been particularly challenging due to cell design complexity in reason of its reactivity; we provide the first data obtained with laser shocks, in a pressure domain up to now unexplored. Mixtures data are in agreement with recent ab initio calculations based on the linear mixing approximation. We measured the optical reflectivity of liquid mixtures and silica, a key component of rocky planets' interiors. From reflectivity data we estimated the electrical conductivity of such components – a crucial parameter for modelling the generation of planetary magnetic fields in the interiors via a dynamo mechanism. Water, ammonia, and water-ethanol-ammonia mixtures exhibit different reflectivity (hence conductivity) behaviours as a function of pressure and temperature. This suggests that pure water should not be used in dynamo models as representative of the icy mixtures. Moreover, we provide the first experimental confirmation of recent ab initio studies showing that the conductivity of silica along isothermal lines is not monotonic at moderate temperatures. Our data provide experimental support for the calculations predicting a dynamo action to occur in super-Earths' and early Earth's magma oceans.

Université Paris-Saclay
Espace Technologique / Immeuble Discovery
Route de l'Orme aux Merisiers RD 128 / 91190 Saint-Aubin, France